FEUP Universidade do Porto
Faculdade de Engenharia

CHARACTERIZATION OF X52, X60 AND X65 STEEL GRADES UNDER MONOTONIC AND ULTRA-LOW-CYCLE FATIGUE LOADING

João Carlos Rego Pereira

2016

Thesis presented to the Faculty of Engineering of the University of Porto
for the Doctor Degree in Mechanical Engineering

Supervisors
António Augusto Fernandes *Full Professor*
Abílio Manuel Pinho de Jesus *Assistant Professor*

GOVERNO DE PORTUGAL
FCT Fundação para a Ciência e a Tecnologia
MINISTÉRIO DA CIÊNCIA, TECNOLOGIA E ENSINO SUPERIOR
UNIÃO EUROPEIA Fundo Social Europeu
QREN QUADRO DE REFERÊNCIA ESTRATÉGICO NACIONAL PORTUGAL 2007.2013
POPH POTENCIAL HUMANO

Aos meus avós

António Roberto Rego

Laura da Conceição Malheiro

Ó Pátria mil vezes Santa
- Meu Portugal, minha terra
Onde vivo e onde nasci!

Na tua História me perco,
E nela tudo aprendi.

Mesmo que fosses pequena
E eu te visse pobre ou nua
- Ninguém ama a sua Pátria por ser grande,
Mas sim por ser sua!

António Botto

The author acknowledges the financial support from Fundação para a Ciência e Tecnologia through the Doctoral grant No. SFRH/BD/80091/2011.

AGRADECIMENTOS

A elaboração da presente dissertação de doutoramento só foi possível com o contributo profissional e pessoal de diversas pessoas. Desta forma desejo aqui, expressar os seguintes agradecimentos:

Aos orientadores científicos, Professor Doutor António Augusto Fernandes e ao Professor Doutor Abílio Pinho de Jesus, pelo seu apoio incondicional, colaboração, disponibilidade e por tudo terem feito para esclarecer as dúvidas que fui tendo ao longo deste percurso;

Ao Doutor Cristóvão Santos pelo auxílio que prestou durante a campanha de ensaios experimentais no desenvolvimento de ferramentas essenciais para a realização dos ensaios;

Aos colegas José Ruano e Bruno Martins pela ajuda nos ensaios cíclicos dos provetes planos lisos que foram sem dúvida os mais "especiais" deste trabalho e ao Romeo Nunes pelo desenvolvimento do sistema de amarras utilizado nos ensaios de flexão cíclica.

À UME (Unidade de Microscopia Eletrónica) da UTAD, em particular à Lisete Fernandes, técnica do Laboratório de microscopia eletrónica pela colaboração fornecida na análise de superfícies de fratura;

Aos meus amigos Fábio Pereira, Luís Silva, José Xavier, José Correia, Joaquim Maeiro e Mário Furtado, que através da sua amizade, camaradagem e incentivo me ajudaram a terminar este trabalho.

Aos meus pais, pela forma como me educaram e por todo o investimento que tiveram na minha formação, este trabalho é também deles.

A toda a minha família que sempre me ofereceu momentos especiais para a atenuar os momentos de maior trabalho;

O agradecimento mais especial é endereçado à minha esposa, Lígia Abelha, por todo o seu carinho e prestação como mulher exemplar, permitiu que me concentrasse o máximo possível neste trabalho.

Sem o apoio de todos este trabalho não teria sido possível.

Agradeço ainda às instituições Faculdade de Engenharia da Universidade do Porto (FEUP), à Universidade de Trás-os-Montes e Alto-Douro (UTAD) onde se realizaram os ensaios small-scale e ao Instituto de Ciência e Inovação em Engenharia Mecânica e Engenharia Industrial (INEGI) pelo suporte e meios colocados à disponsição para a realização de todo o trabalho.

Agradeço à Fundação para a Ciência e Tecnologia, pelo suporte financeiro concedido através da bolsa de doutoramento SFRH/BD/80091/2011.

Agradeço à Comissão Europeia através do Research Fund for Coal and Steel (RFCS) que financiaram o projeto Euporeu ULCF que disponibilou todos os meios materiais necessários à realização dos estudos experimentais.

Também um agradecimento especial aos parceiros do projeto ULCF, em particular ao RWTH/Aachen University e ao OCAS/ArcilorMittal que partilharam os resultados experimentais relativos aos ensaios cíclicos realizados à escala real.

ABSTRACT

Ultra or extreme low-cycle fatigue (ULCF) of steels has deserved increasing interest by the researchers since it corresponds to a fatigue domain not fully understood nor explored. It has been recognized that fatigue damage under extreme loading conditions is representative of several practical applications (e.g. seismic actions, accidental loads) and pipelines are a type of critical components that can undergo such extreme loading conditions. ULCF damage corresponds to a transition damage behaviour between the LCF and the monotonic ductile damage. Therefore studies on ULCF usually needs to cover those bounding damage processes. The characterization of X52, X60 and X65 API piping steels under monotonic and ULCF loading was performed in this work. Also, X60 and X65 steel grades after a thermal treatment were investigated. In detail, an experimental campaign covering distinct small-scale geometries was carried out to derive the monotonic, cyclic elastoplastic as well as the ULCF and LCF damage behaviours. New testing methodologies for monotonic and mainly for ULCF loading were proposed, since existing standards for LCF are not valid for ULCF loading due to significant instabilities, which increases the plastic damage evolution leading to the premature failure of the specimens. Thus, an anti-buckling device was applied in the cyclic tests of smooth specimens in order to minimize the lateral instabilities but those devices did not reveal to be fully effective. The use of notched specimens under tension/compression or bending cyclic tests represents an alternative procedure to investigate the cyclic behaviour under high plastic strain amplitudes, but requiring numerical simulations to evaluate the stress/strain fields at the potential crack initiation location. Also, the support of Digital Image Correlation revealed as a valuable tool for experimental data analysis and models validation, including the boundary conditions. The design of the specimens accounted for different fracture strains, triaxiality and Lode angle parameters. A complete damage characterization was performed for the X60 piping steel resulting life-triaxiality-Lode angle failure fields. The Theory of the Critical Distances was also explored for the LCF and ULCF domains, using available small-scale testing data.

In addition, the ULCF damage behaviour of large-scale elbows and straight pipes subjected to cyclic tests were investigated. The large-scale elbows were produced from line pipes subjected to hot bending process, therefore the thermal process used in the hot bending

manufacturing process was also accounted for in the material testing in order to understand the effect of this process on pipe material. Two steel grades used on pipelines manufacturing were investigated, namely the X60 and X65 piping steels, with the following overall dimensions 16” and w.t. 9.5 mm and 8 5/8” and w.t. 5.59 mm, respectively. The full-scale tests were performed in the context of the European project ULCF (*Ultra Low Cycle Fatigue of Steel Under Cyclic High-Strain Loading Conditions*). In all full-scale tests (elbows or straight pipes) the failure was preceded by cyclic plastic deformation concentration due to local plastic instability (buckling). In order to evaluate the stress/strain loading conditions, finite element simulation of the large-scale elbows and straight pipes were performed aiming at simulating the experimental conditions. J2 plasticity models with non-linear kinematic hardening, calibrated by means of small-scale data were adopted. Moreover, the test data of small-scale tests was used in the identification of damage models (e.g. Coffin-Manson, Xue relations), which in turn were applied to simulate the failure cycles of the full-scale pipe components. In particular, strain-based design guidelines based on the Xue model application, which includes the effect of stress triaxiality and Lode angle parameter was proposed in this work. Finally, the ASME VIII Div.2 procedures were also used to compute the failure cycles of the large-scale elbows and straight pipes, to allow an assessment of these existing procedures.

RESUMO

O estudo do comportamento de aços sujeitos a fenómenos de fadiga oligocíclica extrema tem despertado o interesse dos investigadores pois trata-se de um domínio da fadiga ainda pouco estudado e compreendido. Os fenómenos de fadiga oligocíclica extrema são representativos de diversas ocorrências com interesse prático (ex: ações sísmicas, cargas acidentais) sendo os oleodutos e gasodutos infraestruturas críticas que podem também estar vulneráveis a estas ações extremas. Os mecanismos de dano associados à fadiga oligocíclica extrema estão compreendidos entre a rotura monotónica dúctil e fadiga oligocíclica, pelo que a necessidade de investigar esses dois domínios limite é essencial. No presente trabalho procedeu-se à caracterização de aços utilizados no fabrico de gasodutos, API X52, X60 e X65 sob a ação de carregamentos monotónicos e cíclicos extremos. Também os aços X60 e X65 submetidos a um tratamento térmico foram investigados neste estudo. Com o objetivo de avaliar o comportamento monotónico, as propriedades elastoplásticas cíclicas e os comportamentos à fadiga oligocíclica e oligocíclica extrema, foi realizada uma vasta campanha de ensaios experimentais, em provetes de pequenas dimensões. Dado não existirem normas específicas para a realização de ensaios no domínio na fadiga oligocíclica extrema, são propostas novas metodologias, que visam a redução das instabilidades sofridas pelos provetes durante este tipo de ensaios. Estas instabilidades introduzem deformações plásticas adicionais levando à rotura precoce do material. Para reduzir estas instabilidades foi desenvolvido um sistema anti-encurvadura que foi utilizado nos ensaios de fadiga oligocíclica extrema dos provetes planos lisos que, no entanto, não se revelou totalmente eficaz. Assim, os ensaios em provetes entalhados sob ações de tração/compressão ou ensaios de flexão representam um procedimento alternativo para avaliar o comportamento do material sob a ação de grandes amplitudes de deformação plástica, sendo necessária a realização de simulações numéricas para avaliar o campo de tensões/deformações na localização admissível para a iniciação de fenda. Também o uso da Correlação Digital de Imagem se revelou uma ferramenta importante para a análise dos resultados experimentais e para a validação de modelos, incluindo a validação de condições fronteira. Os provetes usados nos ensaios experimentais foram definidos de modo a permitir a obtenção de diferentes deformações de fratura, triaxilidades e ângulo de Lode. Em particular, para o aço X60, foi realizada uma caracterização completa resultando os campos vida-triaxilidade-ângulo de Lode. A Teoria das Distâncias Críticas também foi explorada

para os domínios de fadiga oligocíclica e oligocíclica extrema, usando os resultados experimentais relativos aos provetes testados de pequenas dimensões.

Para além do estudo experimental e numérico de provetes de pequenas dimensões, foi também investigado o comportamento no domínio da fadiga oligocíclica extrema de componentes à escala real de pipelines, em particular troços retos de tubos sujeitos a ensaios de flexão e joelhos sujeitos a carregamentos tipo push-pull. Os joelhos foram produzidos através de conformação plástica assistido por aquecimento por indução, pelo que o efeito deste processo térmico foi também estudado através de ensaios experimentais realizados em provetes de pequenas dimensões. Os componentes de grandes dimensões foram construídos com base em tubos de aço X60 e X65 com as dimensões de 16” de diâmetro e espessura de parede 9.5 mm e 8 5/8” de diâmetro e espessura de parede de 5.59 mm, respetivamente. Estes ensaios à escala real foram realizados no âmbito do projeto europeu ULCF (*Ultra Low Cycle Fatigue of Steel Under Cyclic High-Strain Loading Conditions).*

A simulação dos ensaios foi realizada recorrendo a modelos de elementos finitos com modelos de plasticidade identificados com os resultados obtidos através do programa de ensaios de caracterização experimental dos aços. Adicionalmente, os dados numéricos e experimentais dos ensaios de pequenas dimensões foram usados para calibrar os modelos de dano (ex.: relação de Coffin-Manson, modelo de Xue) que por sua vez foram utilizados para estimar o número de ciclos para a iniciação da fenda nos ensaios dos componentes de grandes dimensões. Em todos os casos testados/simulados, a rotura foi precedida pela formação de uma instabilidade plástica que concentrou as deformações. Foram propostas orientações gerais para procedimentos que incluem a dependência na vida à fadiga da triaxialidade e do parâmetro relativo ao ângulo de Lode, de modo a atualizar as abordagens deformação-vida existentes em códigos de projeto. Foram ainda aplicados os procedimentos do código ASME VIII-Div.2 permitindo assim a sua avaliação.

CONTENTS

CHAPTER III – SMALL-SCALE TESTS OF API PIPING STEELS

CHAPTER IV – FINITE ELEMENT SIMULATION OF SMALL-SCALE TESTS OF API PIPING STEELS

CHAPTER V – APPLICATION OF THE THEORY OF CRITICAL DISTANCES TO LCF AND ULCF BEHAVIOR OF API PIPING STEELS

CHAPTER VI – FULL-SCALE CYCLIC TESTS OF ELBOWS AND STRAIGHT PIPES

CHAPTER VII – FINITE ELEMENT SIMULATION AND DAMAGE ASSESSMENT OF FULL-SCALE CYCLIC TESTS OF ELBOWS AND STRAIGHT PIPES

CHAPTER VIII – FINAL CONCLUSION AND FUTURE WORKS

LISTS OF FIGURES

CHAPTER I – INTRODUCTION

CHAPTER II – A LITERATURE REVIEW ON MONOTONIC DUCTILE AND CYCLIC DAMAGE OF METALLIC MATERIALS

CHAPTER III – SMALL-SCALE TESTS OF API PIPING STEELS

CHAPTER IV – FINITE ELEMENT SIMULATION OF SMALL-SCALE TESTS OF API PIPING STEELS

CHAPTER V – APPLICATION OF THE THEORY OF CRITICAL DISTANCES TO LCF AND ULCF BEHAVIOR OF API PIPING STEELS

CHAPTER VI – FULL-SCALE CYCLIC TESTS OF ELBOWS AND STRAIGHT PIPES

LISTS OF TABLES

CHAPTER II – A LITERATURE REVIEW ON MONOTONIC DUCTILE AND CYCLIC DAMAGE OF METALLIC MATERIALS

CHAPTER III – SMALL-SCALE TESTS OF API PIPING STEELS

CHAPTER IV – FINITE ELEMENT SIMULATION OF SMALL-SCALE TESTS OF API PIPING STEELS

CHAPTER V – APPLICATION OF THE THEORY OF CRITICAL DISTANCES TO LCF AND ULCF BEHAVIOR OF API PIPING STEELS

CHAPTER VI – FULL-SCALE CYCLIC TESTS OF ELBOWS AND STRAIGHT PIPES

CHAPTER VII – FINITE ELEMENT SIMULATION AND DAMAGE ASSESSMENT OF FULL-SCALE CYCLIC TESTS OF ELBOWS AND STRAIGHT PIPES

NOMENCLATURE

LATIN

b	Fatigue strength exponent
c	Fatigue ductility exponent, ductility exponent
$d\varepsilon^p$	Incremental equivalent plastic strain
f_v^*	Effective void volume fraction
f_v	Current void volume fraction
f_C	Critical porosity
f_F	Failure porosity
f_N	Effective particle of the void nucleation
f	Void volume fraction, frequency
m	Material parameter
n'	Cyclic strain hardening exponent
q	Von Mises stress
q_1	Material parameters
q_1	Material parameters
q_1	Material parameters
r	Isotropic internal variable
s	Damage variable
C	Material constants
C_m	Ductile damage factor
D	Isotropic damage internal variable, Damage variable
D_s	Static damage
D_c	Cyclic damage
D_1, D_2, D_3, D_4, D_5, D_6	Material parameters
$\underline{\underline{\boldsymbol{D}}}^E$	Isotropic elasticity tensor
E	Elastic modulus
F_{Gurson}	Yield surface of Gurson model
G	Shear modulus
$\boldsymbol{I}$	Second order tensor identity
K	Elastic compressibility modulus
K’	Cyclic strain hardening coefficient
L	Lode angle parameter
N	Number of fatigue cycles
N_i	Number of cycles until crack initiation
N_f	Number of cycles until the failure

$\boldsymbol{N}$	Flow vector
P	Hydrostatic pressure
R_δ	Relative displacement ratio
R_ε	Strain ratio
R	Average void radius, thermodynamical forces associated with the isotropic hardening
S	Damage variable
S_N	Standard deviation of the normal distribution
S_t	Transversal area
$\boldsymbol{S}$	Deviatoric stress tensor
T	Energy release rate
T_σ	Stress triaxiality
$VGI_{monotonic}$	Monotonic void growth index
VGI_{cyclic}	Cyclic void growth index
$VGI_{monotonic}^{critical}$	Critical monotonic void growth index
V	Voids volume
V_0	Initial volume of material
Y	Thermodynamical forces associated with damage

GREEK

$\boldsymbol{\alpha}$	Back stress tensor
β	Material constant
γ	Material constant
$\dot{\gamma}$	Plastic multiplier
δ	Relative displacement
$\varepsilon_1, \varepsilon_2, \varepsilon_3,$	Principal strains
ε_a	Strain amplitude
ε_d	Equivalent plastic distortion
ε_{fr}	Residual ductility
ε_m	Mean strain
ε_{max}	Maximum strain
ε_{Pmax}	Maximum tensile plastic strain
ε_d^0	Strain in the first cycle loading
ε_{pD}	Damage strain threshold
$\bar{\varepsilon}_f$	Fracture strain
$\dot{\varepsilon}_v^p$	Equivalent macroscopic plastic strain rate

ε_N	Mean void nucleation
$\boldsymbol{\varepsilon}^E$	Elastic strain tensor
$\boldsymbol{\varepsilon}^P$	Plastic strain tensor
ε'_f	Fatigue ductility coefficient
η	Stress triaxiality
θ	Lode angle
$\bar{\theta}$	Lode angle parameter
λ	Damage coefficient
λ_v	Microvoid elongation ratio
υ	Poisson coefficient
ξ	Normalized third deviatoric stress invariant
$\boldsymbol{\sigma}$	Stress tensor
σ_{y0}	Initial uniaxial yield stress
$\sigma_1, \sigma_2, \sigma_3$	Principal stress
σ_s	Current yield stress
σ'_f	Fatigue strength coefficient
ψ	Free energy
$\Delta\delta$	Displacement range
$\Delta\varepsilon^E/2$	Uniaxial elastic strain amplitude
$\Delta\varepsilon^P/2$	Uniaxial plastic strain amplitude
$\Delta\varepsilon^P$	Uniaxial plastic strain range
$\Delta\varepsilon^E$	Uniaxial elastic strain range
$\Delta\varepsilon_{eq}$	Equivalent strain range
$\Delta\varepsilon^P_{eq}$	Equivalent plastic strain range
$\Delta\varepsilon^E_{eq}$	Equivalent elastic strain range
$\Delta\sigma$	Stress range
Φ	Yield function

ACRONYMS

AM – Area method

API – American Petroleum Institute

ASME – American Society of Mechanical Engineers

BW – Bai and Wierzbicki model

CM – Coffin-Manson relation

DIC – Digital image correlation

GTN – Gurson-Tvergaard-Needleman

GTN-LPD – Gurson-Tvergaard-Needleman-Leblond-Perrin-Devaux

JC – Johnson Cook model

KD – Kanvinde and Deierlein model

LCF – Low-cycle fatigue

LM – Line method

MM-CVGM – Micromechanical void growth model

PM – Point method

TCD – Theory of Critical Distances

ULCF – Ultra-low-cycle fatigue

Chapter I

Introduction

1.1 INTRODUCTION

Pipelines subjected to extreme cyclic loading conditions such as those resulting from earthquakes, support settlements and industrial plant shutdown, among others, may experience large plastic strain amplitudes which may lead to their collapse under the action of a reduced number of cycles. The damage associated with this cyclic phenomenon of especially short duration and extreme intensity is usually named as extreme-low-cycle-fatigue or ultra-low-cycle fatigue (ULCF), the latter terminology being adopted in this work. Moreover, it is commonly accepted to assume this fatigue domain characterized by a reduced number of cycles until the final fracture in the order of N_i <100.

Large plastic deformations suffered by a pipeline can be observed in the Figure 1.1, which illustrates a pipeline after the Kocaeli earthquake occurred in Turkey in 1999 [1]. Elbows and straight pipes can promote the stress and strain concentrations, mainly under bending cyclic action for the straight pipes. ULCF failures of a full-scale straight pipe and an elbow subjected to a bending cyclic test, combined with internal pressure, are illustrated in Figure 1.2. These failures of full-scale components were produced in the framework of the ULCF European Project [2]. The failures resulted from the application of loading histories of high amplitude, promoting the widespread yielding and the damage evolution, concentrated at plastic instabilities generated at the pipeline components during the cyclic action.

The investigation of ULCF damage has deserved little attention in the literature when compared with the bounding damage mechanisms, namely the monotonic ductile damage and the low-cycle fatigue. Since the ULCF damage can be considered a transition damaging process between the monotonic ductile damage and the low-cycle fatigue (LCF), ULCF simulation has been performed using models available for both bounding damaging mechanisms. Experimental testing in the ULCF regime is not abundant in the literature since it poses significant challenges due to the intense plastic deformations. Also existing standards for LCF are not appropriate for ULCF. Therefore, there exists an opportunity for research in both experimental materials characterization as well as in ULCF modelling of steel and respective components.

Figure 1.1 – Failure of pipe during Kocaeli earthquake of 1999 [1].

Figure 1.2 – ULCF failure after experimental tests carried out on: a) straight pipe [3]; b) elbow pipe [4].

This work aims at investigating the ULCF damage mechanisms on three API pipeline steel grades, namely the X52, X60 and X65, through a comprehensive experimental program. ULCF testing is more challenging than monotonic or low-cycle fatigue testing, since it involves high cyclic plastic strain levels, requiring special design of specimens and testing apparatus and improved data reduction techniques. Expertise on ULCF testing will be developed. Existing models for ULCF will be evaluated and enhancements will be proposed. New validated damage models will be applied to model ULCF tests of full-scale pipeline components.

The work described in this thesis was performed under the framework of the ULCF European project (Ultra-Low Cycle Fatigue of Steel Under Cyclic High-Strain Loading Conditions) [2] which provided the piping materials for the presented research as well as cyclic full-scale testing data. The recent ULCF project is a good indication of the interest of such a research on the ULCF on pipeline steels.

1.2 AIM OF THE THESIS

The main goal of the proposed research is to contribute for a better understanding of damage mechanisms associated to ULCF, which has deserved increasing attention in recent years. In particular, the failure of originally crack-free components, subjected to cyclic strains of very high amplitude and low duration (N_i<100 cycles) is to be investigated. Steel grades for pipeline components will be the focus of the proposed investigation. Three steel grades will be selected (X52, X60 and X65) in order to compare high strength materials with lower elongation with materials with a more pronounced yield point elongation. The effects of a thermal treatment on the X60 and X65 steels is also a goal of this research. An extensive experimental program of monotonic, LCF and ULCF tests, covering several geometries of specimens and load combinations will be aimed. These tests should cover a wide range of stress triaxialities and Lode angle parameters [5]. Expertise for ULCF testing will be developed, namely on adequate design of specimens and testing apparatus as well as on test monitoring using full field Digital Image Correlation (DIC). There are no specific standards on ULCF testing and published results on ULCF are very scarce. Using generated experimental data, existing models proposed for ULCF are expected to be evaluated. ULCF models resulting both from extension of monotonic ductile damage models (micromechanical-based models) and LCF models, will be assessed. New developments are expected to be proposed, updating existing models in order to overcome the detected limitations. In particular, the effects of the Lode angle stress parameter (θ), that has been recently understood to have a significant influence on monotonic ductile damage, will be investigated for intermediate values (0<θ<1). The influence of this parameter will be analysed in ULCF and his effect accounted in the ULCF modelling. Validated models for ULCF are expected to be further evaluated using data available regarding the ULCF behaviour of full scale pipeline components. In particular, the performance of the Coffin-Manson relation [6] [7] and the Xue model [8] will be investigated and modifications on theirs formulations proposed in order to increase their simulation performance.

Another important objective of this work is to conduct numerical studies of full-scale elbows and straight pipes by means of finite element simulations using experimental data resulted from an experimental program of full-scale tests performed within the ULCF

European project [2]. The cyclic tests on elbows were performed by Department of Ferrous Metallurgy (RWTH Aachen University) and OCAS N.V. (Zwijnaarde, Belgium) carried out the bending cyclic tests on straight pipes, both were partners of the referred project. This experimental program aimed at characterizing the elastoplastic cyclic and damage behaviour of these large-scale components under ULCF domain. The results of this experimental program will be used for plasticity models validation as well as for the validation of the investigated damage models.

1.3 OUTLINE OF THE THESIS

This PhD thesis is composed by a set of eight chapters, including the current one that reports the introduction, the objectives and the outline of the present work. In the Chapter II, a literature review on monotonic ductile and cyclic damage behaviour of metallic materials is presented. In detail, the formulation of several monotonic ductile damage models and also damage models for the fatigue life prediction under LCF and ULCF domain are revised as well as a review of existing experimental studies on ULCF is presented.

In the Chapter III, the experimental program carried out with small-scale specimens is described, including the experimental results achieved from these tests. This is one important contribution from the present research since it involved a very significant experimental campaign. In addition to the characterization of the fatigue behaviour of each steel, covering both the low and ultra-low-cycle fatigue, the basic mechanical properties of the materials are also addressed. Comparisons between the performances of three piping steels and pipeline materials affected with the thermal treatment typical of elbows manufacturing is also described. A variety of specimens geometries were explored ranging from smooth to notched specimens which will require numerical simulations of each tests regarding the non-uniform specimens in order to allow an appropriate data reduction.

The Chapter IV reports the numerical simulations of the experimental tests described in the Chapter III. In this chapter alternative finite elements models exploring distinct strategies for the definition of the boundary conditions are presented. Effectively, ideal boundary

conditions and updated boundary conditions taken into account the actuator parasitic lateral movement's registered during the cyclic loading, will be considered. Moreover, a new methodology for the application of boundary conditions derived from DIC full-field measurements is also explored. The issue of definition appropriate boundary conditions is raised by the extreme cyclic loading that induces instabilities during the compressive loading excursions. The results of small-scale tests are correlated using the Coffin-Manson relation and the Xue model that are proposed for the fatigue life estimations under LCF and ULCF domain. This procedure allows to investigate the performance of these models on the fatigue life estimation for different specimens' geometries which are associated with distinct fracture strain, stress triaxialities and Lode angle parameter levels.

In the Chapter V, the investigation of LCF and ULCF behaviour of API piping steels by means of the Theory of Critical Distances (TCD) is proposed. The TCD was originally proposed in the literature for the high-cycle fatigue [9]. More recently it was applied to LCF [10]. In this chapter, the TCD will be tested for the LCF/ULCF regimes. The experimental program, covering both smooth and notched plane specimens of three piping steel grades (X52, X60 and X65) was coupled with a numerical analysis, aiming the application of Point, Line and Area methods. In addition, the numerical results of bending cyclic tests and flat-grooved plane specimens of X52 steel are also used to investigate the performance of these methods.

The Chapter VI presents a summary of the experimental program of full-scale fatigue tests performed on elbows and straight pipes. These testes were carried out by RWTH and OCAS under the ULCF European project (*Ultra Low Cycle Fatigue of Steel Under High-Strain Cyclic Loading Conditions*) coordinated by FEUP and results were made available to the partners. These testes will be simulated in the Chapter VII, therefore the experimental tests will be described including important details of the experimental program.

Chapter VII describes the numerical modelling using finite elements analysis of the cyclic full-scale tests performed under ULCF domain, as described in the Chapter VI. The performance of fatigue damage models, namely the Coffin-Manson relation [6] [7], and the updated Xue model [8] are assessed. Additionally the American ASME Boiler & Pressure Vessel Code, Section VIII, Division 2 [11] is applied in order to assess its applicability for the ULCF conditions.

Finally, the main conclusions achieved in this work and proposals for future work will be exposed in the Chapter VIII.

1.4 REFERENCES

[1] Rajaram, C., Terala, S., Singh, A. P., Mohan, K., Rastogi, B. K., Ramancharla, P. K., (2014). "Vulnerability Assessment of Buried Pipelines: A Case Study." Frontiers in Geotechnical Engineering (FGE) - Science and Engineering Publishing Company, 3: 24-26.

[2] Fernandes A.A. et al, (2015), "Ultra low cycle fatigue of steel under cyclic high strain loading conditions," Final Report, European Commission RFSR CT 2011 00029.

[3] Wittenberghe J.V., (2014). "Full scale tests of straight pipes under cyclic." ULCF internal report, OCAS NV.

[4] Schaffrath, S., Eichler, B., Feldmann, M., (2014). "Full Scale tests of elbows under cycle loading (ULCF)." ULCF internal report, RWTH Aachen - Institute of steel construction.4

[5] Wierzbicki T., Bao Y., Lee Y-W., Bai Y., (2005), "Calibration and Evaluation of Seven Fracture Models." International Journal of Mechanical Sciences, 47:719 – 743.

[6] Coffin Jr L.F., (1971), "A note on low cycle fatigue laws." Journal of Materials JMLSA, 6(2):388 – 402.

[7] Manson S.S., (1954), "Behavior of materials under conditions of thermal stress" NACA-TR-1170, National Advisory Committee for Aeronautics.

[8] Xue L., (2007), “A unified expression for low cycle fatigue and extremely low-cycle fatigue and its implication for monotonic loading” International Journal of Fatigue, 30:1691–1698.

[9] Susmel L., (2003), “A unifying approach to estimate the high-cycle fatigue strength of notched components subjected to both uniaxial and multiaxial cyclic loadings.” Fatigue and Fracture of Engineering Materials and Structures 27: 391 – 411.

[10] Susmel, L., Taylor, D., (2010), “An elasto-plastic reformulation of the theory of critical distances to estimate lifetime of notched components failing in the low/medium-cycle fatigue regime,” Journal of Engineering Materials and Technology, 132(2): 210021 – 210028.

[11] ASME Boiler & Pressure Vessel Code, Section VIII, (2013). “Rules for Construction of Pressure Vessels, Division 2 – Alternative Rules”, The American Society of Mechanical Engineers (ASME), New York, USA.

Chapter II

A literature review on monotonic ductile and cyclic damage of metallic materials

2.1 INTRODUCTION

Current design codes procedures for steel structures avoid the brittle fracture of structural components in particular brittle cracking at critical locations (e.g. stress concentrations, joints). Plastic deformation in these locations is desired before final failure (see Figure 2.1). Tough materials and geometries with large deformation capability should be used, allowing ductile failure modes.

Under cyclic loading of high intensity, failure may occur for a reduced number of load reversals. This damage regime is often categorized as ultra-low-cycle fatigue (ULCF). In fact, ULCF damage mechanisms show a mixture of features of both monotonic (void formation and growth) and LCF (crack nucleation and propagation), as shown in Figure 2.2. The combination of the ductile and cyclic damage mechanisms in the ULCF failure, can be observed from the fracture surfaces for these modes of fracture. The fracture surfaces of a monotonic failure and ULCF fatigue failure are represented in the Figure 2.3, for the S185 steel grade [1]. The comparisons of these figures reports a common damage mechanisms regards to the growing and coalescence of the microvoids. The monotonic surface shows deep cavities well distinguished that indicates the growing and the coalescence of the microvoids while the ULCF fracture surface presents cavities with a fibrous aspect. This effect, results from the successive loading reveals associated with large strain amplitudes, leading to the compression and distortion of the material. Figure 2.2 illustrates a typical S-N diagram where it is possible to compare several fatigue regimes, the ULCF fitting in between the monotonic ductile/plastic damage and the LCF.

This chapter will presents a literature review about monotonic ductile/plastic and cyclic plastic damage models, the latter with focus on LCF and ULCF fatigue regimes. Some damage modelling approaches for ULCF are adapted from monotonic ductile/plastic damage approaches, which justifies the review of the monotonic damage models as well. This chapter will also highlight the research on ULCF involving experimental programs.

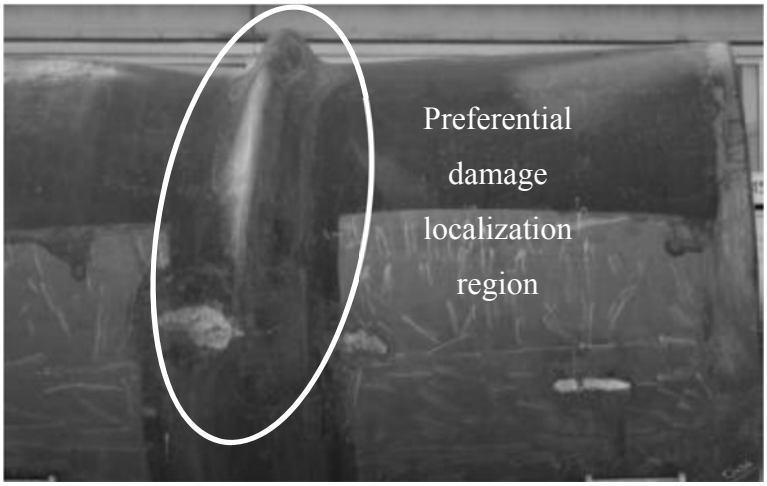

Figure 2.1 – Large plastic deformation associated with damage localization [2].

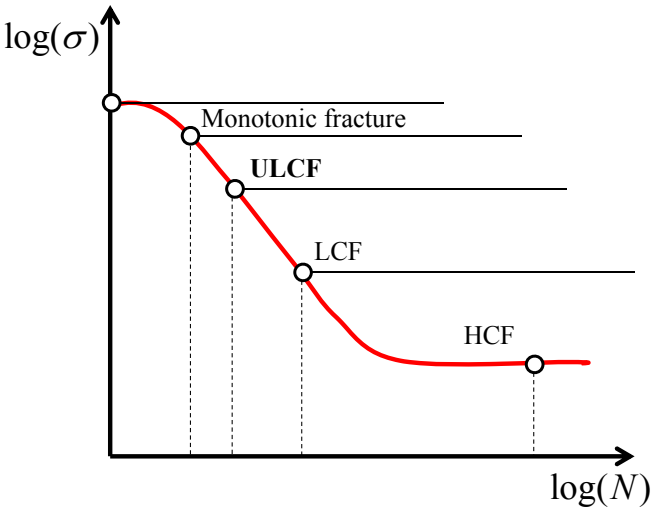

Figure 2.2 – Relation of ULCF damage with other damage mechanisms [3].

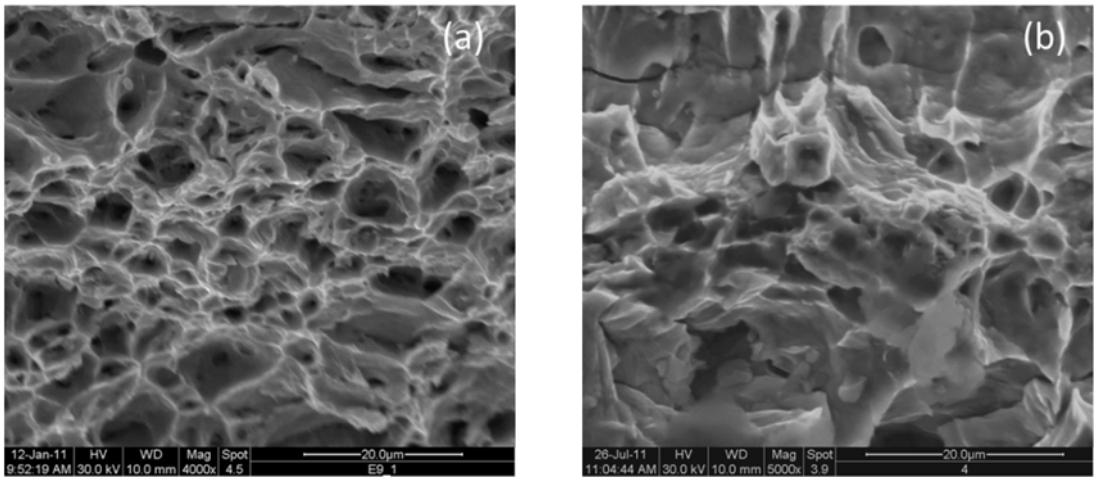

Figure 2.3 – Images of fracture surfaces of the S185 steel grade: a) monotonic fracture [1]; b) ULCF fracture [1].

2.2 MONOTONIC DUCTILE FRACTURE

One of the most important and key concepts in the entire field of Materials Sciences, Solid Mechanics and Engineering is the fracture. In its simplest form, fracture can be described as a single body being separated into pieces by an external loading condition. In general, the fracture concept can be divided in two possible modes of fracture, brittle and ductile. The main difference between brittle and ductile fracture is related to the amount of plastic deformation induced in the material before the final fracture. Ductile materials exhibit large amounts of plastic deformation while brittle materials may show little or no plastic deformation before fracture, as illustrated in Figure 2.4. Tensile stress-strain curves may represent the degree of plastic deformation exhibited by both brittle and ductile materials before fracture. The assessment of the ductile failure of metals still represents an important challenge aiming the evaluation and prediction of the collapse in structural components. Ductile fracture concepts are related with large deformations in metals which can origin the phenomenon of the initiation and growth of cavities and micro cracks, as referred by Kachanov [4].

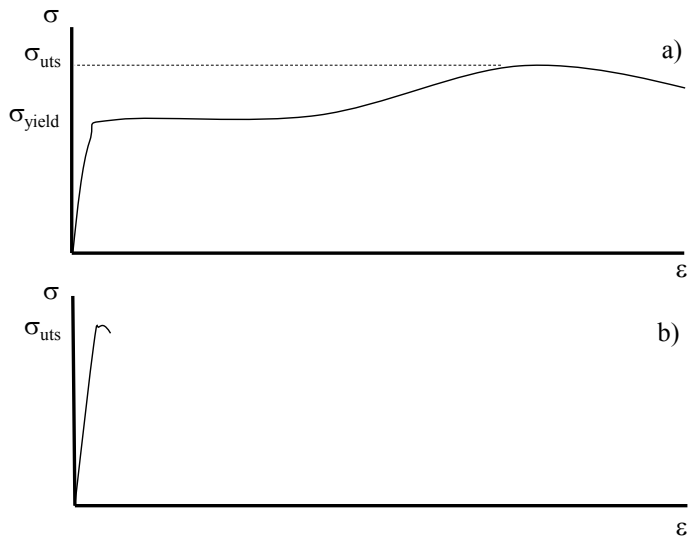

Figure 2.4 – Comparison of tensile stress-strain curves for ductile and brittle materials: a) ductile material; b) brittle material [5].

In general, the most common models for ductile fracture relate the damage with the accumulated plastic strain and the stress triaxiality, as originally proposed by Bridgman

[6]. Based on these assumptions, several models have been proposed in order to describe the ductile fracture mechanism during the loading process in metals. These proposals fall into four classes: empirical criteria, void growth models, the continuum damage mechanics (CDM) and porosity-type models [7].

The empirical models assume that damage accumulation depends on the equivalent plastic strain, weighted by a suitable triaxiality function. Examples of such formulations were proposed by Cockcroft and Latham [8], Datsko and Yang [9], Brozzo [10], Norris [11] and Johnson and Cook [12].

Regarding to the void growth micromechanics based models they show a similar formulation to the empirical models. However, these models are based on voids evolution on the micro scale, as referred by McClintock [13], Rice and Tracy [14] and Kanvinde and Deierlein [15]. For empirical and void growth micromechanics based models, damage and plasticity are usually assumed completely decoupled [16].

Originally introduced by Lemaitre [17] the CDM models are based on a consistent thermodynamics framework, where damage represents the loss of stiffness in the material. Bonora [18] proposed a non-linear damage evolution law instead of the originally linear one proposed by Lemaitre [17].

Concerning the porosity-based models, they have been proposed based on the Gurson [19], Tvergaard and Needleman [20][21] studies. These models assume that the ductile fracture in metallic components is caused by nucleation, growth and coalescence of micro-voids presented inside the material at the level of its microstructure.

Besides the accumulated equivalent plastic strain, the stress triaxiality was early recognized as an influent stress parameter on ductile/plastic damage evolution. However, based on experimental evidences, Clausing [22] postulated that different geometrical conditions could provide distinct ductile fracture behaviors in materials at similar levels of stress triaxiality. McClintock [13] also found that the equivalent plastic strain to failure is lower in torsion than in tension, even if the stress triaxiality in torsion is zero. Thus, these evidences are not consistent with any of the hydrostatic pressure dependence models. A different approach with respect to the classical damage theories was originally proposed by

Bai and Wierzbicki [23], introducing a normalized stress parameter related with the third invariant of the stress tensor, so-called as deviatoric parameter. With this new proposition, the equivalent strain at fracture, the stress triaxiality and the deviatoric parameter allows covering both hydrostatic and the shear type failure modes.

In the following sections a description of some selected models used for monotonic ductile fracture prediction will be presented. In particular, the empirical model developed by Johnson and Cook (JC) [12], the void micro-mechanics based model proposed by Kanvinde and Deierlein (KD) [15], the Lemaitre [17] model based on CDM, the Gurson-Tvergaard-Needleman model (GTN) [19]-[21] for porous metals and the Bai and Wierzbicki model (BW) that considers the influence of deviatoric parameters are presented.

2.2.1 Johnson-Cook model

The JC model proposes the ductile/damage curve which relates the equivalent strain at fracture with the stress triaxiality [12] by means of a monotonic function, represented in the Figure 2.5, and that can be expressed as follows:

$$\bar{\varepsilon}_f = C_1 + C_2 \exp\left(C_3 \eta\right) \tag{2.1}$$

where the stress triaxiality, η, is defined by the ratio between the hydrostatic pressure, p, and the *Von Mises* equivalent stress, q, as follows:

$$\eta = \frac{p}{q} \tag{2.2}$$

C_1, C_2 and C_3 are constants that characterize the material and are determined using the monotonic tensile testing data, addressing distinct stress triaxialities and fracture strains. The determination of the stress triaxiality in the critical region is complex, since it changes during the loading process. To overcome this shortcoming an average triaxiality value can be used as proposed by the following equation:

$$\eta_{av} = \frac{1}{\bar{\varepsilon}_f} \int_0^{\bar{\varepsilon}_f} \eta(\bar{\varepsilon}) d\bar{\varepsilon} \tag{2.3}$$

where $\bar{\varepsilon}_f$ is the strain at fracture.

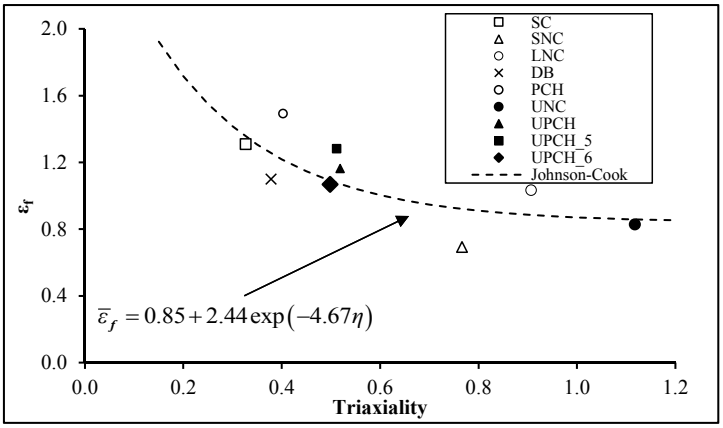

Figure 2.5 – Ductility curve of S185 structural steel [24].

2.2.2 Kanvinde and Deierlein model

Kanvinde and Deierlein (KD) [15] developed a model for ULCF damage based on a generalization of a model for monotonic ductile fracture. In this section the base monotonic ductile damage model is presented. Metallic materials contain voids in their microstructures, which may grow under the action of plastic deformation. Rice and Tracey [14] reported that, for a single spherical void in an infinite continuum, the void growth rate can be described as:

$$dR / R = C \exp(1.5\eta) d\varepsilon_P \tag{2.4}$$

where R is the average void radius, C is a material constant, η is the stress triaxiality and $d\varepsilon_p = \sqrt{(2/3)\boldsymbol{\varepsilon}^P : \boldsymbol{\varepsilon}^P}$ is the incremental equivalent plastic strain. Integrating Eq. (2.5) and normalizing the void radius R with respect to the initial void radius R_0, the following expression is obtained:

$$\ln\left(R/R_0\right)=\int_0^{\varepsilon_p} C\exp(1.5\eta)d\varepsilon_P \tag{2.5}$$

Assuming that the void growth is the controlling parameter of the monotonic fracture, the failure criterion for monotonic damage is based on the critical size of the void radius and can be expressed as:

$$\ln\left(R/R_0\right)_{monotonic}^{critical}=\int_0^{\varepsilon_p^{critical}} C\exp(1.5\eta)d\varepsilon_P \tag{2.6}$$

This expression can be further simplified in order to derive a fracture criterion based on the void growth index, $VGI_{monotonic}$, which is compared to its critical value, $VGI_{monotonic}^{critical}$, as described in Eq. (2.7):

$$\begin{aligned}\ln\left(R/R_0\right)_{monotonic}/C=VGI_{monotonic}=\int_0^{\varepsilon_p}\exp\left(1.5\eta\right)d\varepsilon_p &\le VGI_{monotonic}^{critical}\\ &=\int_0^{\varepsilon_p^{critical}}\exp\left(1.5\eta\right)d\varepsilon_p\end{aligned} \tag{2.7}$$

Eq. (2.7) is the basis of the void growth model for monotonic loading, in which $VGI_{monotonic}^{critical}$ is considered a material constant.

2.2.3 Lemaitre model

Lemaitre [17] proposed a ductile damage model based on the effective stress concept coupled with plasticity. In this section the respective constitutive equations are presented. The plasticity model allows non-linear isotropic and kinematic hardening in the behavior of ductile materials and also includes the evolution of internal damage [17]. The specific free energy, ψ, can be expressed as a function of the set $\{\boldsymbol{\varepsilon}^E, r, D\}$ of state variables:

$$\psi=\psi\left(\boldsymbol{\varepsilon}^E, r, D\right) \tag{2.8}$$

where, $\boldsymbol{\varepsilon}^E$ is the elastic strain tensor, r is the isotropic hardening internal variable and D represents the isotropic damage internal variable. The specific free energy is defined in Eq.

(2.9) as a function of the elasticity-damage and plastic hardening, since they are decoupled [17]:

$$\psi = \psi^{ed}\left(\boldsymbol{\varepsilon}^{E}, D\right) + \psi^{p}\left(r\right) \tag{2.9}$$

where ψ^{ed} is the elastoplastic damage contribution and ψ^{p} define the plastic contribution to the free energy. These two components can be postulated by the following expressions, respectively:

$$\bar{\rho}\psi^{ed}\left(\boldsymbol{\varepsilon}^{E}, D\right) = \frac{1}{2}\boldsymbol{\varepsilon}^{E} : (1-D)\underline{\underline{\boldsymbol{D}}}^{E} : \boldsymbol{\varepsilon}^{E} \tag{2.10}$$

$$\bar{\rho}\psi^{p}\left(r\right) = \bar{\rho}\psi^{I}\left(r\right) \tag{2.11}$$

where $\underline{\underline{\boldsymbol{D}}}^{E}$ represents the isotropic elasticity tensor. To obtain the elasticity law including the damage effect is necessary to perform the derivative of the elastic-damage potential in order to the elastic strain tensor, as follows:

$$\boldsymbol{\sigma} = \bar{\rho}\frac{\partial \psi^{ed}}{\partial \boldsymbol{\varepsilon}^{E}} = (1-D)\underline{\underline{\boldsymbol{D}}}^{E} : \boldsymbol{\varepsilon}^{E}. \tag{2.12}$$

Performing the derivative of the elastic-damage contribution in order to the damage variable and by taking the derivative of the plastic potential with regard to the isotropic hardening variable, the thermodynamical forces related with damage and isotropic hardening internal variable are obtained and expressed, respectively, as follows:

$$-Y \equiv -\bar{\rho}\frac{\partial \psi^{ed}}{\partial D} = \frac{q^2}{6G(1-D)} + \frac{p^2}{2K(1-D)^2}, \tag{2.13}$$

$$R \equiv -\bar{\rho}\frac{\partial \psi^{I}}{\partial r} = R(r), \tag{2.14}$$

where Y is the thermodynamical force associated with damage, q represents the *Von Mises* equivalent stress, p is the hydrostatic pressure, G define the shear modulus, K represents the elastic compressibility modulus and R is the thermodynamical force associated with the isotropic hardening variable. Thus, assuming the existence of the flow potential, ψ, the evolution of the internal variable can be obtained, by:

$$\psi = \Phi + \frac{S}{(1-D)(s+1)}\left(\frac{-Y}{S}\right)^{s+1}, \tag{2.15}$$

where the parameters S and s are damage evolution constants and Φ is the yield function, defined by the following equation:

$$\Phi = \frac{q}{(1-D)} - \sigma_{y_0} - R(r), \tag{2.16}$$

where σ_{y0} is the initial uniaxial yield stress. Taking into account the plastic flow rule definition, the plastic strain rate, $\dot{\varepsilon}^{P}$ and the flow vector, $\boldsymbol{N}$ are defined by:

$$\dot{\varepsilon}^{P} = \dot{\gamma}\frac{\partial \Phi}{\partial \sigma} = \dot{\gamma}\boldsymbol{N}, \tag{2.17}$$

$$\boldsymbol{N} = \sqrt{\frac{3}{2}}\frac{\boldsymbol{S}}{\|\boldsymbol{S}\|}\frac{1}{(1-D)}, \tag{2.18}$$

where $\dot{\gamma}$ is the plastic multiplier and $\boldsymbol{S}$ represents the deviatoric stress tensor. By performing the derivative of the flow potential in order to the thermodynamic forces associated with damage, Y and the derivative with regard to the isotropic hardening variable, r, the evolution law for damage and isotropic hardening internal variables can be established, and given by the following expressions:

$$\dot{D} \equiv \dot{\gamma}\frac{\partial \psi}{\partial Y} = \dot{\gamma}\frac{1}{(1-D)}\left(\frac{-Y}{S}\right)^{s}, \tag{2.19}$$

$$\dot{r} \equiv \dot{\gamma} \frac{\partial \psi}{\partial R} = \dot{\gamma}. \tag{2.20}$$

To complete the description of the constitutive equations of the Lemaitre model, it is necessary to introduce the rate-independent plasticity consistency conditions:

$$\Phi \leq 0, \ \dot{\gamma} \geq 0, \ \dot{\gamma}\,\Phi = 0 \tag{2.21}$$

The CDM model as proposed by Lemaitre represents a class of coupled models, where damage and plasticity are coupled in the constitutive equations or in other words, damage influences the yield plastic function as indicated by Eq. (2.19). Previous models presented in Sections 2.2.1 and 2.2.2 are uncoupled, since damage does not influence the plastic behavior of the material.

2.2.4 Gurson-Tvergaard-Needleman model

Regarding the GTN model, it assumes that the micro defects and micro cavities in the material microstructure can be accountable during the damage evolution process due to an external load. Hence, this process is based on micromechanical assumptions as nucleation, growth and coalescence of voids inside the material, as referred above. As such, failure occurs when the void volume fraction, *f*, reaches the critical value [19]. The void volume fraction is defined as follows:

$$f = \frac{V}{V_0} \tag{2.22}$$

where V represents the voids volume within an initial volume of material, V_0. According to the GTN model, the reduction of resistance is addressed by the introduction of the yield surface described by the plastic potential, F_{Gurson}, [19]-[21]:

$$F_{Gurson} = \frac{q^2}{\sigma_s^2} - 1 + 2q_1 f_v^* \cosh\left(\frac{3}{2} q_2 \frac{p}{\sigma_s}\right) - q_3 f_v^{*2} \tag{2.23}$$

where σ_s represents the current uniaxial yield stress, q is the equivalent stress, q_1, q_2 and q_3 are materials parameters related with the interaction of microvoids. The relationship $q_3=q_1^2$ stands for these material constants. f_v^* is the effective void volume fraction defined as [19]-[21]:

$$f_v^* = \begin{cases} f_v & f_v < f_c \\ f_C + \dfrac{q_1^{-1} - f_C}{f_F - f_C}\left(f_v - f_C\right) & f_v \geq f_c \end{cases} \tag{2.24}$$

where f_v is the current void volume fraction, f_C and f_F are the critical porosity (critical void volume fraction) and failure porosity, respectively. The evolution of void volume fraction can be divided into two parts: void growth rate and void nucleation rate:

$$\begin{aligned} \dot{f}_v &= \dot{f}_g + \dot{f}_n \\ \dot{f}_g &= (1 - f_v)\dot{\varepsilon}_{kk}^p \\ \dot{f}_n &= \frac{f_N \dot{\varepsilon}_v^p}{S_N\sqrt{2\pi}} \exp\left[-\frac{1}{2}\left(\frac{\varepsilon_v^p - \varepsilon_N}{S_N}\right)^2\right] \end{aligned} \tag{2.25}$$

where $\dot{\varepsilon}_v^p$ represents the equivalent macroscopic plastic strain rate, f_N denotes the effective particle of the void nucleation, ε_N is the mean void nucleation and S_N is the standard deviation of the normal distribution [19]-[21]. The flow direction of the GTN plasticity model, is given by the follow expression:

$$\boldsymbol{N} = \boldsymbol{S} + \frac{1}{3} q_1 q_2 f \sigma_y \sinh\left(\frac{q_2 3p}{2\sigma_y}\right)\boldsymbol{I} \tag{2.26}$$

where $\boldsymbol{S}$ represents the deviatoric stress tensor and $\boldsymbol{I}$ is the second order tensor identity.

2.2.5 Bai–Wierzbicki model

Bai and Wierzbicki proposed a ductile damage model that includes the hydrostatic pressure dependency, through the stress triaxiality and the effect of the third deviatoric stress

invariant, through the Lode angle [25]. These effects were coupled to the *Von Mises* plasticity model (based on yield function), by redefining the hardening rule of the material. In the Bai-Wierzbicki model, the hardening rule is based on the accumulated plastic strain, stress triaxiality and the Lode angle parameter. In this subsection the relevant stress parameters are defined and the hardening law defined.

The formulation of Bai-Wierzbicki model requires the definition of several variables, which are expressed in terms of the three invariants of the stress tensor, $\boldsymbol{\sigma}$. Hydrostatic pressure p, the *Von Mises* equivalent stress q and the stress triaxiality η were previously referred. However, for the sake of completeness these parameters are redefined again in Eqs. (2.27), (2.28), and (2.29). The parameter based on the third invariant of the deviatoric stress tensor, is defined in Eq. (2.30).

$$p = \sigma_m = \frac{1}{3} tr(\boldsymbol{\sigma}) = \frac{1}{3}\left(\sigma_1 + \sigma_2 + \sigma_3\right) = \frac{I_1}{3} \tag{2.27}$$

$$q = \left(\frac{3}{2}\boldsymbol{S} : \boldsymbol{S}\right)^{\frac{1}{2}} = \left(\frac{1}{2}\left[\left(\sigma_1 - \sigma_2\right)^2 + \left(\sigma_2 - \sigma_3\right)^2 + \left(\sigma_3 - \sigma_1\right)^2\right]\right)^{\frac{1}{2}} = \left(3J_2\right)^{\frac{1}{2}} \tag{2.28}$$

$$\eta = \frac{p}{q} = \frac{\sigma_m}{q} \tag{2.29}$$

$$r = \left(\frac{9}{2}\boldsymbol{S}\cdot\boldsymbol{S} : \boldsymbol{S}\right)^{\frac{1}{3}} = \left[\frac{27}{2}\det \boldsymbol{S}\right]^{\frac{1}{3}} = \left(\frac{27}{2} S_1 S_2 S_3\right)^{\frac{1}{3}} = \left(\frac{27}{2} J_3\right)^{\frac{1}{3}} \tag{2.30}$$

In the previous equations, $\boldsymbol{S}$ is the deviatoric stress tensor, defined as:

$$\boldsymbol{S} = \boldsymbol{\sigma} - p\boldsymbol{I} \tag{2.31}$$

$\boldsymbol{I}$ is the second order identity tensor and σ_1, σ_2 and σ_3 denote the principal stresses. Concerning the stress triaxiality (Eq. (2.29)), it is defined as the ratio between the pressure and the *Von Mises* equivalent stress. In other words, the stress triaxiality relates the deviatoric and hydrostatic part of the stress state.

Another important parameter of the stress tensor in the formulation of the Bai-Wierzbicki damage model is the Lode angle, θ. This parameter is associated to the normalized third deviatoric stress invariant, ξ [27][28] as defined by Eq. (2.32). According to the range of Lode angle ($0 \leq \theta \leq \pi/3$), the range of ξ is defined as $-1 \leq \xi \leq 1$ [29]. Consequently, the Lode angle can be normalized according to Eq. (2.33)where $\bar{\theta}$ represents the Lode angle parameter assuming the same range of the normalized third deviatoric stress invariant.

$$\xi = \left(\frac{r}{q}\right)^3 = \frac{27}{2}\frac{J_3}{\left(3J_2\right)^{3/2}} = \cos\left(3\theta\right) \tag{2.32}$$

$$\bar{\theta} = 1 - \frac{6\theta}{\pi} = 1 - \frac{2}{\pi}\arccos\xi \tag{2.33}$$

In the Haigh-Westergaard space (see Figure 2.6), the stress vector $\overrightarrow{OP}$ represents the stress state (σ_1, σ_2, σ_3). The vector can be represented using a cylindrical coordinate system (μ, θ, z). The z – *axis* is named hydrostatic axis, where the principal stress have the same value. The plane passing through the origin O and is perpendicular to z − *axis*, is called the deviatoric plane. In cylindrical coordinate system the stress vector can be decomposed into vectors, which are perpendicular to the octahedral plane i.e. $\overrightarrow{OO'}$ and in the octahedral plane i.e. $\overrightarrow{O'P}$. The vector $\overrightarrow{O'P}$ represents the deviatoric term and hydrostatic pressure is described by $\overrightarrow{OO'}$. The direction between the stress vector, $\overrightarrow{OP}$ and π-*plane* or deviatoric plane is given by the angle ϕ which is related with the stress triaxiality. This angle, so-called by elevator angle is responsible for the size of yield surface. In turn, the Lode angle, θ, differentiates the stress state between tension, shear and compression. In the literature, two different definitions can be found for Lode angle. The first one [30]-[32] defines the Lode angle as the angle to the positive direction of the $\sigma_1 = -\sigma_3$ axis, as represented in the Figure 2.7 which illustrates the geometrical representation of the principal stresses on the octahedral plane. On the other hand, in [33]-[36] the Lode angle is defined as the positive angle to the positive direction of σ_1 (see Figure 2.7). In the present work the last definition was used.

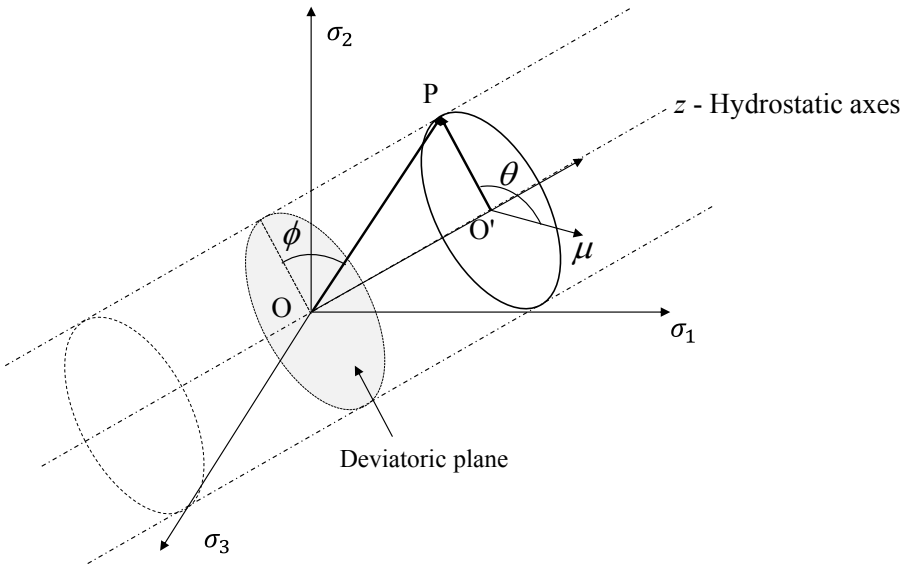

Figure 2.6 – Representation of the stress state vector in the Haigh-Westergaard space and cylindrical coordinates [26].

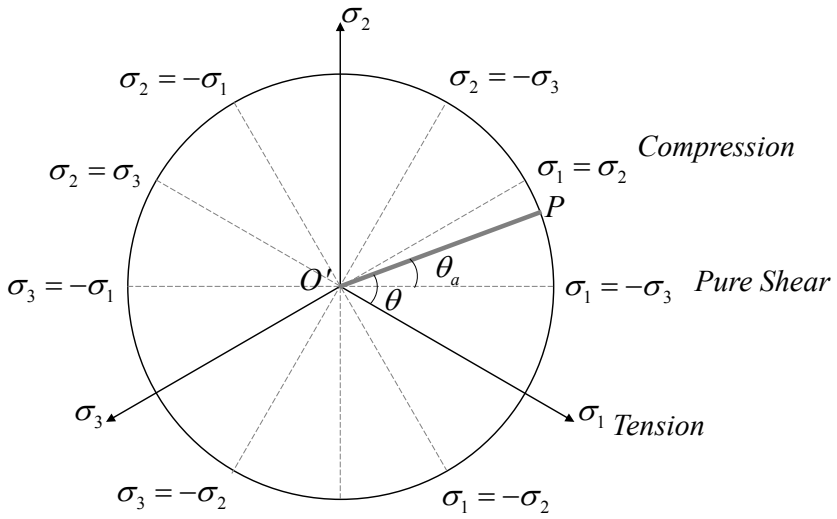

Figure 2.7 – Geometrical representation of the principal stresses on the octahedral plane (adapted from [37]).

Regarding to the yield function, it is dependent of the accumulated plastic strain, the triaxiality and the parameter μ related with Lode angle parameter as expressed in Eq. (2.34). The new proposition for the yield criteria is obtained by replacing the standard hardening rule $\sigma_y(\bar{\varepsilon}^p)$ by $\sigma_y(\bar{\varepsilon}^p, \eta, \mu)$ on the usually plasticity model based on *Von Mises* yield criterion.

$$\Phi = q - \sigma_y\left(\bar{\varepsilon}^P, \eta, \mu\right),$$
$$\Phi = q - \sigma_y\left(\bar{\varepsilon}^P\right)\cdot\left[1 - C_\eta(\eta - \eta_0)\right]\cdot\left[C_\theta^s + \left(C_\theta^{ax} - C_\theta^s\right)\left(\mu - \frac{\mu^{m+1}}{m+1}\right)\right] \tag{2.34}$$

According to the yield criterion definition, the hardening rule is given by the following expression:

$$\sigma_y\left(\bar{\varepsilon}^P, \eta, \mu\right) = \sigma_y\left(\bar{\varepsilon}^P\right)\cdot\left[1 - C_\eta(\eta - \eta_0)\right]\cdot\left[C_\theta^s + \left(C_\theta^{ax} - C_\theta^s\right)\left(\mu - \frac{\mu^{m+1}}{m+1}\right)\right] \tag{2.35}$$

where $\sigma_y(\bar{\varepsilon}^P)$ is the material strain hardening function, C_η, $C_\theta{}^s$, $C_\theta{}^{ax}$, and m represent the material parameters obtained with experimental procedures, η_0 is reference value of the stress triaxiality and μ denotes a parameter defined as a function of the Lode angle.

$$\mu = \frac{\cos(\pi/6)}{1 - \cos(\pi/6)}\cdot\left[\sec\left(\theta - \frac{\pi}{6}\right) - 1\right] \tag{2.36}$$

A simplified expression of the yield function can be obtained through the following functions defined in Eq. (2.37) and Eq. (2.38). The final expression for the yield criteria used in the BW model is given by Eq.(2.39).

$$A(\eta) = \left[1 - C_\eta(\eta - \eta_0)\right] \tag{2.37}$$

$$B(\mu) = \left[C_\theta^s + \left(C_\theta^{ax} - C_\theta^s\right)\left(\mu - \frac{\mu^{m+1}}{m+1}\right)\right] \tag{2.38}$$

$$\Phi = q - \sigma_y\left(\bar{\varepsilon}^P\right)\cdot A(\eta)\cdot B(\mu) \tag{2.39}$$

One key information for the constitutive model formulation is the definition of the flow vector which results from the differentiation of the yield function, $\partial\Phi/\partial\boldsymbol{\sigma}$. The flow vector of the BW plasticity model is given by the following expression:

$$\boldsymbol{N} = \frac{3\alpha}{2q}\boldsymbol{S} + \frac{3\lambda}{2q}\boldsymbol{S}^2 + \frac{\beta}{3}\boldsymbol{I} \tag{2.40}$$

with the parameters α, λ and β defined as follows:

$$\alpha = 1 - \frac{\sigma_y\left(\bar{\varepsilon}^P\right)}{q}\left(C_\eta.B(\mu).\eta\right) \tag{2.41}$$

$$\lambda = \frac{3\sigma_y\left(\bar{\varepsilon}^P\right)A(\eta)D(\theta)}{q^2} \tag{2.42}$$

$$\beta = \frac{\sigma_y\left(\bar{\varepsilon}^P\right)}{q}\left[C_\eta.B(\mu) - \frac{9A(\eta)D(\theta)}{2q^2}\left(tr\left(\boldsymbol{\sigma}^2\right) - \frac{tr(\boldsymbol{\sigma})^2}{3}\right)\right] \tag{2.43}$$

$$D(\theta) = \frac{\sqrt{3}}{2-\sqrt{3}}\frac{\tan(\theta-\pi/6)}{\cos(\theta-\pi/6)}\frac{1}{\sin(3\theta)}\left(C_\theta^{ax} - C_\theta^{s}\right)\left(1-\mu^m\right) \tag{2.44}$$

2.2.5.1 Experimental evidences of triaxiality, Lode angle and plastic strain influences on monotonic ductile failure

In this section a literature review about the influence of the stress triaxiality, Lode angle parameter and the equivalent plastic strain on monotonic ductile failure is described. There are several standards that establish the experimental procedures to perform monotonic tensile tests, namely the Portuguese standard NP EN 10002-1 [38] and the American standard ASTM E646 [39]. These standards refer to small-scale tests on smooth specimens aiming at deriving the basic mechanical strength properties or elastoplastic properties. Additionally, monotonic tensile tests on notched specimens have been proposed to investigate the failure conditions under complex stress states. These complex stress states can be characterized by the stress triaxiality and the Lode angle parameters, which together with the equivalent plastic strain can describe the plastic failure conditions, as demonstrated by Bao [40], Bai [36] and Coppola [16]. In the experimental program performed by Bao [40] on 2024-T351 aluminium alloy, various stress states, covering distinct combinations

of stress triaxialities and deviatoric stress parameters (related with Lode angle parameter), were tested leading distinct fracture strains. The specimens geometries used in this experimental work are illustrated in Figure 2.8 and the different values of fracture strain, stress triaxiality and Lode angle parameter are expressed in the Table 2.1. Plotting the results of Table 2.1 on the plane $\{\eta,\bar{\theta}\}$ it is possible to correlate the stress state with the experimental tests typology. A particular attention was given by Wierzbicki [41] for the condition of plane stress state, σ_3=0, which uniquely relates the stress triaxiality and Lode angle parameter as defined by the Eq. (2.45) which is plotted in the Figure 2.9 including the particular cases: axial symmetry tension and compression and plastic plane strain or generalized shear.

$$\xi = \cos\left[\frac{\pi}{2}\left(1-\bar{\theta}\right)\right] = -\frac{27}{2}\eta\left(\eta^2 - \frac{1}{3}\right) \tag{2.45}$$

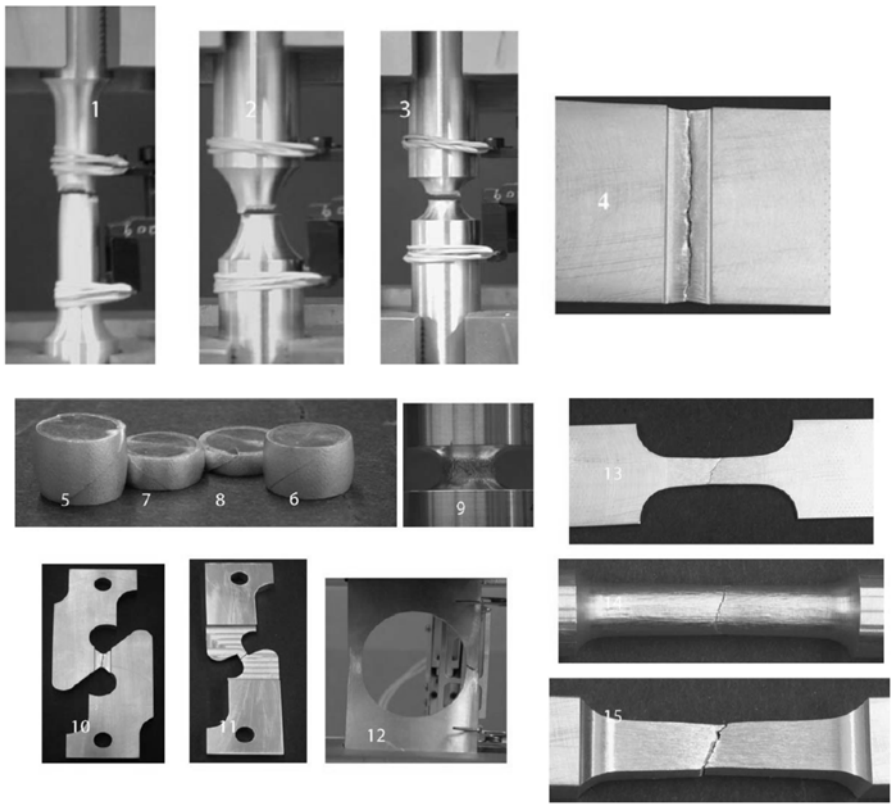

Figure 2.8 – Specimens used on monotonic tests of aluminium performed by Bao [40].

Table 2.1 – Summary of the experimental program carried out by Bao [40].

Test reference	Specimen description	$\bar{\varepsilon}_f$	η	$\bar{\theta}$
1	Round, smooth	0.46	0.40	1.0
2	Round, large notch	0.28	0.63	1.0
3	Round, small notch	0.17	0.93	1.0
4	Flat-grooved	0.21	0.61	0.097
5	Cylinder (d_0/h_0 = 0.5)	0.45	-0.278	-0.91
6	Cylinder (d_0/h_0 = 0.8)	0.38	-0.234	-0.81
7	Cylinder (d_0/h_0 = 1.0)	0.356	-0.233	-0.82
8	Cylinder (d_0/h_0 = 1.5)	0.341	-0.224	-0.80
9	Round notched (compression)	0.62	-0.248	-0.84
10	Flat dog-bone tensile	0.21	0.0124	0.055
11	Flat	0.26	0.117	0.5
12	Plate with a circular hole	0.31	0.343	1.0
13	Dog-bone	0.48	0.357	0.979
14	Pipe	0.33	0.356	0.984
15	Solid bar	0.36	0.369	1.0

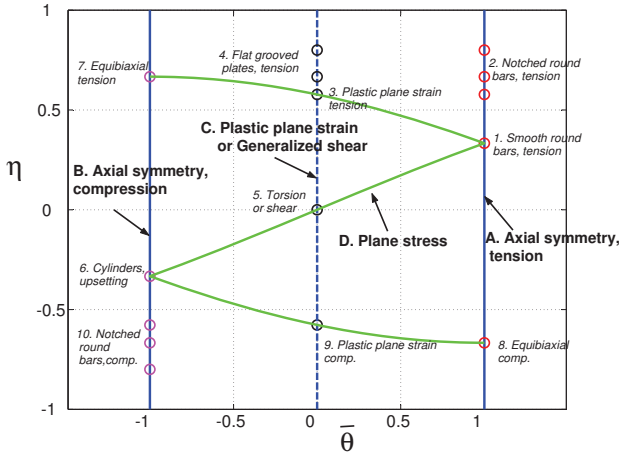

Figure 2.9 – Representation of the failure conditions for different tests on the η, $\bar{\theta}$ plane [40].

As previously referred, in this work the Lode angle is defined as the angle between the actual stress state and the positive direction of σ_1 axis, on the deviatoric plane. In order to better illustrate the evolution of the Lode angle in the principal stress space, numerical simulations under elastic domain were conducted on appropriated geometries, which are represented through the finite element meshes in the Figure 2.10. In detail, three round bars, two flat-grooved specimens with different widths and a pure shear specimen were simulated. The selection of the geometries aimed to cover the different stress state conditions that result in different J_2 and J_3 deviatoric stress invariants.

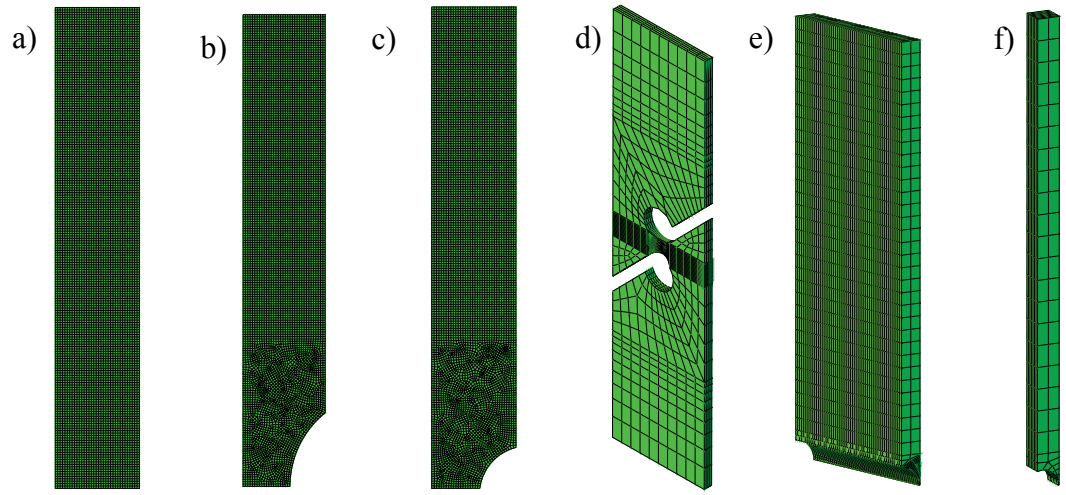

Figure 2.10 – Geometries used in the stress triaxiality and Lode angle parameter assessment: a) smooth round bar; b) round bar with large notch; c) round bar with small notch; d) shear specimen; e) flat-grooved specimen with large width; f) flat-grooved specimens with small width.

The principal stresses of each simulation were normalized and plotted in the space of the three principal stresses (Haigh-Westergaard space), as represented in the Figure 2.11. A relation between the Lode angle parameter and the θ angle is clearly observed. On effect, the angle θ increases with the decreasing of the Lode angle parameter. In other words, the Lode angle assumes 0º for tension ($\bar{\theta}$=1) state and tends to 30º (π/6) in the pure shear ($\bar{\theta}\approx$0). The "+" and "x" marks represent an intermediate stress state of the Lode angle parameter, which are associated to the flat-grooved geometries. For these geometries it would be expected to obtained $\bar{\theta}$=0. However, the pure elastic simulations cannot reproduce the plastic plane strain conditions and the increase of the specimen width is not sufficient to attain this condition. In detail for the specimen with the large width a Lode angle parameter $\bar{\theta}$=0.44, was achieved while for the specimen with small width the Lode angle parameter is $\bar{\theta}$=0.88. The evolution of the stress triaxiality, η can be also analysed from the Figure 2.11. In fact, this parameter defines the projected distance between the origin O and any stress point, in the octahedral plane. The lower value of stress triaxiality results on higher distance to the origin O. This assumption can be supported by the analysis of the data points plotted along σ_1 derived from the finite element simulations of round bar specimens. For the smooth round bar a stress triaxiality of η=0.33 was obtained and in contrast the notch severity leads to an increases of this parameter. The stress state conditions of smooth round bar and pure shear specimens can be analytically derived and they are summarized in the Table 2.2 and Table 2.3, where the triaxiality and Lode angle parameter are given.

Table 2.2 – Analytical procedure for the computation of stress state parameters of smooth round bar specimens.

Smooth round bar
1. Stress conditions $\sigma_1 = \sigma; \sigma_2 = 0; \sigma_3 = 0;$
2. Stress tensors and hydrostatic pressure $[\sigma] = \begin{bmatrix} \sigma & 0 & 0 \\ 0 & 0 & 0 \\ 0 & 0 & 0 \end{bmatrix}; [s] = \begin{bmatrix} \sigma - \sigma/3 & 0 & 0 \\ 0 & -\sigma/3 & 0 \\ 0 & 0 & -\sigma/3 \end{bmatrix}; p = \frac{1}{3}\sigma$
3. Deviatoric stress invariants $J_2 = \frac{1}{2}\left(\left(\frac{2\sigma}{3}\right)^2 + \left(-\frac{\sigma}{3}\right)^2 + \left(-\frac{\sigma}{3}\right)^2\right) = \frac{\sigma^2}{3}$ $J_3 = \frac{2\sigma}{3} \times \left(-\frac{\sigma}{3}\right) \times \left(-\frac{\sigma}{3}\right) = \frac{2\sigma^3}{27}$
4. Stress parameters $\{\eta, \bar{\theta}\}$ $\eta = \frac{p}{q} = \frac{p}{\sqrt{3J_2}} = \frac{\sigma}{3\sqrt{3J_2}} = \frac{\sigma}{3\sqrt{3 \times \frac{\sigma^2}{3}}} = \frac{1}{3}$ $\xi = \frac{27}{2}\frac{J_3}{q^3} = \frac{27}{2} \times \frac{2\sigma^3}{27\sigma^3} = 1$ $\bar{\theta} = 1 - \frac{2}{\pi} a\cos(\xi) = 1$

Table 2.3 – Analytical procedure for the computation of stress state parameters of pure shear specimens.

Pure shear
1. Stress conditions $\sigma_1 = -\sigma_3 = \sigma; \sigma_2 = 0; \sigma_3 = -\sigma;$
2. Stress tensors and hydrostatic pressure $[\sigma] = [s] = \begin{bmatrix} \sigma & 0 & 0 \\ 0 & 0 & 0 \\ 0 & 0 & -\sigma \end{bmatrix}; p = 0$
3. Deviatoric stress invariants $J_2 = \frac{1}{2}\left(\sigma^2 + \left(-\sigma^2\right)\right) = \sigma^2$ $J_3 = 0$
4. Stress parameters $\{\eta, \bar{\theta}\}$ $\eta = \frac{p}{q} = \frac{p}{\sqrt{3J_2}} = \frac{0}{3\sqrt{3J_2}} = 0$ $\xi = \frac{27}{2}\frac{J_3}{q^3} = \frac{27}{2} \times \frac{0}{\sigma^3} = 0$ $\bar{\theta} = 1 - \frac{2}{\pi} a\cos(\xi) = 0$

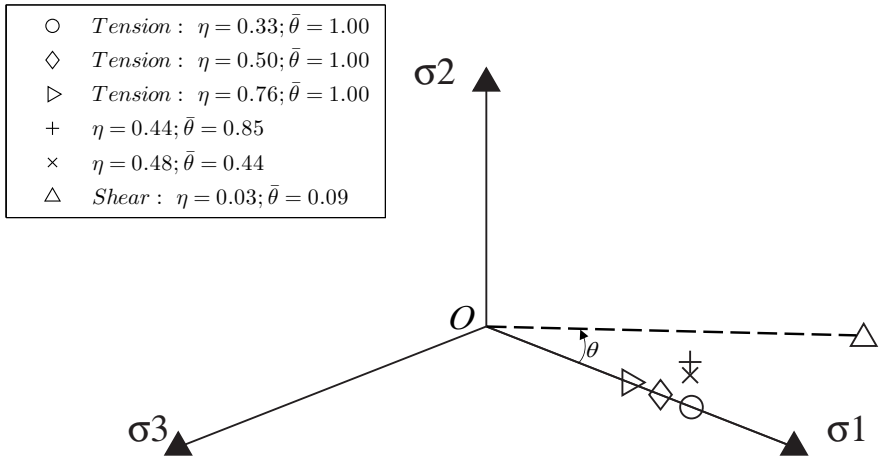

Figure 2.11 – Representation of typical stress states on octahedral plane, resulting from elastic simulation of specimens from Figure 2.10.

The combination of the equivalent strain at fracture (fracture strain) with the respective stress triaxiality and the deviatoric stress parameter allows the definition of the monotonic ductile failure locus. This corresponds to an extension of Wilkin and Johnson–Cook models, which was suggested by Wierzbicki and Xue. The latter researchers suggested a symmetric 3D fracture surface in the stress triaxiality and deviatoric stress parameters space, as represented in Figure 2.12. Nevertheless, the symmetry conditions of the 3D fracture surface for $\bar{\theta} = 0$ is not supported by the experimental evidences. In fact, the upsetting tests performed by Bao [40] allow calibrating the fracture strain in the entire range of stress triaxialities as shown in Figure 2.13. Therefore, two distinct ductility curves can be identify for both $\bar{\theta} = 1$ (corresponding to axial symmetry in deviatoric tension) and $\bar{\theta} = -1$ (corresponding to axial symmetry in deviatoric compression), which means that the loss of ductility in upsetting tests are due to the Lode angle parameter $\bar{\theta}$. These boundary limits together with the condition of $\bar{\theta} = 0$ that corresponds to the plastic plane strain or generalized shear, are sufficient to calibrate the 3D fracture locus in the space of $(\bar{\varepsilon}_f, \eta, \bar{\theta})$. Thus, the following formulation for the 3D fracture surface was proposed by Bai and Wierzbicki [29] (note that these authors used the Lode angle parameter $\bar{\theta}$ instead of the deviatoric stress state parameter, ξ, in the formulation of the fracture locus):

$$\begin{aligned}\bar{\varepsilon}_f\left(\eta,\bar{\theta}\right) &= \left[\frac{1}{2}\left(\hat{\varepsilon}_f^{(+)}+\hat{\varepsilon}_f^{(-)}\right)-\hat{\varepsilon}_f^{(0)}\right]\bar{\theta}^2+\frac{1}{2}\left(\hat{\varepsilon}_f^{(+)}+\hat{\varepsilon}_f^{(-)}\right)\bar{\theta}+\hat{\varepsilon}_f^{(0)} \\ &= \left[\frac{1}{2}\left(D_1e^{-D_2\eta}+D_5e^{-D_6\eta}\right)-D_3e^{-D_4\eta}\right]\bar{\theta}^2+\frac{1}{2}\left(D_1e^{-D_2\eta}-D_5e^{-D_6\eta}\right)\bar{\theta} \\ &\quad +D_3e^{-D_4\eta}.\end{aligned} \tag{2.46}$$

where D_1, D_2, D_3, D_4, D_5, and D_6 represents the material fitting parameters. The analysis of the Eq. (2.46) shows that terms $D_1e^{-D_2\eta}$, $D_3e^{-D_4\eta}$ and $D_5e^{-D_6\eta}$ are associated with the three limiting cases, $\hat{\varepsilon}_f{}^{(+)}$, $\hat{\varepsilon}_f{}^{(-)}$ and $\hat{\varepsilon}_f{}^{(0)}$, respectively. A geometrical representation of the new fracture locus in the 3D space is shown in Figure 2.14. Concerning the 3D fracture locus calibration, at least six different tests are necessary to achieve the six model constants. As referred above the cylinders upsetting tests are adequate to calibrate the boundary limit, $\hat{\varepsilon}_f{}^{(-)}$ while the so-called upper bound limit [23] can be obtained for the monotonic tensile tests of smooth and notched specimens.

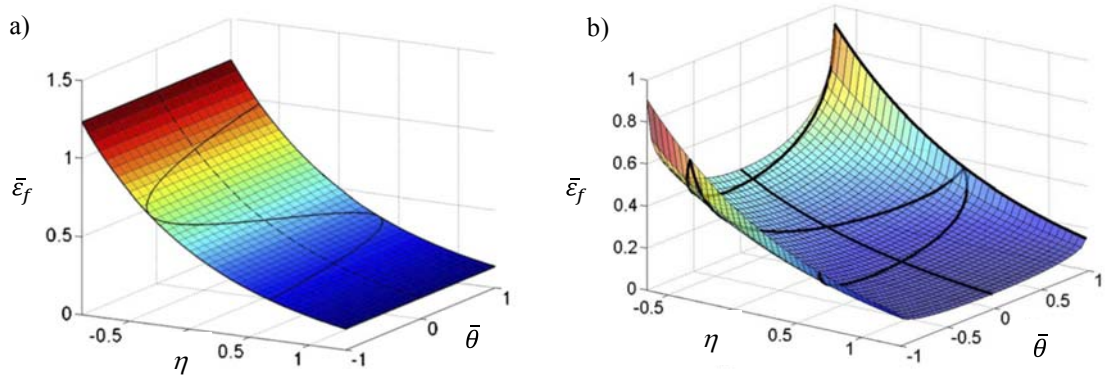

Figure 2.12 – a) The fracture surface independent of $\bar{\theta}$ postulated by Johnson and Cook [12] and b) a 3D symmetric fracture surface dependent of $\bar{\theta}$ developed by Wierzbicki and Xue [41].

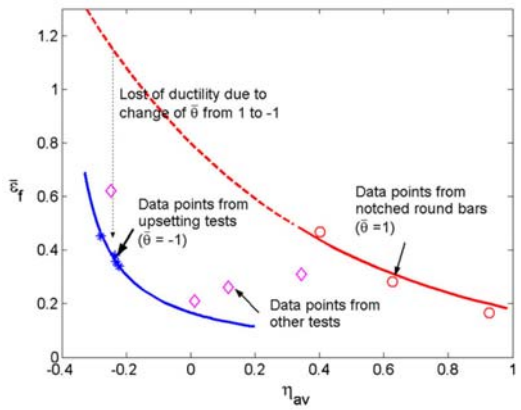

Figure 2.13 – A new interpolation of Bao's data points of aluminum 2024-T351 [29].

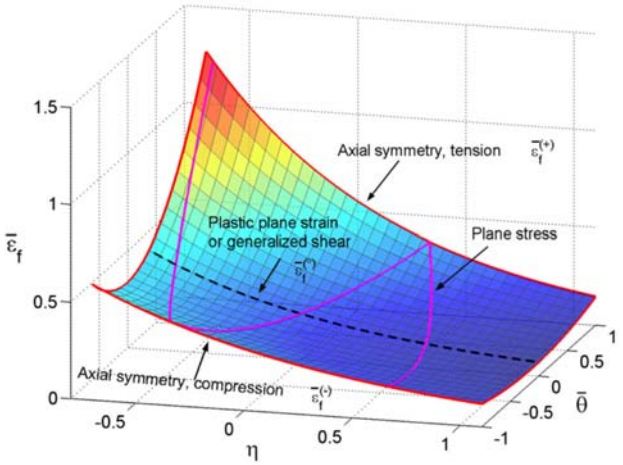

Figure 2.14 – A new design of 3D asymmetric fracture surface [29].

In order to derive the constants D_5 and D_6 that allow the definition of the lower ductility limit of the fracture locus [23], flat grooved, torsion or shear specimens can be used. Therefore, an experimental program of flat grooved plates with different notch radius and torsion of tubular specimen of 1045 steel grade (AISI standard) was conducted (see Figure 2.15) [29]. The flat-grooved specimens provide a wide range of fracture strains and stress triaxialities, keeping constant the Lode angle parameter, $\bar{\theta} = 0$. A different strategy was adopted by Coppola [16] that used torsion and flattening tests to obtain the lower bound limit of the 33MnB5 steel grade (UNI standard). The upper bound and lower bound limits in the space of fracture strain and stress triaxiality are illustrated in the Figure 2.16 using results from Bai and Coppola for two steels. Taking into account the formulation of the 3D fracture surface described previously, the fracture locus obtained by Bai for 1045 steel is illustrated in Figure 2.17. It should be noted that due to lack of experimental tests available under the loading condition of axial symmetric compression, $\bar{\theta} = -1$ the 3D fracture surface was assumed as symmetric.

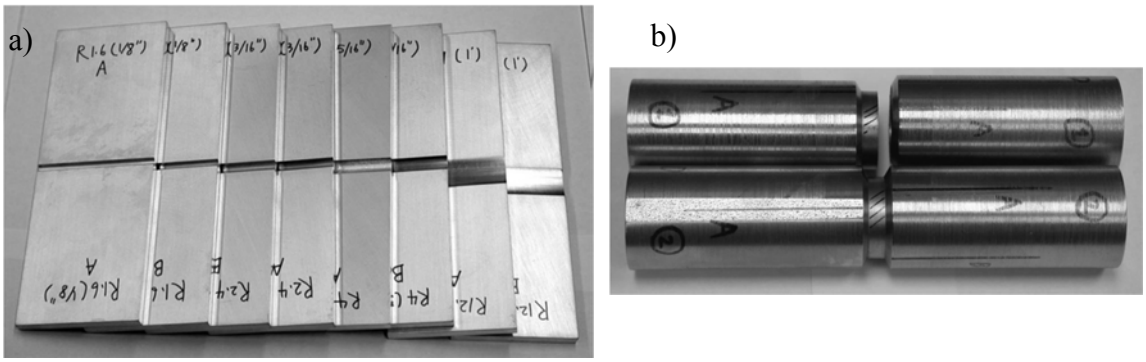

Figure 2.15 – Flat grooved specimens a) and specimens for pure torsion b) of 1045 steel [29].

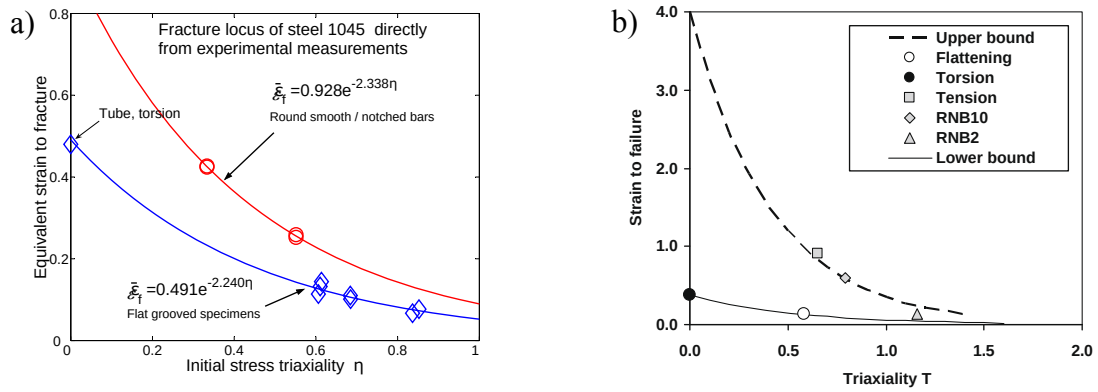

Figure 2.16 – Upper and lower boundary limits in the space of fracture strain and stress triaxiality for two steels: a) Bai experiments [36]; b) Coppola experiments [16].

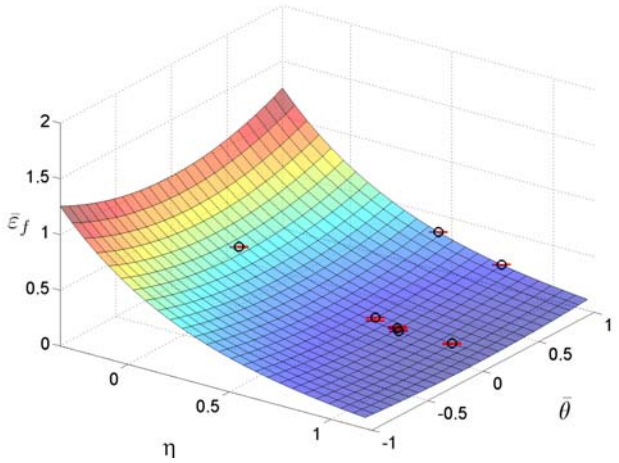

Figure 2.17 – Calibrated 3D fracture surface locus for the 1045 steel from "classical" specimens [36].

Besides the use of the "classical" specimens to calibrate a 3D fracture surface, Bai used a new specimen design with butterfly shape to calibrate the fracture locus in the space of stress triaxiality and equivalent fracture strain [36]. Figure 2.18 shows the butterfly specimen used in the experimental campaign. Some specimens were tested under monotonic loading conditions while others were subjected complex loading conditions to study the loading history effect on fracture. A wide range of stress states was achieved under different loading angles. Therefore, the stress triaxiality, the Lode angle parameter and the fracture strain were computed for each loading case and the results are summarized in the Table 2.4. An optimization procedure was conducted in order to correlate the data points using the 3D failure locus formulation presented previously. This procedure allows deriving a 3D fracture surface for the 1045 steel that is illustrated in the Figure 2.19, which resulted differently from the one evaluated using the so-called "classical" specimens. The

comparison of the two 3D fracture locus for the 1045 steel can be performed by the analysis of Figure 2.20. It should be noted that the fracture locus obtained from "classical specimens" was assumed to be a symmetric surface, thus the red continuous line is representative of the both $\bar{\theta} = 1$ and $\bar{\theta} = -1$ stress conditions. In a general view, it is found that the fracture locus calibrated using butterfly specimens is higher than the one from "classical" specimens [36]. According to Bai, these differences may be supported by the mesh size effect. In fact, the fracture strain will increase when the mesh size decreases [42][43], mainly for ductile material with large deformations.

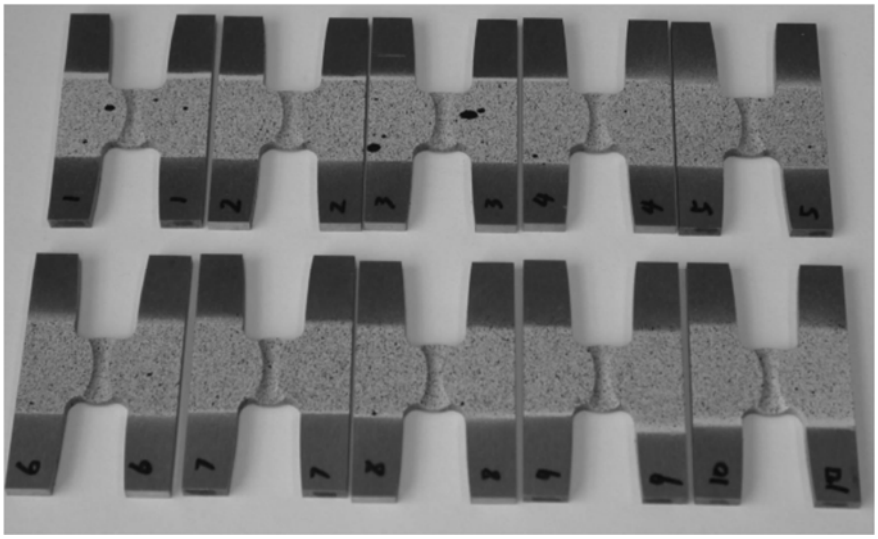

Figure 2.18 – Butterfly specimens tested under monotonic loading conditions [36].

Table 2.4 – Stress state parameters and fracture strains obtained from butterfly specimens for 1045 steel [36].

No.	Loading condition	η	$\bar{\theta}$	$\bar{\varepsilon}_f$
1	+90º, tension	0.8192	0.0955	0.1566
2	+30º, tension and shear	0.6892	0.6563	0.2359
3	+22º, tension and shear	0.6202	0.8482	0.2766
4	+10º, tension and shear	0.3750	0.5176	0.3553
5	+5º, tension and shear	0.2051	0.2442	0.4026
6	+0º, shear	-0.0214	-0.0206	0.8601
7	−5º, compression and shear	-0.1693	-0.3831	0.9655
8	−10º, compression and shear	-0.2547	-0.6081	1.1826

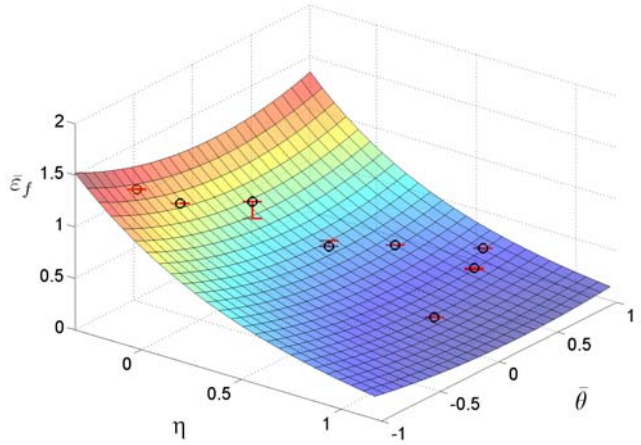

Figure 2.19 – Calibrated 3D fracture surface locus of 1045 steel from butterfly specimens [36].

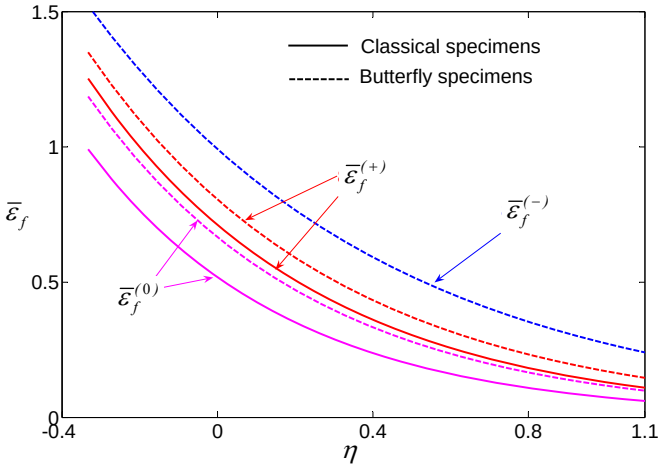

Figure 2.20 – Comparison of two fracture loci of 1045 steel calibrated from classical specimens and butterfly specimens in the plane of equivalent strain to fracture and stress triaxiality [36].

2.3 CYCLIC DAMAGE MODELS

Concerning the ULCF modelling, existing approaches reported in the literature may be classed into coupled and uncoupled ones [24]. Coupled models are supported by the interdependency between plasticity and damage. These models allow the simulation of crack initiation (damage onset) as also the crack propagation (damage spread). An example of these formulations was proposed by Lemaitre [17]. An extension of the GTN model for cyclic loading was proposed by Leblond et al. [44]. In particular, kinematic hardening was introduced in the porous plasticity model formulation, leading to the so called GTN-LPD

model [45]. In the domain of uncoupled models, damage does not influence the plastic behaviour. This approach can be very efficient for crack initiation modelling. There are some propositions in the literature for uncoupled ULCF models, which are supported by distinct physical assumptions. As referred by Komotori and Shimizu [46], the damage mechanism during a fatigue process changes whenever large or small plastic strain amplitudes are experienced. Consequently, fatigue life in ULCF regime is dominated by ductility, i.e., the large plastic deformations achieves an important fraction of the monotonic fracture strain, which may activate damage mechanisms more typical of monotonic damage, such as voids nucleation and growth [24]. Based on these assumptions, a fatigue model has been proposed by Kuroda [47] which divides the ULCF damage into the following three parts: (a) damage due to tensile straining; (b) damage due to ductility exhaustion due to cyclic loading; (c) damage due to crack propagation. Alternatively, Tateishi and Hanji [48] defined the total damage during ULCF loading as a linear summation between a tensile ductile part and a cyclic damage.

Xue [49] proposed an exponential damage rule for fatigue life prediction in the ULCF regime, which overcomes the overestimation limitation of the classical Coffin–Manson approach that has been cited in the literature [50]. Kanvinde and Deierlein [15] proposed a fatigue model based on cyclic behaviour of micro-voids that can also be classed as an uncoupled damage model, which postulates that material degradation, by micro-void growth, is a function of the plastic strain weighted by a triaxiality function.

In the present chapter, several uncoupled models are presented and proposals that have being suggested for the improvement of the performance of existing LCF fatigue models are presented. The classical Coffin-Manson LCF relation [51]-[52], the Tateishi model [48], the Kanvinde and Deierlein model [15] and Xue model [49] among others are described in this section.

2.3.1 Coffin-Manson relation

Coffin and Manson [51][52] proposed an empiric relation, which has been widely used for LCF, i.e. for fatigue domains involving plastic strains but typically not as intense as observed in ULCF regimes:

$$\frac{\Delta\varepsilon^P}{2} = \varepsilon'_f (2N_i)^c \tag{2.47}$$

Eq. (2.47) is represented by a linear relation in a bi-logarithm representation, where $\Delta\varepsilon^P/2$ and N_i are a uniaxial plastic strain amplitude and the number of cycles to crack initiation, respectively; ε'_f is the fatigue ductility coefficient and c is the fatigue ductility exponent, and both are considered material dependent constants. Some authors [47][48][50] have shown that the Coffin-Manson relation does not give a satisfactory description of the ULCF regime, for some tested metals. They report a fatigue life over prediction when the Coffin-Manson relation is used in ULCF domain. The original Coffin-Manson relation was proposed for uniaxial stress-strain conditions, but its generalization for multiaxial stress-strain conditions may be performed using an equivalent multiaxial strain definition. The Coffin-Manson model is assessed latter in the present research in order to verify its performance, since its simplicity is very attractive for using in practical designs. It is the basis of some design codes such as the ASME B&PVC, Section VIII, Div. 2 [53].

2.3.2 Tateishi model

The fatigue prediction model proposed by Tateishi states that the cyclic damage induced during the ULCF loading is a result of monotonic ductile and cyclic damage linear accumulation [48]. This model arises as an extension of Coffin-Manson relation, the main difference consisting in the introduction of a ductile damage factor, C_m, given by Eq. (2.48) :

$$\Delta\varepsilon^P N_i^k = C \cdot C_m$$
$$C_m = \begin{cases} \left(\dfrac{\overline{\varepsilon}_f - \varepsilon_{\max}}{\varepsilon_f - \varepsilon_{pD}} \right)^k & if \quad \varepsilon_{\max} > \varepsilon_{pD} \\ 1.0 & if \quad \varepsilon_{\max} \le \varepsilon_{pD} \end{cases}, \tag{2.48}$$

where k and C are directly obtained from Coffin-Manson relation, ε_{max} is the maximum value of strain and ε_{pD} is the damage strain threshold under pure tension.

2.3.3 Kanvinde and Deierlein cyclic void growth model

The ULCF model proposed by Kanvinde and Deierlein, arises as an extension of the monotonic ductile damage applied to cyclic loading conditions proposed by the same authors. Under cyclic loading, critical regions of the component experiences alternating positive and negative stress triaxialities. When triaxiality is positive, voids will grow; inversely, when triaxiality is negative, voids will shrink (average void radius will reduce). Thus, the sign of the triaxiality is used to differentiate tensile from compressive loading. The sign of the triaxiality governs the voids growth or shrinkage, while the magnitude of triaxiality and the equivalent plastic strain govern the rate of voids growth/shrinkage [15]. For a cyclic loading, Eq. (2.49) can be rewritten in the following more general form:

$$dR / R = sign(\eta) C \exp\left(\left|1.5\eta\right|\right) d\varepsilon_p \tag{2.49}$$

where the *sing(η)* term incorporates the influence of the hydrostatic pressure, p. Therefore, the void growth/shrinkage rate is controlled by the magnitude of the stress triaxiality and the equivalent plastic strain, whilst the sign of the stress triaxiality governs whether voids grow or shrink. The void growth/shrinkage during cyclic loading is captured by the integration of Eq. (2.49) over tensile compressive excursions of loading. The loading cycles can be subdivided into tensile and compressive, based on the sign of stress triaxiality. The evolution of the void radius along the cyclic loading, for tensile and compressive excursions is expressed as:

$$\ln\left(R / R_0\right)_{cyclic} = \sum_{tensile\,cycles} C_1 \int_{\varepsilon_1^P}^{\varepsilon_2^P} \exp\left(\left|1.5\eta\right|\right) d\varepsilon_p \; - \sum_{compressive\,cycles} C_2 \int_{\varepsilon_1^P}^{\varepsilon_2^P} \exp\left(\left|1.5\eta\right|\right) d\varepsilon_p \tag{2.50}$$

The first term of the previous equation contains the cumulative void growth over all tensile excursions. However, each excursion requires the computation of the integral between ε_1^P and ε_2^P plastic strains at the beginning and end of that tensile excursion. The same procedure is used for the compressive excursions, which is distinguished from the negative sign in the second term. The negative sign reflects the assumption that the negative triaxiality will cause void shrinkage. C_1 and C_2 are used to define the different growth or

shrinkage rates. Taking into account the lack of experimental evidence, Kanvinde and Deierlein considered $C_1=C_2=C$, from which the following expression is obtained:

$$\ln\left(R/R_0\right)_{cyclic} = C\left(\sum_{tensile\,cycles}\int_{\varepsilon_1^P}^{\varepsilon_2^P}\exp\left(\left|1.5\eta\right|\right)d\varepsilon_p - \sum_{compressive\,cycles}\int_{\varepsilon_1^P}^{\varepsilon_2^P}\exp\left(\left|1.5\eta\right|\right)d\varepsilon_p\right) \tag{2.51}$$

Following the same convention that previously allowed the definition of the monotonic void growth index, for cycling loading the void growth index is defined as follows:

$$VGI_{cyclic} = \\ = \frac{\ln\left(R/R_0\right)_{cyclic}}{C} = \sum_{tensile\,cycles}\int_{\varepsilon_1^P}^{\varepsilon_2^P}\exp\left(\left|1.5\eta\right|\right)d\varepsilon_p - \sum_{compressive\,cycles}\int_{\varepsilon_1^P}^{\varepsilon_2^P}\exp\left(\left|1.5\eta\right|\right)d\varepsilon_p \tag{2.52}$$

VGI_{cyclic} increases and decreases during cycling, but this parameter cannot assume negative values. If VGI_{cyclic} decreases to zero, it remains at zero until a subsequent "tensile" cycle increases its value above zero. Similarly to monotonic ductile fracture, ULCF failure occurs when VGI_{cyclic} reaches a critical value, $VGI_{cyclic} \leq VGI_{cyclic}^{critical}$. Kanvinde and Deierlein proposed, for the critical cyclic void growth index, $VGI_{cyclic}^{critical}$, an exponential decay function of the critical monotonic void growth index:

$$VGI_{cyclic}^{critical} = VGI_{monotonic}^{cyclic}\exp\left(-\lambda\varepsilon_p^{accumulated}\right) \tag{2.53}$$

where λ is treated as a material-dependent damage coefficient. To compute the $VGI_{cyclic}^{critical}$ it is important to distinguish the equivalent plastic strain that increases over the entire loading and the damage variable, $\varepsilon_p^{accumulated}$, which is defined as the equivalent plastic strain that is accumulated up to the beginning of each tensile excursion of loading. Therefore, the increment of equivalent plastic strain during the current tensile loading does not contribute to the cyclic damage that occurs within that loading increment. The $VGI_{cyclic}^{critical}$ will show a discontinuous stepwise behaviour. However, recent studies carried out by Pereira [24] shows that λ parameter cannot be treated as a material constant but instead it depends on stress state itself. On effect, plotting the $R_{VGI}=VGI_{cyclic}^{critical}/VGI_{monotonic}^{critical}$ (computed for each geometry) against the accumulated equivalent plastic strain a distinct relation for each

tested geometry is evidenced (see Figure 2.21). In addition, an exponential relation can be found between the damage parameter λ and the fracture strain of each geometry as proven by the analysis of Figure 2.22. Consequently, a new exponential damage function was proposed by Pereira [24] to define the R_{VGI}, with the following form:

$$VGI_{cyclic}^{critical} = VGI_{monotonic}^{critical} \times exp\left[-C_1 exp\left(-C_2 \overline{\varepsilon}_f\right) \varepsilon_p^{accumulated}\right], \tag{2.54}$$

where C_1 and C_2 are material parameters and λ becomes dependent on the fracture strain of the component, which in turn depends on the triaxiality level of the component.

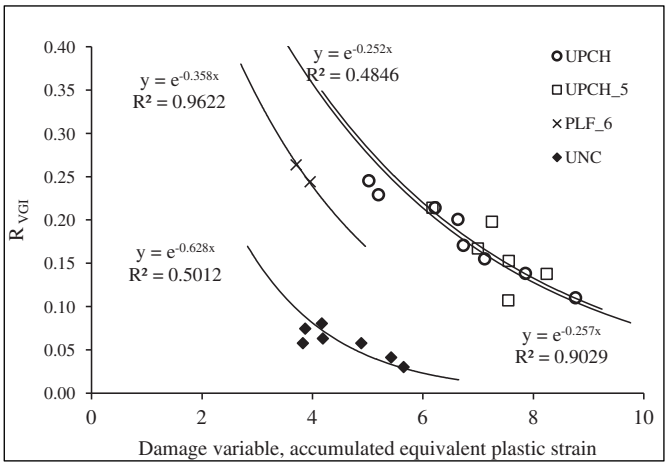

Figure 2.21 – Cyclic damage resistance evolution with the accumulated plastic strain obtained for S185 steel grade [24].

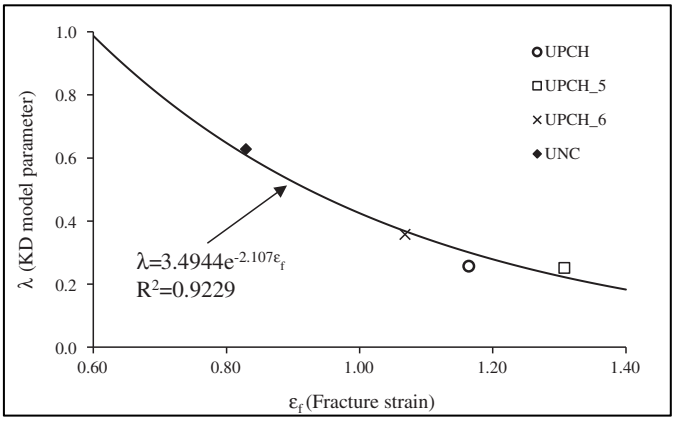

Figure 2.22 – Cyclic damage parameter versus fracture strain for each set of specimens [24].

2.3.4 Xue model

Xue [49] proposed a model for ULCF as an extension of the Coffin-Manson relation and assuming linear damage summation, according to Miner's rule [54]:

$$D = \frac{4n\Delta\varepsilon^P}{4N\Delta\varepsilon^P} = \frac{n}{N}, \tag{2.55}$$

where $\Delta\varepsilon^P$ is the plastic strain amplitude, n is the current number of applied cycles and N is the number of life cycles. The Coffin-Manson relation, is conveniently expressed in the alternative form to the Eq. (2.56):

$$\Delta\varepsilon^P \cdot N_i^k = C \tag{2.56}$$

where c and k are materials constants. Considering a specific type of periodic plastic loading with a strain ratio, $R_\varepsilon=0$, the monotonic loading can be assumed the limiting case of $N=1/2$. For this case, $\Delta\varepsilon^P = \bar{\varepsilon}_f$ and $C=\bar{\varepsilon_f}/2$. Xue also assumed that the cyclic plastic damage is governed by the equivalent plastic distortion, which may be defined using the three principal components of the plastic strain tensor as:

$$\varepsilon_d = \sqrt{\frac{2}{3}}\sqrt{\varepsilon_1^2 + \varepsilon_2^2 + \varepsilon_3^2} \tag{2.57}$$

The equivalent plastic distortion should be distinguished from the equivalent accumulated plastic strain, which takes into account the plastic strain accumulation along the loading [49]. A power law damage rule was proposed for monotonic loading, by differentiating the Coffin-Manson relation and knowing that the incremental plastic distortion is the same as the equivalent plastic strain, for each proportional loading branch as expressed:

$$dD = m\left(\frac{\varepsilon_d}{\bar{\varepsilon}_f}\right)^{(m-1)} \frac{1}{\bar{\varepsilon}_f} d\varepsilon_p \tag{2.58}$$

where $m=1/k$. Integrating Eq. (2.58) along the plastic loading path yields the plastic damage potential function for materials obeying the Coffin-Manson relation:

$$\Psi\left(\frac{\varepsilon_d}{\bar{\varepsilon}_f}\right)=\left(\frac{\varepsilon_d}{\bar{\varepsilon}_f}\right)^m \tag{2.59}$$

Based on experimental data, Xue proposed an alternative to the damage potential function, valid for fatigue life prediction in ULCF regime:

$$\Psi\left(\frac{\varepsilon_d}{\bar{\varepsilon}_f}\right)=\frac{e^{\lambda\frac{\varepsilon_d}{\bar{\varepsilon}_f}}-1}{e^{\lambda}-1} \tag{2.60}$$

where λ is a damage parameter, which is determined from experimental data by regression analysis. Using Eq.(2.60), the number of life cycles, as a function of strain amplitude, can be obtained by differentiation:

$$N_i=\frac{1}{2}\frac{e^{\lambda}-1}{e^{\lambda\left(\frac{\Delta\varepsilon^P}{\bar{\varepsilon}_f}\right)}-1} \tag{2.61}$$

However, Xue verified that neither the power law nor the exponential damage rules fits the complete range of life cycles from both LCF and ULCF regimes. Therefore a new function, based on m and λ parameters, was suggested to predict fatigue life in the range $1/2\sim10^4$ cycles [49]. In order to derive a new damage potential function for the entire fatigue regime, the influence of the plastic damage accumulation and the exponential damage rule for the ULCF regime can be combined through the joint effect of m and λ parameters:

$$\Psi\left(\frac{\varepsilon_d}{\bar{\varepsilon}_f}\right)=\frac{e^{\lambda\left(\frac{\varepsilon_d}{\bar{\varepsilon}_f}\right)^m}-1}{e^{\lambda}-1} \tag{2.62}$$

The damage rate is derived from Eq. (2.62) and expressed in Eq. (2.63) and the strain-life relationship for both LCF and ULCF range is defined by Eq. (2.64):

$$dD = \frac{m\lambda\left(\frac{\varepsilon_d}{\overline{\varepsilon}_f}\right)^{(m-1)} e^{\left(\lambda\left(\frac{\varepsilon_d}{\overline{\varepsilon}_f}\right)^m\right)}}{\left(e^{\lambda}-1\right)} \frac{d\varepsilon_p}{\overline{\varepsilon}_f} \tag{2.63}$$

$$N_i = \frac{1}{2}\frac{e^{\lambda}-1}{e^{\lambda\left(\frac{\varepsilon_d}{\overline{\varepsilon}_f}\right)^m}-1} \tag{2.64}$$

2.3.5 Dufailly and Lemaitre model

In order to estimate the fatigue life time in the range of 1~20 cycles a coupled damage model was proposed by Dufailly and Lemaitre [55]. This model is based on the definition of a kinematic damage law given by Eq. (2.65) which depends on the equivalent plastic strain rate, $\dot{\varepsilon}^P$:

$$\dot{D} = \left(\frac{T}{S}\right)^s \dot{\varepsilon}^P \tag{2.65}$$

$$\dot{\varepsilon}^P = \left(\frac{2}{3}\dot{\boldsymbol{\varepsilon}}^P : \dot{\boldsymbol{\varepsilon}}^P\right)^{1/2} \tag{2.66}$$

where S and s are the material constants. T represents the energy release rate, which is defined in Eq. (2.67) based on the stress triaxiality function, R_υ, expressed in Eq. (2.68) using, in turn, the Poisson coefficient, υ:

$$T = \frac{q^2 R_\upsilon}{2E\left(1-D\right)^2} \tag{2.67}$$

$$R_\upsilon = \frac{2}{3}\left(1+\upsilon\right) + 3\left(1-\upsilon\right)\left(\frac{p}{q}\right)^2 \tag{2.68}$$

The damage initiation can be defined through the accumulated plastic strain limit, $\bar{\varepsilon}^P{}_{accumulated}$, expressed as follows:

$$\varepsilon^{P}_{accumulated} < \bar{\varepsilon}^{P}_{accumulated} \rightarrow \dot{D} = 0 \tag{2.69}$$

Taking into account the ULCF damage mechanism, can be assumed that the accumulated plastic strain achieves the damage threshold at the end of the first cycle, which can be considered $\bar{\varepsilon}^{P}_{accumulated}=0$. The initiation of a macroscope crack is given by the condition, $D=D_c$, where D_c is the critical damage value that could be considered, $D_c=1$ [55]. Following the above assumptions it is possible rewrite the kinematic damage law as:

$$\dot{D} = \left(\frac{q^2 R_{\upsilon}}{2ES\left(1-D\right)^2} \right)^{s} \dot{\varepsilon}^{P}. \tag{2.70}$$

The application of Dufailly and Lemaitre damage relation for extreme cyclic loading can be performed, assuming a perfect plastic behaviour of the material due to the large plastic deformation levels. Therefore, the yield stress of the material, σ_s can be assumed as constant. Consequently, and taking into account the yield plastic criteria expressed in the Eq. (2.71) the damage increment for each cycle is defined in the Eq. (2.72) since q/(1-D) it is assumed as constant for each cycle.

$$\frac{q}{1-D} - \sigma_s = 0 \tag{2.71}$$

$$\frac{\Delta D}{\Delta N} = \left(\frac{\sigma_s^2 R_{\upsilon}}{2ES} \right)^{s} \Delta \varepsilon^{P} \tag{2.72}$$

Assuming a uniaxial tension stress state ($R_{\upsilon}=1$), Eq. (2.72) can be rewritten as:

$$\frac{\Delta D}{\Delta N} = \left(\frac{\sigma_s^2}{2ES} \right)^{s} \Delta \varepsilon^{P} \tag{2.73}$$

where $\Delta\varepsilon^P$ is defined as the plastic strain range. The number of cycles to failure can be computed integrating the previous expression between for following limits: $D \Longrightarrow 0 \longrightarrow 1$ and $N \Longrightarrow 0 \longrightarrow N_f$.

$$N_f = \left(\frac{2ES}{\sigma_s^2} \right)^s \frac{1}{2\Delta\varepsilon^P} \tag{2.74}$$

This relation is a simplified form of the Coffin-Manson relation.

2.3.6 Kuroda model

As referred by Komotori [46], the damage mechanisms during the fatigue process are different between the large and small plastic strain range regimes. Fatigue life in ULCF regime is dominated by ductility exhaustion, while in the LCF regime is governed by crack propagation. A cumulative fatigue damage model to predict the ULCF life was proposed by Kuroda [47], which consisted of an evolution of the works by Du [56]. Du [56] proposed a model for ULCF regime which divides the fatigue damage in two parts. The first part represents the state of a material loaded monotonically to the maximum point during the first cycle and is defined in Eq. (2.75):

$$D_s = \frac{\varepsilon_d^0}{\bar{\varepsilon}_f} \tag{2.75}$$

where ε_d^0 is the strain in the first cycle of loading and $\bar{\varepsilon}_f$ is the strain at fracture determined in a monotonic test. Concerning the second part of damage, it consists of the cyclic damage accumulation of all loading reversals, which can be obtained from Coffin-Manson relation:

$$D_c = \frac{\Delta\bar{\varepsilon}_d N_f^\alpha}{C} \tag{2.76}$$

where $\Delta\bar{\varepsilon}_d$ is the average strain range during the entire cyclic loading [47]. Taking into account the "static" and "cyclic" damage, the total damage can be defined by:

$$D_s + D_c = 1 \tag{2.77}$$

However, this model is not able to account for the effects of ductility exhaustion during cyclic loading nor elucidate clearly the physical meaning of the cyclic damage. Therefore, a new formulation that categorized the damage into the following three parts was developed by Kuroda [47]: (a) damage due to tensile loading; (b) damage due to ductility exhaustion during cyclic loading and (c) damage due to crack propagation. Concerning the damage due to tensile loading, it is verified that fracture occurs when the applied plastic strain reaches the fracture strain, during tensile tests. The damage level can be obtained from the ratio between the maximum tensile plastic strain applied and the plastic strain at fracture:

$$D_{tensile} = \frac{\varepsilon_{P\max}}{\overline{\varepsilon}_f} \tag{2.78}$$

where $\varepsilon_{Pmax}=\varepsilon_m+\varepsilon_{fr}$, ε_m is the mean strain applied initially and ε_{fr} is the residual ductility, as illustrated in Figure 2.23. The residual ductility tests are proposed to obtain unexhausted ductility by measuring the residual strain [47]. More detail information about these tests is described in [57]. Concerning the damage due to ductility exhaustion during cyclic loading, it is assumed that ULCF tests can be related with monotonic tensile tests, as referred by Ohji's hypothesis [58] as follows:

$$\Delta\varepsilon^P = 2\overline{\varepsilon}_f \tag{2.79}$$

$$N_f = 1/4 \tag{2.80}$$

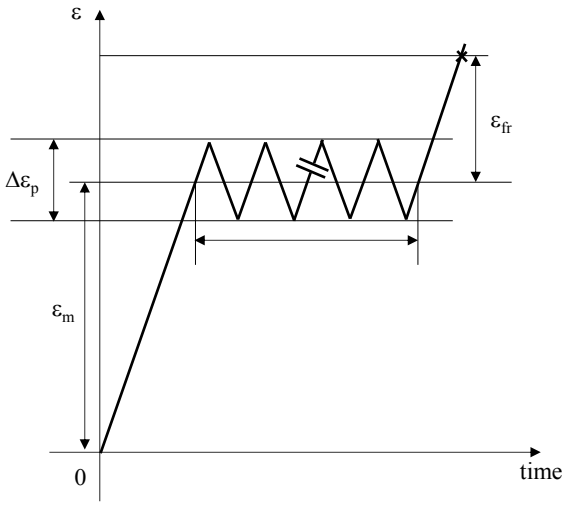

Figure 2.23 – Diagram of the strain pattern for residual ductility tests [47].

Substituting Eqs. (2.79) and (2.80) into Coffin-Mason relation and supposing that fatigue damage is linearly accumulated with strain cycling, as supported by Miner´s rule [54], the damage due to ductility exhaustion under cyclic loading can be expressed by Eq. (2.81):

$$D_{fatigue} = \frac{n}{N_f} = 4n\left(\frac{\Delta\varepsilon^P}{2\overline{\varepsilon}_f}\right)^{a'} \tag{2.81}$$

where $a'=1/\alpha$ and is a material constant which depends on the degree of ductility exhaustion. Besides the accumulated damage along the cyclic loading, the ductility exhaustion also depends on the accumulated damage along the tensile loading. In this way, ductility exhaustion can be obtained adding the $D_{tensile}$ and the $D_{fatigue}$:

$$D_{ductility} = \frac{\varepsilon_{P\max}}{\varepsilon_f} + 4n\left(\frac{\Delta\varepsilon_P}{2\varepsilon_f}\right)^{a'} \tag{2.82}$$

In LCF regime, the fatigue damage is dominated by the crack propagation and not by ductility exhaustion [57]. Damage due crack propagation has less influence when compared with ductility exhaustion during cyclic loading. Therefore it should be taken into account in ULCF regime. This damage is derived from a small crack growth law, proposed by Murakami [59], as expressed follows:

$$\frac{dl}{dn} = \beta \Delta \varepsilon_P^{\gamma} l \tag{2.83}$$

where β and γ are material constants and l represents the crack length. Integrating the previous equation between l_0 and l_f crack lengths, which corresponds to $n=0$ and $n=N_f$ respectively,

$$\int_{l_0}^{l_f} \frac{dl}{l} = \int_0^{N_f} \beta \Delta \varepsilon_P^{\gamma} dn \,, \tag{2.84}$$

results the following equation:

$$\frac{\Delta \varepsilon^P N_f^{\alpha'}}{C'} = 1 \tag{2.85}$$

where $\alpha' = 1/\gamma$ and $C' = \left(\frac{1}{\beta} \ln \frac{l_f}{l_0} \right)^{1/\gamma}$ represent material constants. Thus, the damage due crack propagation can be expressed as follows:

$$D_{crack} = \frac{\Delta \varepsilon^P N_f^{\alpha'}}{C'} \tag{2.86}$$

The relation between damage due to crack propagation and ductility exhaustion, when fracture occurs in ULCF regime, is defined as:

$$D_{ductility} + D_{crack} = 1 \tag{2.87}$$

Substituting Eqs. (2.82) and (2.86) into Eq. (2.87), the generalized expression is obtained, which allows to derive the number of cycles to the material failure, when the condition $n=N_f$ is attained:

$$\frac{\varepsilon_{P\max}}{\bar{\varepsilon}_f} + 4n \left(\frac{\Delta \varepsilon^P}{2\bar{\varepsilon}_f} \right)^{a'} + \frac{\Delta \varepsilon^P n^{\alpha'}}{C'} = 1 \tag{2.88}$$

2.3.7 GTN-LPD model

In order to investigate the possibility of micromechanics based models to characterize the cyclic plastic damage behaviour of the materials, a coupled damage model was developed by Leblond, Perrin and Devaux [44] which was named as LPD model. This model arises from an extension of the GTN model, originally applied in materials following isotropic plastic hardening and subjected to monotonic loading. In LPD model formulation, the GTN yield function is extended to account for kinematic hardening, by replacing the Cauchy stress tensor by the difference of the Cauchy stress and back-stress tensors [45]. The resulting yield function is then represented by the following form:

$$F_{LPD} = \frac{3}{2}\frac{(\mathbf{S}:\mathbf{S})}{\bar{\sigma}_1^2} + 2f_v^* \cosh\left(q_2 \frac{-3tr(\mathbf{S})}{2\bar{\sigma}_2^2}\right) - \left(1 + q_3 f_v^{*2}\right) = 0 \tag{2.89}$$

2.3.8 Micromechanical cyclic void growth model for ULCF

The effects of the stress triaxiality and Lode angle parameters on the microscopic damage mechanisms was investigated by Kiran and Khandelwal [64] by means of a detailed micromechanical study, based on a numerical model of material volume cell that is represented in the Figure 2.24. Material volume cells were loaded cyclically by changing the stress triaxiality values (reported as T_σ by Kiran and Khandelwal) and keeping constant the Lode angle parameter, $|L|=1$ (defined as L by Kiran and Khandelwal). According to the investigation carried out by Karin and Khandelwal considerations about the stress triaxiality influence on microvoids elongation and dilatation were performed [64]:

i) The void volume fraction decreases when the equivalent plastic strain increases at triaxiality levels close to zero.

ii) For low values of triaxiality ($T_\sigma \approx 0.33$) an increase of void volume fraction is verified at positive triaxiality peaks and a decreasing of the microvoid volume occurs for negative peaks of triaxiality.

iii) In turn, the elongation of the microvoids is verified under both positive and negative triaxiality peaks.

iv) With the increase of the stress triaxiality levels the void volume fraction or the microvoid dilation growth more rapidly.

v) Concerning the void elongation, at medium stress triaxiality ($T_\sigma \approx 0.75$), at low equivalent plastic strain values, microvoid elongates in both positive and negative triaxiality cycles; at high stress triaxiality levels ($T_\sigma \approx 1.0$) microvoid increases only in the negative triaxiality cycles [64].

The influence of Lode angle parameter was also inspected on the micromechanical damage mechanism. Thus, material volume cells with a microvoid were submitted to cyclic loads covering several Lode angle parameters levels ($|L| \in \{0, 0.33, 0.67, 1.0\}$) fixing a constant magnitude of triaxiality ($|T_\sigma| \in \{0.33, 0.75, 1.5\}$). The evolution of the void volume fraction and the void elongation ratio for the different levels of Lode angle parameter are presented in Figure 2.25 and Figure 2.26 . Some conclusions about Lode angle parameter together with the stress triaxiality can be pointed out based on the analysis of Figure 2.25 and Figure 2.26 [64]:

i) Regardless the stress triaxiality level, a minimal effect of the Lode angle parameter on the evolution of the void volume fraction is observed.

ii) In turn, a representative impact of the Lode angle parameter is verified on the microvoid elongation, since, higher magnitudes of Lode angle parameter produce less microvoid elongation comparatively to lower magnitudes of Lode angle parameter.

iii) For high stress triaxialities the influence of the Lode angle parameter is more pronounced.

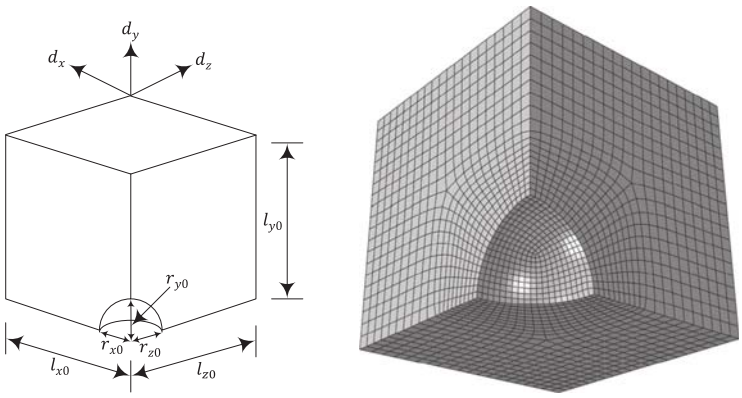

Figure 2.24 – Elemental volume of material with a microvoid: a) geometry; b) finite element model of the material cell [64].

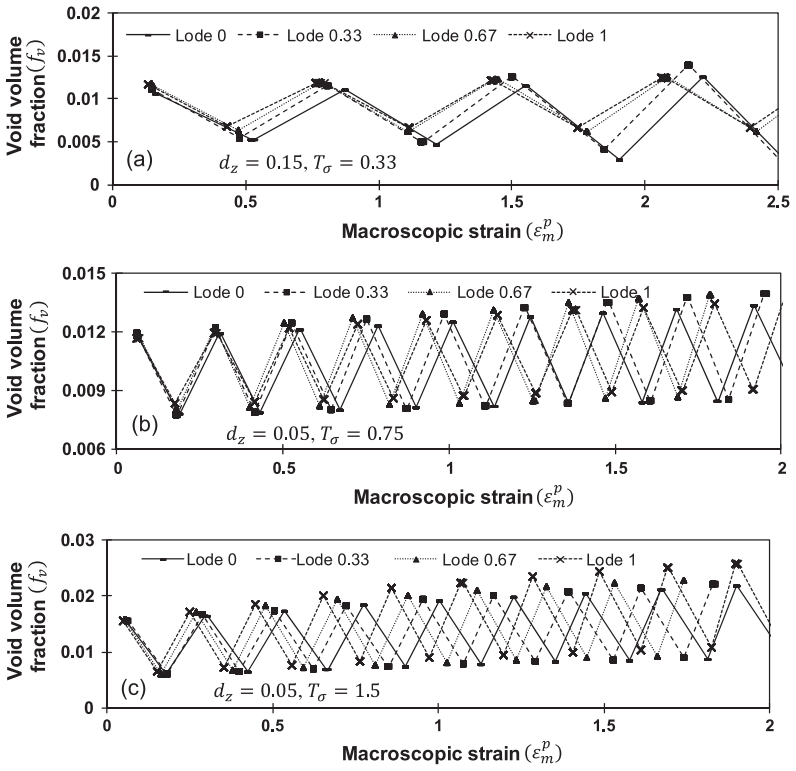

Figure 2.25 – Influence of Lode angle parameter on the evolution of void volume fraction [64].

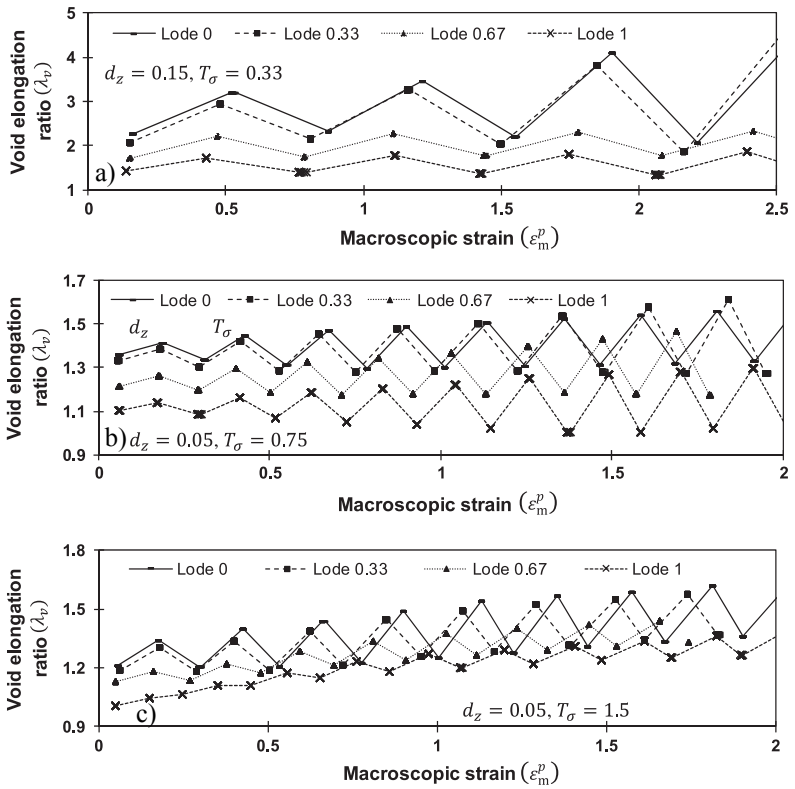

Figure 2.26 – Influence of Lode angle parameter on the evolution of void elongation ratio [64].

The monotonic ductile fracture occurring in steel components is frequently associated with high strain triaxiality levels ($|T_\sigma| \geq 0.75$) [60][61][62] and with applied loads producing a Lode angle parameter close to 1 [63]. Supported on these evidences, a micromechanical cyclic void growth model was developed by Kiran and Khandelwal [64] in order to predict the ULCF failure under high stress triaxialities and Lode parameter magnitude close to 1.0. This model defines the evolution of damage from the microvoid dilation and elongation as follows:

$$D = \left(\frac{f_v}{f_0} \right) \lambda_v - 1 \tag{2.90}$$

where D is the damage variable, f_v is the current void volume fraction that allows quantify the microvoid dilatation, f_0 is the initial void volume fraction and λ_v represents the microvoid elongation ratio which is defined as the ratio between the maximum and minimum (semi) axes length of the deforming microvoid. For a better understanding of the damage evolution as a function of the stress triaxiality and Lode angle parameters, the damage variable (λ_v) obtained from computational simulation of the material volume cell and micromechanical void growth model (MM-CVGM) is plotted against the equivalent plastic strain, fixing the stress triaxiality and Lode angle parameter magnitudes (T_σ=1.25, $|L|$=1), in Figure 2.27. The analysis of the Figure 2.27 suggests a linear law to describe the tensile and the compressive loading path. Thus, the increment damage variable can be defined by:

$$dD = \begin{cases} m_1(T_\sigma)\, d\varepsilon_m^p, & T_\sigma \geq 0 \\ -m_2(T_\sigma)\, d\varepsilon_m^p, & T_\sigma < 0 \end{cases} \tag{2.91}$$

where $m_1(T_\sigma)$ and $m_2(T_\sigma)$ are the magnitudes of the slopes of damage evolution, for tensile (T_σ^+) and compressive (T_σ^-) loading paths. Integrating Eq. (2.91), the damage can be written as:

$$D = \sum_{T_\sigma^+} \int m_1(T_\sigma) d\varepsilon_m^p - \sum_{T_\sigma^-} \int m_2(T_\sigma) d\varepsilon_m^p \tag{2.92}$$

The evolution of the slopes in the positive and negative triaxialities regions, $m_1(T_\sigma)$ and $m_2(T_\sigma)$, respectively, as function of the stress triaxialities levels, can be reproduced by a power law function. Based on this assumption, the damage equation can be rewritten as:

$$D = \sum_{T_\sigma^+} \int a_1 \left|T_\sigma\right|^{b_1} d\varepsilon_m^p - \sum_{T_\sigma^-} \int a_2 \left|T_\sigma\right|^{b_2} d\varepsilon_m^p \tag{2.93}$$

where a_1, a_2, b_1 and b_2 represent the material constants. Nevertheless, Eq. (2.93) is not sufficient to be used as a fracture criterion. In fact, the damage mechanism should be associated to a certain volume of the material for the initiation of the ductile fracture [65]. This volume is characterized through a characteristic length, l^*, as demonstrated in [61]. Taking into account the previous assumptions the MM-CVGM predicts the ductile fracture under extreme cyclic loading conditions when the following condition is verified:

$$\sum_{T_\sigma^+} \int a_1 \left|T_\sigma\right|^{b_1} d\varepsilon_m^p - \sum_{T_\sigma^-} \int a_2 \left|T_\sigma\right|^{b_2} d\varepsilon_m^p \geq D_{cr}, \text{for } r > l^* \tag{2.94}$$

where D_{cr} is the critical damage value and l^* is the characteristic length of the material that should be calibrated from experimental tests.

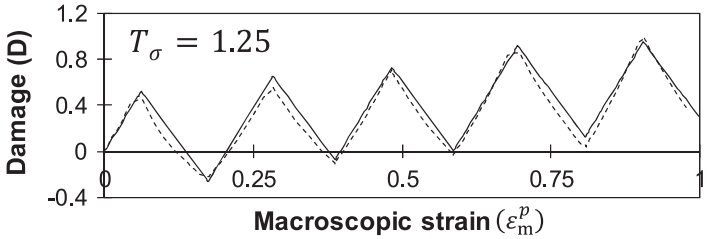

Figure 2.27 – Evolution of damage for T_σ=1.25 predicted using FEM simulation of a material cell (dotted line) and the MM-CVGM (solid line) [64].

This model proposed by Kiran and Khandelwal shows similarities with the model proposed by Kanvinde and Deierlein. Both models are based on micromechanics behaviour of voids in a plastic medium. However, while Kanvinde and Deierlein considers void growth proportional to $\exp\left(\left|1.5\eta\right|\right) d\varepsilon_p$ Kiran and Khandelwal assumes void growth proportional to $a_1 \left|T_\sigma\right|^{b_1} d\varepsilon_m^p$. Both relations show a dependency on stress triaxiality and direct influence of

plastic strain. Kanvinde and Deierlein selected an exponential function to model the influence of the stress triaxiality and Kiran and Khandelwal considered a potential function.

2.3.9 Ohata-Toyoda model

Ohata-Toyoda proposed a damage model for cyclic loading that is an extension of existing well established models for monotonic loading dependent of stress triaxiality [66]. Henceforth the premises of the Ohata-Toyoda model for ULCF are discussed.

The prediction of the monotonic ductile fracture of any structural component can be performed by estimating the stress/strain field derived from a FE analysis. Through the stress and strain fields, the mechanical conditions under which the crack initiation mechanisms can occur are formulated [66]. More specifically, under a tensile loading, the fracture strain at the crack initiation point is assumed by Ohata-Toyoda to be related with the stress triaxiality, which allows the definition of the ductile damage curves, as proposed by the Johnson-Cook formulation [12]. An "effective strain concept", based on the ductile damage curves for ductile cracking of structures under monotonic loading, was proposed at the Osaka University for the prediction of failure by cyclic loading [66]. This assumption implies a nonlinear isotropic/kinematic combined plasticity hardening model as a material model in the numerical simulations that allow reproducing the Bauschinger effects, besides the cyclic hardening/softening [67]. The material damage for ductile cracking under cyclic loading is controlled by the evolution of long-range internal stresses, the so called back-stresses, which enter in the yield function formulation as follows:

$$f\left(\boldsymbol{\sigma}-\boldsymbol{\alpha}\right)-\bar{\sigma}\left(\bar{\varepsilon}_{p}\right)=0 \tag{2.95}$$

where $\boldsymbol{\sigma}$ is the stress tensor, $\boldsymbol{\alpha}$ is the back-stress tensor that represents the centre of the yield surface in the stress space and $\bar{\sigma}(\bar{\varepsilon}_P)$ defines the evolution of the yield strength as a function of the equivalent plastic strain. The plasticity model was defined through the superposition of multiple back-stress components, in accordance with Lemaitre and Chaboche [68] proposal. The evolution of back-stress tensor can be defined as follows:

$$d\boldsymbol{\alpha}^k = \frac{C^k}{\bar{\sigma}}\left(\boldsymbol{\sigma} - \boldsymbol{\alpha}\right) d\bar{\varepsilon}_p - \gamma^k \boldsymbol{\alpha} d\bar{\varepsilon}_p$$
$$\boldsymbol{\alpha} = \sum_{k=1}^{N} \boldsymbol{\alpha}^k \tag{2.96}$$

where C and γ are material constants. Based on the effective damage concept, Ohata and Toyoda proposed the so-called "advanced two-parameter criterion" to evaluate the ductile crack initiation for cyclic loadings [66], in which the equivalent plastic strain and stress triaxiality were adopted as the two mechanical parameters that control ductile cracking [13][69]. The following main ideas can be accomplished together with the analysis of the Figure 2.28. It is observed that only the effective plastic strain, resulting from each cycle, contributes to the damage when the back-stress exceeds the maximal back-stress under the preceding loading cycle. The crack initiation occurs when the accumulation of the effective plastic strain as a function of the stress triaxiality reaches the damage curve obtained from the monotonic loading tests on small scale specimens for the material of interest.

The model by Ohata-Toyoda was proposed for structural components subjected to seismic actions which are simulated by variable increasing amplitude stresses. In this cases the back-stress tensor suffers a progressive shift beyond the previous cycles position, leading to increments on the effective equivalent plastic strain and consequently to a damage increment. However, when external loads are stable, the cyclic elastoplastic response could be also stable and the effective equivalent stress is stationary not promoting any damage which could be not acceptable.

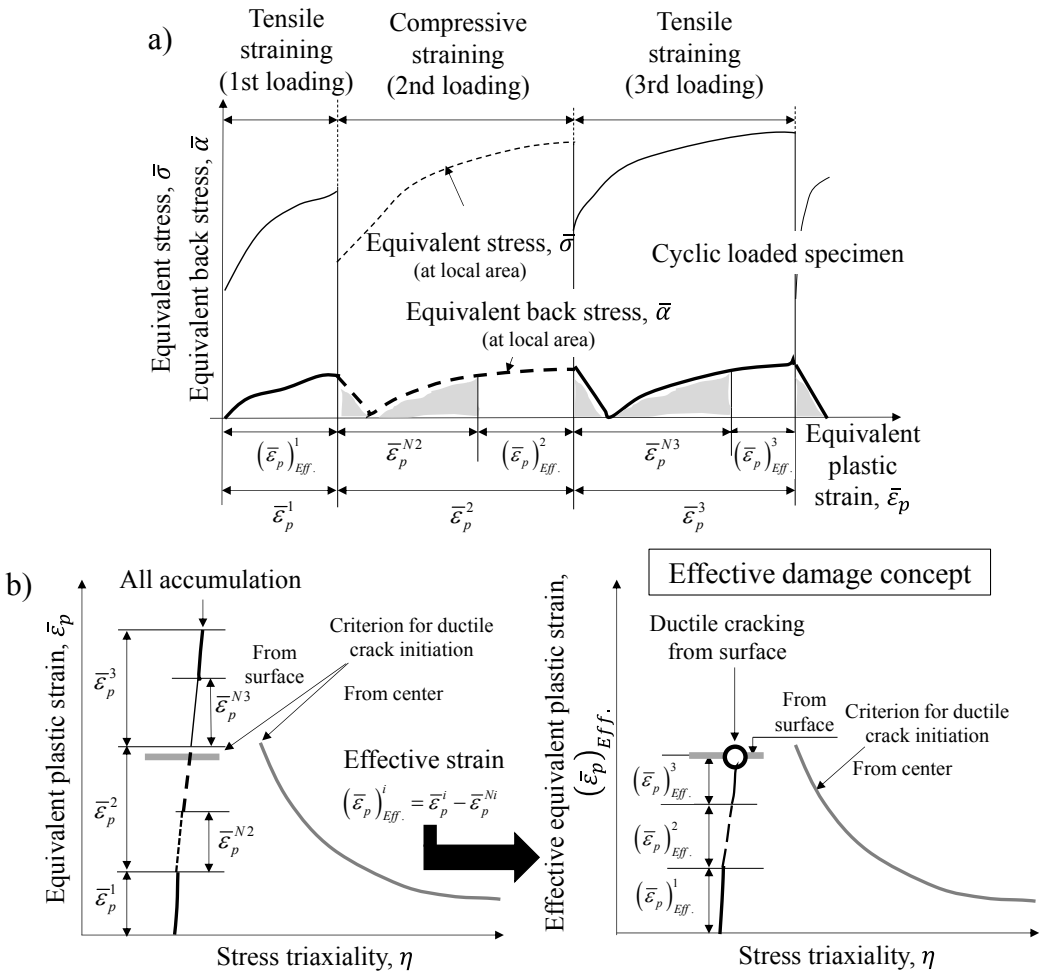

Figure 2.28 – Advanced 2-parameter criterion for ductile cracking of structural members under cyclic loading based on effective damage concept: a) evolution of the equivalent back-stress under cyclic loading; b) effective damage concept [66].

2.4 ULCF TESTING

In this section, a brief reference to experimental works carried out on ULCF domain, published in the literature, are presented. LCF experimental tests are very abundant in the literature and are already normalized which is the case of the American Standard, ASTM E606 [70]. This standard establishes that experimental cyclic tests should be performed on smooth specimens under strain control. Although, at high strain range levels (typically above 2%) smooth specimens may suffer lateral instabilities which promotes the perturbation of the uniaxial stress state. In fact, high strain ranges may lead to anticipated

failure of the specimens. The performance of ULCF tests requires the utilization of strain ranges within 3-10%, which makes impracticable the ASTM E606 procedures. Experimental testing under ULCF domain using smooth specimens is not so common in the literature. The most of the authors adopts notched specimens since it promotes the stress and strain concentration at the notch root.

In order to investigate the effects of the temperature in the cyclic straining and the fatigue behaviour of several metals, Coffin and Tavernelli [71] adopted round bar specimens with a central notch with large radius, as represented in the Figure 2.29. The resulting experimental data is plotted in the Figure 2.30 and was used latter by Xue [49] for the calibration of a damage model for LCF and ULCF domain. Additionally, the use of notched round bar specimens for ULCF testing was also followed from Kanvinde and Deierlein [15] and Ohata [66], as illustrated in the Figure 2.31.

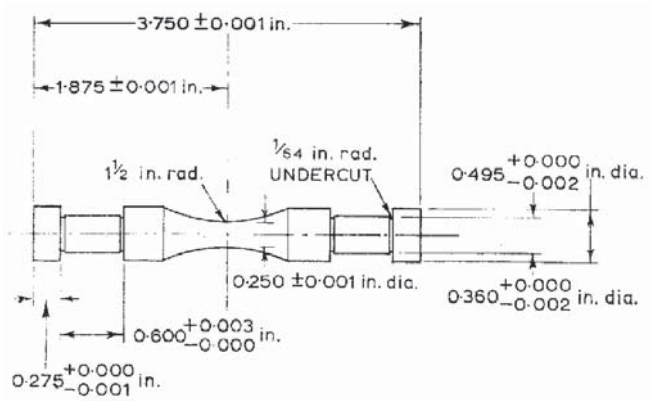

Figure 2.29 –Fatigue specimen for temperature straining/fatigue testing [72].

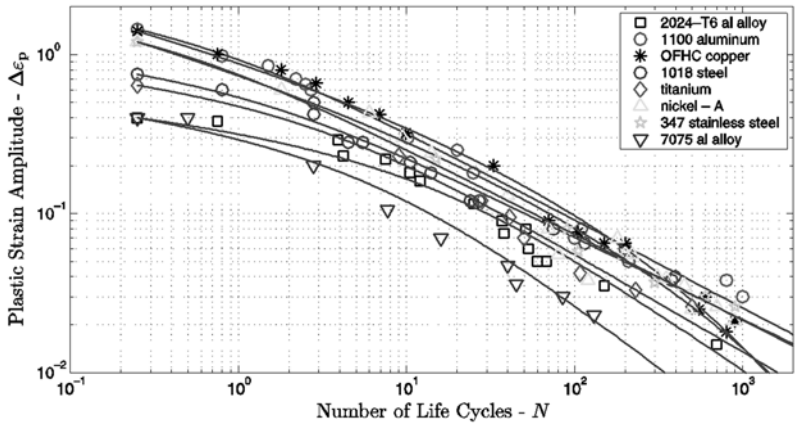

Figure 2.30 – Strain-life relation for several metals. Experimental data from Coffin and Tavernelli [72].

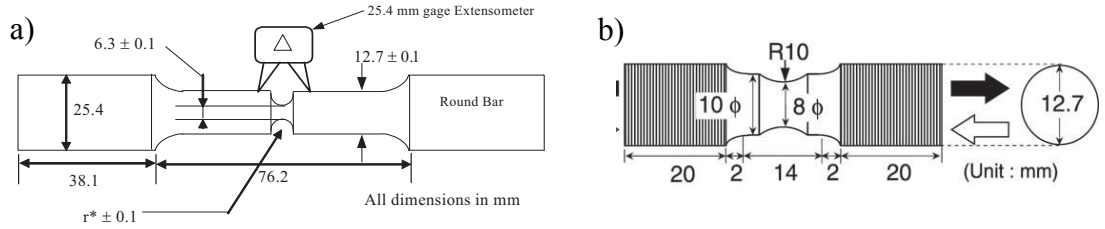

Figure 2.31 – Notched round bar specimens used: a) for cyclic void-growth model calibration proposed by Kanvinde and Deierlein [15]; b) for the evaluation of ductile crack initiation for cyclic loading as proposed by Ohata and Toyoda [66].

In contrast, other authors suggest the use of plane specimens for uniaxial cyclic tests. In detail notched plane specimens, with a circular central hole were used by Pereira [1] to perform ULCF tests on S185 steel grade (see Figure 2.32). Smooth plane specimens were also used for the uniaxial cyclic tests as evidenced in the experimental works of Nip [73] and Rizzo [74]. However, the use of smooth specimens potentially raises instabilities problems during the compressive stages of the loading. This difficulty leads to the development of a gripping system to reduce the specimen instability and lateral plastic deformation. Thus, for the ULCF tests on smooth plane specimens, Nip adopted the specimen geometry and gripping system illustrated in Figure 2.33. Specimens were gripped by friction in the jaws of the testing apparatus as well as positively held by pins at each end [73] (see Figure 2.34). Relative movements between the top and bottom jaws of the testing apparatus were prevented by guide plates [73].

In order to perform LCF tests on thin plates, an anti-buckling device was also designed by Rizzo [74] and is illustrated in the Figure 2.35. Nevertheless, these solutions exhibit some limitations, related to the friction between the specimen and the grip and small instabilities remains, which promotes the specimens plastic accommodation and promotes the damage acceleration. Thus, the potential specimens' instability should be properly considered on the boundary conditions of the finite element models required for the damage models assessment.

Another approach presented in the literature for ULCF testing consists of performing cyclic bending tests. This approach was followed by Tateishi [48], Ohata [66] and Nip [73]. The experimental set-up used in these works is illustrated in Figure 2.36.

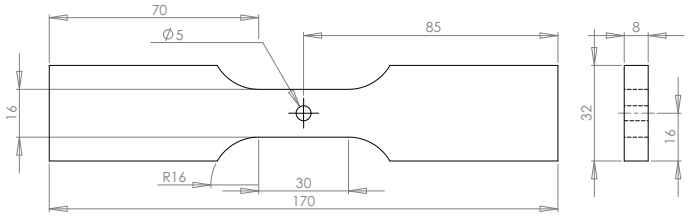

Figure 2.32 – Plane notched specimens in the ULCF testing of S185 steel grade.

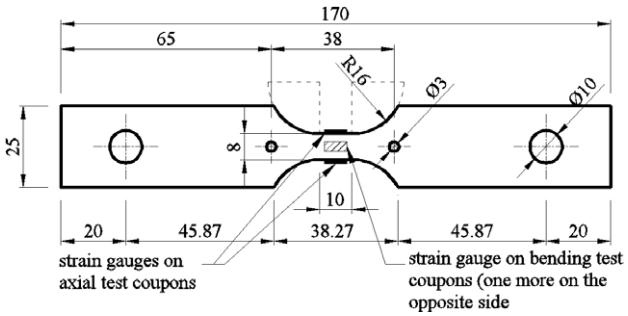

Figure 2.33 – Dimensions of smooth plane specimens used in the Nip experimental works [73].

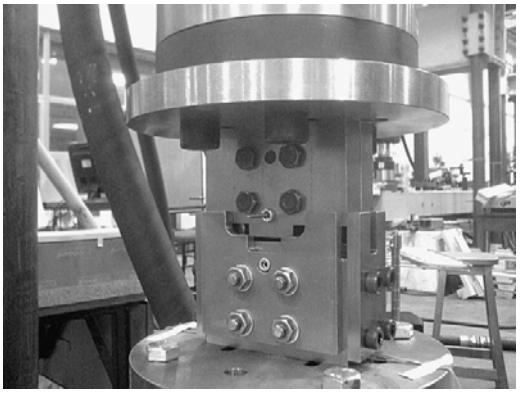

Figure 2.34 – Experimental experimental apparatus of cyclic axial test setup [73].

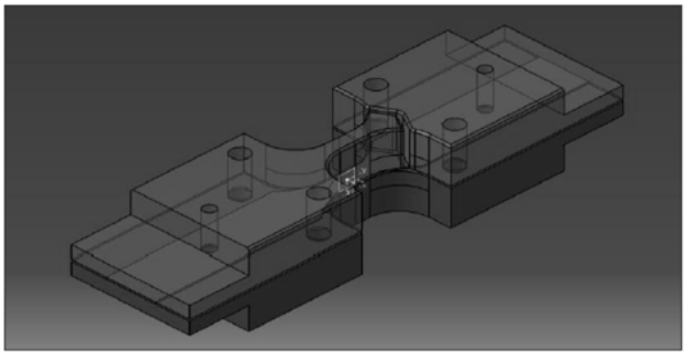

Figure 2.35 – Anti-buckling device developed by Rizzo *et al* [74].

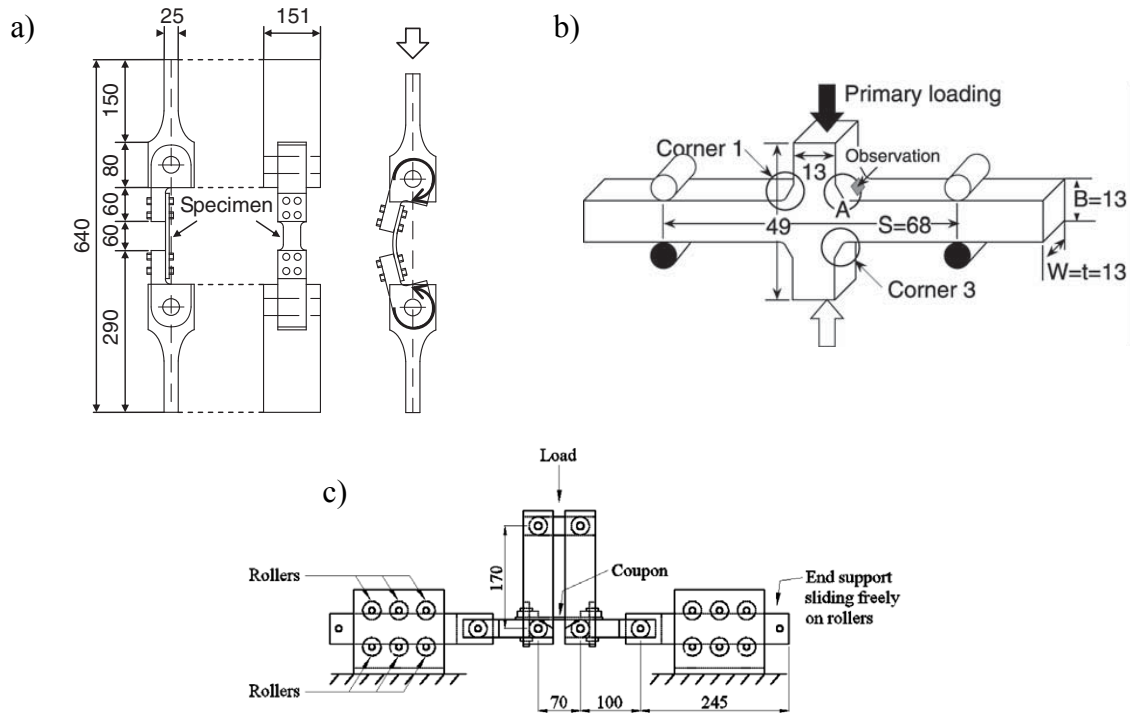

Figure 2.36 – Experimental set-up of cyclic bending tests performed by: a) Tateishi [48]; b) Ohata [66]; c) Nip[73].

2.5 REFERENCES

[1] Pereira J.C.R., (2011), "Behavior of steel components under the action of monotonic and cyclic extreme loading", University of Trás-os-Montes e Alto Douro (in Portuguese).

[2] de Jesus A.M.P., Natal R., Seabra M., Pereira J.C.R., Fernandes A.A., (2013), "Ultra low cycle fatigue of steel under cyclic high strain loading conditions," Midterm Assessment Report, European Commission RFSR CT 2011 00029.

[3] Bleck W., Dahl W., Nonn A., Amlung L., Feldman M., Schäfer D., Eichler B., (2009), "Numerical and experimental analyses of damage behaviour of steel moment connection." Engineering Fracture Mechanics, 76: 31 – 47.

[4] Kachanov L.M., (1986), "Introduction to Continuum Damage Mechanics." Martinus Nijhoff Publishers.

[5] Barson J.M., Rolfe S.T., (1999), "Fracture and Fatigue Control in Structures, Third Edition: Applications of Fracture Mechanics." ASTM

[6] Bridgman P.W., (1952), "Studies in large plastic flow and fracture." New York: McGraw-Hill.

[7] Atkins A.G., (1997), "Fracture mechanics and metal forming: damage mechanics and the local approach of yesterday and today." Fracture research in retrospect – an anniversary volume in honor of George R. Irwin's 90'th birthday, Rotterdam, Brookfield: A.A. Balkema.

[8] Cockcroft M.G., Latham D.L., (1968). "Ductility and the workability of metals." Journal Institute of Metals, 96: 33 – 39.

[9] Datsko, J., Yang, C.T., (1960), "Correlation of bendability of metals with their tensile properties." Transactions ASME, B82:309.

[10] Brozzo P., De Luca B., Rendina R., (1972), "A new method for the prediction of formability in metal sheet, sheet metal forming and formability." In: Proceedings of the 7th biennial conference of the IDDRG.

[11] Norris D., Reaugh J., Moran B., Quinnones D., (1978), "A plastic-strain mean-stress criterion for ductile fracture." Journal of Engineering of Materials, 100:79 – 86.

[12] Johnson G.R., Cook W.H., (1985), "Fracture characteristics of three metals subjected to various strains, strains rates, temperatures and pressures." Engineering Fractures Mechanics, 21: 33 – 48.

[13] McClintock F.A., (1968), "A criterion for ductile fracture by growth of holes." Transactions ASME, Journal of Applied Mechanics, 35: 63 – 71.

[14] Rice J.R., Tracey D.M., (1969), "On the ductile enlargement of voids in triaxial stress fields." Journal of the Mechanics and Physics of Solids, 35: 201 – 217.

[15] Kanvinde A.M., Deierlein G.G., (2007), "Cyclic Void Growth Model to Assess Ductile Fracture Initiation in Structural Steels due to Ultra Low Cycle Fatigue.", Journal of Engineering Mechanics, 133:701 – 702.

[16] Coppola T., Cortese L., Folgarait P., (2009), "The effect of stress invariants on ductile fracture limit in steels." Engineering Fracture Mechanics, 76: 1288 – 13021302.

[17] Lemaitre J., (1985), "A continuous damage mechanics model for ductile fracture." Journal of Engineering Materials and Technology – Transactions ASME, 107: 83–89.

[18] Bonora N., (1997), "A nonlinear CDM model for ductile failure." Engineering Fracture Mechanics, 58:11–28.

[19] Gurson A.L., (1977), "Continuum theory of ductile rupture by void nucleation and growth. Part I: Yield criteria and flow rules for porous ductile media." Transactions ASME, Journal of Engineering Materials, 99: 2 – 15.

[20] Tvergaard V., Needleman A., (1984), "Analysis of the cup-cone fracture in a round tensile bar." Acta Metallurgica, 32:157–169.

[21] Tvergaard V., 1982, "Influence of void nucleation on ductile shear fracture at a free surface." Journal of the Mechanics and Physics of Solids, 30:399–425.

[22] Clausing D.P., (1970), "Effect of plastic strain state on ductility and toughness." International Journal of Fracture Mechanics 6:71–85.

[23] Wierzbicki T., Bao Y., Lee Y-W., Bai Y., (2005), "Calibration and Evaluation of Seven Fracture Models", International Journal of Mechanical Sciences, 47: 719 – 743.

[24] Pereira J.C.R., Xavier J.M.C., de Jesus A.M.P., (2014), "Ultra Low-Cycle Fatigue behavior of a structural steel", Engineering Structures, 20: 214 – 222.

[25] Malcher L., Andrade Pires F.M., César de Sá J.M.A., Andrade F.X.C, (2009), "Numerical integration algorithm of a new model for metal plasticity and fracture including pressure and lode angle dependence." International Journal of Material Forming, 1:443 – 446.

[26] Anandarajah A., (2010), "Computational Methods in Elasticity and Plasticity." Springer.

[27] Malvern, L.E., (1969), "Introduction to the Mechanics of a Continuous Medium." Prentice-Hall, Inc.

[28] Xu, B., Liu, X., (1995), "Applied Mechanics: Elasticity and Plasticity." Tsinghua University Press, Beijing, China.

[29] Bai Y., Wierzbicki T., (2008), "A new model of metal plasticity and fracture with pressure and Lode dependence", International journal of plasticity 24: 1071 – 1096.

[30] Davis R. O., Selvadurai A.P.S., (2002), "Plasticity and Geomechanics", Cambridge Univ Pr.

[31] Xue L., (2007), "Ductile fracture modeling - theory, experimental investigation and numerical verication." PhD thesis, Massachusetts Institute of Technology.

[32] Gao X., Zhang G., Roe C., (2010), "A study on the effect of the stress state on ductile fracture." International Journal of Damage Mechanics, 1975 – 94.

[33] Chen W.F., Han D.J., (2007) "Plasticity for Structural Engineers." J Ross Pub.

[34] Ottosen N.S., Ristinmaa M., (2005) "The Mechanics of Constitutive Modeling." Elsevier Science Ltd.

[35] Yu M., (2006) "Generalized Plasticity". Springer Verlag.

[36] Bai Y., (2003), "Effect of Loading History on Necking and Fracture". Ph.D. thesis. Cambridge, MA: Department of Ocean Engineering, Massachusetts Institute of Technology.

[37] Basaran. M., (2011), "Stress state dependent damage modelling with a focus on the Lode angle influence". PhD Thesis, RWTH Aachen University.

[38] NP EN 10002-1, (2006). "Materiais metálicos", Ensaio de tracção, Parte 1: Método de ensaio à temperatura ambiente, Instituto Português da Qualidade.

[39] ASTM - American Society for Testing and Materials, (2007). "ASTM E646: Standard Test Method for Tensile Strain-Hardening Exponents (n-Values) of Metallic Sheet Materials", ASTM-International, 100 Barr Harbor Drive, P.O. Box C700, West Conshohocken, PA 19428-2959, USA.

[40] Bao Y., (2003), "Prediction of ductile crack formation in uncracked bodies." Ph.D. thesis. Cambridge, MA: Department of Ocean Engineering, Massachusetts Institute of Technology;

[41] Wierzbicki T., Xue L., (2005), "On the effect of the third invariant of the stress deviator on ductile fracture." Impact and Crashworthiness Lab Report 136. Cambridge, MA: Massachusetts Institute of Technology.

[42] Lee Y.W., (2005), "Fracture prediction in metal sheets. PhD thesis, Massachusetts Institute of Technology.

[43] Wierzbicki T., Bao Y., Werner H., (2002), "Ductile fracture, theory, calibration and applications." EuroPAM 2002 Antibes Juan les Pins, France.

[44] Leblond J.B., Perrin G., Devaux J., (1995), "An improved Gurson-type model for hardenable ductile metals." European Journal of Mechanics - A/Solids, 14:499 – 527.

[45] Steglich D., Pirondi A., Bonora N., Brocks W., (2005), "Micromechanical modelling of cyclic plasticity incorporating damage." International Journal of Solids and Structures; 42:337–51.

[46] Komotori J., Shimizu M., (1998), "Fracture mechanism of ferritic ductile cast iron in extremely low cycle fatigue." In: Rie KT, Portella PD, editors. Low cycle fatigue and elasto–plastic behavior of materials. Elsevier Science Ltd 39–44.

[47] Kuroda M., (2001), "Extremely low cycle fatigue life prediction based on a new cumulative fatigue damage model." International Journal of Fatigue, 24:699–703.

[48] Tateishi K., Hanji T., (2004), "Low cycle fatigue strength of butt-welded steel joint by means of new testing system with image technique." International Journal of Fatigue, 26:1349–1356.

[49] Xue L., (2007), "A unified expression for low cycle fatigue and extremely low-cycle fatigue and its implication for monotonic loading." International Journal of Fatigue, 30:1691–1698.

[50] Hatanaka K., Fujimitsu T., (1984), "Some considerations on cyclic stress–strain relation and low cycle fatigue life." Transactions of the Japan Society of Mechanical Engineering - Part A, 50(451) 291–300.

[51] Coffin Jr L.F., (1971), "A note on low cycle fatigue laws." Journal of Materials JMLSA, 6(2):388–402.

[52] Manson S.S., (1954), "Behavior of materials under conditions of thermal stress." NACA-TR-1170, National Advisory Committee for Aeronautics.

[53] ASME Boiler & Pressure Vessel Code, Section VIII, (2013). "Rules for Construction of Pressure Vessels, Division 2 – Alternative Rules", The American Society of Mechanical Engineers (ASME), New York, USA.

[54] Miner MA, 1945. "Cumulative damage in fatigue." Journal of Applied Mechanics Transactions ASME, 67:159–64.

[55] Dufailly, J., Lemaitre, J., 1995. "Modeling Very Low Cycle Fatigue", International Journal of Damage Mechanics, 4.

[56] Du M.L., Li G.C., Zhang Y.Z., Fang W.D., (1992). "Fracture behavior of axisymmetric bars under high triaxial stress and large strain cyclic loading." Fatigue & Fracture of Engineering Materials & Structures, 15: 1009–24.

[57] Kunio T., Shimizu M., Ohtani N., Abe T., (1988), "Microstructural aspects of crack initiation and propagation in extremely low cycle fatigue". Solomon HD, Halford GR, Kaisand LR, Leis BN, editors. Low cycle fatigue: ASTM STP 942. Philadelphia: American Society for Testing and Materials, 751–64.

[58] Ohji K., Miller W.R., Marin J., (1966), "Cumulative damage and effect of mean strain in low-cycle fatigue of a 2024-T351 aluminum alloy". Transactions of the ASME Series D; 88:801–10.

[59] Murakami Y., Harada S., Endo T., Taniishi H., Fukushima Y., (1983), "Correlations among growth law of small cracks, low-cycle fatigue law and applicability of Miner's rule." Engineering Fracture Mechanics, 18:909–24.

[60] Kuwamura H., (1997), "Transition between fatigue and ductile fracture in steel." Journal of Structural Engineering; 123: 864–70.

[61] Kiran R., Khandelwal K., (2013), "Experimental studies and models for ductile fracture in ASTM A992 steels at high triaxiality". Journal of Structural Engineering (ASCE); 140:1–11.

[62] Kanvinde A.M., Fell B.V., Gomez I.R., Roberts M., (2008), "Predicting fracture in structural fillet welds using traditional and micromechanical fracture models." Engineering Structures; 30:3325–35.

[63] Kiran R., Khandelwal K., (2014), "Fast-to-compute weakly coupled ductile fracture model for structural steels." Journal of Structural Engineering, 4:014-018.

[64] Kiran R., Khandelwal K., (2015), "A micromechanical cyclic void growth model for ultra-low cycle fatigue." International Journal of Fatigue, 70:24-37

[65] Mackenzie A.C., Hancock J.W., Brown D.K., (1977), "On the influence of state of stress on ductile failure initiation in high strength steels". Engineering Fracture Mechanics, 9:167–88.

[66] Ohata M., Toyoda M., (2004), "Damage concept for evaluating ductile cracking of steel structure subjected to large-scale cyclic straining", Science and Technology of Advanced Materials, 5:241-249.

[67] Socie D.F., Marquis G.M., (2000), "Multiaxial fatigue", Society of Automotive Engineers, Inc.

[68] Lemaitre J., Chaboche J.L., (1990), "Mechanics of Solid Materials." Cambridge University Press.

[69] Thomason P.F., (1968), "A theory for ductile fracture by internal necking of cavities." Journal of the Institute of Metals. 96 360–365.

[70] ASTM - American Society for Testing and Materials, (1998), "ASTM E606: Standard Test Method for Strain-Controlled Fatigue Testing, ASTM International", In Annual Book ASTM Standards.

[71] Coffin Jr L.F., Tavernelli J.F., (1959), "The cyclic straining and fatigue of metals." Transactions Metallic Society AIME; 215: 794–807.

[72] Tavernelli J.F., Coffin L.F., (1963), "The cyclic strain aging and fatigue of a low carbon steel", Proceedings of the Institution of Mechanical Engineers, Conference Proceedings June 1963 vol. 178: 63 – 70.

[73] Nip K.H., Gardner L., Davies C.M., Elghazouli A.Y., (2008), "Extremely low cycle fatigue tests on structural carbon steel and stainless steel". Journal of Constructional Steel Research 66: 96 – 110.

[74] Rizzo L. et al, (2012), "An efficient and effective methodology and simulation tools for die design and springback compensation for hss and uhss". Final Report, European Commission RFCS-CT-2008-00029.

Chapter III

Small-scale tests of API piping steels

3.1 INTRODUCTION

In this chapter, the experimental program carried out on small-scale specimens is described and results are presented. Both monotonic and cyclic tests were performed on several specimens, the respective geometries being summarized in the Table 3.1 to Table 3.5. Concerning the fatigue tests, both LCF and ULCF domains were investigated. The cyclic tests allowed the evaluation of the cyclic and fatigue properties for a wide variety of strain ranges. These results allowed the calibration of fatigue damage models assessed latter in this research. Additionally, monotonic tensile tests were performed for each specimen's series allowing the evaluation of the basic material properties. Monotonic tensile tests are important since some fatigue damage models (e.g. Xue model) incorporate monotonic parameters in their formulation, as for example the monotonic fracture strain. This parameter is related with the stress state parameters, namely the triaxiality and the Lode angle.

The image acquisition system, ARAMIS® v6.02 by GOM [1] was coupled with the monotonic tensile tests, allowing the assessment of the specimen necking progress until final fracture. In addition, Digital Image Correlation (DIC) was used together with the fatigue tests in order to derive the full field information of specimens' surfaces.

The microstructures of the tested piping steels, with and without thermal treatment, were also conducted using an optical microscope, allowing investigate the influence of the thermal cycle on material's microstructure. The fracture surfaces of some specimens were also analysed by means of Scanning Electron Microscope (SEM).

3.2 PIPING STEELS AND SPECIMENS DESCRIPTION

Experimental tests were performed covering three piping steels, namely the X52, X60 and X65 piping steels (specifications according to the American Petroleum Institute - API). Moreover, concerning the X60 and X65 steel grades tests, monotonic and cyclic tests

were also carried out using steel samples extracted from pipes that were subjected to the same thermal cycle applied to produce elbows by hot bending manufacturing process. Hereafter the X60 and X65 piping steels that were subjected to the thermal treatment are named as X60TT and X65TT, respectively. These materials were made available through the ULCF (*Ultra-low-cycles fatigue of Steel Under Cyclic High-Strain Loading Conditions*) RFCS European project. Figure 3.1 illustrates the different straight pipes used in this work. Figure 3.1a) represents the X52 pipe with an outside diameter (OD) of 168 mm and wall thickness (Wt) of 4.78 mm; Figure 3.1b) illustrates X60 pipes with OD=406 mm and Wt=9.5 mm; Figure 3.1c) shows two X65 pipes with OD=219mm and Wt=5.6mm. All specimens were extracted from the pipe material, along the longitudinal direction, as schematized in Figure 3.2. The side faces were milled and grinded in order to achieve plane faces with low surface roughness.

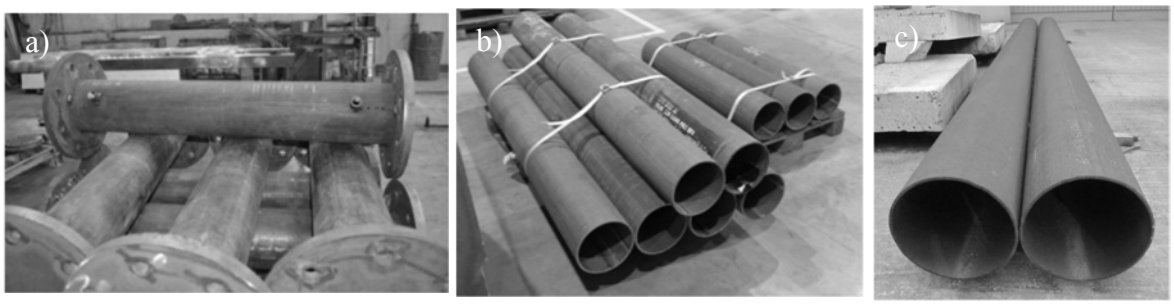

Figure 3.1 – Straight pipes made of API steels: a) X52; b) X60; c) X65 grade.

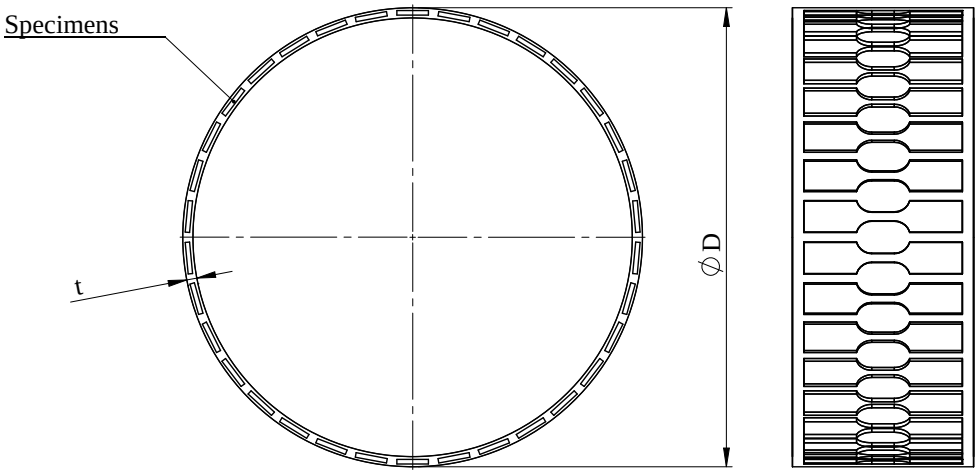

Figure 3.2 – Cutting/machining plan of specimens along the longitudinal direction of the straight pipes (t=Wt; D=OD).

Concerning the X52 piping steel, tensile smooth plane (dog-bone) and plane notched, cyclic smooth plane and notched plane and cyclic bending (smooth, notched and flat side

grooved) specimens were machined. The aim of each test series, the geometries of the specimens and the gauge length of dynamic extensometer set for each test are referenced in the Table 3.1. Figure 3.3 to Figure 3.5 show the geometries of the specimens listed in the Table 3.1.

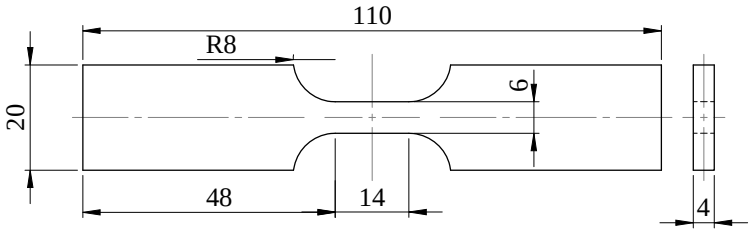

Figure 3.3 – Smooth plane specimen geometry of X52 piping steel (X52_SP).

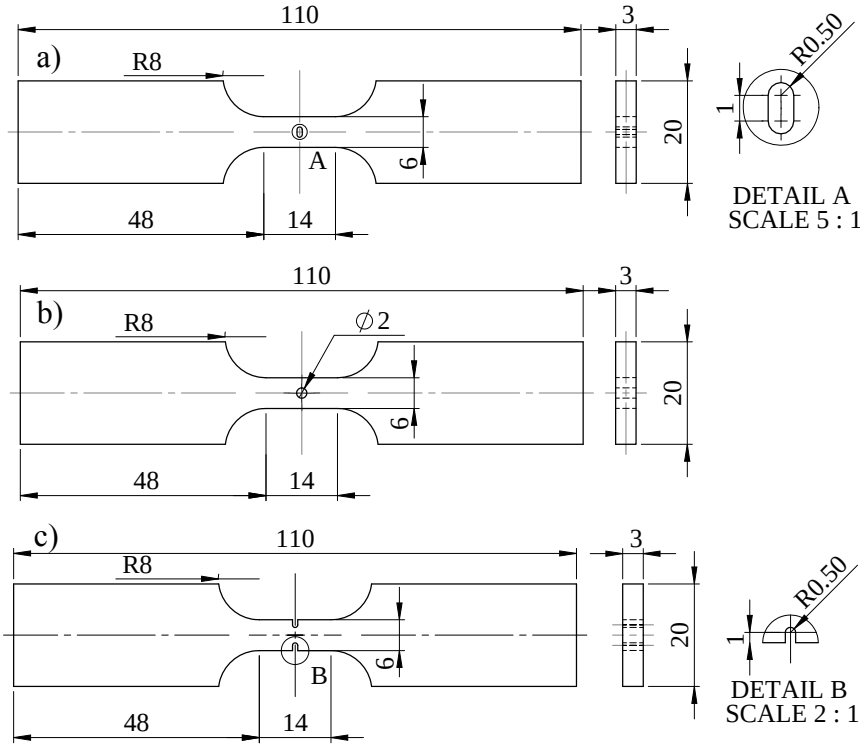

Figure 3.4 – Notched plane specimens' geometries of X52 piping steel: a) central oval hole (X52_OH); b) central circular hole (X52_CH); c) side notch (X52_SN).

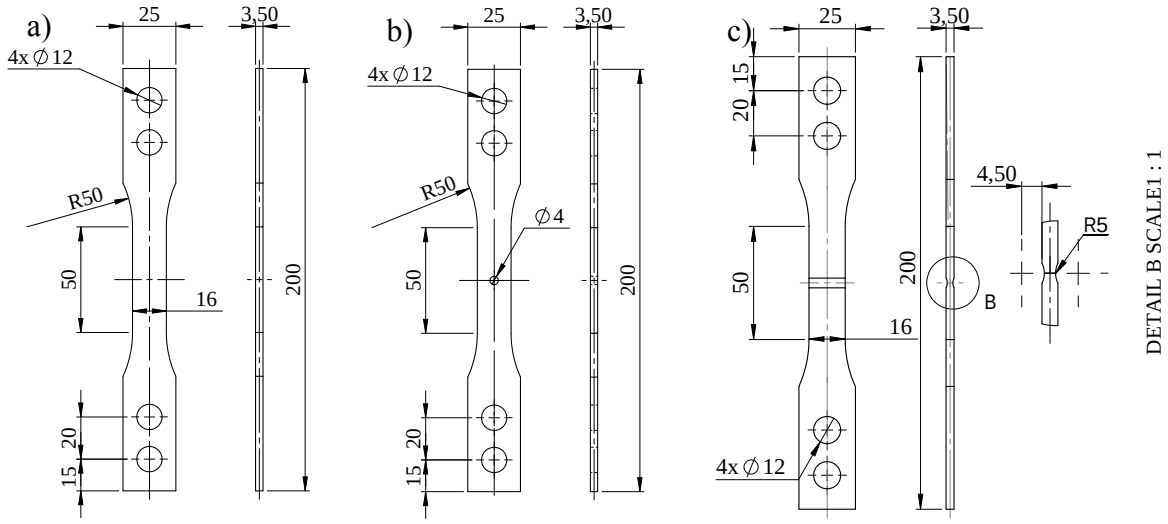

Figure 3.5 – Specimens geometries of X52 piping steel used in the cyclic bending tests: a) smooth plane (X52_BSP); b) notched plane (X52_BNP); c) plane flat grooved (X52_BFG).

Table 3.1 – Specimens' series of X52 piping steel.

Specimen reference	Specimen and test type	Scope of test	Figure no	Gauge length [mm]
X52_SP	Tensile smooth plane	Stress-strain curve, basic material properties	Figure 3.3	12.5
X52_CH X52_OH X52_SN	Tensile notched plane	Fracture strain, triaxiality and Lode angle parameter influence	Figure 3.4	12.5
X52_SP	Cyclic smooth plane	Kinematic hardening material behaviour	Figure 3.3	12.5
X52_CH X52_OH X52_SN	Cyclic notched plane	Triaxiality and Lode angle parameter influence	Figure 3.4	12.5
X52_BSP	Bending smooth plane	Cyclic response of wrinkles under severe load reversals, for different stress triaxialities and Lode angle parameter	Figure 3.5	Not used
X52_BNP	Bending notched plane			Not used
X52_BFG	Bending flat grooved			Not used

Smooth and notched plane and round specimens were machined for the small-scale tests of X60 piping steel. Additionally, experimental tests on tensile and cyclic flat grooved and also plane shear specimens were conducted. With respect to the material with thermal treatment, tensile and cyclic tests were carried out on smooth and notched plane specimens. Table 3.2 summarizes the scope of each test series as also the number of the figures illustrating the specimens' geometries which can be observed in Figure 3.6 to Figure 3.12. The gauge length of the dynamic extensometer used in both monotonic and cyclic tests is also evidenced in the Table 3.2.

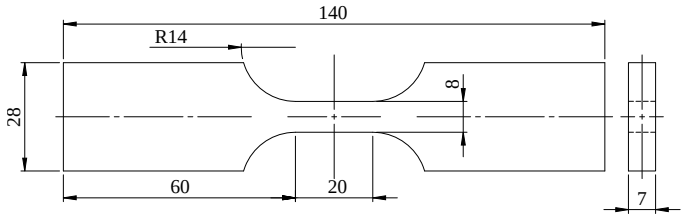

Figure 3.6 – Smooth plane specimen geometry of X60 piping steel (X60_SP).

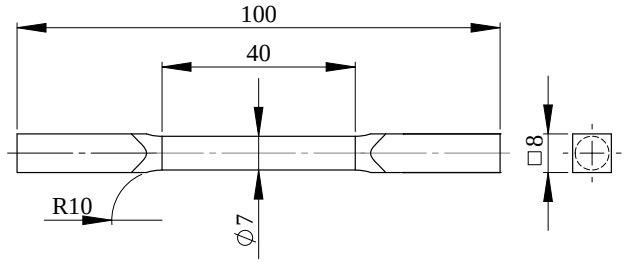

Figure 3.7 – Round bar specimen geometry of X60 piping steel (X60_RB).~

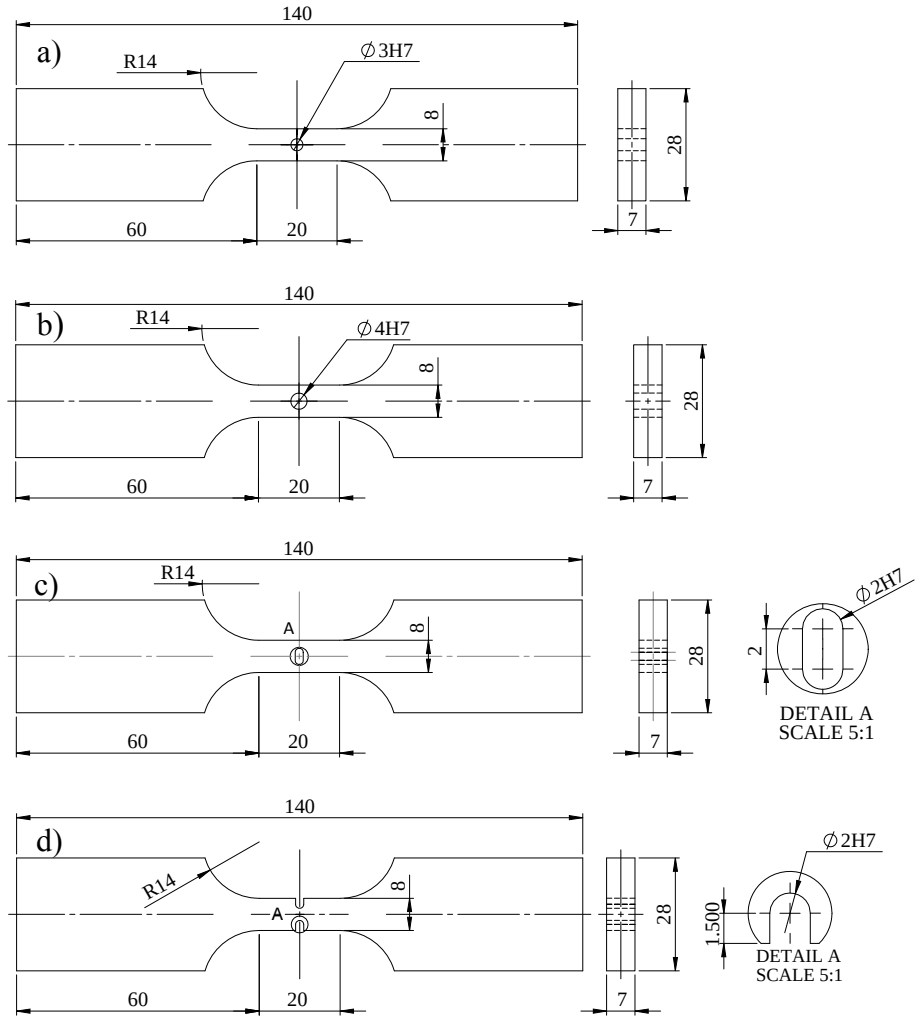

Figure 3.8 – Notched plane specimens' geometries of X60 piping steel: a) central circular hole with a diameter of 3mm (X60_CHS); b) central circular hole with a diameter of 4mm (X60_CHB); c) central oval hole (X60_OH); d) side notch (X60_SN).

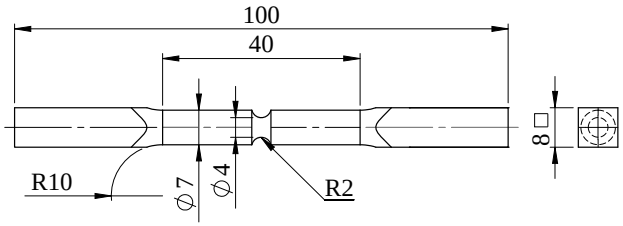

Figure 3.9 – Notched round bar with small notch of X60 piping steel, (X60_RBS).

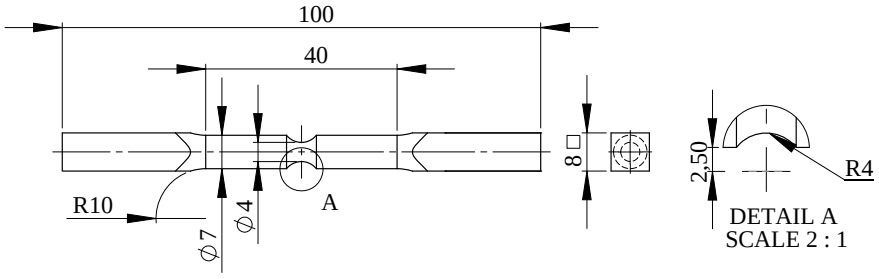

Figure 3.10 – Notched round bar with large notch of X60 piping steel, (X60_RBL).

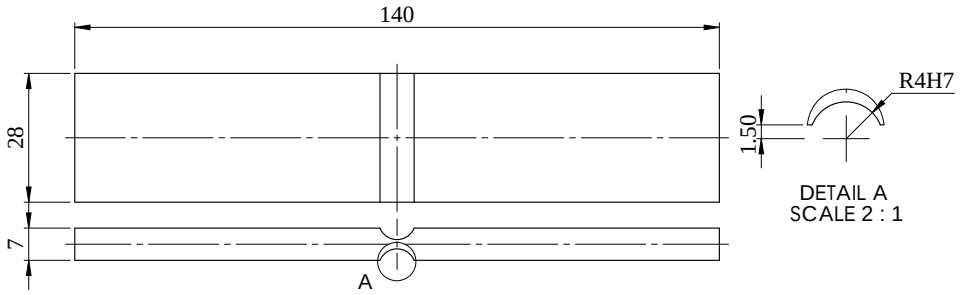

Figure 3.11 – Flat grooved specimen of X60 piping steel (X60_FG).

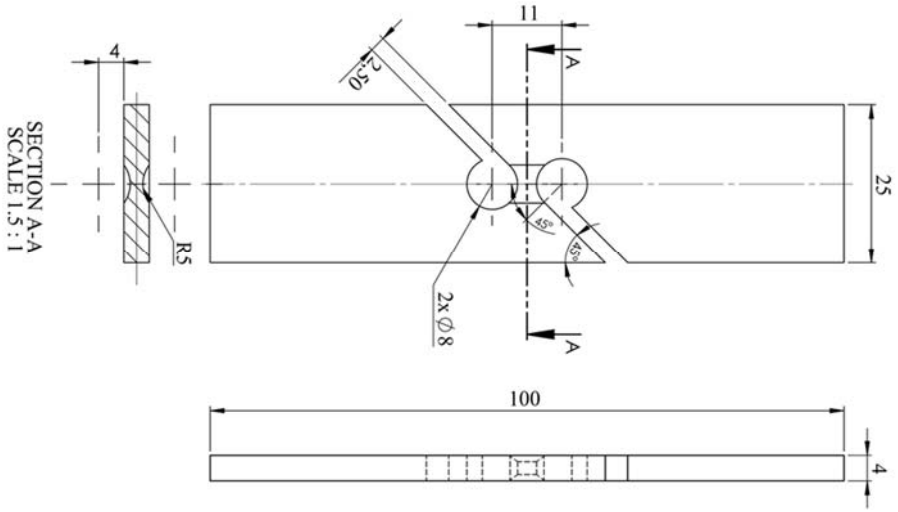

Figure 3.12 – Plane shear specimen of X60 piping steel (X60_PSG).

Table 3.2 – Specimens' list of X60 piping steel.

Specimen reference	Specimen and test type	Scope of test	Figure no	Gauge length [mm]
X60_SP	Tensile smooth plane	Stress-strain curve, basic material properties	Figure 3.6	12.5
X60_RB	Tensile round bar		Figure 3.7	12.5
X60_RBS X60_RBL	Tensile notched round bar	Upper bound identification	Figure 3.9 Figure 3.10	12.5
X60_CHS X60_CHB X60_OH X60_SN	Tensile notched plane	Fracture strain, triaxiality and Lode angle parameter influence	Figure 3.8	12.5
X60_FG	Tensile flat grooved	Lower bound identification	Figure 3.11	25
X60_PSG	Tensile shear	Lower bound identification	Figure 3.12	50
X60_SP	Cyclic smooth plane	Kinematic hardening material behaviour	Figure 3.6	12.5
X60_CHS X60_CHB X60_OH X60_SN	Cyclic notched plane	Triaxiality and Lode angle parameter influence	Figure 3.8	12.5
X60_FG	Cyclic flat grooved	Triaxiality and Lode angle parameter influence	Figure 3.11	25
X60_PSG	Cyclic shear	Triaxiality and Lode angle parameter influence	Figure 3.12	50

The X65 steel grade was also characterized by means of monotonic and cyclic (ULCF+LCF) tests since this material was also selected for fatigue tests of straight pipes, in a similar way as proposed for the other two steel grades, X52 and X60. The experimental program of X65 piping steel included tensile and cyclic tests on smooth and notched plane specimens as also flat grooved specimens. Table 3.3 gives an overview of the specimens tested concerning the X65 steel characterization. Figure 3.13 and Figure 3.14 exhibits the geometry of the specimens tested aiming the X65 steel grade characterization.

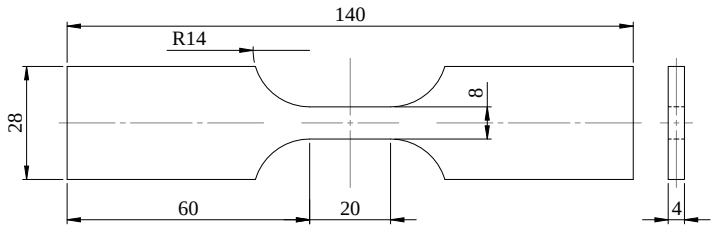

Figure 3.13 – Smooth plane specimen geometry of X65 piping steel (X65_SP).

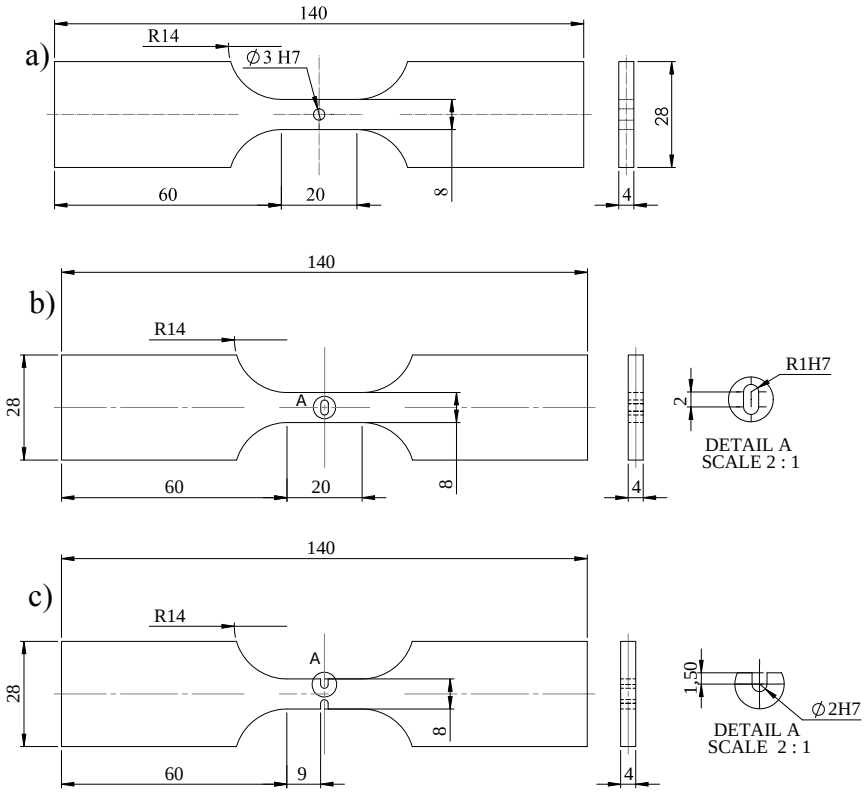

Figure 3.14 – Notched plane specimens' geometries of X65 piping steel: a) central circular hole (X65_CH); b) central oval hole (X65_OH); c) side notch (X65_SN).

Table 3.3 – Specimens' summary of X65 piping steel.

Specimen id.	Specimen and test type	Scope of test	Figure no	Gauge length [mm]
X65_SP	Tensile smooth plane	Stress-strain curve, basic material properties	Figure 3.13	12.5
X65_CH X65_OH X65_SN	Tensile notched plane	Fracture strain, triaxiality and Lode angle parameter influence	Figure 3.14	12.5
X65_SP	Cyclic smooth plane	Kinematic hardening material behaviour	Figure 3.13	12.5
X65_CH X65_OH X65_SN	Cyclic notched plane	Triaxiality and Lode angle parameter influence	Figure 3.14	12.5

The X60 and X65 steel grades after suffering a thermal process that was applied in the full-scale elbows manufacturing were also characterized using monotonic and cyclic tests. The thermal process consisted of a heating until 950ºC±20ºC followed by rapid cooling, using water applied on the outer surface of the tubes, during the hot bending process. A tempering/stress relieve treatment consisting of a stage at 510ºC−520ºC, during 30 minutes, followed by slow cooling (175ºC/hour), was applied afterwards. The experimental program conducted on X60 and X65 steel grades subjected to the referred

thermal process is described in Table 3.4 and Table 3.5, respectively. With respect to the specimens' geometries, the smooth plane specimens of X60TT and X65TT steel grades assumes the dimensions of the smooth plane specimen of X65 (see Figure 3.13) while the geometry of the notched plane specimens of X60TT and X65TT is shown in Figure 3.15.

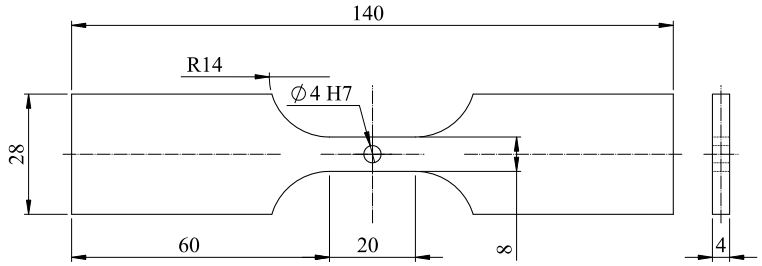

Figure 3.15 – Notched plane specimen geometry of X60TT and X65TT piping steels.

Table 3.4 – Specimens' list of X60 piping steel after thermal treatment (X60TT).

Specimen id.	Specimen and test type	Scope of test	Figure no	Gauge length [mm]
X60TT_SP	Tensile smooth plane	Stress-strain curve, basic material properties	Figure 3.13	12.5
X60TT_CH	Tensile notched plane	Fracture strain, triaxiality and Lode angle parameter influence	Figure 3.15	12.5
X60TT_SP	Cyclic smooth plane	Kinematic hardening material behaviour	Figure 3.13	12.5
X60TT_CH	Cyclic notched plane	Triaxiality and Lode angle parameter influence	Figure 3.15	12.5

Table 3.5 – Specimens' list of X65 piping steel after thermal treatment (X65TT).

Specimen id.	Specimen and test type	Scope of test	Figure no	Gauge length [mm]
X65TT_SP	Tensile smooth plane	Stress-strain curve, basic material properties	Figure 3.13	12.5
X65TT_CH	Tensile notched plane	Fracture strain, triaxiality and Lode angle parameter influence	Figure 3.15	12.5
X65TT_SP	Cyclic smooth plane	Kinematic hardening material behaviour	Figure 3.13	12.5
X65TT_CH	Cyclic notched plane	Triaxiality and Lode angle parameter influence	Figure 3.15	12.5

3.3 EXPERIMENTAL PROGRAM DETAILS

The experimental tests were conducted in a close-loop servo hydraulic machine, INSTRON® 8801. In order to measure/control the longitudinal strain/displacements of the specimens an INSTRON® 2620-602 dynamic extensometer, with limit displacements of ±2.5 mm was used. The base gauge length of the dynamic extensometer was adjusted in accordance with the specimen geometry/size. Gauge lengths of 12.5, 25 and 50 mm were available. The load cell rated to 100kN was used. Monotonic tensile tests were performed under displacement control under a cross-head velocity of 1 mm/min. The dynamic extensometer allows the measurement of an ultimate longitudinal strain of 20% (gauge length of 12.5 mm). However due to the high elongation experienced by the smooth specimens, the gauge was removed at a strain of approximately 17%. The image acquisition system ARAMIS® v6.02 by GOM was coupled with the monotonic tensile tests, allowing the assessment of the specimen necking progress until final fracture. The experimental set-up is shown in Figure 3.16.

An experimental program of cyclic tension-compression tests were conducted under both low-cycle fatigue ($10^2<N_i<10^4$) and ultra-low-cycle fatigue ($10^0<N_i<10^2$) regimes, covering two distinct strain ratios for smooth specimens or two displacement ratios for notched, flat grooved and shear specimens, namely $R_{\varepsilon,\delta}=-1$ and $R_{\varepsilon,\delta}=0$. An approximate constant average strain rate of $d\varepsilon/dt=0.8$ or average relative displacement rate of $d\delta/dt=0.8$ were adopted in the cyclic tests. The frequency of the cyclic tests was set as a function of the strain/relative displacement. Additionally, cyclic bending tests were carried out on X52 piping steel specimens. An adequate experimental set-up was designed to in order to apply an eccentric load on the specimens. More details about the experimental campaign of the bending cyclic tests will be given later.

Smooth specimens tested under ULCF domain may exhibit lateral movements due to plastic instability of the specimens observed at compressive reversals. These lateral instabilities may be significant since it induce additional stresses and strains due to undesired bending effects. It is important to note that there are neither standards nor guidelines available about ULCF testing. In order to minimize the lateral instabilities

during testing, the grip system is complemented by two side rigid plates producing a sandwich with the specimen in the middle, as illustrated in Figure 3.17a), but allowing a small clearance between the gauge length of the specimen and the side plates to avoid high friction. However, when high strain ranges are applied aiming fatigue lives less than 10^2 cycles, the anti-buckling device is not fully effective and the specimens suffer invariably instabilities, as illustrated in Figure 3.17b). Besides the clearance between the specimen and the side plates, the horizontal compliance of the machine actuator is responsible for allowing that reported instabilities.

The lateral movements of the actuator, allowed additional plastic deformations on the specimens, increasing the accumulated equivalent plastic strain during the cyclic loading. For that reason, to quantify the influence of the lateral movements on the evolution of the accumulated equivalent plastic strain, it was decided to measure these displacements in the ULCF tests of the X60TT and X65TT steel grades [4]. The measurements were performed using two LVDTs displacement sensors, from Applied Measurements Limited®, with a displacement range of $\pm 2.5mm$. The LVDT sensors were placed perpendicular to each other and to the loading direction, as represented in Figure 3.18a). The data acquisition was performed using the SPIDER®8 DAC equipment. The LVDT experimental set-up is shown in the Figure 3.18b).

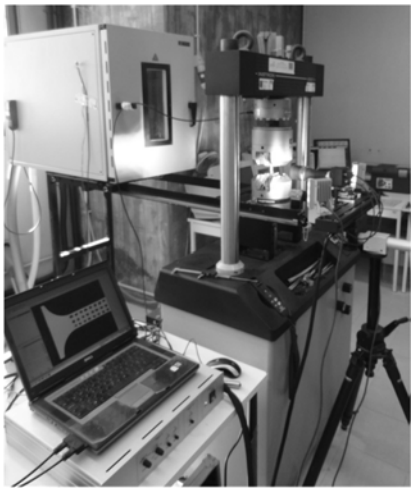

Figure 3.16 – Experimental set-up used in the static tensile tests of the smooth specimens.

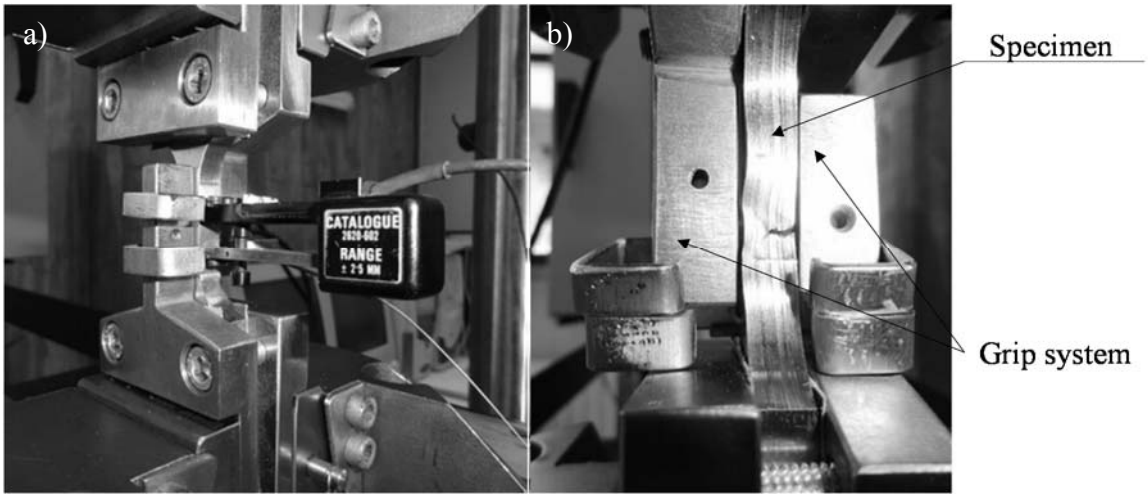

Figure 3.17 – Anti-buckling device used in ULCF tests: a) smooth specimen before testing with the clip gauge mounted; b) smooth specimen after ULCF test showing instability signals.

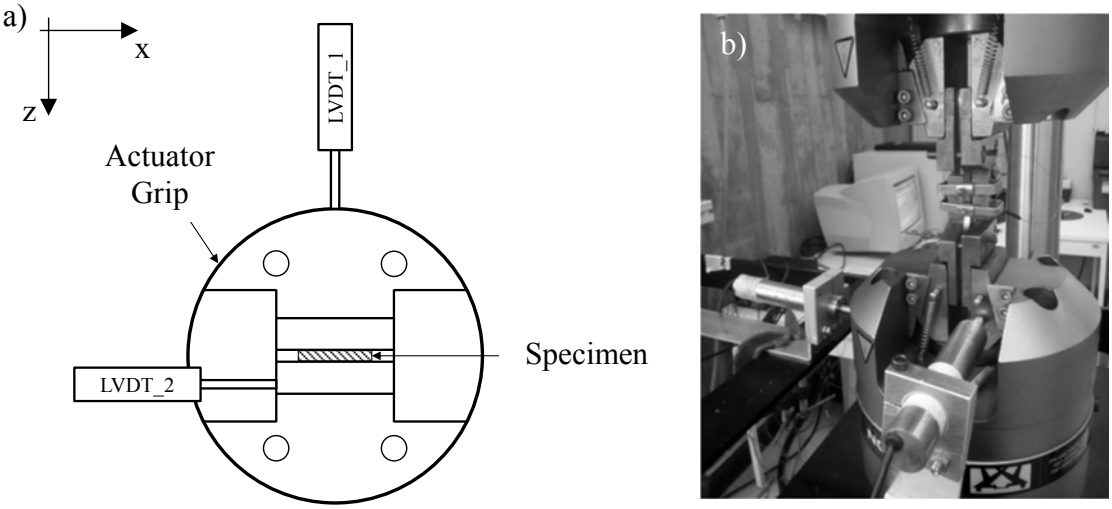

Figure 3.18 – LVDT's measurement system of lateral displacement: a) LVDT's position relative to specimen location (top view); b) experimental set-up of LVDT sensors coupled with the test machine.

In this work, the 2D Digital Image Correlation method was selected taking advantage of its potential when coupled with mechanical tests performed using a universal testing machine, together with relatively simple specimen preparation. This optical method was coupled with monotonic tensile and cyclic tests of notched specimens aiming at evaluating the displacement and strain fields at the regions of interest. The DIC method measures the full-field displacements of an object by comparing the similarity of patch features in images acquired at distinct mechanical/testing time configurations. The reference image (undeformed configuration) is usually subdivided into correlation domains (e.g. square subsets) by selecting a number of pixels/subsets. It is assumed that the spatial distribution of pixel grey levels within each subset defines a unique and local

fingerprint of the surface with suitable contrast and isotropy. The size of the subsets must be carefully defined in a compromise between correlation and interpolation errors, since an independent value of the displacement is measured per subset. A sub-pixel correlation algorithm calculates the position (centre) of each facet on the deformed configuration, therefore determining the displacement field across the region of interest. The DIC method can be used on both 2D and 3D (also called stereovision) configurations [1][2]. DIC 2D measures the in-plane displacements of a (quasi-)planar surface of interest, and it requires the utilization of only one digital camera. In turn, the stereovision set-up provides both in-plane and out-of-plane displacements (although with different resolutions), but it requires the use of two identical optical systems (i.e., digital camera, lenses, aperture, focal length…). The stereovision system has the advantage of taking into account (at least at a certain extent) both parasitic out of- plane movements and contraction effect (Poisson's effect) that may occur during a tensile mechanical loading. Moreover, it can be more properly applied to specimens with moderate curved surfaces. Although, it requires a calibration procedure of the stereovision system, which is time consuming and induces an additional uncertainty on the displacement measurements coming from the evaluation of the camera model parameters. Therefore, in this work the 2D ARAMIS® v6.02 system by GOM was used. The optical devices and measuring parameters are summarized in the Table 3.6. The surfaces of the specimens were prepared in order to define a textured pattern suitable for DIC. A random pattern (speckle) was created over the surface of interest by means of aerosol spray painting. The surface was firstly polished using 300-grit sandpaper. A background white matte paint was then applied followed by a spread distribution of black painting dots.

Table 3.6 – Optical system components and measurement parameters.

CCD Cameras	Baumer Optronic FWX20 (8 bits, 1624x1236 pixels)
Lens	TC2336 Telecentric lens *Magnification: 0.24373%* *Field of view:29.31×22.1mm* *Workingdistance:103.573 mm* *WorkingF-number:8* Far-Field Microscope: Zoom 70XL (Aux lens 0.25X and 2.0X TV Tube) *Magnification: Low: 0.27; High: 1.9* *Field of view: Low (1/4"): 7.2×9.7; High (1/4"): 1.0×1.3* *Low (1/3"): 9.5×12.7; High (1/3"): 1.3×1.8* *Low (1/2"): 12.7×17.0; High (1/2"): 1.8×2.4* *Low (2/3"): 17.5×23.4; High (2/3"): 2.5×3.3* *Working distance: 310 mm* Nikon: Nikon AF 28-105mm f_3.5-4.5D IF Zoom Nikko *Focal length: 100mm* *WorkingF-number:8*
Project parameter – subset	
Subset size	15x15 pixels^2 (0.27×0.27mm^2)
Subset step	15x15 pixels^2 (0.27×0.27mm^2)
Project parameter – strain	
Strain length	7x7 subsets^2 (1.89×1.89 mm^2)
Validity code	55%
Strain computation method	Total
Resolution	
Displacement	2x10^{-2} pixel
Strain	0.02-0.04%

The typical speckle pattern obtained with this marking technique is shown in the Figure 3.19. When applied, the lens aperture, the LED lighting intensity and the shutter time were set in order to enhance the image contrast (pixel grey levels spread as much as possible over the entire dynamic of the camera sensor), but avoiding pixel saturation and preventing motion blur in the images during the exposure time when testing. The facet size (number of pixels per subset) and the facet step (distance between adjacent facet centres) were set to 15×15 pixels^2, taking into account the size of the region of interest, the optical magnification and the quality of the speckle obtained by spray painting. In post-processing, the strain fields were evaluated from the displacement fields by numerical differentiation using a base strain length of 7 subsets. The displacement and strain resolution associated to the DIC measurements are, respectively, in the range of 2×10^{-2} pixel and 0.02% [2]. In addition, this optical system was also coupled with bending cyclic tests allowing the assessment of the deformed shape of the specimens for the extreme position of cyclic loading, by means of a contrast between the specimen

(painted white) with a black background. Figure 3.20 shows the deformed shape obtained during the first cycle of such bending tests.

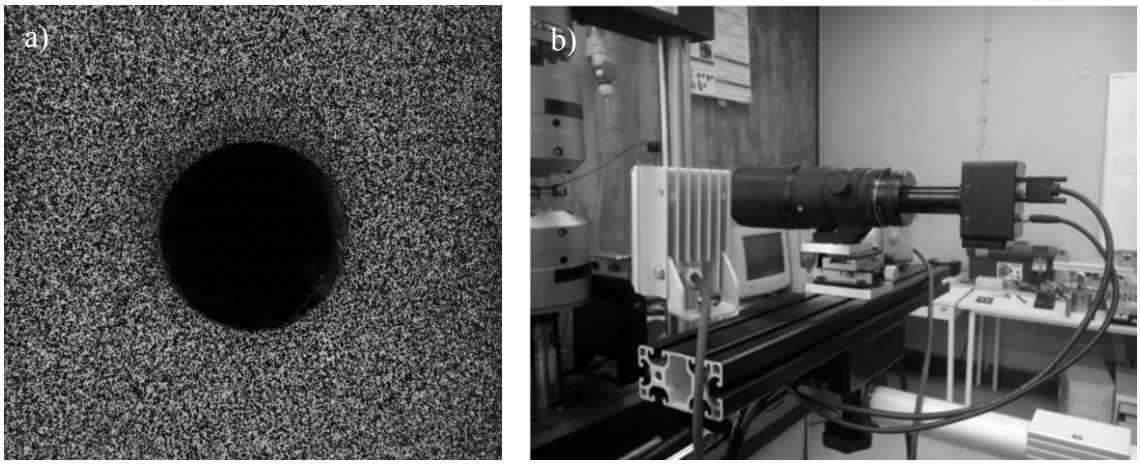

Figure 3.19 – DIC system: a) speckle pattern used in the DIC and b) experimental set-up used for DIC application.

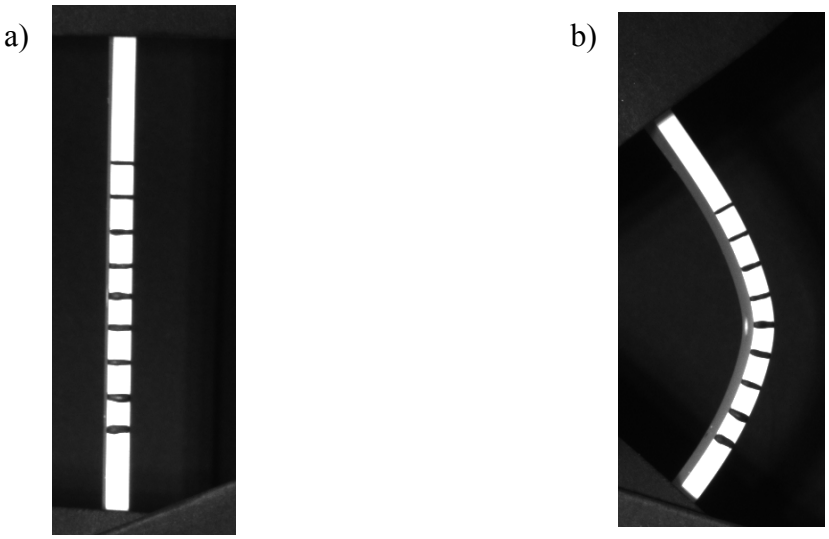

Figure 3.20 – Assessment of the deformed shape of specimen U_BNP_5: a) initial configuration; b) bent configuration.

In order to analyse the material microstructures (metallographic analysis), several images were acquired from an optical microscope. A polishing process was applied to the samples using water sand paper with a decreasing levels of abrasion (180, 220, 320, 500, 800 and 1000) and polishing clothes (3μm and 6μm). Then, the samples were emerged in a solution of Nital-10% in order to emphasize the grain boundaries. Additionally, fracture surface of some specimens were analysed by SEM (Philips® FEI/Quanta 400).

3.4 EXPERIMENTAL RESULTS

An overview of the experimental results from the small-scale tests performed in this study is presented in this section. Three API 5L pipe steel grades, namely the X52, X60, X65 were selected and tested. The experimental program incorporates monotonic and cyclic tests, carried out with several specimen series that were previously described. Concerning the X60 and X65 steel grades, monotonic and cyclic tests were also carried out using steel samples extracted from pipes that were subjected to the same thermal cycle applied to produce elbows with hot bending manufacturing process.

3.4.1 Experimental results of the X52 piping steel

3.4.1.1 Basic tensile properties

The X52 piping steel is used for pipeline transportation systems in the petroleum and natural gas industries and is manufactured in accordance with the American Petroleum Institute specification API 5L. The chemical properties and the mechanical properties requirements of the X52 piping steel are presented in the Table 3.7 and Table 3.8 [3]. Table 3.9 summarizes the mechanical properties, including the yield stress ($\sigma_{y/0.2\%}$) and the ultimate tensile strength (σ_{UTS}) that were obtained from the monotonic tensile tests carried out on smooth plane specimens.

Table 3.7 – Chemical properties of X52 piping steel, API 5L – PSL2 (maximum values) [3].

C [%]	Mn [%]	P [%]	S [%]	V [%]	Nb [%]	Ti [%]
0.28	1.2	0.03	0.03	a	a	a

a: The sum of the Niobium, Vanadium, and Titanium concentrations shall be < 0.06%

Table 3.8 – Mechanical properties requirements of X52 piping steel, API 5L – PSL2 (minimum values) [3].

Piping steel	$\sigma_{y/0.2\%}$ [MPa]	σ_{UTS} [MPa]
X52	360	520

Table 3.9 – Static mechanical properties of the X52 piping steel.

	$\sigma_{y/0.2\%}$ [MPa]	σ_{UTS} [MPa]
Mean	368.53	555.88
Std. Deviation	5.26	1.58
CoV [%]	1.43	0.28

The analysis of the Table 3.9 allows concluding that the experimental results follow the specifications presented in the API standard [3]. Figure 3.21 show the conventional stress-strain curves for the same specimens, until the ultimate tensile strength levels. As referred previously the dynamic extensometer displacement limit was not sufficient to measure the longitudinal strain until the final fracture of the specimens. The elastic, yield plateau (detail view in Figure 3.22) and plastic region are clearly observed.

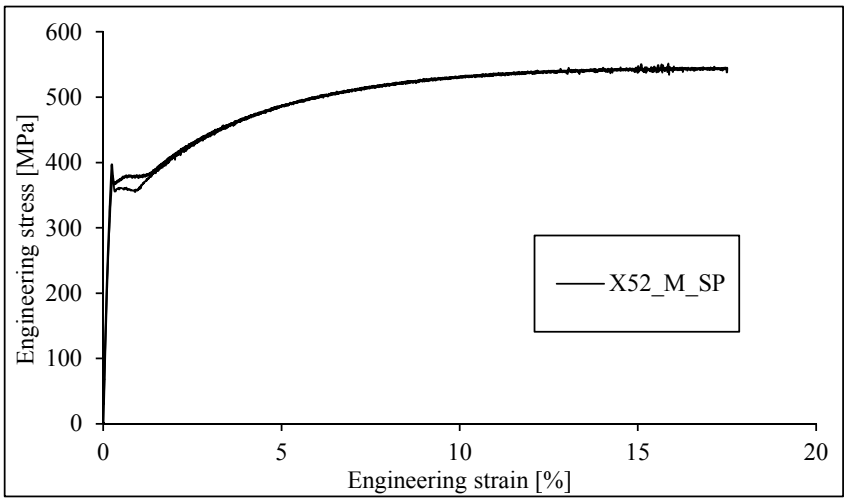

Figure 3.21 – Conventional stress-strain curves of smooth plane specimens of X52 piping steel.

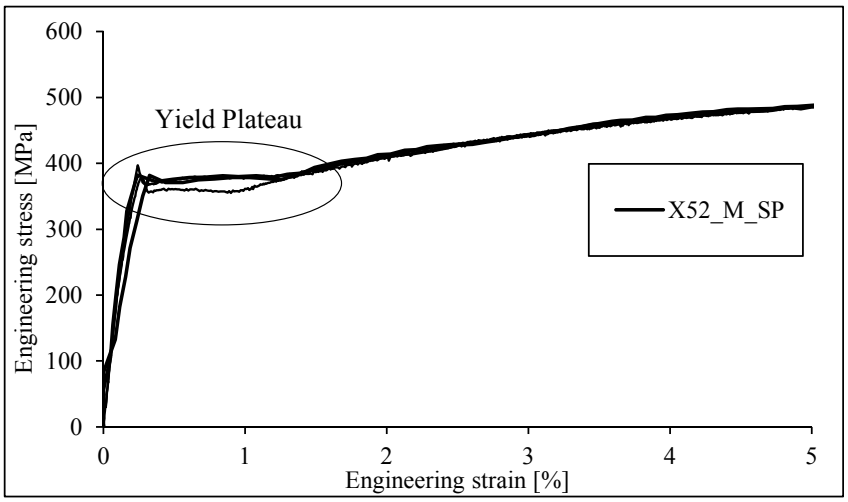

Figure 3.22 – Detail view of yield plateau of the stress-strain curves from the smooth plane specimens of X52 piping steel.

3.4.1.2 Quasi-static monotonic tensile test results

In order to evaluate the entire monotonic behavior of X52 piping steel, the load values were plotted against the lateral necking for the smooth plane specimens. Through the processing of the recorded images during the monotonic tensile tests, it was possible to obtain the experimental lateral necking data. Nevertheless, these results are not the most suitable approach to evaluate the monotonic ductile behavior of the material. In fact, the lateral necking only accounts for transversal deformation of the specimen. Figure 3.23 exhibits the load-relative displacement (lateral necking) of smooth plane of X52 piping steel. The recorded load-displacements curves of the notched specimens' series of X52 piping steel are illustrated in Figure 3.24 to Figure 3.26. The elastic, plastic region and loss of strength due to necking effect and damage of the material can be clearly observed. A good agreement between the curves of same specimens' geometries is verified. Since notched plane specimens have less capacity of longitudinal deformation, the dynamic extensometer was suitable to follow the entire specimen deformation during the tensile tests. Different notch severities were considered for the referred specimens, thus it is expectable to obtain different levels of monotonic parameters, namely monotonic fracture strain, triaxiality and Lode angle parameters, which have to be assessed through numerical simulation. Figure 3.27a) shows the fracture surface of a smooth plane specimen of X52 piping steel where can be observed the fibrous appearance of the material that characterizes the ductile fracture. Microvoids are the typical microstructure feature of the plastic failure, which are clearly identified in the Figure 3.27b).

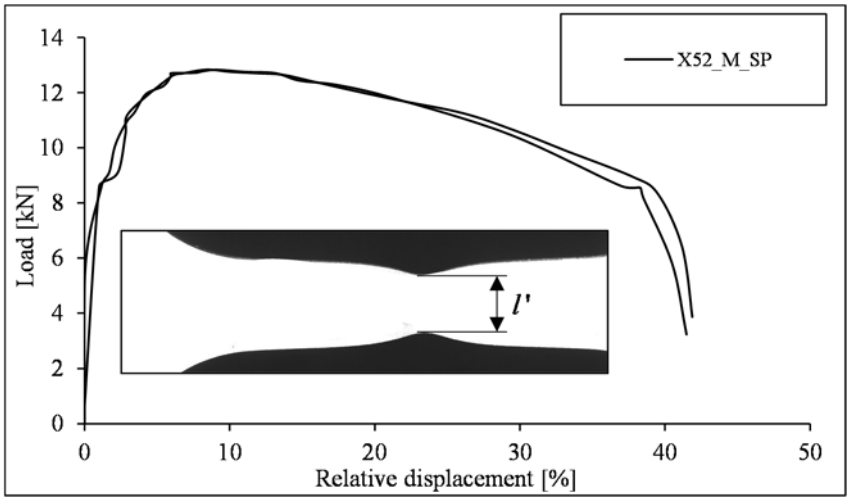

Figure 3.23 – Monotonic load-relative displacement (lateral necking) curves of smooth plane specimens of X52 piping steel.

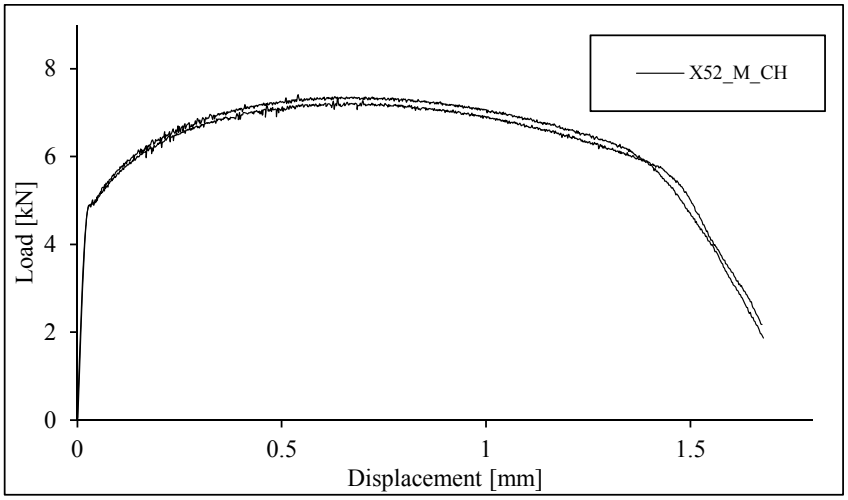

Figure 3.24 – Monotonic load-displacement curves of the X52_CH notched specimens series.

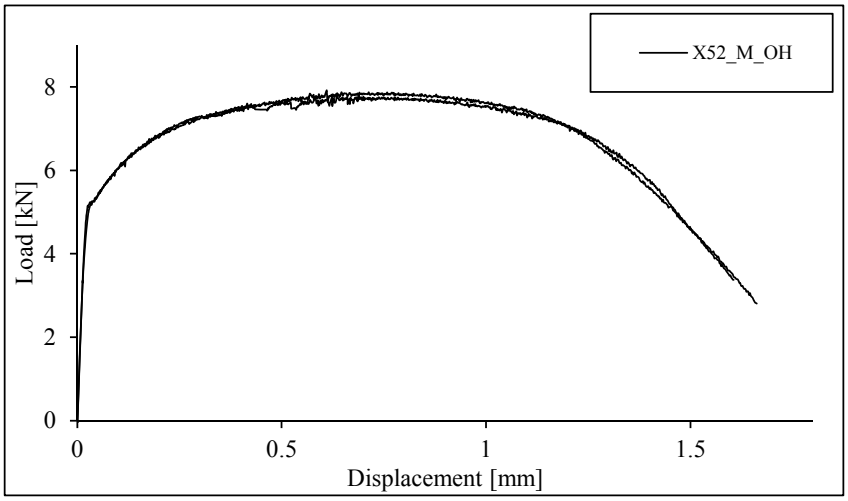

Figure 3.25 – Monotonic load-displacement curves of the X52_OH notched specimens series.

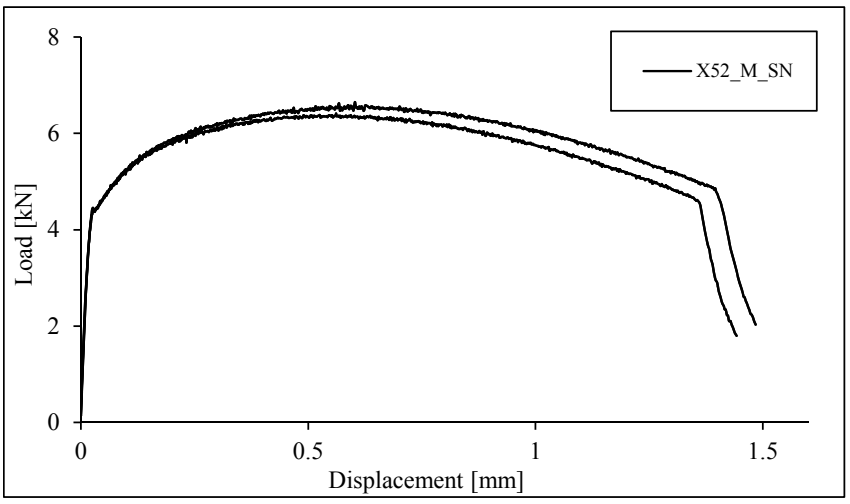

Figure 3.26 – Monotonic load-displacement curves of the X52_SN notched specimens series.

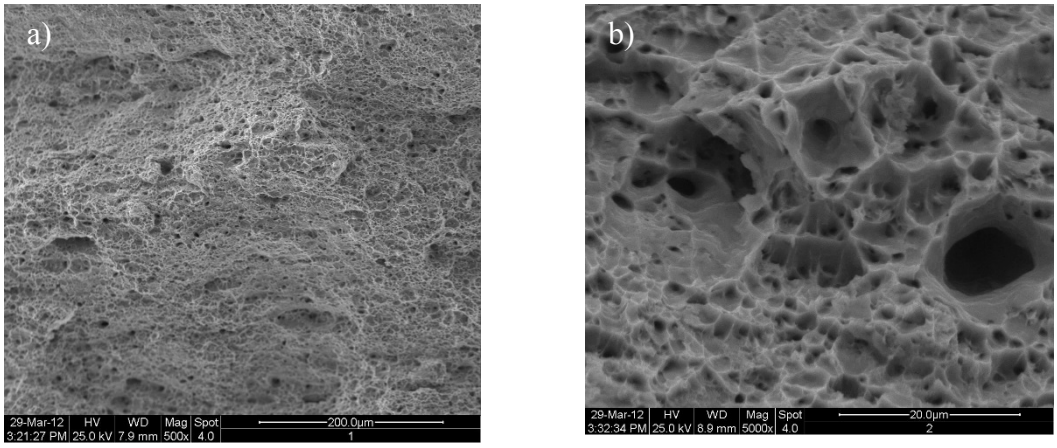

Figure 3.27 – Facture surface of a smooth plane specimen of X52 piping steel subjected to monotonic failure: a) general of material porosity view; b) detail view of material porosity with microvoids pattern.

3.4.1.3 Experimental results of cyclic tension-compression tests on smooth specimens

The experimental data obtained from LCF and ULCF tests of smooth plane specimens of X52 piping steel is present in the Table 3.10. The capital letters *L* and *U* in the specimen identification denotes LCF and ULCF tests, respectively. The transversal area (S_t), the strain ratio (R_ε), the test frequency (f) , the strain range ($\Delta\varepsilon$), the number of cycles to crack initiation (N_i), the stress range at the section of specimen ($\Delta\sigma$) and the plastic ($\Delta\varepsilon^P$) and elastic ($\Delta\varepsilon^E$) strain ranges of the tests performed are presented. The fatigue life was investigated until crack initiation. Therefore, a criterion to identify the number of cycles to crack initiation was suggested, by plotting the maximum load values along the number of cycles, as shown in Figure 3.28. The fatigue crack initiation was assumed to occur when the load values deviates from the linear trend with respect to the number of cycles, which corresponds to the macroscopic fatigue crack propagation. This methodology was extrapolated for all axial tension-compression cyclic tests performed in this work.

The plastic strain range was computed from the width of stabilized hysteresis loops at the mean life of the specimen. Based on the total strain range, the elastic strain range was derived by subtracting the plastic strain range to the total strain range. Uniaxial stress state and uniform strain field were assumed in this procedure. The experimental stress and strain amplitudes of stabilized hysteresis cycles are correlated together in order to derive

the cyclic curve of the material. This relation can be described by the Ramberg-Osgood equation, as follows [5]:

$$\frac{\Delta\varepsilon}{2} = \frac{\Delta\varepsilon^E}{2} + \frac{\Delta\varepsilon^P}{2} = \frac{\Delta\sigma}{2E} + \left(\frac{\Delta\sigma}{2K'}\right)^{1/n'} \tag{3.1}$$

where E is the Young modulus, K' and n' are the cyclic strain hardening coefficient and cyclic strain hardening exponent, respectively. The stress and strain amplitudes are plotted in a log-log scale in order to obtain the cyclic parameters involved in Ramberg-Osgood relation [5]. To analyse the influence of the ULCF experimental data on the assessment of cyclic parameters two distinct approaches are followed described. In the first case only LCF data was considered (see Figure 3.29) to compute the cyclic parameters while in the second approach both LCF and ULCF were plotted together to identify the main contribution of the ULCF experimental tests on the computation of the cyclic curve parameters. Table 3.11 summarizes the cyclic parameters derived from these approaches. Comparisons between cyclic curves derived from LCF and ULCF plus LCF data are represented in Figure 3.31. As can be observed, the cyclic curves shift downward when ULCF data is considered.

Table 3.10 – Experimental program of cyclic tests of smooth specimens of X52 piping steel.

Specimens	S_t [mm^2]	R_ε [–]	f [Hz]	$\Delta\varepsilon$ [%]	N_i [cycles]	$\Delta\sigma$ [MPa]	$\Delta\varepsilon^P$ [%]	$\Delta\varepsilon^E$ [%]
L0_SP_1	22.98	0	0.4000	1.00	1750	806.12	0.603	0.397
L0_SP_2	22.91	0	0.4000	1.00	2300	802.13	0.610	0.390
L0_SP_3	23.14	0	0.2667	1.50	488	865.95	1.046	0.454
L0_SP_4	23.02	0	0.2667	1.50	465	869.21	1.051	0.449
L0_SP_5	23.00	0	0.2000	2.00	320	914.40	1.508	0.492
L0_SP_6	23.09	0	0.2000	2.00	350	904.45	1.489	0.511
L0_SP_7	23.25	0	0.1600	2.50	184	942.49	1.968	0.532
L0_SP_8	23.10	0	0.1600	2.50	251	943.73	1.983	0.517
L0_SP_9	23.07	0	0.8000	0.50	29000	630.10	0.190	0.310
L0_SP_10	22.99	0	0.5333	0.75	3200	739.14	0.395	0.355
L0_SP_11	22.71	0	0.5333	0.75	7010	718.52	0.393	0.357
L0_SP_12	22.60	0	0.8000	0.50	18000	641.28	0.201	0.299
L0_SP_13	22.78	0	0.1455	2.75	240	935.49	2.220	0.530
L0_SP_14	23.34	0	0.1333	3.00	181	941.72	2.455	0.545
L0_SP_15	22.96	0	0.1455	2.75	162	947.92	2.189	0.561
L0_SP_16	23.10	0	0.1333	3.00	156	949.90	2.437	0.563
L-1_SP_1	23.12	-1	0.2000	2.00	330	884.10	1.493	0.507
L-1_SP_2	22.99	-1	0.2000	2.00	290	914.75	1.494	0.506
L-1_SP_3	23.26	-1	0.4000	1.00	2150	785.66	0.600	0.400
L-1_SP_4	23.12	-1	0.2667	1.50	720	827.59	1.006	0.494
L-1_SP_5	22.91	-1	0.1333	3.00	90	980.85	2.450	0.550
L-1_SP_6	22.84	-1	0.2667	1.50	680	851.69	1.034	0.466
L-1_SP_7	22.81	-1	0.1600	2.50	182	959.58	1.948	0.552
L-1_SP_8	23.07	-1	0.5333	0.75	3750	739.08	0.386	0.364
L-1_SP_9	22.68	-1	0.1600	2.50	211	921.23	1.950	0.550
L-1_SP_10	22.77	-1	0.4000	1.00	2050	776.09	0.543	0.457
L-1_SP_11	22.79	-1	0.8000	0.50	27500	636.94	0.191	0.309
L-1_SP_12	22.84	-1	0.8000	0.50	28000	647.18	0.189	0.311
L-1_SP_13	22.57	-1	0.5333	0.75	6000	737.20	0.382	0.368
L-1_SP_14	22.94	-1	0.1455	2.75	155	967.38	2.211	0.539
L-1_SP_15	22.96	-1	0.1455	2.75	130	977.78	2.199	0.551
U0_SP_1	23.78	0	0.0800	5.00	*			
U0_SP_2	23.66	0	0.1143	3.50	117	958.65	2.889	0.611
U0_SP_3	23.48	0	0.1000	4.00	*			
U0_SP_4	23.63	0	0.1000	4.00	70	1026.53	3.422	0.578
U0_SP_5	23.93	0	0.0941	4.25	87	1010.00	3.601	0.649
U0_SP_6	23.85	0	0.1000	4.00	*			
U0_SP_7	23.89	0	0.0941	4.25	121	1001.39	3.569	0.681
U0_SP_8	23.78	0	0.0889	4.50	46	976.46	3.780	0.720
U0_SP_9	23.91	0	0.0889	4.50	41	1062.28	3.874	0.626
U0_SP_10	23.68	0	0.0727	5.50	27	1091.59	4.921	0.579
U0_SP_11	23.85	0	0.0800	5.00	35	1032.47	4.348	0.652
U0_SP_12	23.66	0	0.0667	6.00	24	1101.85	5.348	0.652

* invalid test

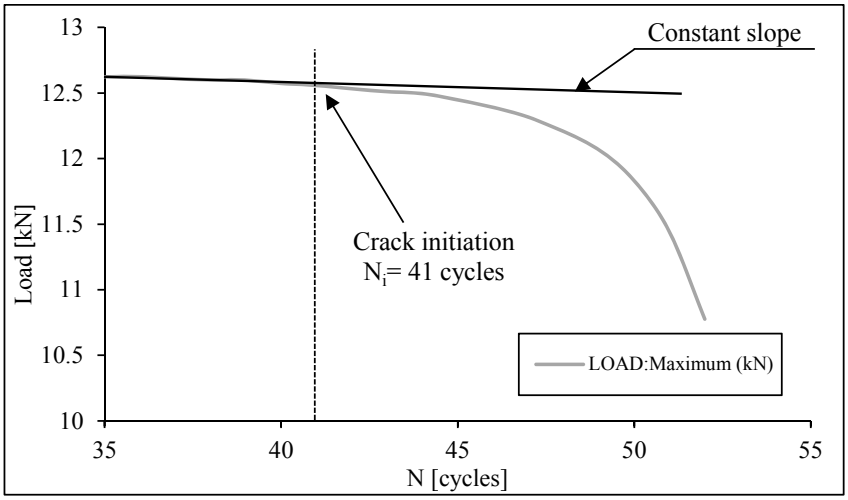

Figure 3.28 – Criterion to assess the fatigue crack initiation (e.g. X52_U0_SP_12 specimen).

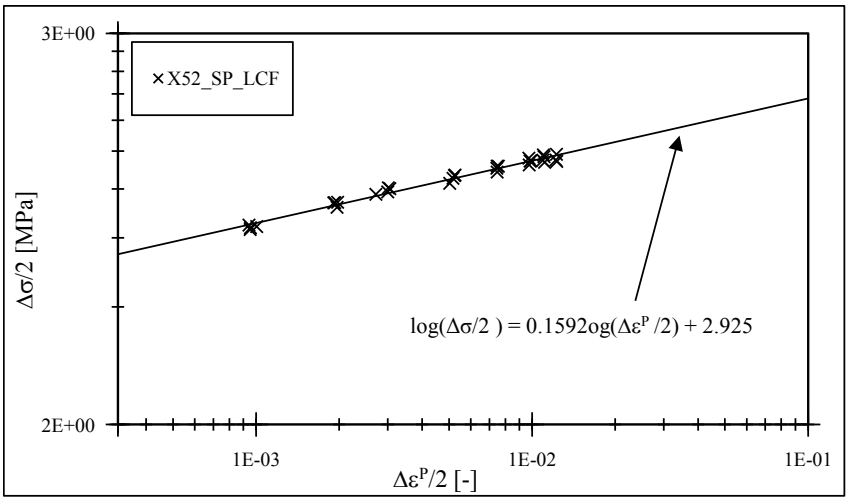

Figure 3.29 – Stress-plastic strain amplitude of X52 piping steel, under LCF domain.

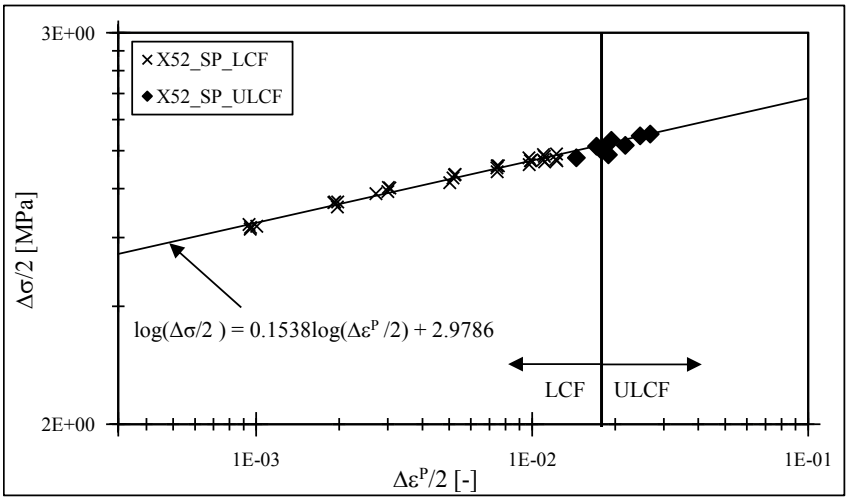

Figure 3.30 – Stress-plastic strain amplitude of X52 piping steel, under LCF plus ULCF domain.

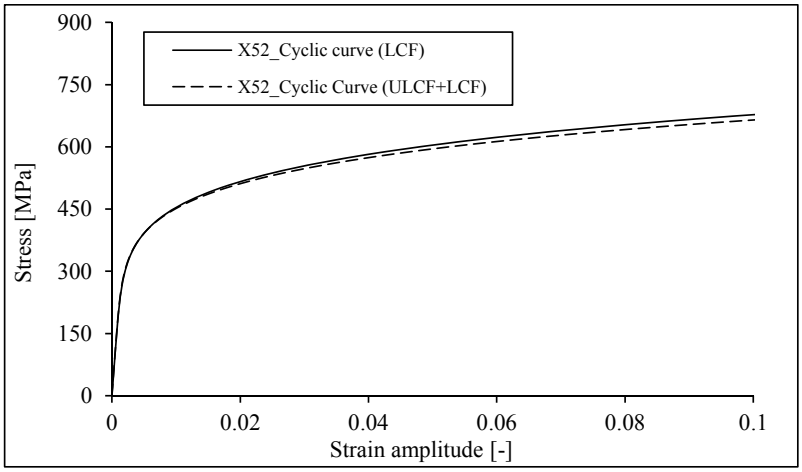

Figure 3.31 – Cyclic curves of X52 piping steel obtained with LCF and LCF plus ULCF experimental data.

Table 3.11 – Cyclic parameters of the X52 piping steel obtained from LCF data and LCF plus ULCF data.

Experimental Data Source	*K'* [MPa]	*n'*
LCF	982.88	0.1592
LCF+ULCF	951.92	0.1538

For both strain ratios used in the cyclic tests of the X52 piping steel, the evolution of the cyclic stress amplitude with the number of cycles was derived for the applied strain ranges. These results can be observed in Figure 3.32 and Figure 3.33, respectively. For the average levels of the applied strain ranges (0.75% and 1.0%) the material exhibits a stabilized behaviour, for the whole cyclic loading. The analysis of the experimental data also shows a cyclic hardening for higher strain range levels (3.0%, 2.5%, 2.0 % and 1.5%) between the first and the second cycle, followed by a stabilized behaviour. Additionally, for lower strain range levels (e.g. 0.5%) a cyclic softening is verified between the first and the second cycle. This softening increases progressively along the cyclic loading. The strain-life relations for the X52 steel are now presented. LCF test data are usually presented using relations between the strain amplitude and the number of reversals until crack initiation, *2Ni*. This relation results from the superposition of the elastic and plastic strain effects, defined respectively by Basquin [6] and Coffin-Manson relations [7][8]:

$$\frac{\Delta\varepsilon}{2}=\frac{\Delta\varepsilon^{E}}{2}+\frac{\Delta\varepsilon^{P}}{2}=\frac{\sigma_{f}^{'}}{E}(2N_{i})^{b}+\varepsilon_{f}^{'}(2N_{i})^{c} \tag{3.2}$$

where σ'_f is the fatigue strength coefficient, b is the fatigue strength exponent, ε'_f is the cyclic ductility coefficient and c is the ductility exponent. The constants involved in Morrow's formulation were obtained splitting the total strain-life relation into elastic and plastic strains *versus* life relations. The evolution of the elastic, plastic and total strain *versus* life relations were obtained correlating together the data from both strain ratios, since a negligible influence of the strain ratio was verified in the strain-life relation. Figure 3.34 exhibits the strain-life curves of the X52 piping steel based on the LCF experimental data only. The influence of ULCF on the estimation of strain-life relation is taken into account by plotting the LCF and ULCF data simultaneously in the same graph, as can be observed in the Figure 3.35. The parameters of Morrow's relation resulted from these procedures are summarized in the Table 3.12. Main differences are found for cyclic ductility coefficient and ductility exponent, which are related with the plastic strain component of the experimental data.

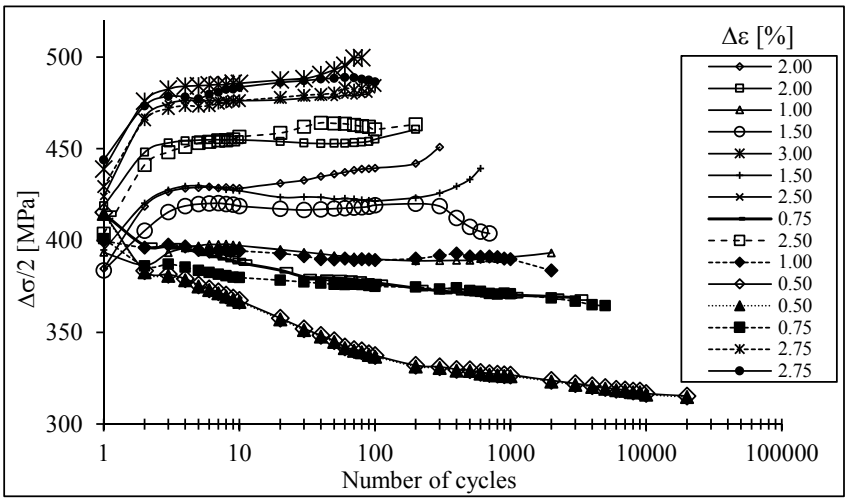

Figure 3.32 – Evolution of the stress amplitude with number of cycles for smooth plane specimens tested under R_ε=-1, X52 piping steel.

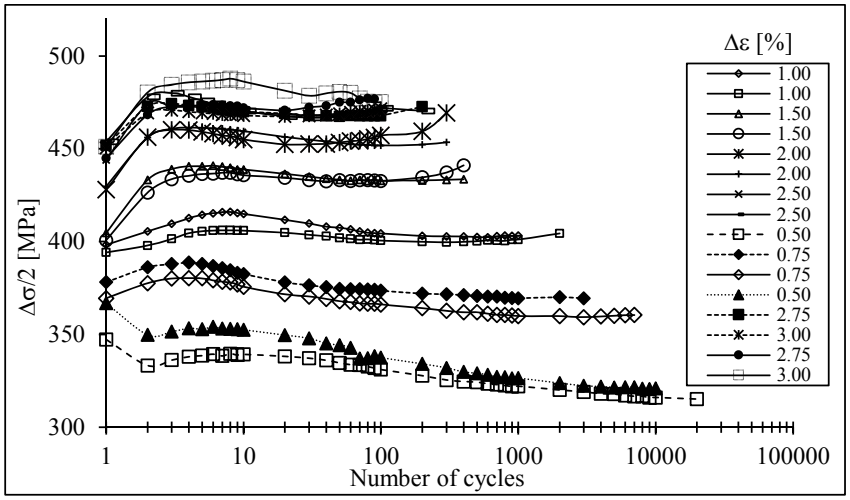

Figure 3.33 – Evolution of the stress amplitude with number of cycles for smooth plane specimens tested under R_ε=0, X52 piping steel.

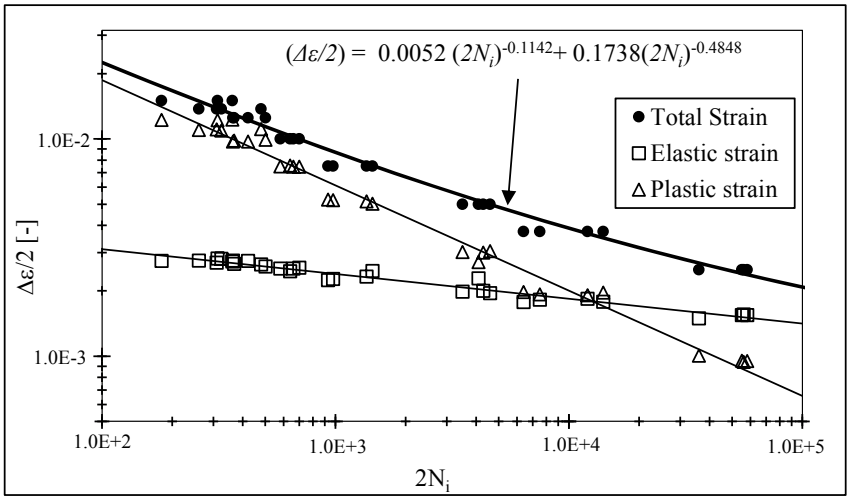

Figure 3.34 – Total strain-life curves of X52 piping steel obtained from LCF data (smooth plane specimens).

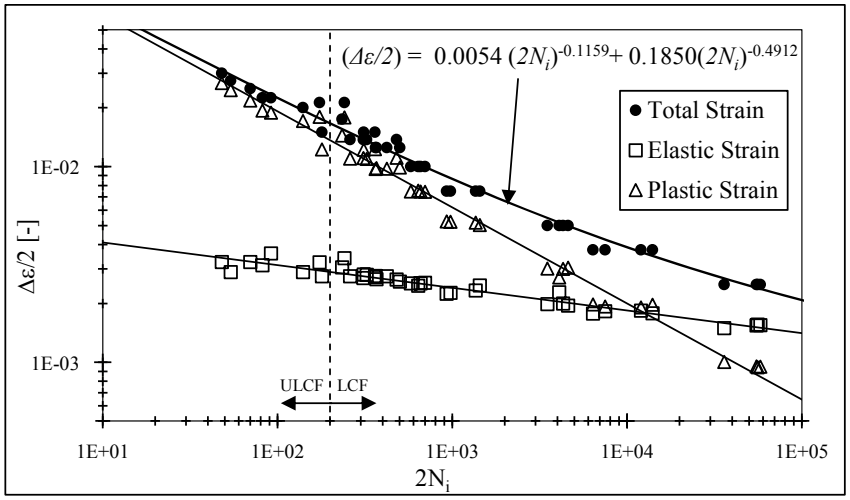

Figure 3.35 – Total strain-life curves of X52 piping steel obtained from LCF plus ULCF data (smooth plane specimens).

Table 3.12 – Parameters of Morrow's relation derived from LCF and LCF plus ULCF data, of X52 piping steel.

Experimental Data Source	σ'_f [MPa]	b	ε'_f	c
LCF	1073.17	-0.1142	0.1738	-0.4848
LCF+ULCF	1112.40	-0.1159	0.1850	-0.4912

The fracture surfaces of the smooth plane specimens tested under ULCF domain of X52 piping steel were examined. The analysis of the fracture surface aims to identify characteristic features of a fatigue failure under large plastic strain cyclic conditions. Figure 3.36 illustrates a typical ULCF fracture surface where it is possible to observe the crack initiation location (1), the crack propagation phase characterized by beachmarks (2) and the final plastic failure (3). Under ULCF domain the plastic strains are intense, thus the beachmarks are more noticeable. These features mark the progress of the crack at various stages of the cyclic loading. The ULCF failure mechanisms results of a mixture of LCF and monotonic ductile failure [9]. These assumptions are supported by the analysis of the Figure 3.37 where is possible to identify the microcracks typical of LCF fracture (Figure 3.37a)) and the cavities with a fibrous aspect which results from the growth and coalescence of microvoids (Figure 3.37a)). The progress of the fatigue crack per cycle, resulting in the beachmarks formation, is accompanied by plastic failure with microvoids formation, growth and coalescence.

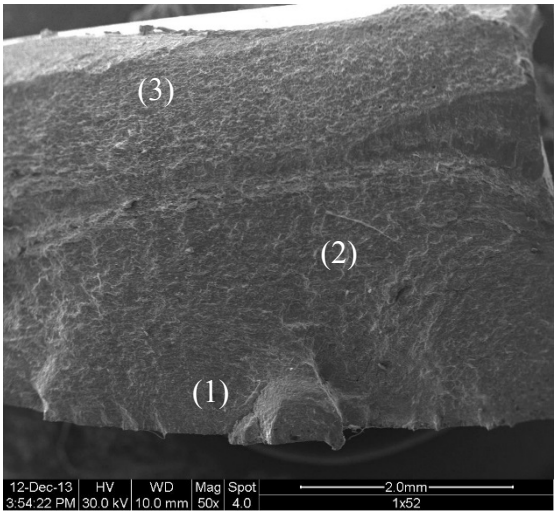

Figure 3.36 – Fracture surface of smooth plane specimens of X52 piping steel, tested under ULCF domain ($\Delta\varepsilon$=5%).

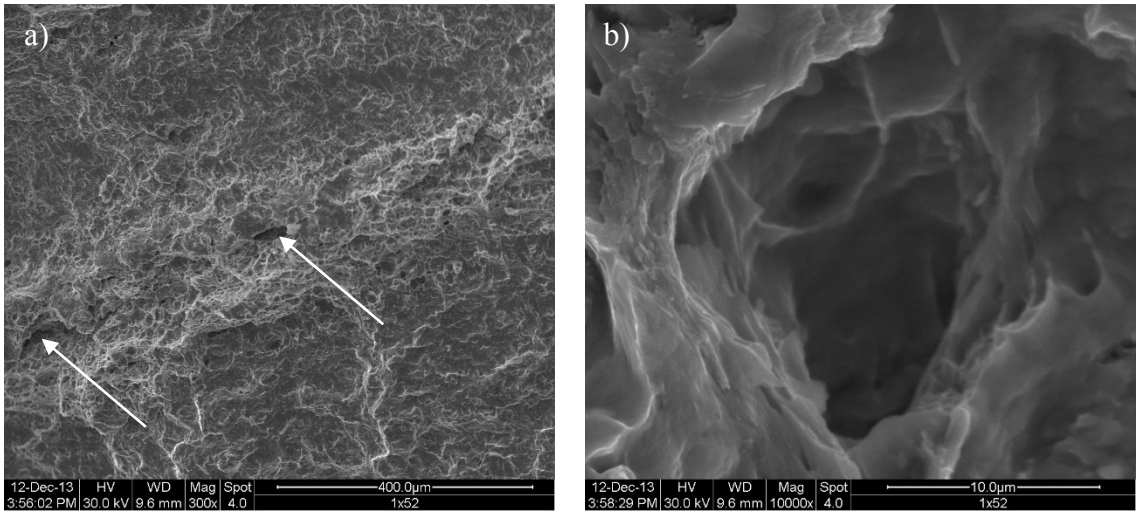

Figure 3.37 – Fracture surface of smooth plane specimens of X52 piping steel, tested under ULCF domain: a) detail view of microcracks; b) detail view of a microvoid.

3.4.1.4 Experimental results of cyclic tension-compression tests on notched specimens

Cyclic tests under LCF and ULCF domain were also performed on notched plane specimens of X52 steel grade. The geometries of those specimens were previously presented in the Section 3.2. The use of notched specimens allowed the investigation of the stress state parameters influence on ductile fracture as well as the reduction of instability problems at the compressive reversals of ULCF tests. Thus, with moderate remote displacement range levels, fatigue cycles lower than 10^2 were obtained. Regarding X52 piping steel three different kinds of notches were considered. Table 3.13 to Table 3.15 summarize the experimental data covered by both LCF and ULCF domains of notched plane specimens. It is possible to observe the specimens reference (designation), the relative displacement ratio, R_δ, the relative displacement range, $\Delta\delta$, the test frequency, f and the number of cycles to crack initiation. The criterion set for the crack initiation of the smooth plane specimens (see Figure 3.28) was also considered for the notched plane specimens. The cyclic tests of notched specimens were performed under displacement control, using the dynamic extensometer with a gauge length of L_0=12.5mm. The relative displacement or pseudo strain, δ, is defined by the ratio of displacement imposed within the gauge length. In fact, the notch presence leads to a non-uniform stress/strain field whereby is not possible to correlate the displacement imposed and the maximum strain at the notch using a simple direct formulation. The methodology of displacement control is

exemplified in Figure 3.38 and was used for all cyclic tests carried out on the notched specimens of piping steels investigated in this work.

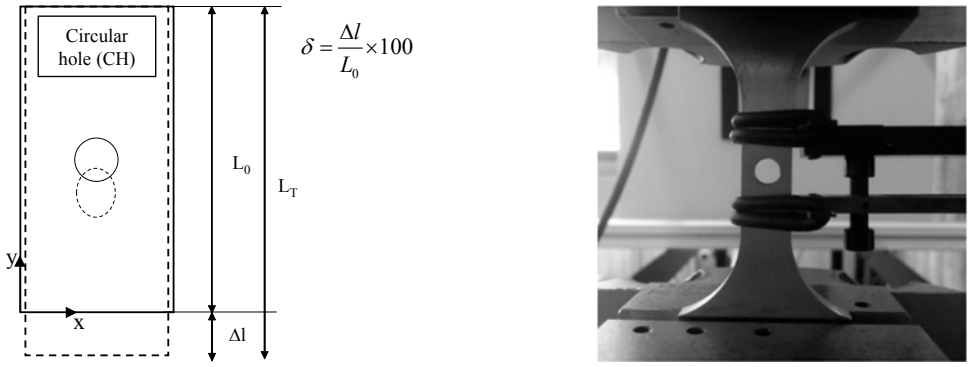

Figure 3.38 – Methodology of displacement control used in the cyclic tests of notched plane specimens: a) gauge region and relative displacement definition; b) notched plane specimen (CH series) with clip gauge.

Table 3.13 – Experimental program of cyclic tests of CH series of X52 piping steel.

Specimens reference	***Rδ* [–]**	***f* [Hz]**	***Δδ* [%]**	***Ni* [cycles]**
L-1_CH_01	-1	0.5333	0.75	140
L-1_CH_02	-1	0.8000	0.50	410
L-1_CH_03	-1	1.6000	0.25	5201
U-1_CH_01	-1	0.2667	1.00	72
U-1_CH_02	-1	0.2667	1.25	52
U-1_CH_03	-1	0.2000	1.50	34
U-1_CH_04	-1	0.2000	2.00	17
U-1_CH_05	-1	0.1778	2.25	13
U0_CH_01	0	0.2000	2.00	20
U0_CH_02	0	0.1778	2.25	14
U0_CH_03	0	0.2667	1.50	36
U0_CH_04	0	0.3200	1.25	51
U0_CH_05	0	0.2286	1.75	22

Table 3.14 – Experimental program of cyclic tests of SN series of X52 piping steel.

Specimens reference	***Rδ* [–]**	***f* [Hz]**	***Δδ* [%]**	***Ni* [cycles]**
L-1_SN_01	-1	0.8000	0.50	1021
L-1_SN_02	-1	1.0000	0.40	1713
L-1_SN_03	-1	0.5333	0.75	324
L-1_SN_04	-1	1.3333	0.30	3949
U-1_SN_01	-1	0.7500	1.50	29
U-1_SN_02	-1	1.0000	2.00	16
U-1_SN_03	-1	0.8750	1.75	23
U-1_SN_04	-1	0.5000	1.00	65
U-1_SN_05	-1	1.1250	2.25	13
U-1_SN_06	-1	0.6250	1.25	55
U0_SN_01	0	0.3200	1.25	50
U0_SN_02	0	0.1778	2.25	14
U0_SN_03	0	0.2000	2.00	20
U0_SN_04	0	0.2286	1.75	26
U0_SN_05	0	0.4000	1.00	60
U0_SN_06	0	0.2667	1.50	35

Table 3.15 – Experimental program of cyclic tests of OH series of X52 piping steel.

Specimens reference	R_δ [–]	f [Hz]	$\Delta\delta$ [%]	N_i [cycles]
L-1_OH_01	-1	0.5333	0.75	80
L-1_OH_02	-1	0.8000	0.50	240
L-1_OH_03	-1	1.0000	0.40	435
L-1_OH_04	-1	1.3333	0.30	1381
L-1_OH_05	-1	2.0000	0.20	9300
U-1_OH_01	-1	0.1778	2.25	9
U-1_OH_02	-1	0.2000	2.00	11
U-1_OH_03	-1	0.2286	1.75	12
U-1_OH_04	-1	0.2667	1.50	19
U-1_OH_05	-1	0.3200	1.25	30
U-1_OH_06	-1	0.2667	1.50	18
U0_OH_01	0	0.2286	1.75	14
U0_OH_02	0	0.1778	2.25	11
U0_OH_03	0	0.2000	2.00	13
U0_OH_04	0	0.4000	1.00	53
U0_OH_05	0	0.3200	1.25	38
U0_OH_06	0	0.2667	1.50	22

3.4.1.5 Experimental results of cyclic bending specimens

To overcome the instability phenomena observed during the ULCF tests of smooth specimens, an anti-buckling device or the notched specimens can be used as previously shown. However, for extremely high strain levels the anti-buckling system could not be sufficient to fully solve the effect of the specimens' instabilities. The use of notched specimens to overcome the instability problems, raises some difficulties regarding the data reduction, due to the multiaxial stress/strain fields generated, being necessary the finite element analysis of these tests. Based on these assumptions bending cyclic tests on smooth specimens arises as an alternative procedure to derive ULCF data. Bending cyclic tests generates bending plastic deformations on the material, leading to the failure. This loading scenario can be found in cyclic bending of pipelines induced by local plastic instability. The cyclic bending tests were also conducted on notched and flat-grooved specimens, which allow investigating the stress triaxiality and Lode angle parameters influence (refer to Figure 3.5 and Figure 3.39 for specimen's geometries). The experimental program of cyclic bending tests was carried out on a servo hydraulic INSTRON® 8801 universal test machine, at room temperature, under displacement control with a displacement ratio, R_d =0 and using a load cell rated for 5kN. The experimental set-up of bending cyclic tests is represented in Figure 3.40. A grip system was designed to induce an eccentric compressive load, as shown schematically in Figure 3.40a).

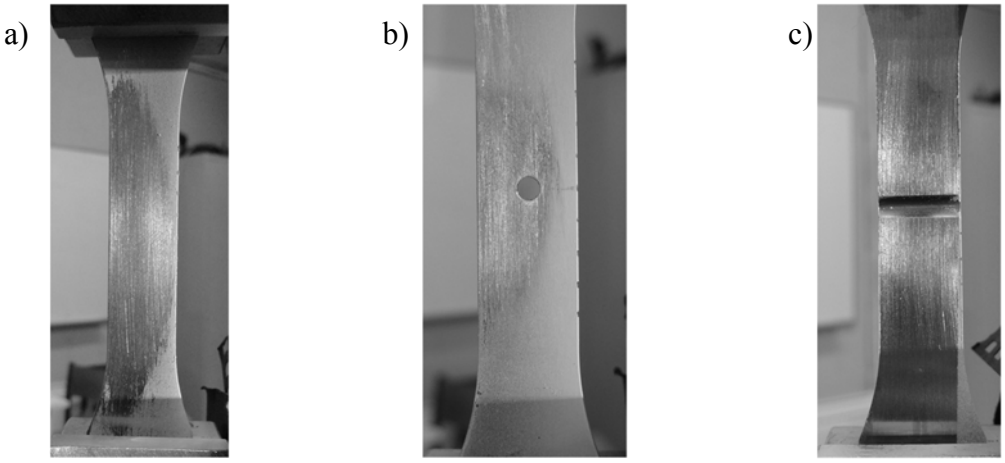

Figure 3.39 – Specimens used in cyclic bending tests: a) smooth plane specimens; b) notched plane specimen; c) flat-grooved specimen.

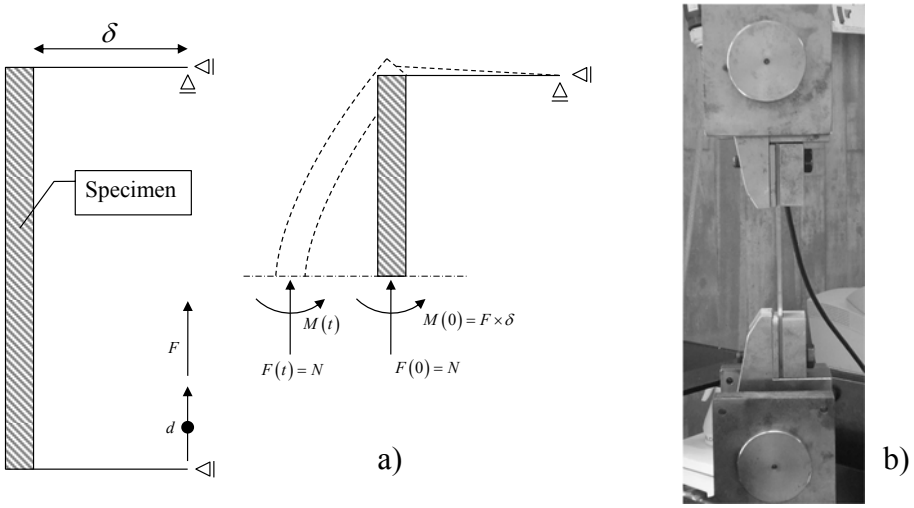

Figure 3.40 – Cyclic bending tests: a) loading conditions of cyclic bending tests; b) grip system mounted in the universal testing machine.

The applied displacement range, Δd and the number of cycles to crack initiation, N_i are summarized in the Table 3.16, Table 3.17 and Table 3.18 for the three specimens' series. Taking into account the displacement limit allowed by the servo-hydraulic machine, a maximum displacement range of 150 mm was set for the smooth specimens to obtained fatigue life cycles less than 100 cycles. Two displacement ranges was used in cyclic bending tests and a poor correlation regarding the fatigue life was obtain. In contrast, the notched and flat-grooved specimens exhibit a higher strain concentration that promoted a higher damage evolution and consequently a reduced number of cycles to crack initiation were attained. This effect allowed a well detention of the crack initiation instant from the analysis of consecutive pictures that were taken during the cyclic tests. This procedure

indicated the local of cracking initiation. In the case of smooth plane specimens subjected to the cyclic bending tests, the damage evolution is slower whereby is not reproduced immediately in the global response which raised some difficulties for the assessment of the number of cycles for the crack initiation. The number of cycles resulted from this methodology is compared with the displacement range used for the cyclic bending tests of notched plane and flat-grooved specimens in the Figure 3.41. A potential law was used to correlate the experimental data and a high coefficient of determination was obtained for both tests series.

Table 3.16 – Experimental results of smooth plane specimens of cyclic bending tests (U_BSP series).

Specimens reference	Δd [mm]	N_i [cycles]
U_BSP_1	150	78
U_BSP_2	150	51
U_BSP_3	150	47
U_BSP_4	150	74
U_BSP_5	150	69
U_BSP_6	150	90
U_BSP_7	120	34
U_BSP_8	120	106

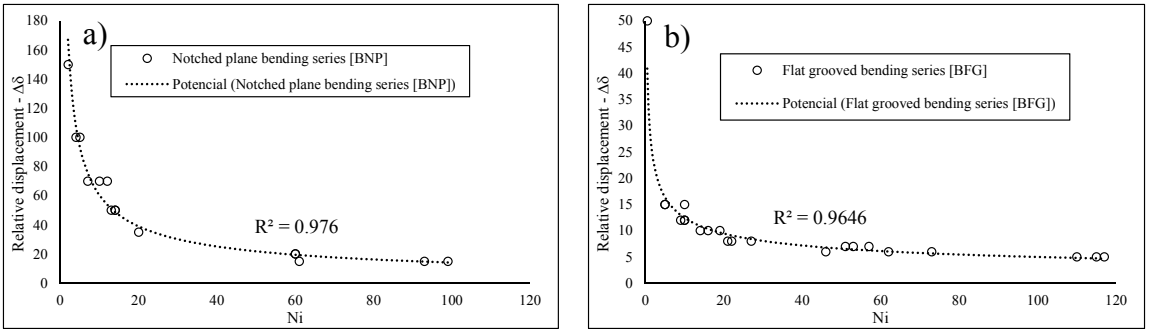

Figure 3.41 – Relative displacement plotted against of number of cycles to crack initiation: a) notched plane specimens; b) flat-grooved specimens.

Table 3.17 – Experimental results of notched plane specimens subjected to cyclic bending tests (U_BNP series).

Specimens reference	Δd **[mm]**	N_i **[cycles]**
U_BNP_1	100	4
U_BNP_2	150	2
U_BNP_3	70	10
U_BNP_4	70	7
U_BNP_5	70	12
U_BNP_6	50	14
U_BNP_7	50	13
U_BNP_8	50	14
U_BNP_9	35	20
U_BNP_10	100	5
U_BNP_11	20	60
U_BNP_12	20	60
U_BNP_13	15	93
U_BNP_14	15	99
U_BNP_15	15	61

Table 3.18 – Experimental results of flat-grooved plane specimens subjected to cyclic bending tests (U_BFG series).

Specimens reference	Δd **[mm]**	N_i **[cycles]**
U_BFG_1	50	0.5
U_BFG_2	15	10
U_BFG_3	10	14
U_BFG_4	10	16
U_BFG_5	7	53
U_BFG_6	10	19
U_BFG_7	7	51
U_BFG_8	7	57
U_BFG_9	5	110
U_BFG_10	5	115
U_BFG_11	5	117
U_BFG_12	6	62
U_BFG_13	6	46
U_BFG_14	6	73
U_BFG_15	8	27
U_BFG_16	8	22
U_BFG_17	8	21
U_BFG_18	12	9
U_BFG_19	12	10
U_BFG_20	12	10
U_BFG_21	15	5
U_BFG_22	15	5

In order to obtain information about the longitudinal strain history during the cyclic loading, VISHAY® strain gauges with the reference EP-08-125AC-350 and a gage factor of $2.100 \pm 0.5\%$ were glued to some notched specimens' surfaces using the adhesive M-bond A-12. The location of strain gauge in the notched plane surface is schematically represented in Figure 3.42a).The strain gauges and the adhesive were selected taking into

account the high strain levels verified in this type of loading. The characteristic equation of the strain gauges is given by:

$$\frac{\Delta R}{R} = S_a \left(\varepsilon_a + K_t \varepsilon_t \right) \tag{3.3}$$

where $\Delta R/R$ is the resistance variation, S_a represents the gage factor, ε_a and ε_t defines the axial and transverse strain and the K_t is given by the ratio of S_t/S_a where S_t is the transverse sensibility factor. The deformation along to transverse direction is insignificant when compared with axial strain. Thus, the Eq. (3.3) can be rewritten as follows:

$$\varepsilon_a = \frac{\Delta R}{R} \frac{1}{S_a} \tag{3.4}$$

Load axial strain curve derived from the strain gauges is illustrated in the Figure 3.42b) and a reduction effect on axial strain is clearly observed. These results will be helpful in order to validate the plasticity models used in the cyclic simulations of these tests. Additional experimental results will be present and compared with numerical response in the Chapter IV. The experimental load-displacement curves of bending cyclic tests were also acquired and they are represented in the Figure 3.43 to Figure 3.45.

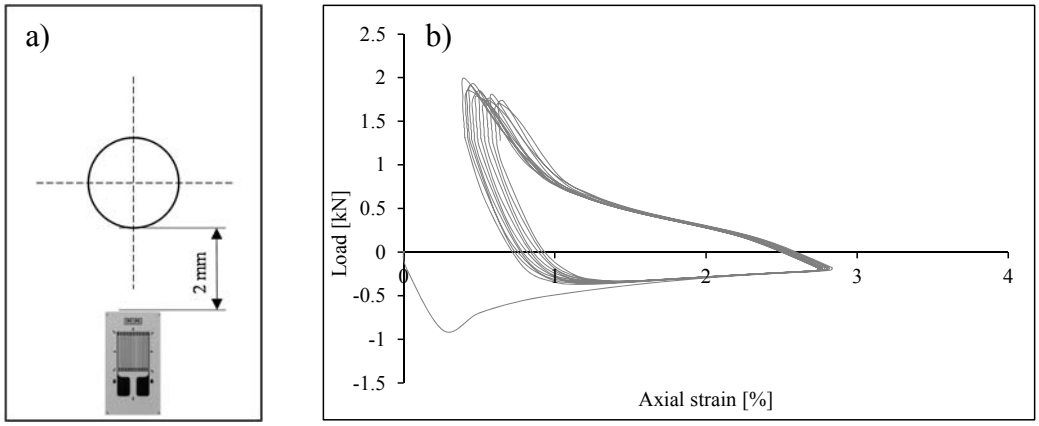

Figure 3.42 – Instrumentation of the cyclic bending test of a notched plane specimen: a) location of the strain gauges at the notched specimen surface; b) load-axial strain relation for the U_BNP_06 specimen (X52 steel grade).

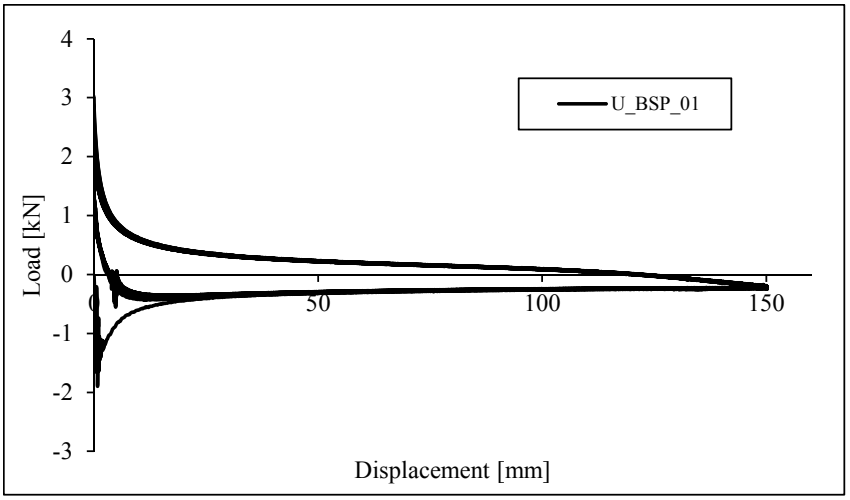

Figure 3.43 – Illustration of a load-displacement curve of a smooth specimen tested under cyclic bending (X52 steel grade).

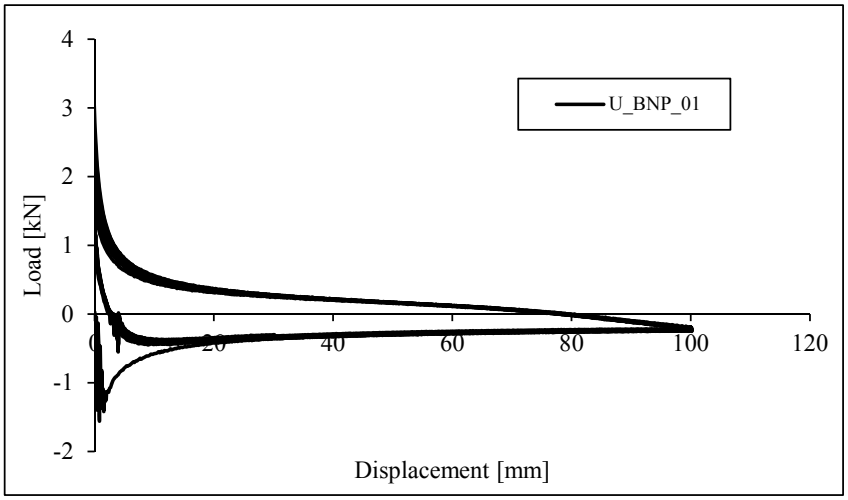

Figure 3.44 – Illustration of a load-displacement curve of a notched specimen tested under cyclic bending (X52 steel grade).

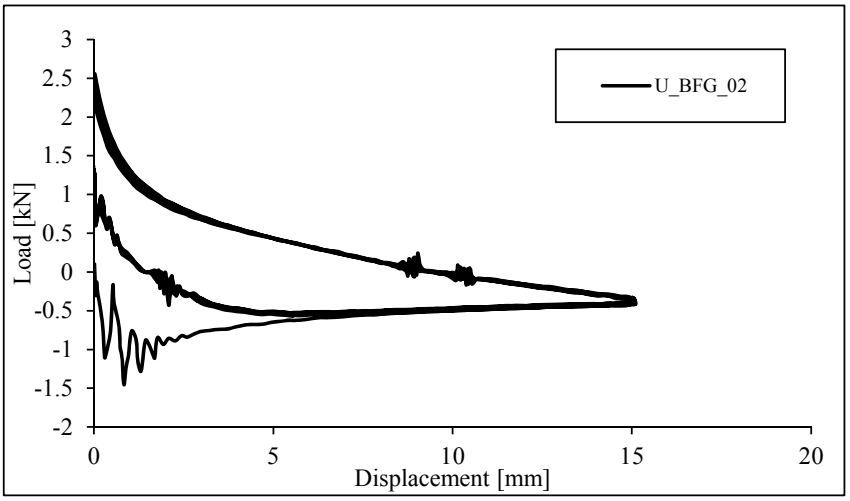

Figure 3.45 – Illustration of a load-displacement curve of a flat-grooved specimen tested under cyclic bending (X52 steel grade).

Experimental evidences in smooth specimens' tests showed that the crack initiation occurred at the middle of the side surface of the specimens at curvature centre side, as illustrated in Figure 3.46a) and at the opposite edges to the curvature centre side as presented in Figure 3.46b). Concerning the notched specimens, in general, a first macroscopic crack stars at the notch root at curvature centre side (Figure 3.47a)) and then another crack appears in opposite specimen face, as can be observed in Figure 3.47b). The same sequence of cracks initiation was found for flat-grooved specimens. Figure 3.48 illustrates the crack initiation location for the flat-grooved specimens in the cyclic bending tests.

a) b)

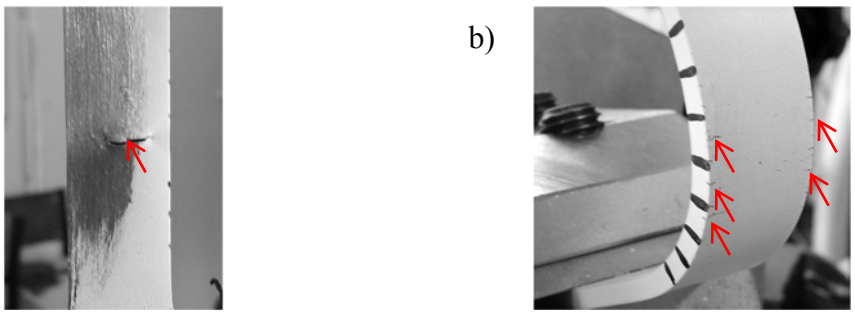

Figure 3.46 – Crack initiation location on smooth specimens tested under cyclic bending (X52 steel grade): a) crack initiation at the middle of surface at the centre curvature side; b) crack initiation at the edges opposite to the curvature centre side.

a) b)

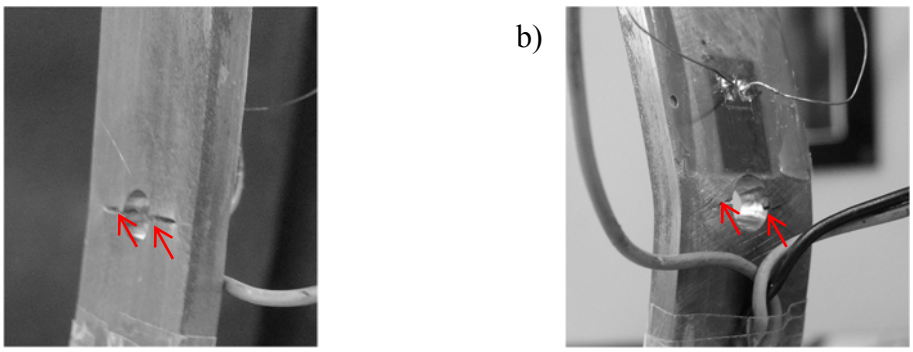

Figure 3.47 – Crack initiation location on notched specimens tested under cyclic bending (X52 steel grade): a) crack initiation at the notch root of surface at the centre of curvature side; b) crack initiation at the opposite face.

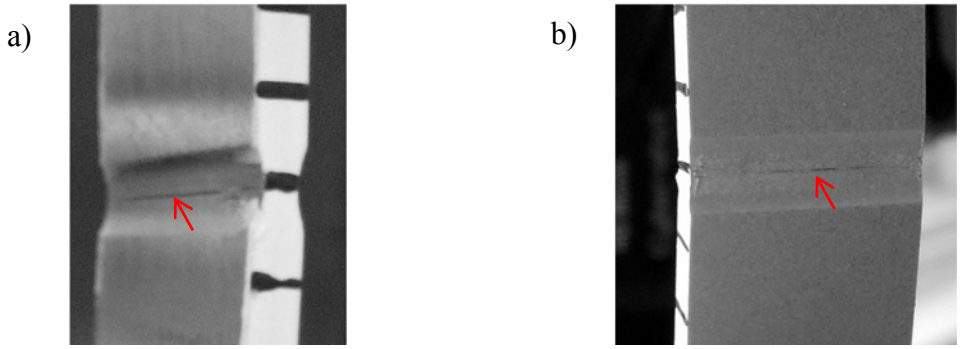

Figure 3.48 – Crack initiation location on flat-grooved specimens tested under cyclic bending (X52 steel grade): a) crack initiation at the notch root on surface at the centre curvature side; b) crack initiation at the opposite face.

In order to investigate the failure mechanisms associated with large plastic strain levels, the fracture surfaces of smooth and notched specimens were analysed and illustrated in Figure 3.49. For both cases, the fatigue failure is dominated by crack growth, which is supported by beachmarks (1) presence in the fracture surface. These features mark the progress of the crack at various stages of loading. Under ULCF domain the crack growth per cycle is higher, thus the beachmarks are more noticeable in the fracture surfaces. The analysis of crack initiation location on the fracture surface confirms the experimental observations performed during the cyclic tests.

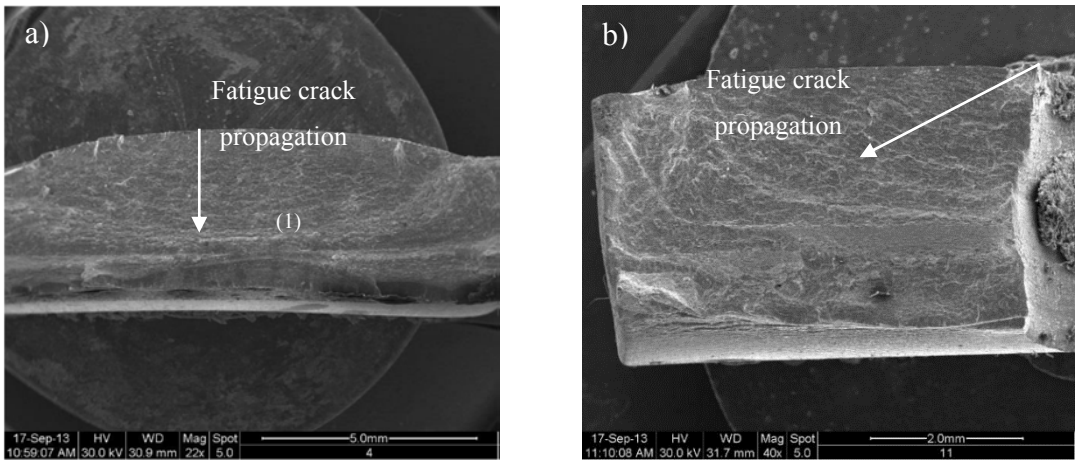

Figure 3.49 – Fracture surfaces of specimens of X52 steel tested under cyclic bending: a) smooth plane specimen; b) notched plane specimen.

3.4.2 Experimental results of the X60 piping steel

3.4.2.1 Basic tensile properties

Such as the X52 steel grade, the X60 piping steel is used to manufacture pipelines following the steel specifications API 5L – PSL1 [3]. Table 3.19 and Table 3.20 show the chemical and mechanical properties according the API standard. The mechanical properties obtained from the monotonic tensile tests carried out on smooth plane specimens of X60 piping steel are presented in the Table 3.21. Moreover, in the Table 3.22 the mechanical properties of X60TT are also shown [4]. The thermal treatment induced a reduction on yield stress as supported by the analysis of Table 3.21 and Table 3.22. Similar values of ultimate tensile strengths were found for both materials.

Table 3.19 – Chemical properties of X60 piping steel, API 5L – PSL1 (maximum values) [3].

C [%]	Mn [%]	P [%]	S [%]	V [%]	Nb [%]	Ti [%]
0.28	1.4	0.03	0.03	a	a	a

a: The sum of the Niobium, Vanadium, and Titanium concentrations shall be < 0.15%

Table 3.20 – Mechanical properties requirements of X60 piping steel, API 5L – PSL1 (minimum values) [3].

Piping steel	$\sigma_{y/0.2\%}$ [MPa]	σ_{UTS} [MPa]
X60	415	520

Table 3.21 – Static mechanical properties of X60 piping steel.

	$\sigma_{y/0.2\%}$ [MPa]	σ_{UTS} [MPa]
Mean	512	556.82
Std. Deviation	12	1.58
CoV [%]	2.34	0.35

Table 3.22 – Static mechanical properties of X60 piping steel with thermal treatment (X60TT) [4].

	$\sigma_{y/0.2\%}$ [MPa]	σ_{UTS} [MPa]
Mean	452.89	537.54
Std. Deviation	5.35	4.67
CoV [%]	1.18	0.87

The conventional stress-strain curves of the X60 and X60TT steel grades were plotted together in the Figure 3.50. In contrast to X52 piping steel, the X60 steel grade does exhibit the yield stress plateau. Moreover, the material after the thermal treatment recovers the yield stress plateau, as can be observed in the Figure 3.50. The conventional

stress-strain curves of both materials show a relative low scatter. In addition, tensile tests on round bar specimens (RB series) of X60 piping steel were performed. For round bar tensile tests, a feature tracking method was applied. Feature tracking method is defined as an optical method, where circular marks are painted on the surfaces of the specimens (see Figure 3.51). This tracking was done by a computational algorithm that allowed the computation of the displacements of the target features in a sequence of images grabbed during the object deformation by an external loading. From feature tracking algorithm, the relative displacement between the marks 1 and 6 was computed and plotted against load values. The experimental load-displacement curves of cylindrical smooth specimens are illustrated in the Figure 3.51. The conventional stress-strain curves were also computed and represented in the Figure 3.52. The longitudinal stress was computed by dividing the load values by the initial section. With respect to the longitudinal strain, it was obtained from relative displacements divided by the gauge length of 25mm (initial distance between marks 1 and 6). The elastic regime, the plastic region and the loss of strength capacity due to damage evolution are clearly observed. The recorded images during the loading process of X60_RB specimens, were used to measure the actual diameter of the round specimens, which allowed the computation of the true stress values. In order to compute the true strain values, the logarithm strain definition was used. Up to specimen necking, the strain value is given by $\varepsilon = \ln(l/l_0)$. After necking, the true strain is computed by $\varepsilon = \ln(A_0/A)+\varepsilon_{necking}$, where A_0 and $\varepsilon_{necking}$ are the initial section and the true strain, respectively, at the necking instant. The true stress-strain curve is plotted in the Figure 3.53. The yield and ultimate tensile stresses from RB tests are presented in the Table 3.23. These values are within the specified range of API 5L and there are very close of SP series results.

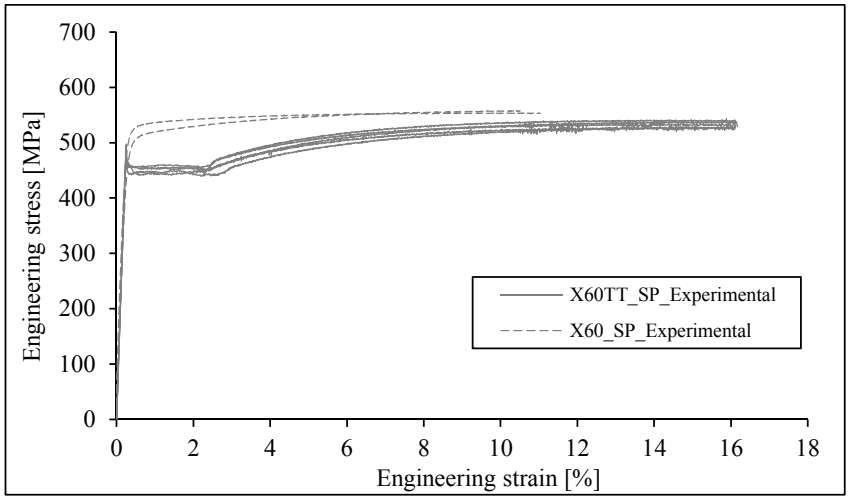

Figure 3.50 – Conventional stress-strain curves of X60 piping steel with and without thermal treatment (SP specimen series).

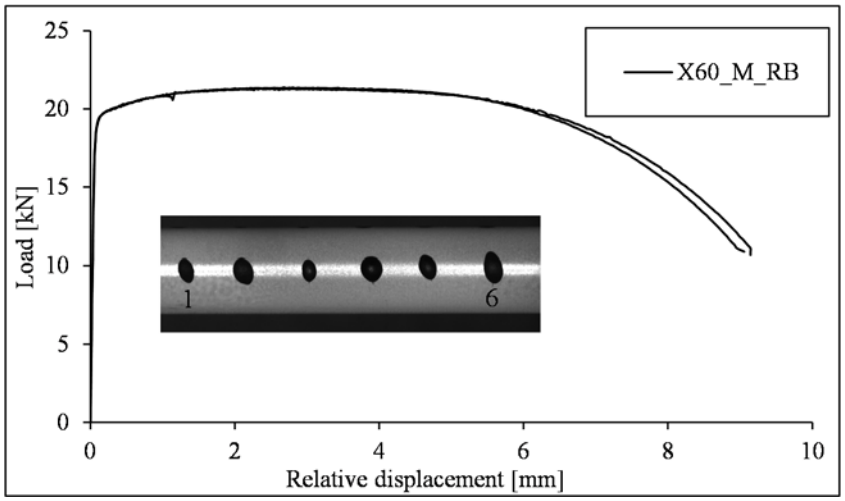

Figure 3.51 – Load-relative displacement curves of RB specimens of X60 piping steel.

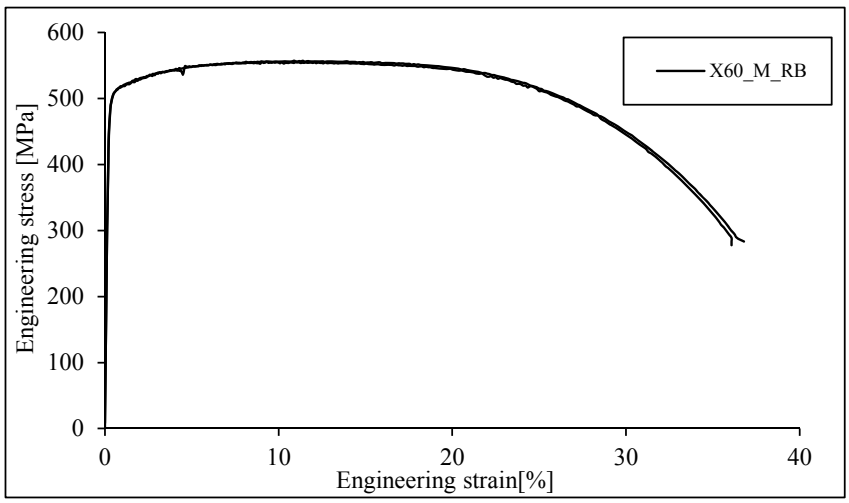

Figure 3.52 – Conventional stress-strain curves of RB specimens of X60 piping steel.

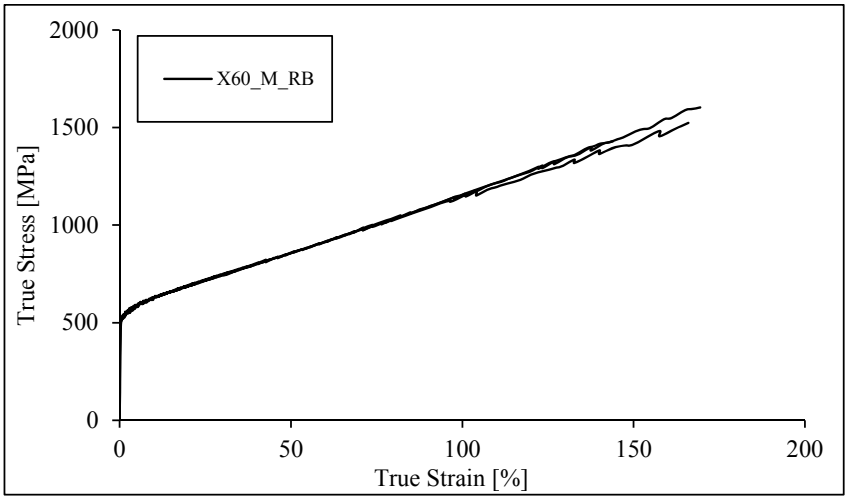

Figure 3.53 – True stress-true strain curves of RB specimens series of X60 piping steel.

Table 3.23 – Static mechanical properties of X60 piping steel obtained from RB tensile tests.

	$\sigma_{Y/0.2\%}$ [MPa]	σ_{UTS} [MPa]
Mean	511	556.82
Std. deviation	5.79	2.53
CoV [%]	1.13	0.45

Regarding to the material microstructure, the effect of thermal treatment can be investigated from the analysis of the Figure 3.54 and Figure 3.55. A reduction of grain size is verified for the samples of material with thermal treatment. Besides this effect, the grain orientation was also affect by the thermal treatment process. The original material shows a specific grain orientation due to the plastic metal forming, which is eliminated after the heat treatment. The thermal processing includes a tempering treatment that allows the material recrystallization.

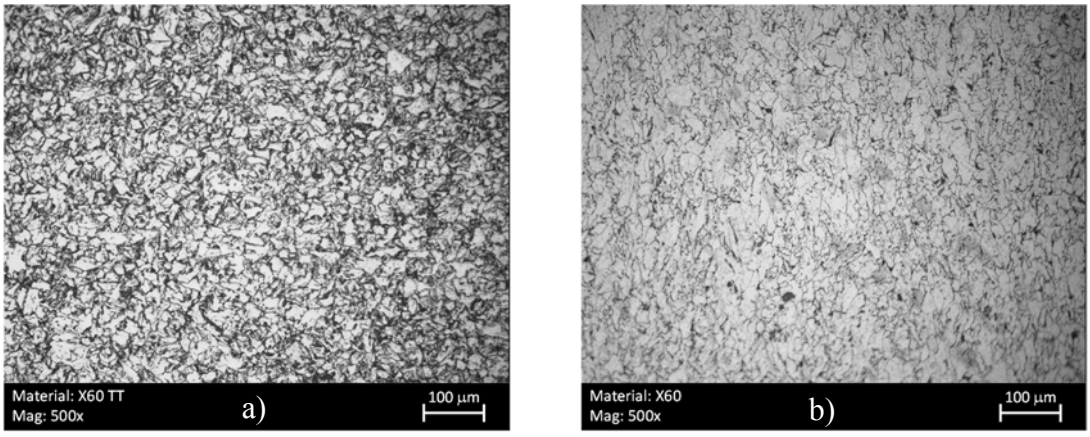

Figure 3.54 – Microstructures of the X60 piping steel for a magnification of 500x: a) with thermal treatment [4]; b) without thermal treatment.

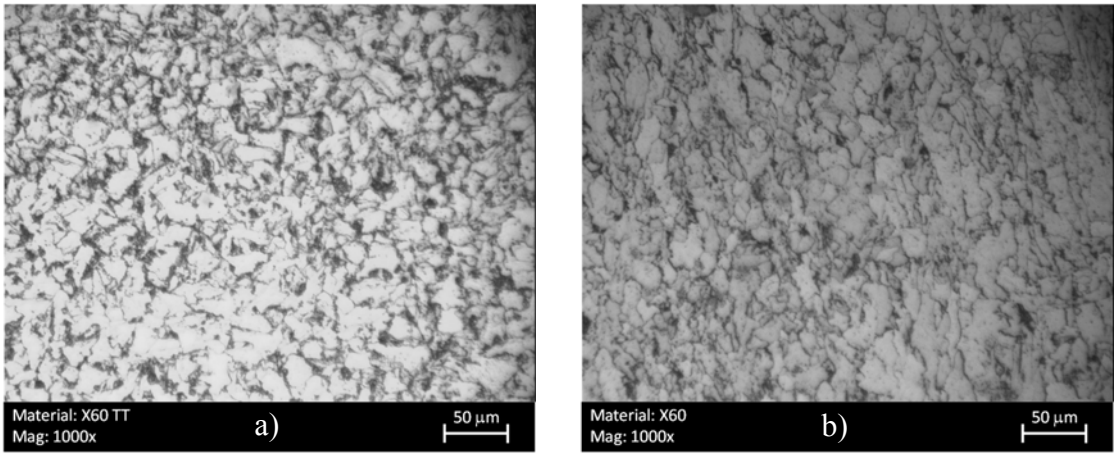

Figure 3.55 – Microstructure of the X60 piping steel for a magnification of 500x: a) with thermal treatment [4]; b) without thermal treatment.

3.4.2.2 Quasi-static monotonic tensile test results

In this section, experimental results from the monotonic tensile tests of the X60 piping steel are presented. Similarly to the monotonic tensile tests performed on smooth specimens of X52 steel grades, the X60 smooth specimens deformed shape was recorded using the ARAMIS® optical system. The processing of the images led to the assessment of the lateral necking of the smooth specimens. Load-relative displacement curves computed from the lateral necking of the smooth specimens are represented in the Figure 3.56 and Figure 3.57 for X60 piping steel. The same procedure was performed to derive the experimental curves regarding the X60 steel subjected to the thermal treatment [4]. The analysis of Figure 3.56 and Figure 3.57 reveal a greater relative displacement by the base X60 piping steel material when compared with the material with thermal treatment. Nevertheless the lateral necking is just one perspective for the material ductility. Comparisons about the effect of the thermal process on the ductility behaviour will be presented in the Chapter IV, by means of numerical analysis.

Figure 3.58 to Figure 3.66 show the load-displacement curves from monotonic tensile tests of notched specimens, including notched plane, notched bar, flat grooved specimens. In addition, results from shear tests of X60 piping steel are presented. With respect to X60 steel grade subjected to a thermal process only one notched specimen' series was tested. In all these tests, the dynamic extensometer was appropriate to track the specimen longitudinal deformation at a region of interest. The reference length of the dynamic

extensometer was adjusted for each specimen's series in order to monitor the displacements as remotely as possible. Figure 3.67 illustrates the clip gauge extensometer mounted on a notched round bar, a notched plane, a flat-grooved and a shear specimen with different gauge lengths (see Table 3.2).

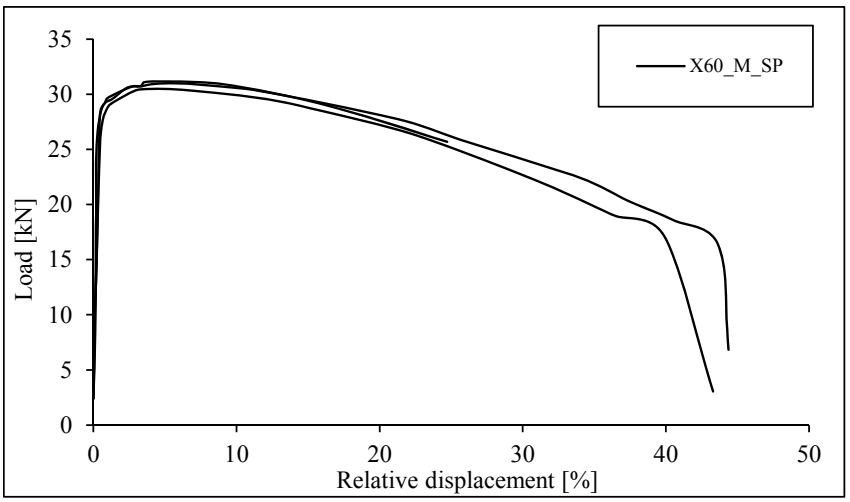

Figure 3.56 – Load-relative displacement (lateral necking) curves from smooth plane specimens of X60 piping steel.

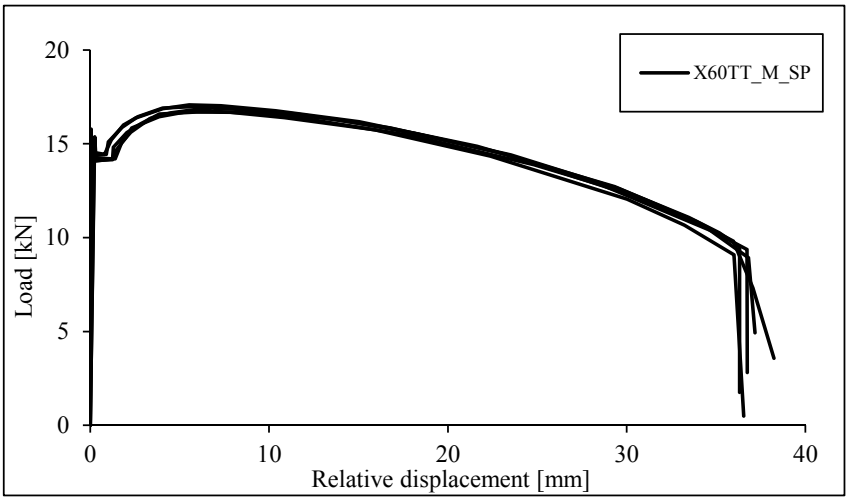

Figure 3.57 – Load-relative displacement (lateral necking) curves from smooth plane specimens of X60TT piping steel [4].

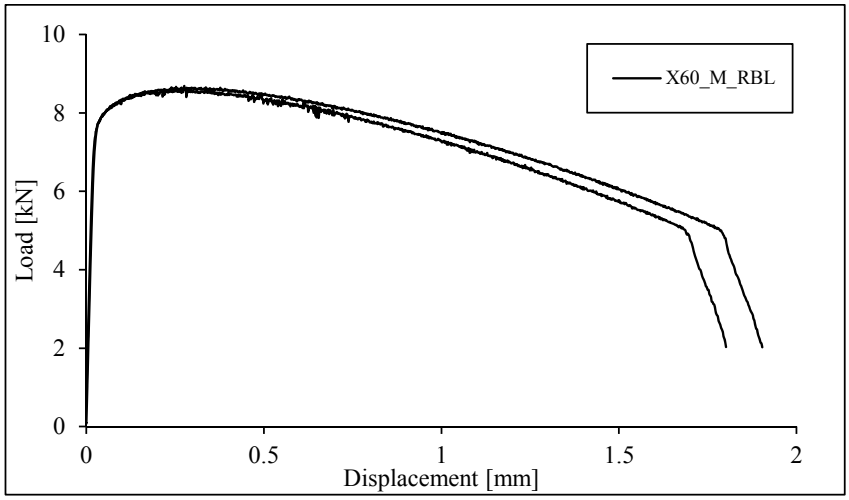

Figure 3.58 – Load-displacement curves from round bar specimens with large notch of X60 piping steel.

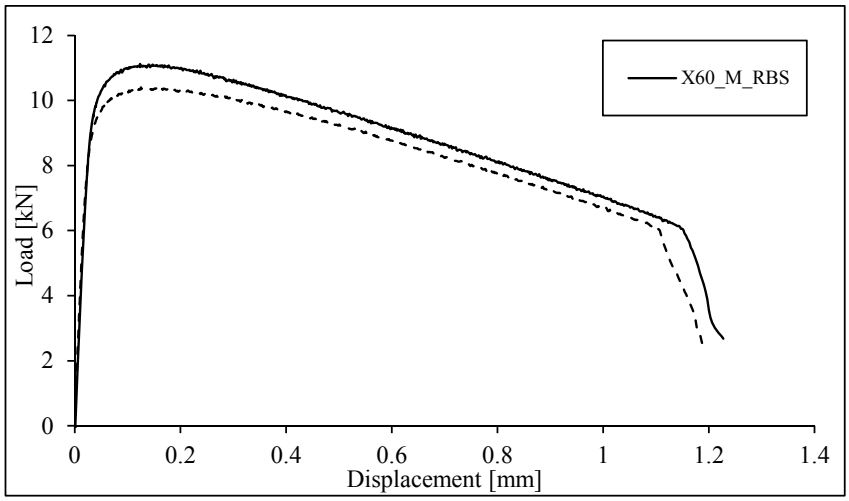

Figure 3.59 – Load-displacement curves from round bar specimens with large notch of X60 piping steel.

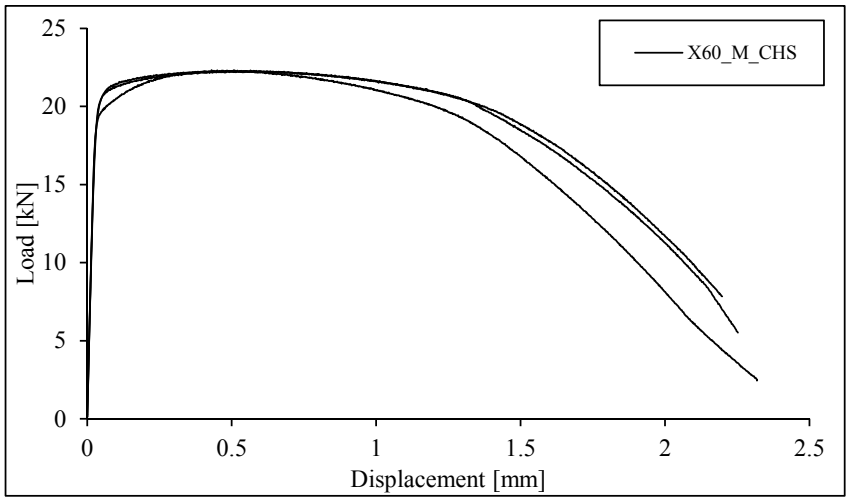

Figure 3.60 – Load-displacement curves from notched plane specimens of X60 piping steel, CHS series.

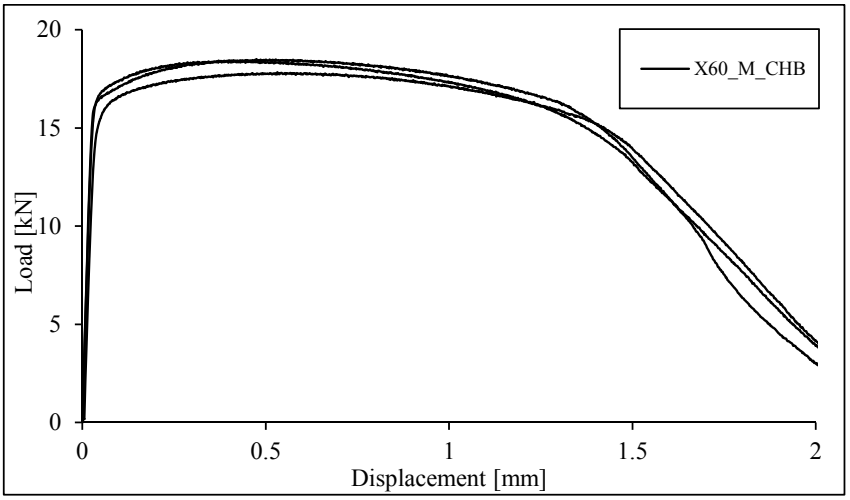

Figure 3.61 – Load-displacement curves from notched plane specimens of X60 piping steel, CHB series.

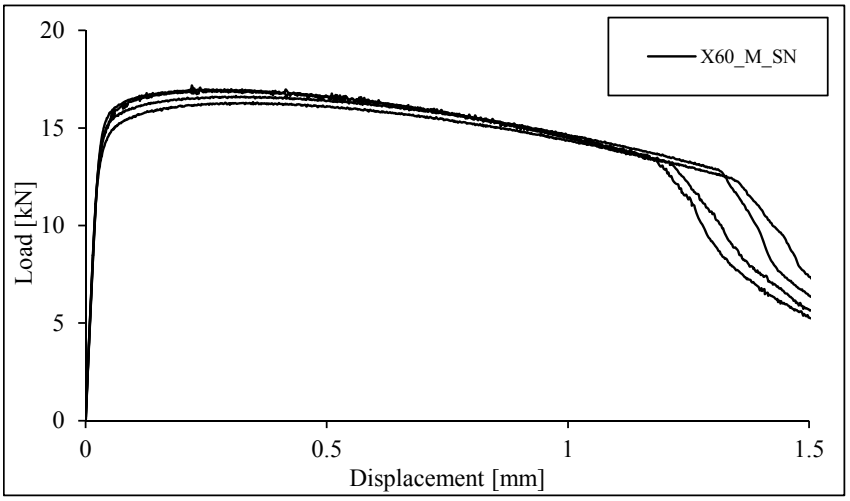

Figure 3.62 – Load-displacement curves from notched plane specimens of X60 piping steel, SN series.

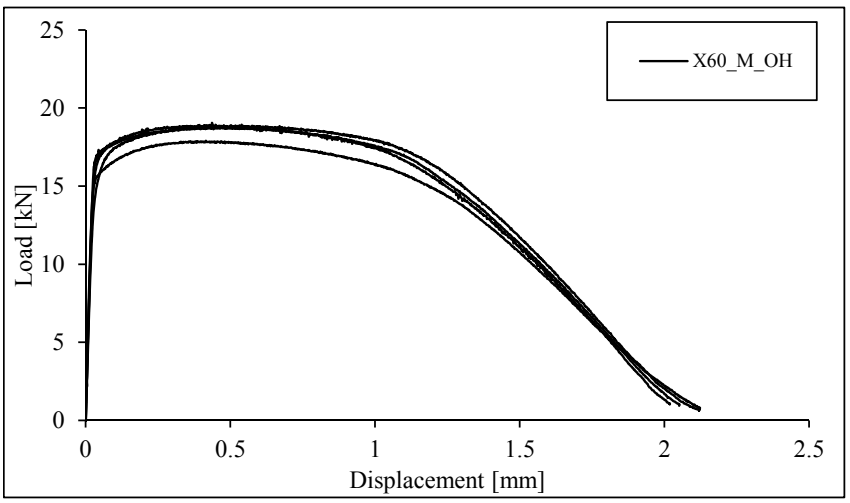

Figure 3.63 – Load-displacement curves from notched plane specimens of X60 piping steel, OH series.

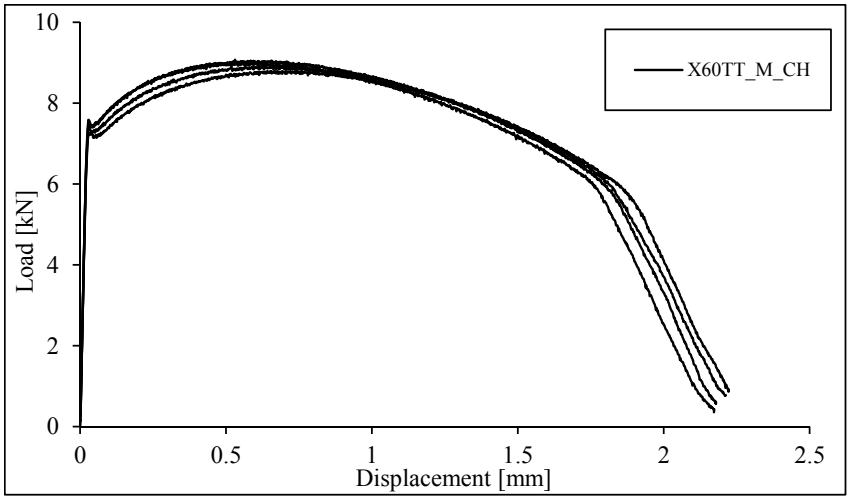

Figure 3.64 – Load-displacement curves from notched plane specimens of X60 piping steel with thermal treatment, CH series.

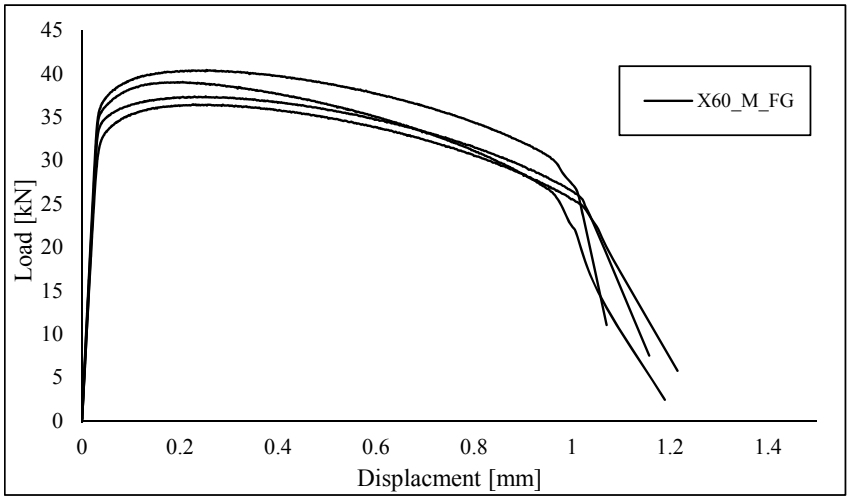

Figure 3.65 – Load-displacement curves from flat-grooved specimens of X60 piping steel.

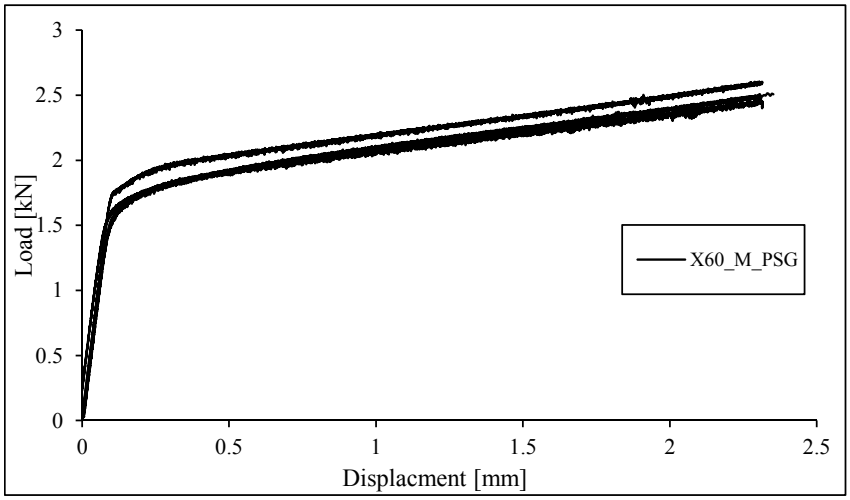

Figure 3.66 – Load-displacement curves from plane shear specimens of X60 piping steel.

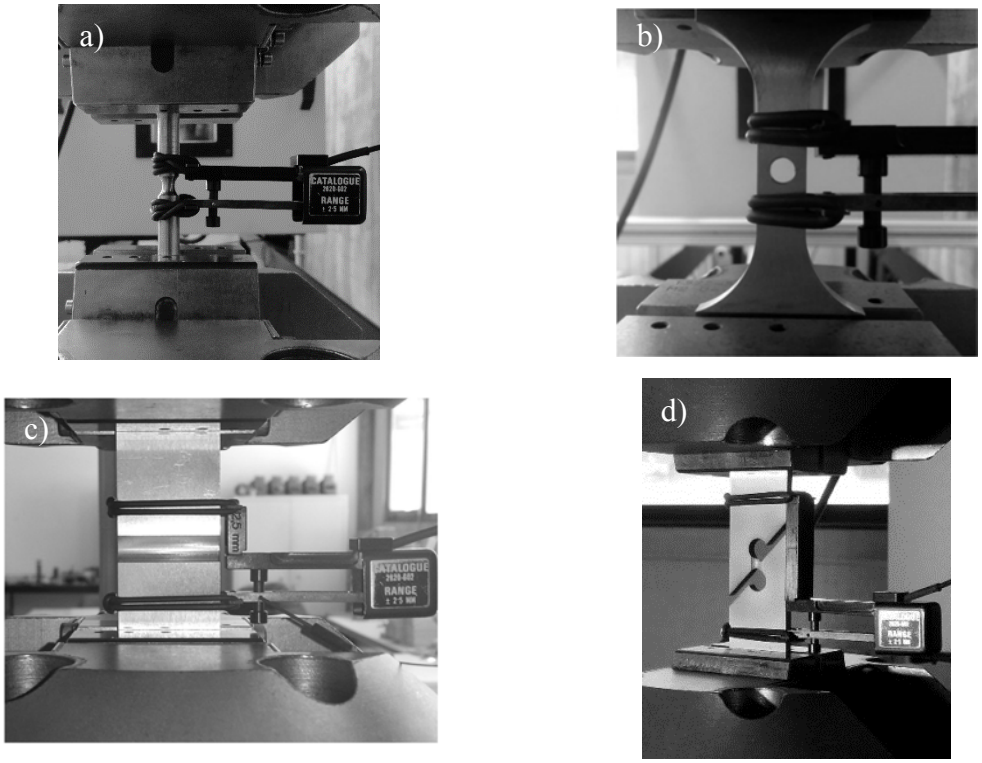

Figure 3.67 – Experimental set-up with detail view of clip gauge: a) notched round bar specimen; b) notched plane specimen; c) flat-grooved specimen; d) plane shear specimen.

The fracture surfaces of a smooth plane specimen and a flat-grooved specimen can be observed in the Figure 3.68 and Figure 3.69, respectively. The fracture surfaces illustrate the classic characteristics of a monotonic ductile fracture, in detail the fibrous appearance, the porosity and an overall rough appearance. The surfaces consist of microvoids and dimples (see Figure 3.68b) and Figure 3.69b)). This aspect of ductile fracture occurs in later deformation stages after necking. First, small microvoids initiate in the interior of the material. Next, deformation continues and the microvoids enlarge to form a crack. The crack continues to grow and spreads laterally towards the edges of the specimen. Finally, crack propagation is rapid along a surface that makes about 45 degree angle with the tensile stress axis. The new fracture surfaces have a very irregular appearance.

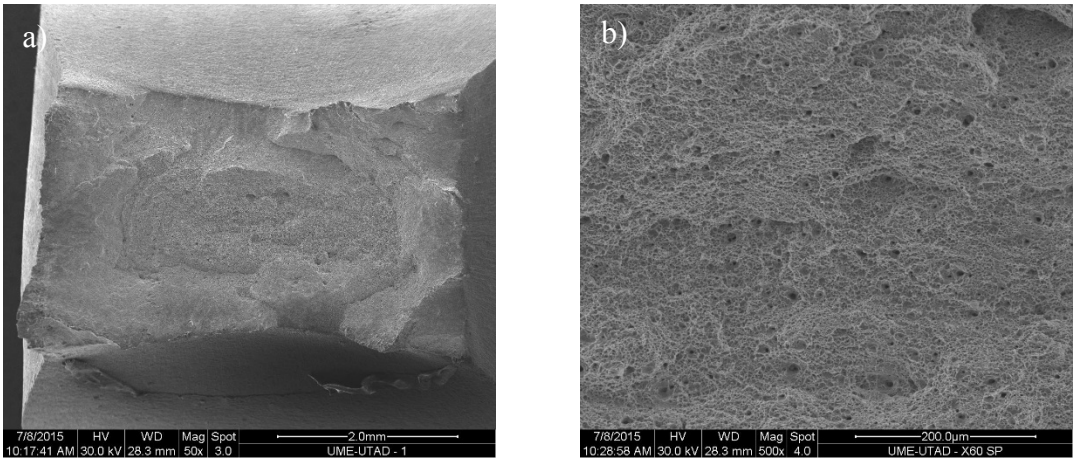

Figure 3.68 – Facture surface of a smooth plane specimen of X60 piping steel: a) general view; b) detail view of material porosity.

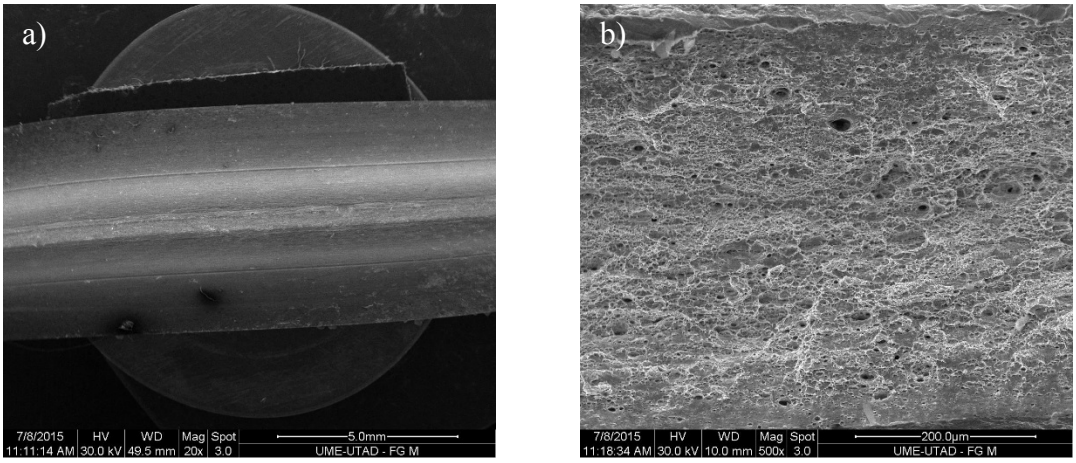

Figure 3.69 – Facture surface of a flat-grooved specimen of X60 piping steel: a) general view; b) detail view of material porosity.

3.4.2.3 Experimental results of cyclic tension-compression tests on smooth specimens

Table 3.24 and Table 3.25 summarize the experimental program of LCF and ULCF tests performed on smooth plane specimens of X60 piping steel without and with thermal treatment, respectively. The number of cycles to crack initiation and the plastic and elastic strain ranges were computed following the same procedure described in the experimental cyclic tests performed for smooth specimens of X52 piping steel.

Table 3.24 – Experimental program of cyclic tests performed on smooth specimens of X60 piping steel.

Specimens Reference	S_t [mm^2]	R_ε [–]	f [Hz]	$\Delta\varepsilon$ [%]	N_i [cycles]	$\Delta\sigma$ [MPa]	$\Delta\varepsilon^P$ [%]	$\Delta\varepsilon^E$ [%]
L0_SP_1	55.71	0	0.2667	1.50	835	862.768	1.059	0.441
L0_SP_2	55.74	0	0.2667	1.50	452	889.817	1.021	0.479
L0_SP_3	55.66	0	0.2000	2.00	463	937.149	1.487	0.513
L0_SP_4	55.79	0	0.2000	2.00	400	892.045	1.495	0.505
L0_SP_5	55.30	0	0.0800	5.00	100	964.300	4.435	0.565
L-1_SP_1	55.80	-1	0.3200	1.25	1113	896.320	0.789	0.461
L-1_SP_2	55.64	-1	0.3200	1.25	1054	915.268	0.782	0.468
L-1_SP_3	55.53	-1	0.4000	1.00	2016	807.465	0.579	0.421
L-1_SP_4	56.33	-1	0.4000	1.00	2075	819.901	0.607	0.393
L-1_SP_5	56.06	-1	0.2000	2.00	225	967.557	1.503	0.497
L-1_SP_6	55.75	-1	0.2000	2.00	347	943.057	1.512	0.488
U0_SP_1	56.07	0	0.0667	6.00	67	1058.55	5.349	0.651
U0_SP_2	55.69	0	0.0571	7.00	31	1130.30	6.303	0.697
U0_SP_3	55.95	0	0.0500	8.00	26	1094.62	7.384	0.616
U0_SP_4	55.09	0	0.0571	7.00	*			
U0_SP_5	55.42	0	0.0667	6.00	71	1000.17	5.366	0.634
U0_SP_6	55.63	0	0.0615	6.50	51	1032.54	5.896	0.604
U0_SP_7	55.64	0	0.0533	7.50	*			
U0_SP_8	56.06	0	0.0667	6.00	*			
U0_SP_9	55.69	0	0.0571	7.00	48	1036.62	6.322	0.678
U0_SP_10	55.89	0	0.0500	8.00	*			
U0_SP_11	55.58	0	0.0500	8.00	*			
U0_SP_12	55.89	0	0.0615	6.50	71	1036.57	5.823	0.677
U0_SP_13	55.64	0	0.0533	7.50	*			
U0_SP_14	55.69	0	0.0533	7.50	28	1107.18	5.823	1.677
U0_SP_15	55.82	0	0.0500	8.00	26	1013.28	6.807	1.193

* invalid tests

Table 3.25 – Experimental program of cyclic tests performed on smooth specimens of X60 piping steel, with thermal treatment [4].

Specimens Reference	**S_t [mm²]**	**R_ε [–]**	***f*** **[Hz]**	**$\Delta\varepsilon$ [%]**	**N_i [cycles]**	**$\Delta\sigma$ [MPa]**	**$\Delta\varepsilon^P$ [%]**	**$\Delta\varepsilon^E$ [%]**
L-1_SP_01	31.74	-1	0.5000	0.80	2300	700.709	0.462	0.338
L0_SP_02	*							
L0_SP_03	31.62	0	0.2667	1.50	640	790.483	1.076	0.424
L0_SP_04	31.60	0	0.4000	1.00	1200	736.005	0.610	0.390
L0_SP_05	31.74	0	0.3333	1.20	700	757.162	0.784	0.416
L0_SP_06	31.56	0	0.6667	0.60	7000	634.343	0.279	0.321
L0_SP_07	31.70	0	0.5000	0.80	2400	686.857	0.453	0.347
L0_SP_08	31.70	0	0.3333	1.20	840	758.595	0.777	0.423
L0_SP_09	31.54	0	0.4000	1.00	1800	721.528	0.614	0.386
U0_SP_1	31.72	0	0.2000	2.00	340	836.409	1.578	0.422
U0_SP_2	31.76	0	0.1333	3.00	180	864.304	2.486	0.514
U0_SP_3	31.58	0	0.1000	4.00	110	886.448	3.439	0.561
U0_SP_4	31.62	0	0.0889	4.50	66	948.255	4.004	0.496
U0_SP_5	31.72	0	0.0889	4.50	80	914.133	3.944	0.556
U0_SP_6	31.70	0	0.0800	5.00	68	929.373	4.439	0.561
U0_SP_7	31.70	0	0.0800	5.00	76	936.916	4.469	0.531
U0_SP_8	31.78	0	0.0727	5.50	46	956.040	4.979	0.521
U0_SP_9	31.74	0	0.0727	5.50	58	931.166	4.965	0.535
U0_SP_10	*							
U0_SP_11	31.74	0	0.0667	6.00	38	967.907	5.425	0.575
U0_SP_12	31.82	0	0.0667	6.00	60	923.058	5.446	0.554
U0_SP_13	31.62	0	0.0615	6.50	44	956.042	5.921	0.579

* invalid tests

The cyclic parameters of the Ramberg-Osgood [5] relation are presented in the Table 3.26 for the base X60 piping steel. The cyclic parameters were obtained by plotting the stress amplitude against the plastic strain amplitude fitting a linear function in a log-log scale, as can be observed in Figure 3.70 and Figure 3.71. As occurred in the analysis of the X52 steel grade results, significant differences are observed when the cyclic parameters obtained from LCF only or LCF plus ULCF data, which are supported by the analysis of Figure 3.72. The effect of ULCF data on the estimation of cyclic parameters addressed for X52 piping steel is repeated in the analysis of X60 experimental results. A shift down correction of the cyclic curves derived from LCF plus ULCF data is observed.

Table 3.26 – Cyclic parameters of X60 piping steel obtained from LCF data only and LCF plus ULCF data.

Experimental Data Source	***K'* [MPa]**	***n'***
LCF	854.87	0.1232
LCF+ULCF	732.49	0.0964

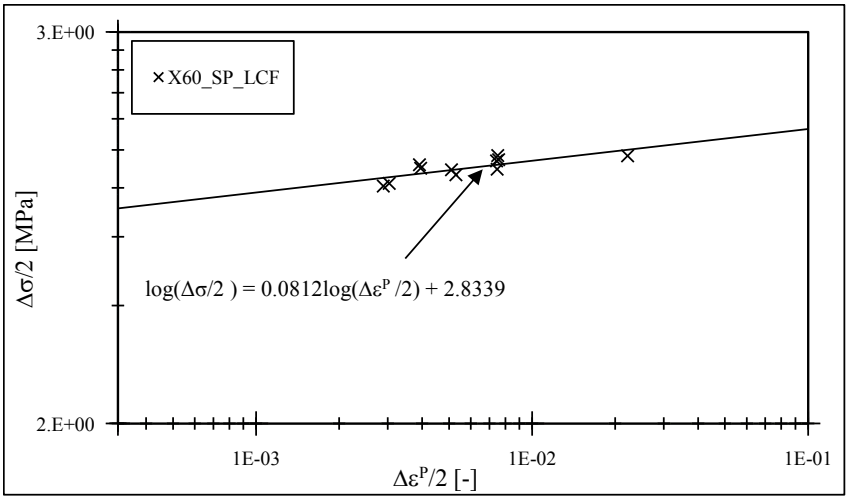

Figure 3.70 – Stress amplitude *versus* plastic strain amplitude of X60 piping steel, under LCF domain.

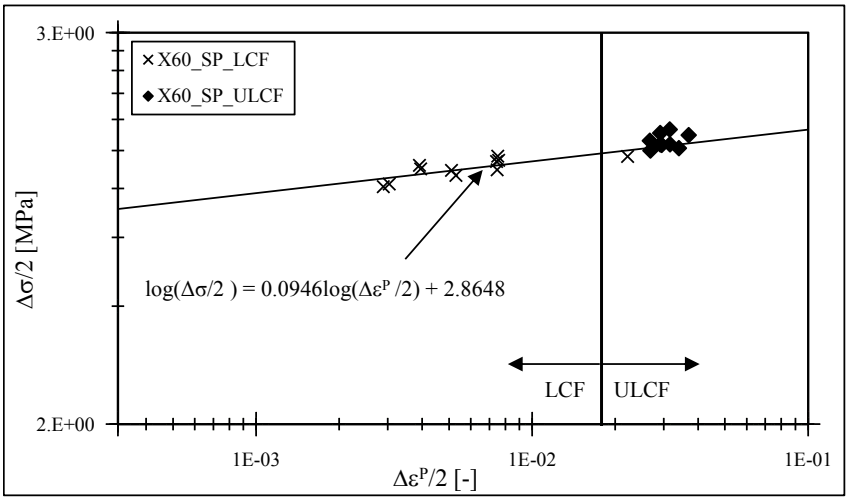

Figure 3.71 – Stress amplitude *versus* plastic strain amplitude of X60 piping steel, under LCF plus ULCF domains.

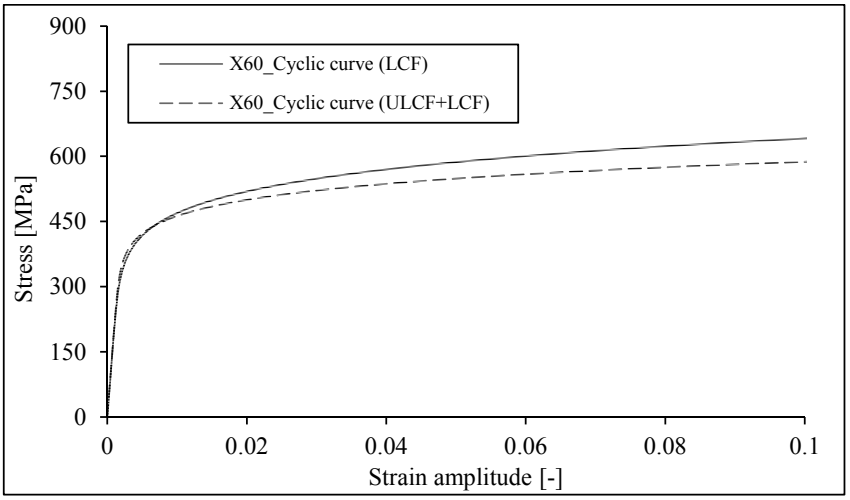

Figure 3.72 – Cyclic stress-strain curves of X60 piping steel obtained with LCF only and LCF plus ULCF experimental data.

The stress amplitude versus plastic strain amplitude relation for the X60 piping steel with and without thermal treatment are compared in the Figure 3.73. The same comparison, but concerning the complete cyclic curves is presented in the Figure 3.74. The effect of thermal treatment promote a reduction of the cyclic hardening in the X60 steel grade. In fact, for the same strain levels the material exposed to the thermal treatment exhibits lower stress levels when compared to the original material. Moreover, with the increasing of strain values, both cyclic curves tend to the same stress levels. The cyclic parameters of the Ramberg-Osgood relation [5] of X60 piping steel with thermal treatment (X60TT) are presented in Table 3.27.

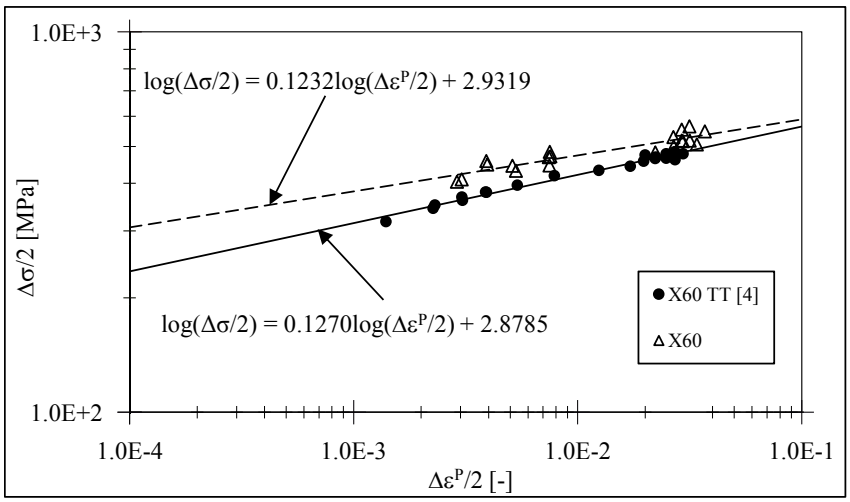

Figure 3.73 – Comparison of the stress amplitude versus plastic strain amplitude relations under LCF plus ULCF domains, between X60 piping steel with and without thermal treatment.

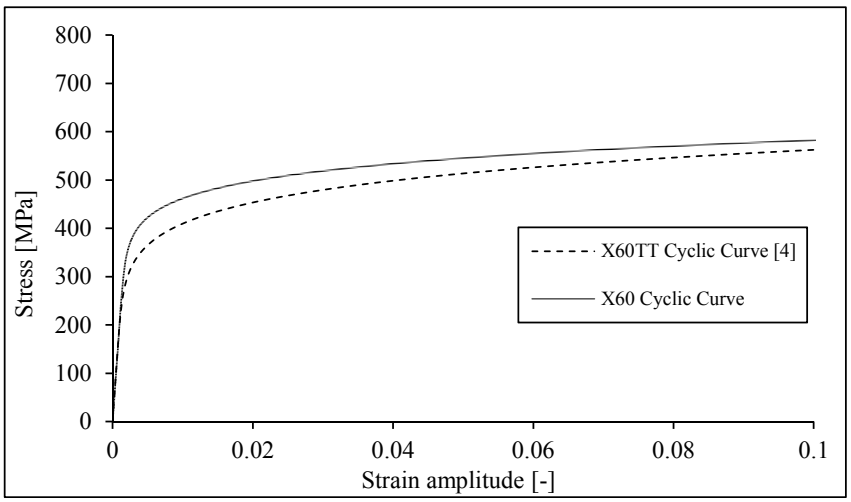

Figure 3.74 – Cyclic curves of X60 piping steel with and without thermal treatment (smooth specimens).

Table 3.27 – Cyclic parameters of X60 piping steel with thermal treatment obtained from LCF plus ULCF data [4].

Experimental Data	***K'* [MPa]**	***n'***
LCF+ULCF	755.96	0.1270

The evolution of stress amplitude as a function of the number of cycles to crack initiation is plotted respectively in Figure 3.75 and Figure 3.76 for LCF and ULCF tests of smooth plane specimens of X60 piping steel. A continuous softening can be observed independently of the strain range applied in the cyclic tests. A similar procedure was performed for the material subjected to the thermal process in order to investigate its effect in the material cyclic behaviour. The thermal treatment does not affect the cyclic softening of the X60 steel grade [4], the same trend observed for the X60 steel being verified.

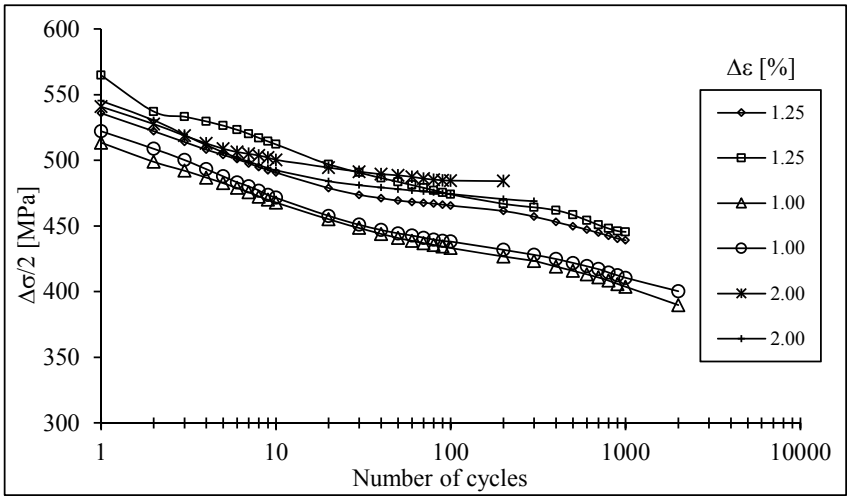

Figure 3.75 – Evolution of the stress amplitude with the number of cycles of the specimens tests under LCF domain, X60 piping steel.

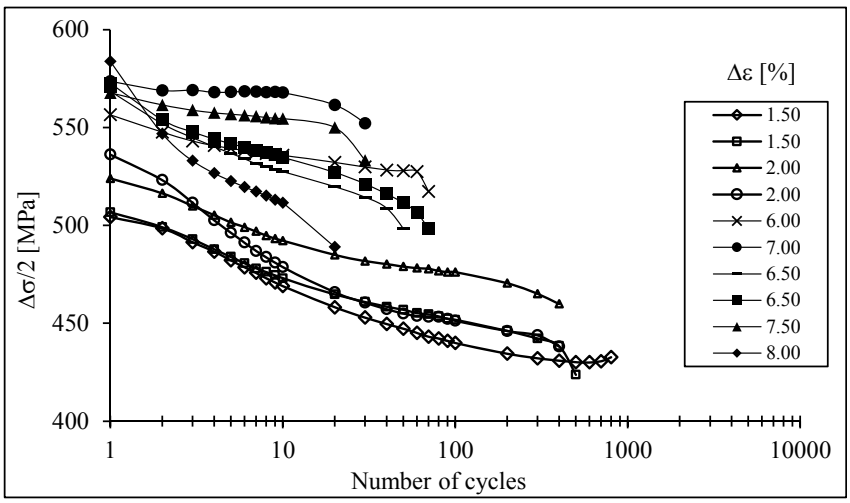

Figure 3.76 – Evolution of the stress amplitude with the number of cycles of the specimens tests under ULCF domain, X60 piping steel.

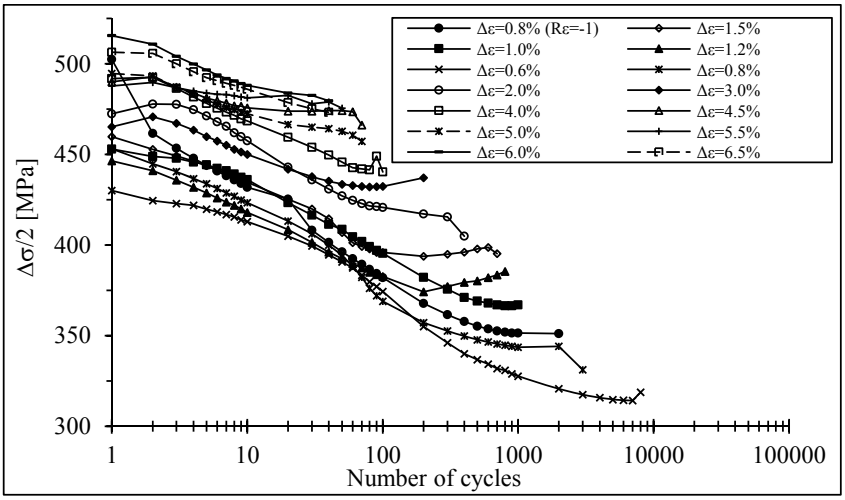

Figure 3.77 – Evolution of the stress amplitude with the number of cycles of the cyclic smooth plane specimens of X60TT steel grade [4].

The strain components, namely total, elastic and plastic strain are plotted against the number of reversals until crack initiation in Figure 3.78 taking into account the experimental data from the LCF regime. Similarly, LCF plus ULCF strain data are correlated together and plotted against with the number of reversals. This procedure allows estimating the parameters involved in the Morrow relation Eq.(3.2), previously described. As verified for X52 piping steel, the inclusion of ULCF data on the Morrow's parameters identification leads to a sensitive modification on these values. In order to compare the fatigue life performance of the X60TT steel grade, the global strain-life curves were also derived and represented in the Figure 3.80. The influence of the thermal process is negligible regarding the fatigue life performance, as supported by the analysis of Figure 3.81. Although, the base material shows a slightly higher fatigue strength, more noticeable at the LCF domain. Table 3.28 summarizes the Morrow's parameters derived from experimental data of smooth specimens of X60 piping steel, including the base and treated materials.

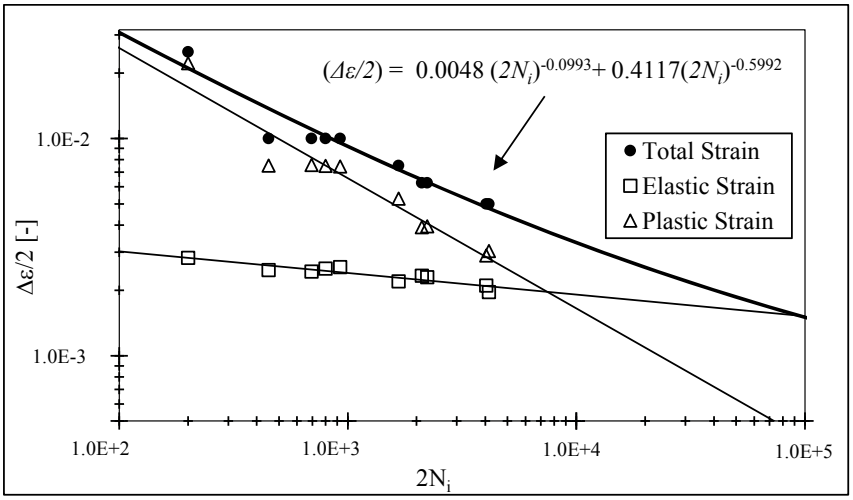

Figure 3.78 – Global strain-life curves of the X60 piping steel obtained from LCF data.

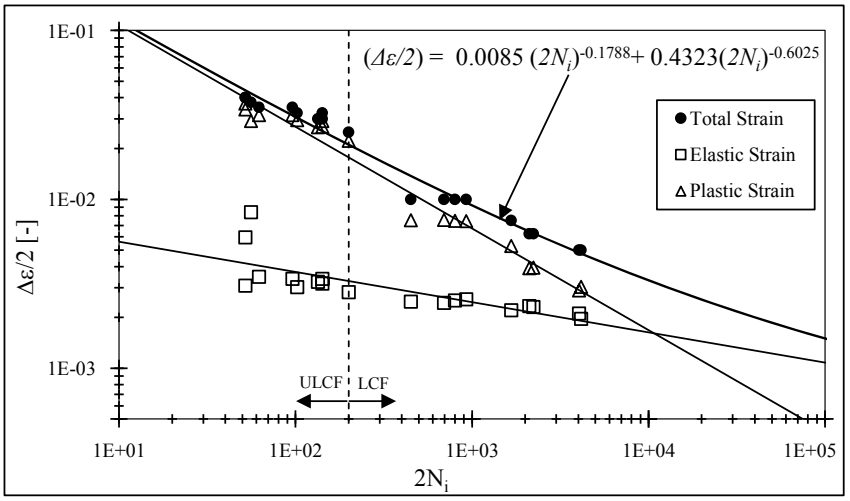

Figure 3.79 – Global strain-life curves of the X60 piping steel obtained from LCF plus ULCF data.

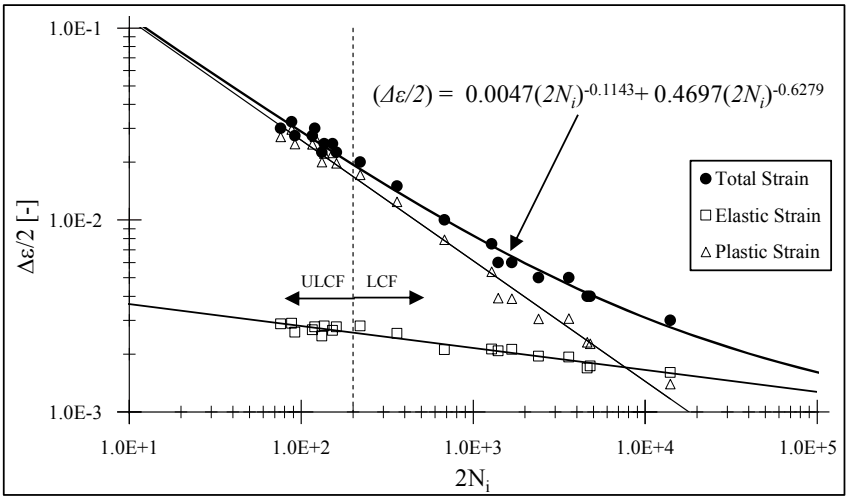

Figure 3.80 – Global strain-life curves of the X60 piping steel with thermal treatment obtained from LCF plus ULCF data [4].

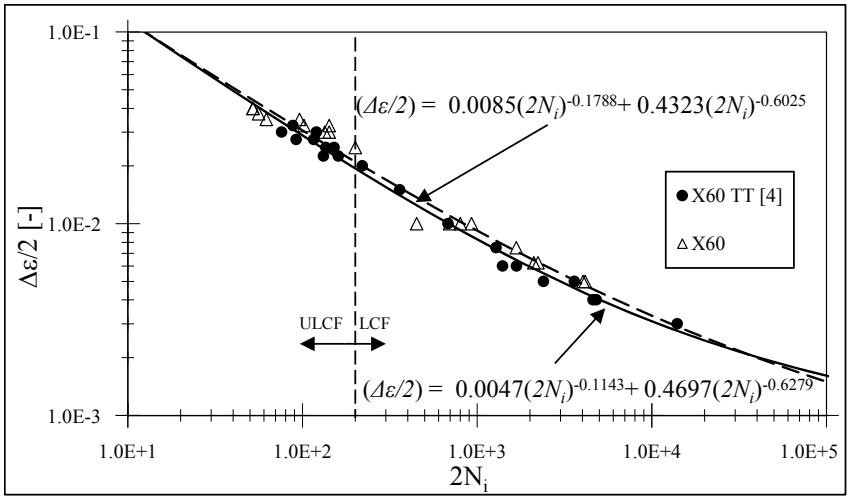

Figure 3.81 – Comparison between global strain-life curves of X60 piping steel with and without thermal treatment.

Table 3.28 –Morrow's relation parameters derived from LCF only and LCF plus ULCF data, of X60 piping steel.

Experimental Data Source	σ'_f [MPa]	b	ε'_f	c
LCF	988.80	-0.0993	0.4117	-0.5992
LCF+ULCF	1751.00	-0.1788	0.4323	-0.6025
LCF+ULCF (X60TT) [4]	968.20	-0.1143	0.4697	-0.6279

Figure 3.82 shows the aspect of a fracture surface with a detailed view of a microcrack of a smooth plane specimen subjected to ULCF loading. The crack propagation path is clearly observed being characterize by the beachmarks, which results from the opening and closure of the macroscopic crack. The fracture surface resulted from ULCF loading shows similar facets of plastic failure. The growing and coalescence mechanism of microvoids is common in ductile and ULCF fracture mechanism. Figure 3.83 shows a detailed view of a microvoid. Comparison between LCF and ULCF fractures surfaces, of X60 piping steel with thermal treatment can be observed in Figure 3.84. As expectable the ULCF fracture surface present a higher plastic fracture area and consequently a reduced area relative to the crack propagation. The crack progress per cycle is more noticeable for the ULCF facture specimen.

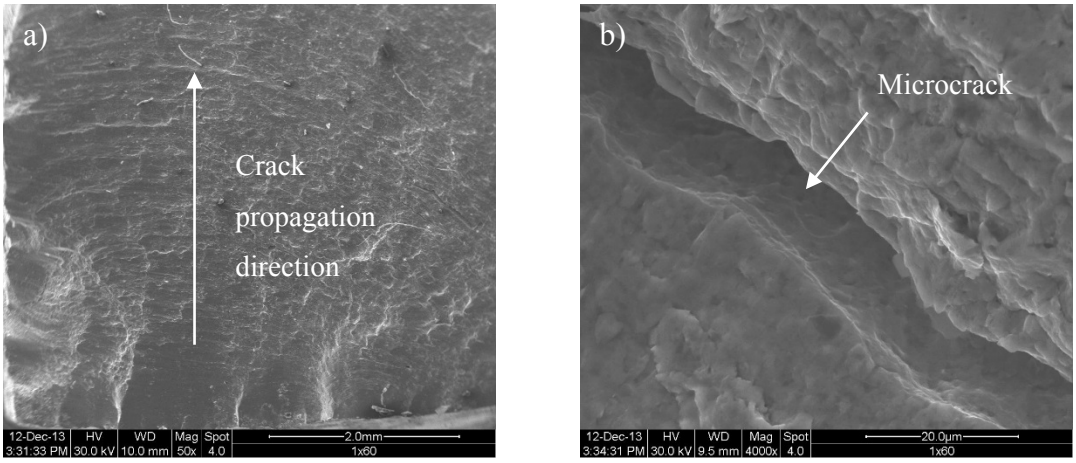

Figure 3.82 – Fracture surface of smooth plane specimens of X60 piping steel, tested under ULCF domain (X60_U0_SP_05, Δε=7%): a) path of macroscopic crack propagation; b) microcrack existent in the fracture surface.

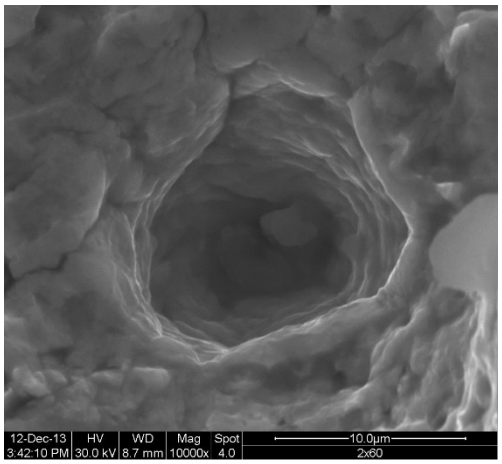

Figure 3.83 – Detail view of a microvoid present in the fracture surface of a smooth plane specimen tested under ULCF domain (X60_U0_SP_07, Δε=7.5%).

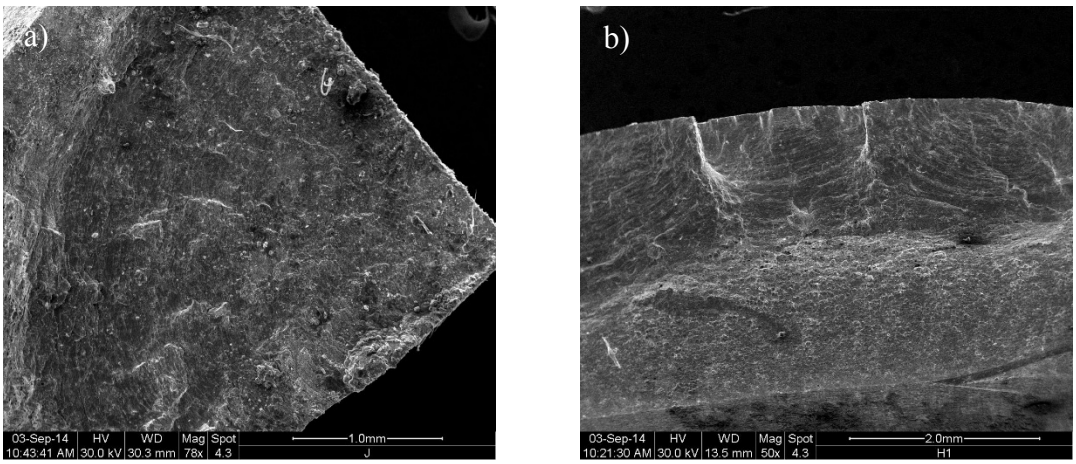

Figure 3.84 – Fracture surfaces of smooth plane specimens (X60TT): a) LCF specimen, Δε=1.2%; b) ULCF specimen, Δε=6.0% [4].

3.4.2.4 *Experimental results of cyclic tension-compression tests on notched specimens*

In this section the experimental results of notched plane specimens of X60 piping steel, including the notched plane series of the material subjected to the thermal process, are presented. These results are summarised in the Table 3.29 to Table 3.33. The cyclic tests of notched specimens were performed under displacement control, using the dynamic extensometer with the gauge length specified in the Table 3.2. Concerning the evaluation of the number of cycles to crack initiation, the criterion illustrated in Figure 3.28 was followed again in this material.

Table 3.29 – Experimental program of cyclic tests performed on CHS series of X60 piping steel.

Specimens reference	R_δ *[–]*	f *[Hz]*	$\Delta\delta$ *[%]*	N_i *[cycles]*
L-1_CHS_01	-1	0.8000	0.50	430
L-1_CHS_02	-1	0.5000	0.80	120
L-1_CHS_03	-1	1.3333	0.30	7129
L-1_CHS_04	-1	1.0000	0.40	891
U-1_CHS_01	-1	0.2000	2.00	12
U-1_CHS_02	-1	0.2000	2.00	14
U-1_CHS_03	-1	0.1600	2.50	10
U-1_CHS_04	-1	0.1600	2.50	10
U-1_CHS_05	-1	0.1455	2.75	9
U-1_CHS_06	-1	0.1455	2.75	9
U-1_CHS_07	-1	0.1333	3.00	7
U-1_CHS_08	-1	0.1333	3.00	8
U-1_CHS_09	-1	0.1143	3.50	6
U-1_CHS_10	-1	0.1143	3.50	5
U0_CHS_01	0	0.2000	2.00	14
U0_CHS_02	0	0.2000	2.00	15
U0_CHS_03	0	0.1600	2.50	10
U0_CHS_04	0	0.1600	2.50	10
U0_CHS_05	0	0.1455	2.75	9
U0_CHS_06	0	0.1455	2.75	8
U0_CHS_07	0	0.1333	3.00	8
U0_CHS_08	0	0.1333	3.00	7
U0_CHS_09	0	0.1143	3.50	6
U0_CHS_10	0	0.1143	3.50	6

Table 3.30 – Experimental program of cyclic tests performed on CHB series of X60 piping steel.

Specimens reference	R_δ [–]	f [Hz]	$\Delta\delta$ [%]	N_i [cycles]
L-1_CHB_01	-1	0.5000	0.80	125
L-1_CHB_02	-1	1.0000	0.40	975
L-1_CHB_03	-1	0.8000	0.50	550
L-1_CHB_04	-1	1.3333	0.30	4644
U-1_CHB_01	-1	0.2000	2.00	17
U-1_CHB_02	-1	0.2000	2.00	21
U-1_CHB_03	-1	0.1600	2.50	11
U-1_CHB_04	-1	0.1600	2.50	12
U-1_CHB_05	-1	0.1455	2.75	9
U-1_CHB_06	-1	0.1455	2.75	9
U-1_CHB_07	-1	0.1333	3.00	8
U-1_CHB_08	-1	0.1333	3.00	8
U-1_CHB_09	-1	0.1250	3.20	7
U-1_CHB_10	-1	0.1250	3.20	7
U0_CHB_01	0	0.2000	2.00	18
U0_CHB_02	0	0.2000	2.00	18
U0_CHB_03	0	0.1600	2.50	11
U0_CHB_04	0	0.1600	2.50	14
U0_CHB_05	0	0.1455	2.75	9
U0_CHB_06	0	0.1455	2.75	9
U0_CHB_07	0	0.1333	3.00	8
U0_CHB_08	0	0.1333	3.00	9
U0_CHB_09	0	0.1143	3.50	7
U0_CHB_10	0	0.1081	3.70	7

Table 3.31 – Experimental program of cyclic tests performed on SN series of X60 piping steel.

Specimens reference	R_δ [–]	f [Hz]	$\Delta\delta$ [%]	N_i [cycles]
L-1_SN_01	-1	0.8000	0.50	583
L-1_SN_02	-1	0.5000	0.80	161
L-1_SN_03	-1	1.0000	0.40	1205
L-1_SN_04	-1	1.1429	0.35	2579
U-1_SN_01	-1	0.2000	2.00	24
U-1_SN_02	-1	0.2000	2.00	27
U-1_SN_03	-1	0.1600	2.50	20
U-1_SN_04	-1	0.1600	2.50	21
U-1_SN_05	-1	0.1333	3.00	14
U-1_SN_06	-1	0.1333	3.00	11
U-1_SN_07	-1	0.1231	3.25	11
U-1_SN_08	-1	0.1231	3.25	9
U-1_SN_09	-1	0.1231	3.25	10
U-1_SN_10	-1	0.1429	2.80	12
U0_SN_01	0	0.2000	2.00	32
U0_SN_02	0	0.2000	2.00	27
U0_SN_03	0	0.1600	2.50	15
U0_SN_04	0	0.1600	2.50	19
U0_SN_05	0	0.1333	3.00	12
U0_SN_06	0	0.1333	3.00	12
U0_SN_07	0	0.1231	3.25	10
U0_SN_08	0	0.1231	3.25	10
U0_SN_09	0	0.1231	3.50	9
U0_SN_10	0	0.1231	3.70	8

Table 3.32 – Experimental program of cyclic tests performed on OH series of X60 piping steel.

Specimens reference	R_δ [–]	f [Hz]	$\Delta\delta$ [%]	N_i [cycles]
L-1_OH_01	-1	0.5714	0.70	145
L-1_OH_02	-1	1.0000	0.40	686
L-1_OH_03	-1	0.8000	0.50	305
U-1_OH_01	-1	0.2000	2.00	12
U-1_OH_2	-1	0.2000	2.00	12
U-1_OH_03	-1	0.2286	1.75	15
U-1_OH_04	-1	0.2286	1.75	16
U-1_OH_05	-1	0.2667	1.50	22
U-1_OH_06	-1	0.2667	1.50	22
U-1_OH_07	-1	0.1818	2.20	10
U-1_OH_08	-1	0.1818	2.20	9
U-1_OH_09	-1	0.1667	2.40	7
U-1_OH_10	-1	0.1600	2.50	7
U0_OH_01	0	0.2000	2.00	12
U0_OH_02	0	0.2000	2.00	12
U0_OH_03	0	0.2286	1.75	15
U0_OH_04	0	0.2286	1.75	14
U0_OH_05	0	0.2667	1.50	23
U0_OH_06	0	0.2667	1.50	24
U0_OH_07	0	0.1818	2.20	12
U0_OH_08	0	0.1818	2.20	10
U0_OH_09	0	0.1667	2.40	9
U0_OH_10	0	0.1600	2.50	6

Table 3.33 – Experimental program of cyclic tests performed on CH series of X60TT [4].

Specimens reference	R_δ [–]	f [Hz]	$\Delta\delta$ [%]	N_i [cycles]
L0_CH_01	0	0.5000	0.80	140
L0_CH_02	0	0.6667	0.60	240
L0_CH_03	0	1.3333	0.30	1600
L0_CH_04	0	1.0000	0.40	500
U0_CH_01	0	0.2000	2.00	26
U0_CH_02	0	0.2000	2.00	22
U0_CH_03	0	0.1600	2.50	18
U0_CH_04	0	0.1600	2.50	15
U0_CH_05	0	0.1333	3.00	10
U0_CH_06	0	0.1333	3.00	12
U-1_CH_01	-1	0.2000	2.00	20
U-1_CH_02	-1	0.2000	2.00	22
U-1_CH_03	-1	0.1600	2.50	13
U-1_CH_04	-1	0.1600	2.50	11
U-1_CH_05	-1	0.1333	3.00	11
U-1_CH_06	-1	0.1333	3.00	9

3.4.2.5 Experimental results of cyclic tests performed on flat grooved and shear specimens

In order to investigate the influence of Lode angle parameter on fatigue tests, cyclic tests on flat grooved specimens and plane shear specimens were conducted under displacement

control conditions, on X60 piping steel. Different reference lengths were set for the clip gauge that was mounted at the specimen centres (see Figure 3.67). The specimens design aims at producing plastic plane strain conditions or shear, both corresponding to a Lode angle parameter, $\bar{\theta} = 0$. These aspects will be further discussed in the Chapter IV, supported by the numerical data derived from FEM analysis. The experimental program of flat-grooved specimens included ULCF tests whereas LCF and ULCF regimes were covered in the cyclic tests of plane shear specimens. The detailed results of the experimental program are summarized in the Table 3.34 for FG series and in the Table 3.35 for the PSG series. The relative displacement ratio, R_δ, the relative displacement range, $\Delta\delta$, the test frequency, f and the number of cycles to crack initiation, N_i are given in the tables.

Table 3.34 – Experimental program of cyclic tests performed with FG series of X60 piping steel.

Specimens	R_δ [–]	f [Hz]	$\Delta\delta$ [%]	N_i [cycles]
U-1_FG_01	-1	0.8000	0.50	112
U-1_FG_02	-1	0.2667	1.50	4
U-1_FG_03	-1	0.4000	1.00	10
U-1_FG_04	-1	0.4000	1.00	15
U-1_FG_05	-1	0.2667	1.50	5
U-1_FG_06	-1	0.5000	0.80	22
U-1_FG_07	-1	0.5000	0.80	22
U-1_FG_08	-1	0.6667	0.60	72
U-1_FG_09	-1	0.6667	0.60	61

Table 3.35 – Experimental program of cyclic tests performed with PSG series of X60 piping steel.

Specimens	R_δ [–]	f [Hz]	$\Delta\delta$ [%]	N_i [cycles]
L0_PSG_01	0	0.8000	0.50	500
L0_PSG_02	0	0.6667	0.60	278
L0_PSG_03	0	1.0000	0.40	1000
L0_PSG_04	0	1.3333	0.30	8810
L0_PSG_05	0	0.8000	0.50	560
L0_PSG_06	0	0.5714	0.70	190
U0_PSG_01	0	0.2667	1.50	26
U0_PSG_02	0	0.2500	1.60	20
U0_PSG_03	0	0.2500	1.60	*
U0_PSG_04	0	0.2500	1.60	17
U0_PSG_05	0	0.2353	1.70	17
U0_PSG_06	0	0.2353	1.70	16
U0_PSG_07	0	0.2222	1.80	11
U0_PSG_08	0	0.2222	1.80	14
U0_PSG_09	0	0.2000	2.00	10
U0_PSG_10	0	0.4000	1.00	68
U0_PSG_11	0	0.1600	2.50	9
U0_PSG_12	0	0.2667	1.50	28

*invalid test

The fracture surface of a flat-grooved specimens was also analysed. A typical fracture surface of a ULCF test can be observed in the Figure 3.85, which includes the crack propagation path and the beachmarks characteristic of the crack progress along the specimen cross-section. In addition, a fracture surface of a plane shear specimens of X60 piping steel is also illustrated in Figure 3.86. The analysis of the fatigue crack growth at the plane shear specimen shows a predominant transgranular fracture mode, with a flat and brilliant surface (see Figure 3.86a)). At higher growth rates, as verified in the ULCF cyclic tests, the fracture surfaces remain transgranular, but with evidence of striations and the shear facets, as represented in Figure 3.86b).

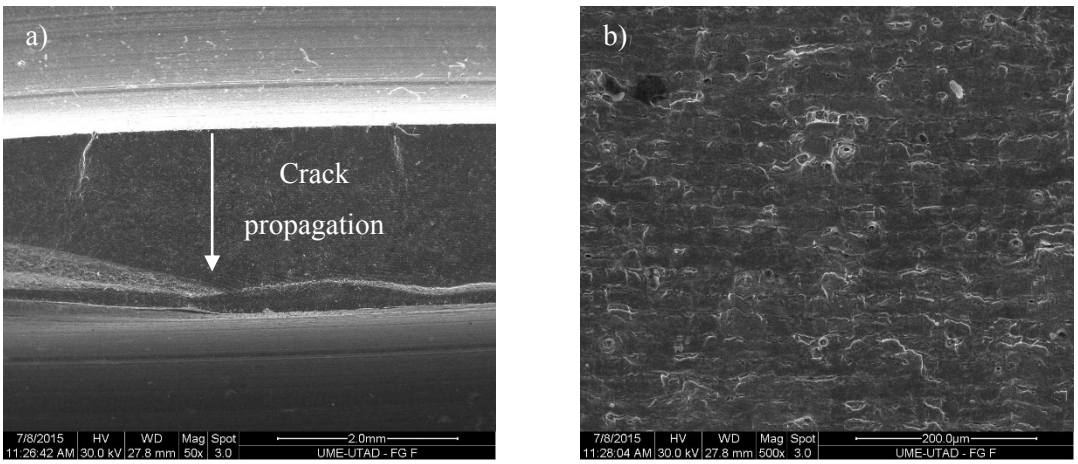

Figure 3.85 – Fracture surface of a flat-grooved specimen of X60 piping steel, tested under ULCF regime: a) crack propagation path; b) beachmarks relative to the macroscope crack path.

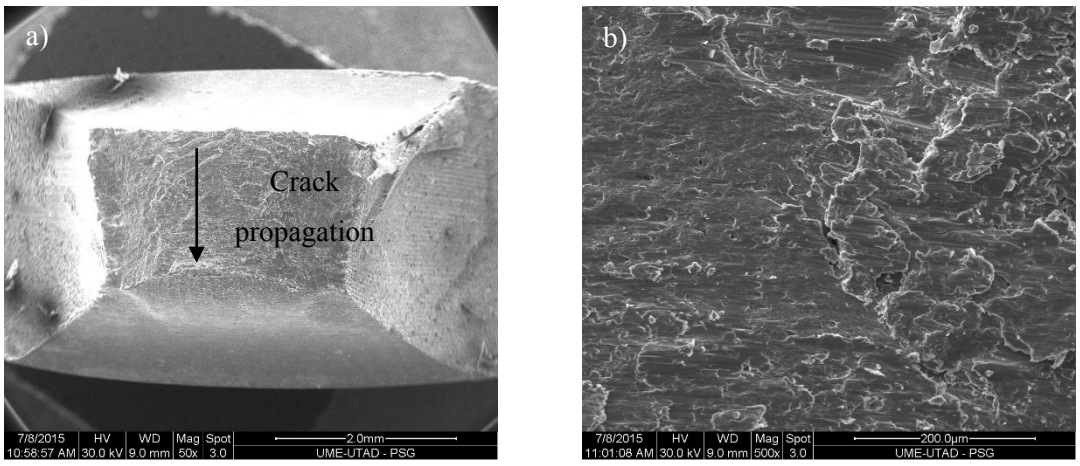

Figure 3.86 – Fracture surface of a plane shear specimen of X60 piping steel, tested under ULCF regime: a) crack propagation path; b) close view of the fracture surface.

3.4.3 Experimental results of the X65 piping steel

3.4.3.1 Basic tensile properties

The X65 piping steel is also used in the manufacturing of pipelines following the API 5L – PSL1 specifications [3]. The chemical and mechanical properties according to the API standard are shown in Table 3.36 and Table 3.37. Monotonic tensile tests were conducted on smooth plane specimens to address the mechanical properties of the X65 piping steel, which are presented in Table 3.38. Additionally, the mechanical properties derived for the X65TT steel [4] are presented in the Table 3.39. The X65 piping steel does not exhibit the yield stress plateau similarly to that verified for the X60 piping steel. In contrast, the thermal treatment induces a softening on the material monotonic behaviour, showing a very pronounced yield stress plateau. A reduction of the yield stress as also the ultimate tensile strength can be observed in the Figure 3.87. In general, the influence of the thermal treatment is more perceived for the X65 piping steel, when compared with the experimental response of the X60 piping steel.

Table 3.36 – Chemical properties of X65 piping steel, API 5L – PSL1 (maximum values) [3].

C [%]	Mn [%]	P [%]	S [%]	V [%]	Nb [%]	Ti [%]
0.28	1.4	0.03	0.03	a	a	a

a: The sum of the Niobium, Vanadium, and Titanium concentrations shall be < 0.15%

Table 3.37 – Mechanical properties requirements of X65 piping steel, API 5L – PSL1 (minimum values) [3].

Piping steel	$\sigma_{y/0.2\%}$ [MPa]	σ_{UTS} [MPa]
X65	450	535

Table 3.38 – Static mechanical properties of X65 piping steel.

	$\sigma_{y/0.2\%}$ [MPa]	σ_{UTS} [MPa]
Mean	601.85	644.81
Std. Deviation	11.09	5.80
CoV [%]	1.84	0.9

Table 3.39 – Static mechanical properties of X65 piping steel with thermal treatment (X65TT) [4].

	$\sigma_{y/0.2\%}$[MPa]	σ_{UTS} [MPa]
Mean	471.09	537.54
Std. Deviation	12.38	9.88
CoV [%]	2.63	1.83

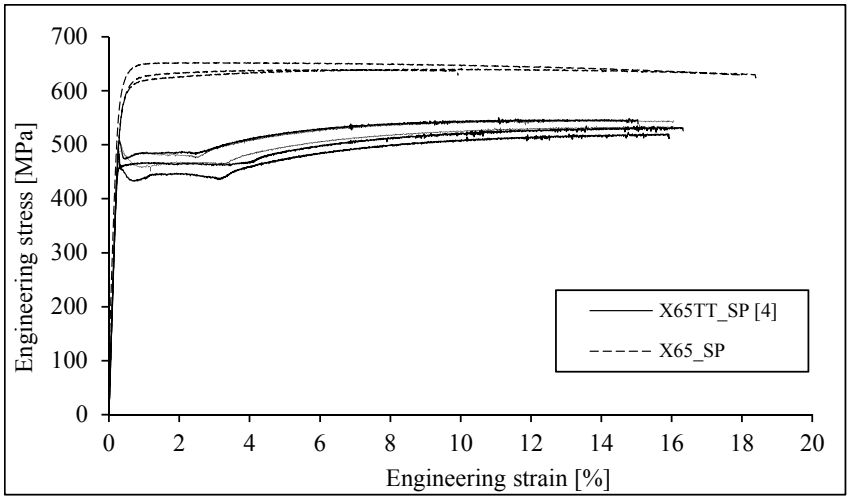

Figure 3.87 – Conventional stress-strain curves obtained for the X65 piping steel with and without thermal treatment using smooth plane specimens.

Concerning the material microstructure, the thermal treatment results on similar adjustments observed for the X60 piping steel. The material subjected to the thermal process presents a decreasing grain size with higher amounts of pearlite at the grain joints as observed in the Figure 3.88 and Figure 3.89. In contrast, with the original material, the material with thermal treatment does not show a specific grain orientation – a random grain orientation is observed with approximate equiaxial form.

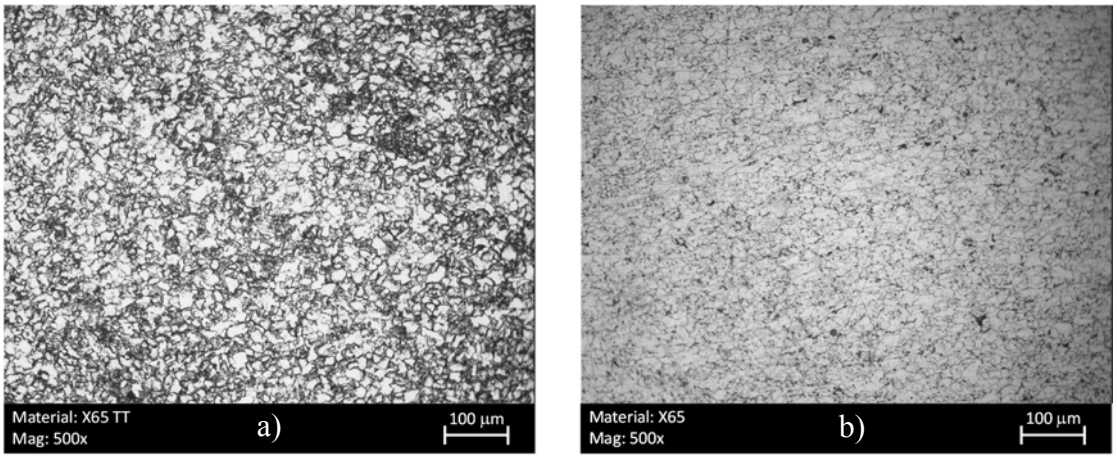

Figure 3.88 – Microstructures comparison for the X65 piping steel for a magnification of 500x: a) with thermal treatment (X65TT); b) without thermal treatment [4].

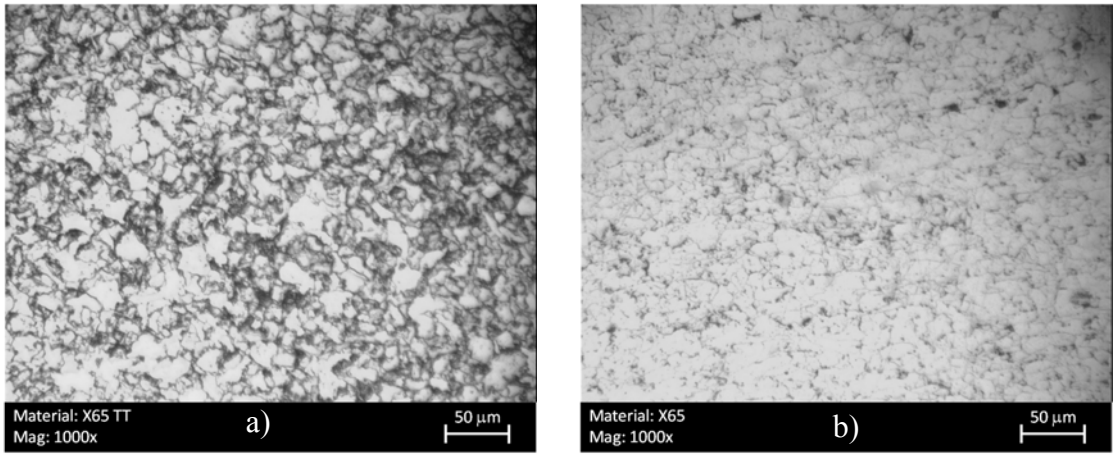

Figure 3.89 – Microstructures comparison for the X65 piping steel for a magnification of 1000x: a) with thermal treatment (X65TT); b) without thermal treatment [4].

3.4.3.2 Quasi-static monotonic tensile test results

The experimental results from the monotonic tensile tests of the X65 piping steel are further discussed in this section and additional results presented. Smooth plane specimens deformed shape was accessed using the ARAMIS® optical system, along with the monotonic tensile tests execution. This procedure allows the derivation of the experimental data concerning the load-relative displacement curves of smooth plane specimens. It should be noted that the relative displacements were computed from the specimen's lateral necking as performed for the X52 and X60 piping steels. These results are illustrated for the base material and for the material with thermal treatment in Figure 3.90 and Figure 3.91. The analysis of these figures shows a greater relative displacement suffered by the X65 piping steel with thermal treatment when compared with the base piping material. Nonetheless the lateral necking is one of the feature that can be investigated by the monotonic tests and in Chapter IV, this information will be very important to calibrate numerical simulations that will allow the evaluation of the effect of the thermal process in the material ductility. The load-displacement curves from monotonic tensile tests performed on X65 piping steel are illustrated in Figure 3.90 to Figure 3.95. These experimental curves includes the results of notched plane specimens. One series of a notched plane specimens was tested for the X65 piping steel with thermal treatment. The longitudinal displacements were measured with a clip extensometer with a reference length of 12.5 mm for all tested notched plane specimens.

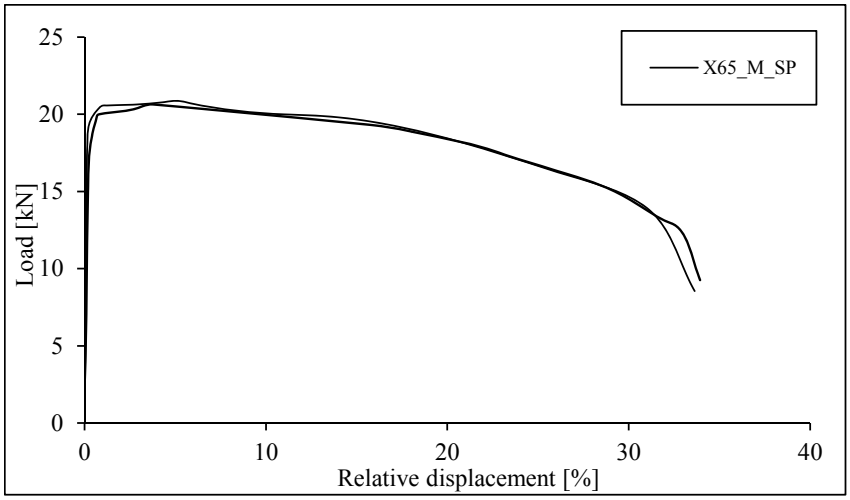

Figure 3.90 – Load-relative displacement (lateral necking) curves obtained from tests of smooth plane specimens of X65 piping steel.

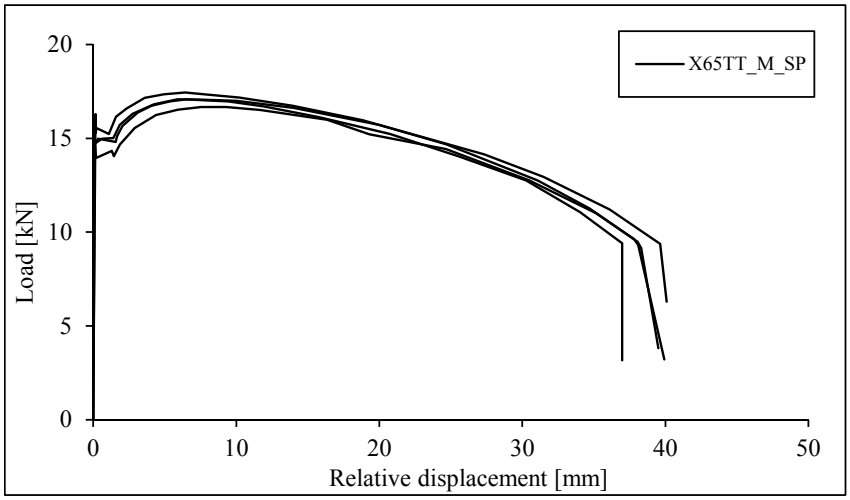

Figure 3.91 – Load-relative displacement (lateral necking) curves from tests of smooth plane specimens of X65 piping steel, with thermal treatment.

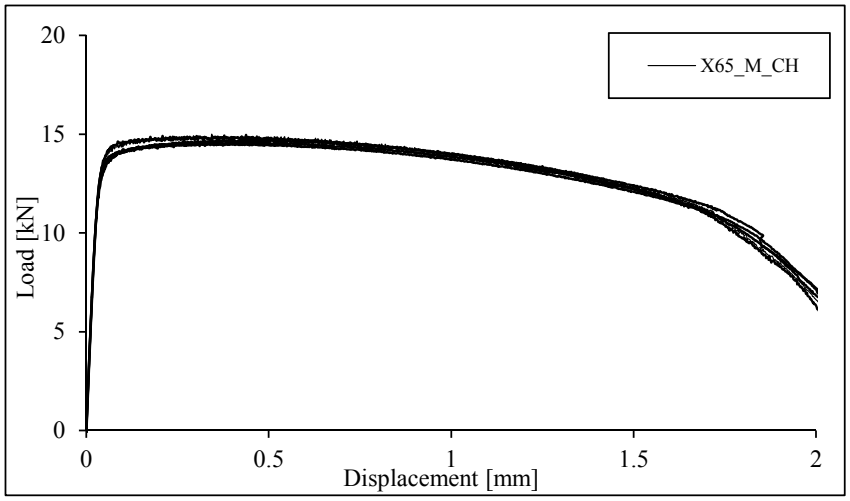

Figure 3.92 – Load-longitudinal displacement curves from tests of notched plane specimens of X65 piping steel, CH series.

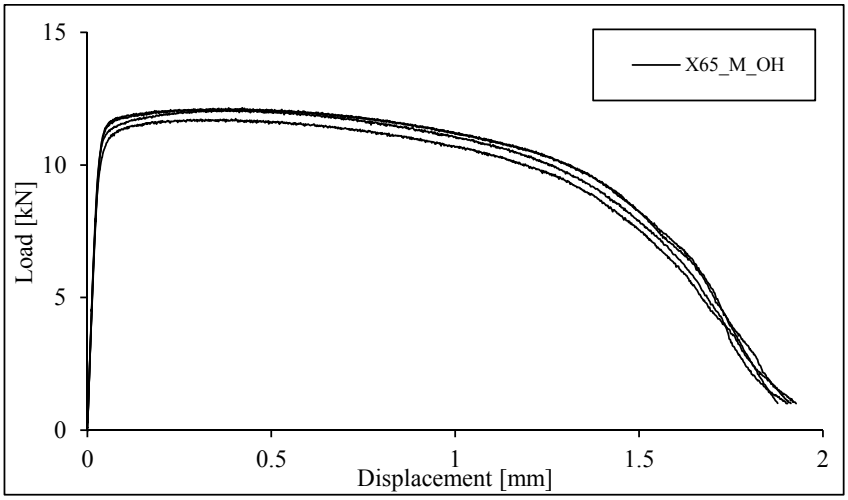

Figure 3.93 – Load-longitudinal displacement curves from tests of notched plane specimens of X65 piping steel, OH series.

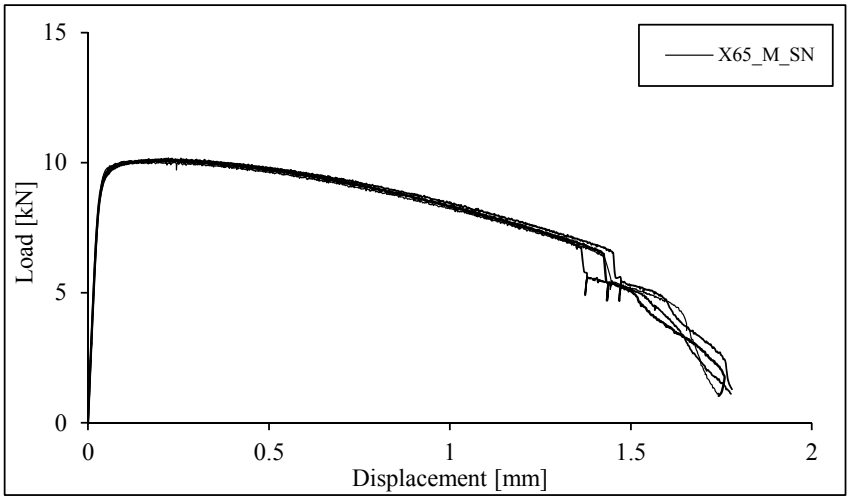

Figure 3.94 – Load-longitudinal displacement curves from tests of notched plane specimens of X65 piping steel, SN series.

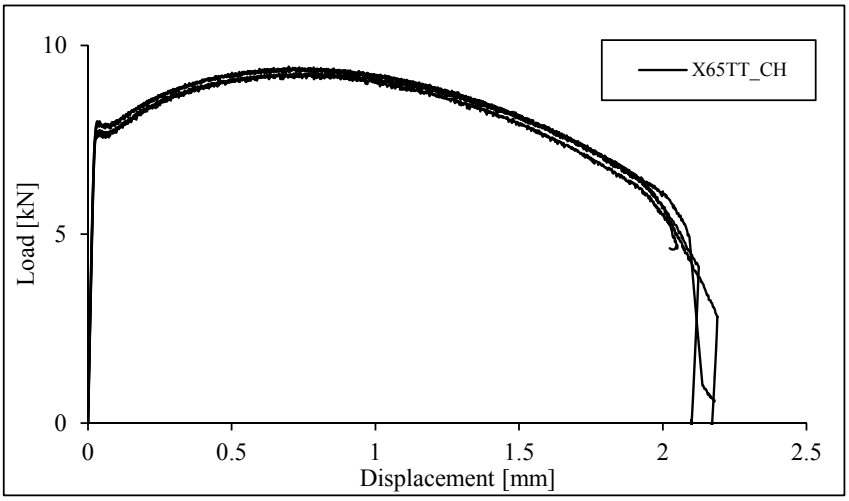

Figure 3.95 – Load-longitudinal displacement curves from tests of notched plane specimens of X65 piping steel with thermal treatment, CH series.

An unusual fracture surface with a central crack of a smooth plane specimen of X65 piping steel is observed in the Figure 3.96a). In order to clarify this effect, two possible scenarios may be envisaged, related with manufacturing process and hydrogen presence. Usually this feature is a consequent of the manufacturing process since the pipes of X65 steel grades were obtained from hot rolled plates. Consequently, the plates may have the memory of the central segregation of the original cast. This effect was not observed for X52 and X60 because they are seamless tubes, so the manufacturing route is completely different. Other possibility consists in the presence of hydrogen during the manufacturing process that can lead to this kind of crack. Due to its small size the hydrogen atom can easily migrate to the metal lattice, where it has a great mobility. Under certain conditions hydrogen can initiate cracks [10]. Despite of fracture surface shows a planar aspect the typical shape of a monotonic tensile test can be found in the Figure 3.96b).

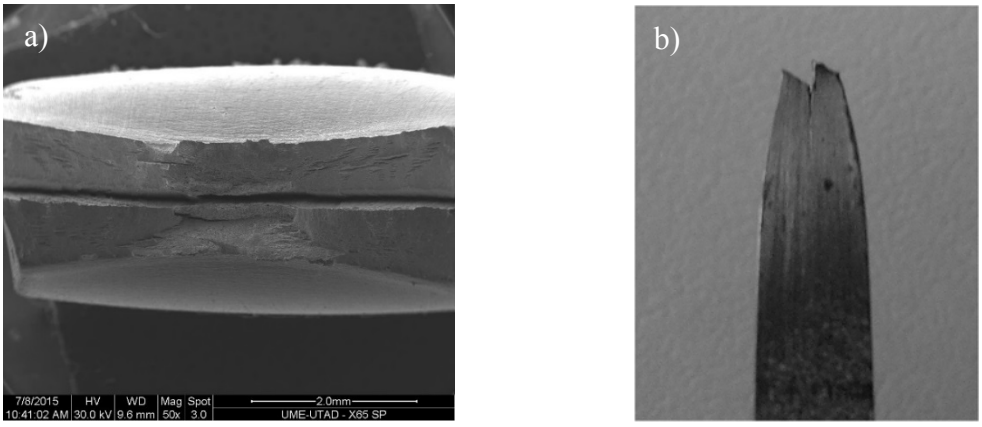

Figure 3.96 – Facture surface of a smooth plane specimen of X65 piping steel: a) general surface view; b) lateral/side view.

3.4.3.3 Experimental results of cyclic tension-compression tests on smooth specimens

The experimental program of LCF and ULCF tests carried out smooth plane specimens of X65 piping steel are summarized in the Table 3.40. In addition, the cyclic tests on smooth plane specimens affected with thermal treatment, covered both LCF and ULCF domains are also presented in the Table 3.41 [4]. The number of cycles until crack initiation and the plastic and elastic strain ranges were computed using the same procedure described for the previous materials.

Table 3.40 – Experimental program of cyclic tests performed on smooth specimens of X65 piping steel.

Specimens reference	S_t [mm^2]	R_ε [–]	f [Hz]	$\Delta\varepsilon$ [%]	N_i [cycles]	$\Delta\sigma$ [MPa]	$\Delta\varepsilon^P$ [%]	$\Delta\varepsilon^E$ [%]
L0_SP_1	32.28	0	0.4000	1.00	750	1026.333	0.484	0.516
L0_SP_2	32.68	0	0.5000	0.80	2050	992.797	0.327	0.473
L0_SP_3	32.64	0	0.2667	1.50	230	1090.188	1.023	0.477
L0_SP_4	32.30	0	0.4000	1.00	595	1063.713	0.507	0.493
L0_SP_5	32.54	0	0.3333	1.20	350	1095.458	0.707	0.493
L0_SP_6	32.58	0	0.5000	0.80	2796	983.948	0.311	0.489
L0_SP_7	32.46	0	0.6667	0.6	7696	732.418	0.290	0.310
L-1_SP_1	32.40	-1	0.3333	1.20	300	1099.102	0.713	0.487
L-1_SP_2	32.16	-1	0.2667	1.50	150	1124.769	0.980	0.520
L-1_SP_3	32.12	-1	0.5333	0.75	1800	978.500	0.295	0.455
L-1_SP_4	32.32	-1	0.5333	0.75	1600	996.920	0.281	0.469
L-1_SP_5	32.18	-1	0.5000	0.80	1720	967.893	0.322	0.478
L-1_SP_6	32.70	-1	0.6667	0.60	5300	935.646	0.167	0.433
L-1_SP_7	32.50	-1	0.4000	1.00	820	1030.289	0.509	0.491
U0_SP_1	32.54	0	0.1000	4.00	36	1252.613	3.352	0.648
U0_SP_2	32.22	0	0.0889	4.50	50	1252.613	3.797	0.703
U0_SP_3	32.38	0	0.0800	5.00	41	1252.613	4.263	0.737
U0_SP_4	32.56	0	0.0727	5.50	17	1274.605	4.891	0.609
U0_SP_5	32.58	0	0.0727	5.50	*			
U0_SP_6	32.38	0	0.0727	5.50	22	1268.693	4.757	0.743
U0_SP_7	32.48	0	0.0667	6.00	*			
U0_SP_8	32.40	0	0.0667	6.00	16	1261.115	5.332	0.668
U0_SP_9	32.30	0	0.0571	7.00	*			
U0_SP_10	32.32	0	0.0615	6.50	*			
U0_SP_11	32.28	0	0.0615	6.50	20	1240.891	5.800	0.700
U0_SP_12	32.70	0	0.0571	7.00	*			

* invalid test

Table 3.41 – Experimental program of cyclic tests of smooth specimens performed on X65 piping steel, with thermal treatment [4].

Specimens reference	S_t [mm^2]	R_ε [–]	f [Hz]	$\Delta\varepsilon$ [%]	N_i [cycles]	$\Delta\sigma$ [MPa]	$\Delta\varepsilon^P$ [%]	$\Delta\varepsilon^E$ [%]
L0_SP_1	32.18	0	0.5000	0.80	3000	700.079	0.426	0.374
L0_SP_2	32.30	0	0.4000	1.00	780	758.11	0.60	0.40
L0_SP_3	32.14	0	0.3333	1.20	680	775.364	0.787	0.413
L0_SP_4	32.52	0	0.4000	1.00	1600	735.067	0.605	0.395
L0_SP_5	32.26	0	0.5000	0.80	2400	726.023	0.429	0.371
L0_SP_6	32.54	0	0.3333	1.20	440	792.058	0.806	0.394
L0_SP_7	32.10	0	0.6667	0.60	10000	720.359	0.238	0.362
L0_SP_8	32.18	0	0.5000	0.80	1400	712.848	0.432	0.368
U0_SP_1	32.24	0	0.1000	4.00	104	929.074	3.486	0.514
U0_SP_2	32.02	0	0.0889	5.00	54	943.053	4.460	0.540
U0_SP_3	32.12	0	0.0800	5.00	50	965.099	4.424	0.576
U0_SP_4	32.18	0	0.0727	6.00	34	985.071	5.418	0.582
U0_SP_5	*							
U0_SP_6	32.36	0	0.0727	5.50	50	970.901	4.911	0.589
U0_SP_7	32.14	0	0.0667	6.00	36	965.367	5.435	0.565
U0_SP_8	*							
U0_SP_9	32.28	0	0.0727	5.50	56	946.516	4.919	0.581
U0_SP_10	32.06	0	0.0615	6.50	38	993.484	5.917	0.583
U0_SP_11	32.14	0	0.0615	6.50	32	982.595	5.942	0.558

* invalid tests

The mathematical relation proposed by Ramberg-Osgood [5] is usually used to describe the elastoplastic cyclic behaviour of the materials. The parameters involved in this relation were computed by plotting the stress amplitude against the plastic strain amplitude fitting a linear function in a log-log scale. Figure 3.97 and Figure 3.98 show the stress amplitude *versus* plastic strain amplitude resulted from LCF data only and LCF plus ULCF data, which allows addressing the cyclic parameters of the X65 piping steel as included in Table 3.42. Significant differences are observed namely for the cyclic strain hardening parameter. This evidence is confirmed by the analysis of the Figure 3.99 that compares the cyclic curves using the LCF data only and the LCF plus ULCF data. As already verified for the X52 and X60 steel grades, when ULCF data is used to derive the cyclic curves, a shift downward is observed.

Table 3.42 – Cyclic parameters of the X65 piping steel obtained from LCF data only and LCF plus ULCF data.

Experimental Data	***K'* [MPa]**	***n'***
LCF	938.64	0.0986
LCF+ULCF	732.49	0.0964

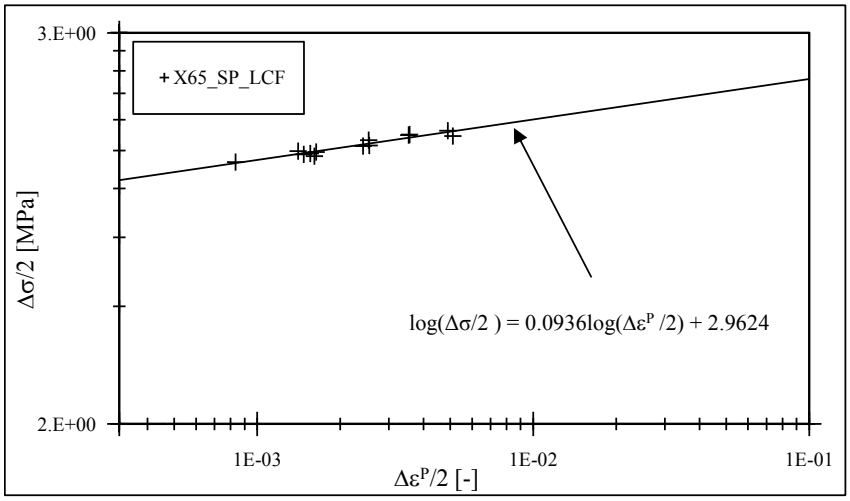

Figure 3.97 – Stress amplitude *versus* plastic strain amplitude relation of the X65 piping steel, under LCF domain.

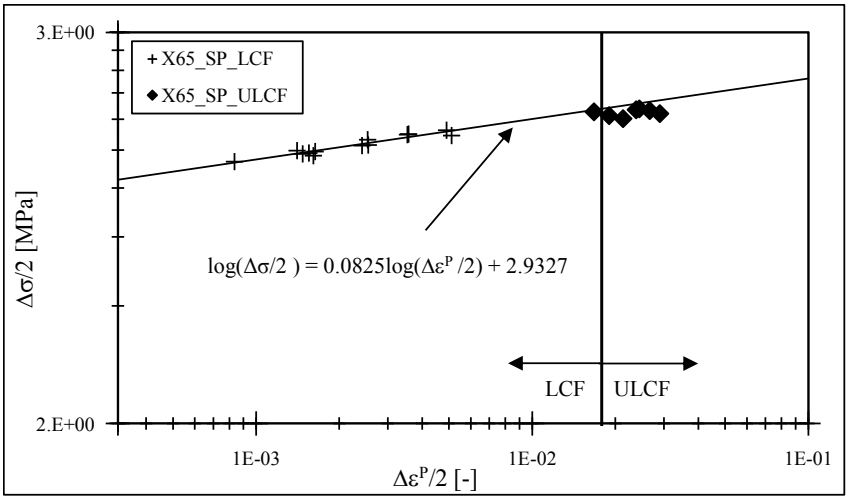

Figure 3.98 – Stress amplitude *versus* plastic strain amplitude relation of the X65 piping steel, under LCF plus ULCF domain.

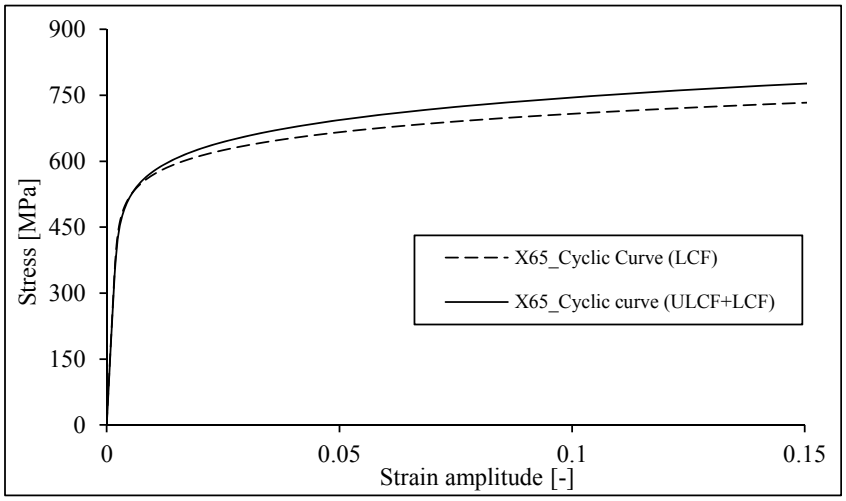

Figure 3.99 – Cyclic curves of the X65 piping steel obtained with LCF data only and LCF plus ULCF experimental data.

The comparisons of monotonic properties indicates that the thermal treatment of the X65 piping steel leads to considerable differences when compared with the results of X60 piping steel. Thus, it is also expected significant modifications in cyclic testing results. Comparisons between the X65 piping steel with and without thermal treatment are illustrated in Figure 3.100 and Figure 3.101 that show stress-plastic strain amplitude relations and the cyclic curves of base material and the thermal affected material, respectively. The effect of thermal treatment promotes very significant reduction of the cyclic hardening in the X65 steel grade. Table 3.43 shows the cyclic parameters obtained from LCF plus ULCF data of X65 piping steel with thermal treatment.

Table 3.43 – Cyclic parameters of X65 piping steel with thermal treatment obtained from LCF plus ULCF data [4].

Experimental Data	***K'* [MPa]**	***n'***
LCF+ULCF	737.22	0.1151

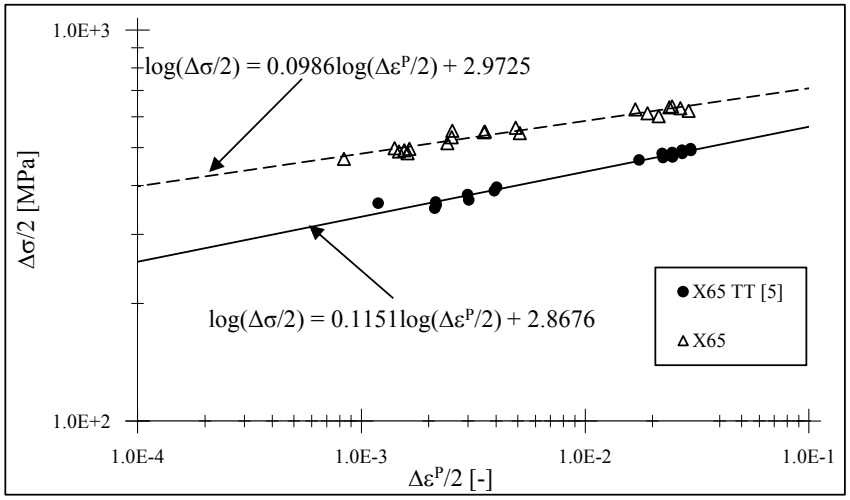

Figure 3.100 – Comparison of stress-plastic strain amplitude under LCF plus ULCF domain, between X65 piping steel with and without thermal treatment.

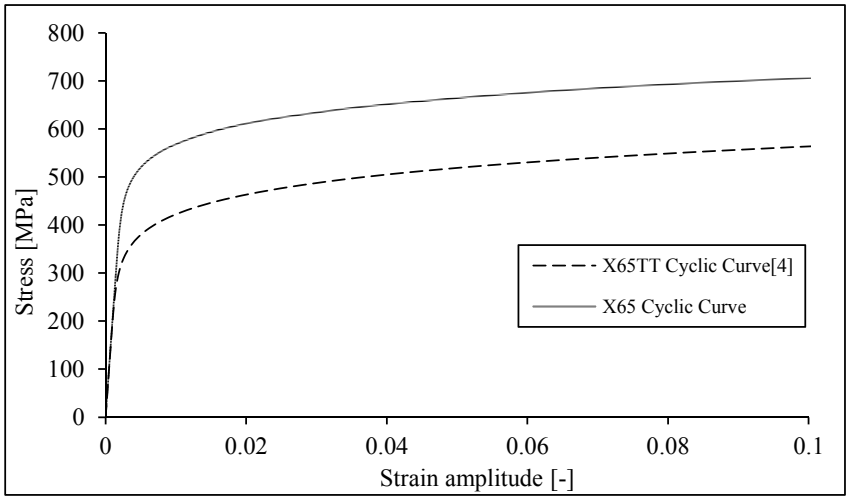

Figure 3.101 – Cyclic curves of X65 piping steel with and without thermal treatment.

Figure 3.102 illustrates the stress amplitude evolution with the number of cycles, where can be observed a progressive softening for all strain ranges applied in the cyclic tests. The evolution of stress amplitude against the number of cycles was also obtained for the material with thermal treatment and represented in the Figure 3.103. As expected, for the same strain ranges, the material with thermal treatment shows lower stress levels when compared with the non-affected material. In addition, for the high strain ranges, the stress

amplitude assumes fundamentally a stabilized behaviour with a slight softening. For the lower strain rages a pronounced softening is clearly observed.

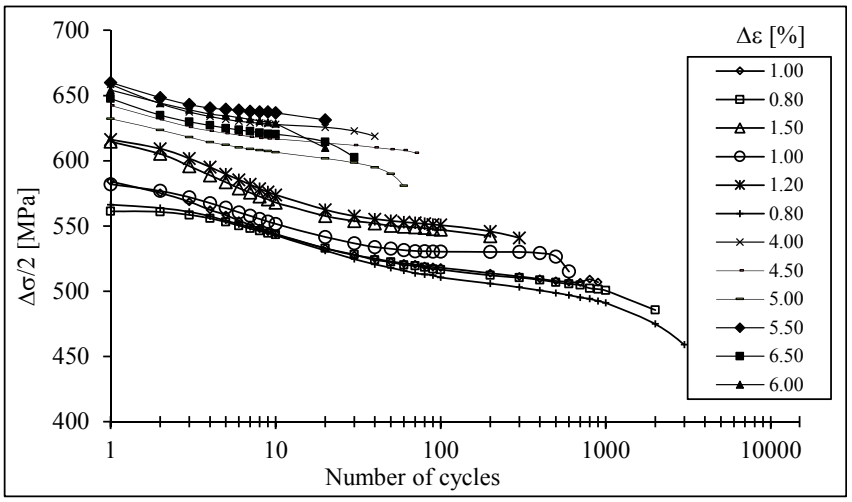

Figure 3.102 – Evolution of the stress amplitude with the number of cycles for the cyclic tests of smooth plane specimens of X65 piping steel.

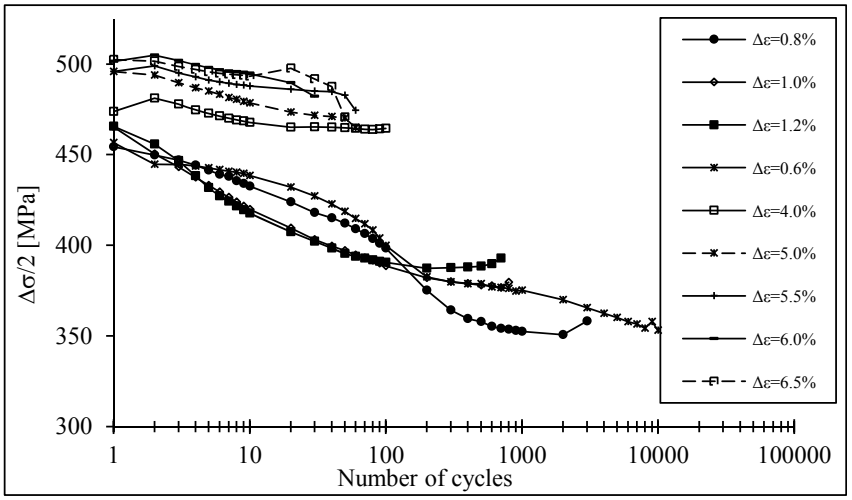

Figure 3.103 – Evolution of the stress amplitude with number of cycles for the cyclic tests of smooth plane specimens of X65TT steel grade [4].

In order to investigate the strain-life relation of the X65 piping steel under LCF regime, the total, elastic and plastic strains were correlated with the number of reversals until crack initiation as shown in Figure 3.104. The influence of ULCF domain was investigated correlating both LCF and ULCF data as represented in Figure 3.105. The parameters of the Morrow's relation were obtained from these approaches and they are presented in the Table 3.44. Significant modifications on the parameters of Morrow's relation can be found. Extrapolations of strain-life relations for ULCF regime may be

erroneous, if the estimation of Morrow relation parameters are performed only with LCF data. Figure 3.106 shows the total, plastic and elastic strain plotted against the number of reversals to crack initiation of smooth plane specimens with thermal treatment. In contrast to the X60 piping steel, the effect of thermal treatment is significant. In fact, the material subjected to a thermal process shows a higher fatigue strength mainly for ULCF regime. The parameters of Morrow relation obtained from the cyclic tests of smooth specimens with thermal treatment are presented in the Table 3.44.

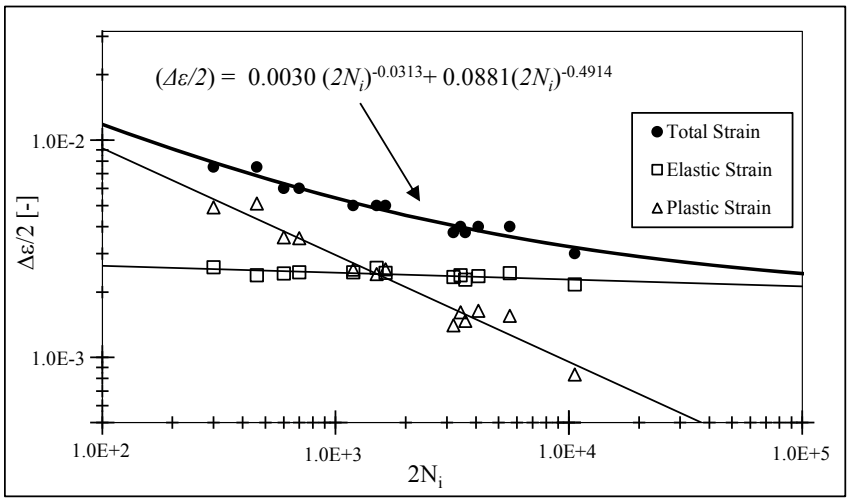

Figure 3.104 – Global strain-life curves of the X65 piping steel obtained from LCF data.

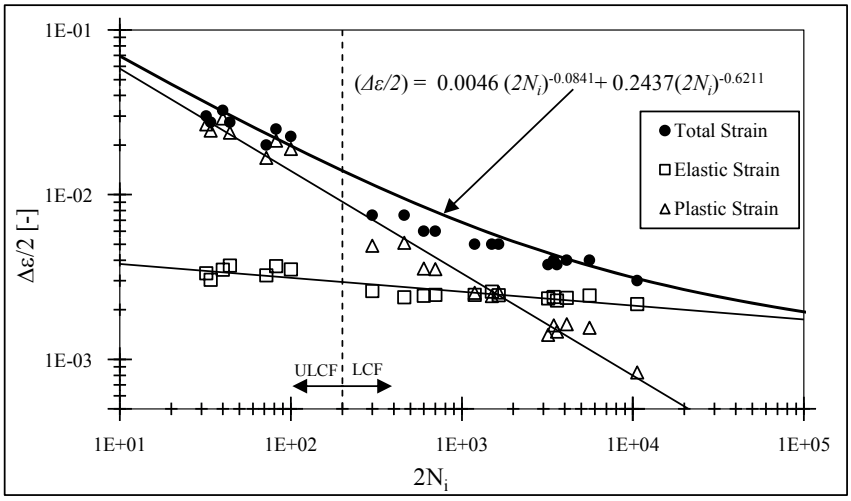

Figure 3.105 – Global strain-life curves of X65 piping steel obtained from LCF plus ULCF data.

Table 3.44 – Parameters of Morrow's relation derived from LCF data only and LCF plus ULCF data, of X65 piping steel.

Experimental Source Data	σ'_f [MPa]	b	ε'_f	c
LCF	984.16	-0.0993	0.0881	-0.4914
LCF+ULCF	1751.00	-0.1788	0.4323	-0.6025
LCF+ULCF (X65TT) [4]	908.59	-0.1011	0.3825	-0.6152

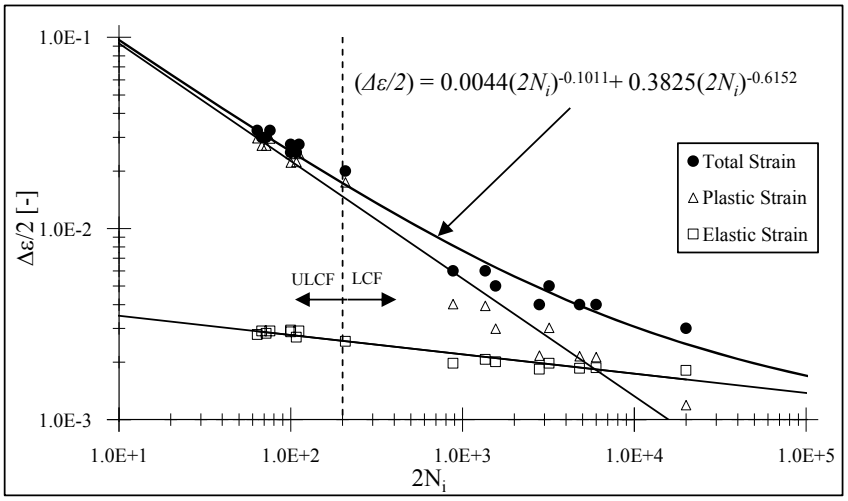

Figure 3.106 – Global strain-life curves of the X65 piping steel with thermal treatment obtained from LCF plus ULCF data [4].

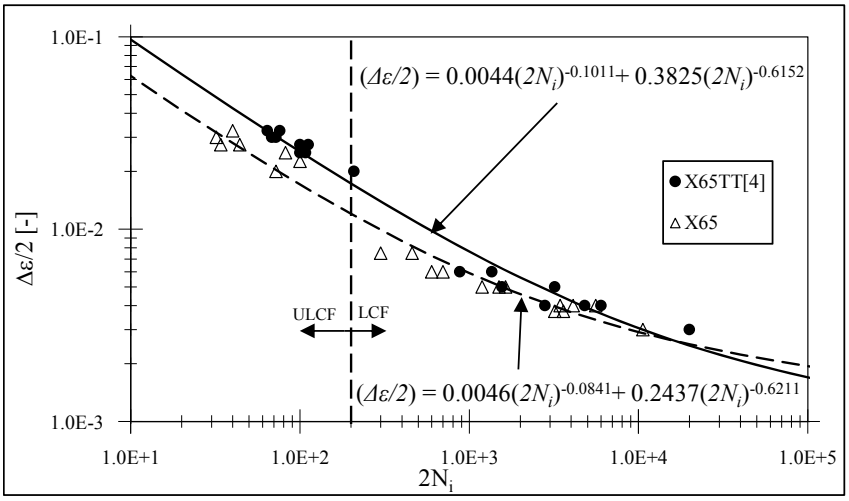

Figure 3.107 – Comparison between strain-life curve of the X65 piping steel with and without thermal treatment.

The fracture surface of a specimen tested under ULCF domain of X65 piping steel is illustrated in Figure 3.108a). The photographs associated to the fatigue failure under large plastic levels can be observed. The crack initiation occurs at the middle of specimens' side surface and the crack progress is marked by fatigue striations. The final plastic failure can be also observed. These aspects are common in the analysis of fracture

surfaces under ULCF domain of the three steel grades investigated in this work. A mixture of ductile damage and cyclic damage is represented in the Figure 3.108b) where is possible to identify the cavities with a fibrous aspect which results from the growth and coalescence of microvoids. The crack advance per cycle results from some degree of ductile damage.

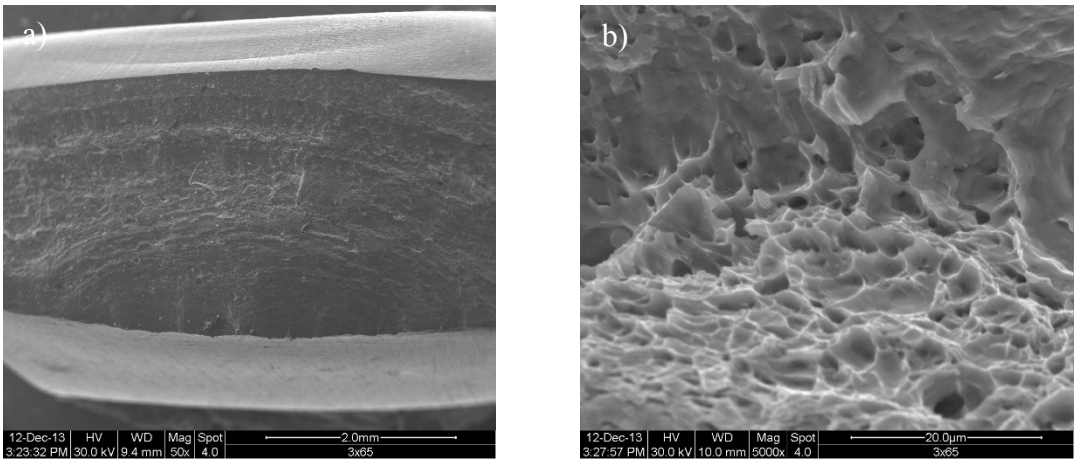

Figure 3.108 – Fracture surface of smooth plane specimens of X65 piping steel, tested under ULCF domain (X65_U0_SP_08, Δε=6%): a) path of macroscopic crack propagation; b) aspect of the fracture surface at one striation transition.

3.4.3.4 Experimental results of cyclic tension-compression tests performed on notched specimens

LCF and ULCF tests were also conducted on notched plane specimens of X65 piping steel. The relative displacement δ, is computed by the ratio of imposed displacement and the reference gauge length. The specimens' reference, the relative displacement range $\Delta\delta$, the relative displacement ratio, R_δ, the test frequency, f and the number of cycles to crack initiation, N_i are presented in the Table 3.45 to Table 3.47 for notched specimens of base material and in the Table 3.48 for the notched series of the material with thermal treatment. As it has been performed so far, the number of cycles to crack initiation were computed based on procedures shown in Figure 3.28.

Table 3.45 – Experimental program of cyclic tests performed on CH specimen series of X65 piping steel.

Specimens reference	R_δ [–]	f [Hz]	$\Delta\delta$ [%]	N_i [cycles]
L-1_CH_01	-1	0.5000	0.80	145
L-1_CH_02	-1	2.0000	0.20	*
L-1_CH_03	-1	1.0000	0.40	1450
L-1_CH_04	-1	0.8000	0.50	420
L-1_CH_05	-1	1.1429	0.35	400
L-1_CH_06	-1	1.0000	0.40	2205
U-1_CH_01	-1	0.2000	2.00	20
U-1_CH_02	-1	0.2000	2.00	21
U-1_CH_03	-1	0.1818	2.20	18
U-1_CH_04	-1	0.1818	2.20	18
U-1_CH_05	-1	0.1481	2.70	13
U-1_CH_06	-1	0.1481	2.70	13
U-1_CH_07	-1	0.1333	3.00	11
U0_CH_01	0	0.2000	2.00	22
U0_CH_02	0	0.2000	2.00	22
U0_CH_03	0	0.1600	2.50	13
U0_CH_04	0	0.1600	2.50	14
U0_CH_05	0	0.1333	3.00	11
U0_CH_06	0	0.1333	3.00	10
U0_CH_07	0	0.1250	3.20	9

*invalid test

Table 3.46 – Experimental program of cyclic tests performed on SN specimen series of X65 piping steel.

Specimens reference	R_δ [–]	f [Hz]	$\Delta\delta$ [%]	N_i [cycles]
L-1_SN_01	-1	1.1429	0.35	2700
L-1_SN_02	-1	1.0000	0.40	1400
L-1_SN_03	-1	0.8000	0.50	452
L-1_SN_04	-1	0.5000	0.80	185
L-1_SN_05	-1	0.6667	0.60	340
U-1_SN_01	-1	0.2000	2.00	23
U-1_SN_02	-1	0.2000	2.00	22
U-1_SN_03	-1	0.1600	2.50	19
U-1_SN_04	-1	0.1600	2.50	18
U-1_SN_05	-1	0.1333	3.00	15
U-1_SN_06	-1	0.1333	3.00	15
U-1_SN_07	-1	0.1231	3.25	13
U-1_SN_08	-1	0.1231	3.25	13
U0_SN_01	0	0.2000	2.00	22
U0_SN_02	0	0.2000	2.00	*
U0_SN_03	0	0.1600	2.50	17
U0_SN_04	0	0.1600	2.50	18
U0_SN_05	0	0.1333	3.00	13
U0_SN_06	0	0.1333	3.00	14
U0_SN_07	0	0.1231	3.25	12

*invalid test

Table 3.47 – Experimental program of cyclic tests performed on OH specimen series of X65 piping steel.

Specimens reference	R_δ [–]	f [Hz]	$\Delta\delta$ [%]	N_i [cycles]
L-1_OH_01	-1	0.5000	0.80	78
L-1_OH_02	-1	0.6667	0.60	180
L-1_OH_03	-1	0.8000	0.50	390
L-1_OH_04	-1	1.0000	0.40	590
L-1_OH_05	-1	1.3333	0.30	2800
U-1_OH_01	-1	0.2000	2.00	15
U-1_OH_02	-1	0.2000	2.00	13
U-1_OH_03	-1	0.1600	2.50	9
U-1_OH_04	-1	0.1600	2.50	9
U-1_OH_05	-1	0.1333	3.00	6
U-1_OH_06	-1	0.1333	3.00	7
U-1_OH_07	-1	0.1231	3.25	4
U0_OH_01	0	0.2000	2.00	*
U0_OH_02	0	0.2000	2.00	11
U0_OH_03	0	0.1600	2.50	*
U0_OH_04	0	0.1600	2.50	9
U0_OH_05	0	0.1333	3.00	7
U0_OH_06	0	0.1333	3.00	6
U0_OH_07	0	0.1231	3.25	15

*invalid tests

Table 3.48 – Experimental program of cyclic tests performed on CH specimen series of X65 piping steel, with thermal treatment.

Specimens references	R_δ [–]	f [Hz]	$\Delta\delta$ [%]	N_i [cycles]
L0_CH_01	0	0.5000	0.80	130
L0_CH_02	0	0.6667	0.60	260
L0_CH_03	0	1.3333	0.30	1600
L0_CH_04	0	1.0000	0.40	1000
U-1_CH_01	-1	0.2000	2.00	24
U-1_CH_02	-1	0.2000	2.00	22
U-1_CH_03	-1	0.1600	2.50	15
U-1_CH_04	-1	0.1600	2.50	15
U-1_CH_05	-1	0.1333	3.00	9
U0_CH_01	0	0.2000	2.00	24
U0_CH_02	0	0.2000	2.00	26
U0_CH_03	0	0.1600	2.50	18
U0_CH_04	0	0.1600	2.50	17
U0_CH_05	0	0.1333	3.00	12
U0_CH_06	0	0.1333	3.00	11

3.5 COMPARISONS OF API PIPING STEELS PERFORMANCE

The extensive experimental program carried out on X52, X60 and X65 piping steels allow the identification of the main static and cyclic properties that are compared in this section. Figure 3.109 illustrates the conventional stress-strain curves of the three steel grades investigated in this work. It can be observed that X52 steel grade, showing a clearly defined yield stress plateau assumes the lowest yield stress value, followed by the X60 and X65 piping steels. Concerning the ultimate tensile strengths of the X52 and X60 steels shows a similar levels while X65 presents the highest value. The discussion about the ductility of these materials will be done by means of FEM analysis in Chapter IV, since the finite element simulations will be used to simulate the failure conditions of the specimens and assess the maximum longitudinal deformation.

In addition the cyclic curves associated to each steel grades were also derived from the cyclic tests under LCF and ULCF domain of smooth plane tests. The cyclic curves are plotted together in the Figure 3.110. The analysis of the cyclic curves shows that the X65 piping steel exhibits a higher cyclic hardening while a similar cyclic elastoplastic behaviour is found for both X52 and X60 piping steels at low strains. The strain-life relations are compared together in the Figure 3.111. In general, X52 and X65 shows a similar fatigue behaviours. The fatigue behaviour of the X60 tend to be distinct mainly under ULCF regime, showing a higher fatigue resistance for ULCF conditions.

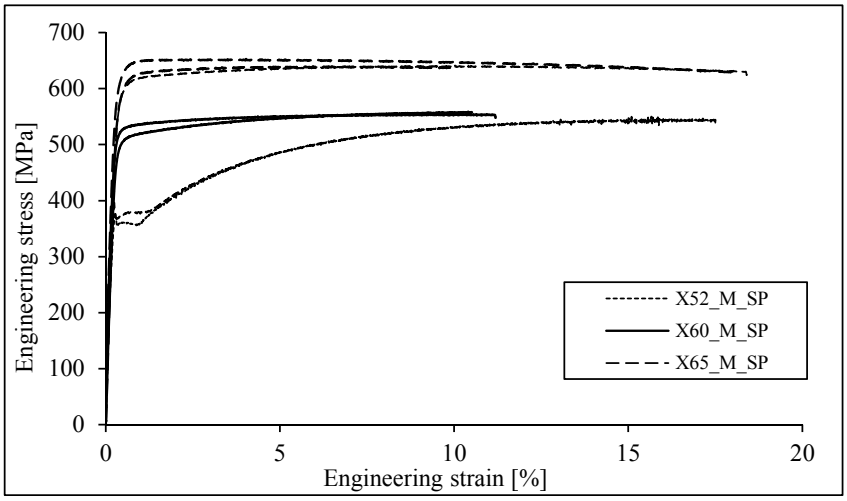

Figure 3.109 – Comparison of conventional stress-strain curves of X52, X60 and X65 piping steels (smooth plane specimens).

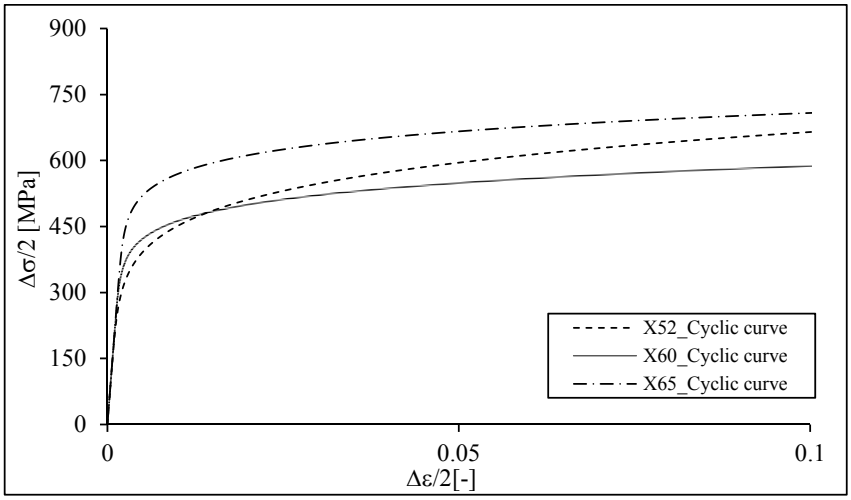

Figure 3.110 – Comparison of cyclic curves of X52, X60 and X65 piping steels (smooth plane specimens).

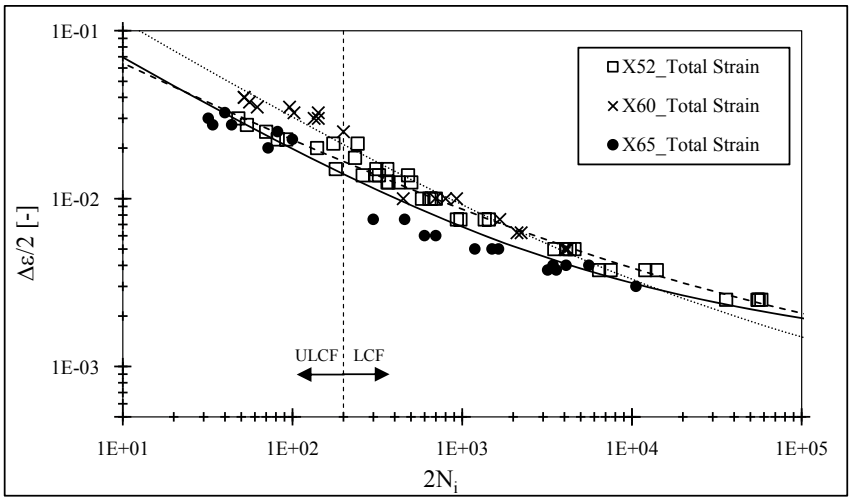

Figure 3.111 – Comparisons between strain-life relation of X52, X60 and X65 piping steels covering both the ULCF and LCF regimes (smooth plane specimens).

3.6 CONCLUSIONS

The monotonic ductile behaviour of three piping steels were investigated in this section. An extensive experimental work was carried out, by using several specimens' configurations, namely smooth and notched specimens. For some steel grades additional special tests were performed which is the case of the flat grooved and plane shear specimens used for the X60 steel grade. Concerning the smooth specimen's tests, they allowed to identify the typical mechanical properties of each material and establish

comparisons between ductility/strength performances. In fact, X65 presents a higher yield stress as also a higher ultimate tensile strength. X52 and X60 exhibits a similar ultimate tensile strength. X52 assumes the lowest yield stress value. X60 piping steel reveals higher ductility until material monotonic fracture. Monotonic tests on notched, flat grooved and plane shear specimens provided different levels of fracture strains, stress triaxialities and lode angle parameters.

Cyclic tension-compression tests on smooth, notched, flat-grooved, plane shear specimens and cyclic bending tests were performed under LCF and ULCF fatigue domain. The results obtained from tested smooth specimens showed that the X60 piping steel exhibits a higher fatigue resistance under both LCF and ULCF domains. With respect to the elastoplastic cyclic behaviour, cyclic curves were obtained taking into account both LCF and ULCF data. This analysis allowed to conclude that strain hardening of cyclic curve reduces when ULCF data is accounted. Based on this assumption, in order to fully define the cyclic behaviour of these materials it is recommended to perform experimental tests in both fatigue domains, since distinct parameters can be obtained if only LCF or ULCF regimes are accounted separately.

High strain range levels applied on the smooth specimens produces lateral movement during the compressive reversal, even using a strain ratio of R_ε=0. The use of an anti-buckling system coupled to the smooth plane specimens overcomes partially this shortcoming but for extreme high strain level some instability still may be observed. Thus, the actuator movements during the ULCF tests of the smooth specimens of the steels grades affected with thermal process were measured using an LVDT's system. The experimental data obtained from LVDTs measurements will be explored in the Chapter IV in order to evaluate more accurate boundary conditions to be used in the numerical simulations of the ULCF tests on smooth plane specimens, in particular to account for the lateral instabilities. Alternatively, tensile-compression cyclic tests on notched specimens and cyclic bending tests can be used to investigate the ULCF cyclic behaviour of the steels. However, a non-linear finite element analysis of these tests should be performed in order to assess the history of the damage parameters involved in the fatigue damage models, as will be shown latter in this thesis.

ULCF experimental data derived from cyclic bending tests will be used to validate the fatigue damage models, which are calibrated using the uniaxial cyclic tests. In detail, the experimental load-displacement curves, the data acquired from strain gauges and the specimen deformed shape assessed from the acquisition of consecutive images during the bending cyclic tests will be compared with the numerical results in the Chapter IV. Moreover, the cyclic tests carried out on flat grooved and shear plane specimens provides special stress state conditions, associated with a Lode angle parameter of $\bar{\theta} = 0$ aiming to investigate the influence of this parameter on the elastoplastic cyclic behaviour of the steel grades. However, finite element simulation are required to achieve the stress/strain loading history in the specimens' critical regions which will be presented latter in this work.

The effect of the thermal treatment on X60 and X65 steel grades was also investigated in this section. For both steels a reduction of mechanical strength was verified. Additionally, the X60 and X65 piping steels with thermal process exhibits a pronounced yield plateau, typical of carbon steels, which was caused by the tempering treatment applied after the metal forming of elbows. Concerning the thermal cycle effects, very significant impact on both cyclic elastoplastic and fatigue relations was observed, with more emphasis on X65 steel. A reduction in the cyclic yield stresses and an increase of the fatigue resistance was verified for the X65 steel pipe. For the X60 steel grade, no noticeable effect of the thermal cycle on fatigue behaviour of the material was reported.

Samples of fracture surfaces of some specimens subjected to monotonic and cyclic tests were analysed. In general, the monotonic fracture surfaces exhibits the classic characteristics of monotonic ductile fractures, namely the fibrous appearance, the porosity and larger necking regions and an overall rough appearance. From another point of view, fracture surfaces associated of ULCF tests show similar features from fatigue and ductile fracture appearances. Due to the high strain levels, growing and coalescence mechanisms of microvoids were observed. The microcracks typical of LCF and the fatigue striation marking the crack progress were clearly identified. An uncommon fracture surface was found for a smooth plane specimen of X65 piping steel. Two possibilities were point out in order to justify the presence of the central crack. The manufacturing process of the straight pipe and the presence of hydrogen causing a blister cracking were appointed as possible reasons for this characteristic fracture behaviour.

3.7 REFERENCES

[1] ARAMIS commercial software. GOM (http://www.gom.com/)

[2] Xavier J., de Jesus A., Morais J., Pinto J., (2012), "Stereovision measurements on evaluating the modulus of elasticity of wood by compression tests parallel to the grain." Construction and Building Materials, 26(1):207 – 215.

[3] American Petroleum Institute, (2007), "Specification for Line Pipe - ANSI/APISpecification 5L", 44ª Edition

[4] Ruano, J., (2015), "Effect of thermal treatment in the ultralow cycle fatigue behavior of pipeline steels", MSc Thesis, UTAD (in Portuguese).

[5] Ramberg, W., Osgood, W. R., (1943), "Description of stress-strain curves by three Parameters", NACA Tech. Note No.902.

[6] Basquin, O.H., (1910), "The Exponential Law of Endurance Tests," Proceedings of the American Society for Testing and Materials, 10: 625-630.

[7] Coffin, L.F., (1954), "A study of the effects of cyclic thermal stresses on a ductile metal," Trans. ASME, 76: 931-950.

[8] Manson, S.S., (1954), "Behaviour of materials under conditions of thermal stress," National Advisory Committee for Aeronautics, NACA TN-2933.

[9] Kuwamura, H., Yamamoto, K., (1997). "Ductile crack as a trigger of brittle fracture in steel." Journal Structural Engineering, 1236:729 – 735.

[10] Möser M., Schmid V., (1997). “Fractography and mechanism of hydrogen cracking – the fisheye concept”, Acad. of Sci. of GDR, Inst. of Solid State Physics and Electron Microscopy, 4020 Halle, German Democratic Republic.

Chapter IV

Finite element simulation of small-scale tests of API piping steels

4.1 INTRODUCTION

Finite element simulations of small scale specimens presented in the Chapter III, are present in this chapter. Plasticity models used for monotonic and cyclic simulations were calibrated, which allowed the identification of the stress/strain histories at the critical locations of the specimens. These results were accounted, particularly in the fatigue damage models in order to estimate the number of cycles until the crack initiation.

The numerical simulations were performed in commercial code ABAQUS 6.12® [1]. In this study the numerical simulations of the monotonic, cyclic tension-compression and cyclic bending tests were considered. Moreover, the instability verified in the ULCF tests of smooth specimens was also reproduced from the numerical simulations. This procedure aims at assessing the capacity of the damage models under real loading conditions. The elasto-plastic properties and boundary conditions of the numerical models were identified and calibrated from the comparison between the numerical results and the experimental data of the small-scale specimens. The experimental displacement ranges obtained from LVDT sensors were applied directly in the finite element simulations of cyclic tests of X60 and X65 piping steels with thermal treatment. A criteria based on the LVDT sensors measurements was developed and applied in the numerical simulations of the smooth specimens of X52, X60 and X65 steel grades.

A new methodology for the application of local boundary conditions is also presented in this chapter. This procedure, consist in the application of local boundary conditions derived from the displacement field obtained from the DIC that was used in the cyclic tests of notched plane specimens. The deformed shape of cyclic bending tests was accessed by mean of optical methods and comparisons between experimental and numerical results were also covered.

The evaluation of the stress/strain histories at the specimens' critical locations allowed the identification of the constants involved in the damage models. In more detail, the monotonic fracture strain, the average stress triaxiality and the average Lode angle parameters were obtained from monotonic tensile simulations in order to calibrate the

monotonic fracture surface proposed by Bai and Wierzbicki [2] for the X60 piping steel. This model is extrapolated for the cyclic loading conditions to investigate the triaxiality and the Lode angle parameters influence in the elasto-plastic cyclic behaviour. Moreover, the performance of the classical fatigue life relation proposed by Coffin-Manson [5][6] and the Xue [7] were investigated through comparisons between the fatigue life prediction and the experimental results.

4.2 NUMERICAL ANALYSIS OF QUASI-STATIC TENSILE TESTS

Finite element simulations of quasi-static tensile tests allow the identification of the parameters located at the critical regions that characterize the stress/strain state at the final fracture. These parameters are involved in the formulation of some damage models used for the fatigue life prediction. In fact, the formulation of Xue [7] model includes the dependency of the fracture strain, which in turn is dependent of the stress state and the specimen geometry. Thus, all specimens were modelled in order to achieve the monotonic properties. In this section the numerical models and the numerical results are presented and compared with the experimental data.

4.2.1 Finite element models

Plane, flat-grooved and plane shear specimens were modelled using 3D 8-noded isoparametric solid finite elements with reduced integration, C3D8R, available in the commercial code ABAQUS 6.12® [1]. Taking into account the symmetry boundary conditions, whenever possible, only 1/8 of the geometries are modelled. The round bar specimens were modelled using planar elements with reduced integration CAX4R. The axisymetry of round specimens was taken into account in the numerical modelling. Consequently, the numerical models of plane (smooth and notched) specimens, the flat-grooved specimens as also round bar specimens were build considering the symmetry and axisymetry conditions schematized in Figure 4.1 to Figure 4.2. The displacements of the nodes laying at the symmetry planes were restrained along the direction normal to that symmetry planes. A mesh refinement was deemed suitable for the proposed analyses in

order to reduce the mesh size effect on the computation of stress and strain fields. The numerical models of plane, cylindrical, flat-grooved and plane shear specimens as well as a detail view of the mesh refinements can be observed in the Figure 4.4 to Figure 4.7.

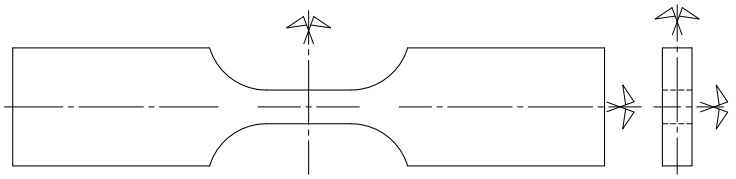

Figure 4.1 – Symmetry conditions of the plane specimens.

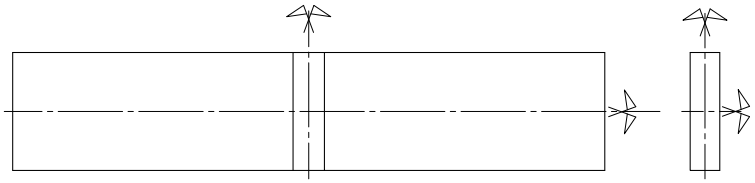

Figure 4.2 – Symmetry conditions of the flat-grooved specimens.

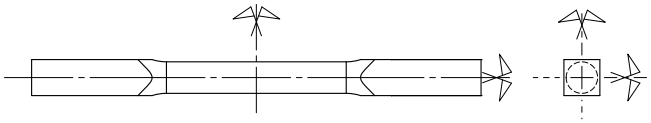

Figure 4.3 – Symmetry conditions of the round bar specimens.

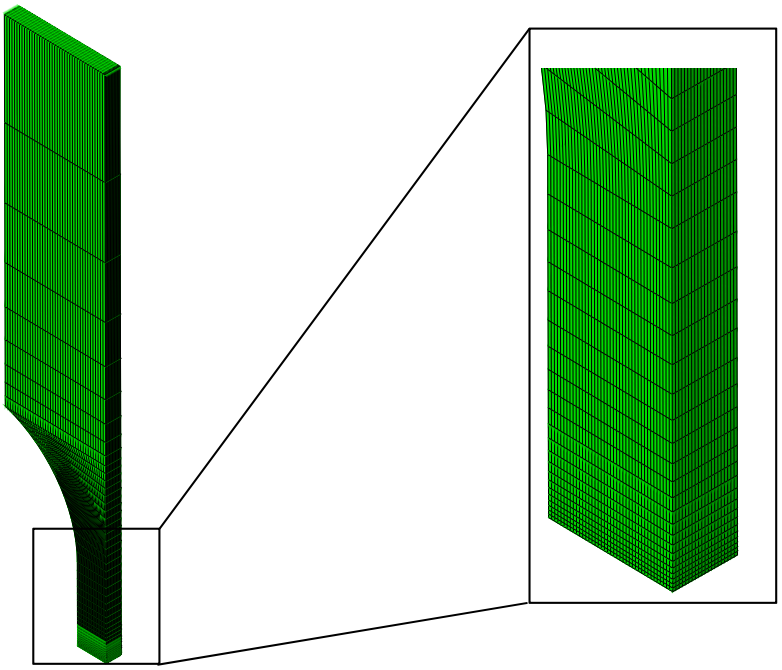

Figure 4.4 – Numerical model of a smooth plane specimens using 1/8 of the whole geometry.

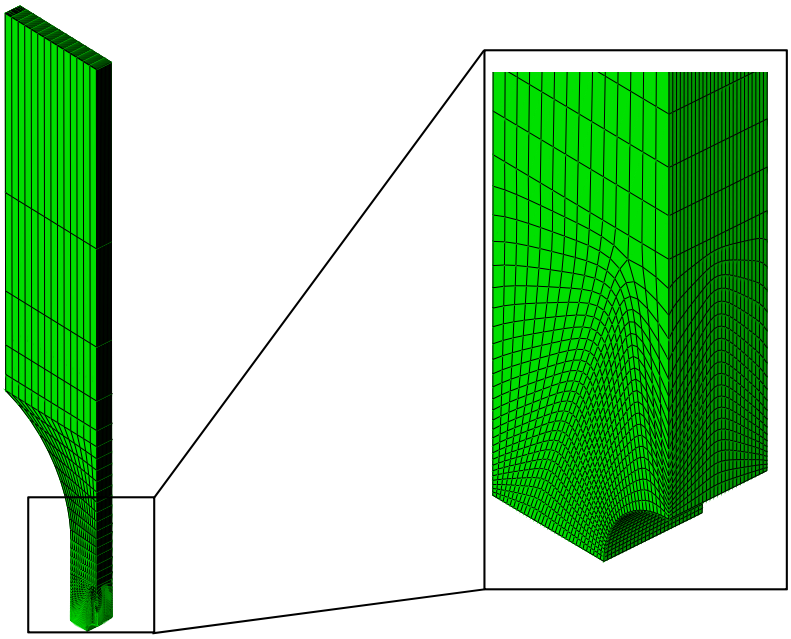

Figure 4.5 – Numerical model of a notched plane specimen using 1/8 of the total geometry.

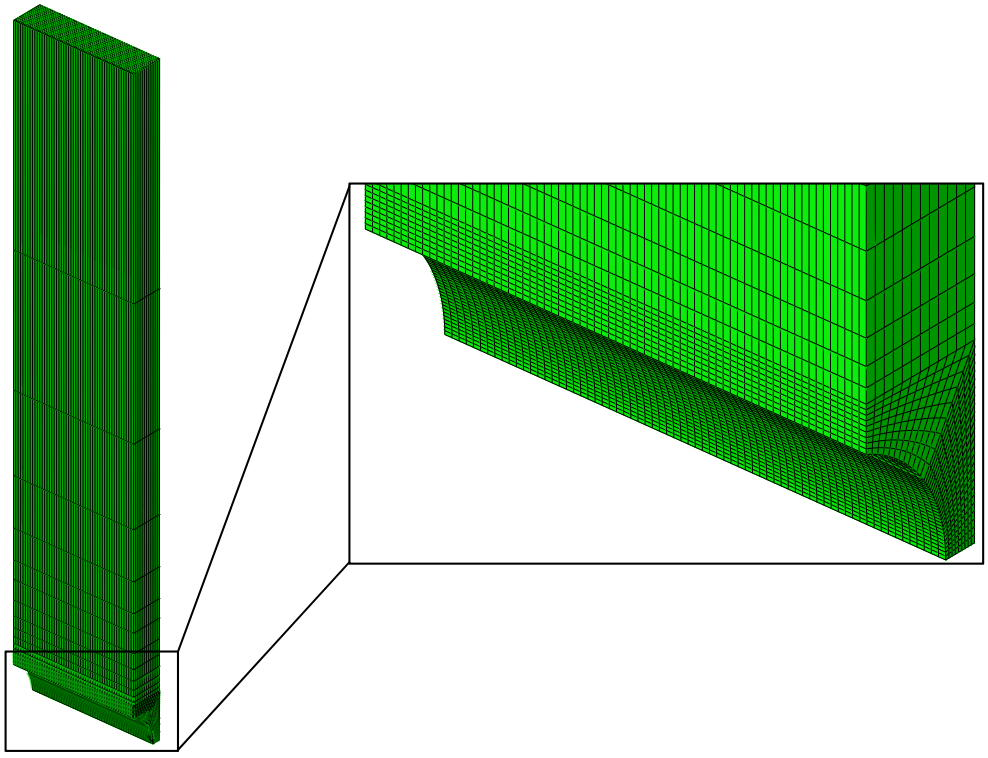

Figure 4.6 – Numerical model of a flat-grooved specimen using 1/8 of the total geometry.

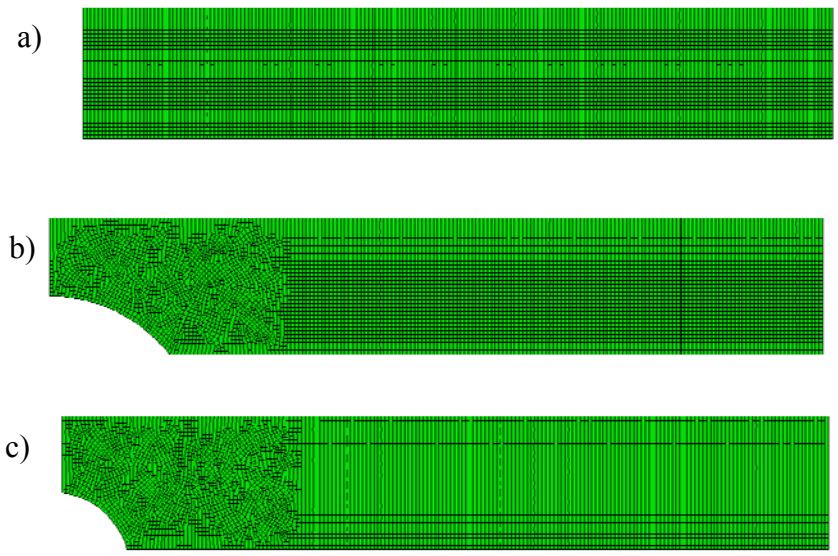

Figure 4.7 – Numerical models of round bar specimens using the axisymmetric conditions: a) smooth round bar; b) round bar with large notch; c) round bar with small notch.

4.2.2 Calibration of plasticity models

Finite element simulations of the monotonic tensile tests were performed adopting a plasticity model based on the J2 yield criterion, with multilinear isotropic hardening [1]. This kind of plasticity model is able to reproduce the non-linear plastic behavior including the necking, until the plastic damage onset. In fact, the damage evolution is only possible to evaluate using coupled damage models, as for instance the Gurson model. Therefore, the plasticity model was applied to simulate the material behavior until the failure initiation of the specimens. In order to define the plasticity model, a uniaxial stress-strain curve needs be introduced, establishing a compromise between the overall experimental data. This curve was determined by a trial and error procedure using the stress-strain relation described by the Ludwik's equation [8]:

$$\sigma = \sigma_0 + K \varepsilon^n \tag{4.1}$$

where σ_0 is the yield stress, K is the strength coefficient and n is the strain hardening exponent. The stress-strain curves computed for each material are represented in the Figure 4.8. Additionally, the stress-strain curves used to define the plasticity model of the steels affected with the thermal process are also illustrated in the Figure 4.9. Since the monotonic

behavior of piping steels with thermal treatment shows a yield stress plateau, this aspect was taken into account in the definition of stress-strain curves. In order to ensure the specimens' failure, remote displacements were applied in the specimen end. However, the displacement values for a node located at the clip gauge knife edge location, which is turn depends of the gauge length assumed for each specimens' series were monitored. This node is situated at the lateral specimen surface where the clip gauge knife edge contacts with the specimen. As regards the smooth specimens, the displacement histories were acquired for a suitable node to access the lateral necking measurement. These results allowed to establish the comparisons between numerical and experimental curves. Then, the numerical curves are plotted together with experimental curves obtained for X52, X60 and X65 piping steels. The results derived for the material with thermal treatment are also illustrated.

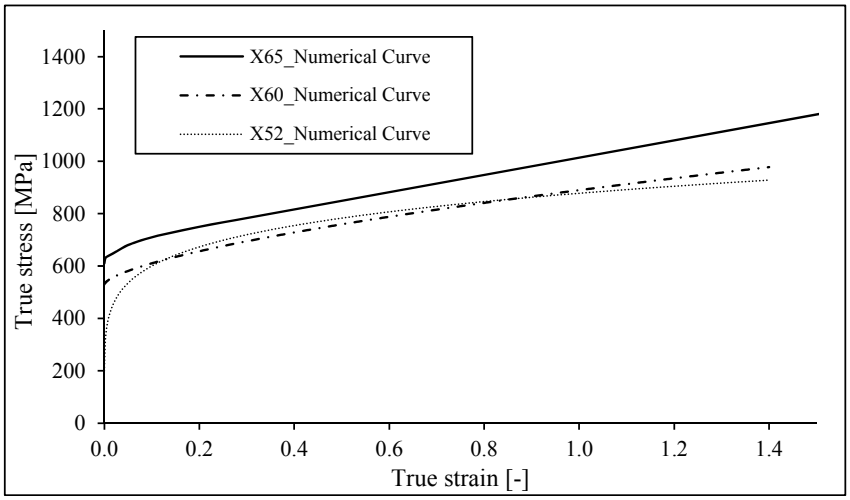

Figure 4.8 – Uniaxial true stress-true strain curves used for the plasticity model definition.

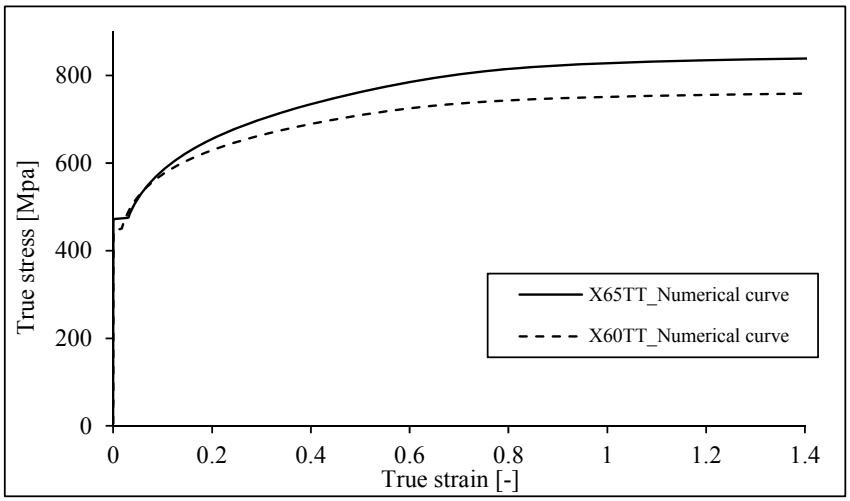

Figure 4.9 – Uniaxial true stress-true strain curves used for the plasticity model definition, of piping steels with thermal treatment.

4.2.2.1 Numerical fitting of experimental monotonic curves of the X52 piping steel

Comparisons between experimental and numerical load-displacement curves for the plane specimens of X52 piping steel are illustrated in Figure 4.10 to Figure 4.13. In particular, the numerical curve of the smooth specimen illustrates the effect of the lateral necking while the displacement values of the notched plane specimens were directly obtained from the clip gauge. The analysis of the figures, above mentioned, shows a good agreement between experimental and numerical data, in the plastic region including the load reduction prior ductile damage effects become noticeable. Supported on this numerical adjustments, an extended engineering stress-strain curve was proposed for the smooth specimens made of X52 piping steel since it was not possible to generate by testing due to the limitations in the clip gauge limit displacements. The experimental data available for this specimen was only correlated with the numerical response until the clip gauge limits.

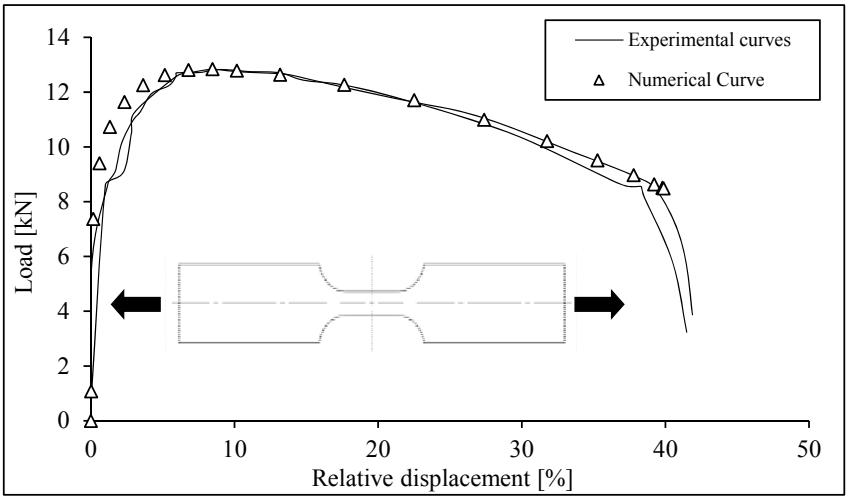

Figure 4.10 – Load-relative displacement (lateral necking) experimental and numerical curves obtained for the smooth specimens of X52 piping steel.

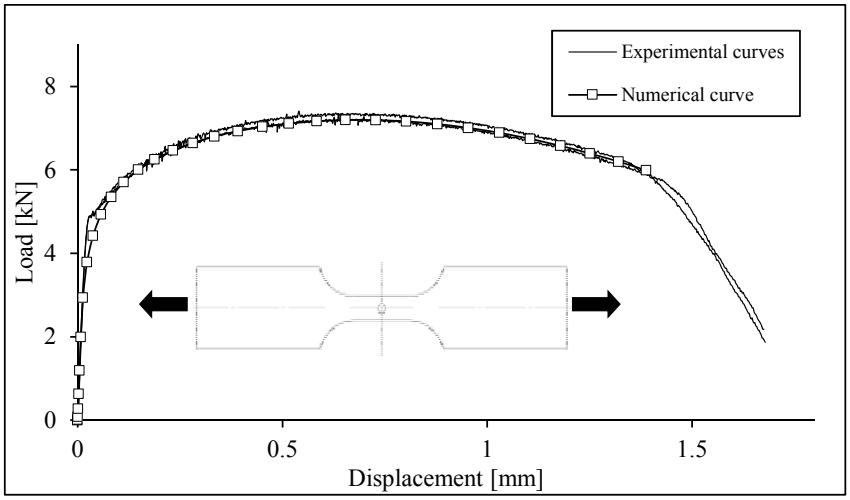

Figure 4.11 – Load-displacement experimental and numerical curves obtained for the X52_CH specimen series.

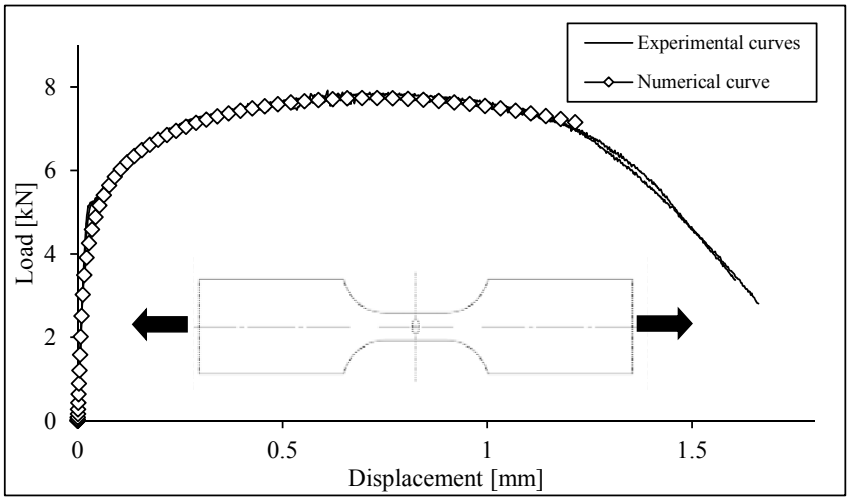

Figure 4.12 – Load-displacement experimental and numerical curves obtained for the X52_OH specimen series.

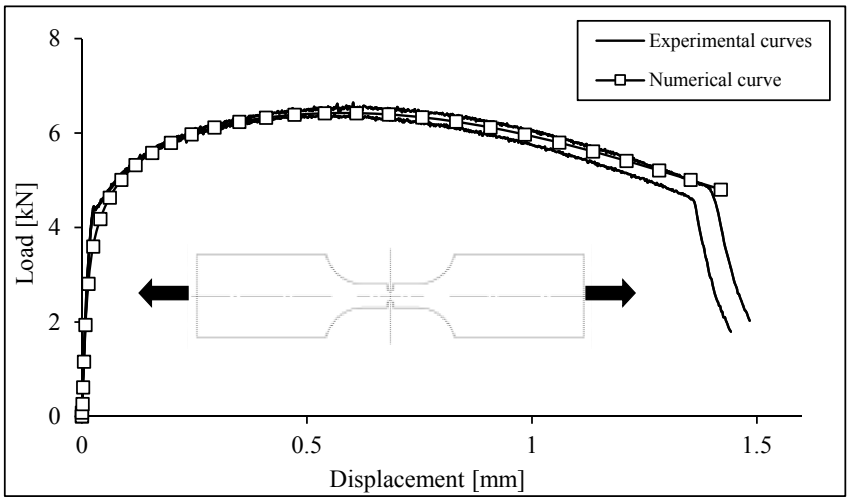

Figure 4.13 – Load-displacement experimental and numerical curves obtained for the X52_SN specimen series.

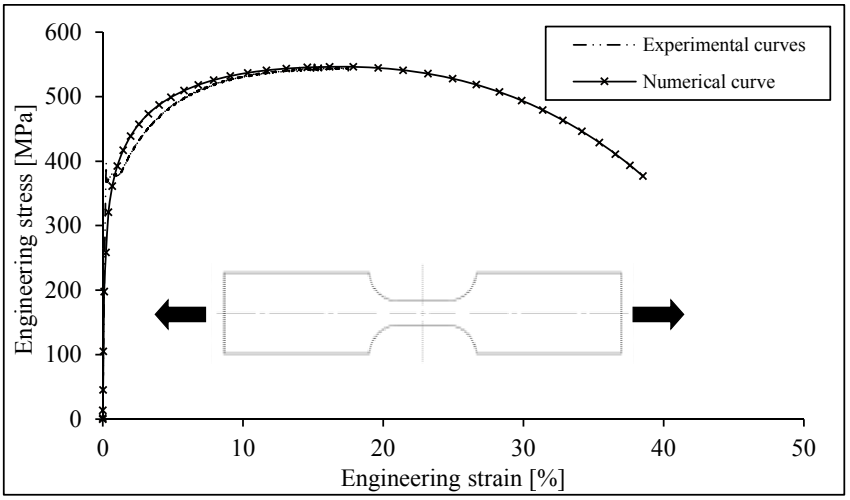

Figure 4.14 – Engineering stress-strain curve obtained for the smooth specimens of X52 piping steel, with extended numerical data until specimen failure.

4.2.2.2 Numerical fitting of the experimental monotonic curves of the X60 piping steel

Figure 4.15 to Figure 4.24 illustrates the load-displacement experimental curves correlated with the numerical response from the finite element simulations. Despite the large number of specimen geometries considered in the monotonic tensile tests, a good performance of the plasticity model is verified. In general, a good compromise between numerical and experimental results is identified. The numerical results related to the lateral necking of the smooth specimens are slightly overestimated, however good adjustments can be found for notched plane, round bar, flat-grooved and plane shear specimens. It should be noted that, due to the limitations of clip gauge, the experimental data of smooth round bar specimens (see Figure 4.16) was measured by means of diameter reduction.

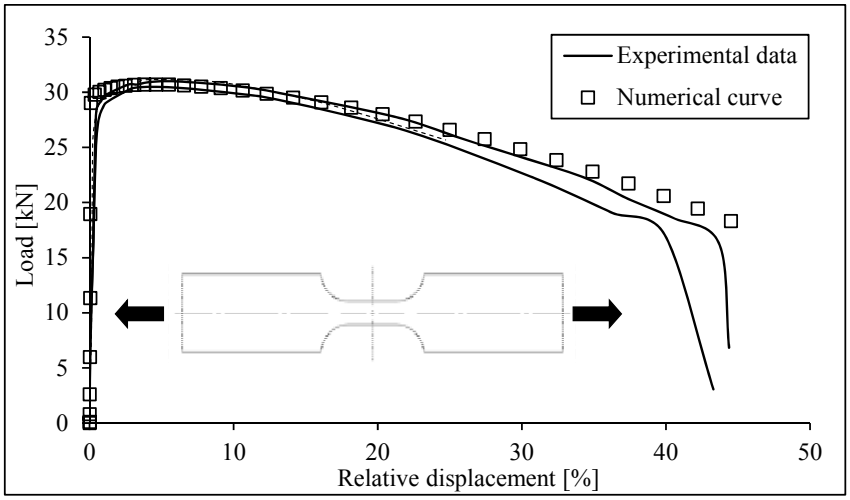

Figure 4.15 – Load-relative displacement (lateral necking) experimental and numerical curves obtained for X60_SP specimens series.

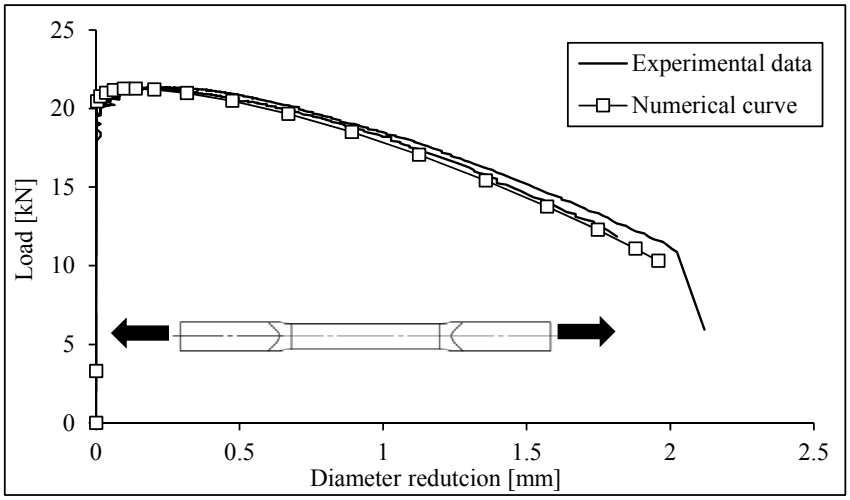

Figure 4.16 – Load-displacement experimental and numerical curves obtained for X60_RB specimen series.

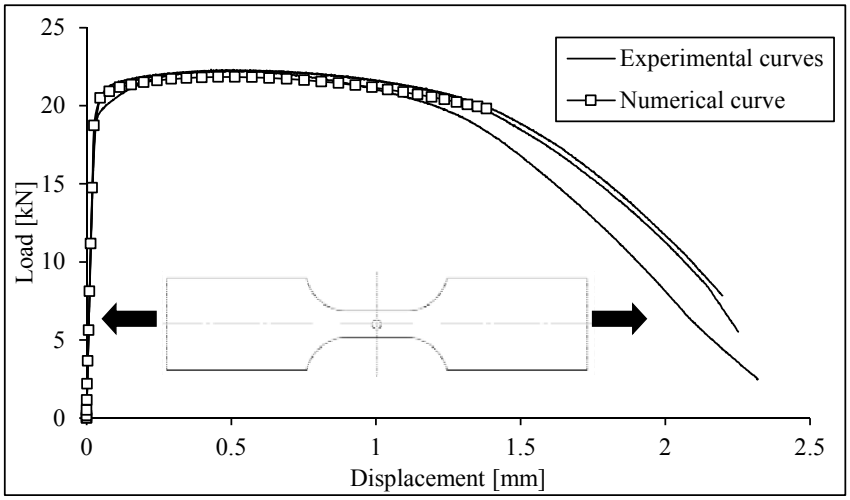

Figure 4.17 – Load-displacement experimental and numerical curves obtained for X60_CHS specimen series.

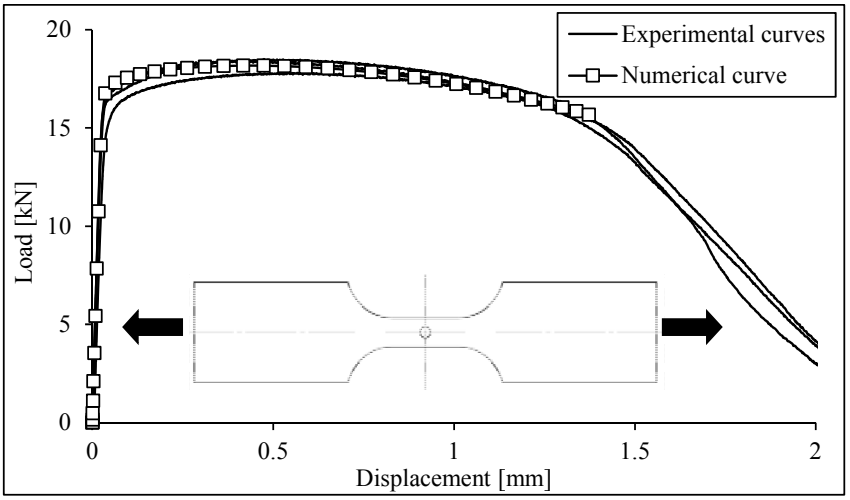

Figure 4.18 – Load-displacement experimental and numerical curves obtained for X60_CHB specimen series.

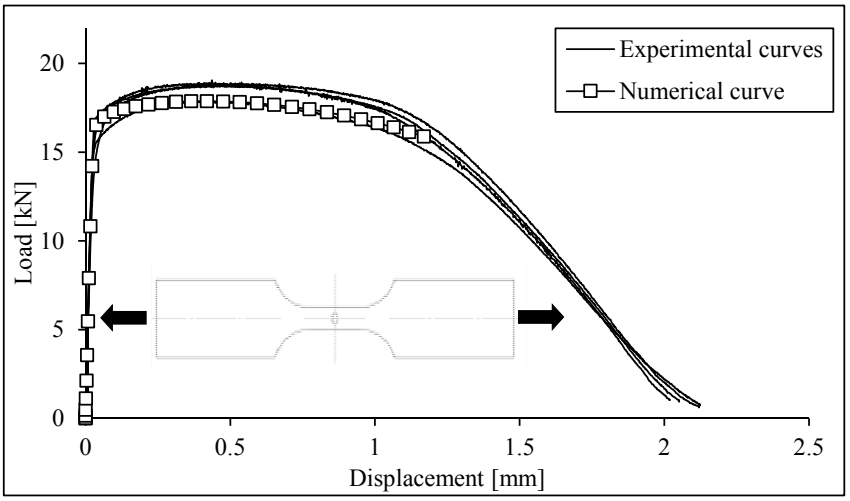

Figure 4.19 – Load-displacement experimental and numerical curves obtained for X60_OH specimen series.

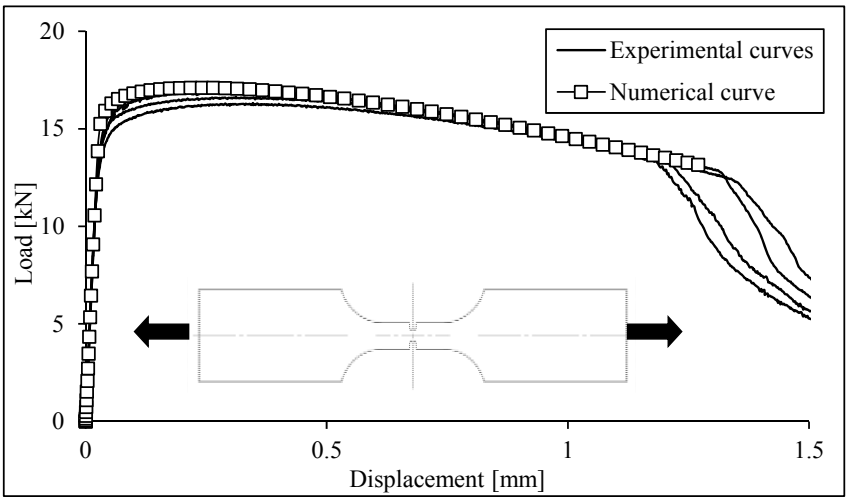

Figure 4.20 – Load-displacement experimental and numerical curves obtained for X60_SN specimen series.

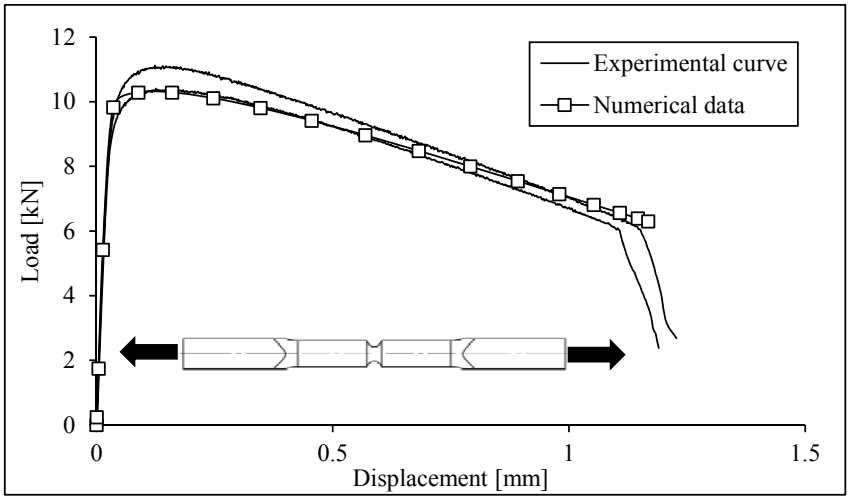

Figure 4.21 – Load-displacement experimental and numerical curves obtained for X60_RBS specimen series.

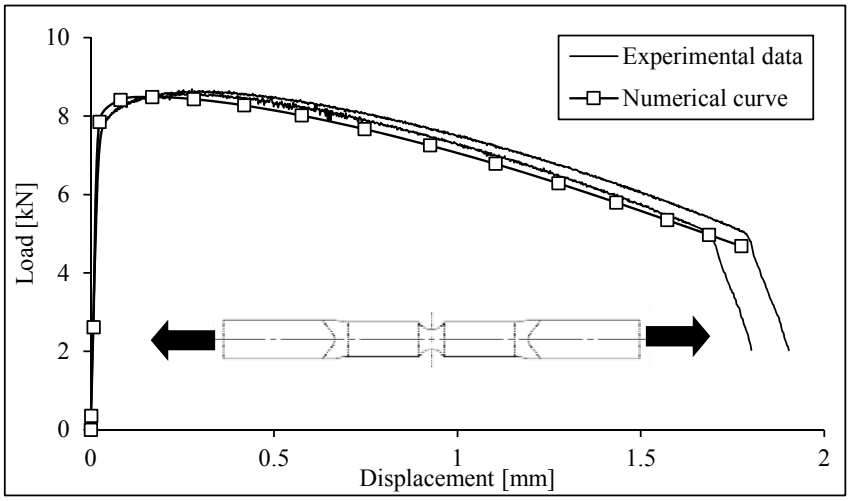

Figure 4.22 – Load-displacement experimental and numerical curves obtained for X60_RBL specimen series.

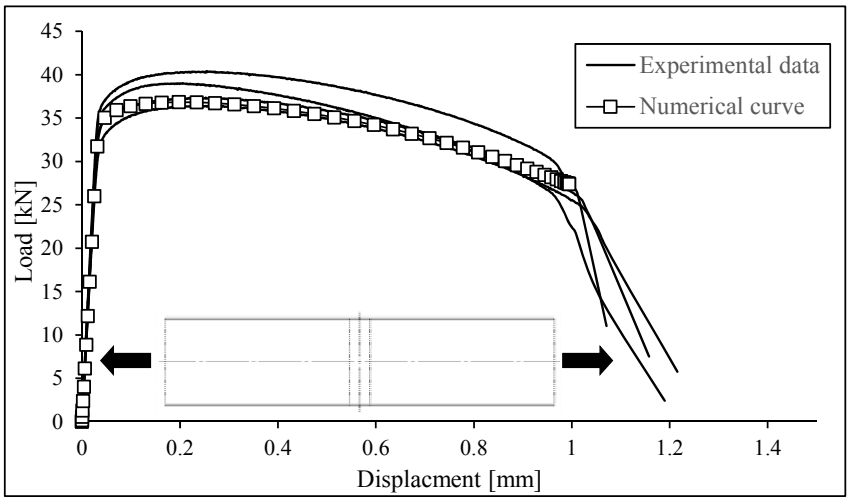

Figure 4.23 – Load-displacement experimental and numerical curves obtained for X60_FG specimen series.

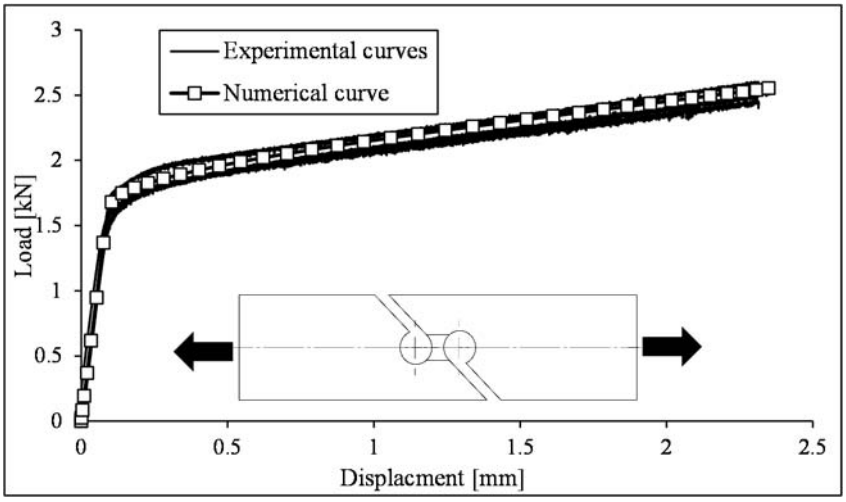

Figure 4.24 – Load-displacement experimental and numerical curves obtained for X60_PSG specimen series.

Numerical results were also computed for the smooth and notched plane specimens made of X60 steel with the thermal treatment which were plotted against the experimental load-displacement results, as shown in Figure 4.25 and Figure 4.26. In general, the plasticity model provides a satisfactory correlation including the yield stress plateau. It is also observed that the sudden degradation of specimens is not reproduced by the plasticity model, since it is an uncoupled damage model.

The good performance of the plasticity model with isotropic hardening allowed to extend the experimental data of smooth plane specimens of X60 piping steel until the facture, similarly to what was performed for the X52 piping steel. The extended engineering stress-strain curves for the X60 piping steel with and without thermal treatment are represented in the Figure 4.27. Engineering stress-strain numerical curves allows to investigate the material ductility and the effect of the thermal process. The analysis of Figure 4.27 shows that the thermal treatment leads to a ductility reduction of the X60 piping steel. It is also observed that the thermal process applied to the material results in a recovery of the yield plateau, which is typical of low carbon steels.

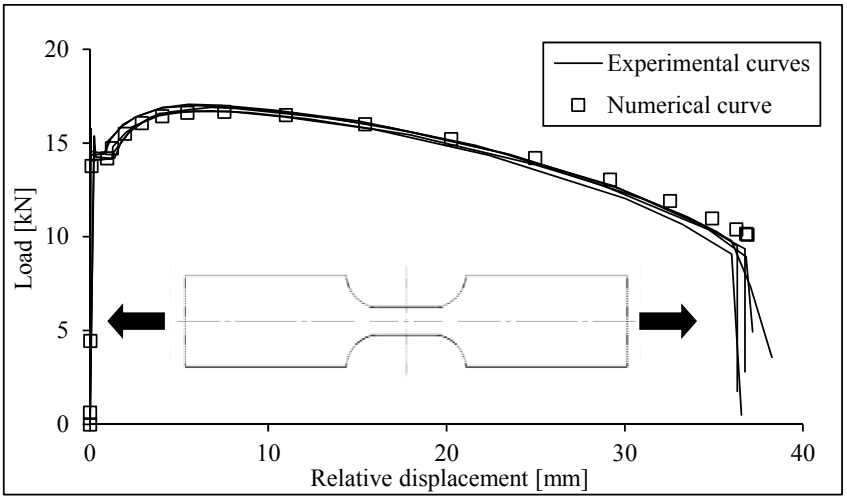

Figure 4.25 – Load-relative displacement (lateral necking) experimental and numerical curves obtained for the smooth specimens of X60 piping steel, with thermal treatment.

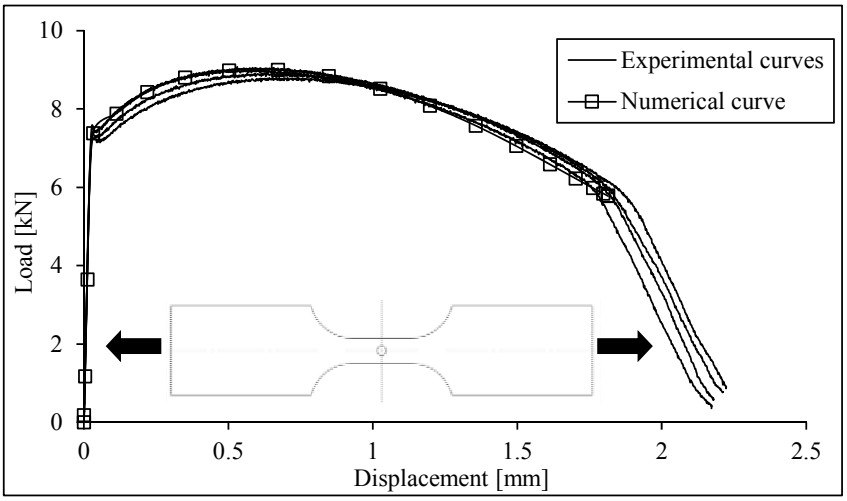

Figure 4.26 – Load-displacement experimental and numerical curves obtained for the X60TT_CH specimen series.

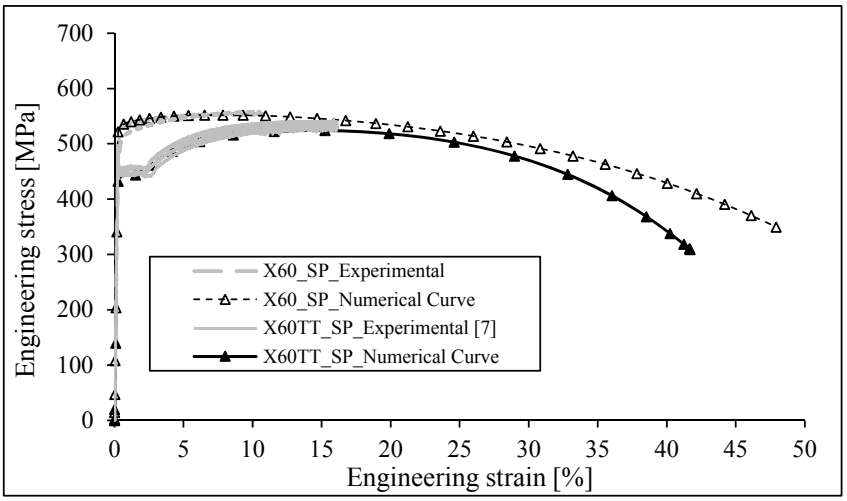

Figure 4.27 – Engineering stress-strain curve derived for the smooth specimens of X60 piping steel with and without thermal treatment, with extended numerical data.

4.2.2.3 Numerical fitting of the experimental monotonic curves of the X65 piping steel

Comparisons between numerical and experimental load-displacement curves for plane and flat-grooved specimens of X65 piping steel are illustrated in Figure 4.28 to Figure 4.31. In particular, the numerical curve derived for the smooth specimen represents the lateral necking effect while for the notched plane specimens the displacement values represent the displacement at clip gauge length. A good agreement between the experimental and the numerical data, in the plastic region, including the load reduction prior ductile damage effects become noticeable, is clearly observed. In order to reproduce the final degradation of the specimens coupled plasticity-damage models are recommended.

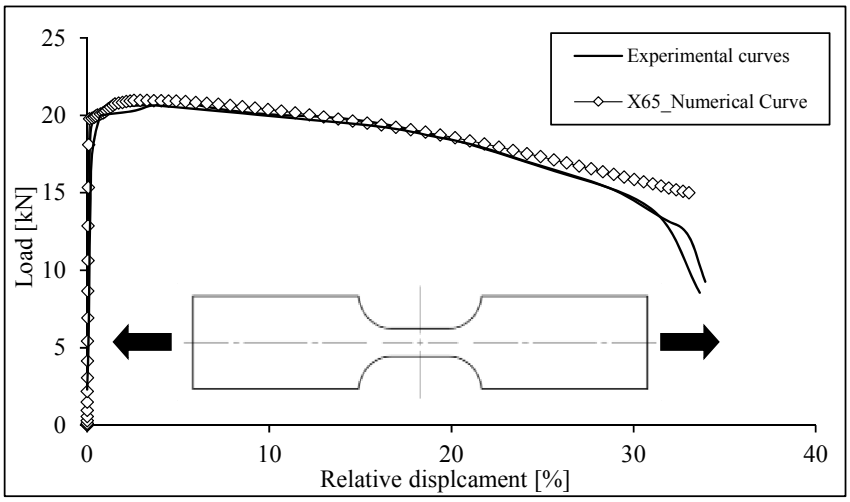

Figure 4.28 – Load- relative displacement (lateral necking) experimental and numerical curves obtained for smooth specimens of X65 piping steel.

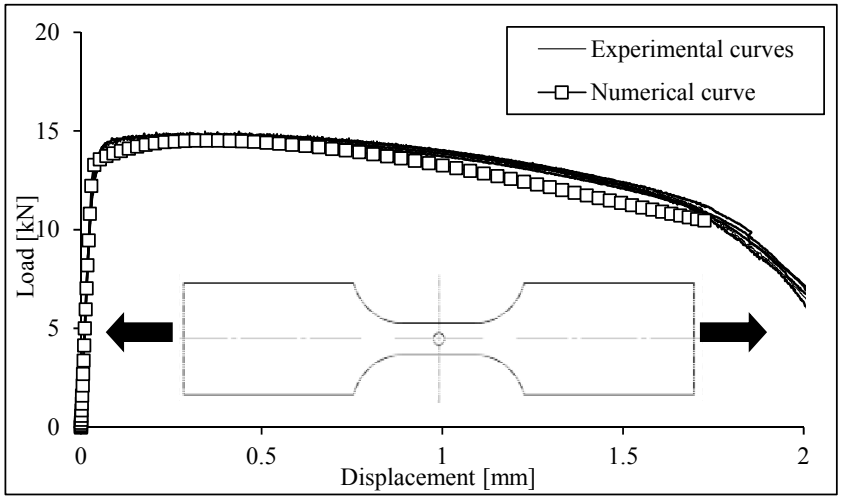

Figure 4.29 – Load-displacement experimental and numerical curves obtained for X65_CH specimen series.

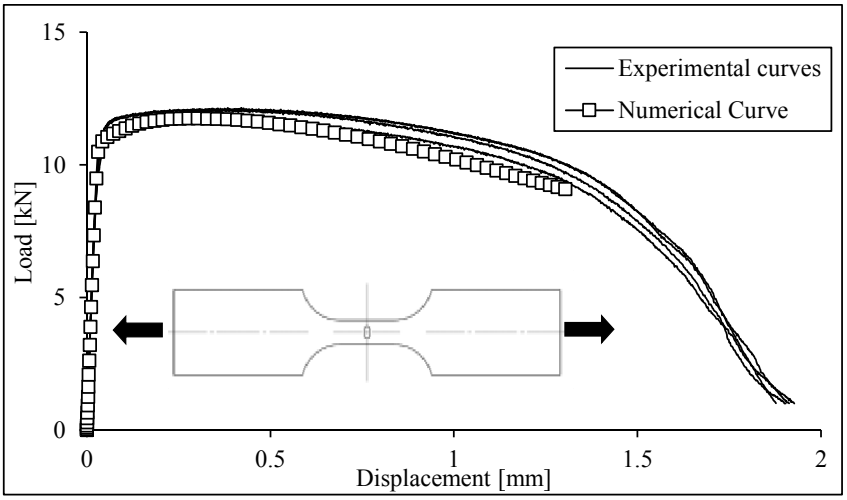

Figure 4.30 – Load-displacement experimental and numerical curves obtained for the X65_OH specimen series.

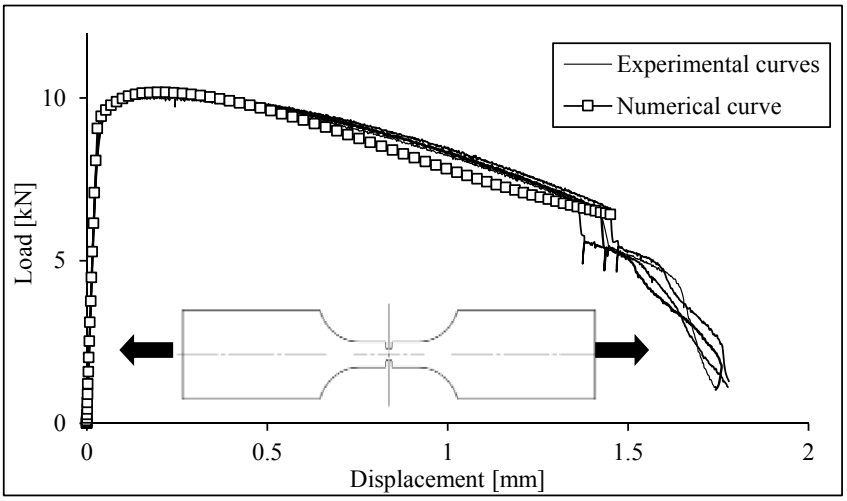

Figure 4.31 – Load-displacement experimental and numerical curves obtained for the X65_SN specimen series.

In addition, numerical simulations were also performed in order to derive the numerical data of smooth and notched plane specimens with made of X65 steel grade with thermal treatment. Figure 4.32 and Figure 4.33 compares the experimental and numerical results. A satisfactory agreement between numerical and experimental curves is observed. The plasticity model is also able to reproduce the yield plateau visible in the experimental results. Based on the good performance of the numerical models in the description of monotonic ductile behavior, the engineering stress-strain curves were extended until specimen damage onset, using the numerical models developed for the smooth specimens. These results are illustrated in the Figure 4.34, which allows the evaluation of the thermal process effect of the X65 piping steel. In this case the thermal process increases the ductility

of the material. The influence of thermal process is more noticeable in the monotonic ductile behavior of the X65 steel grade when compared with the X60 piping steel.

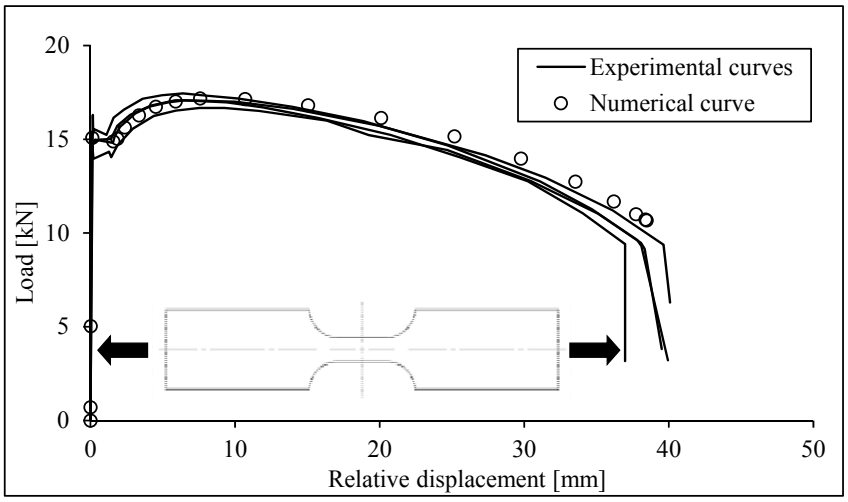

Figure 4.32 – Load- relative displacement (lateral necking) experimental and numerical curves obtained for smooth specimens of X65 piping steel, with thermal treatment.

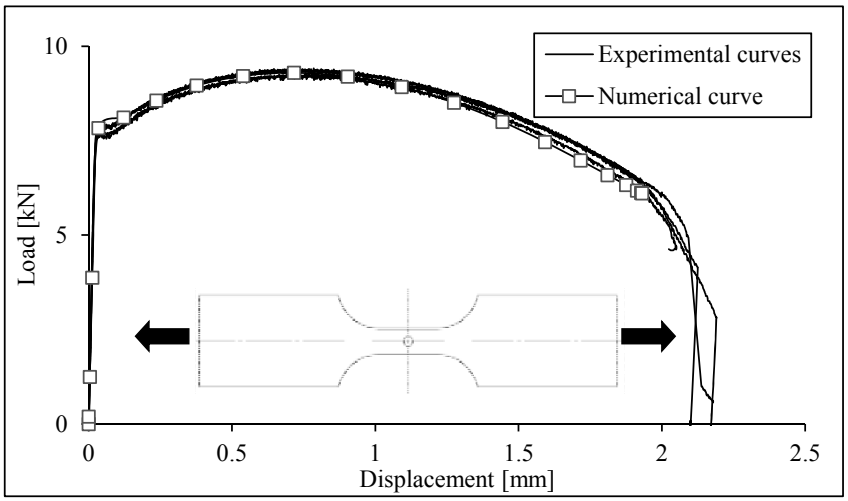

Figure 4.33 – Load-displacement experimental and numerical curves obtained for the X65TT_CH specimen series.

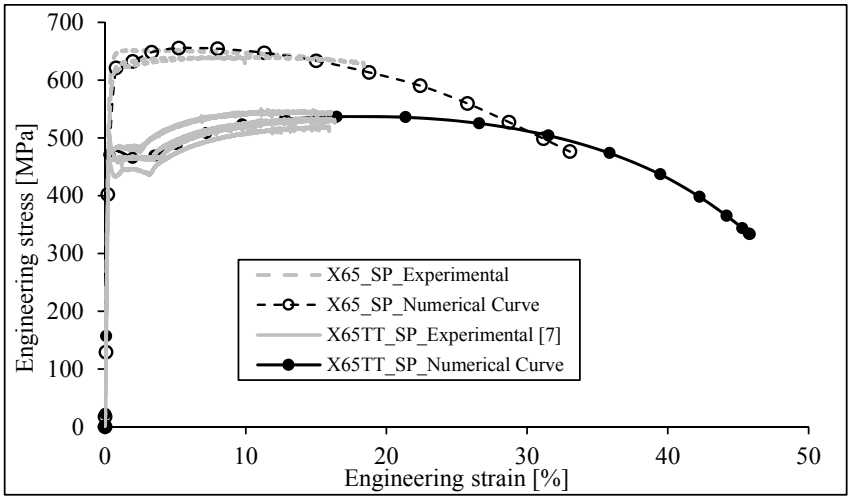

Figure 4.34 – Engineering stress-strain curves derived for the smooth specimens of X65 piping steel with and without thermal treatment, with numerical data extended until specimen failure.

4.2.3 Analysis of numerical results of monotonic tensile tests

In general, the plasticity models with isotropic hardening used in the finite element simulations of the monotonic tensile tests are able to follow the experimental elastoplastic behaviours of the materials. The analyses of the numerical responses, mainly for the smooth plane specimens of X60 and X65 piping steels (see Figure 4.15 and Figure 4.25) shows an overestimation of lateral necking of specimens from the maximum load value. It should be noted that the experimental procedure used to measure the lateral necking of the specimens shows some limitations when applied to the tests with large plastic deformation. In fact, a 2D optical system does not allow to capture the out-of-plane displacements suffered by the samples during the necking process leading to a significant degradation of the full-field measurements at those stages [10]. Regarding to the load-displacement predictions of the other specimen series, a good compromise was obtained between the numerical and experimental data. The finite element simulations of monotonic tensile tests allowed the computation of the parameters involved in some damage models for fatigue life prediction, such as the equivalent monotonic fracture strain, which is an input of the Xue model formulation. These results will be discussed later together with the fatigue life predictions using the Xue model. The extended stress-strain data of conventional stress-strain curves were proposed until specimen damage initiation by means of finite element simulations, which are represented in the Figure 4.35, simultaneously for the three piping steels. From this inverse method, assumptions about ductility of material can be assumed. In fact, X52

and X65 assumes a similar elongation at final fracture, although X60 steel reveals higher ductility at failure.

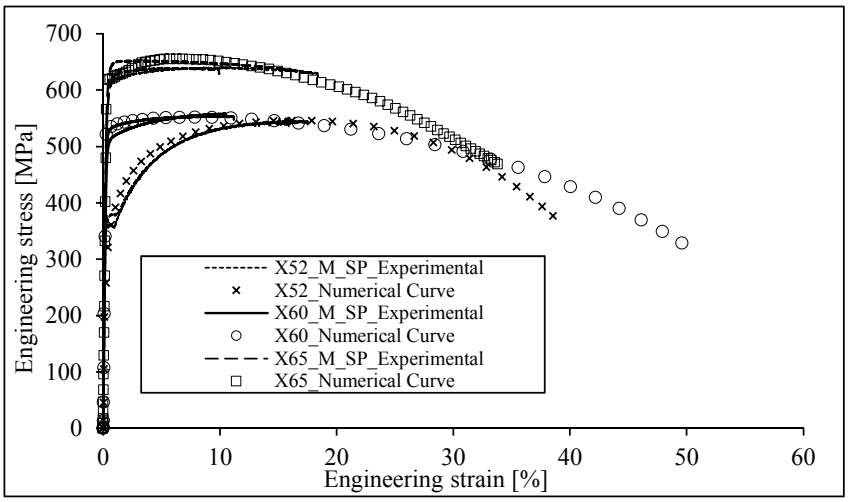

Figure 4.35 – Comparison of engineering stress-strain curves from smooth specimens of X52, X60 and X65 piping steels.

4.2.4 3D fracture locus of the X60 piping steel

The calibration of the 3D fracture locus proposed by Bai and Wierzbicki [11] requires the identification of six parameters (see Eq (2.46)), which can be obtained from the experimental program carried out with the specimens of the X60 piping steel. Since there is no data points available under axial symmetric compression loading condition ($\bar{\theta} = -1$), the 3D fracture surface is assumed to be symmetric. Therefore, especially attention should be given for two groups of tests, namely the smooth plane and the round bars corresponding to axial symmetry in deviatoric tension ($\bar{\theta} = 1$) and the flat-grooved and plane shear specimens corresponding to plastic plane strain or generalized shear ($\bar{\theta} = 0$). Thanks to the finite element analysis the equivalent fracture strains, the stress triaxiality and Lode angle parameters were accessed at the critical location of the specimens. Since the two stress state parameters are variable during the loading process, average values are used, according to the definitions given by [2]:

$$\eta_{av} = \frac{1}{\bar{\varepsilon}_f} \int_0^{\bar{\varepsilon}_f} \eta(\bar{\varepsilon}) d\bar{\varepsilon} \tag{4.2}$$

$$\bar{\theta}_{av} = \frac{1}{\bar{\varepsilon}_f} \int_0^{\bar{\varepsilon}_f} \bar{\theta}(\bar{\varepsilon}) d\bar{\varepsilon}. \tag{4.3}$$

A summary of the data points computed from the numerical simulations of the monotonic tensile tests discussed in the Chapter III is listed in Table 4.1 for X60 piping steel. For each specimen series, the equivalent strains at fracture, the stress triaxiality and the Lode angle parameters are presented. Since the effect of the Lode angle parameter on fracture strain is not uniform for different stress triaxialities, it is proposed to construct the fracture locus based on the bounding effects of the Lode angle on failure locus, i.e., on the material ductility. As referred above, these limits can be achieved for $\bar{\theta} = 1$ and for $\bar{\theta} = 0$, if a symmetric fracture locus is assumed. Concerning the upper bound limit, it can be directly extracted from the Table 4.1 by plotting the fracture strain against the stress triaxiality, which allow to derive D_1 and D_2 parameters of Eq. (2.47) that defines the 3D ductile surface. Nevertheless, the lower bound limit cannot be fully assessed from the data points presented in the Table 4.1. Despite flat-grooved and the plane shear specimens exhibit $\bar{\theta} = 0$, the fracture strain and triaxiality are unable to be correlated by an exponential function suitable to achieve the constants D_5 and D_6. Furthermore, this evidence was also experienced by Bai [2], when he used two groups of specimens, namely the so called classical specimens and the butterfly specimens to obtain the 3D fracture locus, as described in the Chapter II. Thus, the plane shear grooved specimens can be treated as a kind of butterfly specimen, therefore it should be tested under the loading conditions of Table 2.2 to allow the identification of the 3D fracture surface. These shortcomings concerning the limitations of the available experimental data for the evaluation of the fracture failure locus lead to the development of a numerical procedure able to model the final degradation of the specimens, by means of a coupled plasticity-damage model.

Table 4.1 – Summary of test results on X60 piping steel.

Specimen series	$\bar{\varepsilon}_f$	η_{av}	$\bar{\theta}_{av}$
SP	1.46	0.62	0.99
RB	1.69	0.67	1.00
RBS	1.28	0.90	1.00
RBL	0.91	1.16	1.00
CHS	0.72	0.78	0.60
CHB	0.83	0.76	0.50
OH	0.96	0.84	0.30
SN	0.79	1.21	0.76
FG	1.01	0.87	0.02
PSG	0.64	0.07	0.05

Some failure results were generated by numerical simulation using an elastoplastic-damage model to simulate additional flat-grooved specimens covering stress triaxialities other than the values included in the experimental program. The reproduction of the final degradation of the specimens was simulated by means of the coupled plastic-damage model by Gurson–Tvergaard–Needleman model (GTN) [15]-[17]. With this procedure is expected to obtain additional fracture strains and triaxiality data that allow the identification of lower bound limit. Two supplementary flat-grooved specimens, based on the geometry of the FG series, with different notch radius are proposed. In more detail, two thicknesses in the minimal cross-section (t) are assigned to these specimens: t=3.2mm with a notch radius of 2 mm (FG_R=2) and t=1.9mm with a notch radius of 12 mm (FG_R=12). The numerical models (finite element meshes) of these specimens are illustrated in the Figure 4.36. Symmetry conditions were assumed and 8-noded isoparametric solid elements with reduced integration, C3D8R applied in ABAQUS®. Besides the plasticity model with isotropic hardening, the use of the GTN model requires the introduction of material constants that governs the damage evolution (see Section 2.2.4). The constants of the GTN model were calibrated using a fitting procedure between numerical and experimental data available for the flat-grooved tested series. This coupled damage-plasticity model for monotonic fracture allows the description of the monotonic behavior of the material including the loss of strength capacity at fracture, as can be seen in Figure 4.37, which compares the experimental and numerical load–displacement curves of flat-grooved specimens. The plane strain conditions is common between the three tested flat-grooved specimens, so we can argue that the GTN constants are representative of those plane strain conditions. In other words the GTN formulation is not sensitive to the third invariant of stress tensor, consequently, the determination of material constants using the experimental data of other specimen series covering distinct Lode angles could lead to distinct parameters. The resulting parameters of GTN model identified for the X60 piping steel are summarized in Table 4.2, taking into account plane strain conditions.

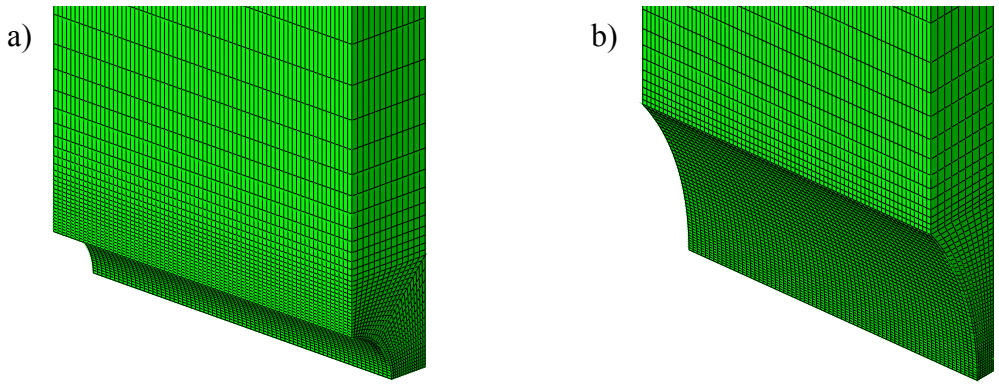

Figure 4.36 – Numerical models of flat-grooved specimens: a) notch radius of 2mm; b) notch radius of 12mm.

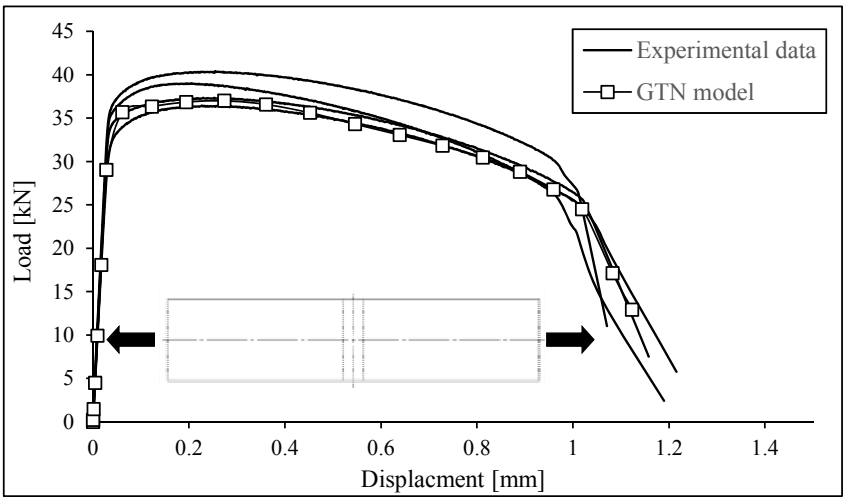

Figure 4.37 – Comparison of experimental load-displacement curves of tested flat-grooved specimens (R=4), with the predicted numerical curves derived using the GTN model.

Table 4.2 – Constants of the GTN model for the X60 piping steel under plain strain conditions.

f_0	ε_N	S_N	f_N	f_C	f_F
1e-5	1.00	0.1	0.001	0.05	0.1

The numerical response achieved with GTN model is compared with the numerical result obtained with the uncoupled J2-plasticity model with isotropic hardening in Figure 4.38 and Figure 4.39 for the numerical flat-grooved specimens. The final degradation of the specimen is clearly observed and this indication was helpful in the identification of the damage onset and the estimation of the fracture strain, the stress triaxiality and the Lode angle parameters, using the same procedure adopted in this work for all the experimental specimens. The resulting parameters are summarized in the Table 4.5. Correlating the numerical data of the flat-grooved specimens the lower bound ductility limit, results the constants D_5 and D_6.

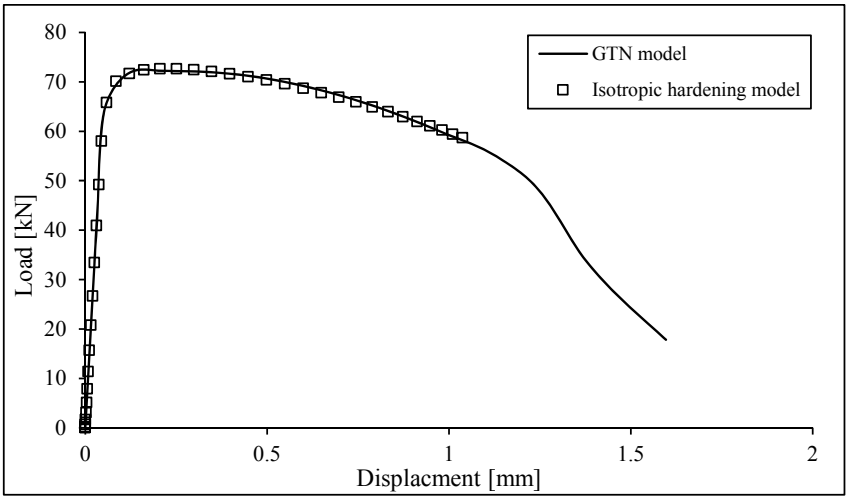

Figure 4.38 – Comparison between numerical responses obtained with the GTN plasticity-damage model and the J2-isotropic hardening plastic model for the numerical specimen, FG (R=12).

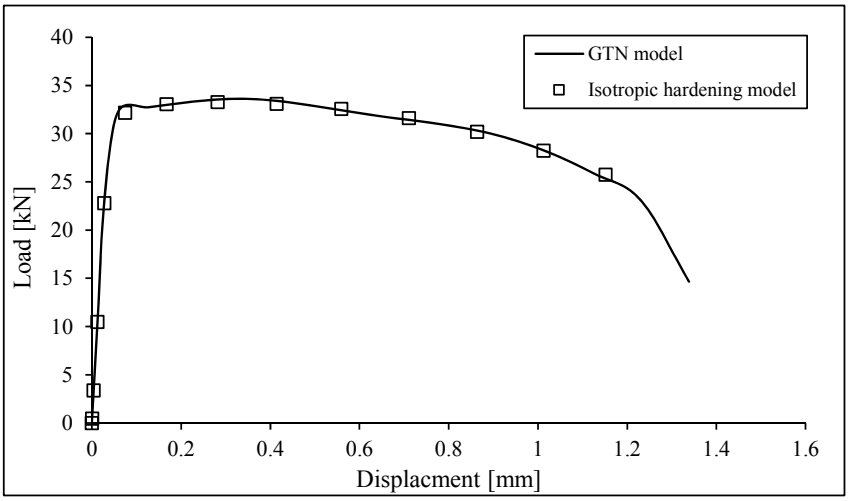

Figure 4.39 – Comparison between numerical responses obtained with GTN plasticity-damage model and the J2-isotropic hardening model for the numerical specimen, FG (R=2).

Table 4.3 – Summary of the numerical results for flat-grooved specimens including the tested specimen.

Specimen series	$\bar{\varepsilon}_f$	η_{av}	$\bar{\theta}_{av}$
FG (R=4)	1.01	0.87	0.02
FG (R=2)	0.91	1.12	0.02
FG (R=12)	1.20	0.79	0.02

The upper bound and lower bound limits in the space of fracture strain and stress triaxiality are illustrated in the Figure 4.40. The loss of ductility in the flat-grooved specimens due to Lode angle parameter, which changes from 1 to 0 is observed. This effect is more noticeable to stress triaxialities lower to 1. The calibrated parameters of the fracture locus equation proposed by Bai [2] are listed in Table 4.4. The appearance of upper and lower bound limits obtained from the so-called classical specimens or reference specimens shows a similar

aspect to the fracture locus of high ductility steels, derived by Coppola [3][4], which in turn supports the identification and utilization of this surface for future applications. It should be noted that $D_1=D_5$ and $D_2=D_6$ since the fracture surface was assumed symmetric with respect to $\bar{\theta} = 0$. A 3D geometrical representation of the fracture locus is illustrated in Figure 4.41. It is shown that the 3D fracture locus agrees well with the data points, of smooth plane (SP Series)/round bar (RB Series) specimens and flat-grooved specimens (FG series) (lower limit). In addition, the results of notched plane series (NP series) were also plotted in the space of fracture strain, triaxiality and Lode angle parameter and a satisfactory agreement with the 3D fracture surface can be observed. This data show intermediate values of the stress and strain parameters which are not the most appropriate data for the identification of the failure locus.

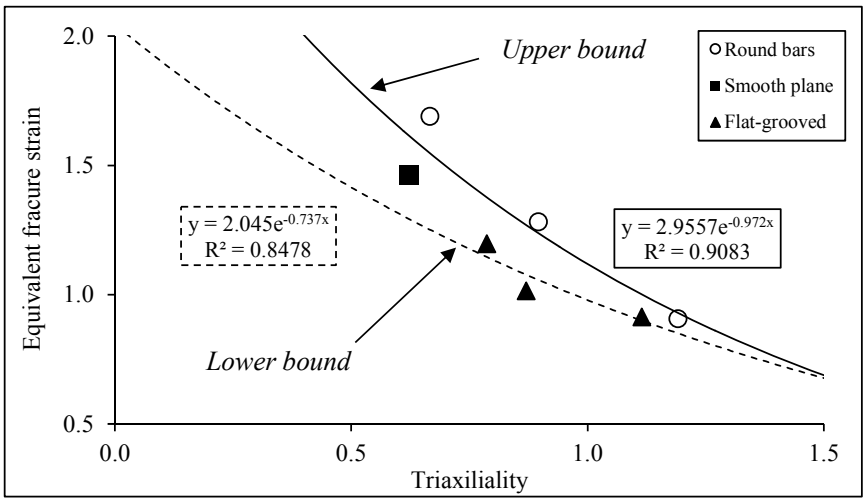

Figure 4.40 – Upper and lower bound limits of the X60 steel ductility behavior in the space of fracture strain and stress triaxiality.

Table 4.4 – Calibrated parameters of the fracture surface of the X60 piping steel.

D_1	D_2	D_3	D_4	D_5	D_6
2.956	0.972	2.045	0.737	2.956	0.972

The identification of the 3D fracture surface is dependent on the accuracy of the plasticity model used in the finite element simulations, even though a good compromise has been achieved until the damage onset between the numerical and experimental data. Figure 4.42 represents the fracture strain-triaxiality and triaxiality-Lode angle parameter 2D-plane which allows to clarify the location of notched plane points in the 3D fracture surface. The 3D fracture surface, will be used to compute the strain fracture, ($\bar{\varepsilon_f}$) incorporated in the

original formulation of Xue model that has been proposed to perform fatigue life predictions under both LCF and ULCF domain.

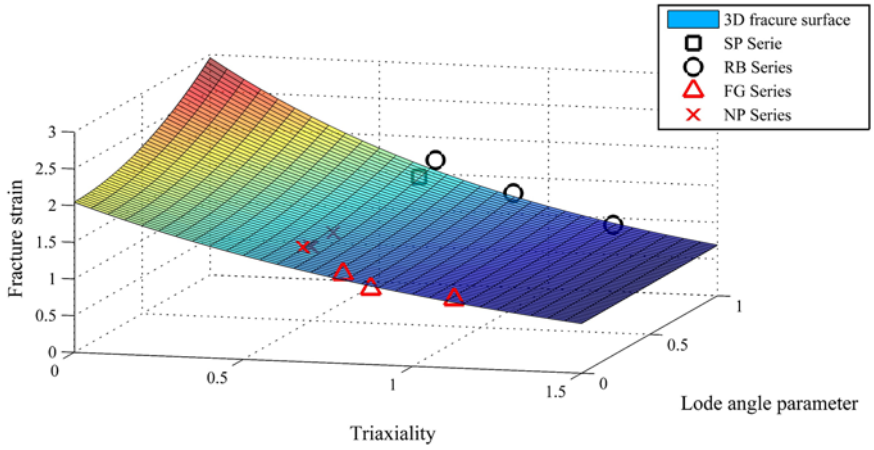

Figure 4.41 – Ductile fracture locus obtained for the X60 piping steel.

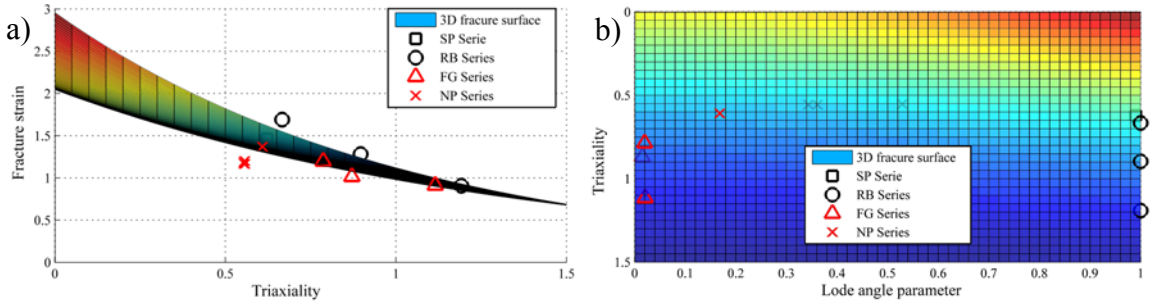

Figure 4.42 – Calibrated 3D fracture surface for the X60 piping steel: a) fracture strain and stress triaxiality 2D projection in the lode angle direction; b) stress triaxiality and lode angle parameter 2D-plane/projection along the fracture strain axis.

4.3 NUMERICAL ANALYSIS OF CYCLIC TENSION-COMPRESSION TESTS

Numerical simulations of cyclic tests are required for the computation of cyclic parameters involved in the ULCF damage models. The experimental data obtained from cyclic tests was used in order to calibrate the plasticity models with kinematic hardening. In this section, a description of the numerical modelling of the uniaxial tension-compression tests using the ideal boundary conditions (without the lateral displacements) is presented. In addition, numerical predictions were performed by means of the Coffin-Manson [5] [6]

relation and Xue [7] model for smooth and plane notched specimens and compared with experimental results shown in the Chapter III.

4.3.1 Finite element models

The finite element simulations of the cyclic tension-compression tests were performed taking into account the finite element models presented in the Section 4.2.1. In order to reproduce the cyclic behaviour of the specimens, the plasticity model with isotropic hardening was replaced by the plasticity model with kinematic hardening. As referred above, cyclic tests were performed with local (clip gauge) displacement control. The displacement data acquired during the cyclic tests should be used in order to compare with the numerical response. Based on this assumptions, a remote displacement was applied on the nodes located in the end of specimens and calibrated cycle-by-cycle, to achieve the local displacement values derived from the clip gauge monitoring. The experimental cyclic curves achieved from LCF and ULCF tests were helpful to derive the numerical uniaxial stress-strain curve introduced in the plasticity model. The plasticity model is based on the second invariant of the stress tensor with nonlinear kinematic hardening (Chaboche model). The kinematic hardening models the translation of the yield surface while its size and shape is kept constant [12]. This kinematic hardening is required to model conveniently the Bauschinger effect of the material. To account for the kinematic hardening, the yield surface is given by:

$$F = f\left(\boldsymbol{\sigma} - \boldsymbol{\alpha}\right) - \sigma^0 = 0 \tag{4.4}$$

where $\boldsymbol{\alpha}$ is the backstress tensor that represents the centre of the yield surface in the stress space, σ^0 is the a material constant which represents the size of yield surface. In this work, the plasticity model was defined through the superposition of multiple backstress components, in accordance with Lemaitre and Chaboche [13] preposition. The evolution of backstress tensor is then defined as follows:

$$d\boldsymbol{\alpha}^k = \frac{C^k}{\bar{\sigma}}(\boldsymbol{\sigma} - \boldsymbol{\alpha})\, d\bar{\varepsilon}_p - \gamma^k \boldsymbol{\alpha}\, d\bar{\varepsilon}_p$$
$$\boldsymbol{\alpha} = \sum_{k=1}^{N} \boldsymbol{\alpha}^k \tag{4.5}$$

In the following subsections, comparisons of numerical and experimental hysteresis loops as also the parameters of plasticity model, with non-linear kinematic hardening are presented.

4.3.1.1 Calibration of the non-linear kinematic hardening model for the X52 piping steel

In order to identify the kinematic hardening model parameters (e.g. Chaboche's model) a direct or inverse procedure was used. The numerical curves correlated with the experimental cyclic curve is represented in the Figure 4.43 and a good correlation can be observed. The parameters used for the plasticity model definition, represented in the Table 4.5, also resulted from the fitting of the plasticity model to the experimental hysteresis cycles, including the first monotonic loading path. Comparisons between experimental and numerical responses derived from cyclic tests on plane specimen cyclic tests of X52 piping steel are presented in Figure 4.44 to Figure 4.47. The analysis of these figures reveals a good performance of the plasticity model with non-linear kinematic hardening in particular concerning the reproduction of the elastoplastic cyclic behaviour of the X52 steel grade.

Table 4.5 – Parameters of the plasticity model, with non-linear kinematic hardening, calibrated for the X52 piping steel.

σ_{ced} [MPa]	C_1	γ_1	C_2	γ_2	C_3	γ_3
400	13000	150	2800	20	700	1

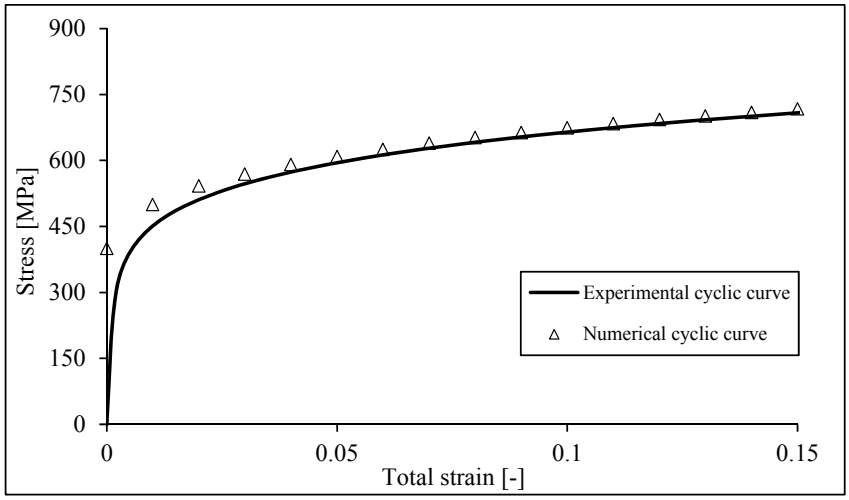

Figure 4.43 – Experimental cyclic curve and the numerical cyclic curve introduced to define the plasticity model of the X52 piping steel.

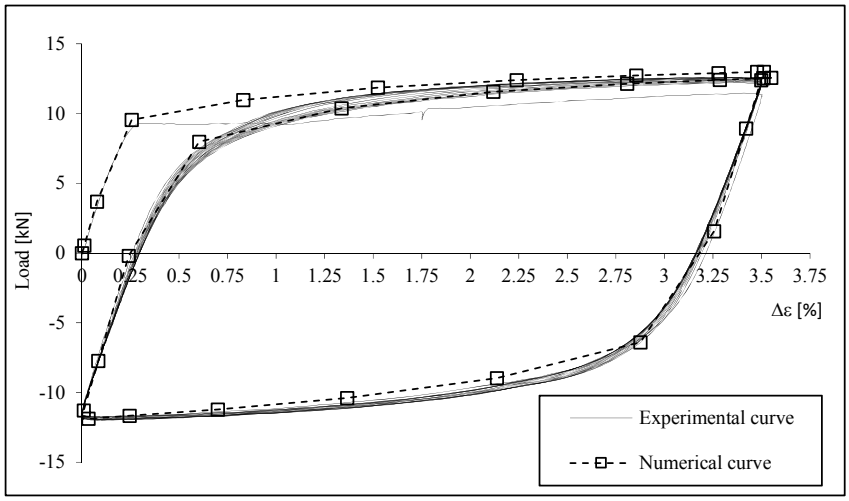

Figure 4.44 – Load-strain hysteresis cycles including numerical response obtained for the U0_SP_02 specimen of X52 piping steel.

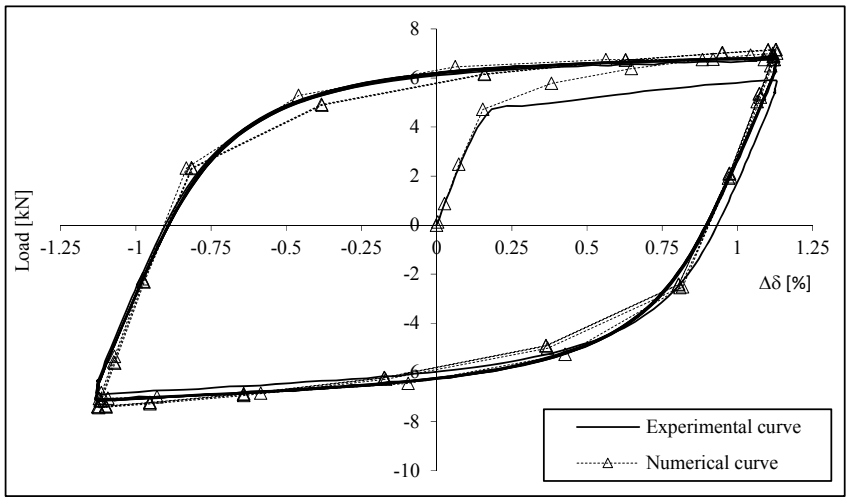

Figure 4.45 – Load-relative displacement hysteresis cycles including numerical response obtained for U-1_CH_05 specimen of X52 piping steel.

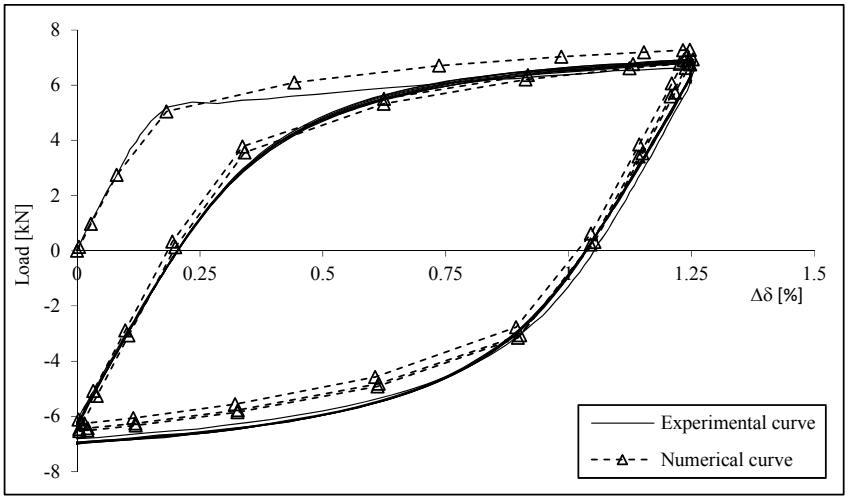

Figure 4.46 – Load-relative displacement hysteresis cycles including numerical response obtained for U0_OH_05 specimen of X52 piping steel.

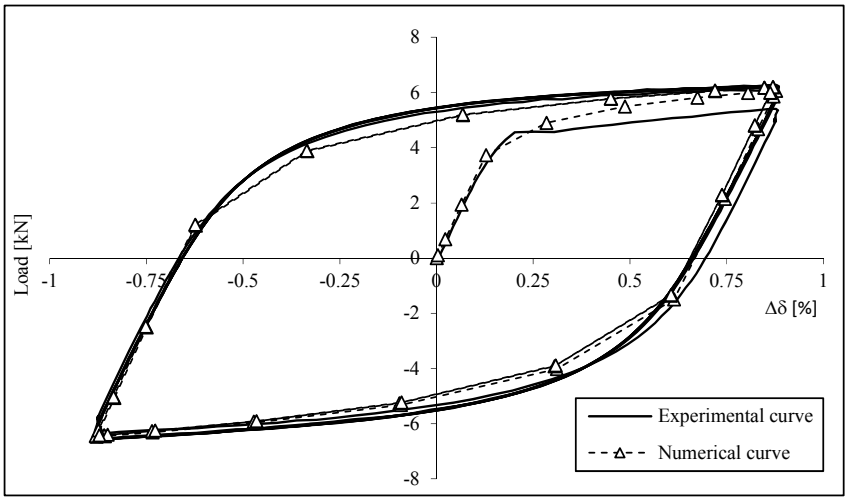

Figure 4.47 – Load-relative displacement hysteresis cycles including numerical response obtained for U-1_SN_03 specimen of X52 piping steel.

4.3.1.2 Calibration of the non-linear kinematic hardening model for the X60 piping steel

The calibration of non-linear kinematic hardening model for X60 piping steel is now presented. This procedure also includes the identification of the plasticity model for the X60 piping with thermal treatment. The Chaboche parameters resulted from this fitting are presented in the Table 4.6 and Table 4.7. Figure 4.48 and Figure 4.49 compares the cyclic curve derived from LCF and ULCF tests of smooth specimens and the respective predicted numerical curves. As can be observed, some deviation is verified around the yield region. Nevertheless, this situation does not represent a major drawback of the model under ULCF

regime, which is characterized by high plastic strain values. The numerical hysteresis cycles are plotted together with the numerical data in Figure 4.50 to Figure 4.56 exhibiting a good agreement between numerical and experimental results.

Table 4.6 – Parameters of the plasticity model, with non-linear kinematic hardening calibrated for the X60 piping steel.

σ_{ced} [MPa]	C_1	γ_1	C_2	γ_2	C_3	γ_3
410	52000	450	2000	80	450	2.5

Table 4.7 – Parameters of plasticity model, with non-linear kinematic hardening calibrated for the X60 piping steel, with thermal treatment.

σ_{ced} [MPa]	C_1	γ_1	C_2	γ_2	C_3	γ_3
355	32200	350	2250	50	700	2.6

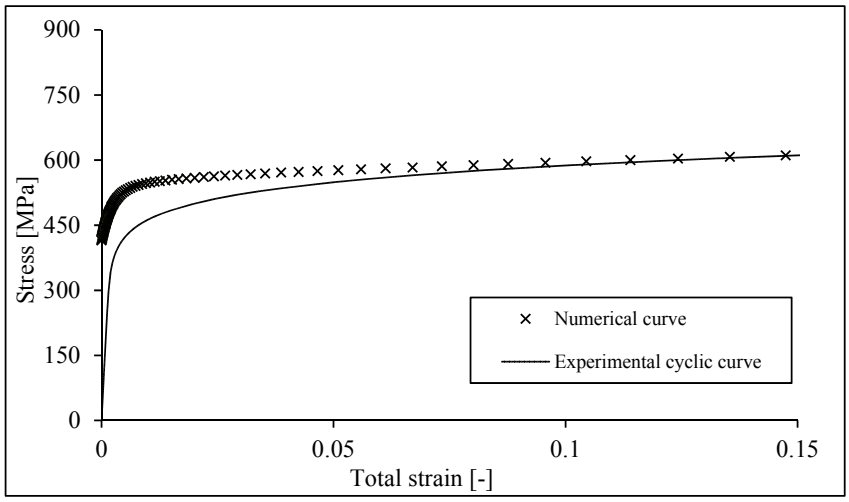

Figure 4.48 – Experimental cyclic curve and numerical curve introduced to define the plasticity model of X60 piping steel.

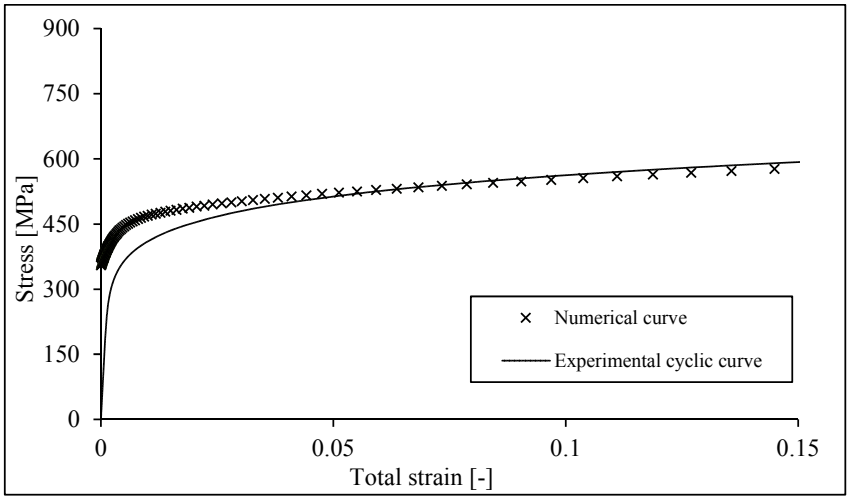

Figure 4.49 – Experimental cyclic curve and numerical curve introduced to define the plasticity model of the X60 piping steel, with thermal treatment.

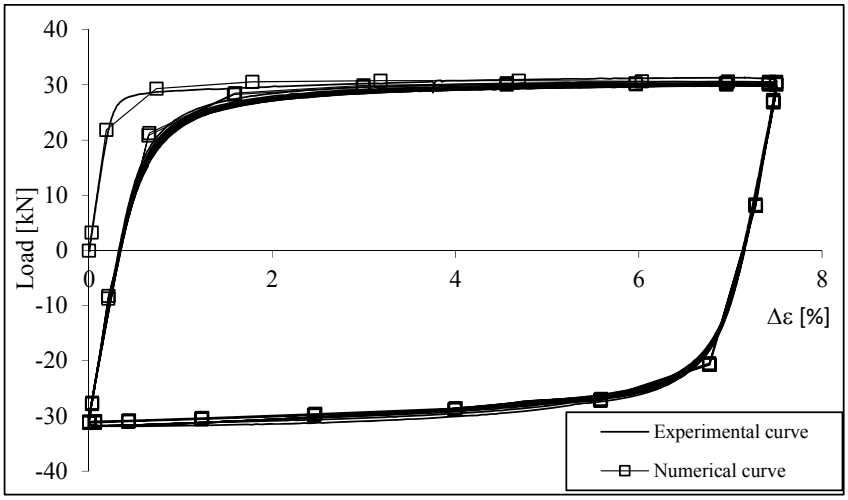

Figure 4.50 – Load-strain hysteresis cycles including numerical response obtained for the U0_SP_08 specimen of X60 piping steel.

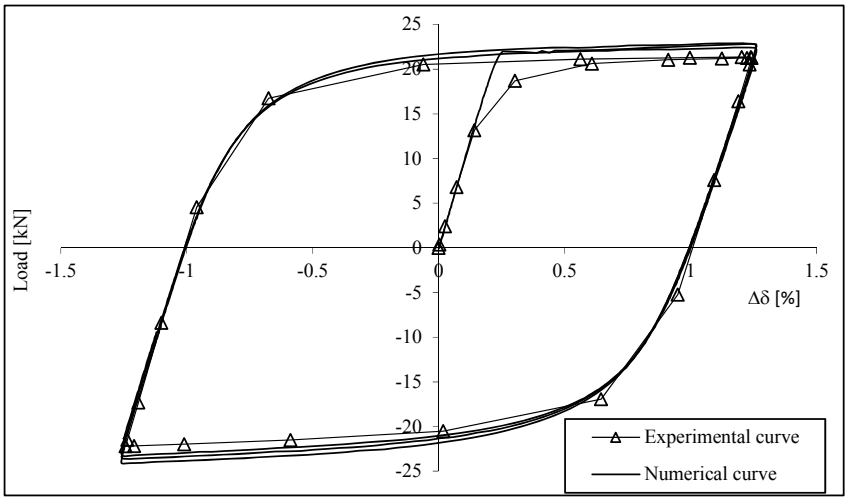

Figure 4.51 – Load-relative displacement hysteresis cycles including numerical response obtained for the U-1_CHS_03 specimen of X60 piping steel.

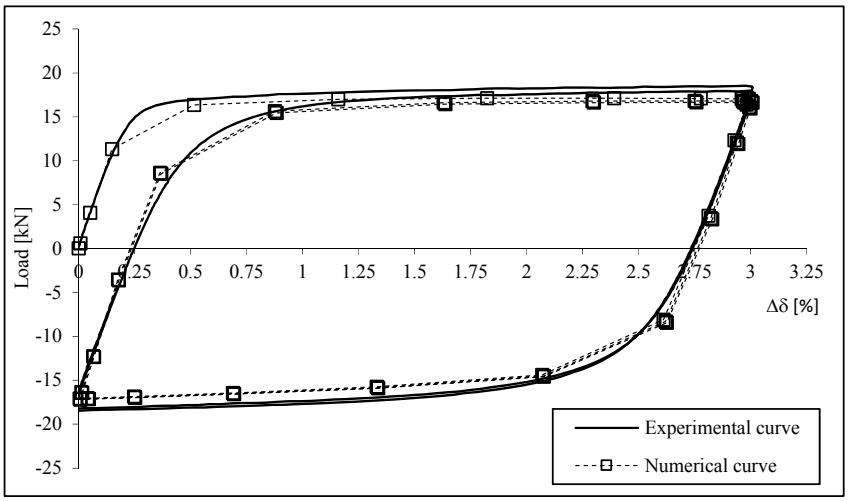

Figure 4.52 – Load-relative displacement hysteresis cycles including numerical response obtained for the U-1_CHB_08 specimen of X60 piping steel.

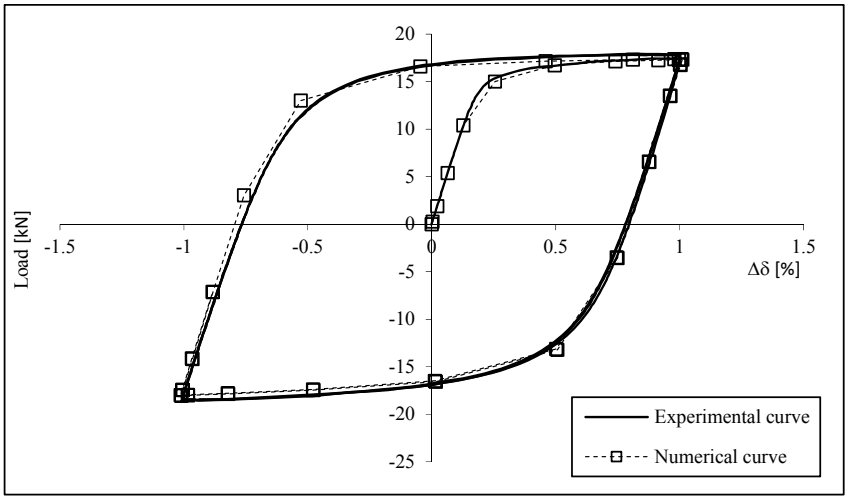

Figure 4.53 – Load-relative displacement hysteresis cycles including numerical response obtained for the U-1_OH_01 specimen of X60 piping steel.

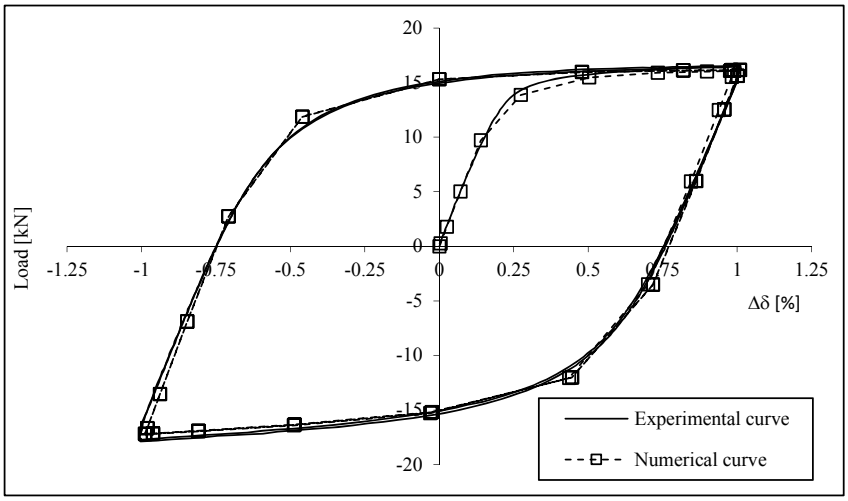

Figure 4.54 – Load-displacement hysteresis cycles including numerical response obtained for the U-1_SN_01 specimen of X60 piping steel.

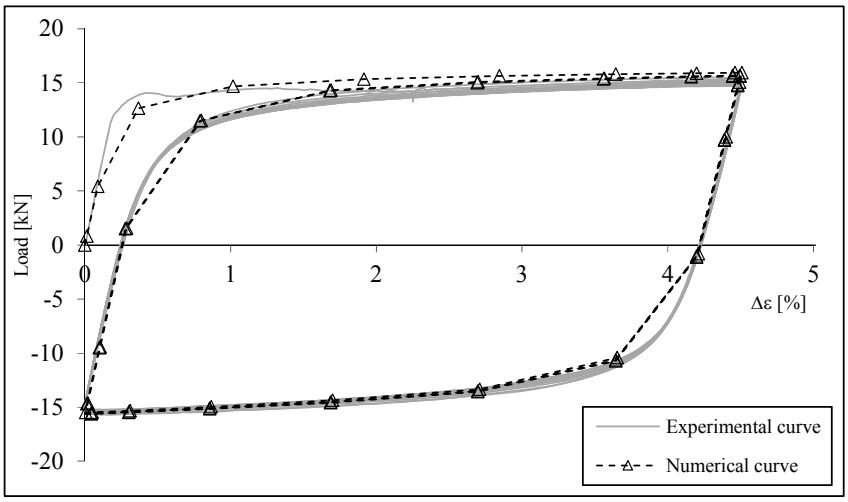

Figure 4.55 – Load-strain hysteresis cycles including numerical response obtained for the U-1_SP_04 specimen of X60 piping steel, with thermal treatment.

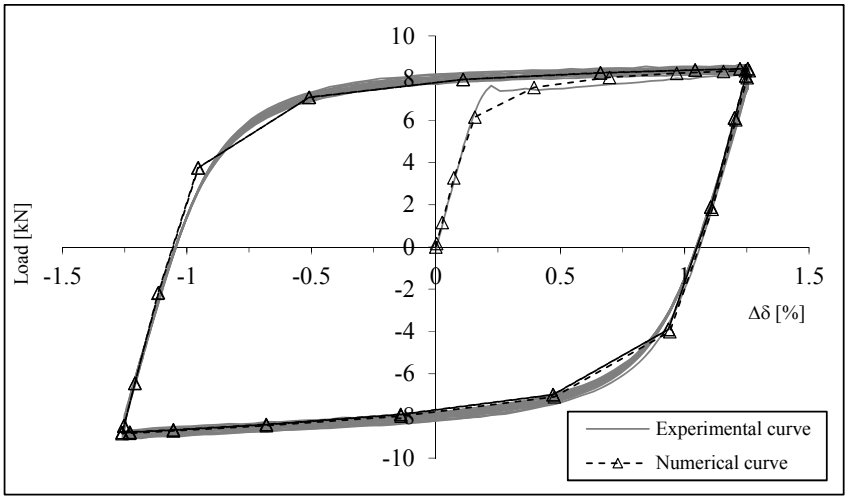

Figure 4.56 – Load-relative displacement hysteresis cycles including numerical response obtained for the U-1_CH_03 specimen of X60 piping steel, with thermal treatment.

4.3.1.3 Calibration of the non-linear kinematic hardening model for the X65 piping steel

The plasticity model of the X65 piping steel was also derived using the same procedure described for X52 and X60 steel grades. The parameter of plasticity models used to define the non-linear kinematic behaviour of the base material and the material with thermal treatment are presented in the Table 4.8 and Table 4.9, respectively. The experimental cyclic curves were also compared with the numerical uniaxial stress-strain curve in the Figure 4.57 and Figure 4.58. Similarly to the X60 piping steel, a deviation of the numerical curve relative to the experimental curve can be observed in the yield region, particularly for the material subjected to the thermal process. Comparisons between experimental and numerical responses derived for the cyclic tests of plane specimens of X65 piping steel are presented in Figure 4.59 to Figure 4.64 and a good compromise between the numerical and experimental data can be observed, despite the deviations observed in the cyclic curves.

Table 4.8 – Parameters of the plasticity model, with non-linear kinematic hardening, calibrated for X65 piping steel.

σ_{ced} [MPa]	C_1	γ_1	C_2	γ_2	C_3	γ_3
470	75000	900	6000	35	50	2

Table 4.9 – Parameters of plasticity model, with non-linear kinematic hardening, calibrated for X65 piping steel, with thermal treatment.

σ_{ced} [MPa]	C_1	γ_1	C_2	γ_2	C_3	γ_3
370	40000	630	6500	90	620	2.6

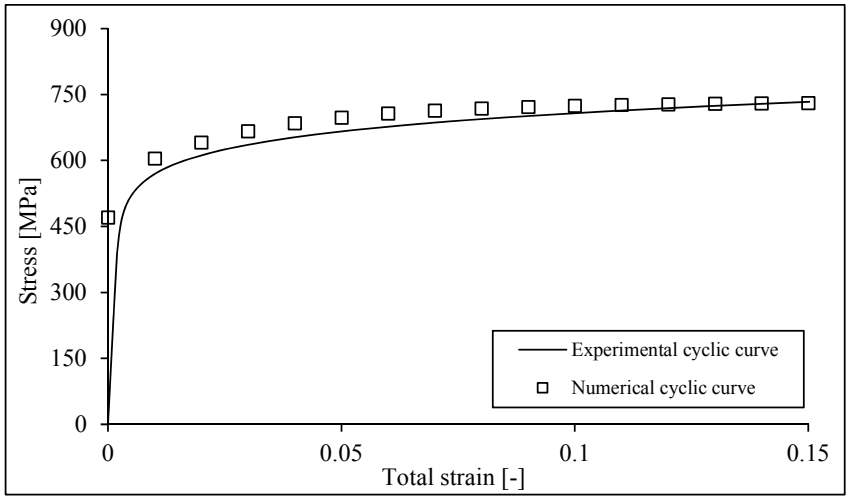

Figure 4.57 – Experimental cyclic curve and numerical curve introduced to define the plasticity model of the X65 piping steel.

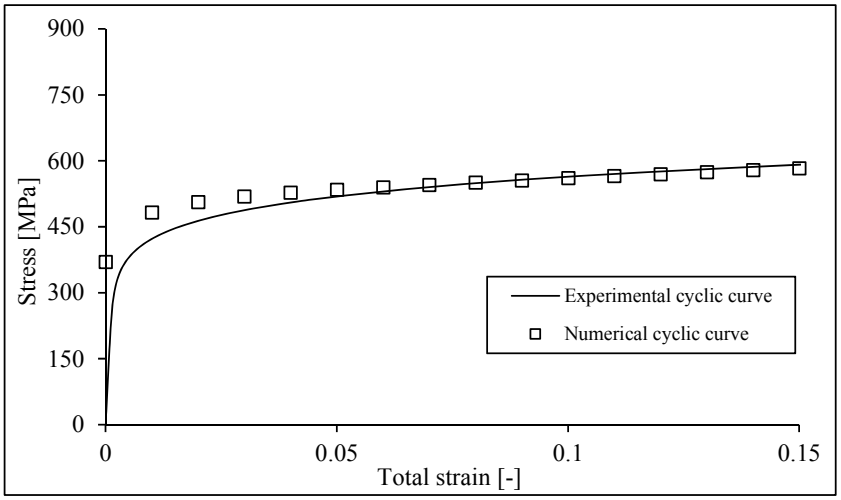

Figure 4.58 – Experimental cyclic curve and numerical curve introduced to define the plasticity model of the X65 piping steel, with thermal treatment.

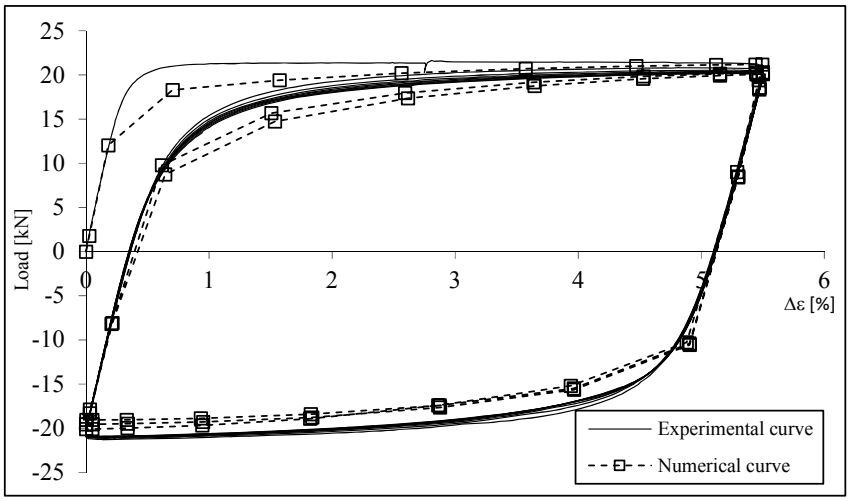

Figure 4.59 – Load-strain hysteresis cycles including numerical response derived for the U0_SP_02 specimen of X65 piping steel.

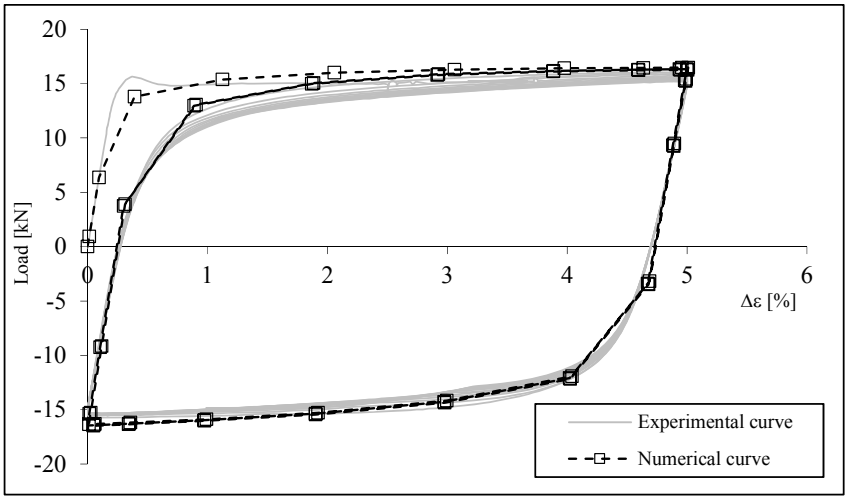

Figure 4.60 – Load-strain hysteresis cycles including numerical response derived for the U0_SP_08 specimen of X65 piping steel, with thermal treatment.

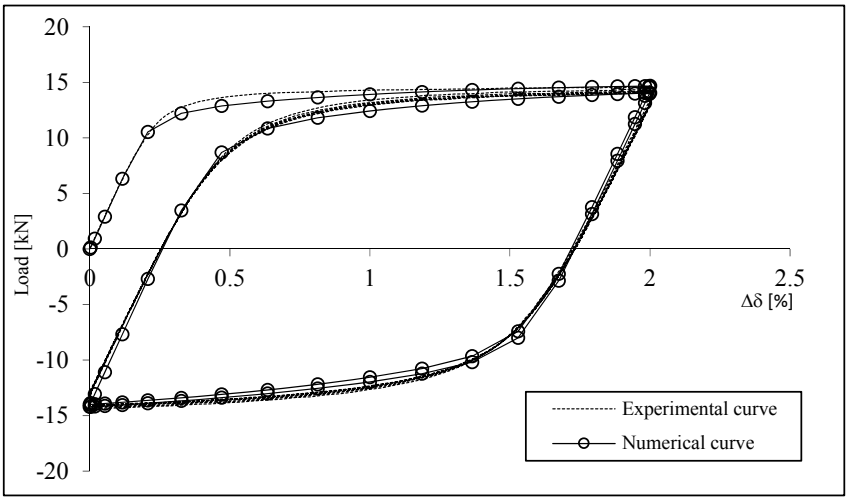

Figure 4.61 – Load-relative displacement hysteresis cycles including numerical response derived for the U0_CH_01 specimen of X65 piping steel.

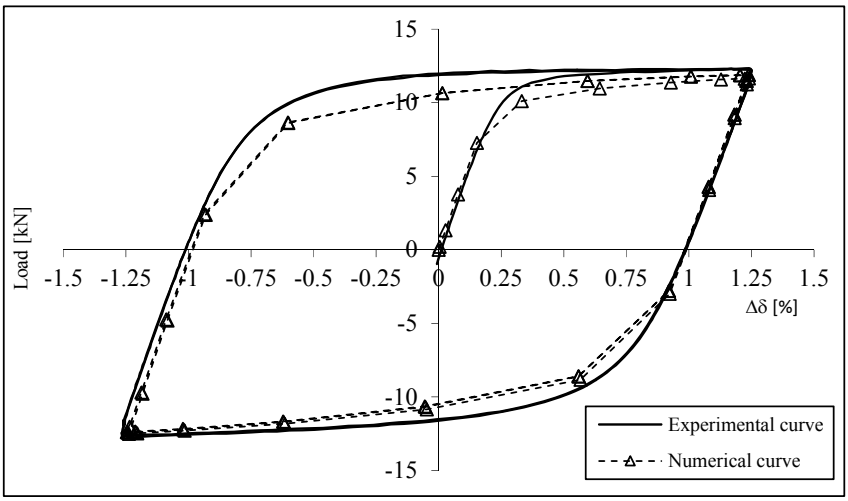

Figure 4.62 – Load-relative displacement hysteresis cycles including numerical response derived for the U0_OH_01 specimen of X65 piping steel.

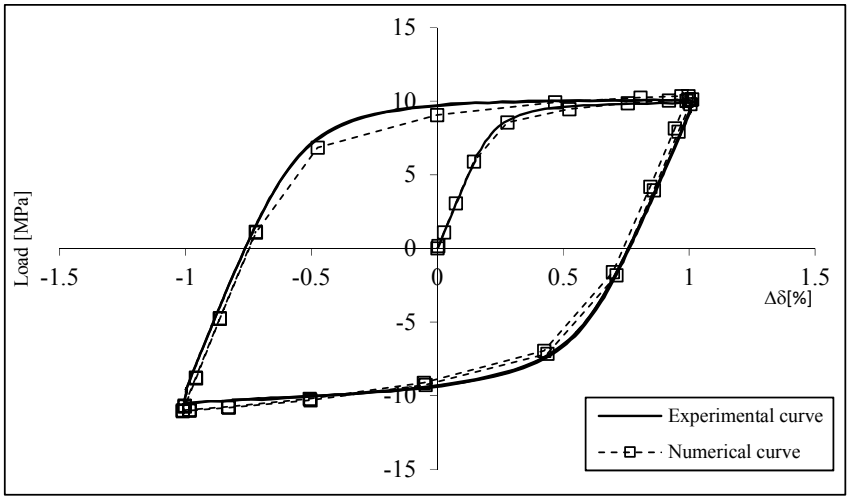

Figure 4.63 – Load-relative displacement hysteresis cycles including numerical response derived for the U-1_SN_01 specimen of X65 piping steel.

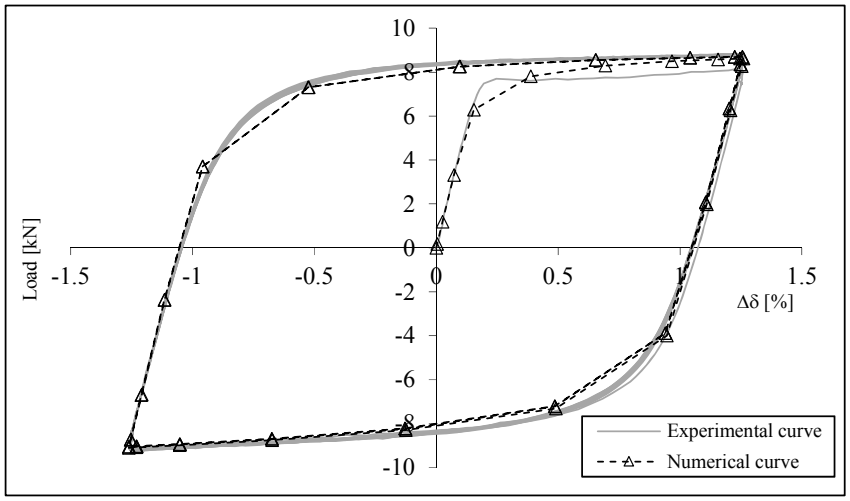

Figure 4.64 – Load-relative displacement hysteresis cycles including numerical response derived for the U-1_CH_03 specimen of X65 piping steel, with thermal treatment.

4.3.2 Fatigue damage models evaluation

In this section, the performance of uncoupled damage models on fatigue life prediction is investigated. Taking into account the restrictions of uncoupled damage models, the number of cycles to failure extracted from the experimental tests were corresponded to macroscopic crack initiation, as referred in the Chapter III. Finite element simulations allowed to identify the strain history evolution during the cyclic loading. In order to introduce the multiaxial effects typical of notched specimens, a multiaxial strain approach is suitable to perform the fatigue life estimations. Thus, the computation of the equivalent plastic strain range was obtained in accordance with ASME formulation [14] as follows:

$$\Delta\varepsilon_{eq}^{P}=\frac{\sqrt{2}}{3}\sqrt{\left(\Delta p_{11}-\Delta p_{22}\right)^{2}+\left(\Delta p_{22}-\Delta p_{33}\right)^{2}+\left(\Delta p_{33}-\Delta p_{11}\right)^{2}+\frac{3}{2}\left(\Delta p_{12}^{2}+\Delta p_{23}^{2}+\Delta p_{31}^{2}\right)} \quad (4.6)$$

where Δp_{ij} denotes the plastic strain component variation between two consecutive reversal points. In fact, a modified formulation of Coffin-Manson relation was used in this work. Instead of the longitudinal plastic strain amplitude, the equivalent plastic amplitude definition was used, as expressed in Eq. (4.7). Similarly, an extended version of Coffin-Mason model was proposed by Xue, in order to predict fatigue life in both LCF and ULCF domains. This model was originally proposed for test data with a strain ratio R_{ε}=0 and takes into account the equivalent plastic distortion (always positive) instead of the equivalent plastic strain, typically used. However, correction coefficients are necessary to be used in fatigue cycles formulation if other strain ratios are used. Since equivalent plastic distortion is always positive one real cycle may lead to plastic distortion cycles. In fact, this strain ratio coefficients dependency is point out as a limitation of the original Xue model. This limitation may be overcome if the current plastic distortion is replaced by the equivalent plastic strain in the Xue model formulation. The number of cycles to crack initiation can be computed using Eq. (4.8).

$$\frac{\Delta\varepsilon_{eq}^{P}}{2}=\varepsilon_{f}^{'}\left(2N_{i}\right)^{c} \quad (4.7)$$

$$N_{i}=\frac{e^{\lambda}-1}{e^{\lambda\left(\frac{\Delta\varepsilon_{eq}^{P}}{\bar{\varepsilon}_{f}}\right)^{m}}-1} \quad (4.8)$$

4.3.2.1 Fatigue assessment of X52 piping steel

The parameters of the Coffin-Manson relation were simultaneously obtained using LCF and ULCF data from the X52 piping steel. These parameters were computed correlating the equivalent plastic strain amplitude with the number of reversals until the crack initiation, as illustrated in the Figure 4.65. As referred above, the equivalent plastic strain amplitude was achieved by means of finite elements analysis. The fatigue ductility coefficient and fatigue ductility exponent are presented in the Table 4.10. In general, the

experimental data of all specimens shows some degree of correlation. Although, some deviations are found when Coffin-Manson parameters are used to estimate the number of cycles to crack initiation for some specific data. This effect is especially noticeable for smooth specimen's data under ULCF domain as can be observed by the analysis of the Figure 4.66. The Coffin-Manson relation tends to overestimate the number of fatigue cycles of smooth specimens, but good fatigue life predictions are obtained for notched plane specimens. Accuracy bands were added to Figure 4.66, a double and half-life criterion being used for LCF domain. For ULCF regime a progressive criterion was used, reducing the accuracy band from LCF to 1.33x and 0.75x of experimental fatigue life in the ULCF (N_i=1 cycle).

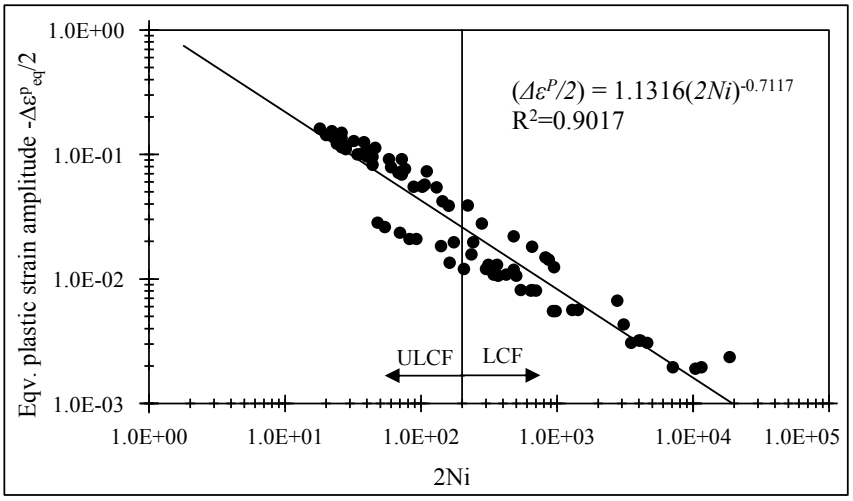

Figure 4.65 – Equivalent plastic amplitude *versus* number of reversals to crack initiation of small-scale data for the X52 piping steel.

Table 4.10 – Coffin-Manson parameters obtained for the X52 piping steel.

ε_f	c	R^2
1.1316	-0.7117	0.9017

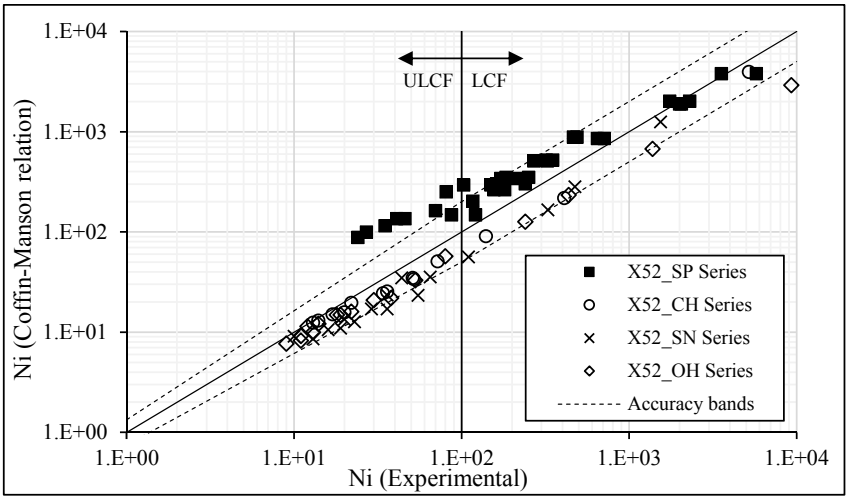

Figure 4.66 – Comparison of the experimental data and Coffin-Manson relation for the X52 piping steel.

In order to compute the *m* and λ parameters of the Xue model, the equivalent plastic strain of the smooth and notched specimens is plotted against the number of cycles to macroscopic crack initiation, in Figure 4.67. In opposition to the Coffin-Manson relation, the Xue model distinguishes the specimen's series through the definition of the fracture strain, $\bar{\varepsilon}_f$.

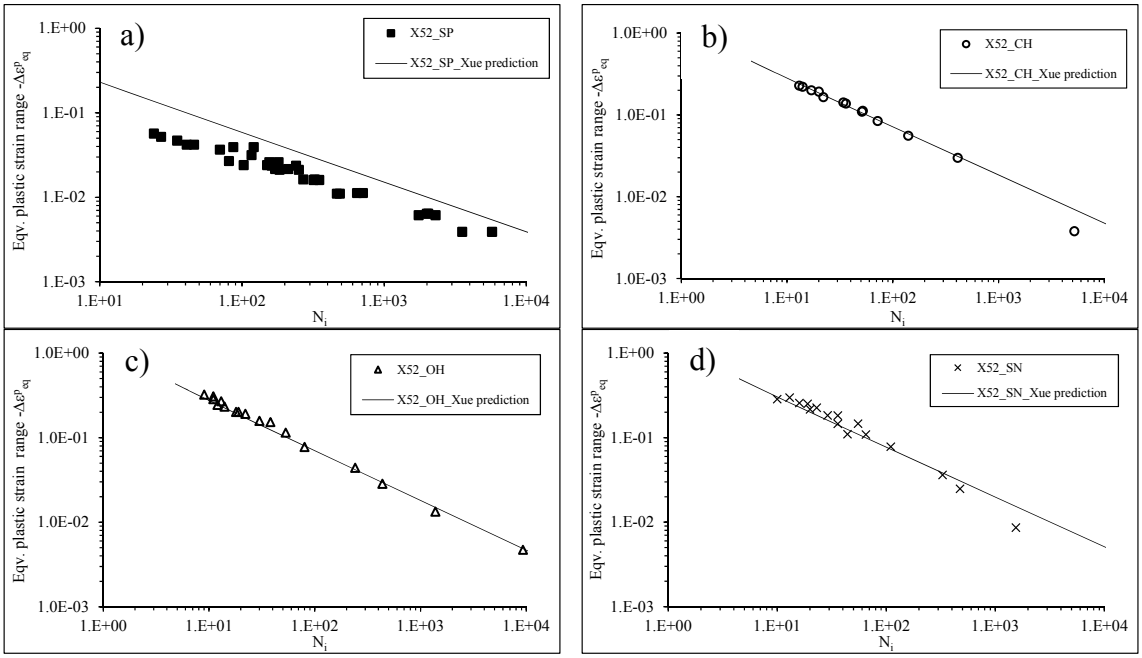

Figure 4.67 – Equivalent plastic range *versus* number of reversals of small-scale specimens of X52 piping steel: a) SP series: b) CH series; c) OH series; d) SN series.

It should be noted that $\bar{\varepsilon}_f$ was computed directly from the numerical simulations of the monotonic tensile tests, but at the node experiencing the crack initiation under the cyclic loading. This node may not coincide with the one where the monotonic fracture may start. In other words, this parameter measures a pseudo total deformation capacity for a particular location when this specimen is subjected to monotonic loading. This total deformation capacity is only real if the monotonic and fatigue failure locations coincide with each other. In fact, for the monotonic loading, the fracture of the smooth specimens starts inside the material, whereas the fatigue failure is dominated by growth of a crack, which begins at the surface of the smooth specimens. Concerning the notched plane specimens the critical location under a monotonic or cyclic loading is coincident and it is localize at the notch root. Table 4.11 summarizes the fracture strain associated to each specimen series. Both *m* and λ parameters are used to correlated overall results. Comparisons between experimental results and Xue model predictions are exposed in Figure 4.68. In general, good predictions are attained with Xue model for both ULCF and LCF regimes mainly for notched specimen series. As already verified for Coffin-Manson relation, the Xue model tends overestimate the fatigue life of smooth specimens. The performance of these fatigue damage models is reported in the Figure 4.69. In general, Coffin-Manson relation provides the better fatigue life correlations. The calibration of these models resulted from the global fitting of the overall results, which did not accounted for the differences associated to distinct specimen geometries. Nevertheless, these results will be reassessed later.

Table 4.11 – Parameters of Xue model computed for X52 plane specimens.

Specimen Series	$\bar{\varepsilon}_f$	m	λ
SP	1.09	1.7	-0.8
CH	1.34		
OH	1.31		
SN	1.44		

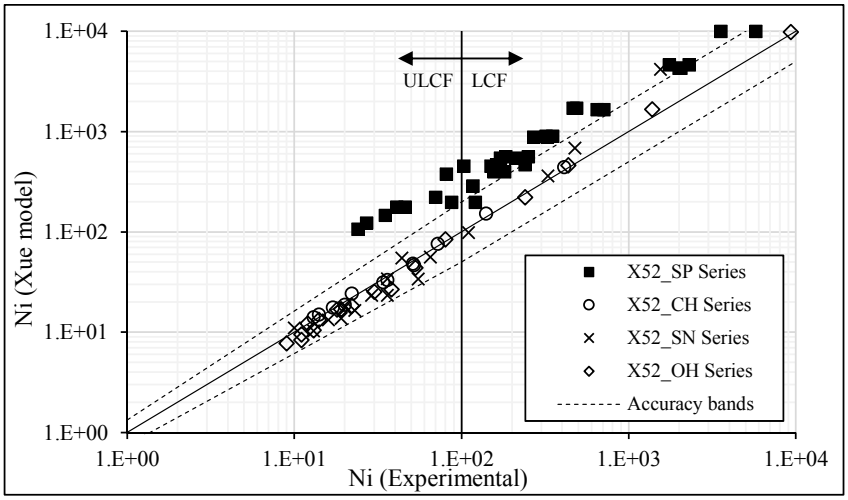

Figure 4.68 – Comparison of experimental data and Xue model predictions for the X52 piping steel.

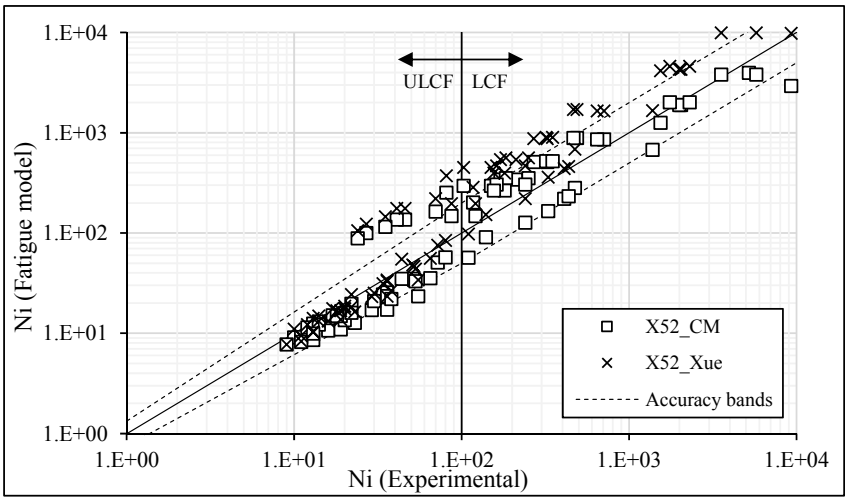

Figure 4.69 – Comparison of experimental data and fatigue damage model predictions for the X52 piping steel.

4.3.2.2 Fatigue assessment of X60 piping steel

Figure 4.70 shows the equivalent plastic strain amplitude against the number of cycles on a log-log scale for the X60 piping steel with and without thermal treatment, including the smooth and notched plane series. From this plot, the parameters of the Coffin-Manson relation were derived and presented in the Table 4.12. In order to investigate the performance of the Coffin-Manson relation on the fatigue life prediction of smooth and notched plane series simultaneously, the number of cycles to crack initiation was computed and plotted against the experimental number of cycles in Figure 4.71 and Figure 4.72, for the base material and for the material subjected to the thermal cycle, respectively.

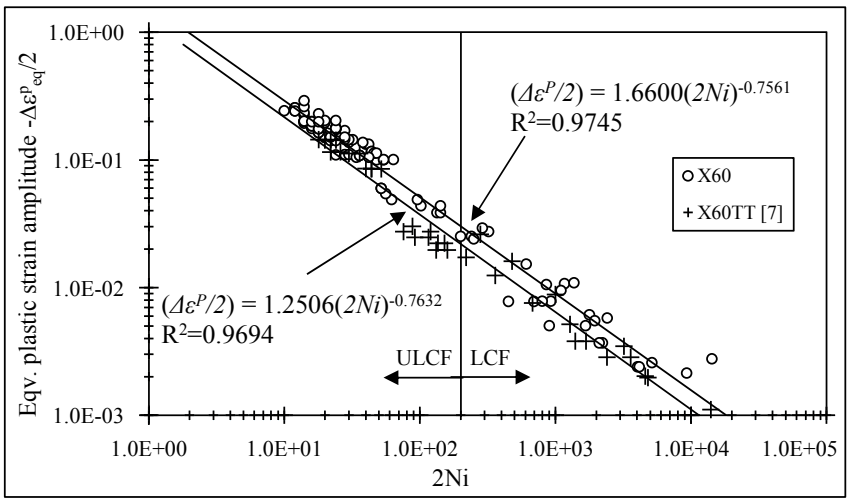

Figure 4.70 – Equivalent plastic strain amplitude *versus* number of reversals to crack initiation of small-scale X60 piping steel, with and without thermal treatment.

Table 4.12 – Coffin-Manson parameters obtained for X60 piping steel, with and without thermal treatment.

Steel	ε_f	c	R^2
X60	1.6600	-0.7561	0.9745
X60TT	1.2505	-0.7632	0.9694

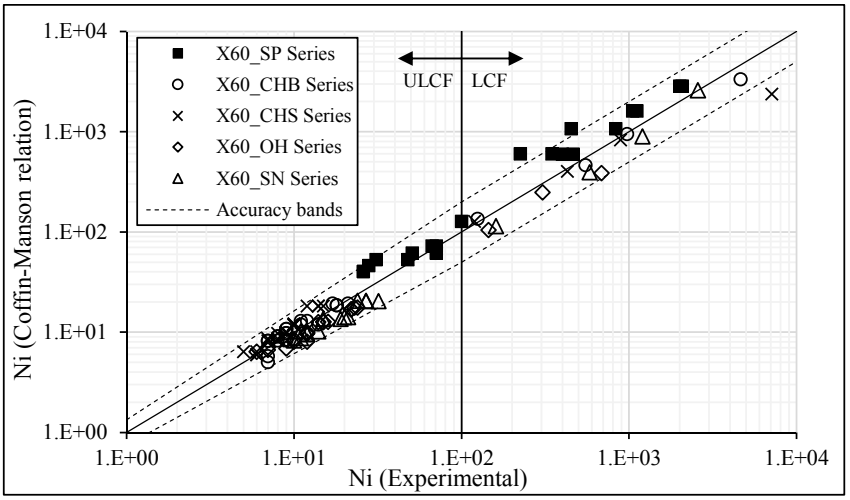

Figure 4.71 – Comparison of experimental data and Coffin-Manson predictions for the X60 piping steel.

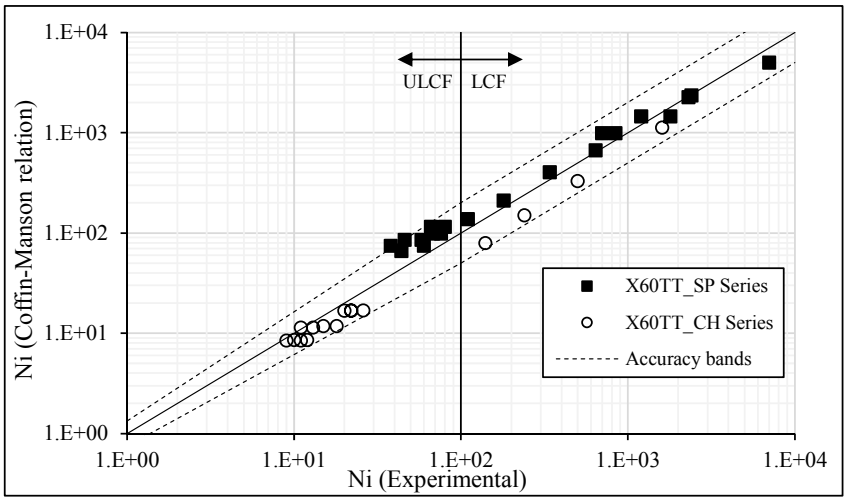

Figure 4.72 – Comparison of experimental data and Coffin-Manson relation for the X60 piping steel, with thermal treatment.

In general, the Coffin-Manson produces satisfactory results on estimating the number of cycles. Although, differences between smooth and notched plane specimens' series are clearly identified, since the equivalent plastic strain values of both series are distinct. The accuracy bands used in the presentation of X52 piping steel results were also considered in this discussion. Figure 4.73 and Figure 4.74 illustrates the equivalent plastic strain of smooth and notched specimens as a function of the number of cycles to macroscope crack initiation, for the X60 piping steel without and with thermal treatment, respectively. These representations allow to estimate the parameters of the Xue model, which are summarized in Table 4.11 for the base material and material with thermal treatment. The analysis of these figures reports a good correlation for notched specimens data and some

scatter/deviation for smooth specimen results. Figure 4.75 and Figure 4.76 compare the fatigue life predictions obtained with the Xue model and the experimental data. Xue model also provides satisfactory results specially, with a better performance for notched plane specimens. Comparisons between Coffin-Manson relation and Xue model can be observed in Figure 4.77 and Figure 4.78, for base material and for material with thermal treatment, respectively. As occurred for X52 piping steel, the use of Xue model results on significant improvements concerning the fatigue life predictions. However, this tendency is not verified for smooth plane specimens. In fact, Coffin-Manson relation provides better fatigue life estimations for these specimens, especially under LCF domain, which indicates that the equivalent plastic strain levels of smooth and notched plane specimens are very close and the effect of the fracture strain on LCF domain can be considered negligible. Concerning the material affected with the thermal treatment, the numerical predictions achieved with the Xue and CM relation are equivalent, since the fracture strains of both specimen series are similar.

Table 4.13 – Parameters of Xue model computed from of X60 plane specimens (base and heat treated materials).

Specimen Series	$\bar{\varepsilon}_f$	m	λ
X60_SP	1.32	1.41	1.25
X60_CHS	1.16		
X60_CHB	1.20		
X60_OH	1.37		
X60_SN	1.18		
X60TT_SP	1.45	1.32	0.6
X60TT_CH	1.52		

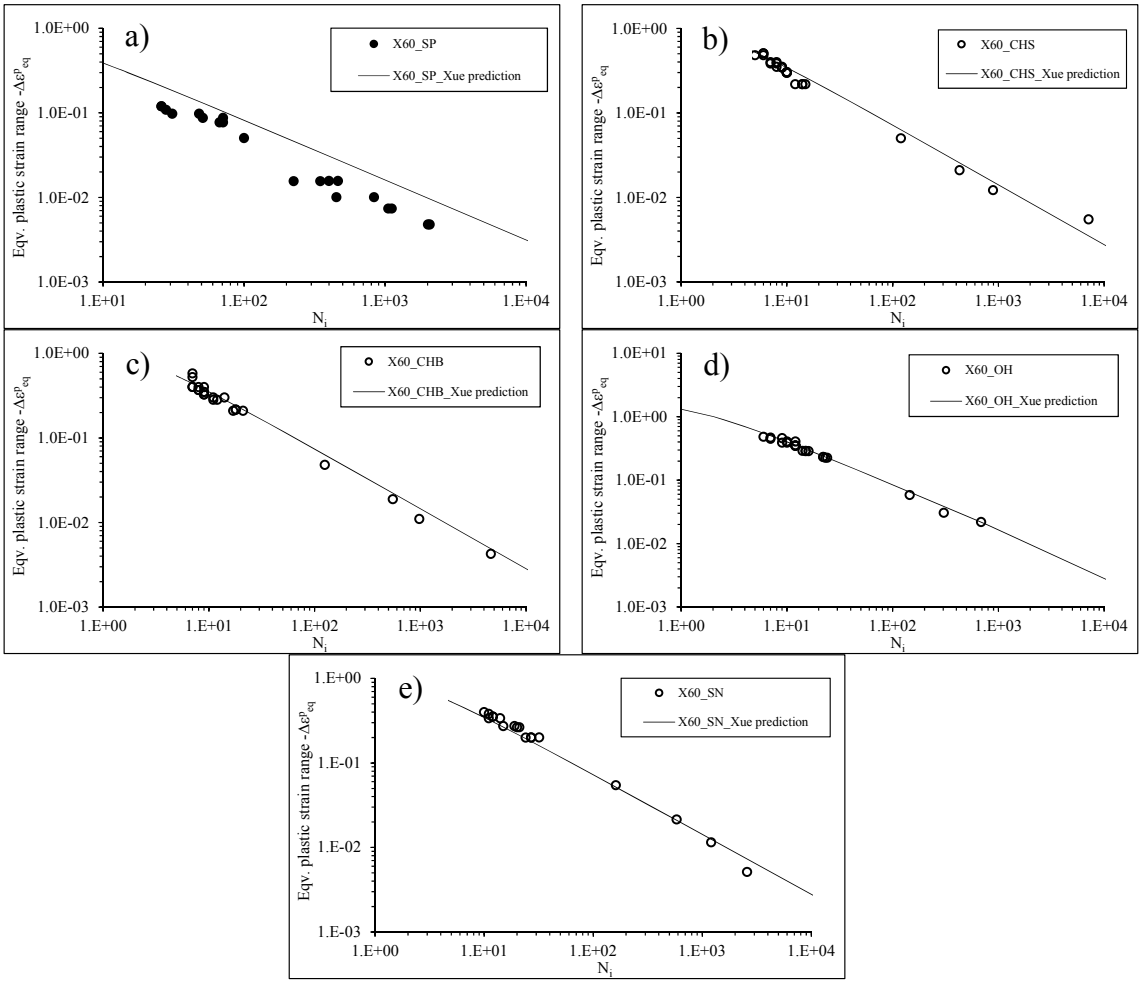

Figure 4.73 – Equivalent plastic range *versus* number of reversals of small-scale tests of X60 piping steel: a) SP series: b) CHS series; c) CHB series; d) OH series; e) SN series.

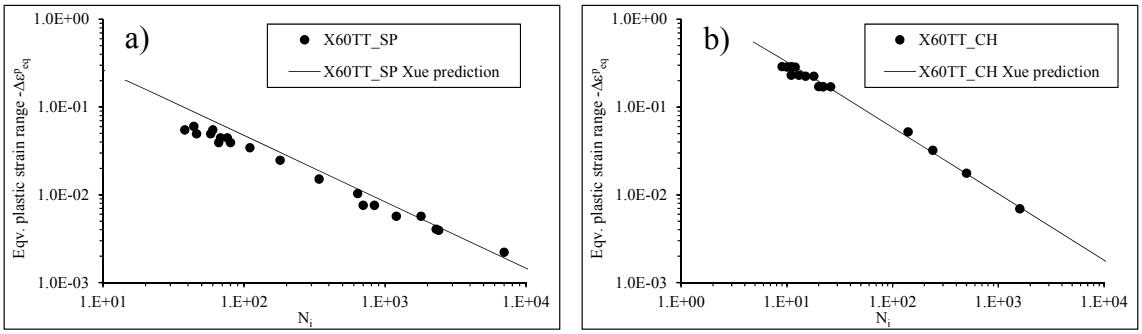

Figure 4.74 – Equivalent plastic strain range *versus* number of cycles of small-scale tests of X60 piping steel with thermal treatment: a) SP series: b) CH series.

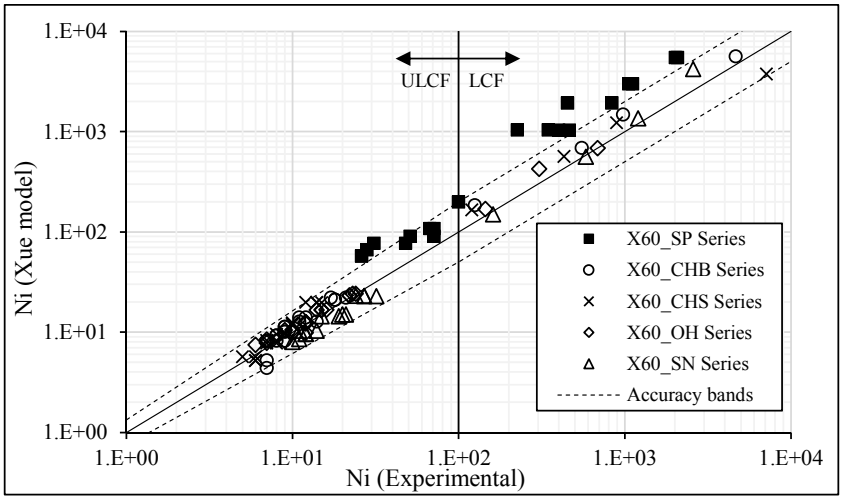

Figure 4.75 – Comparison of experimental data and Xue model for the X60 piping steel.

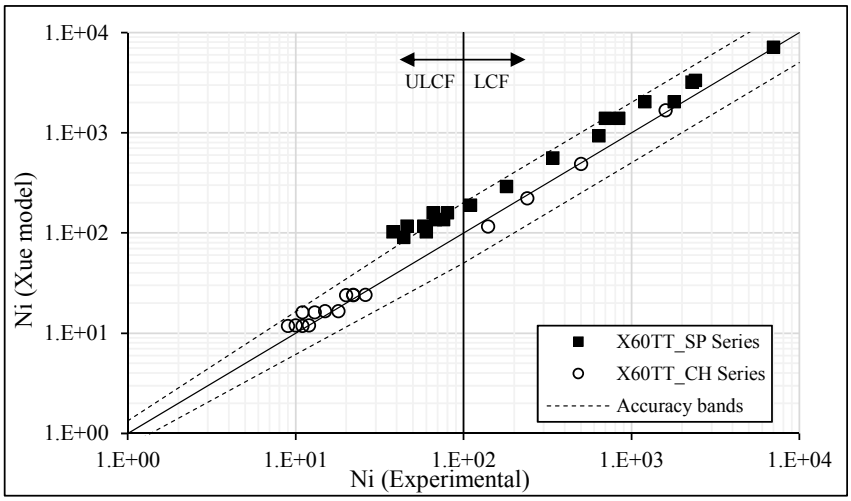

Figure 4.76 – Comparison of experimental data and Xue model for the X60 piping steel, with thermal treatment.

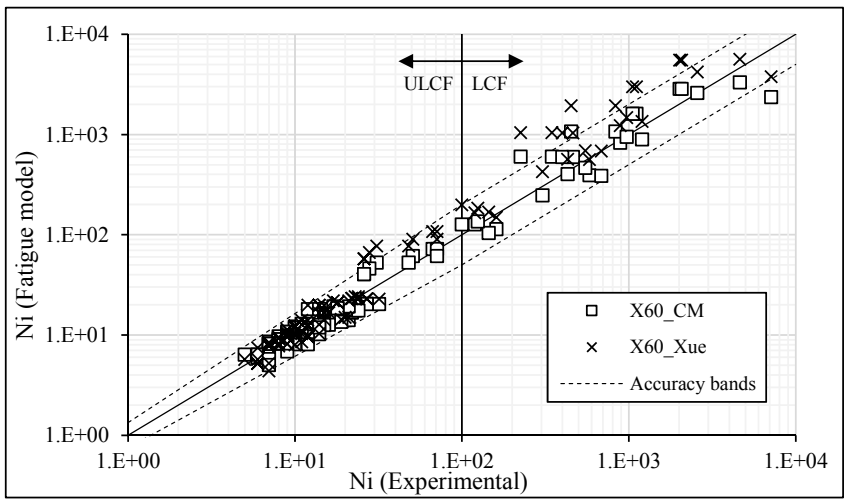

Figure 4.77 – Comparison of experimental data and selected fatigue damage models predictions for the X60 piping steel.

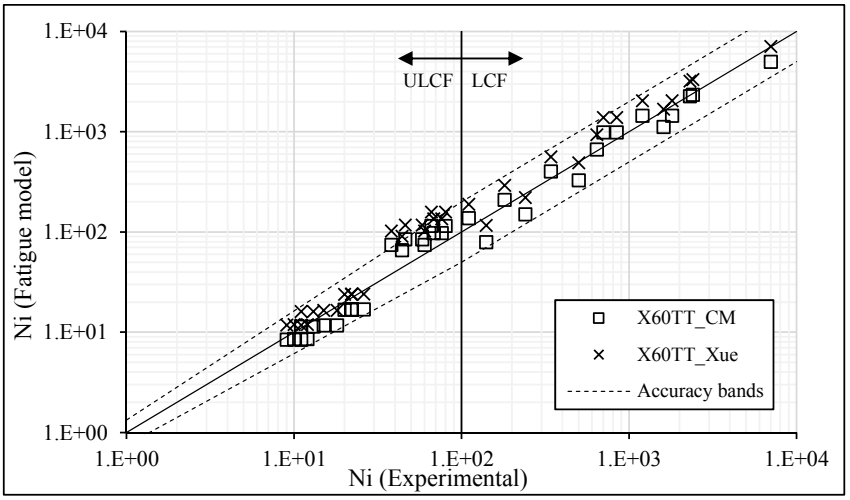

Figure 4.78 – Comparison of experimental data and fatigue damage models predictions for the X60 piping steel, with thermal treatment.

4.3.2.3 Fatigue assessment of X65 piping steel

As accomplished for the X52 and X60 piping steels, the performance of the Coffin-Manson relation was also investigated for the X65 steel grade. The equivalent plastic strain amplitude is plotted against the number of cycles to crack initiation in a log-log scale, see Figure 4.79. In this way, the global parameters of the Coffin-Manson relation were computed and presented in the Table 4.14. Based on these results, fatigue life predictions can be estimated for small-scale tests of X65 piping steel. Comparisons between the experimental number of cycles and the number of cycles predicted from Coffin-Manson relation can be observed in the Figure 4.80 and Figure 4.81 for the material without and with thermal treatment, respectively. Concerning the base material, a poor correlation can be observed mainly for the smooth plane specimens and SN specimen series. On the other hand, satisfactory results were achieved with Coffin-Manson relation on the fatigue life predictions of small-scale tests performed on the material subjected to a thermal process. In general, all data points fall inside the proposed accuracy band, concerning the description of the X52 piping steel results.

Table 4.14 – Coffin-Manson parameters obtained for the X65 piping steel, with and without thermal treatment.

Specimen Series	ε'_f	c	R^2
X65	1.8047	-0.8320	0.9000
X65TT	1.2137	-0.7778	0.9381

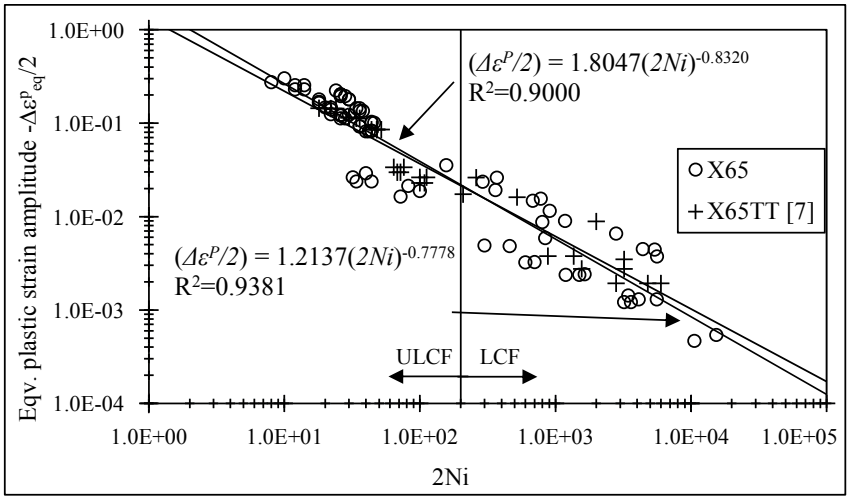

Figure 4.79 – Equivalent plastic amplitude *versus* number of reversals obtained with small-scale specimens of X65 piping steel, without and with thermal treatment.

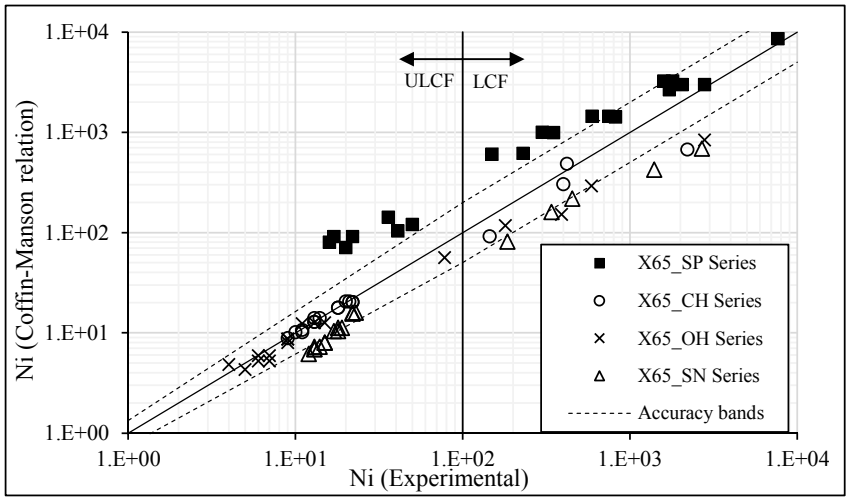

Figure 4.80 – Comparison of experimental data and Coffin-Manson predictions for the X65 piping steel.

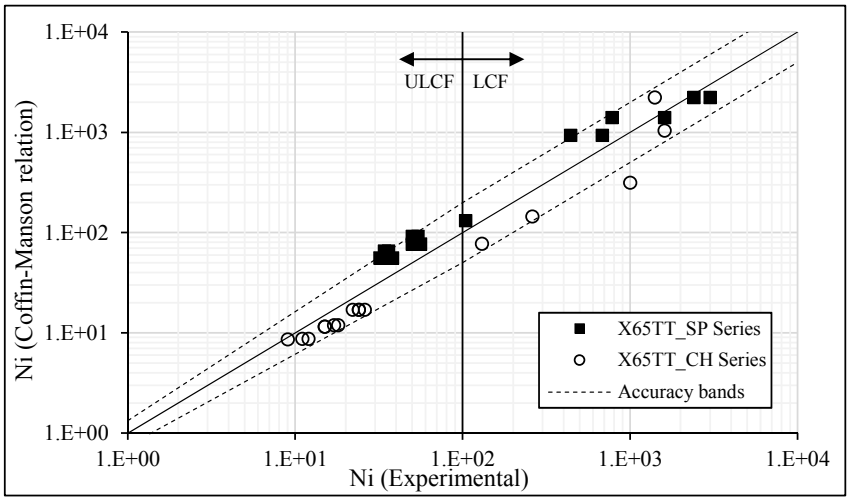

Figure 4.81 – Comparison of experimental data and Coffin-Manson predictions for the X65 piping steel, with thermal treatment.

The m and λ parameters of the Xue model were also evaluated for the X65 piping steel, which resulted from a global fitting of the small-scale test results (see Table 4.15). The small-scale tests carried out on the material with thermal treatment were also included in this study. This results are illustrated in Figure 4.82 and Figure 4.83 for the base material and for the material affected with the thermal treatment, respectively. The data points of the notched specimens are well correlated with the prediction lines of the Xue model, however some deviation can be identified for smooth plane specimens, mainly under ULCF regime. These evidences are reinforced by the analysis of Figure 4.84 and Figure 4.85 that illustrate the numerical predictions obtained with the Xue model for the material without and with thermal treatment.

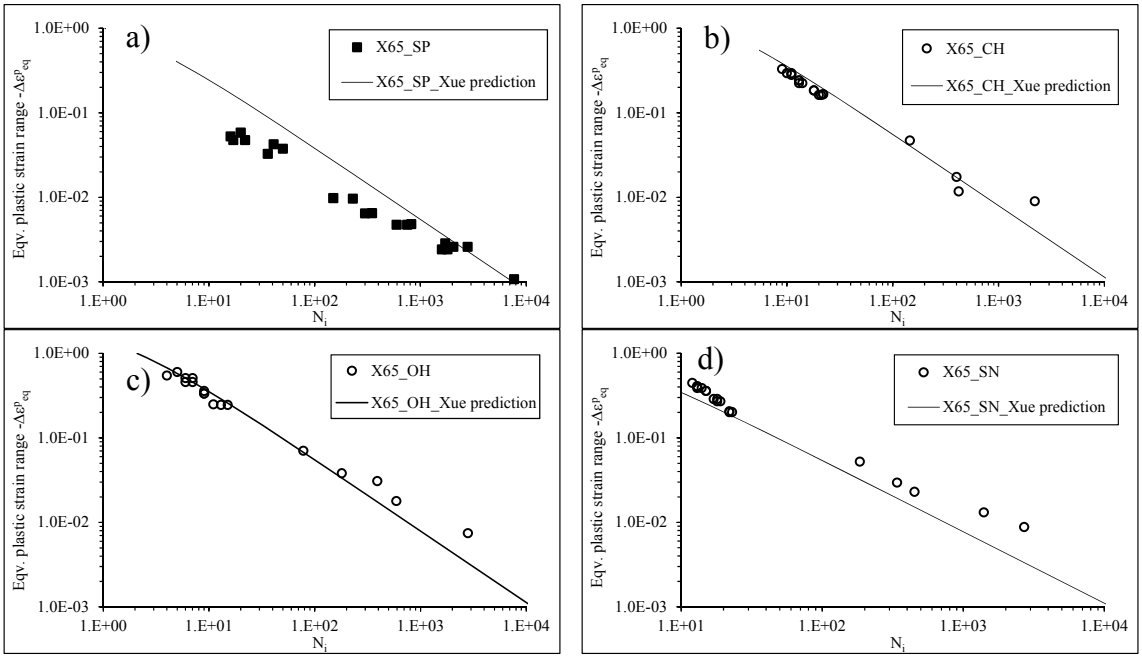

Figure 4.82 – Equivalent plastic range *versus* number of reversals to crack initiation of small-scale tests of X65 piping steel: a) SP series: b) CH series; c) OH series; d) SN series.

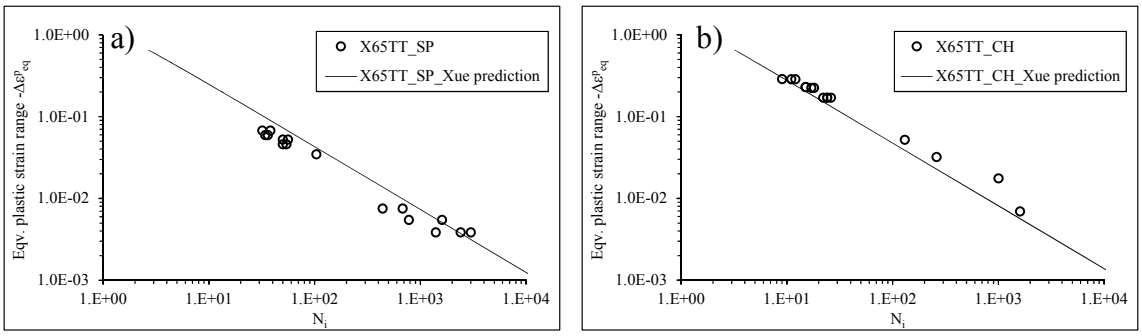

Figure 4.83 – Equivalent plastic range *versus* number of reversals to crack initiation of small-scale tests of X65 piping steel with thermal treatment: a) SP series: b) CH series.

Table 4.15 – Parameters of the Xue model computed for the X65 plane specimens (without and with thermal treatment).

Specimen Series	$\bar{\varepsilon}_f$	m	λ
X65_SP	1.02	1.18	1.35
X65_CH	1.48		
X65_OH	1.46		
X65_SN	1.44		
X65TT_SP	1.27	1.3	0.4
X65TT_CH	1.52		

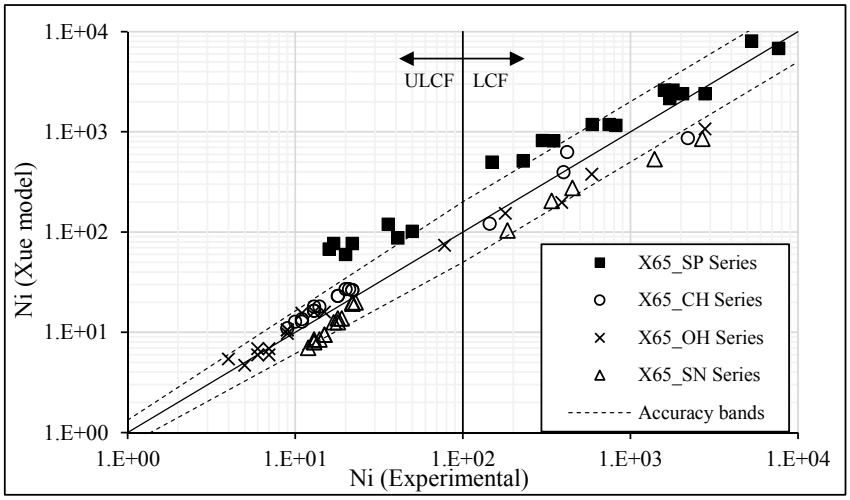

Figure 4.84 – Comparison of experimental data and Xue model predictions for the X65 piping steel.

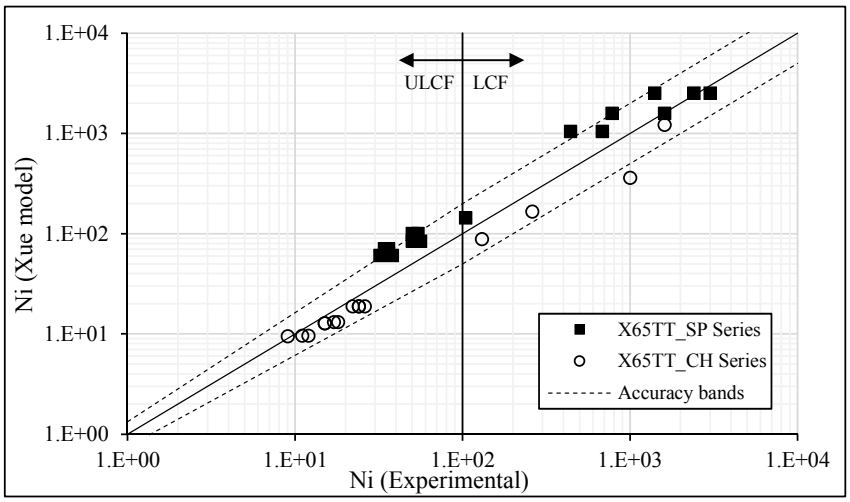

Figure 4.85 – Comparison of experimental data and Xue model predictions for the X65 piping steel, with thermal treatment.

The performance of Coffin-Manson and Xue relations are compared in Figure 4.86 and Figure 4.87, for base and heat-treated material. As occurred for the X52 piping steel, the Xue model provided significant improvements in the description of overall experimental data points, including smooth and notched plane specimens, under both LCF and ULCF

domains. Although, the worst predictions are systematically obtained for the smooth plane specimens. Consequently, in order improve the fatigue life predictions of the smooth plane specimens, a new approach based on updated numerical simulations will be presented in the next section.

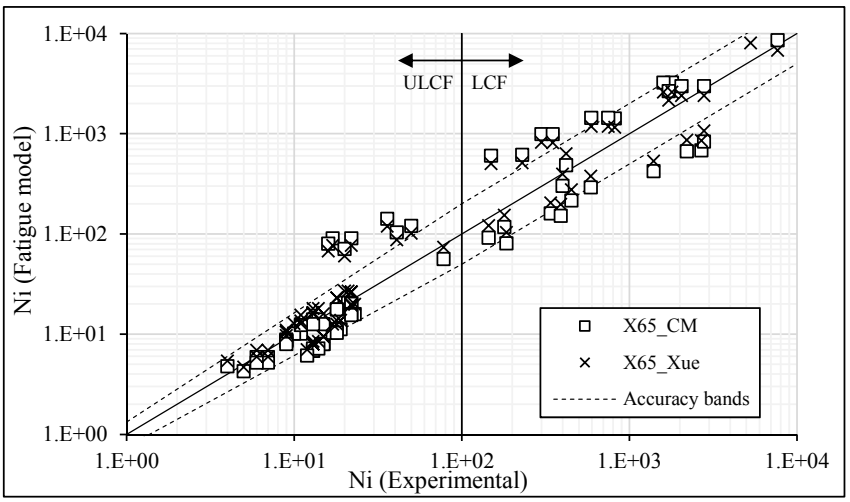

Figure 4.86 – Comparison of experimental data and fatigue damage models predictions for the X65 piping steel.

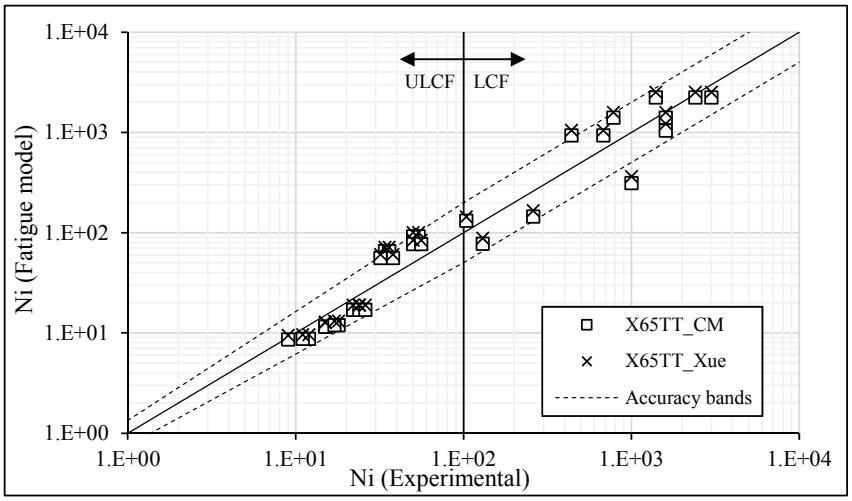

Figure 4.87 – Comparison of experimental data and fatigue damage models predictions for the X65 piping steel, with thermal treatment.

4.4 NUMERICAL ANALYSIS OF TENSION-COMPRESSION CYCLIC TESTS WITH THE APPLICATION OF LATERAL DISPLACEMENTS

As mentioned in Chapter III, lateral instabilities were observed during the ULCF tests of smooth specimens even using the anti-buckling system which minimized to some extent that lateral parasitic displacements. The lateral instabilities promote additional plastic deformations which were not considered in finite element simulations presented in the previous section. The ideal boundary conditions do not reproduce the lateral movements of the specimens gripping. Indeed, new simulations were performed for all smooth specimens under cyclic loading, taking into account the lateral displacements of the actuator. Since the LVDT sensors were only used in the cyclic tests of smooth plane specimens of X60 and X65 piping steel with thermal treatment a criterion was developed in order to estimate the lateral instabilities on the cyclic simulations of the smooth specimens of the X52 and X60 piping steels. This new numerical study will be described along the following subsections.

4.4.1 Finite element models

The new numerical formulation for the application of finite elements models requires the application of multiaxial displacements, which in turn does not allow to consider the symmetry conditions verified in the smooth plane specimens. Thus, updated geometrical models are proposed taking into account the definition of the full geometry of the specimens, as illustrated in Figure 4.88. Also 3D 8-noded isoparametric solid elements with reduced integration, C3D8R, were used to build the numerical models of the complete specimen geometry. The plasticity models with kinematic hardening described in the Section 4.3 were adopted for these simulations. As mentioned above, to reproduce the lateral instability, the displacements of the actuator, measured from two LVDT sensors were used. Cyclic displacements were imposed through two LVDT sensors (see Figure 3.18).

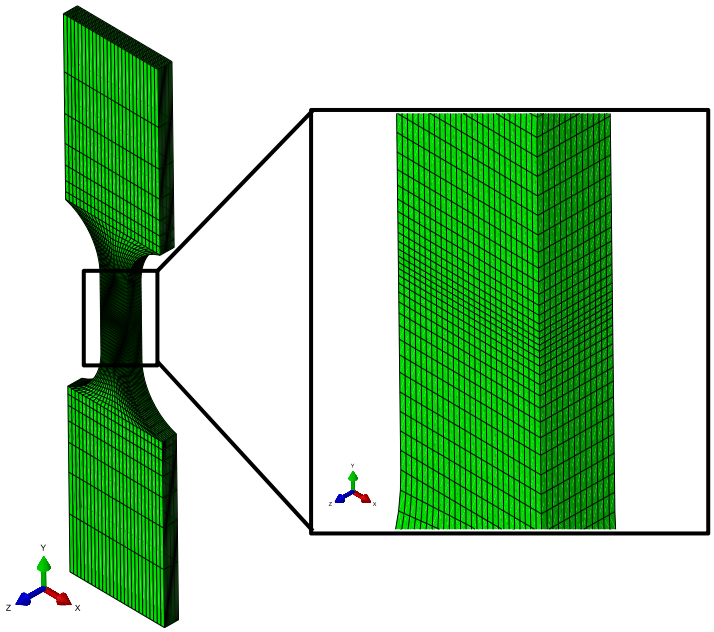

Figure 4.88 – Numerical model of a smooth plane specimens using total geometry.

Updated boundary conditions were applied at the nodes located on top and bottom of a region of interest, which corresponds to the gripping area of the specimens, as can be observed in the Figure 4.89. Since the superior grip is fixed, the degrees of freedom of these nodes were constrained. Supported on experimental observations, the lateral displacements were applied only during the compressive stages. The intensity of these displacements corresponds to the amplitude of experimental displacements, measured for each direction (see Figure 4.90). A criterion based on specimen mean life was used to set the displacement value. The calibration of the longitudinal remote displacements of specimens was based on an iterative process similarly to the previous simulations in order to result the same local clip gauge displacements. The measurements of lateral instabilities were only performed for ULCF tests, therefore extrapolations of these results were conducted to the LCF domain. In order to find a correlation between the experimental LVDTs measurements and the axial strain range, the amplitude of the displacements norm measured with the pair of LVDTs was plotted against the strain range applied in the cyclic tests which can be observed in Figure 4.91. In general, the correlation of these variables shows a decreasing lateral/parasitic displacement amplitudes with the reduction of the range of the applied remote strain range. Also for null axial loading, the lateral/parasitic displacements should also null. The angle β of the displacement vector was also correlated with the value of the strain range (see Figure 4.92), which allowed computing the displacement amplitude

associated to each LVDT direction. The β direction is defined in the Figure 4.90, as the angle between the axis of LVDT_1 and the transversal displacement vector $\vec{u}$.

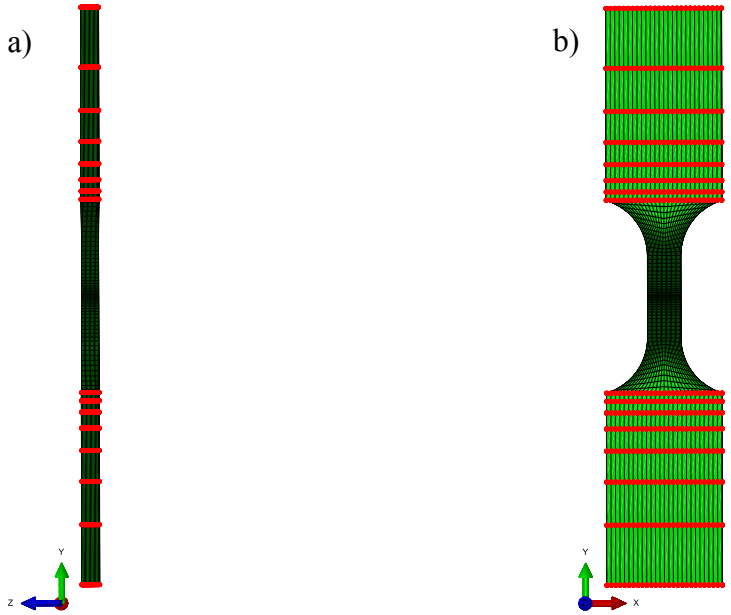

Figure 4.89 – Set of nodes used to apply the boundary conditions for the full model of the specimens: a) lateral view; b) front view.

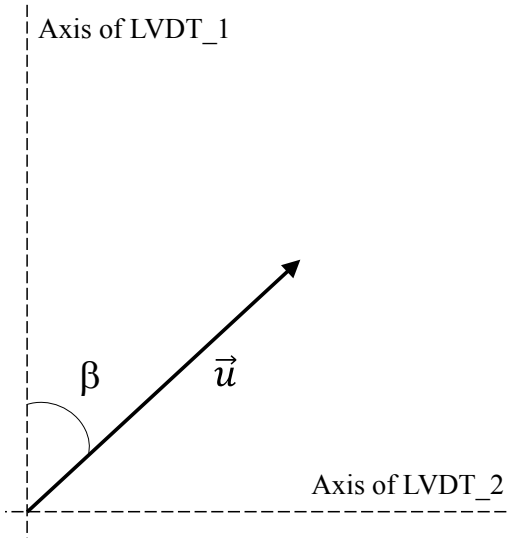

Figure 4.90 – Decomposition of the lateral movements, β.

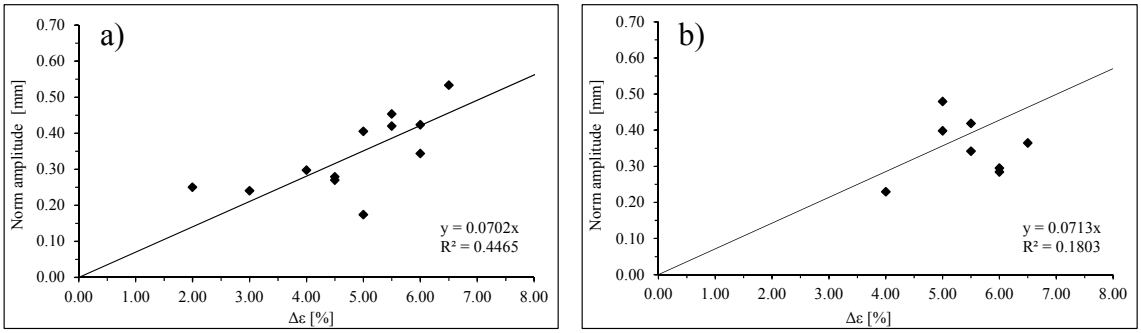

Figure 4.91 – Correlation of the norm of the lateral actuator movements for the ULCF tests: a) X60 piping steel with thermal treatment; b) X65 piping steel with thermal treatment.

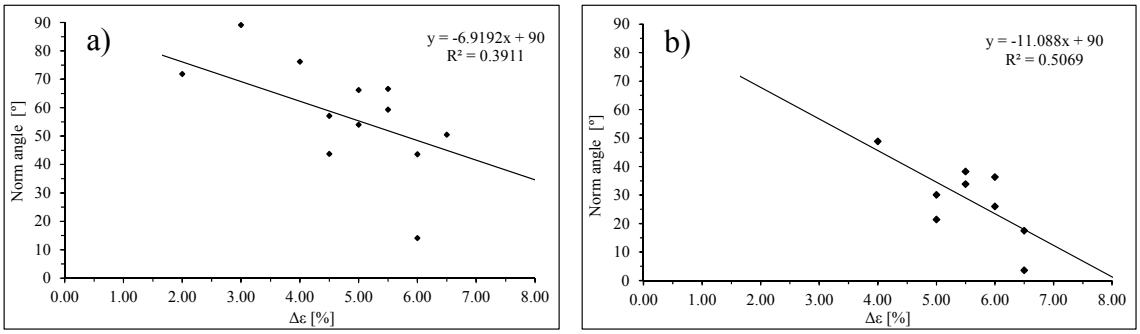

Figure 4.92 – Correlation of the orientation, β, of lateral movements during ULCF tests and the applied strain range: a) X60 piping steel with thermal treatment; b) X65 piping steel with thermal treatment.

The trend lines used in the graphs of Figure 4.91 were defined from the origin since is expected that the specimens' instability tend to be negligible with the decreasing of the applied strain range. The same preposition was adopted for the norm angle, but in this case the intersection of y-axis was defined as 90º. The linear equations presented Figure 4.91 and Figure 4.92 were used to attain the displacements introduced in the boundary conditions. These displacements were accounted in this study being applied directly in the boundary conditions of the numerical models of the smooth specimens of the X65 piping steel, since the smooth plane specimens of X65 and X65TT exhibited the same geometry. Based on the experimental measurements of X65TT tests, a criterion was developed in order to apply the lateral instabilities on the cyclic simulations of the smooth specimens of the X52 and X60 piping steels. The criterion consisted on scaling the displacement amplitudes obtained for the X65TT cyclic tests using a scale factor Figure 4.93 illustrates the influence of the proposed correction factor in the numerical response that is determined, in particular in the compressive stage. The choice of a scale factor of 2 still resulted on a very good agreement between the numerical and experimental results in the simulation of

the stabilized response for the X52 and X60 piping steels. A scale factor of 3 would produce a substantial deviation of the numerical curve from the first compression peaks which indicates an excessive deformation of the specimens, which is not validated by the experimental evidence. The deformed shape of a smooth plane specimen tested considering the lateral movements is illustrated in Figure 4.94. The finite element models allow to reproduce the real behaviour of the specimens and the asymmetry due to the imposition of lateral movements is clearly observed. Despite not corresponding to the specimen illustrated in Figure 4.94, Figure 4.95 allows the comparison of the experimental and numerical deformed shape. The same comparison can be performed from the analysis of Figure 3.18.

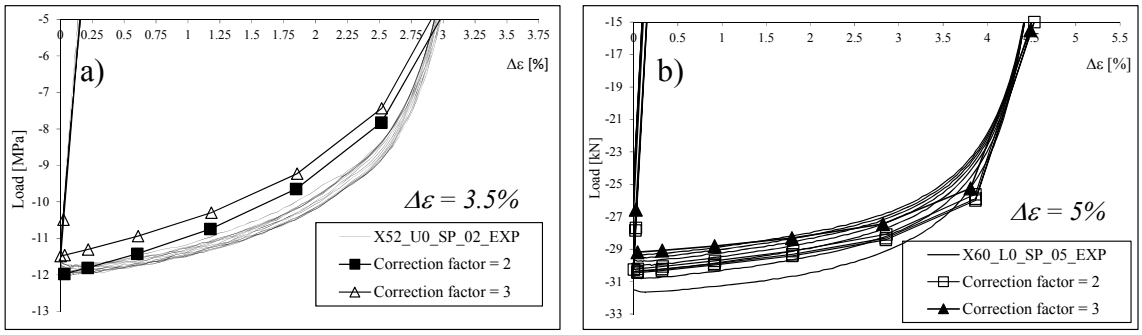

Figure 4.93 – Influence of the correction factor of the LVDT data on the numerical load-deformation response for X52 (a) and X60 (b) piping steels (smooth plane specimens).

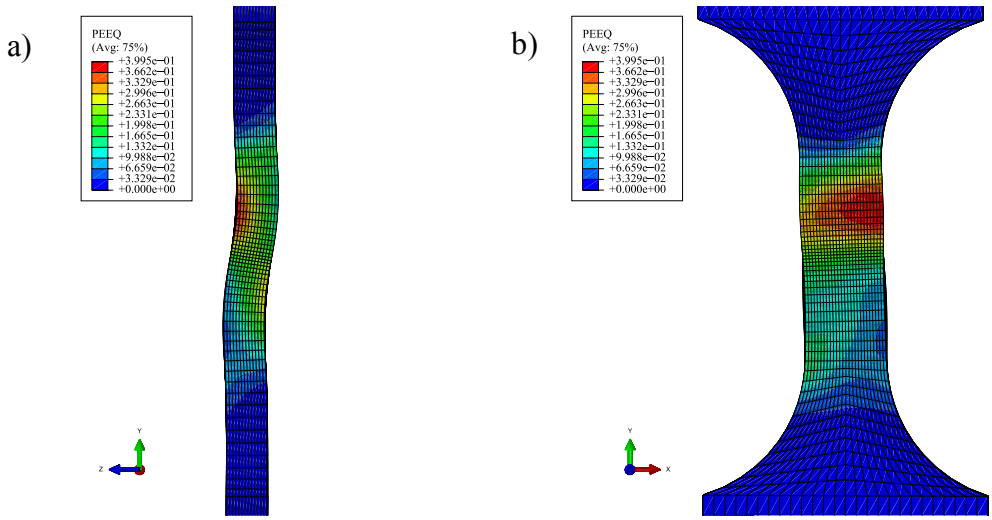

Figure 4.94 – Accumulated equivalent plastic strain field obtained at the compressive reversal stage, taking into account the lateral movements of actuator: a) side view; b) front view.

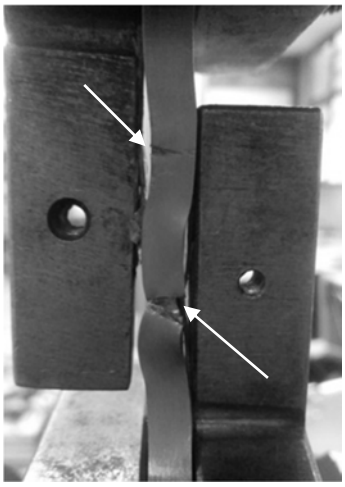

Figure 4.95 – Deformed shape of a smooth plane specimen after ULCF tests.

4.4.2 Fatigue damage models re-evaluation

Based on the numerical simulations carried out on the smooth plane specimens with the lateral instabilities, the performance of the fatigue damage models described above are assessed again. The smooth plane specimens were re-analysed and the equivalent plastic strain range was computed at the critical location taking into account the effect of the lateral instability. Concerning the numerical results of the notched specimens, the same values for the equivalent plastic strain ranges were assumed from previous calculations. In addition, the numerical data of flat-grooved specimens of X60 piping steel was considered in this analysis aiming at verifying the influence of the monotonic ductile fracture on fatigue life predictions under large levels of plastic deformations. In this way, updated model parameters were computed for the Coffin-Manson relation and improved fatigue life predictions regarding to smooth plane specimens were obtained using the parameters of the Xue model, assessed in the previous section.

4.4.2.1 Fatigue life assessment of the X52 piping steel

After the computation of the equivalent plastic strain by mean of the numerical simulations of smooth plane specimens, the overall results of X52 small-scale tests were correlated again in Figure 4.96 and new Coffin-Manson parameters were obtained and presented in the Table 4.16. This procedure results in better correlation of overall data points as supported by the increase of the determination coefficient. Moreover, the fatigue life

predictions using the updated Coffin-Manson relation were also improved as shown in Figure 4.97. However, some deviations are still verified on fatigue life estimations for the smooth plane specimens which are expected to be solved with the application of the model proposed by Xue. The equivalent plastic strain amplitude computed for the smooth specimens taking into account the instabilities are plotted in Figure 4.98.

Table 4.16 – Updated Coffin-Manson parameters obtained for X52 piping steel.

ε'_f	c	R^2
1.0058	-0.6462	0.9664

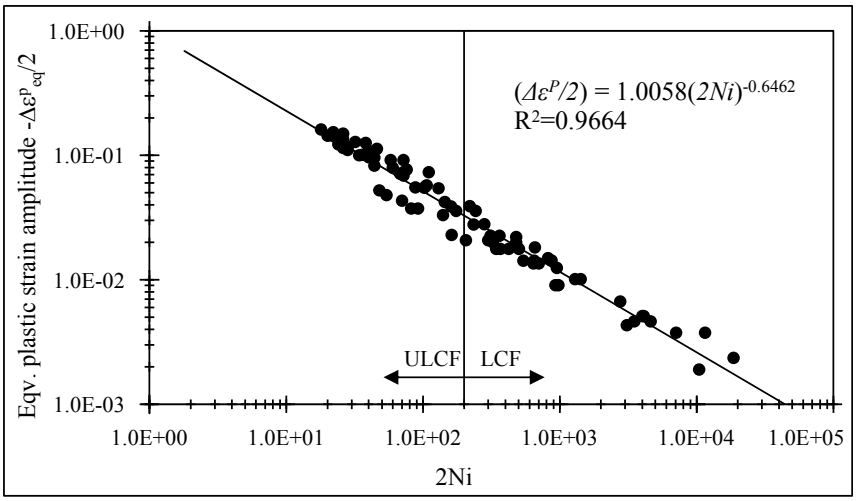

Figure 4.96 – Equivalent plastic amplitude *versus* number of reversals obtained for small-scale data of X52 piping steel, including the updated results from the smooth plane specimens.

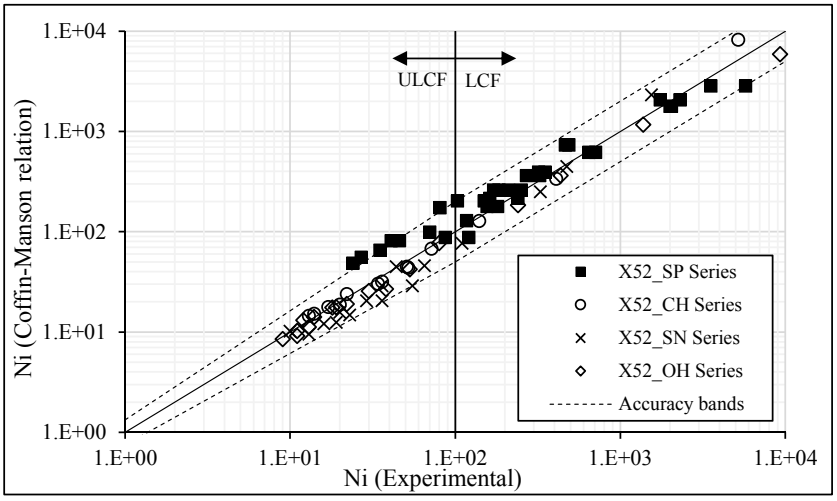

Figure 4.97 – Comparison of experimental data and Coffin-Manson results obtained for the X52 piping steel, including the numerical results from smooth plane specimens considering lateral instabilities.

The parameters of Xue model were computed previously, since no modifications are required for the definition of the trend line of this fatigue model. Comparisons between experimental results and Xue model predictions are presented in the Figure 4.99. In general, good predictions are attained with Xue model for both ULCF and LCF regime, including the data points of smooth plane specimens. The performance of the Coffin-Manson relation and Xue model taking into account the numerical simulations with lateral instabilities is investigated from the analysis of Figure 4.100. In contrast to the first approach, where the smooth plane specimens were simulated following the ideal boundary conditions, the new fatigue data from the simulation of the smooth specimens taking into account the instabilities are in close agreement with the prediction line.

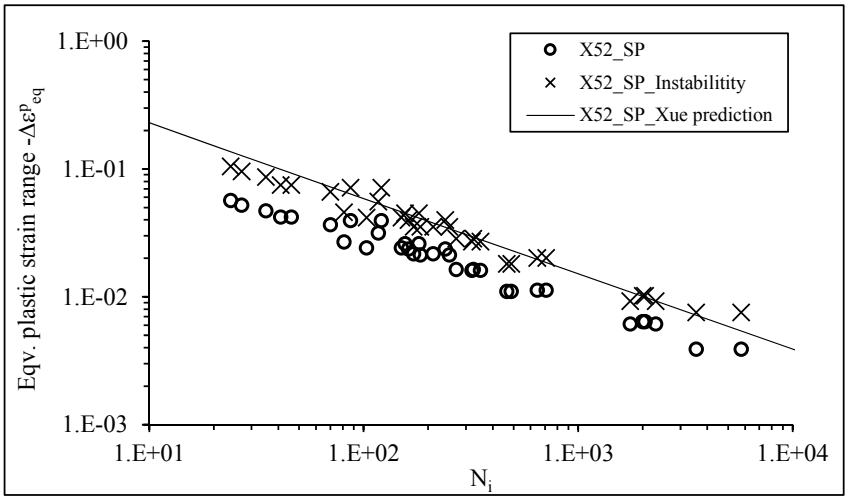

Figure 4.98 – Comparison of equivalent plastic range *versus* number of cycles resulted for the smooth plane specimens of X52 piping steel, with and without lateral instabilities.

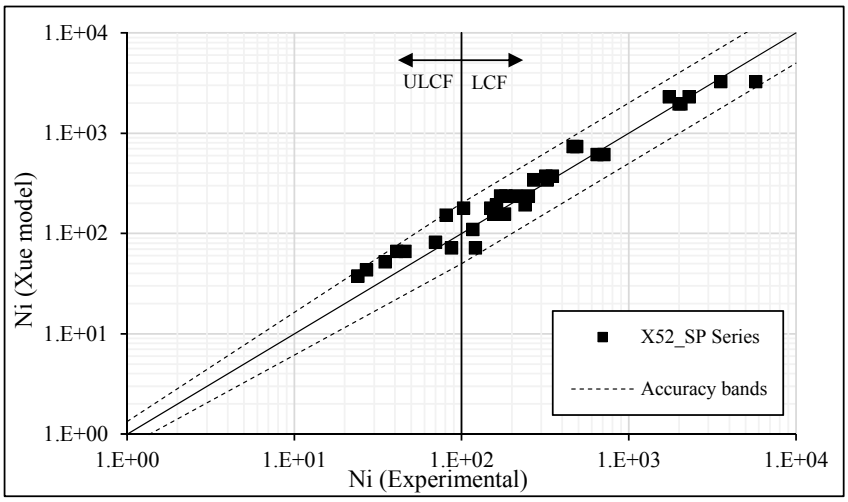

Figure 4.99 – Comparison of experimental data and Xue model resulted for the smooth plane specimens with lateral instabilities of X52 piping steel.

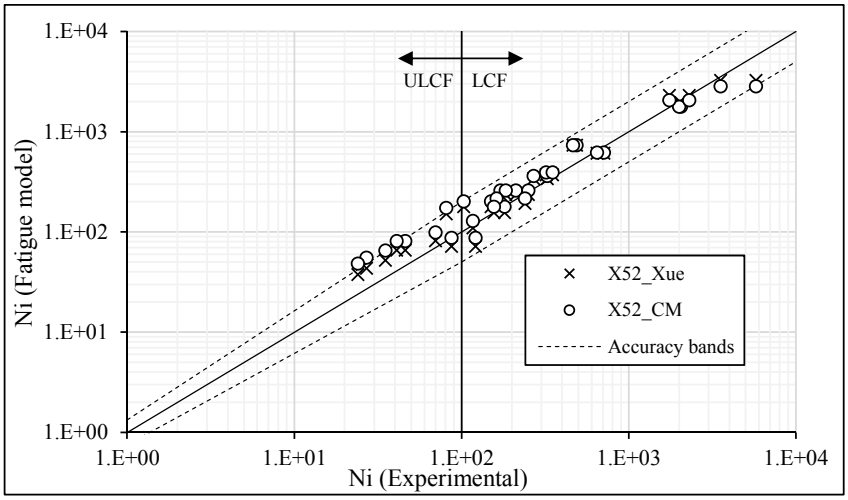

Figure 4.100 – Comparison of experimental data and fatigue damage models predictions obtained for smooth plane specimens of X52 piping steel.

4.4.2.2 Fatigue life assessment of the X60 piping steel

In addition to the numerical results of smooth specimens simulated with lateral instabilities the flat-grooved specimen series were also included in this analysis. The use of this specimen series aims at clarifying the influence of the stress triaxiality and Lode angle parameter on fatigue life behaviour under large plastic strain levels for a geometry that exhibited low ductile monotonic behaviour. As verified in the Section 4.2.4 the flat-grooved and plane shear specimens corresponding to plastic plane strain or generalized shear, ($\bar{\theta} = 0$). However, different stress triaxialities levels are assumed for flat-grooved and plane shear specimens, as observed in Table 4.1. The plane-shear specimens shows a stress triaxiality close to 0, while the triaxiality of flat-grooved specimens is within the range of values obtained for the remaining specimen series. Consequently, the numerical data of flat-grooved specimens will be included to obtain the updated parameters of Coffin-Mason relation and fatigue life prediction for these specimens will be performed by the Xue model previously calibrated. Comparison between numerical and experimental hysteresis cycles for a flat-grooved specimen is illustrated in Figure 4.101. The correlation of numerical and experimental response, allow to validate the use of numerical models for the cyclic simulations of flat-grooved specimen series. Figure 4.102 displays the equivalent plastic strain amplitude *versus* the number of cycles on a log-log scale of global results of X60 piping steel with and without thermal treatment. These results include the data points relative to the flat-grooved specimen series. The parameters of the Coffin-Manson relation

achieved from this analysis are expressed in Table 4.12. Fatigue life predictions were performed and compared with the experimental data in Figure 4.103 and Figure 4.104, for the base material and the material subjected to the thermal cycle, respectively. The analysis of previous results shows that Coffin-Manson relation produces satisfactory fatigue life predictions, after simulating the lateral instability of the smooth plane specimens.

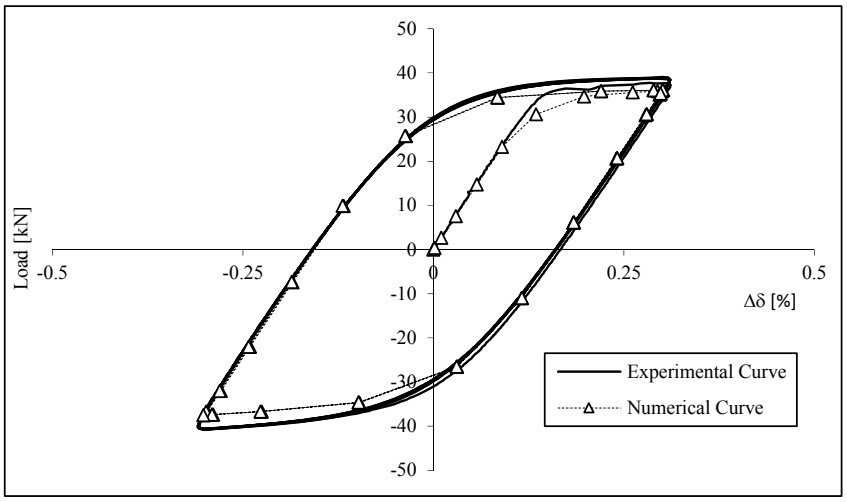

Figure 4.101 – Load-relative displacement hysteresis cycles including numerical response obtained for the U-1_FG_08 specimen of X60 piping steel.

Table 4.17 – Coffin-Manson parameters obtained for the X60 piping steel, with and without thermal treatment.

	ε_f	c	R^2
X60	1.3954	-0.7016	0.9313
X60TT	1.4096	-0.7370	0.9894

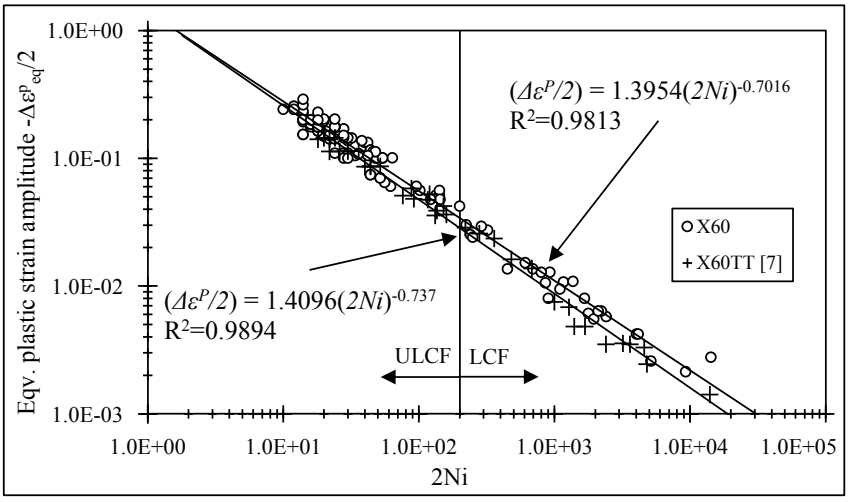

Figure 4.102 – Equivalent plastic amplitude *versus* number of reversals obtained for small-scale specimens of X60 piping steel, with and without thermal treatment, including the numerical results with lateral instability.

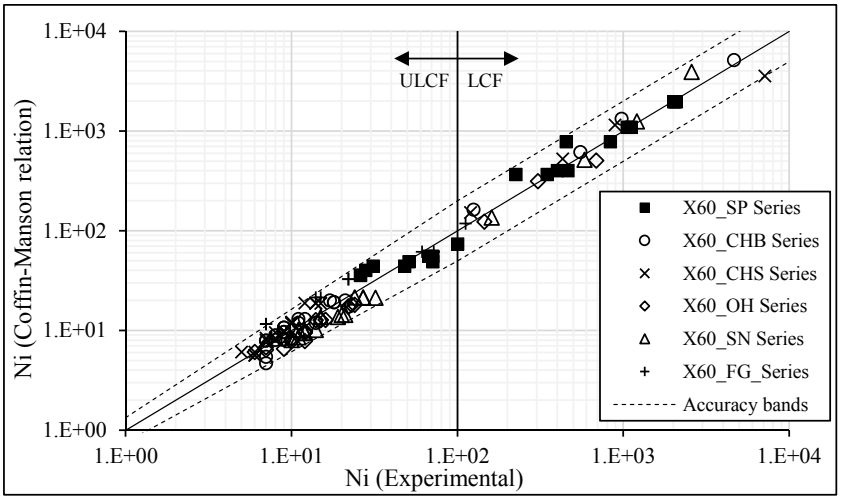

Figure 4.103 – Comparison of experimental data and Coffin-Manson relation for the X60 piping steel, including the numerical results with lateral instability and the flat-grooved specimen series.

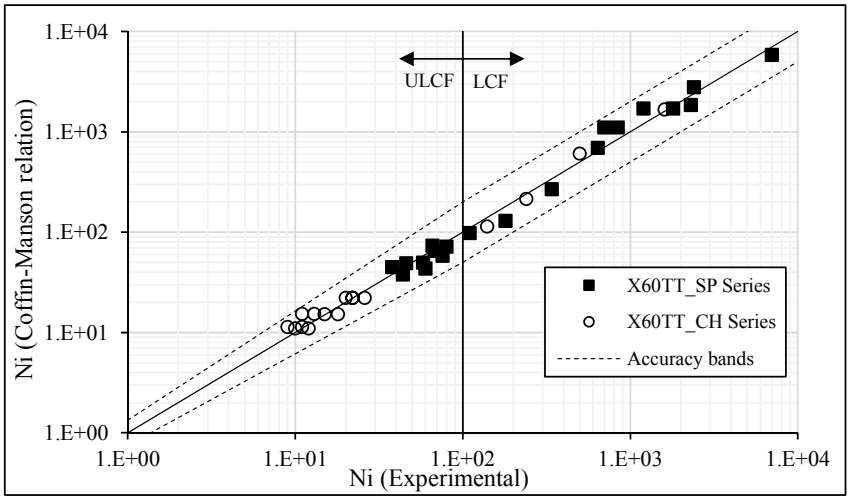

Figure 4.104 – Comparison of experimental data and Coffin-Manson relation obtained for the X60 piping steel, with thermal treatment, including the numerical results of smooth plane specimens with lateral instability.

The comparisons of the simulated S-N lines of the Xue model and the data points of smooth specimens and flat grooved specimens are illustrated in Figure 4.105 to Figure 4.107. As observed, the data points relative to the numerical simulations with lateral instability are closer to the prediction Xue lines. A good correlation is also observed between the data points of flat-grooved specimens and the prediction line given by the Xue model. As referred previously, the fracture strain of the flat-grooved specimens ($\bar{\varepsilon}_f$=1.015) used in Xue model formulation was derived from the monotonic simulation at the stress conditions where the fatigue crack occurs. The parameters of Xue model were computed before, since no modifications are required for the definition of the trend line of this fatigue model. These

results are reflected on the good fatigue life estimations illustrated in the Figure 4.108 and Figure 4.109, for the material without and with thermal treatment. Taking into account the reproduction of lateral instabilities on the cyclic simulations of smooth plane specimens, both Coffin-Manson relation and Xue model produce satisfactory fatigue life estimations. Figure 4.110 compares the performance of the fatigue models investigated in this study taking into account the flat-grooved specimen series only since this specimen geometry showed the most distinct monotonic ductile fracture strain, in the lower bound ductility. Both Coffin-Manson relation and Xue model provided good results. However, the analysis of Figure 4.110 reports a better performance of the Xue model. In fact, the data points derived from this model, mainly for reduce fatigue lives, are closer to the reference line (solid black line).

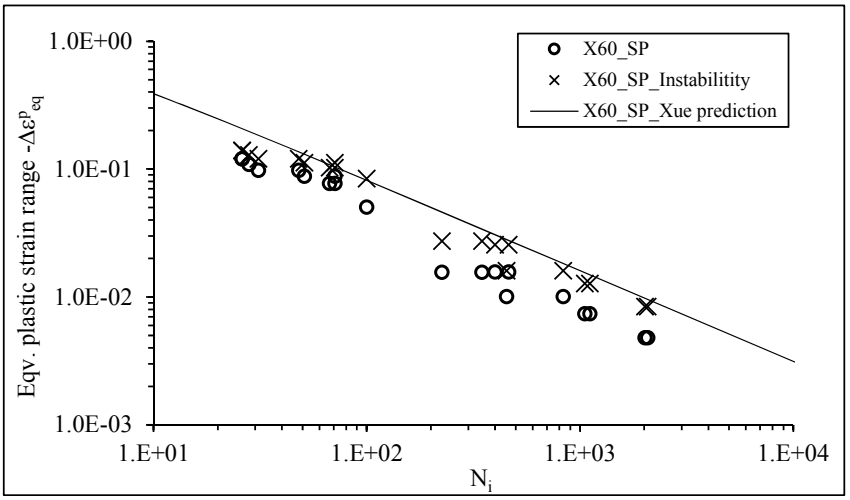

Figure 4.105 – Comparison of equivalent plastic range *versus* number of cycles obtained for the smooth plane specimens of X60 piping steel with and without lateral instabilities.

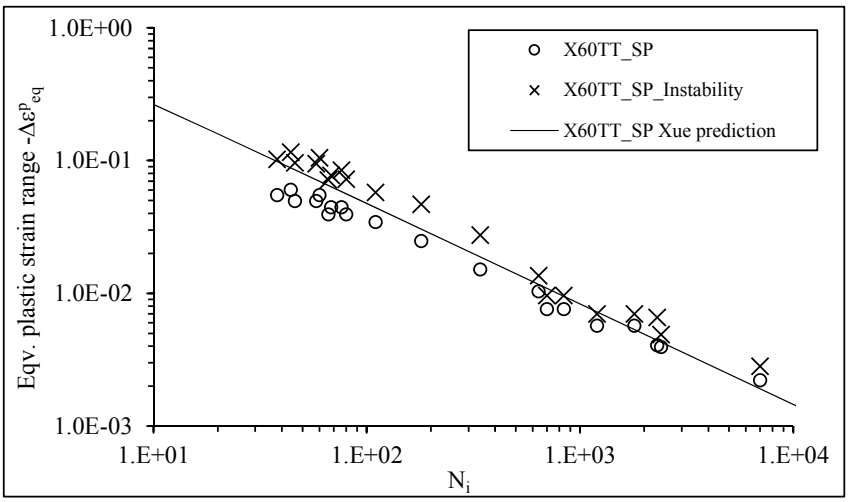

Figure 4.106 – Comparison of equivalent plastic range *versus* number of cycles obtained for smooth plane specimens of X60 piping steel, with thermal treatment, with and without lateral instabilities.

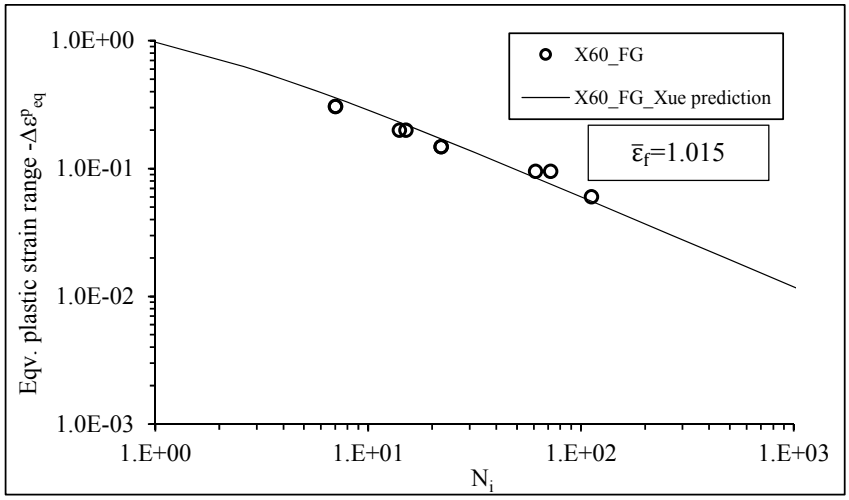

Figure 4.107 – Comparison of equivalent plastic range *versus* number of cycles of flat-grooved specimens of X60 piping steel.

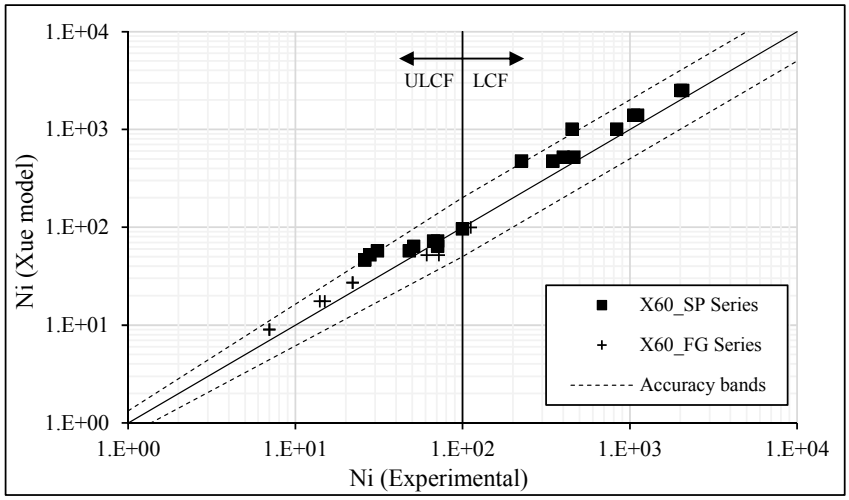

Figure 4.108 – Comparison of experimental data and Xue model predictions obtained for the smooth plane and flat-grooved specimens of X60 piping steel with lateral instability simulation.

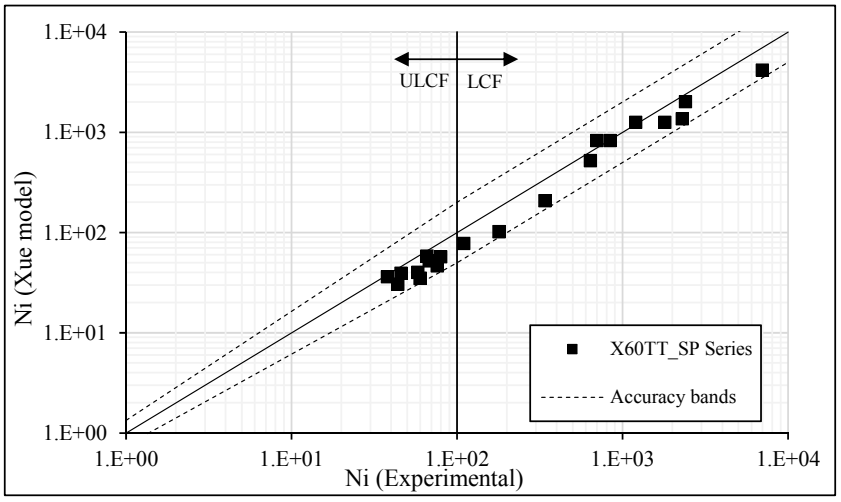

Figure 4.109 – Comparison of experimental data and Xue model predictions for the smooth plane specimens of X60 piping steel, with thermal treatment, with lateral instability.

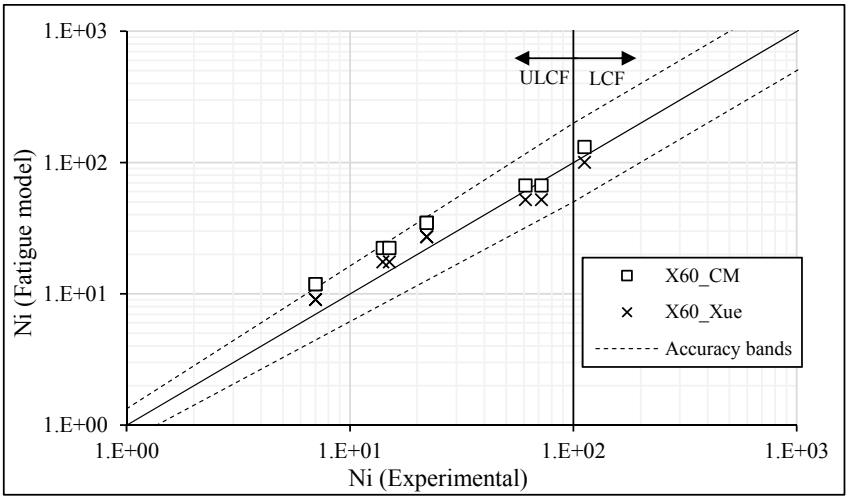

Figure 4.110 – Comparison of experimental data and fatigue damage model predictions for flat-grooved specimens of X60 piping steel.

As exposed along this work, the fatigue life predictions obtained using the Xue model are dependent of the fracture strain (see Table 4.13), which has been measured from the monotonic simulations at the node that reaches the conditions for crack initiation, when this specimen is subjected to cyclic loading. As previously referred, this parameter measures the total deformation capacity for a particular location when this specimens is subjected to a static loading. Nevertheless, some limitations can be appointed with this methodology. Besides the already referred potential discrepancy between the fatigue and monotonic crack initiation locations, it is always required to perform monotonic tensile tests on the specimens covered in the fatigue tests. Also, performing monotonic tests may be not feasible for a particular geometry or loading condition such as bending tests on smooth plane specimens which may not exhibit a clear failure. For large-scale applications the determination of fracture strain may bring also some difficulties, concerning both economical aspects as well as the difficulty to capture the same failure locations in both cyclic and monotonic loading. The impossibility to get ductile failure under certain loading conditions may also apply in such cases (e.g. bending of a pipe). Based on these assumptions a new approach for the application of Xue model is now proposed. With this formulation the fatigue tests and the monotonic tests may no longer be based on the same specimens' geometries. The monotonic tests may be optimized to generate the failure locus for a sufficient domain of stress triaxialities and Lode angle parameters. The use of reference monotonic tensile tests allow the identification of a reliable fracture locus, in particular the lower and upper bounds. This fracture locus needs to cover the triaxialities and Lode angle parameters expected in the fatigue tests, where fatigue cracks are likely to

occur. In detail, the computation of the fracture strain will be dependent of the stress triaxiality and Lode angle parameter at the end of tensile loading path which corresponds to the growth or expansion of the microvoids [18]. The stress state parameters are plotted against the equivalent plastic strain range in Figure 4.111 for different tested specimens. These parameters assumes a nearly constant behavior independently of the applied levels of equivalent plastic strain ranges, therefore average values for these parameters were considered. The 3D fracture surface previously calibrated by means of monotonic tensile tests of X60 piping steel will be used to estimate the fracture strain for each specimen geometry at the fatigue crack location. The average stress triaxiality and Lode angle parameter computed along the cyclic simulations and the fracture strain computed using the calibrated 3D ductile surface are summarized in the Table 4.18. The distribution of these parameters on the 3D fracture surface can be observed in the Figure 4.112. In order to investigate the influence of the triaxiality and Lode angle parameter on ductile monotonic fracture and fatigue failure, the stress triaxiality and Lode angle parameters were compared by plotting the results obtained with cyclic simulations against the values achieved from monotonic simulations, as illustrated in the Figure 4.113. In general, no modifications are observed when we move from monotonic ductile domain to the elastoplastic cyclic regime, with the exception regarding the triaxiality of the smooth plane specimen. On effect, the necking effect observed during the monotonic tensile tests promotes significant modifications on multiaxial state leading to the increase of the triaxiality (η_{av}=0.63). In the case of cyclic loading the triaxiality assumes the typical value of smooth plane specimens (η_{av}=0.33) since the necking effect is not achieved.

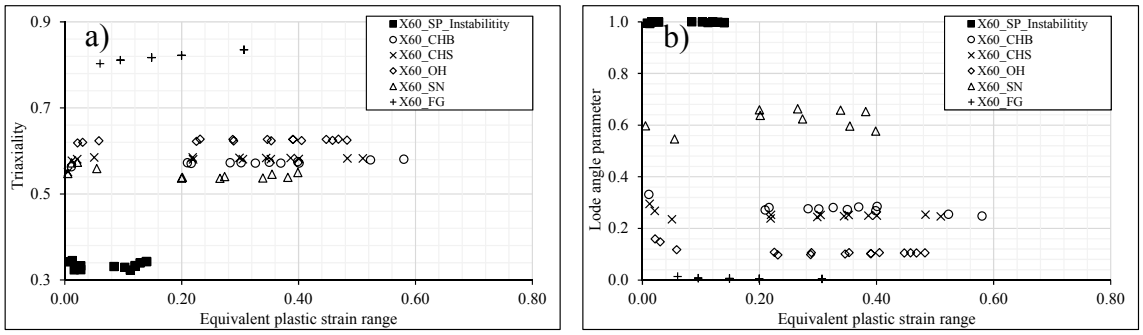

Figure 4.111 – Evolution of stress triaxiality (a) and lode angle parameter (b) as a function of equivalent plastic strain range.

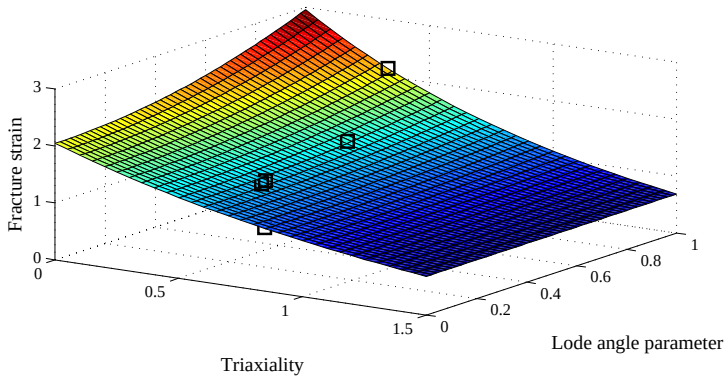

Figure 4.112 – 3D fracture surface of the X60 piping steel with data characterizing the small-scale cyclic tests.

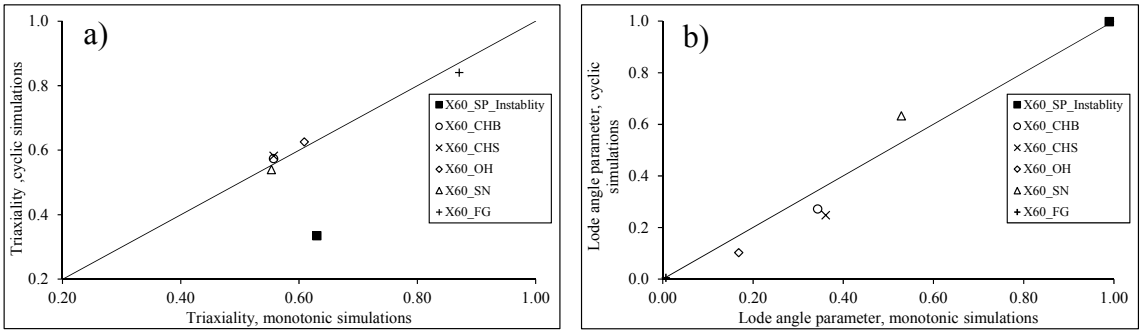

Figure 4.113 – Comparisons between stress triaxiality (a) and lode angle parameter (b) computed from monotonic and cyclic simulations.

Table 4.18 – Average stress triaxiality and Lode angle parameter obtained from cyclic simulations and fracture strain computed from the 3D fracture surface.

Specimen series	***3D fracture surface***	***Cyclic loading simulations***	
	$\bar{\varepsilon}_f$	η_{av}	$\bar{\theta}_{av}$
SP	2.14	0.33	1.00
CHB	1.37	0.57	0.27
CHS	1.36	0.58	0.25
OH	1.29	0.63	0.10
SN	1.52	0.54	0.63
FG	1.10	0.84	0.01

Figure 4.114 illustrates the equivalent plastic strain as a function of the number of cycles to macroscopic crack initiation for smooth and notched plane specimens and including the flat grooved specimens, correlated with prediction lines of Xue model, using updated fracture strains. The prediction lines of Xue model are now dependent of the fracture strain which is computed by means of 3D ductile fracture surface for the fatigue crack initiation location. The resulting m and λ parameters were modified to m=0.5 and λ=1.35 in order to update the correlations. Based on these parameters fatigue life estimations were compared with the experimental data as represented in the Figure 4.115. In general, satisfactory life estimations are attained with this new approach.

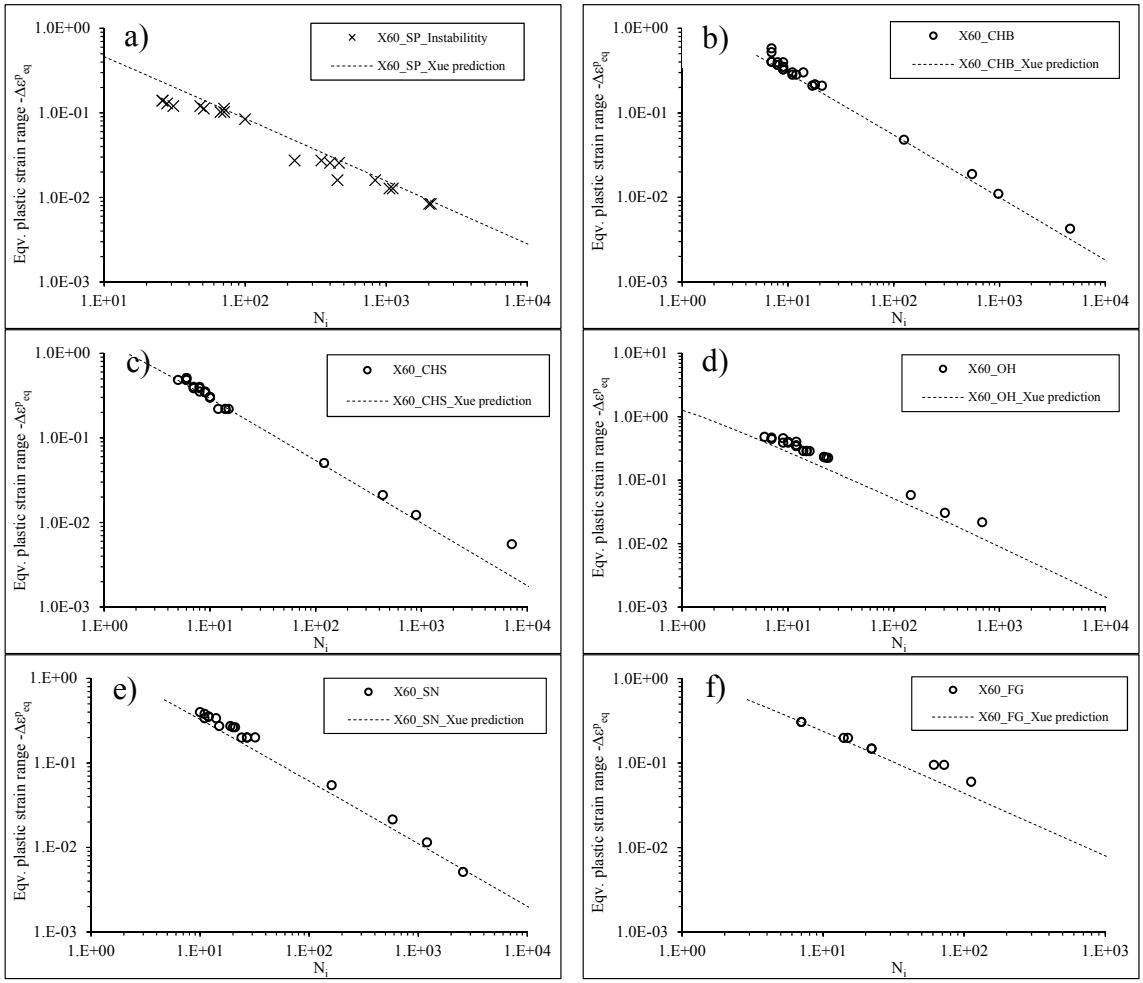

Figure 4.114 – Equivalent plastic range *versus* number of cycles to crack initiation for small-scale specimens of X60 piping steel: a) SP series: b) CHB series; c) CHS series; d) OH series; e) SN series; f) FG series.

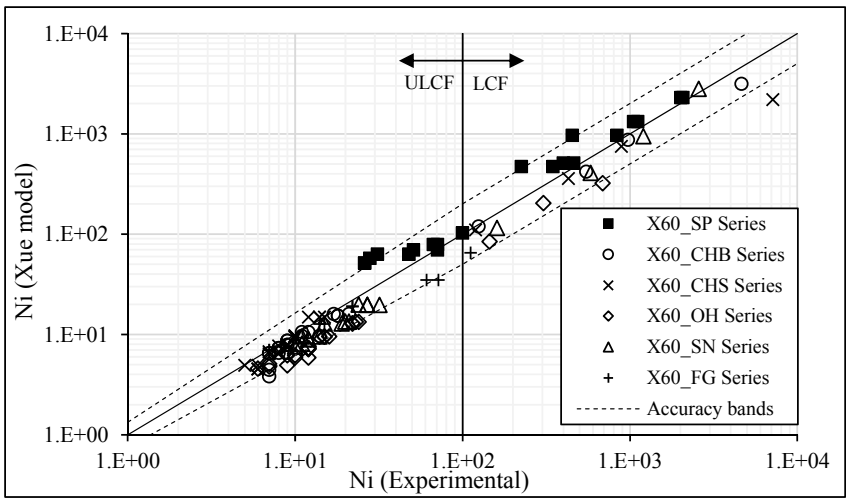

Figure 4.115 – Comparison of experimental data and Xue model predictions for the X60 piping steel, using fracture strains computed directly from the ductile fracture locus.

The influence of stress state parameters, namely the stress triaxiality and Lode angle parameters can be better understood considering a particular case of the round bar specimen. The typical values of the stress state parameters under a cyclic loading (η_{av}=0.33 and $\bar{\theta}_{av} = 1$ were considered to determine the number of cycles according to the Xue model formulation. Figure 4.116 illustrates the evolution of the equivalent plastic strain range against the number of cycles proposed by the Xue model formulation. The square mark pointed in the graph defines an equivalent plastic strain range, $\Delta\varepsilon^{P}_{eq}$=0.5 and a number of cycles, N_i=6 cycles that will be used to normalize a 3D surface which relates the number of cycles with the stress triaxiality and the Lode angle parameter, as represented in the Figure 4.117. This procedure aiming at investigating the influence of the stress state parameters on the fatigue behavior of ductile metals for a specific equivalent plastic strain range. The number of cycles for each stress state were computed using the Xue model, since it gives the dependency of the fatigue life from the monotonic fracture strain, which in turn depends on the stress state parameters. As expectable this fatigue life surface exhibits a similar aspect to the 3D ductile surface proposed by BW model. The fatigue life reduces with increasing triaxiality and decreasing Lode angle parameter. Based on these assumptions a new methodology for the identification of typical strain-life curves are proposed. Figure 4.118 and Figure 4.119 illustrate the strain-life surfaces which take into account the effect of the triaxiality and the Lode angle parameter, respectively. The analysis of both figures reports two clarifications concerning the level of the equivalent plastic strain range. In fact, for high plastic strain levels, $\Delta\varepsilon^{P}_{eq}$>0.3, the strain-life surface is less sensitive to the stress parameters, while for equivalent plastic strain ranges lower than $\Delta\varepsilon^{P}_{eq}$<0.3 the effect of the triaxiality and Lode angle parameter are more noticeable. The stress state parameters progressively controls the admissible fatigue life domain being identified the upper and lower bound limits regarding to the fatigue resistance of the material. However, these influences of the stress parameters on the strain-life relation are being discussed in terms of the absolute values of the fatigue lives, but a small variation in the number of cycles for the ULCF domain may represent a very high relative variation in terms of the fatigue lives. Fixing an interval for the equivalent plastic strain range, the domain of the number of fatigue cycles narrows significantly with the increase of the triaxiality and Lode angle parameter. For a particular case of η=0.33 and $\bar{\theta} = 1$ the interval of the number of cycles is N_i= [9-528] cycles, in contrast for η=1.3 and $\bar{\theta} = 1$ the range of fatigue life is N_i= [2-147] cycles. The same analysis may be performed for the Lode angle parameter, which

shows a similar influence on the cyclic behavior of the ductile metals. For the plane strain or generalized shear $\bar{\theta} = 0$ and η=0.33 the admissible number of cycles is N_i= [6-482] cycles, while for the axial symmetry in tension $\bar{\theta} = 1$ and η=0.33 the fatigue life is within the following range N_i= [9-714] cycles. The life intervals previously referred corresponded to an applied plastic strain range of $\Delta\varepsilon^P$= [0.02-0.5]. A very significant influence of the stress parameters on the number of fatigue cycles is verified for the referred applied strain range.

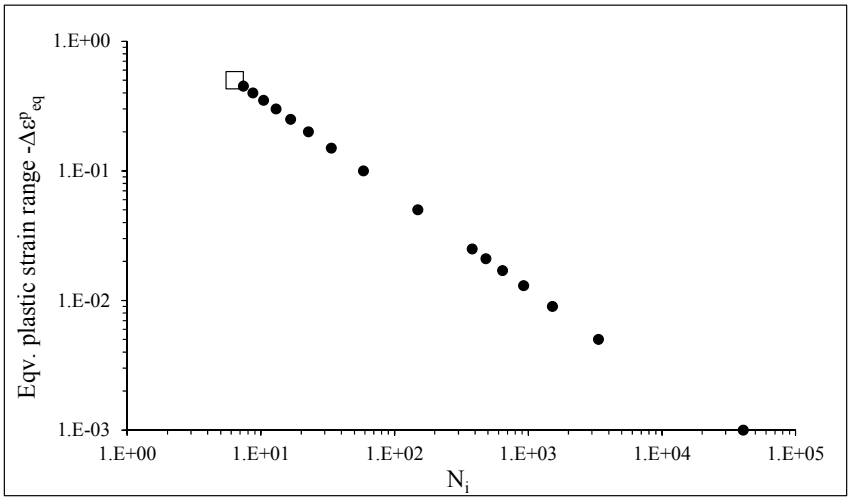

Figure 4.116 – Equivalent plastic strain range *versus* number of cycles for the X60_RB specimen predicted accordingly the Xue model formulation.

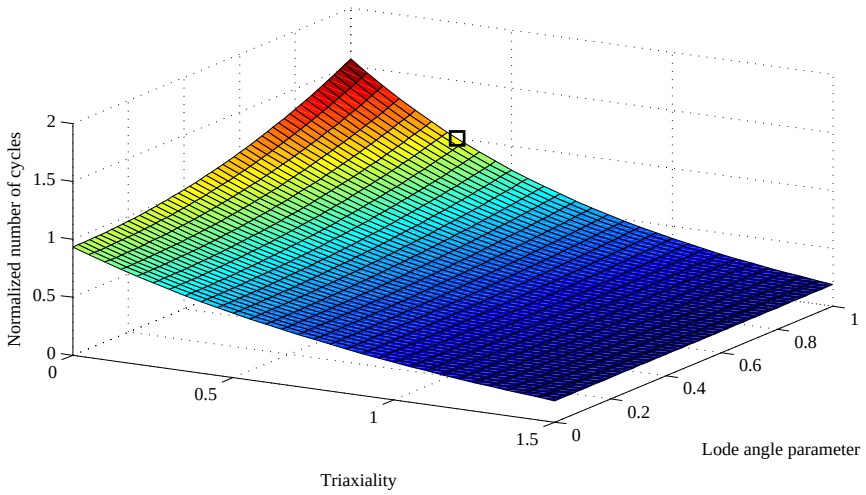

Figure 4.117 – Normalized 3D fatigue surface, dependent of the stress state parameters.

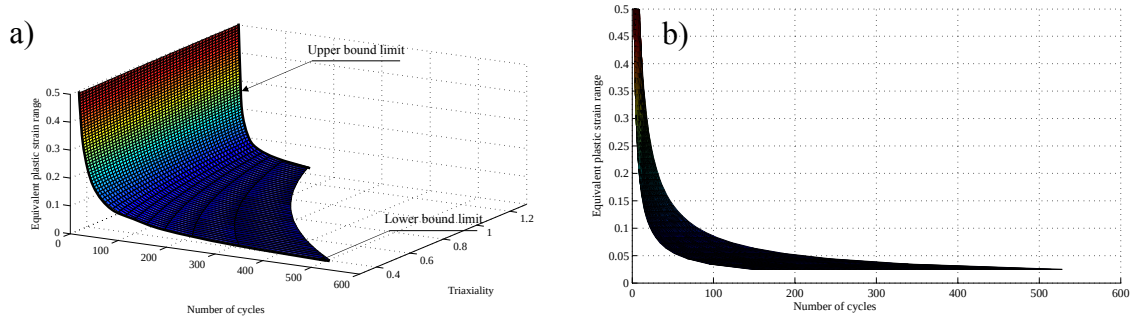

Figure 4.118 – Strain-life surfaces as a function of the stress triaxiality and $\bar{\theta}$=1: a) identification of lower and upper bound limits concerning the triaxiality; b) strain-life field.

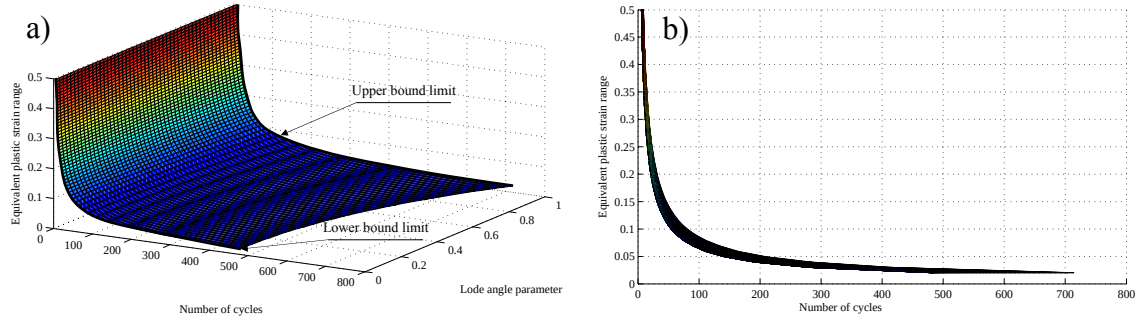

Figure 4.119 – Strain-life surfaces as a function of Lode angle parameter and η=0.33 a) identification of lower and upper bound limits concerning the Lode angle parameter; b) strain-life field.

The consistency of this new fatigue proposal can be checked through the plotting of the experimental strain-life data of the small-scale specimens of X60 piping steel in the strain-life surface, which relates one of the stress parameter the number of cycles and the equivalent plastic strain range. The representation in the same strain-life surface of each specimen series depends on stress state parameter values, one of these parameters should be common to the series, as can be appointed for the specimen series with a central hole (CHS and CHB) that shows a very similar values for the triaxiality. In order to illustrate both series in the $\Delta\varepsilon^{P}_{eq}$-$N_i$-$\bar{\theta}$ space the mean value of triaxiality (η=0.57) was assumed (see Figure 4.120). Furthermore, the results obtained for smooth plane and flat-grooved specimen series were also plotted in the space of $\Delta\varepsilon^{P}_{eq}$-$N_i$-$\bar{\theta}$ and $\Delta\varepsilon^{P}_{eq}$-$N_i$-$\eta$ respectively as observed in the Figure 4.121 and Figure 4.122. In general these representations show a good compromise between the experimental data points and the strain-life surfaces. The process for the fatigue life assessment under different stress/strain conditions presented in this section can be considered as a new methodology, which could be incorporated in the design guidelines. The fatigue dependency on both triaxiality and Lode angle parameters and the interdependency of ULCF damage and material monotonic ductility capacity is

encompassed in a new methodology that is summarized in a step-by-step form in the Table 4.19. This methodology was only fully demonstrated for the X60 steel since the experimental data available was the most complete one.

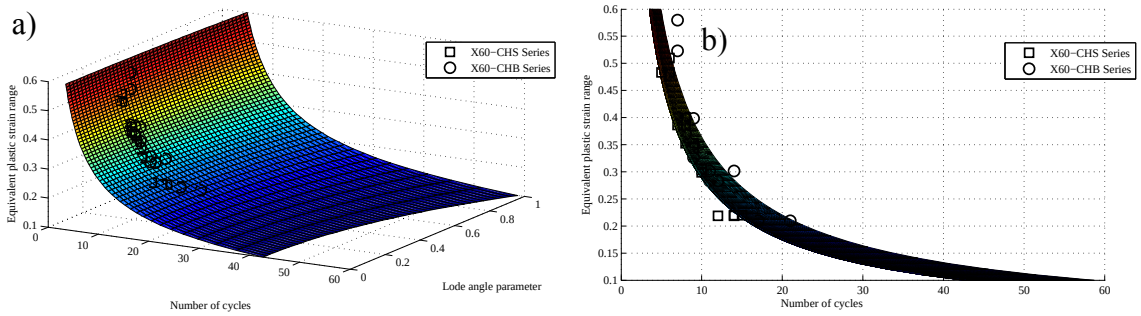

Figure 4.120 – Strain-life surface of notched plane specimen series (CHS and CHB) of X60 piping steel for η=0.575: a) $\Delta\varepsilon^{P}_{eq}$-$N_i$-$\bar{\theta}$ space; b) $\Delta\varepsilon^{P}_{eq}$-$N_i$ plane.

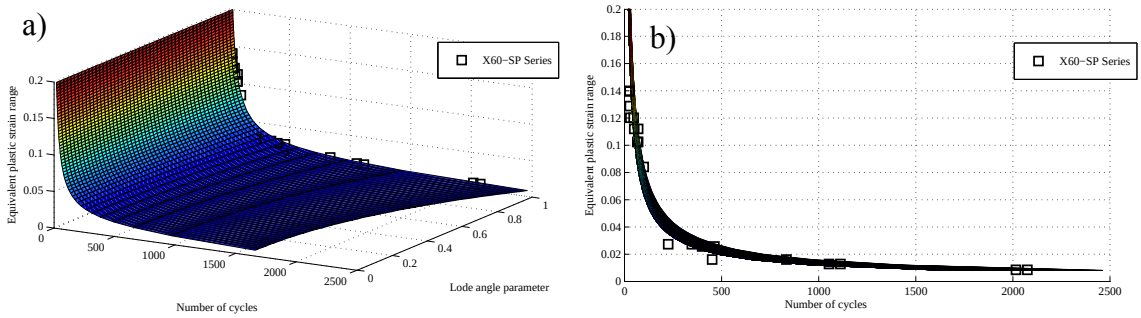

Figure 4.121 – Strain-life surface of smooth specimen series of X60 piping steel for η=0.33: a) $\Delta\varepsilon^{P}_{eq}$-$N_i$-$\bar{\theta}$ space; b) $\Delta\varepsilon^{P}_{eq}$-$N_i$ plane.

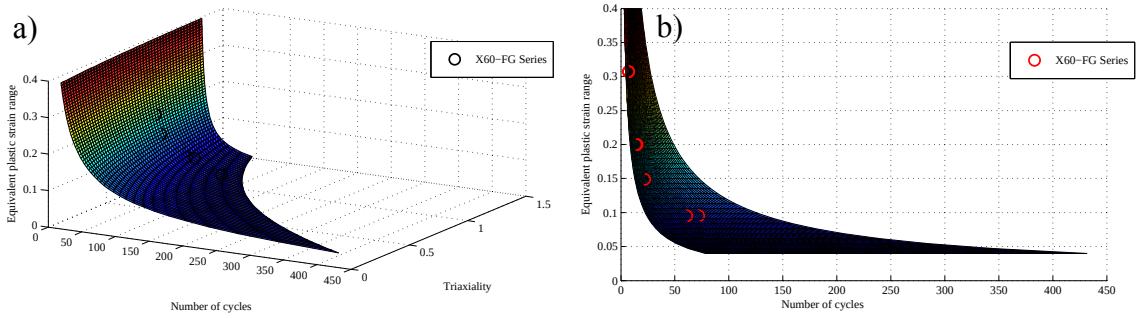

Figure 4.122 – Strain-life surface of flat-grooved specimen series of X60 piping steel for $\bar{\theta}$=0: a) $\Delta\varepsilon^{P}_{eq}$-$N_i$-$\eta$ space; b) $\Delta\varepsilon^{P}_{eq}$-$N_i$ plane.

Table 4.19 – Methodology for the application of BW-Xue model for the fatigue life assessment under large plastic strain conditions.

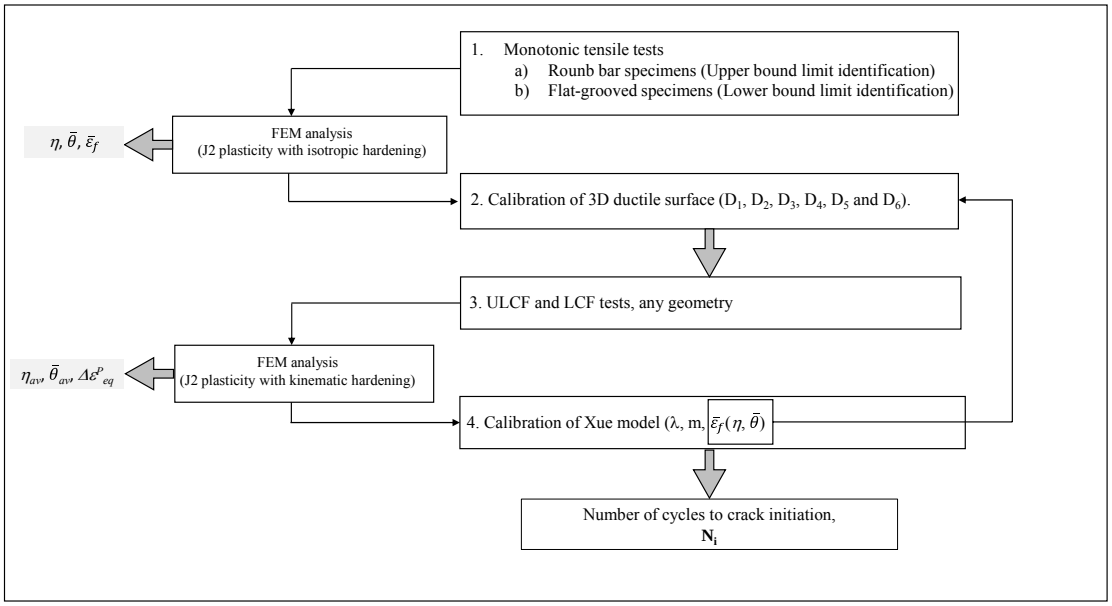

4.4.2.3 Fatigue life assessment of the X65 piping steel

Figure 4.123 illustrates the relationship between the equivalent plastic strain amplitude and the number of reversals obtained for the X65 piping steel without and with thermal treatment, resulting the Coffin-Manson parameters. The strain results already includes the simulation of the lateral instabilities observed in the smooth plane specimen testing (see Table 4.20). The analysis of this figure reports some scatter, despite some acceptable determination coefficients being observed for both testing series.

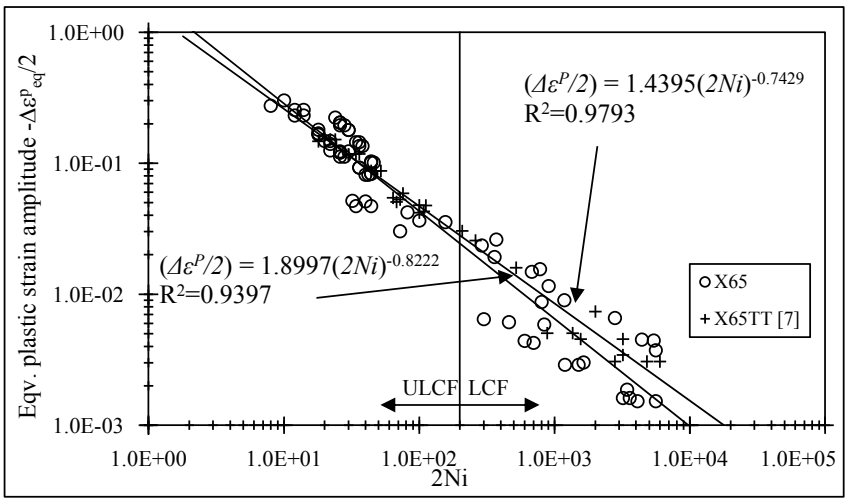

Figure 4.123 – Equivalent plastic amplitude *versus* number of reversals of small-scale specimens made of X65 piping steel, with and without thermal treatment, including lateral instabilities.

Table 4.20 – Coffin-Manson parameters obtained for X65 piping steel, with and without thermal treatment.

	ε'_f	c	R^2
X65	1.8997	-0.8222	0.9397
X65TT	1.4395	-0.7429	0.9793

The numerical predictions obtained with Coffin-Manson relation for X65 piping steel without and with thermal treatment are shown in Figure 4.124 and Figure 4.125 respectively, taking into account that the results of smooth specimens were simulated with the reproduction of the lateral instabilities. As verified for the X60 piping steel, significant improvements are obtained when the equivalent plastic strain is computed accounting for the lateral instabilities. However, these improvements are not sufficient to result the most satisfactory results, mainly for SP and SN series.

Comparisons between experimental results and Xue model predictions are illustrated in Figure 4.126 and Figure 4.127. It should be referred that the prediction lines of the Xue model were kept constant, since the parameters of Xue model including the fracture strain of smooth plane specimens were not modified. As verified, the limitations of Coffin-Manson relation are overcame when the equivalent plastic strain range is addressed from the elastoplastic simulations of smooth plane specimens with the introduction of the lateral movements of the actuator. Based on these results, good fatigue life predictions are expected with the use of Xue model. Figure 4.128 and Figure 4.129 evidences the performance of each fatigue model investigated in this work. On the one hand similar results were attained with both models for the material subjected to the thermal treatment. On the other hand, the Xue model provides the better fatigue life estimations for the base material. For this material, the influence of the monotonic fracture strain was helpful to improve the performance of the Xue model.

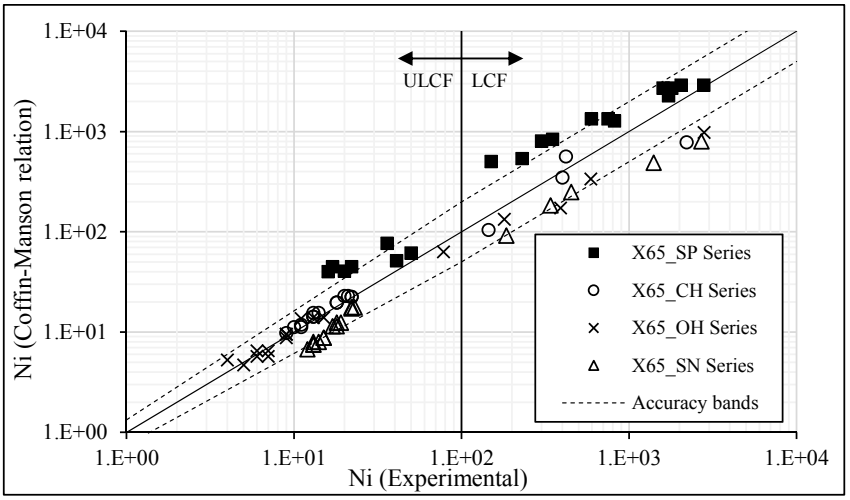

Figure 4.124 – Comparison of experimental data and Coffin-Manson predictions resulted for the X65 piping steel, including the numerical results with lateral instabilities.

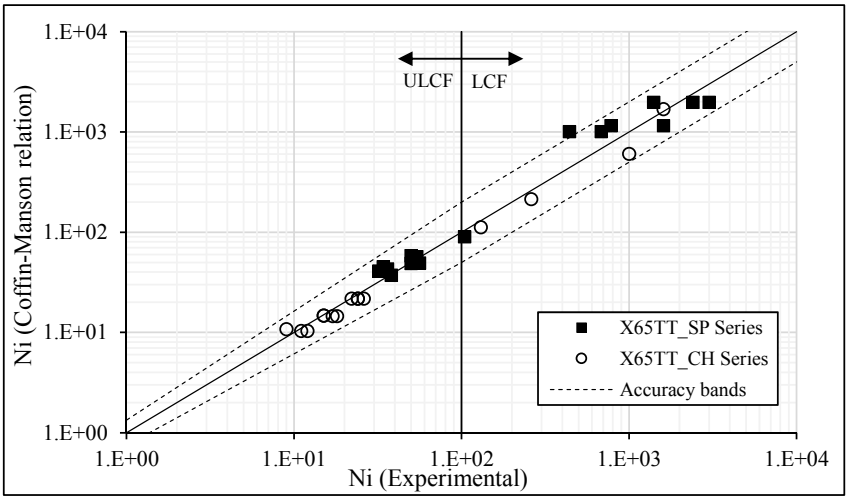

Figure 4.125 – Comparison of experimental data and Coffin-Manson predictions obtained for the X65 piping steel, with thermal treatment including the numerical results of smooth plane specimens with lateral instabilities.

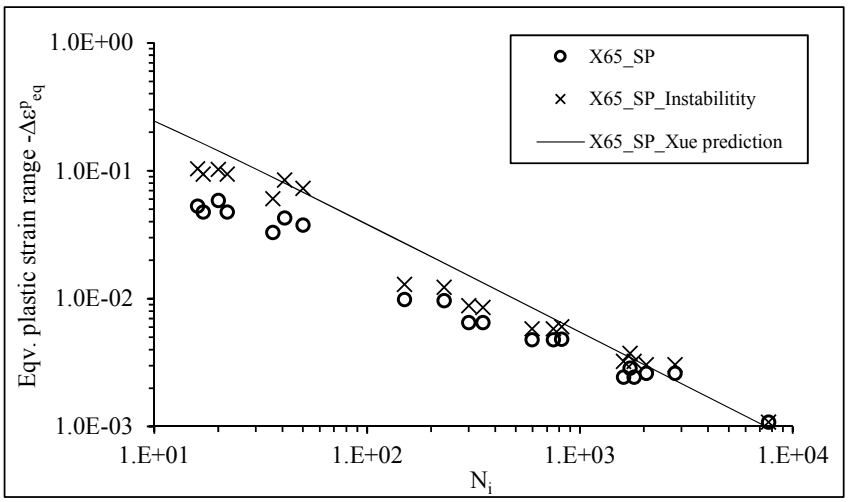

Figure 4.126 Equivalent plastic range *versus* number of cycles obtained for the smooth plane specimens with and without lateral instabilities of X65 piping steel (experimental data and Xue model predictions).

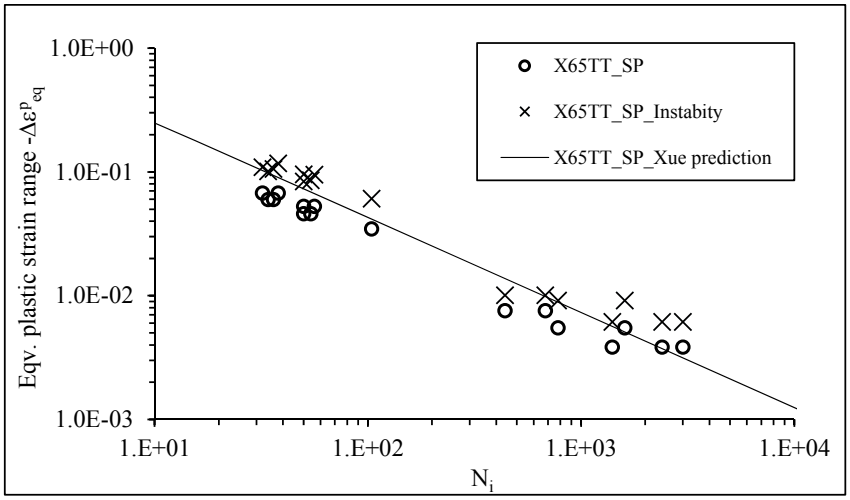

Figure 4.127 – Comparison of experimental data and Xue model predictions obtained for the smooth plane specimens of X65 piping steel, with thermal treatment, accounting for lateral instabilities.

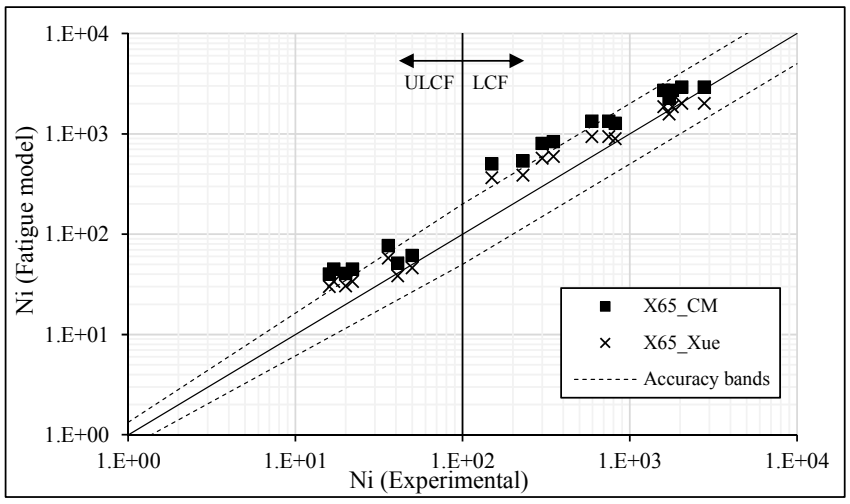

Figure 4.128 – Comparison of experimental data and fatigue damage models predictions for the smooth plane specimens of X65 piping steel.

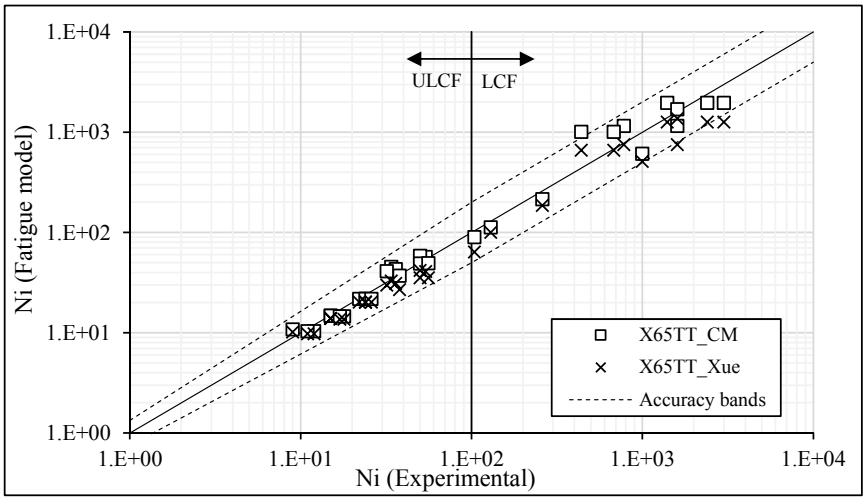

Figure 4.129 – Comparison of experimental data and fatigue damage models predictions for smooth plane specimens of X65 piping steel, with thermal treatment.

4.5 METHODOLOGY FOR ULCF DATA REDUCTION USING LOCAL BOUNDARY CONDITIONS

The identification of the parameters involved in the damage models requires a compromise between numerical and experimental approaches, since the necessary stress/strain parameters cannot be computed uniquely by experimental measurements. Thanks to the full-field optical techniques it is possible to generate global as well as local testing information in order to calibrate the numerical models. Additionally, in terms of large plastic deformations, as occurred in monotonic and ULCF loading, non-contact optical methods are advantageous over point-wise contact counterpart techniques such as strain gauges and extensometers due to their physical limitations [19].

The use of notched plane specimens on ULCF tests emerged as an effective alternative to the smooth plane specimens, since the notch presence contributes to the instability reduction during the cyclic loading. Furthermore, shorter fatigue lives are attained using notched plane specimens in contrast with the results of smooth plane specimens. However, a finite element analysis to derive the stress/strain histories at the critical locations is always required with the use of notched plane specimens, as mentioned in Chapter III. The use of DIC on the ULCF tests of notched plane specimens allows the development of a new numerical approach. This new approach consists on the application of local boundary conditions obtained from the displacement fields at the region of interest of the specimens, as presented in Figure 4.130a). Only CH and OH series were included in this formulation for the 5 steel grades under investigation (X52, X60, X60TT, X65 and X65TT). The process will be illustrated using only few results in order to keep the description as short as possible.

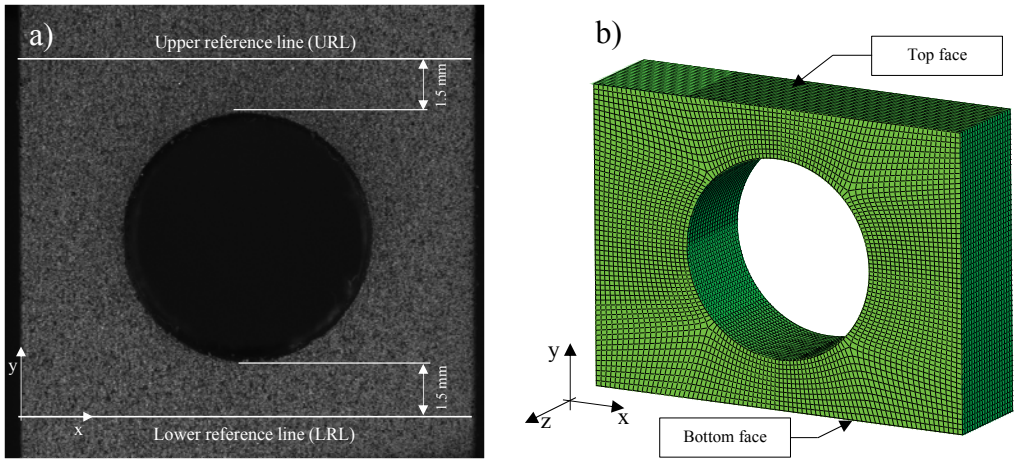

Figure 4.130 – Definition of local boundary conditions for the numerical simulation of notched specimens (CH series): a) region of interest of notched plane specimens delimited by the upper and lower reference lines; b) finite element mesh of notched plane specimens.

Taking into account the field information obtained from DIC it is possible to evaluate the displacements evolution in the loading (U_y) and transversal direction (U_x), along to the reference lines situated 1.5 mm from the notch limit, as illustrated in Figure 4.130a). This two lines define the total height of numerical model, as represented in Figure 4.130b). The numerical models of the specimens were built taking into account uniform conditions along the thickness direction, using 3D solid elements with reduced integration, C3D8R. The transposition of the two displacement components, measured along the URL and LRL to the top and bottom faces of the numerical models was performed by the application of a polynomial function (degree 8), which was fitted to the experimental displacement values measured from the DIC for the total width of specimens. Figure 4.131 and Figure 4.132 reports the experimental data correlated with the numerical fit, for the two displacement components on the URL and LRL, at the stage/image 25. This procedure was carried out for all stages/images, in order to monitor the complete cyclic loading history. It should be noted that the images acquisition was synchronized with tensile/compressive load peaks.

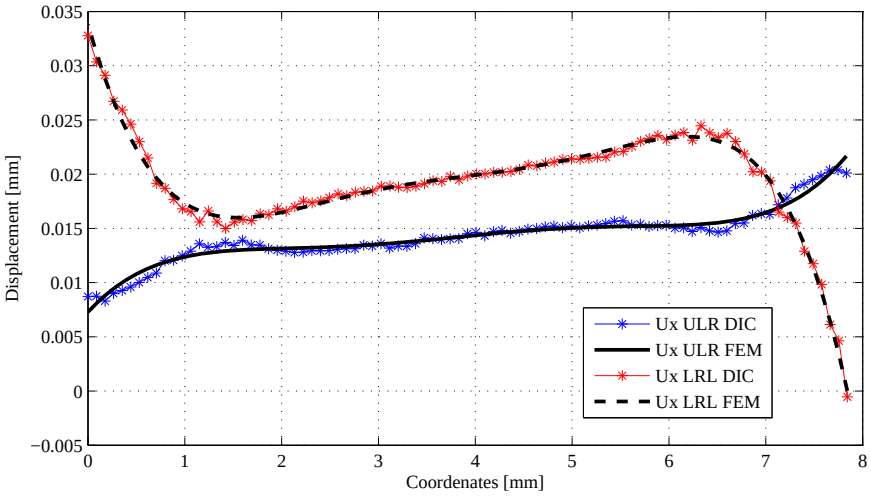

Figure 4.131 – Correlation between *Ux* displacements obtained from DIC and the displacements applied in the numerical model (X65_U0_OH_04).

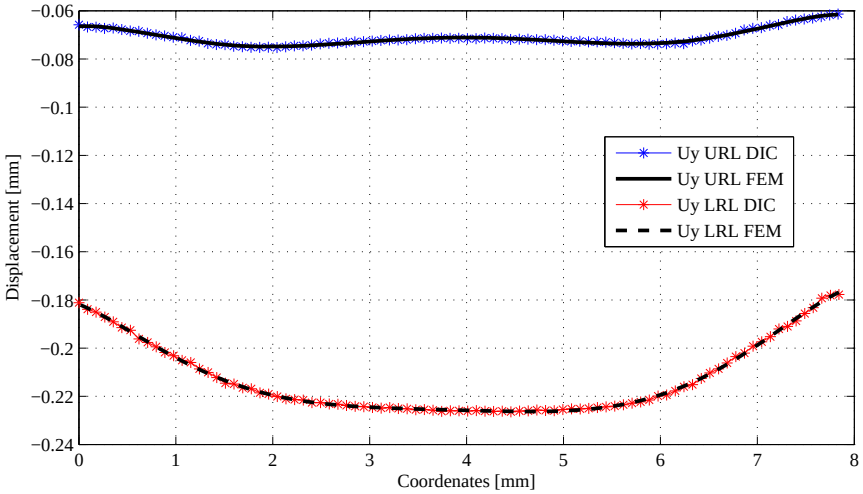

Figure 4.132 – Correlation between *Uy* displacements obtained from DIC and the displacements applied in the numerical model (X65_U0_OH_04).

In addition to monitoring all cyclic loading without having to resort to the iterative remote/local-clip gauge method, this methodology allows reproducing the effects of any in-plane instability suffered by notched plane specimens. Even though significantly lower than of smooth plane specimens, these instabilities, may be associated to the high strain levels and geometrical deviations of the notches with respect to the geometrical centre of specimens, which promotes a progressive asymmetric deformation effect on the specimen. These evidences are supported by the analysis of Figure 4.133 and Figure 4.134, being visible an asymmetry in the displacement fields (*Ux* and *Uy*). Figure 4.135 and Figure 4.136 show the strain fields where, as expected, the strain concentration around the hole vicinity can be observed.

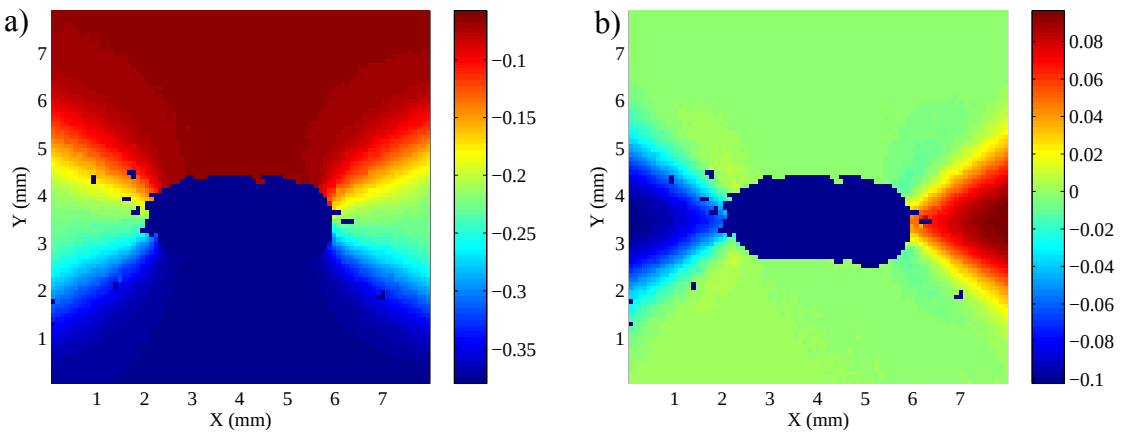

Figure 4.133 – Experimental displacement field mapping obtained for the U0_OH_04 specimen of X65 piping steel, at the stage 18: a) loading direction; b) transverse to loading direction.

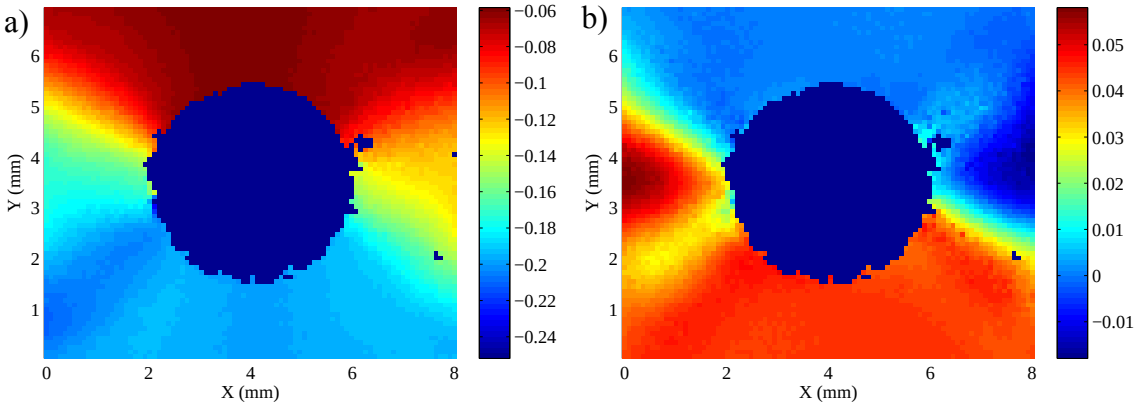

Figure 4.134 – Experimental displacement field mapping obtained for the U-1_CH_04 specimen of X65 piping steel with thermal treatment, at the stage 25: a) loading direction; b) transverse to loading direction.

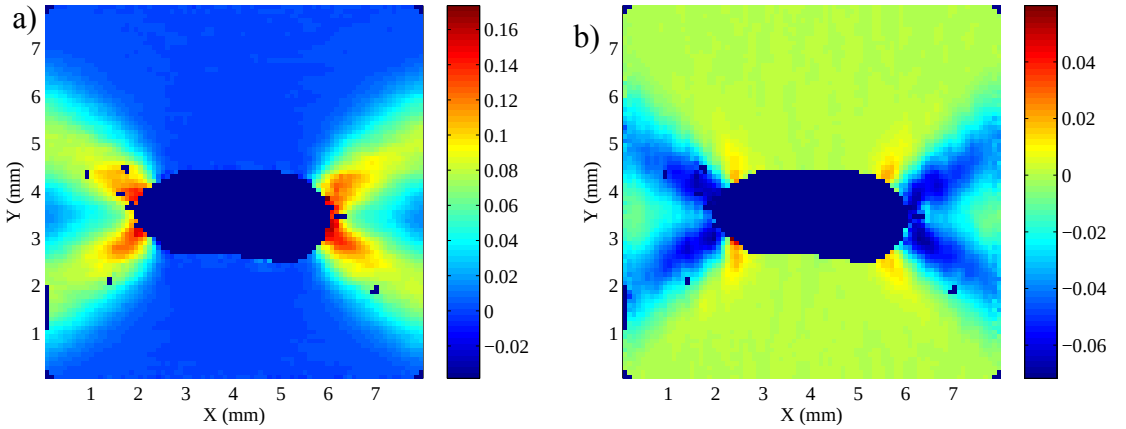

Figure 4.135 – Experimental strain field mapping resulted for the U0_OH_04 specimen of X65 piping steel at the stage 18: a) loading direction; b) transverse to loading direction.

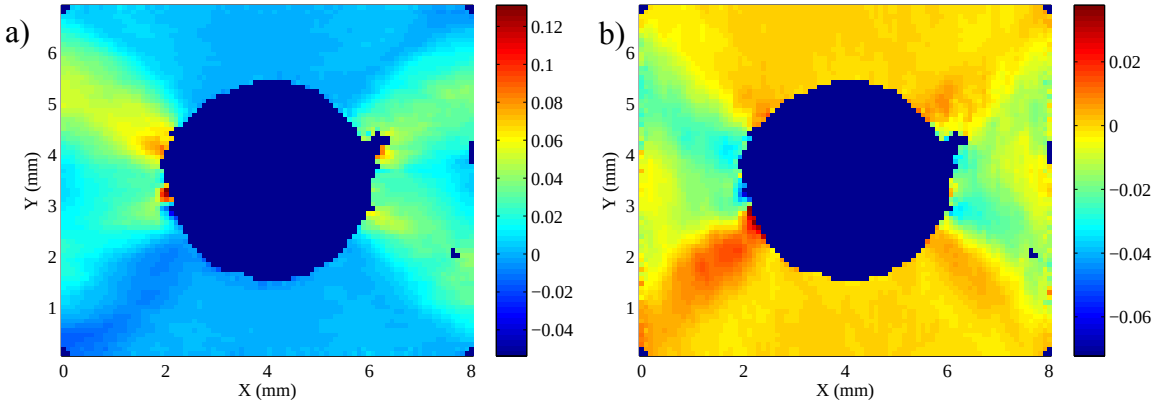

Figure 4.136 – Experimental strain field mapping of U-1_CH_04 specimen of X65 piping steel with thermal treatment at the stage 25: a) loading direction; b) transverse to loading direction.

As referred above, the boundary conditions derived from DIC were applied to the numerical models with the material described by the previously referred plasticity model with kinematic hardening, addressed in the Section 4.3.1. Consequently, this methodology can be used as a validation mechanism of the plasticity models introduced in the numerical simulations. Thus, the load levels obtained from finite element simulations should be similar to experimental data results, until to the macroscopic crack initiation, since the damage evolution during the crack propagation is described by the plasticity model. A good compromise between the experimental and numerical results can be observed in Figure 4.137, which illustrate the comparison between the numerical and experimental data for some selected specimens.

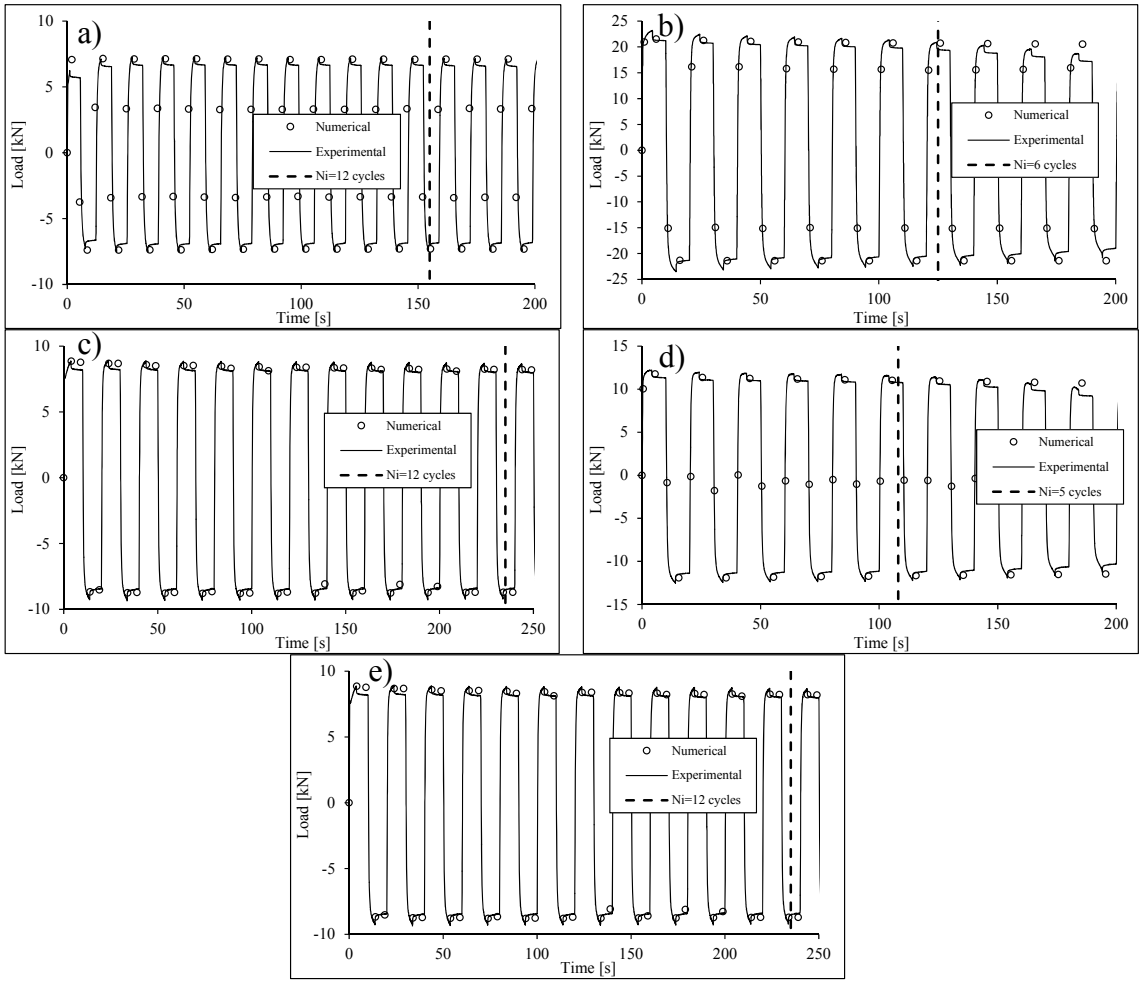

Figure 4.137 – Experimental *versus* numerical loads obtained from the new methodology for the application of local boundary conditions: a) U-1_OH_3 specimen of X52 piping steel; b) U0_CHS_10 specimen of X60 piping steel; c) U-1_CH_4 specimen of X60TT piping steel; e) U0_OH_7 specimen of X60 piping steel; f) U0_CH_5 specimen of X65 piping steel.

Comparisons between the experimental and numerical displacements fields can also support the validity of this new approach to simulate the cyclic loading under ULCF, including the small instabilities suffered by the specimens under large plastic strain levels. The displacements and strain fields obtained from the finite element simulations are illustrated in Figure 4.137 to Figure 4.141. The analysis of these figures results on satisfactory agreement between the displacement/strain fields in the region of interest. In order to minimize the computational costs of the numerical simulations presented in the Section 4.3, three symmetry planes were considered there. However this theoretical assumptions lead to a single critical node around the notch. The application of current approach based on local boundary conditions requires the complete specimen width modelling. In this way, the location of the critical node is not evident and two potential critical nodes were considered in this analysis.

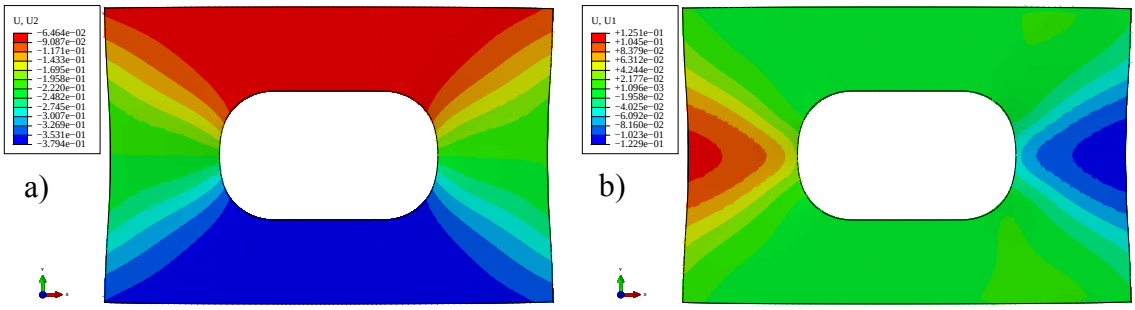

Figure 4.138 – Numerical displacement field maps obtained with the application of local boundary conditions method for the U0_OH_04 specimen of X65 piping steel at the stage 18: a) loading direction; b) transverse to loading direction.

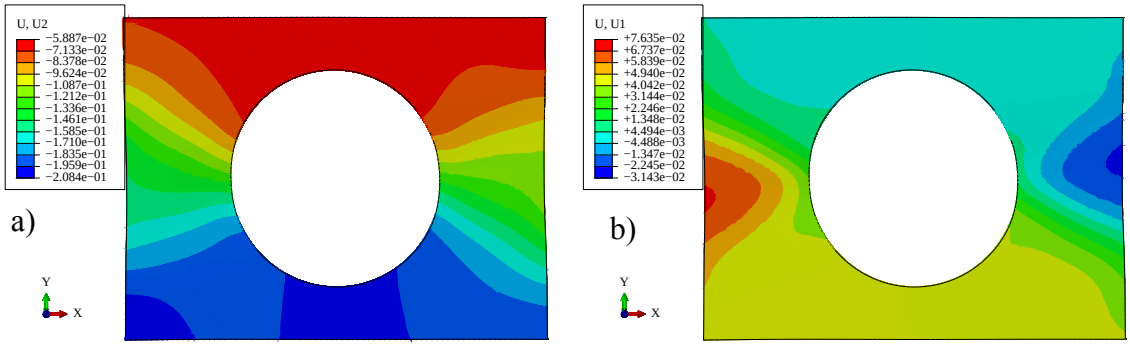

Figure 4.139 – Numerical displacement field maps obtained with the application of local boundary conditions method for the U-1_CH_04 specimen of X65 piping steel with thermal treatment at the stage 25: a) loading direction; b) transverse to loading direction.

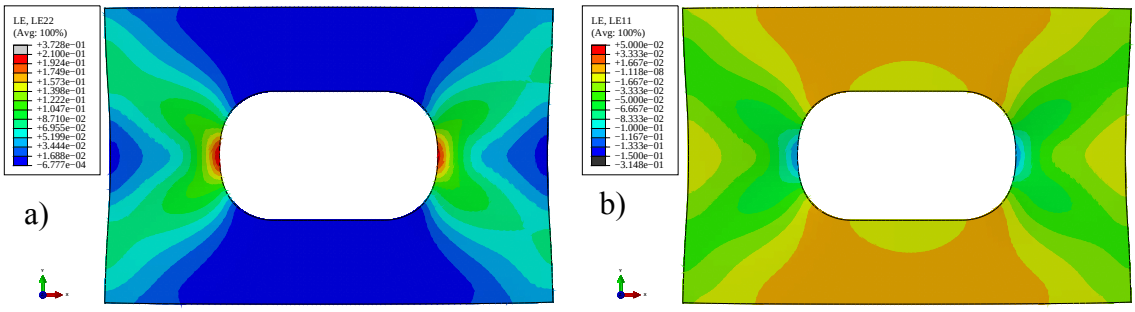

Figure 4.140 – Numerical strain field maps obtained with the application of local boundary conditions method for the U0_OH_04 specimen of X65 piping steel at the stage 18: a) loading direction; b) transverse to loading direction.

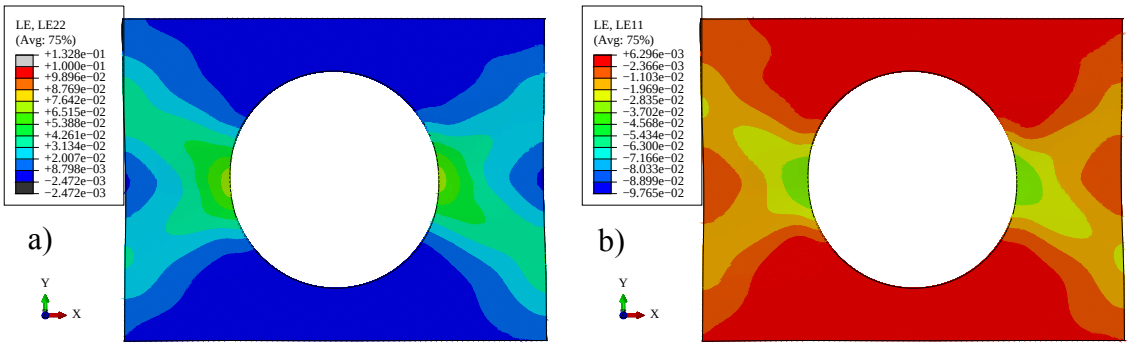

Figure 4.141 – Numerical strain field maps obtained with the application of local boundary conditions method for the U-1_CH_04 specimen of X65 piping steel with thermal treatment at the stage 25: a) loading direction; b) transverse to loading direction.

The equivalent plastic strain was computed for each critical node and compared with the numerical results obtained from the simulation of 1/8 specimens using ideal boundary conditions, as illustrated in Figure 4.142 to Figure 4.145. The two procedures resulted on the computation of similar equivalent plastic strain levels for some geometries, but for other geometries the simulations based on local boundary conditions resulted lower equivalent strains than estimated by the symmetrical model. In general, the two selected critical nodes resulted in very close strain values.

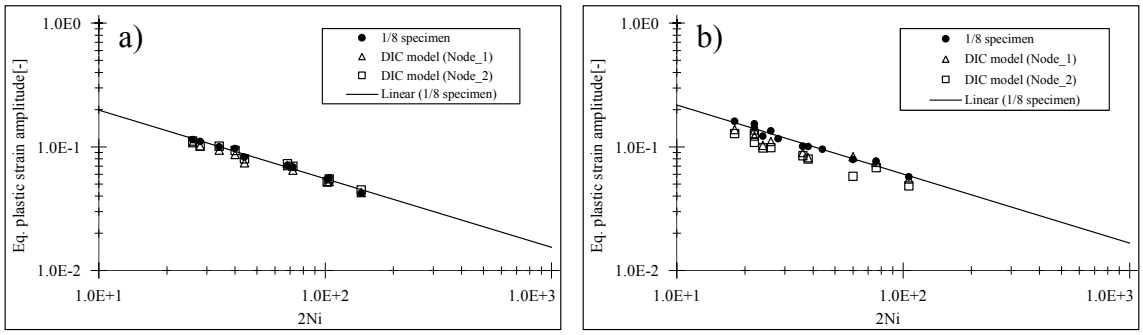

Figure 4.142 – Comparison between the equivalent plastic strain amplitudes computed using an 1/8 symmetrical model and the local model based on updated boundary conditions supported by DIC, obtained for the X52 piping steel: a) CH series; b) OH series.

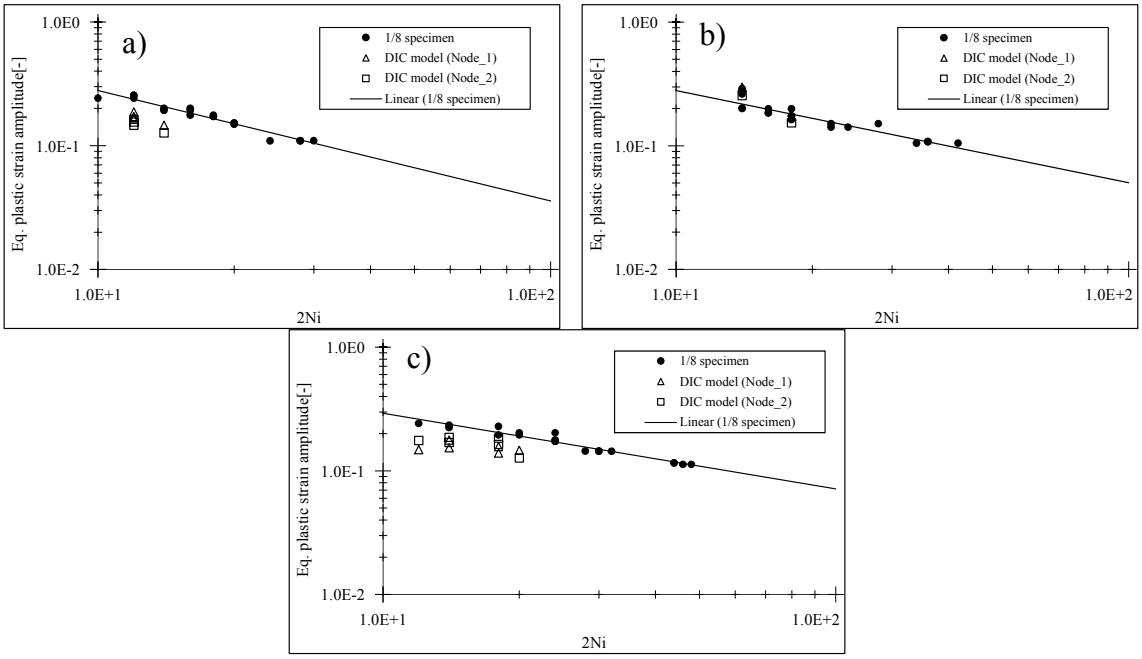

Figure 4.143 – Comparison between the equivalent plastic strain amplitudes computed using an 1/8 symmetrical model and the local model based on updated boundary conditions supported by DIC, obtained for the X60 piping steel: a) CHS series; b) CHB series; c) OH series.

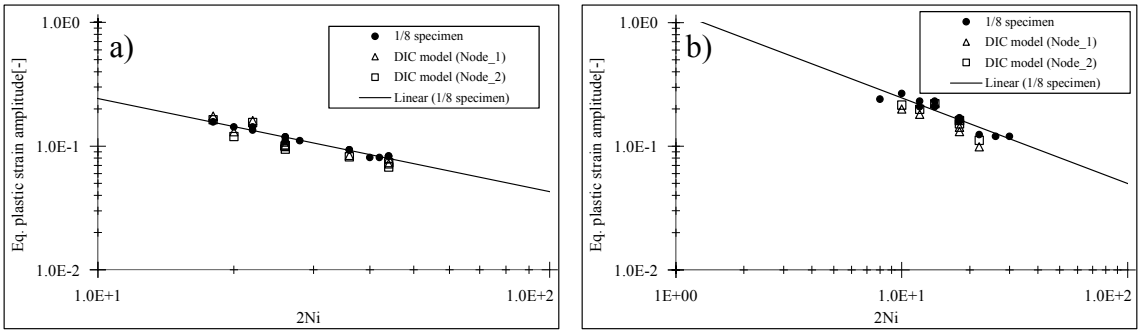

Figure 4.144 – Comparison between the equivalent plastic strain amplitudes computed using an 1/8 symmetrical model and the local model based on updated boundary conditions supported by DIC, obtained for the X65 piping steel: a) CH series; b) OH series.

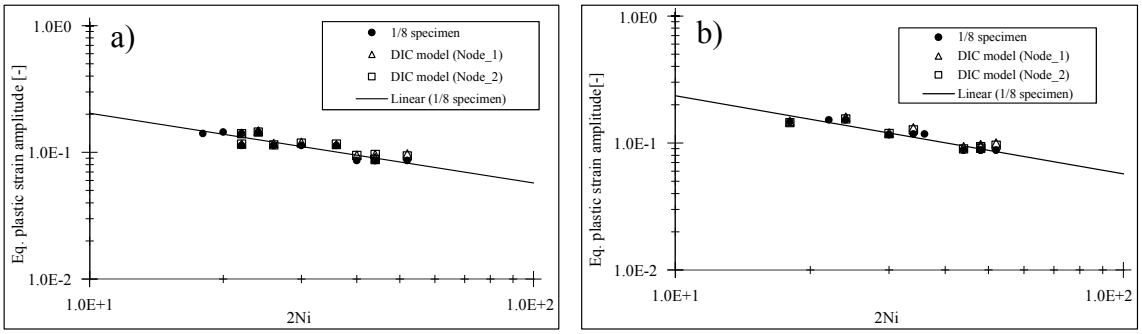

Figure 4.145 – Comparison between the equivalent plastic strain amplitudes computed using an 1/8 symmetrical model and the local model based on updated boundary conditions supported by DIC, obtained for notched (CH) specimens: a) X60TT piping steel; b) X65TT piping steel.

4.6 NUMERICAL ANALYSIS OF BENDING CYCLIC TESTS

Numerical simulations of cyclic bending tests, including smooth, notched and flat-grooved plane specimens of X652 steel, were performed in ABAQUS 6.12®. The plasticity model with kinematic hardening previously presented and validated for smooth and notched specimens under tension/compression loading was used. Regarding the geometry using in the numerical model, besides the specimen, the grip and pin were also considered in the finite element model of the bending setup. The contact definition between the pin and grip hole was set as surface-to-surface contact and pin and grip hole surfaces were chosen as master and slave surfaces, respectively. The finite element mesh proposed for the notched specimen is illustrated in Figure 4.146. Isoparametric solid elements with 8-nodes, C3D8R were used in the numerical models. Taking into account the symmetry planes of the bending test, only ¼ of numerical model was considered. Comparisons between experimental and numerical load-displacement curves are illustrated in Figure 4.147, which allowed the validation of the plasticity model as well as the proposed full numerical model. A satisfactory agreement between two experimental and numerical responses was verified for both cases. In addition, the axial strain acquired from strain gauges is plotted together with the numerical data and a good correlation can be observed (see Figure 4.148). The validation of plasticity model is strengthened from the specimen deformed shape assessment. In fact, the experimental deformed shape of the specimens was acquired by means an optical system, where consecutive images were recorded for the compressive and tensile stages. These images were subjected to a post-processing in order to derive the contour of the specimens. Figure 4.149 presents the deformed shape, derived by finite element analysis, plotted against experimental data, for a smooth and a notched specimen, respectively. For both cases, a very good correlation is found for the extreme positions of the loading. In fact, with this procedure it is guaranteed that the entire loading process is covered for the finite element simulations. Thus, it is expected that the evolution of the strain/stress parameters are in accordance with the values experienced by the specimen even simulating only the stabilized behaviour of the specimens.

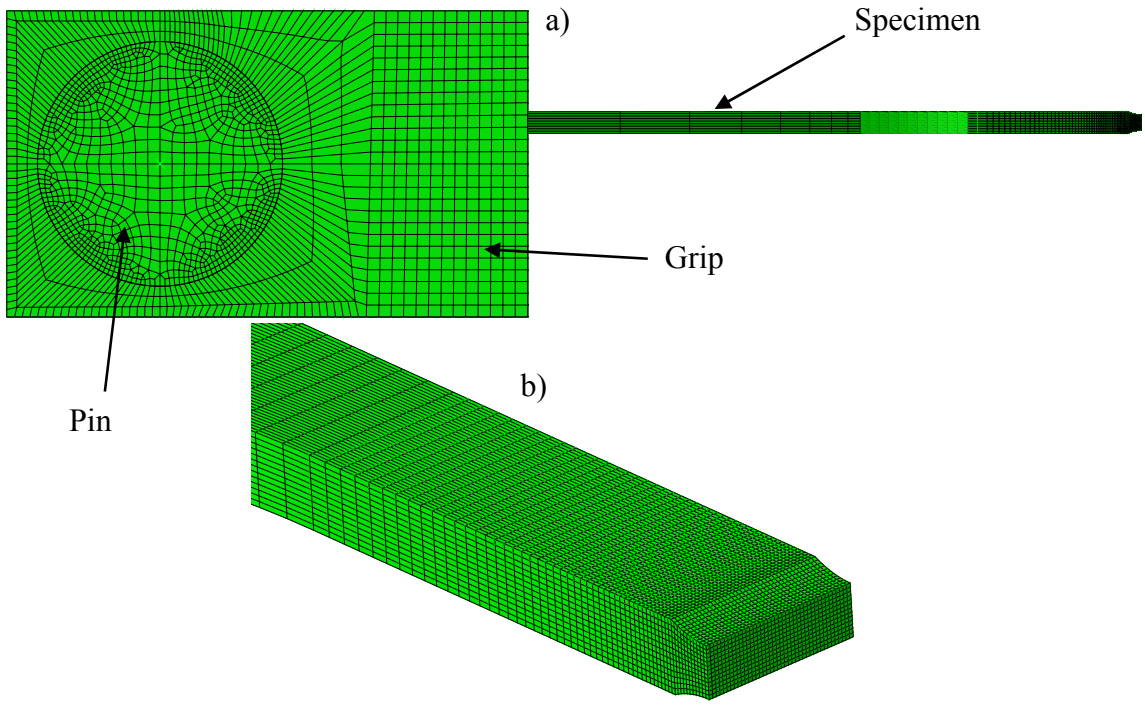

Figure 4.146 – Finite element mesh of the side notched specimen with the gripping system: a) overall view; b) refined mesh at the central cross section of the specimen.

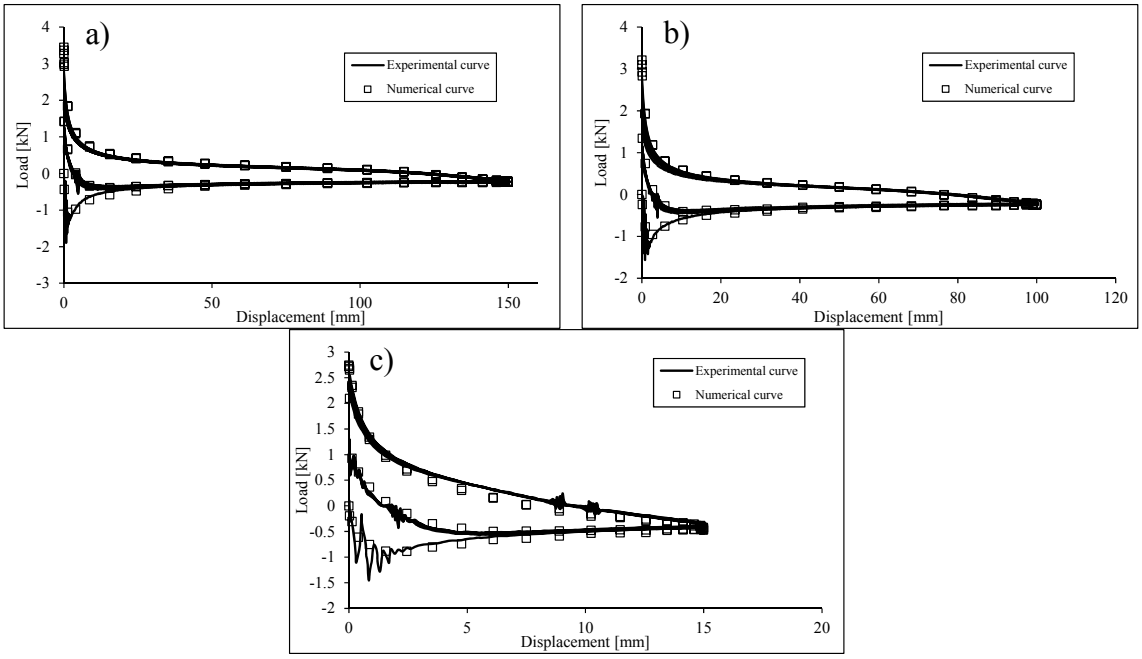

Figure 4.147 – Numerical load-displacement curves correlated with experimental data: a) smooth plane specimens, U_BSP_1; b) notched specimen, U_BNP_1; c) flat-grooved specimen, U_BFG_2.

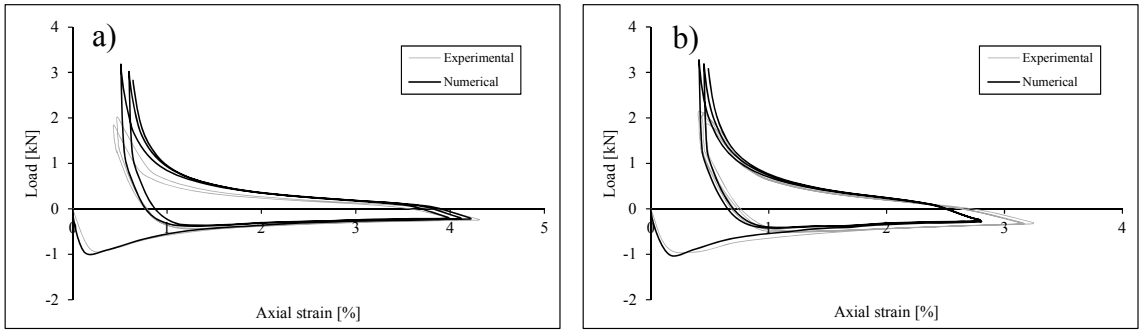

Figure 4.148 – Comparison between experimental and numerical load-axial strain of: a) U_BNP_02 specimens of X52 piping steel; b) U_BNP_03 specimen of X52 piping steel.

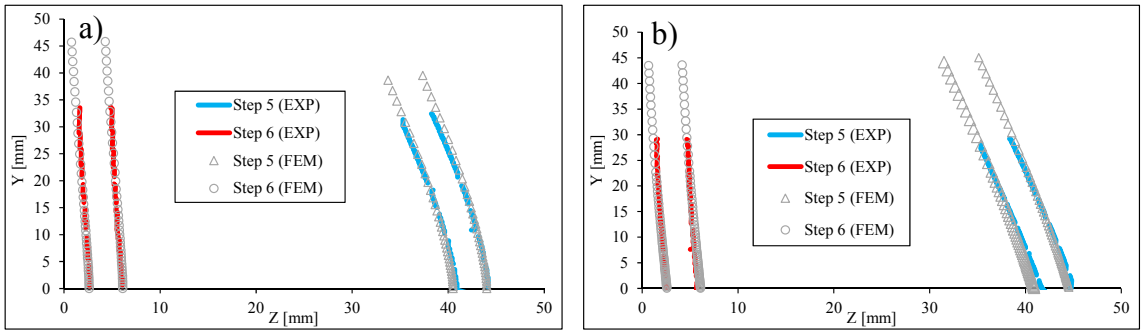

Figure 4.149 – Numerical deformed shape correlated with experimental data: a) U_BNP_13 specimen of X52 piping steel; b) U_BFG_2 specimen of X52 piping steel.

In order to identify the critical location at the specimen cross section, the accumulated equivalent plastic strain and the triaxiality field were obtained. The coordinate system used to map the accumulated equivalent plastic strain and triaxiality is illustrated in Figure 4.150. Based on the identification of the critical point/node, the parameters involved in the fatigue prediction models will be assessed. Bai and Wierzbicki [2] have postulated that monotonic ductile fracture is characterized by the equivalent plastic strain, the triaxiality and the normalized parameter related with the third invariant of the stress tensor, so-called as deviatoric parameter. Based on this assumptions the accumulated equivalent plastic strain mapping is presented in Figure 4.151, the triaxiality field is presented in Figure 4.152 while Figure 4.153 shows the Lode angle parameter map for the third tensile reversal/stage. With respect to the smooth specimens, the analysis of the equivalent plastic strain field at the specimen cross section indicates two potential critical locations for the crack initiation. Concerning the notched and flat-grooved plane specimens, the location of the critical point/node is at the notch root that corresponds to the higher values of the equivalent plastic strain. This evidence can be achieved from the analysis of the fracture surfaces illustrated in the Chapter III. With respect to the triaxiality and deviatoric parameters for smooth and

notched plane specimens they assume alternate values between positive and negative ones. The transition of positive to negative values is associated with neutral axes location at the specimen central section. A distinct mapping of lode angle parameters for flat-grooved specimen is observed. In general, the central section of specimen shows lode angle parameter around to $\bar{\theta} = 0$, which defines the plain strain conditions.

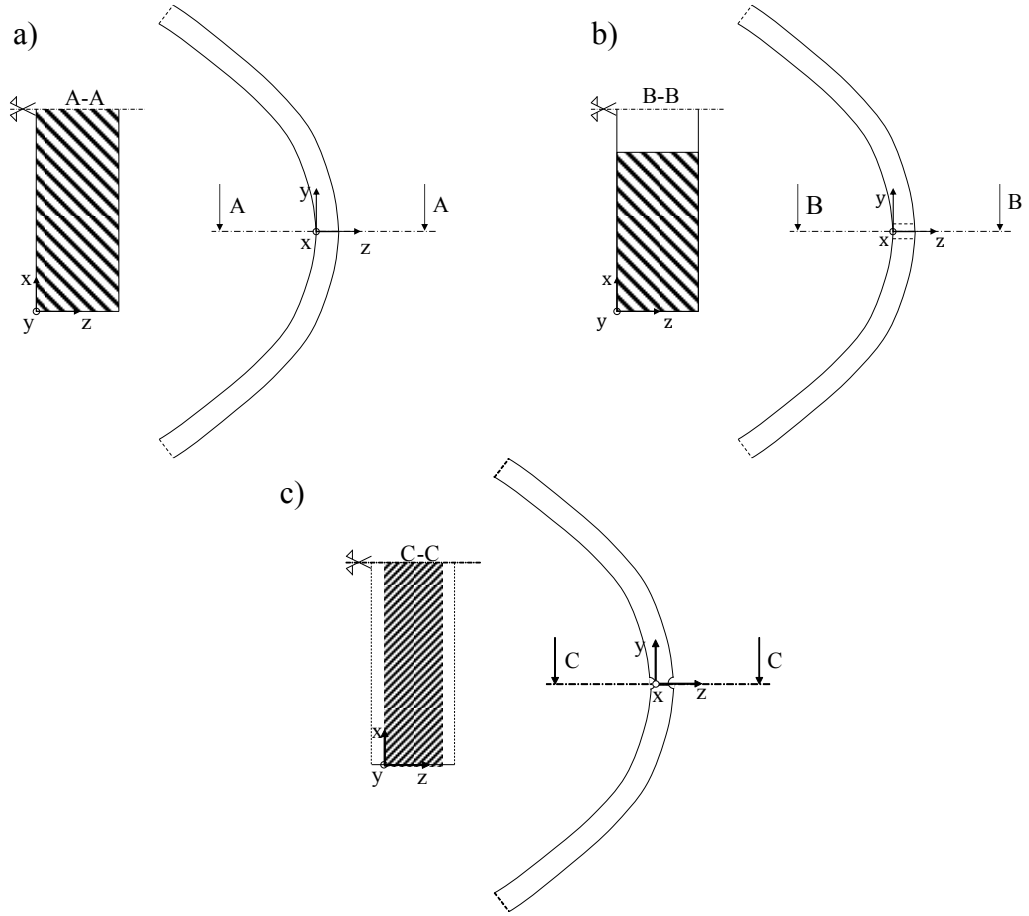

Figure 4.150 – Local coordinate system of central critical cross section used for damage variables mapping: a) smooth plane specimens; b) notched plane specimens; c) flat-grooved plane specimens.

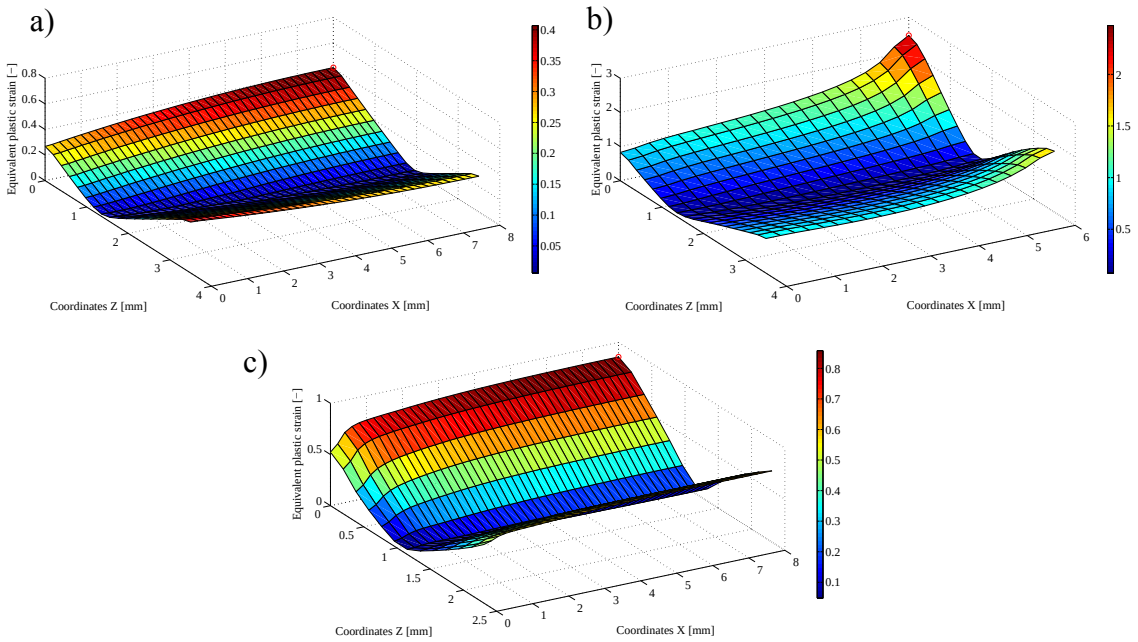

Figure 4.151 – Mapping of accumulated equivalent plastic strains computed for: a) smooth specimen (U_BSP_1); b) notched specimen (U_BNP_1); c) flat-grooved specimen (U_BFG_2).

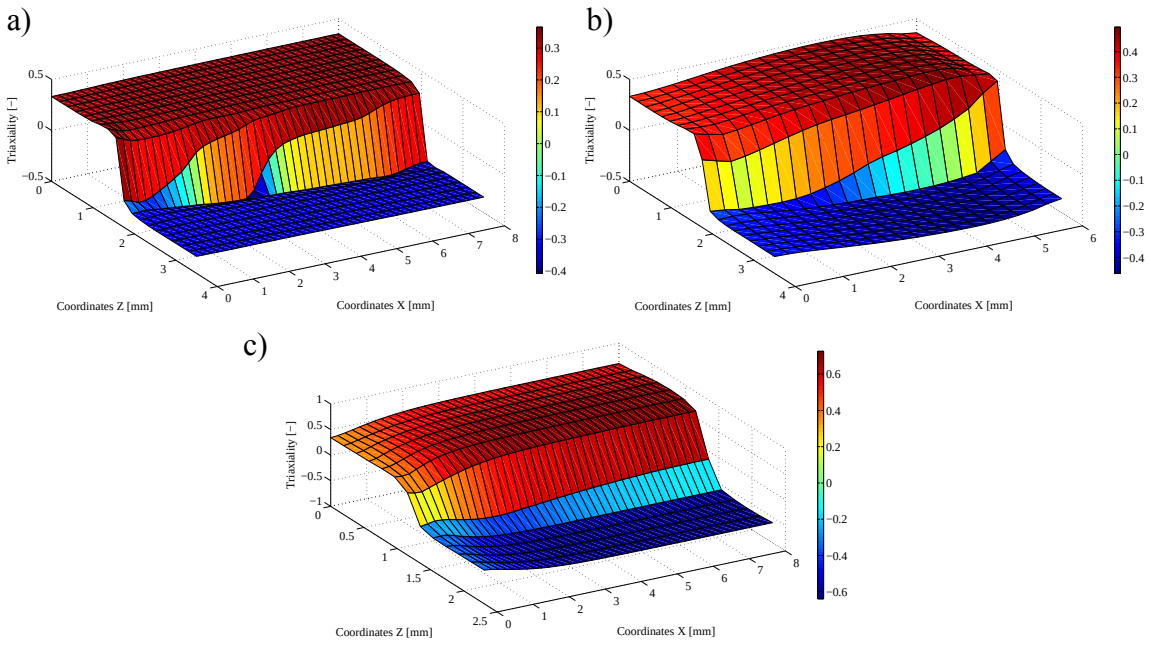

Figure 4.152 – Mapping of stress triaxiality computed for: a) smooth specimen (U_BSP_1); b) notched specimen (U_BNP_1); c) flat-grooved specimen (U_BFG_2).

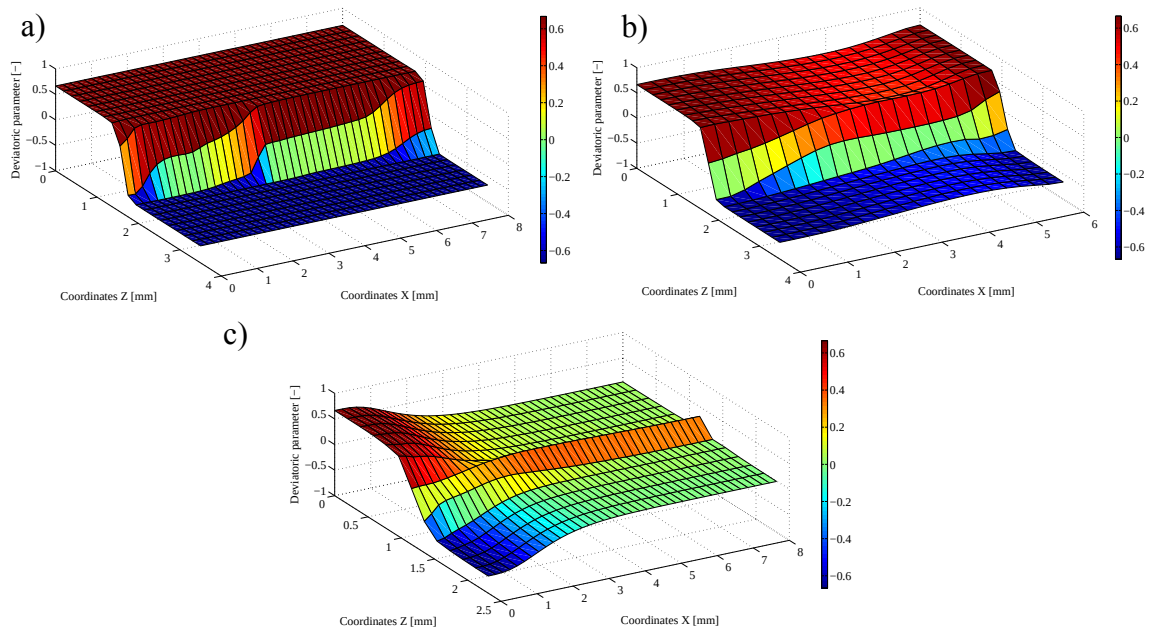

Figure 4.153 – Mapping of lode angle parameter computed for: a) smooth specimen (U_BSP_1); b) notched specimen (U_BNP_1); c) flat-grooved specimen (U_BFG_2).

Based on numerical data reduction provided from finite element analysis, fatigue life predictions were processed using the two uncoupled damage models investigated in this work, namely, Coffin-Manson relation and the Xue model. Since, only two displacement ranges were tested in the cyclic bending tests of smooth plane specimens and a poor correlation regarding the fatigue lives was obtained, these results will not be included on fatigue life estimations of bending cyclic tests. Fatigue life predictions for notched and flat-grooved of bending cyclic tests were performed taking into account the Coffin-Manson parameters achieved from the overall results of tensile-compression small-scale tests (Figure 4.96). Figure 4.155 compares the experimental results with the number of cycles derived from the Coffin-Mason relation. The analysis of this figure reveals good correlations between the reference line and the data points of notched plane series, although the Coffin-Mason relation is not able to estimate the fatigue life of flat-grooved specimens. It is worth to note that the equivalent plastic strain range levels experienced by the notched plane series subjected to a bending cyclic loading are in the same range of the equivalent plastic strain range of axial tension-compression cyclic tests, leading to similar number of fatigue cycles. In contrast the inability of the Coffin-Manson relation to account the effect of plane strain conditions, where fatigue cracking occurs, is evidenced through the poor fatigue life estimations for the flat-grooved specimens. In fact the Coffin-Manson relation overestimates the number of cycles until crack initiation of flat-grooved specimens.

The application of the Xue model for the fatigue life assessment requires the knowledge of the monotonic fracture strain associated with each specimen geometry (notched and flat-grooved) tested in this work, but for the X52 steel the ductile fracture surface was not available due to the lack of experimental data. Concerning the notched plane specimens, it should to be noted that the displacement range allowed by the servo-hydraulic machine was 150mm which was not sufficient to perform a monotonic bending test until failure on the notched plane specimens. Since the use of the Coffin-Manson relation exhibited a similar performance to the predictions performed for the axial tension-compression tests, the monotonic fracture strain of notched plane specimens (X52_CH series, see Table 4.11) is proposed for the notched specimens under cyclic bending loading. In contrast, a monotonic bending test (Δd=50mm) was performed on a flat-grooved specimen, which allowed obtaining the monotonic fracture strain under a bending loading. The experimental curve of monotonic bending test of U0_BFG_01 specimen is correlated with numerical response in Figure 4.154a) while the Figure 4.154b) illustrates the equivalent plastic strain filed used to derive the monotonic fracture strain. Figure 4.156 shows the monotonic fracture values and the strain-life data, the experimental values and the predicted lines by the Xue model, for both notched and flat-grooved specimens. The Xue model was previously identified (see Table 4.11). As expectable, the introduction of the monotonic fracture strain, which normalizes the equivalent plastic strain range leads to an enhancement of the fatigue life estimations, mainly for flat-grooved specimens as can be observed in the Figure 4.157. The influence of the monotonic ductile behaviour is clearly observed from the results of the bending cyclic tests, since the introduction of the fracture strain produces significant improvement on the fatigue life prediction. Moreover, even for different values of lode angle parameter, the fracture strain parameter is able to distinguish the fatigue life behaviour of the specimens subjected to bending cyclic tests.

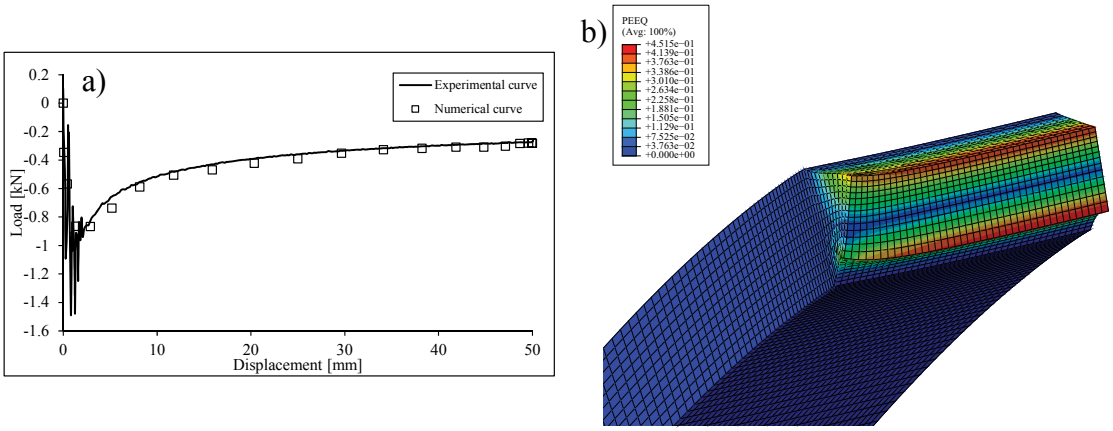

Figure 4.154 – a) Comparison of experimental and numerical load-displacement curve of U0_BGF_01 specimen; b) equivalent plastic strain field at the specimens critical location.

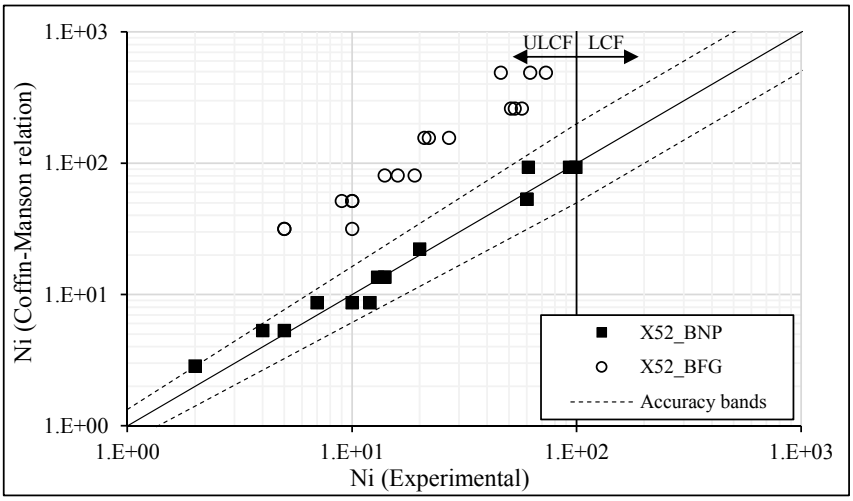

Figure 4.155 – Comparison of experimental data and Coffin-Manson predictions for the bending cyclic tests performed on notched plane and flat-grooved plane specimen series.

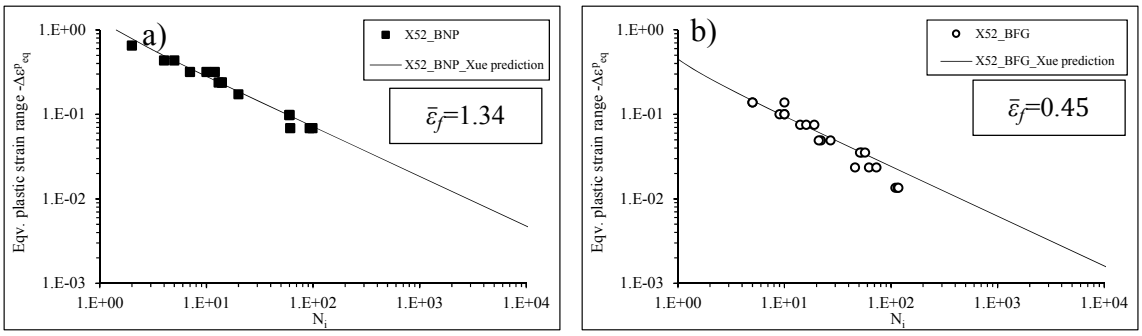

Figure 4.156 – Equivalent plastic range *versus* number of cycles for bending cyclic tests of X52 piping steel – experimental data *versus* Xue predictions: a) notched plane series; b) flat-grooved series.

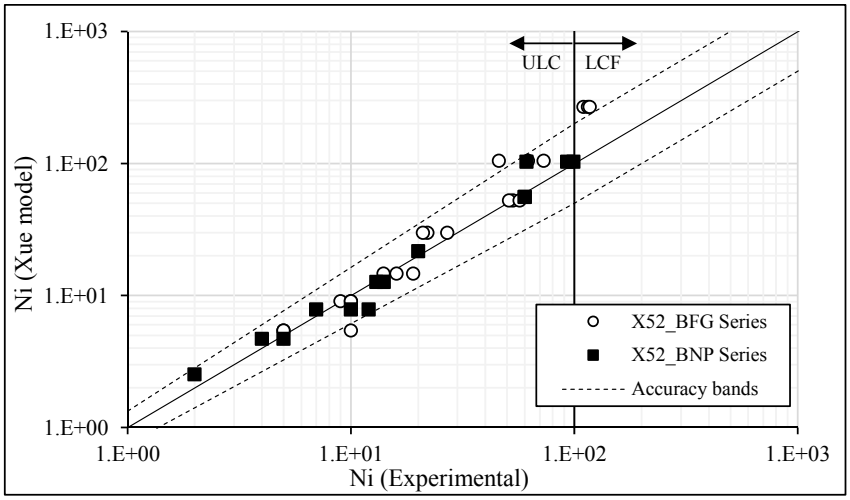

Figure 4.157 – Comparison of experimental data and Xue model predictions for the notched and flat-grooved bending cyclic tests.

4.7 CONCLUSIONS

In this chapter the numerical simulations of experimental tests described in the Chapter III were presented. In addition to the simulation of the cyclic tests of smooth and notched specimens, numerical simulations of monotonic tensile tests were also performed, in order to obtain the fracture strains, the stress triaxialities and Lode angle parameters. The simulation of the smooth specimens' cyclic tests were performed following two strategies regarding to the application of boundary conditions. In the first approach, the ideal boundary conditions were applied and in a second stage, the lateral displacements of the actuator were considered promoting the additional plastic deformations on the smooth specimens.

In order to identify the plasticity model with isotropic hardening used on monotonic simulations, the stress-strain curve for each material was derived, establishing a compromise between the overall available experimental data. These curves were determined by a trial and error. The experimental data obtained from the cyclic tests was used to calibrate the plasticity models with cyclic hardening that were considered in the simulation of cyclic tests.

The monotonic and fatigue behavior, including LCF and ULCF regimes of X52, X60 and X65 piping steels were investigated in this work. In particular the stress-strain curves from the monotonic tensile tests of smooth specimens were extended until the damage onset, which allowed to conclude about the ductility of the three piping steels. The X60 steel grade exhibits a higher ductility whereas X52 and X65 steel grades show a similar elongation until the final failure. The influence of the thermal treatment on the monotonic ductile behavior was also investigated for the X60 and X65 piping steels. In detail, X65 piping steel has a higher ductility when compared with the X60 piping steel. The thermal treatment promotes different effects on the ductility behavior of these steels grades, increasing the ductility of X65 piping steel and reducing it in the X60 piping steel. Additionally, based on the experimental program carried out on specimens of X60 piping steel, the 3D fracture locus proposed by Bai and Wierzbicki was calibrated using reference axisymmetric and flat-grooved specimens' data that allowed directly the evaluation of the upper and lower ductility bound limits. Additionally, the numerical data of notched plane specimens, which provides intermediate values of Lode angle parameter, were also correlated with 3D fracture surface and a good compromise between the fracture surface and the data was observed.

Taking into account the numerical data resulted from the finite element simulation of the cyclic tests, the performance of the Coffin-Manson relation and Xue model under both LCF and ULCF regimes was investigated. In order to introduce the multiaxial effects typical of notched specimens, a multiaxial strain approach was used to perform the fatigue life estimations. The parameters of the Coffin-Manson relation were computed directly from the global results of all specimens of each steel grade. The parameters involved on Xue model formulation were computed by a trial and error procedure in order to establish a good compromise of the overall available results. The boundary conditions applied on the smooth plane specimens were updated, resulting on increased equivalent plastic strains. This detail allows improving the performance to the Coffin-Manson relation and Xue model on fatigue life prediction of smooth and notched plane specimens. In general, the model proposed by Xue that includes the normalization of the strain range by the fracture strain produces the best fatigue life predictions. Moreover, an alternative procedure for the computation of fracture strain and Xue model application was proposed. In detail, the stress triaxiality and Lode angle parameter were evaluated at the end of tensile loading reversals (load peaks) and then used to compute the fracture strains by means of 3D fracture surface

previously calibrated through monotonic tensile tests. The fracture strain of each specimen was accounted for the Xue model application and satisfactory fatigue life estimations were reached. Stress state parameters should be accounted for the fatigue life prediction under ULCF domain, besides the strain range. Fatigue strength reduces with the increasing of triaxiality and the decreasing of Lode angle parameter in the same way as ductile damage evolves with these parameters. The influence of these stress parameters has been fully investigated on ductile damage but this is not the case for the fatigue phenomenon. The process for the fatigue life assessment under different stress/strain conditions presented in this work can be considered as a new methodology which could be incorporated in the future design guidelines that currently are based on equivalent plastic strain range approach only. Also, an expedite approach is proposed to overcome some limitations associated to the fracture strain computation, namely to reduce the number of monotonic experimental tests which in many cases cannot be performed experimentally.

Regarding to the boundary conditions, a new approach based on the application of local boundary conditions obtained from DIC was proposed. This method was applied to the notched plane specimens allowing to reproduce the effects of any instability suffered by notched plane specimens during the cyclic tests of ULCF. This procedure only produced small changes in the equivalent plastic strain computed for each critical node, when compared with the numerical results obtained from the simulation of 1/8 of the specimens. Thus, it is concluded that the use of notched samples on ULCF domain is an effective alternative to the use smooth plane specimens since it limits the instabilities from compressive loading.

In this work the behavior of X52 steel pipe under ULCF regime was also investigated by means of an experimental program of bending cyclic tests, carried out on smooth, notched and flat-grooved specimens. Bending cyclic tests are able to evaluate ULCF fatigue behavior satisfactorily representing an alternative procedure to derive ULCF data. The performance of Coffin-Manson relation and Xue model, typically used in the tensile/compressive tests were assessed. The Xue model allowed the estimation of the fatigue life of both notched and flat-grooved specimens. In fact, this model shows a good performance taking into account the fracture strain derived from monotonic tensile tests and considering positive stress triaxiality levels and a lode angle parameter within the range$0 \leq \bar{\theta} \leq 1$, as also proven from the tensile-compression cyclic tests.

4.8 REFERENCES

[1] ABAQUS, 2012, User's manual version 6.12, Hibbitt, Karlsson, and Sorensen, Inc., Providence, R.I.

[2] Wierzbicki, T., Bao, Y., Lee, Y-W., Bai Y., (2005), "Calibration and Evaluation of Seven Fracture Models", Int. J. Mech. Sci., 47: 719-743.

[3] Coppola, T., Cortese, L., Folgarait, P., (2009), "The effect of stress invariants on ductile fracture limit in steels", Eng. Frac. Mech. 76:1288-1302.

[4] "Ultra low cycle fatigue of steel under cyclic high strain loading conditions," Deliverable D3 - Development of constitutive models and implementation into finite element software, European Commission RFSR CT 2011 00029.

[5] Coffin, L.F., (1954), "A study of the effects of cyclic thermal stresses on a ductile metal", Trans Am Soc Mech Eng, 76: 931–950.

[6] Manson, S.S., 1954. "Behavior of materials under conditions of thermal stress", Technical Report NACA-TR-1170, National Advisory Committee for Aeronautics.

[7] Xue, L., (2008), "A unified expression for low cycle fatigue and extremely low cycle fatigue and its implication for monotonic loading", International Journal of Fatigue, 30: 1691–1698.

[8] Ludik, P., (1909), "Elemente der Technologischen Mechanik" VerlagVon Julius, Springer Leipzig, 32.

[9] Ruano, J., (2015), "Effect of thermal treatment in the ultralow cycle fatigue behaviour of pipeline steels", MSc Thesis, UTAD (in Portuguese).

[10] Xavier, J., Pereira, J.C.R., de Jesus A.M.P., (2014), "Characterization of steel components under monotonic loading by means of image-based methods", Optics and Lasers in Engineering, 50: 142-153.

[11] Bai Y., (2003), "Effect of Loading History on Necking and Fracture". Ph.D. thesis. Cambridge, MA: Department of Ocean Engineering, Massachusetts Institute of Technology.

[12] Khan A.S., Huang S., (1995), "Continuum Theory of Plasticity". John Wiley & Sons, Inc.

[13] Lemaitre J., Chaboche J.L., (1990), "Mechanics of Solid Materials". Cambridge University Press.

[14] ASME, ASME Boiler and Pressure Vessel Code, (2004), ASME, New York.

[15] Gurson A.L., (1977), "Continuum theory of ductile rupture by void nucleation and growth. Part I: Yield criteria and flow rules for porous ductile media." J. Eng. Mater.-T. ASME, 99(1): 2-15.

[16] Tvergaard V., Needleman A., (1984), "Analysis of the cup-cone fracture in a round tensile bar." Acta Metallurgica, 32:157–169.

[17] Tvergaard V., (1982), "Influence of void nucleation on ductile shear fracture at a free surface." Journal of the Mechanics and Physics of Solids, 30:399–425.

[18] Kanvinde A.M., Deierlein G.G., 2007, "Cyclic void growth model to assess ductile fracture initiation in structural steels due to ultra-low cycle fatigue", Journal of Engineering Mechanics-ASCE, 133(6):701-712.

[19] Rastogi P., (2000), "Photomechanics." Berlin, Heidelberg: Springer Verlag.

Chapter V

Application of the Theory of Critical Distances to LCF and ULCF behavior of API piping steels

5.1 INTRODUCTION

Fatigue damage models for ULCF life assessment typically involve similar parameters as adopted in monotonic ductile models, as for example the accumulated equivalent plastic strain, the fracture strain, the stress triaxiality and Lode angle parameters as reported by some authors [1][4]. Besides these parameters, the equivalent plastic strain range typically used in LCF also assumes an important role on ULCF modelling. Based on these parameters the calibration of a ULCF model is dependent of a very specific experimental program involving both monotonic and ULCF tests coupled with finite element analyses, which are required to compute the referred parameters at locations where cracking is likely to occur. In what concerns the ULCF modelling, controlling parameters have been computed at nodes of the finite element model, however, this could be in contradiction with the Theory of Critical Distances (TCD) that suggests that the average of the critical parameters around the specified potential critical location could be more representative of the damage process than the peak values.

In order to establish correlations for both static and fatigue failure of smooth and notched specimens, the Theory of Critical Distances has been originally used with specimens experiencing linear-elastic behavior in the vicinity of the notch root. This theory was initially introduced by Neuber [5][6] and Peterson [7] and has been continuously developed and re-discovered by several researchers over extensive experimental campaigns and assuming linear-elastic local approaches [8][9]. On effect, Whitney and Nuismer [10] defined the characteristic length to calculate the brittle failures in notched details of composite materials, relating the smooth material strength and the material toughness. This concept was reformulated and applied to the fatigue domain by Tanaka [11] and Taylor [12]. Ductile metals under high levels of cyclic plasticity at the critical locations experience a reduction on the number of cycles to failure. This scenario is typically addressed under a strain-based approach framework, where the finite element simulations represent a crucial role in the modelling of the elastoplastic conditions at the damage process zone. Recent studies [13] have shown that TCD can be successfully used to predict the fatigue failure under low-cycle fatigue conditions.

Having in mind the succeeded application of the TCD on LCF modelling, this chapter aims at addressing the performance of this theory on both LCF and ULCF domains. The experimental data derived from an extensive program carried out on small-scale specimens of X52, X60 and X65 piping steels are used for this purpose. In addition to the typical smooth specimens' geometries also notched specimens were subjected to tension/compression cyclic tests. In fact, the ULCF materials characterization is facilitated by the use of notched specimens, since they reduce the instability problems that high plastic strain levels may induce in the specimens. Additionally to the uniaxial cyclic tests also cyclic bending tests on notched specimens were considered which included alternative stress/strain gradients in the tests results. Consequently, the TCD appears naturally as an approach facilitating the data reduction from such distinct source geometries including notched and smooth specimens and different loading scenarios, overcoming the challenges of the resulting non-uniform stress/strain fields. The TCD will be explored in this chapter covering the point, line and area methods in order to check the best appropriate TCD approaches for the API steels. A unified strain-life relation will be sought for the piping steels together with a characteristic material length, in order to result a practical tool for pipeline strain-based design under extreme cyclic loading conditions.

5.2 FUNDAMENTALS OF THE THEORY OF CRITICAL DISTANCES

The failure prediction under high-cycle fatigue domain, particularly for notched details, could be too conservative if the linear-stress conditions at the notch root are considered, as reported by Neuber [5]. According to Neuber, the cyclic damage in the process zone is governed by an effective stress, which results by averaging of the linear-elastic stresses over a specified material length [14]. This postulate can be extended to other fatigue regimes involving cyclic plastic deformations, such as the LCF. In order to estimate the fatigue lives under this specific fatigue domain a strain-based approach was recommended aiming at increasing the predictive capability as originally proposed by Coffin [15] and Manson [16]. Therefore, the classical strain-life approach to address the fatigue life for any kind of notched components may be reformulated according to the

TCD assumptions if the strain/stress field acting on the process fatigue location is known [17].

The application of the TCD can be done following different strategies, namely the Point Method (PM), Line Method (LM), Area Method (AM) and Volume Method (VM) [8]. The main goal of these methods is to achieve a given "characteristic length" which is used to describe an elastoplastic stress/strain state that is equivalent to the entire stress/strain field in the process damage zone. In detail, for the PM the effective stress/strain is computed directly from the stress/strain function, at a certain distance from the notch root, as proposed by Peterson [7] (see Figure 5.1a)). Concerning the LM formulation, Neuber [5] assumed that the effective stress/strain results from the strain/stress averaged over a line with a characteristic length, as illustrated in Figure 5.1b). For the implementation of the AM, the effective strain/stress is computed by averaging the stress/strain data over an area (e.g. semicircle with the geometrical centre coincident with the strain concentrator peak) as schematically represented in Figure 5.1c) [12]. Similar arguments can be presented for the VM. To apply the PM, LM and AM the critical distances are expressed as $L_{PM} = L/2$, $L_{LM} = 2L$ and $L_{AM} = L$, respectively where L is the material characteristic length, which does not depend on the specific features of the strain/stress spectrum of field [14]. Regarding the strain-based approach, and adopting the nomenclature of Figure 5.1, the LM, PM and AM can be expressed as follows [14]:

$$\varepsilon_{eff} = \varepsilon_2\left(\theta = 0, r = \frac{L}{2}\right) = \varepsilon_a \tag{5.1}$$

$$\varepsilon_{eff} = \frac{1}{2L}\int_0^{2L} \varepsilon_2\left(\theta = 0, r\right)dr = \varepsilon_a \tag{5.2}$$

$$\varepsilon_{eff} = \frac{1}{1.1}\frac{1}{\pi L^2}\int_0^{\pi/2}\int_0^{L} \varepsilon_2\left(\theta, r\right)\cdot r \cdot dr \cdot d\theta \cong \varepsilon_a \tag{5.3}$$

where ε_a is the strain amplitude. The TCD has been demonstrated successful for LCF conditions [13]. Nevertheless the application of the TCD under ULCF conditions has never been demonstrated before. Therefore, in this chapter the TCD in the forms of PM, LM and AM will be assessed for conditions of LCF and ULCF and results will be compared with those resulting from the application of the peak values from the influent

damage variables evaluated at the notch root, called in this chapter as critical node approach, which was the base of the analyses presented in the Chapter IV.

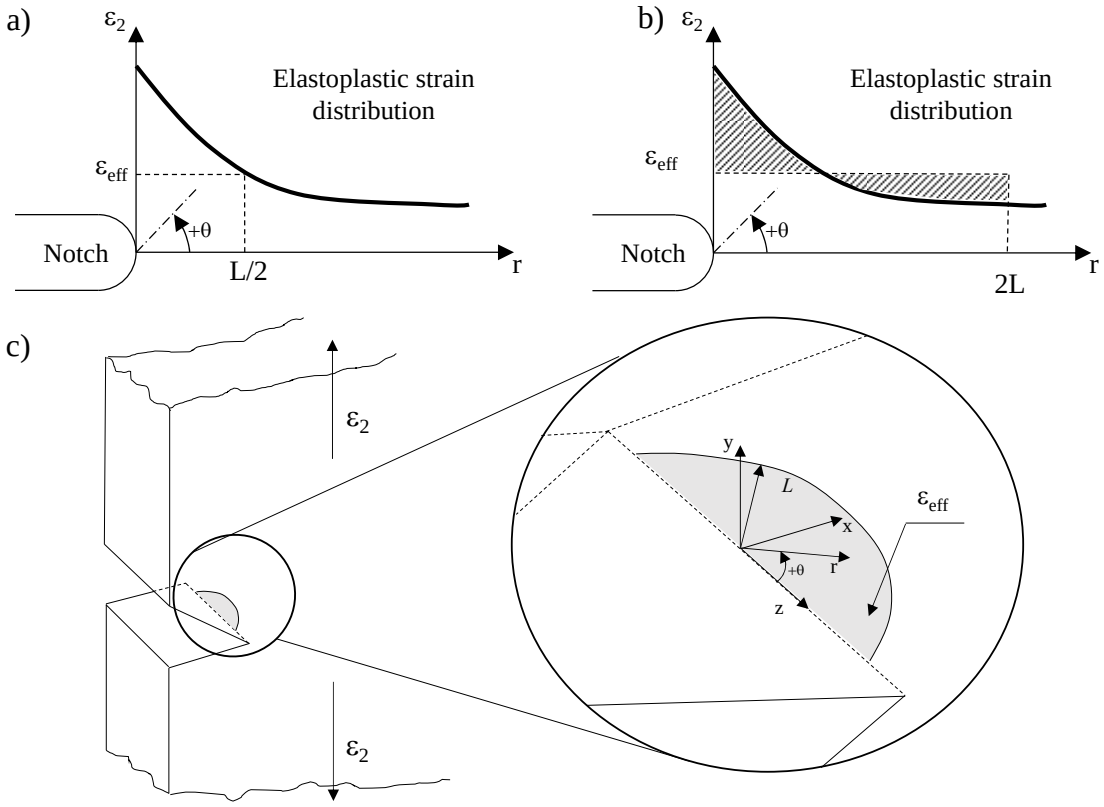

Figure 5.1 – Diagram of PM (a), LM (b) and AM (c) to achieve the effective strain.

5.3 CRITICAL NODE APPROACH

In contrast to the critical node approach presented in the Chapter 4, which only includes the plastic strain component, in this chapter a critical node approach based on both elastic and plastic strain components is presented. As performed in the Chapter 4, in order to account for the multiaxial effects introduced by the notches, an equivalent strain definition proposed by ASME [18] was used to compute the equivalent plastic strain ranges (see Equation 4.6). This formulation was also extended to derive the equivalent elastic strain range, as given by Eq. (5.4):

$$\Delta\varepsilon_{eq}^{E}=\frac{\sqrt{2}}{3}\sqrt{\left(\Delta e_{11}-\Delta e_{22}\right)^{2}+\left(\Delta e_{22}-\Delta e_{33}\right)^{2}+\left(\Delta e_{33}-\Delta e_{11}\right)^{2}+\frac{3}{2}\left(\Delta e_{12}^{2}+\Delta e_{23}^{2}+\Delta e_{31}^{2}\right)}, \quad (5.4)$$

where Δe_{ij} denotes the elastic strain component variation between two consecutive reversal points. Consequently, to address the strain-life relations of the X52, X60 and X65 piping steels, Morrow's relation [19] was used. This relation results from the superposition of the elastic and plastic strain components, defined respectively by Basquin [20] and Coffin-Manson relations [15][16]:

$$\frac{\Delta\varepsilon_{eq}}{2}=\frac{\Delta\varepsilon_{eq}^{E}}{2}+\frac{\Delta\varepsilon_{eq}^{P}}{2}=\frac{\sigma_{f}^{'}}{E}(2N_{i})^{b}+\varepsilon_{f}^{'}(2N_{i})^{c}. \quad (5.5)$$

The parameters of Morrow relation (σ'_f: fatigue strength coefficient; b: fatigue strength exponent; ε'_f: fatigue ductility coefficient; c: fatigue ductility exponent) were computed correlating the elastic and plastic equivalent strain ranges with the number of cycles until crack initiation for all tested specimens and respective values are summarized in the Table 5.1. It should be noted that the data points relative to the smooth plane specimens were obtained from the numerical simulations considering the lateral instabilities. The total strain-life curves are plotted in Figure 5.2 to Figure 5.4 for the three piping steels investigated in this work. Some scatter is found between the notched and smooth specimen series, mainly in the ULCF domain. In fact, the notch presence promotes local strain concentration and a consequent strain gradient in the plastic strain field. The use of an equivalent strain range definition was not enough to overcome this modelling difficulty. Using the parameters of the Morrow's relation and the equivalent plastic strain ranges derived from finite element simulations of each specimen simulation, fatigue life estimations were computed and compared with the experimental results as can be observed in the Figure 5.5 to Figure 5.7. The fatigue predictions included both LCF and ULCF data. Accuracy bands were added to the graphs with a twice (2x)/half(0.5x)-life criterion being used for the LCF domain and a progressive accuracy band used for ULCF, reducing its width (increasing accuracy) from twice/half-life in the LCF to 1.33x/0.75x of experimental fatigue lives at N_i=1 cycle. Satisfactory fatigue life estimations were addressed for notched specimens under ULCF and LCF regimes, although some scatter is verified for X65 piping steel from 100 cycles. Nevertheless the Morrow's relation using a

critical node approach does not provide good predictions for smooth specimens in both fatigue domains addressed in this study, mainly for X52 and X65 piping steels.

Table 5.1 – Parameters of Morrow's relation obtained from critical node approach.

Piping steel grades	σ'_f [MPa]	b	ε_f	c
X52	803.40	-0.0834	1.0058	-0.6462
X60	618.00	-0.0419	1.3954	-0.7016
X65	782.80	-0.0587	1.8997	-0.8222

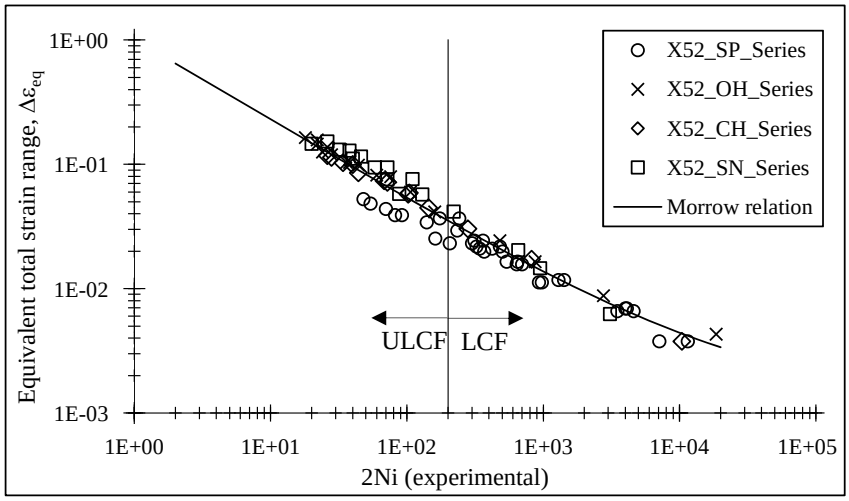

Figure 5.2 – Total strain-life data of the X52 piping steel and correlation using Morrow relation with critical node approach.

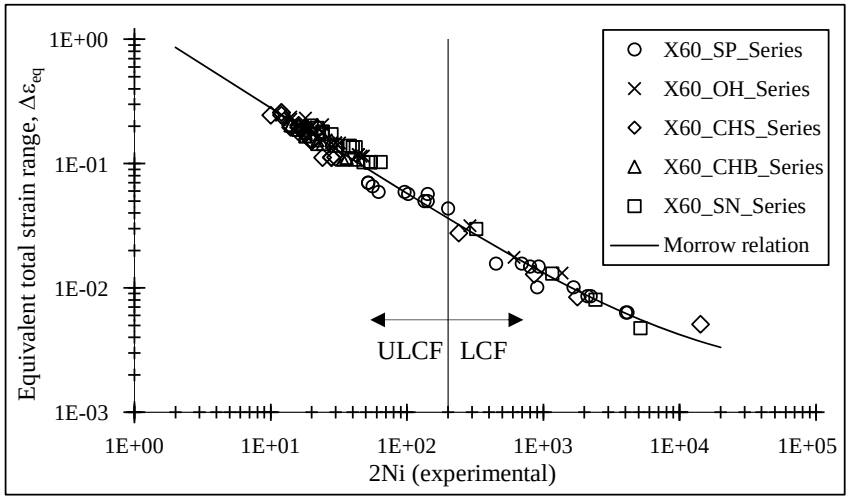

Figure 5.3 – Total strain-life data of the X60 piping steel and correlation using Morrow relation with critical node approach.

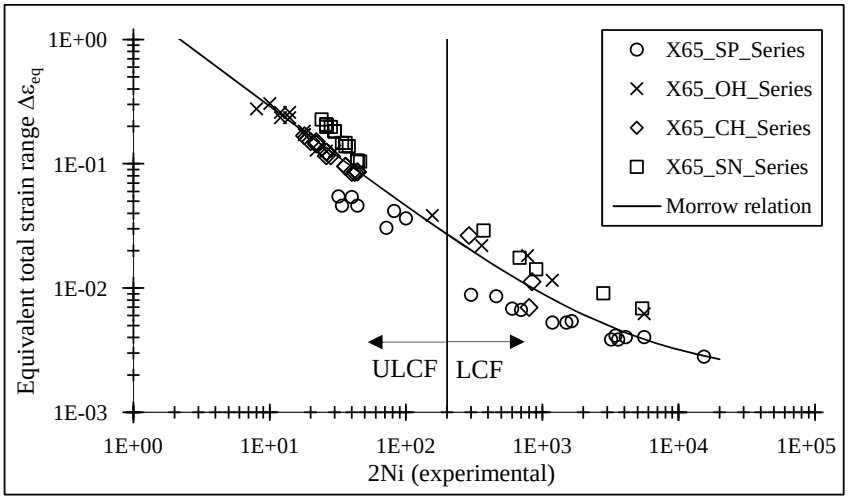

Figure 5.4 – Total strain-life data of the X65 piping steel and correlation using Morrow relation with critical node approach.

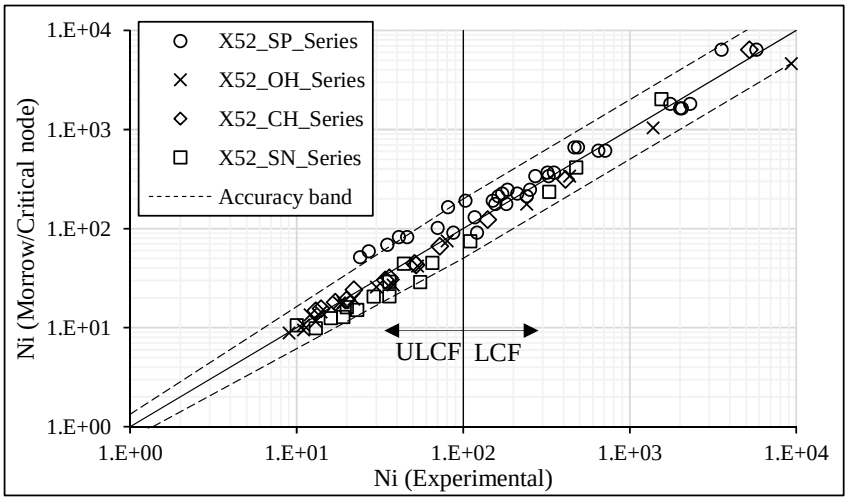

Figure 5.5 – Comparison of experimental data and Morrow approach predictions, based on critical node values, for the X52 piping steel.

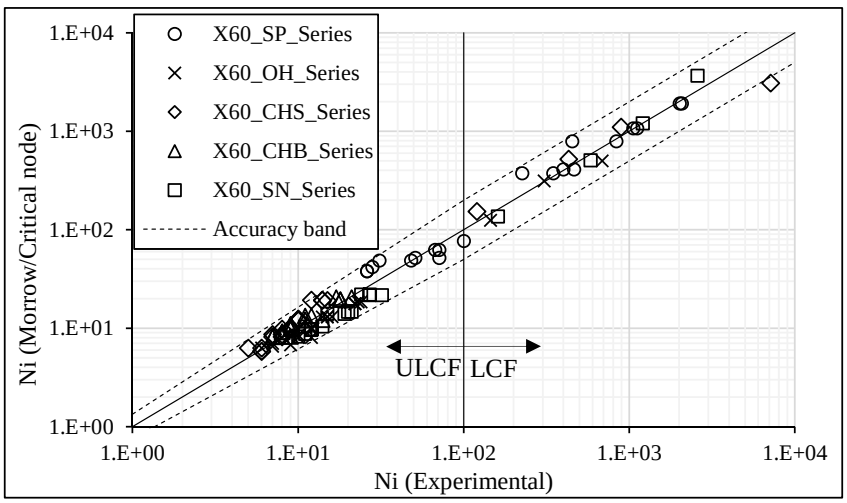

Figure 5.6 – Comparison of experimental data and Morrow approach predictions, based on critical node values, for the X60 piping steel.

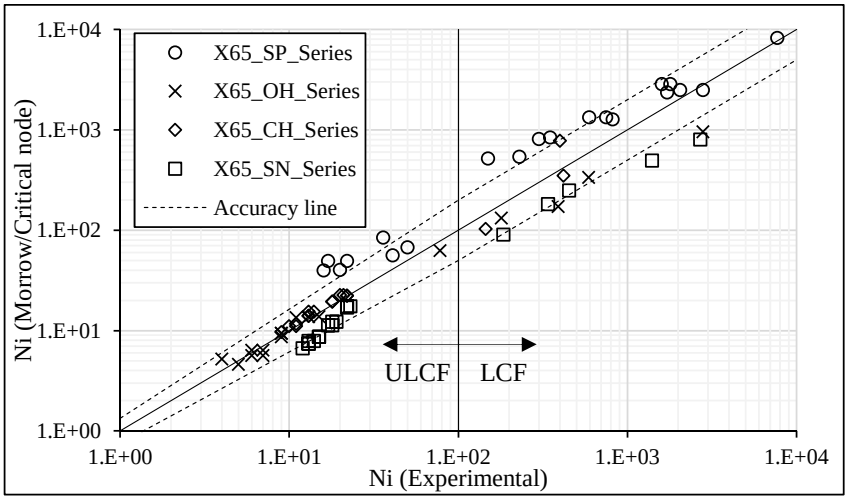

Figure 5.7 – Comparison of experimental data and Morrow approach predictions, based on critical node values, for the X65 piping steel.

5.4 CALIBRATION OF THE TCD METHOD ON LCF AND ULCF LIFE PREDICTION

In this section the TCD is applied together with the Morrow relation for the materials and specimen geometries considered in the previous section. The PM, LM and AM are applied to compute the elastic and plastic effective strains that will be correlated with the number of reversals until the crack initiation. These correlations provide updated Morrow parameters that will be used to estimate the lifetime of smooth and notched plane specimens of X52, X60 and X65 piping steels. The total and plastic strain fields were computed for the specimen's cross-sections as shown schematically in the Figure 5.8. In that figure, the frame origin was placed at the potential crack initiation location. The resulting strain maps allowed the understanding of the strain gradients around the hypothetical crack initiation and propagation path. The equivalent total strain range in a cross-section assessed at a tensile peak for a notched (X52-U-1_OH_01) and smooth specimen (X52-U0_SP_12) can be observed in the Figure 5.9. The analysis of the Figure 5.9a) and Figure 5.9b) allows the identification of the critical locations at mid-thickness and notch root corner, respectively. The main crack propagation direction was assumed along the z axis (plate width), with x axis standing for the thickness direction of the notched specimens.

The simulation of the cyclic tests of smooth specimens accounted for lateral instabilities that may arise from high compressive stress/strains, therefore the crack initiation location could be variable despite of occurring at the specimens' surface [20]. Thus, the crack propagation direction was set from the node with higher equivalent total strain (critical node) along the x axis (thickness direction) with constant z. The evolution of equivalent total strain along the crack propagation direction is represented in the Figure 5.9c) for the strain distribution shown in Figure 5.9a). Combining the formulations of the TCD expressed in the Eq. (5.1) and Eq. (5.2) and the hypothetical crack path orientation at the crack propagation plane, the effective equivalent total and plastic strains were computed for each specimen. Regarding to PM, the effective strain components were directly obtained from the evolution of the equivalent total and plastic strains along the crack path while for the LM the effective total and plastic strains were computed by means of numerical integration of a polynomial function fitted to the equivalent total and plastic strain along the crack path. Moreover, concerning the AM, the effective strain was calculated by averaging the strain data over a circular area with the geometrical centre coincident with the strain concentrator/critical node, as represented in Figure 5.10c).

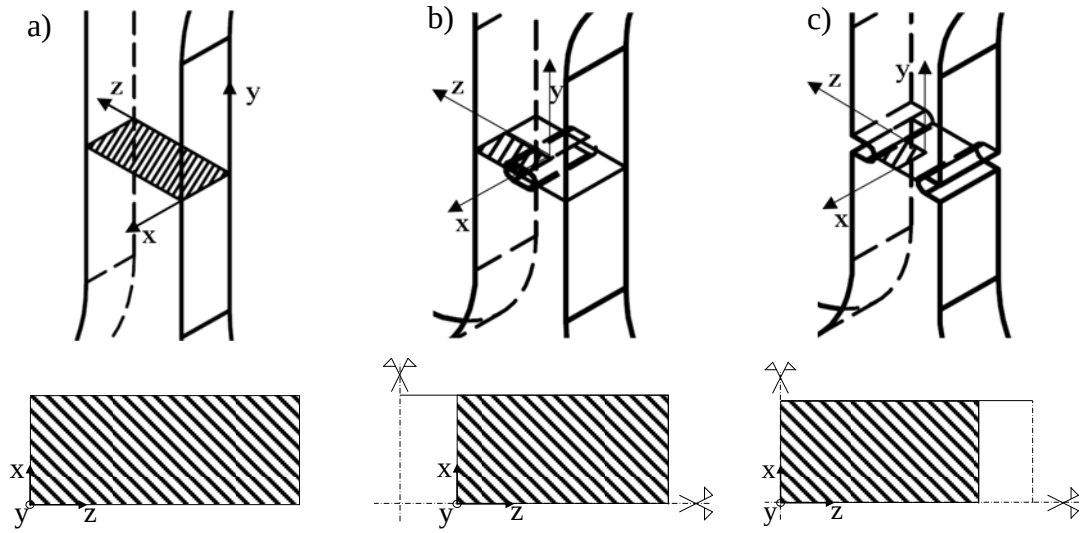

Figure 5.8 – Local coordinate system at central cross-section used for the strain range mapping: a) smooth plane specimens; b) CH and OH series; c) SN series.

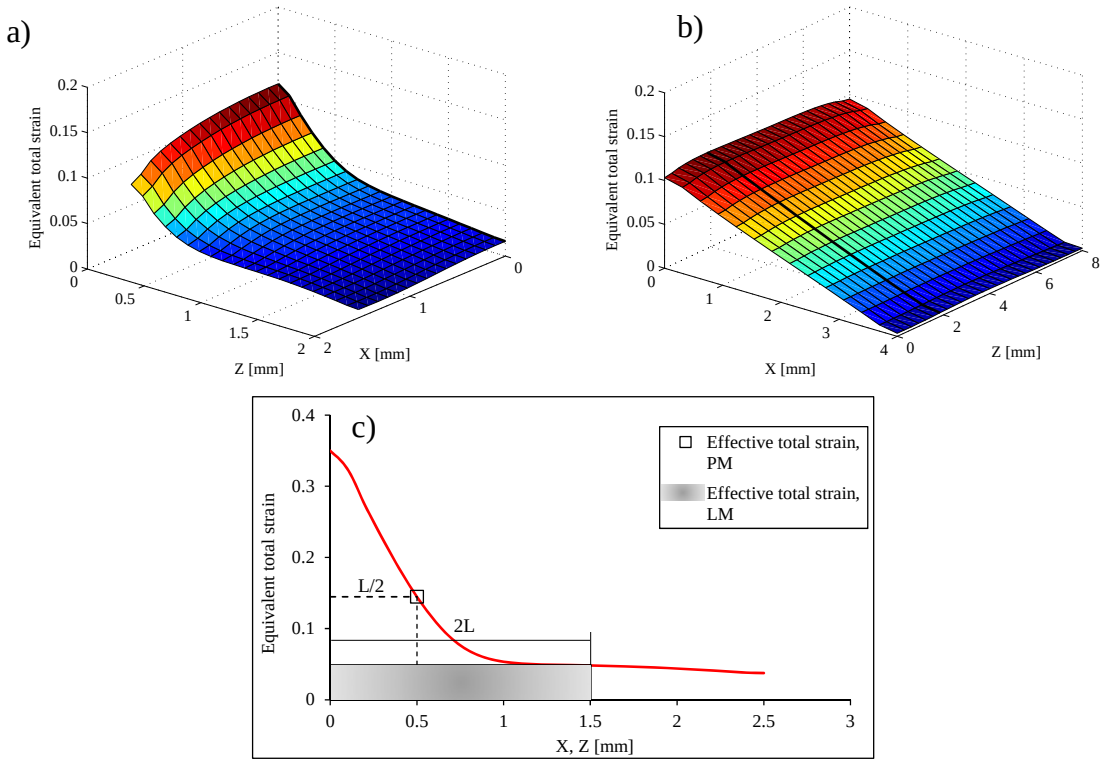

Figure 5.9 – Map of the equivalent total strain range computed for the tensile loading reversal for: a) X52_U0_CH_04 specimen; b) X65_U0_SP_08 specimen. c) Evolution of equivalent total strain along the main crack direction, X60_U-1_CHS_5 specimen.

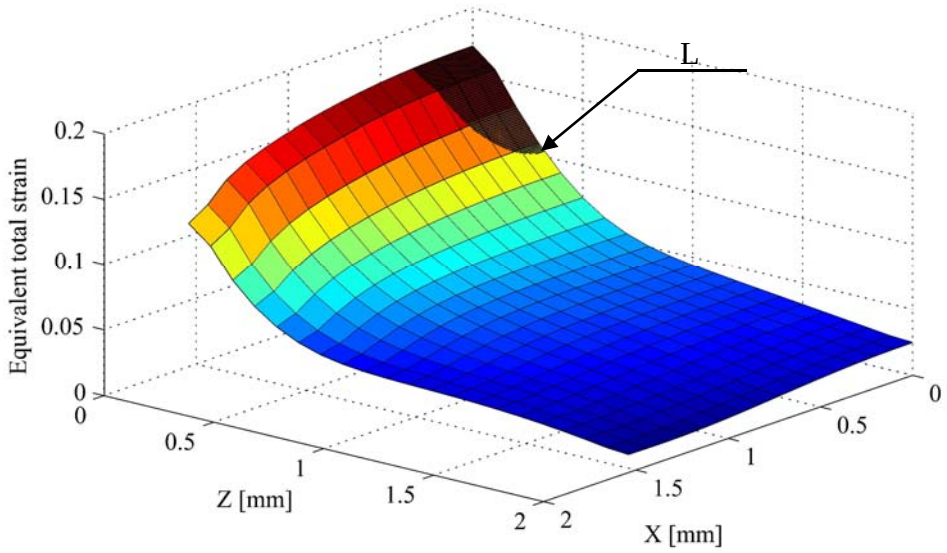

Figure 5.10 – Illustration of the effective equivalent total strain computation by means of TCD/AM: circular region where strains are averaged (see Eq. (5.3)).

The methodology for the assessment of the critical distance L is described below. On effect, to estimate the critical distance L to be applied with the PM, LM and AM a try and error (iterative) method was proposed aiming at maximizing the correlation between the

experimental data and the Morrow's relation. In detail, the PM, LM and AM were applied covering several critical distances (*L* values), which resulted on several fatigue life estimations using the Morrow's relation. The correlation between the experimental number of cycles and numerical fatigue life predictions was measured from the determination coefficient, R^2 that resulted from the least squares method. The values of the determination coefficients were plotted against the distance *L*, as represented in the Figure 5.11 and a polynomial function with six degree order was used to fit the data. The proposed method for *L* identification corresponds to an inverse approach and the validity of the proposed critical distances should be measured by the maximum of the correlation coefficient between the Morrow relation and the experimental data from distinct sources/notched details. Table 5.2 summarizes the maximum correlation coefficients and the resulting critical distances associated with the respective TCD method. In general, reasonable correlation coefficients were verified and comparisons between critical distances achieved for the three piping steels shows that X60 steel presents lower values regarding all TCD approaches. This assumption can be supported by the satisfactory results already attained with the critical node approach. The critical distance *L* presented in Table 5.2, is now used to compute the elastic/plastic strain components by means of PM, LM and AM.

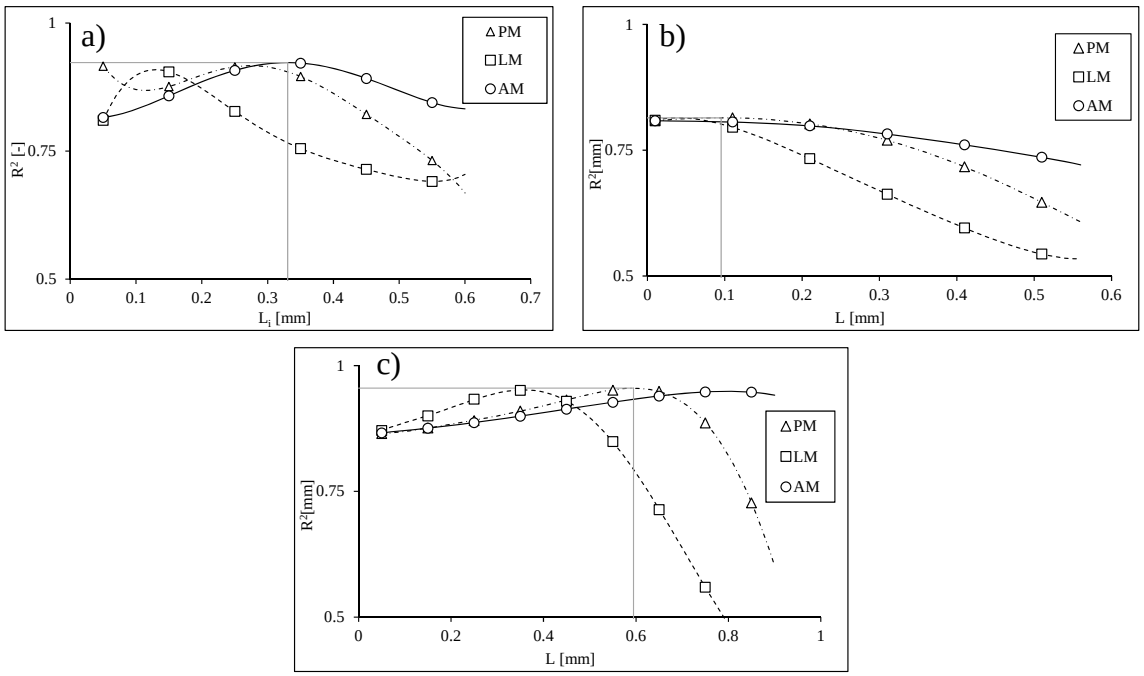

Figure 5.11 – Determination coefficient R^2 as function of distance L_i: a) X52 piping steel; b) X60 piping steel; c) X65 piping steel.

Table 5.2 – Maximum determination coefficients, respective critical distances associated TCD method.

Piping steel	R^2	*L [mm]*	TCD method
X52	0.9226	0.3305	AM
X60	0.8145	0.0955	PM
X65	0.9551	0.5946	PM

The use of the TCD on fatigue life correlation of smooth and notched components based on Morrow's relation represents an improvement when a comparison is established with the results obtained with the critical node approach. The plots of total strain-life data using the critical distance applied to the three TCD methods are illustrated in Figure 5.12 to Figure 5.14. These figures report the three cases referred in Table 5.2. The analysis of the Figure 5.12 to Figure 5.14 shows significant enhancements for ULCF results. This is more visible for the smooth specimens' data. The TCD formulations led to an update the parameters of the Morrow's relation which will be related with the methodology used to compute the elastic/plastic strain components. The updated parameters of Morrow's relation associated with each approach and materials are given in Table 5.3.

Table 5.3 – Parameters of Morrow relation of X52, X60 and X65 piping steels obtained with PM, LM and AM.

Piping steel	σ'_f MPa]	*b*	ε'_f	*c*	*TCD method*
X52	742.57	-0.0763	0.7929	-0.6507	PM
	699.60	-0.0715	0.5752	-0.6315	LM
	762.20	-0.0778	0.8516	-0.6561	AM
X60	613.24	-0.0401	1.401	-0.7058	PM
	599.22	-0.0372	1.3096	-0.7030	LM
	614.19	-0.0403	1.3981	-0.7059	AM
X65	744.81	-0.0542	0.9977	-0.7764	PM
	739.48	-0.0569	0.7469	-0.7623	LM
	750.67	-0.0550	1.1602	-0.7855	AM

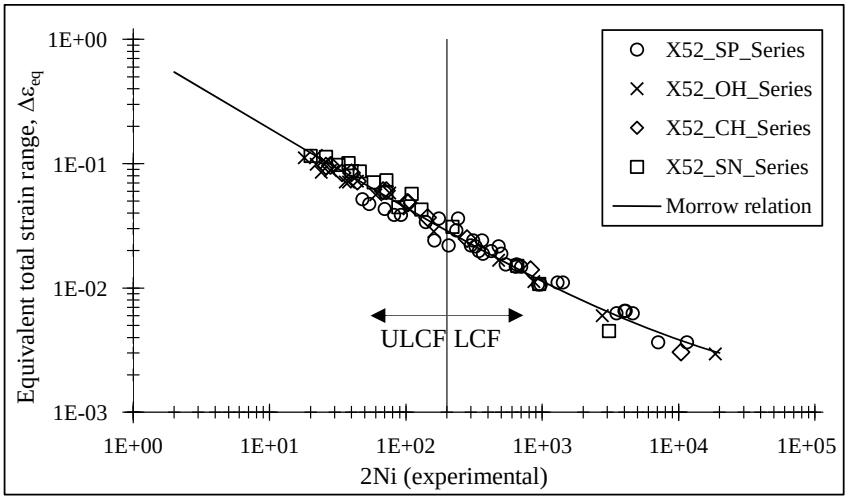

Figure 5.12 – Total strain-life data of the X52 piping steel and correlation using Morrow relation with AM.

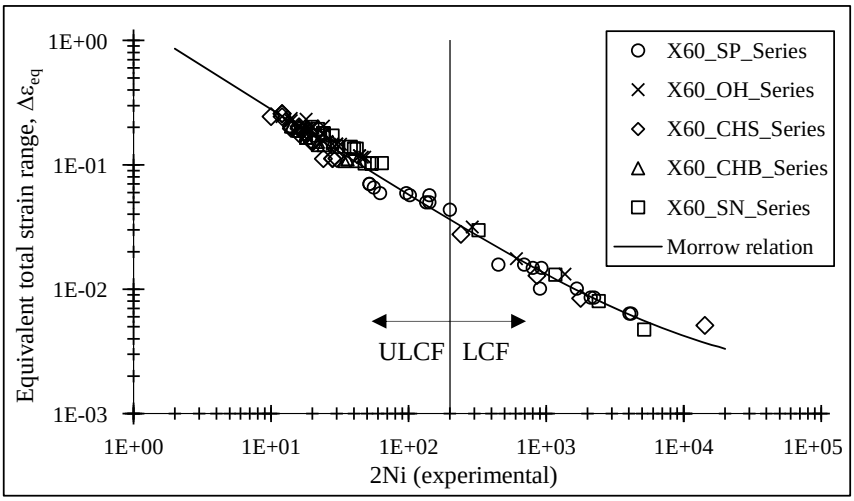

Figure 5.13 – Total strain-life data of the X60 piping steel and correlation using Morrow relation with PM.

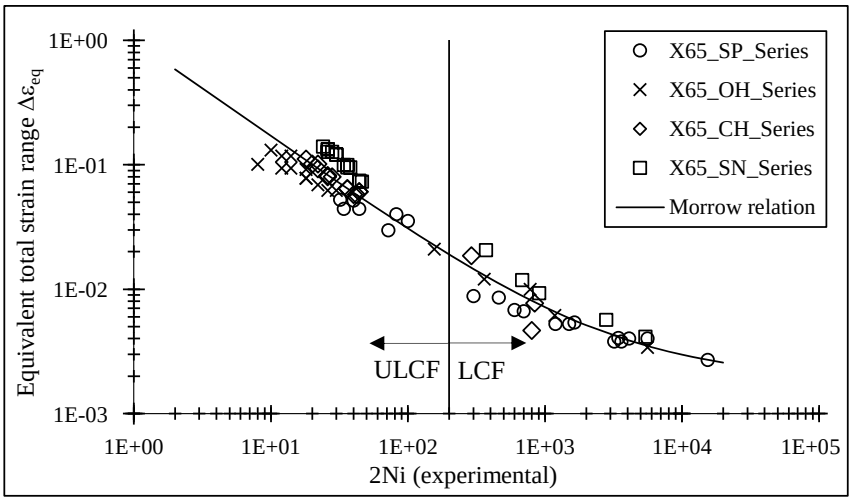

Figure 5.14 – Total strain-life data of the X65 piping steel and correlation using Morrow relation with PM.

Fatigue lifetime predictions were performed using the parameters of Morrow relation presented in Table 5.3 and compared with experimental results, as illustrated in Figure 5.15 to Figure 5.20. In a global overview of the results, the three approaches for TCD application proposed in this study, produced very satisfactory results when compared with the critical node approach, mainly for X52 and X65 piping steels. Particularly the smooth specimen's data was better correlated with the notched data, demonstrating Morrow's relation as a suitable approach to model both smooth and notched fatigue data in the LCF/ULCF regimes. The application of AM results on the best fatigue life predictions (points falling inside the accuracy band) of X52 and X65 piping steel, despite of the critical distance of X65 steel grade has been computed by means of PM. Concerning the X60 piping steel, similar fatigue life estimations are observed independently of the TCD method. The same accuracy bands proposed for critical node approach were used in the proposed comparisons. In addition, to enhance the good performance of TCD method, improved accuracy bands are proposed and added to the comparison of experimental and numerical data. For ULCF domain a progressive condition was used, reducing the accuracy band from LCF to 1.25x and 0.8x of experimental fatigue life in the ULCF (Ni=1 cycle). For LCF regime the double and half-life criterion was replaced by a 1.75x and 0.57x criterion. Even using more conservative accuracy bands the TCD method is able to estimate the fatigue life of smooth and notched specimens under ULCF and LCF domains, mainly for X52 and X60 piping steel.

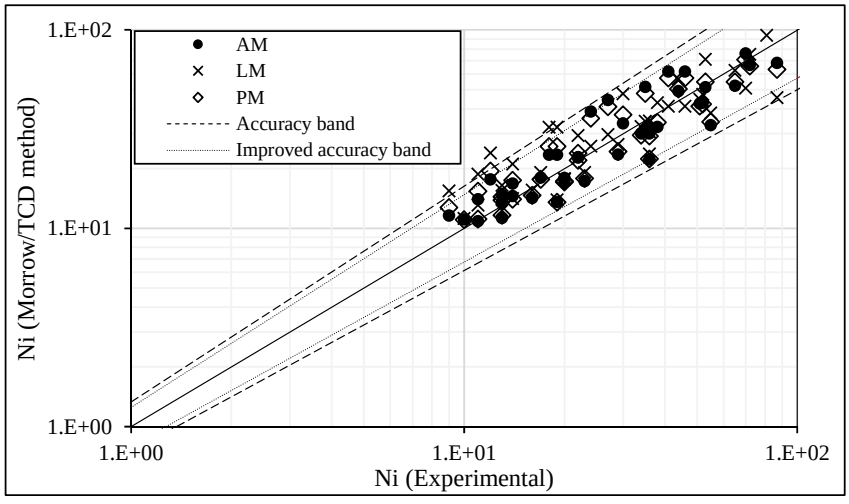

Figure 5.15 – Comparison of experimental data and Morrow/TCD methods predictions for X52 piping steel under ULCF domain.

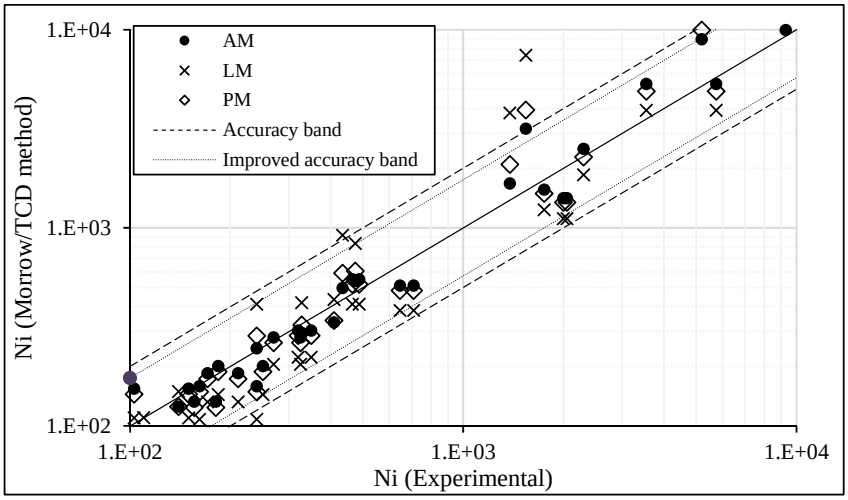

Figure 5.16 – Comparison of experimental data and Morrow/TCD methods predictions for X52 piping steel under LCF domain.

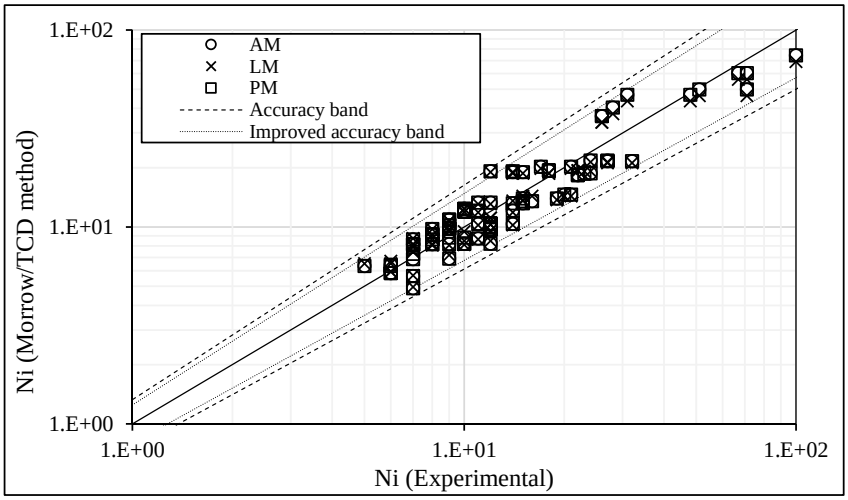

Figure 5.17 – Comparison of experimental data and Morrow/TCD methods predictions for X60 piping steel under ULCF domain.

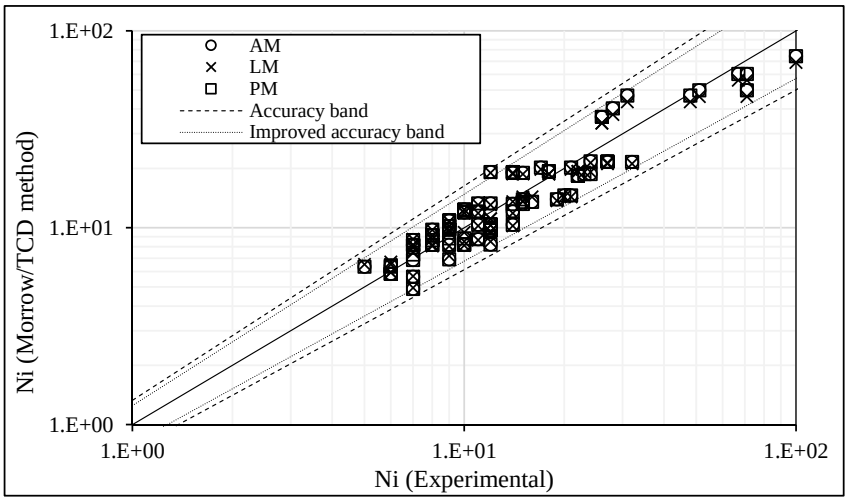

Figure 5.18 – Comparison of experimental data and Morrow/TCD methods predictions for X60 piping steel under LCF domain.

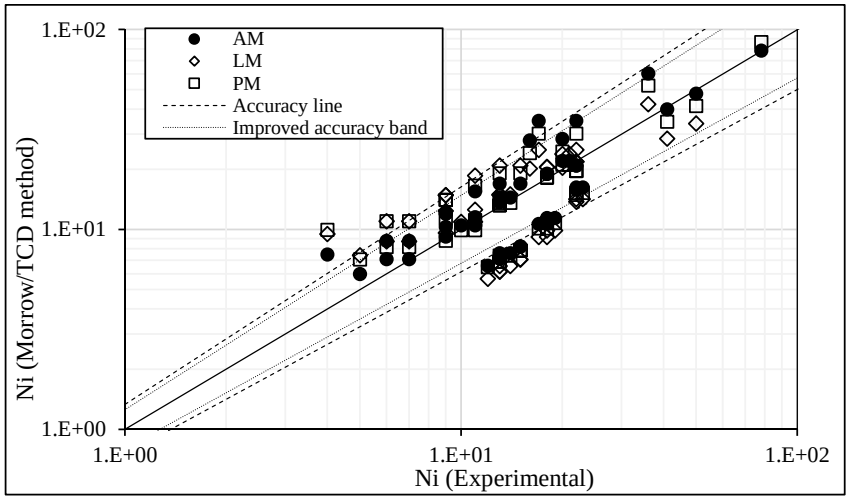

Figure 5.19 – Comparison of experimental data and Morrow/TCD methods predictions for X65 piping steel under ULCF domain.

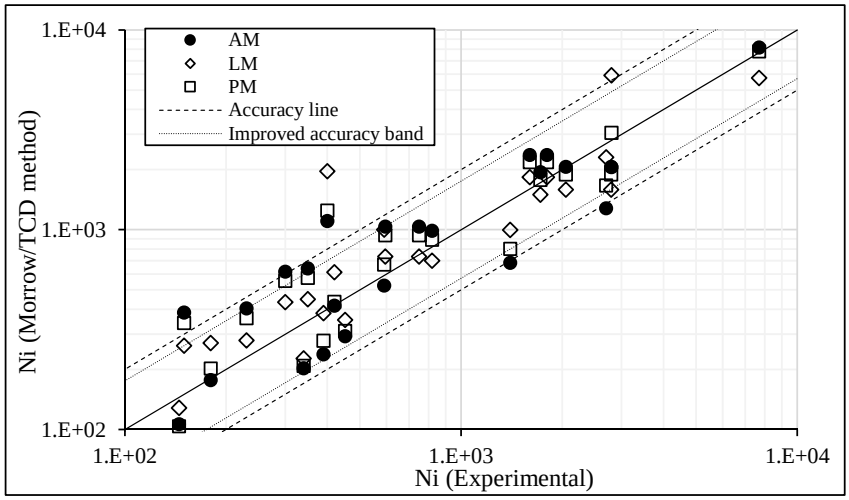

Figure 5.20 – Comparison of experimental data and Morrow/TCD methods predictions for X65 piping steel under LCF domain.

5.5 APPLICATION OF TCD TO THE FATIGUE PREDICTION OF CYCLIC BENDING TESTING RESULTS AVAILABLE FOR THE X52 STEEL

The numerical data of tensile/compression cyclic tests were used to investigate the performance of the TCD approaches in the simultaneous fatigue life prediction of ULCF and LCF domains. The application of PM, LM and AM resulted in the determination of characteristic lengths, associated to each piping steel. Based on these characteristic lengths, the global parameters of the Morrow's strain-life relation were obtained.

In this section, the Morrow relation and the characteristic length obtained for the X52 piping steel will be applied to the fatigue life predictions for the cyclic bending tests performed for the X52 steel (refer to Section 4.xx for details). Both notched and flat-grooved specimens of X52 piping steel are recalled in this section. Figure 5.21 and Figure 5.22 compare the experimental results with the number of cycles computed with the TCD approach for the X52. Similar results to the critical node approach, presented in the Chapter 4 are observed and the best fatigue life predictions are obtained with the application of AM. The analysis of these figures reveals good correlations between the reference line and the data points of the notched plane series, however the Morrow relation applied by means of TCD formulation is not adequate to estimate the fatigue life of the flat-grooved specimens subjected to bending cyclic loading. As verified in the Chapter 4, the flat-grooved specimens exhibit a plane strain state, which results in a Lode angle parameter around to $\bar{\theta} = 0$ and a lower monotonic fracture strain, ($\bar{\varepsilon}_f$=0.45). In contrast, the smooth and plane notched specimens present positive values regarding the Lode parameter and higher fracture strains. The loss of ductility due to Lode angle reduction is clearly evidenced from these results, thus the strain field information only is not able to perform adequate life estimations. The effect of stress state conditions on fatigue life estimation is more important than accounting for the strain gradient around the critical location of the specimens.

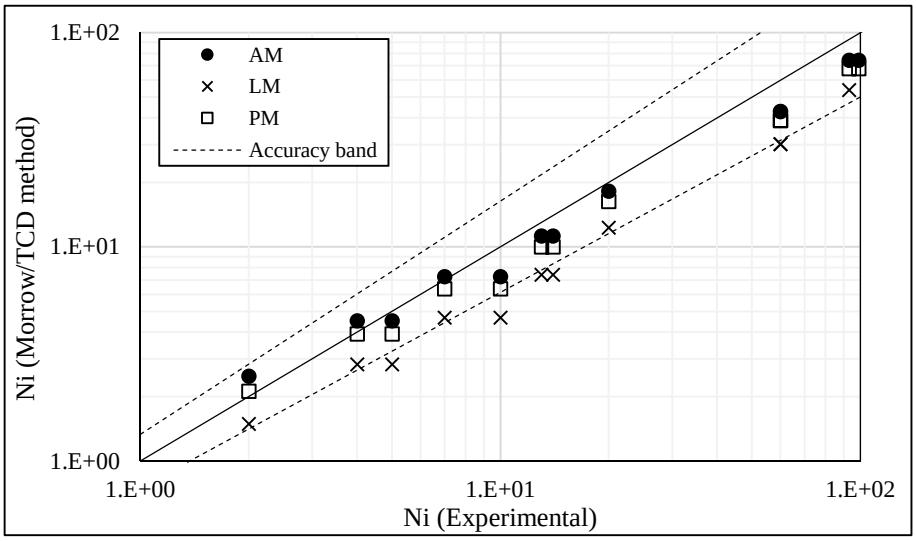

Figure 5.21 – Comparison of experimental data and Morrow/TCD method predictions for notched plane specimens of X52 steel under cyclic bending.

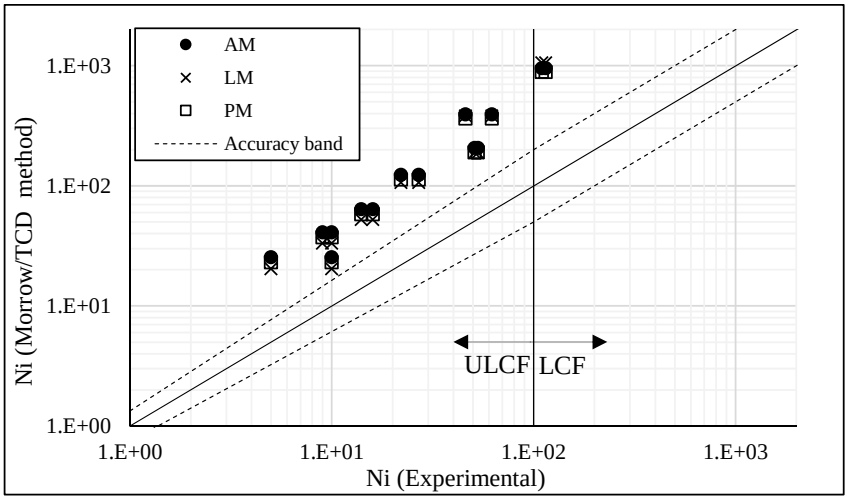

Figure 5.22 – Comparison of experimental data and Morrow / TCD methods for flat-grooved plane specimens of X52 steel under cyclic bending.

5.6 CONCLUSIONS

The performance of the TCD on ULCF and LCF life prediction was investigated in this chapter considering a strain-based model. The total, plastic and elastic strain components were computed following a multiaxial strain approach definition. The Morrow relation was able to reproduce the strain-life behavior of the X52, X60 and X65 piping steels, covering both fatigue regimes investigated in this work. Although generally accepted that both fatigue regimes may exhibit distinct damage mechanisms, the Morrow relation was still able to correlate the experimental data in both regimes. The elastoplastic TCD applied in the form of PM, LM and AM was able to predict the fatigue failure under high plastic strain levels with more accuracy than the typical approach based on the critical node. However the different approaches for the TCD resulted in distinct characteristic lengths. In general, successful results for smooth and notched specimens were obtained independently of the adopted methodology. However, AM seems to be the most accurate method since it accounts for the gradients in both directions. Elastoplastic finite element simulations allowed the definition of the potential crack propagation paths and were essential to derive the elastic and plastic strain distribution along it, mainly for the notched specimens. In addition, a semi-circular area with the geometrical center

coincident with the tip of the strain concentrator and with a fix radius was defined to compute the equivalent strain components.

The critical distances were found for each material and can be treated as a material property. The X60 piping steel can be considered as the least sensitive to the TCD since assumes the lower values for the critical distance. In order to check the consistency and accuracy of the TCD under cyclic loading with high strain conditions, different notched specimen geometries were used.

Additionally, alternative loading conditions as reproduced by bending cyclic tests were investigated for the X52 steel. Different monotonic fracture strains, triaxialities and Lode angle parameters are covered by this set of specimens. The application of the TCD with the Morrow multiaxial strain-life approach was not enough to address the diversity of fatigue data. However, this is not a problem that can be attributed to the TCD but to the damage approach considered. Nevertheless the use of the TCD together a good damage estimator can lead to improved predictions. Instead of using the Morrow's approach, the Xue's approach should be implemented with the TCD approach in order to account properly for both stress triaxiality and Lode angle parameters. In this case, besides the strain range defined as an effective strain range, based on a characteristic length, the equivalent plastic strain, which is a monotonic parameter, needs to be computed using the same effective concepts.

5.7 REFERENCES

[1] Xue L., (2007), “A unified expression for low cycle fatigue and extremely low-cycle fatigue and its implication for monotonic loading.” International Journal of Fatigue, 30:1691–1698.

[2] Kanvinde A.M., Deierlein G.G., 2007, “Cyclic void growth model to assess ductile fracture initiation in structural steels due to ultra-low cycle fatigue”, Journal of Engineering Mechanics-ASCE, 133(6):701-712.

[3] Tateishi K., Hanji T., (2004), “Low cycle fatigue strength of butt-welded steel joint by means of new testing system with image technique.” International Journal of Fatigue, 26:1349–1356.

[4] Pereira J.C.R., de Jesus A.M.P., Fernandes A.A., (2016), “Identification of 3D fracture ductile fracture locus for X60 piping steel and calibration of Xue-Pereira model for ULCF”, submitted to the International Journal of Fatigue.

[5] Neuber, H., 1958. “Theory of Notch Stresses: Principles for Exact Calculation of Strength With Reference to Structural Form and Material. Berlin,” Springer-Verlag (2nd edition).

[6] Neuber, H., (1961), “Theory of Stress Concentration for Shear-Strained Prismatical Bodies with Arbitrary Nonlinear Stress-Strain Law,” ASME J. Appl. Mech. 28: 544–50.

[7] Peterson, R.E., (1959), “Notch Sensitivity,” In: Metal Fatigue, G. Sines and J. L. Waisman, eds., McGraw Hill, New York, 293–306.

[8] Taylor, D, (2007), "The Theory of Critical Distances: A New Perspective in Fracture Mechanics," Oxford: Elsevier.

[9] Susmel, L., Taylor, D., (2008), "Fatigue Design in the Presence of Stress Concentrations," J. Stain Anal. 38 (5): 443-452.

[10] Whitney, J.M., Nuismer, R.J., (1974), "Stress fracture criteria for laminated composites containing stress concentrations," J Compos Mater, 8: 253–65.

[11] Tanaka, K., (1983), "Engineering formulae for fatigue strength reduction due to crack-like notches," Int J Fract, 22: 39–45.

[12] Taylor, D., (1999), "Geometrical effects in fatigue: a unifying theoretical model," International Journal of Fatigue, 21: 413–20.

[13] Susmel, L., Taylor, D., (2010), "An elasto-plastic reformulation of the theory of critical distances to estimate lifetime of notched components failing in the low/medium-cycle fatigue regime," Journal of Engineering Materials and Technology, 132(2): 210021–210028.

[14] Susmel, L., Taylor, D., (2008), "On the use of the Theory of Critical Distances to predict static failures in ductile metallic materials containing different geometrical features," Engineering Fracture Mechanics 75: 4410–4421

[15] Coffin, L.F., (1954), "A study of the effects of cyclic thermal stresses on a ductile metal," Transactions ASME, 76: 931-950.

[16] Manson, S.S., (1954), "Behaviour of materials under conditions of thermal stress," National Advisory Committee for Aeronautics, NACA TN-2933.

[17] Susmel, L., Taylor, D., (2015), “Estimating lifetime of notched components subjected to variable amplitude fatigue loading according to the elasto-plastic Theory of Critical Distances", Journal of Engineering Materials and Technology, 137(1): 11008-11023.

[18] ASME, (2004) ASME Boiler and Pressure Vessel Code, ASME, New York.

[19] Morrow, J.D., (1965), “Cyclic plastic strain energy and fatigue of metals,” International Friction, Damping and Cyclic Plasticity, ASTM, STP 378: 45-87.

[20] Basquin, O.H., (1910), “The Exponential Law of Endurance Tests,” Proceedings of the American Society for Testing and Materials, 10: 625-630.

Chapter VI

Full-scale cyclic tests of elbows and straight pipes

6.1 INTRODUCTION

In the present chapter, an experimental program of ULCF tests carried out on large-scale tests of elbows and straight pipes of X60 and X65 API steel grades is described. The experimental program was developed as part of the ULCF European project (*Ultra Low Cycle Fatigue of Steel Under Cyclic High-Strain Loading Conditions*). The cyclic tests on elbows were performed by the Department of Ferrous Metallurgy of Aachen University (RWTH). OCAS N.V. (Zwijnaarde, Belgium) carried out the cyclic bending test on straight pipes. Both institutions were partners of the referred project. The experimental program consisted on cyclic tests under ULCF domain aiming to evaluate the fatigue behaviour of these components when subjected to high cyclic strain ranges that could result from intensive actions such as seismic actions.

The materials of such piping components were already tested in the Chapter III and constitutive models identified in the Chapter IV. The materials used to manufacture the elbows consisted of X60 and X65 steels with the thermal cycle (X60TT and X65TT). The materials used for the cyclic bending tests of the straight pipes were the X60 and X65 API steel grades.

The availability of such cyclic ULCF full-scale tests of pipe components is very limited in the literature due to the very high costs of such kind of tests. Therefore the data provided in by the ULCF project was used in this thesis in order to validate the modelling approaches proposed in the Chapter IV. This chapter will present an overview of the experimental results of the full-scale tests, but more details can be found in the literature [1]-[4].

6.2 FULL-SCALE TESTS OF ELBOWS UNDER CYCLIC LOADING

A total of eight full-scale cyclic tests on elbows were carried out, four of each steel grade, X60TT and X65TT steels respectively. For each material, two distinct geometries were

also considered, which consisted on using elbows with angles of 45º and 90º. In addition to cyclic push-pull external loading, the elbows were also subjected to internal pressure.

6.2.1 Description of the materials and full-scale specimens

The elbows were obtained from straight pipe sections which have been applied a hot-forming/bending process to create a central curved section of the tube, resulting in distinct sections: a central zone of the elbow and two straight sections at the ends of which displacements are imposed by hydraulic actuators. The common value of three times the diameter (R = 3xD) has been selected for the fillet radius of the elbow. Concerning the length of both straight pipe sections, a value of five times the diameter (L = 5xD) has been selected. The overall dimensions of the elbow are represented in the Figure 6.1.~

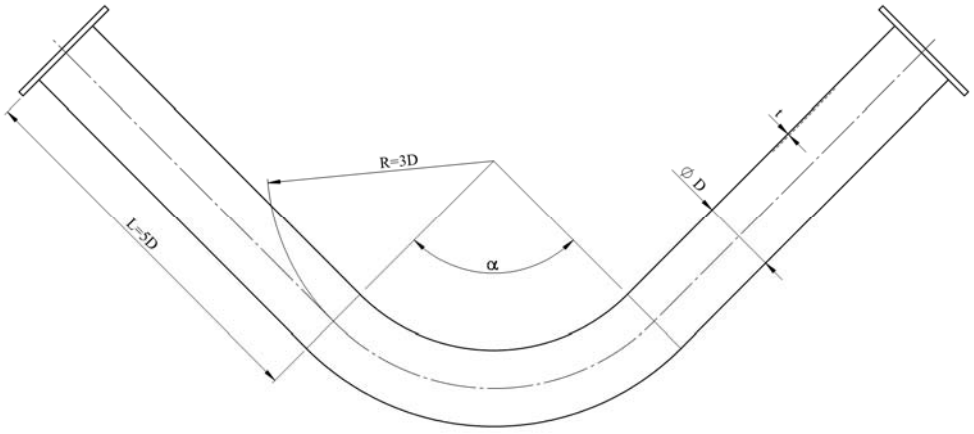

Figure 6.1 – Overall dimensions of the elbow specimens [5].

The initial straight pipes were manufactured by OCAS NV® and were bent by FABRICOM® located in Strijen, Netherlands. As referred in the Chapter III, the thermal process consisted of a heating until 950ºC±20ºC followed by rapid cooling, using water applied on the outer surface of the tubes, during bending. In order to obtain a uniform microstructure, a heat treatment consisting in a temper was applied, after the bending process. A temper consisting on a stage at 510ºC−520ºC, during 30 minutes, followed by slow cooling (175ºC/hour), was applied. Finally two flanges were welded to the ends of the straight sections, which were used for the gripping system. This procedure was executed by Claus Queck GmbH in Germany. For the application of the inner pressure during the experimental tests, hydraulic hoses were connected to the head plates of the specimens. The

connection was performed by an internal thread. Table 6.1 summarizes the elbows used in the cyclic tests.

Table 6.1 – Summary of elbows specimens.

Specimen	Steel grade	Diameter [in]	Wall thickness [mm]	Elbow angle [°]	Internal pressure [Bar]
SP1	X60TT	16.0	9.5	90	80
SP2					20
SP3				45	20
SP4					80
SP5	X65TT	8.625	5.59	90	95
SP6					24
SP7				45	95
SP8					24

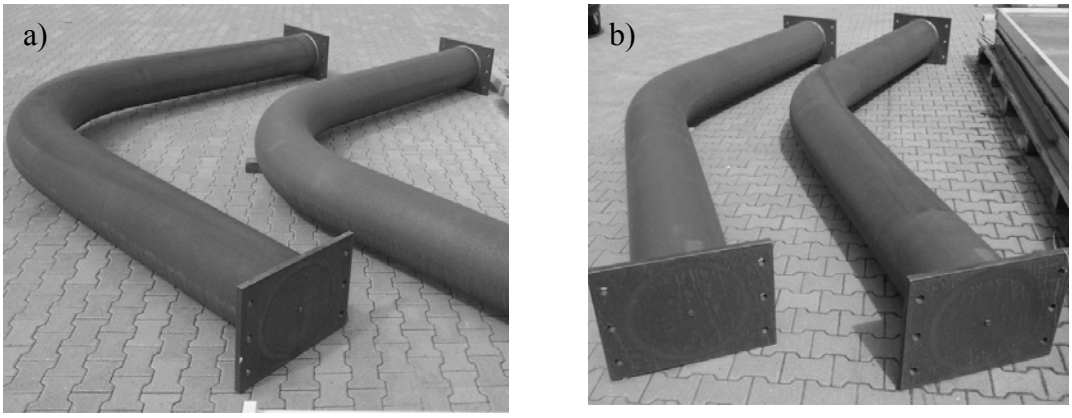

Figure 6.2 – Elbows of X60 piping steel: a) SP1 and SP2 specimens; b) SP3 and SP4 specimens [5].

Figure 6.3 – Elbows of X65 piping steel: SP5 to SP8 specimens [5].

All elbows were subjected to diameter, perimeter and thickness measurements since during the forming process these dimensions may suffer variations and those variations may have a significant influence the testing results. A slide gauge, tape ruler and an ultrasonic device

were used to measure the diameter (D), perimeter (P) and the thickness (t), respectively. Figure 6.4 shows the measuring points on the specimens. The vertical (D_{1-5}) and horizontal (D_{3-7}) diameter as well as the perimeter of each specimen for the section A to O was measured. Concerning the thickness, values for the points 1 to 8 for sections A to O were recorded. The average measurements that have been taken according to the measurements scheme illustrated in the Figure 6.4 are given in Table 6.2 and Table 6.3. The measured diameters along the straight pipe shows a good correlation with the nominal values. Although, the bending process promotes slight differences on the vertical and horizontal diameter in the elbow pipe (section E to section K). The thickness values also differ significantly for the points 1 to 8 in the range of the elbow pipe. In detail, due to bending process, which promotes tensile-compression stresses, the thickness increases in the outer area (point 4, 5 and 6) and decreases in the inner area (points 1, 2 and 8).

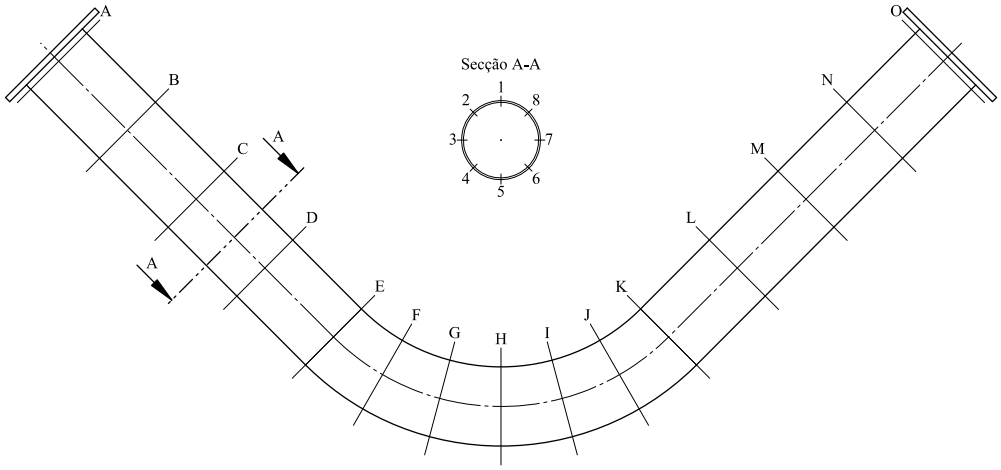

Figure 6.4 – Section with measuring points adopted for the elbows [5].

Table 6.2 – Mean measurements of the vertical and horizontal diameter, perimeter and thickness for SP1 to SP4 specimens (dimension in mm) [5].

Parameter	SP1		SP2		SP3		SP4	
	Straight pipe	**Elbow pipe**	**Straight pipe**	**Elbow pipe**	**Straight pipe**	**Elbow pipe**	**Straight pipe**	**Elbow pipe**
D_{1-5}	407.75	401.80	407.56	401.60	407.88	400.70	407.50	402.20
D_{3-7}	406.63	408.80	406.94	408.50	406.63	409.80	406.88	408.20
P	1283.19	1278.00	1283.13	1277.40	1283.25	1278.90	1283.00	1279.60
t_1	9.43	11.15	9.47	11.25	9.46	11.13	9.49	11.26
t_2	9.46	10.57	9.45	10.61	9.92	11.19	9.66	10.90
t_3	9.49	9.45	9.50	9.53	9.49	9.45	9.42	9.45
t_4	9.48	8.64	9.52	8.69	9.49	8.62	9.46	8.64
t_5	9.48	8.32	9.51	8.37	9.56	8.32	9.53	8.37
t_6	9.44	8.63	9.48	8.67	9.59	8.64	9.56	8.68
t_7	9.40	9.41	9.48	9.51	9.54	9.46	9.55	9.54
t_8	9.73	10.29	9.13	10.39	9.49	10.58	9.50	10.68

Table 6.3 – Mean measurements of vertical and horizontal diameter, perimeter and thickness for SP5 to SP8 specimens (dimension in mm) [5].

Parameter	SP5		SP6		SP7		SP8	
	Straight pipe	Elbow pipe	Straight pipe	Elbow pipe	Straight pipe	Elbow pipe	Straight pipe	Elbow pipe
D_{1-5}	219.94	213.40	220.31	212.90	219.69	213.42	219.69	213.50
D_{3-7}	219.94	222.40	219.94	223.10	220.19	222.92	219.88	222.75
P	693.44	687.60	693.56	688.00	693.38	688.70	692.75	685.80
t_1	5.69	6.68	5.66	6.67	5.71	6.88	5.71	6.79
t_2	5.67	6.27	5.64	6.29	5.65	6.36	5.65	6.36
t_3	5.67	5.66	5.65	5.67	5.70	5.74	5.67	5.71
t_4	5.68	5.20	5.67	5.20	5.63	5.26	5.67	5.27
t_5	5.68	5.07	5.65	5.09	5.52	4.99	5.68	5.12
t_6	5.65	5.20	5.65	5.22	5.49	5.10	5.63	5.23
t_7	5.55	5.53	5.55	5.55	5.36	5.49	5.55	5.61
t_8	5.64	6.27	5.64	6.30	5.49	6.24	5.64	6.35

6.2.2 Description of the experimental setup

During the cyclic tests, the elbows were subjected to push-pull displacements resulting in cyclic bending of the elbow. Also, an internal pressure was applied by means of pressurized water. The displacements were applied by means of two hydraulic cylinders with a maximum displacement of 400mm. Figure 6.5a) illustrates the hinges used to connect the cylinders to the flanges of the straight pipe sections. This system was designed in order to allow the connection between the specimen and a reaction wall using hydraulic cylinders. The experimental setup is illustrated in Figure 6.5b). Taking into account the different specimen geometries the position of the actuator supports can be adjusted. To apply the inner pressure during the cyclic tests a hole in the center of the head plates was included to connect the hydraulic hoses to the specimens head plates. Table 6.4 summarizes the nominal values of inner pressures applied to each specimen. The inner pressure for the experimental tests was applied with a hand pump. Due to the cyclic bending deformation of the specimen, a fluctuation on the inner pressure was observed. Thus, an analogue manometer that was used for the first specimen, was replaced by a digital device to record the inner pressure fluctuations over the time. This information was latter used in the numerical simulations.

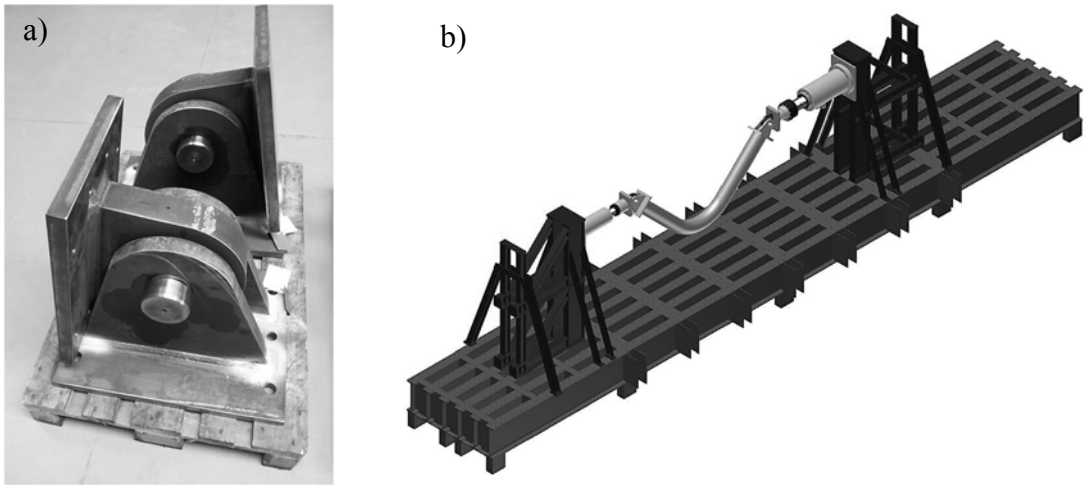

Figure 6.5 – a) Hinges used in cyclic bending tests; b) overview of the overall test setup [5].

Table 6.4 – Inner nominal pressures applied for each specimen.

X60 elbows		X65 elbows	
Specimen	**Pressure [bar]**	**Specimens**	**Pressure [bar]**
SP1	80	SP5	95
SP2	20	SP6	24
SP3	20	SP7	95
SP4	80	SP8	24

The reaction forces were measured by load cells placed in between the cylinders and the hinges. In addition, a pull wire displacement transducer (WDT) was connected to the hinges at the ends of the pipe in order to accurately monitor the displacements of the specimen ends, as schematically represented in Figure 6.6. Moreover, the specimens' ovalization at the elbows central section was monitored using laser devices mounted at a special-purpose steel frame attached on each specimen, as can be observed in Figure 6.7. However, some instabilities regarding this system were observed, which hindered the monitoring of the specimen ovalization until the final failure.

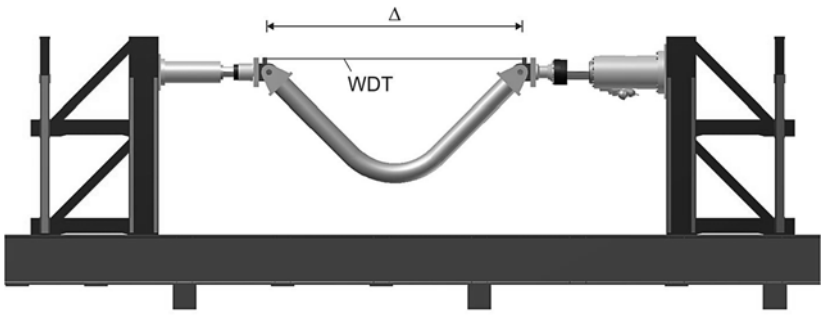

Figure 6.6 – Displacement measurement with a WDT [5].

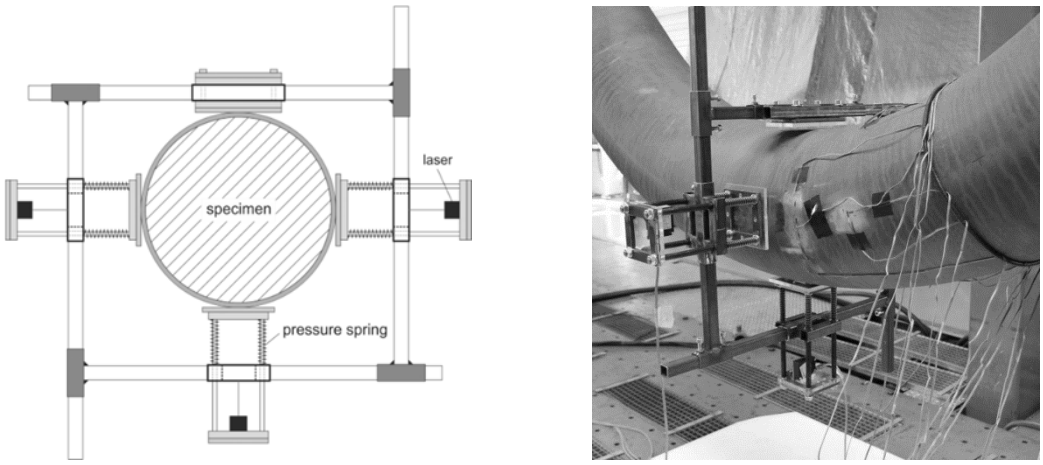

Figure 6.7 – a) Schematic of the ovalization measuring equipment [5]; b) ovalization measuring equipment applied on SP2 specimen [5].

6.2.3 Description of the cyclic testing procedure for the elbows

The ULCF testing program of the elbows followed the *"Recommended Testing Procedure for Assessing the Behaviour of Structural Steel Elements under Cyclic Loads"*, published by the European Convention for Constructional Steelwork (ECCS) [6]. The complete procedure recommends a total of three tests as follows:

1. Monotonic tension displacement increasing test
2. Monotonic compression displacement increasing test
3. Cyclic test with increase of displacement/amplitudes

The preliminary monotonic tests are used to derive the plastic limits of the structural component under tension e_y^+ and compression e_y^-, which will be used to define the cyclic loading. The recommendation allows to compute these parameters from finite element analysis that represents an advantage when there is a limited amount of specimens.

Numerical models were built in the commercial code ABAQUS® and were based on the nominal dimensions, namely the diameter (D) and thickness (t) of each specimen. In detail, D=16" (D=406.4mm) and t=9.5mm was assumed for SP1 to SP4 of X60 piping steel, and D=8 5/8" (D=219.1mm) and t=5.59mm for the specimens SP5 and SP8. In the total, a number of 16 simulations are required. The geometry of the numerical model of specimen SP1 and SP2 is illustrated in Figure 6.8. Due to a lack of small scale tests on X65 material, at the time of all numerical simulations, for the definition of the material cyclic parameters results from the X60 material were adopted. The numerical results relative to the monotonic load-displacement curves are illustrated in the Figure 6.9 for the SP1 specimen, including

the tangents for the evaluation of the yield loads, F_y, and the corresponding displacements, e_y. The parameters addressed from the 16 simulations and covering all the materials/geometries are presented in the

Table 6.5. In order to simplify the application of the displacements during the tests, the average value e_y which results from the e_y^+ and e_y^- was used as a reference value.

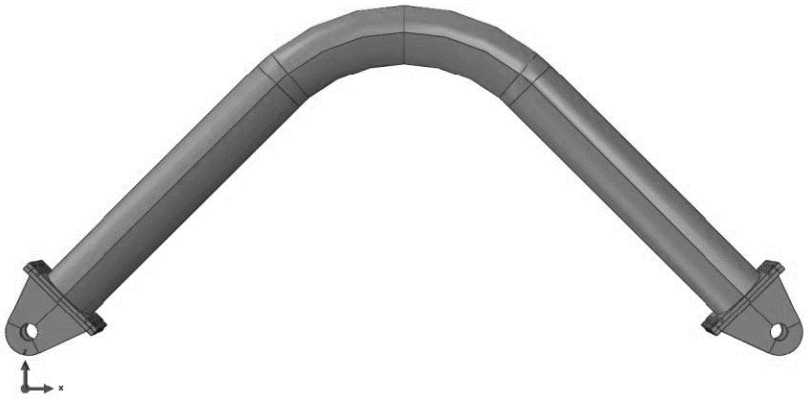

Figure 6.8 – Geometrical model of SP1 specimen [5].

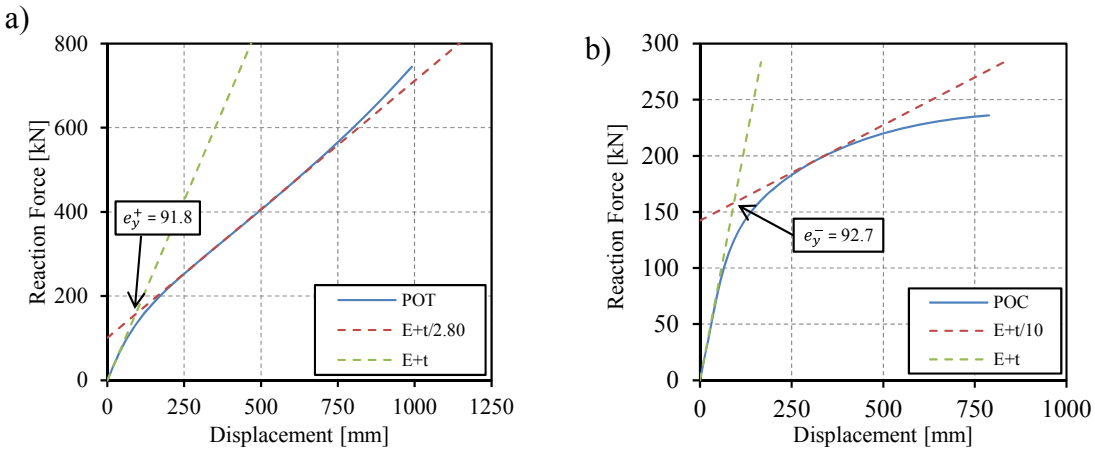

Figure 6.9 – Monotonic load-displacement curves used to compute the parameters involved in the cyclic tests of SP1 specimen: a) tensile/pull loading; b) compressive/push loading [5].

Table 6.5 – Parameters extracted from numerical simulations of the elbows [5].

Specimen	F_y^+	e_y^+	F_y^-	e_y^-	e_y
[-]	[kN]	[mm]	[kN]	[mm]	[mm]
SP1	157.1	91.8	-157.9	-92.7	±90
SP2	116.4	86.9	-105.7	-79.4	±82
SP3	316.5	27	-319.9	-27.6	±28
SP4	304.5	31.3	-247.2	-25.8	±28
SP5	43.6	57.3	-47.3	-57.2	±60
SP6	32.4	48.8	-33	-50	±50
SP7	84.9	16.3	-92.7	-17.1	±17

SP8	79.6	17.2	-75.3	-16.5	±17

Regarding to the cyclic tests, the recommendations of ECCS recommend an increasing amplitude testing, starting with 4 cycles under the elastic domain in progressive increments as follows: $0.25e_y$, $0.5e_y$, $0.75e_y$ and $1.0e_y$. For the plastic regime it is suggested the application of 3 cycles with the amplitudes $2e_y$, $4e_y$ and $6e_y$. Nevertheless, based on experience of previous cyclic tests, the use of the referred amplitudes tend to lead to a failure close to the monotonic fracture. Thus, the displacement amplitudes in the plastic domain were changed in order to reproduce failures in the ULCF regime but not so close to the monotonic failure. The number of cycles and the displacements amplitudes for the plastic regime are represented in Table 6.6 for each tested elbow.

Table 6.6 – Displacement loading histories applied during the ULCF tests of the elbows.

SP1		**SP2**		**SP3**		**SP4**		**SP5**		**SP6**		**SP7**		**SP8**	
Cycles	**Amplitudes (x e_y)**	**Cycles**	**Amplitudes (x e_y)**	**Cycles**	**Amplitudes (x e_y)**	**Cycles**	**Amplitudes (x e_y)**	**Cycles**	**Amplitudes (x e_y)**	**Cycles**	**Amplitudes (x e_y)**	**Cycles**	**Amplitudes (x e_y)**	**Cycles**	**Amplitudes (x e_y)**
3	1.5	3	1.5	3	1.5	3	1.5	3	1.5	3	1.5	3	1.5	3	1.5
3	2.0	3	2.0	3	2.0	3	2.0	3	2.0	3	2.0	3	2.0	3	2.0
3	2.5	3	2.5	3	2.5	3	2.5	3	2.5	3	2.5	3	2.5	3	2.5
3	3.0	3	3.0	3	3.0	3	3.0	3	3.0	3	3.0	3	3.0	3	3.0
3	3.5	3	3.5	3	3.5	3	3.5	3	3.5	3	3.5	3	3.5	3	3.5
15	4.0	3	4.0	3	4.0	3	4.0	3	4.0	3	4.0	3	4.0	3	4.0
-	-	27	4.4	3	4.5	3	4.5	6	4.3	3	4.5	3	4.5	3	4.5
-	-	-	-	3	5.0	3	5.0	-	-	7	5.0	3	5.0	3	5.0
-	-	-	-	3	5.5	3	5.5	-	-	-	-	-	-	2	5.5
-	-	-	-	1	6.0	1	6.0	-	-	-	-	-	-	-	-

6.2.4 Experimental results

During the cyclic tests, a distinctive ductile behavior could be observed, where the location and shape of the buckles is strongly dependent on the magnitude of loading, geometry and applied inner pressure. The exact point where damage started and fatigue cracks developed was strongly dependent on the occurrence of these buckles [5]. The experimental results of the ULCF tests of the elbows are presented in the Table 6.7, the specific failure cycle and the corresponding location of the first visible buckle, the macroscopic crack initiation and the final fracture cycles are described. The hysteresis cycles, the inner pressure time history and the histories of vertical and horizontal displacements promoted by the elbow ovalization are illustrated in Figure 6.10 to Figure 6.40. In addition, photos of the final

specimen fracture are also shown. The hysteresis cycles, relating the applied load and the mean displacements, were obtained for the entire cyclic loading. Regarding the pipe ovalization, a stabilized behavior is identified that is correlated with the displacement amplitudes. However, at high displacement levels which leading to widespread yielding the stabilized behavior is not observed. With respect to the inner pressure, a significant fluctuation is observed with the application of the loading phases. This fluctuation may influence the development of the final instabilities. In the images of the final failure zone, we can observe the plastic instability prior to macroscopic crack initiation, which in turn leads to the eventual collapse.

Table 6.7 – Summary of the experimental results from the ULCF tests of full-scale elbows.

Specimen	**Visible buckle**	**Macroscopic crack initiation**	**Final failure**	**Failure location**
	[Cycle]	**[Cycle]**	**[Cycle]**	**[Section]**
SP1	23	29	34	G-H
SP2	25	43	49	H-I
SP3	23	26	32	H
SP4	26	29	32	H
SP5	19	25	28	J-K
SP6	26	29	32	H
SP7	21	25	28	H-I
SP8	24	26	30	H

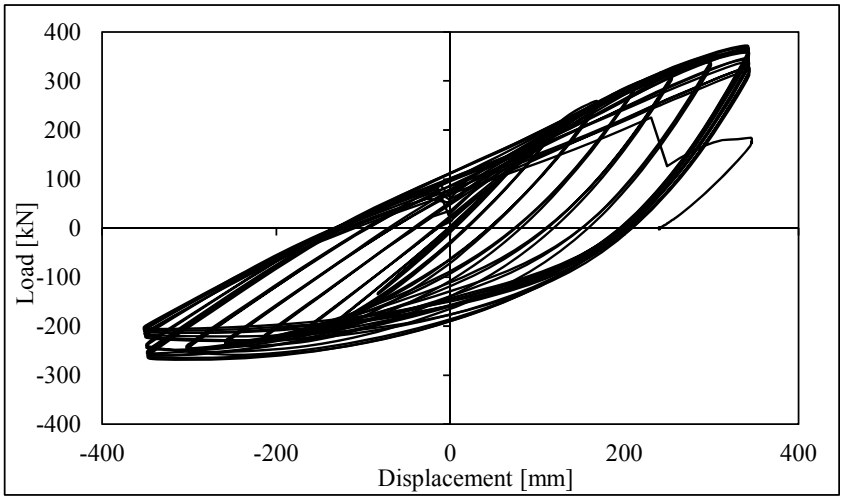

Figure 6.10 – Experimental cyclic load-displacement curves obtained for the SP1 elbow.

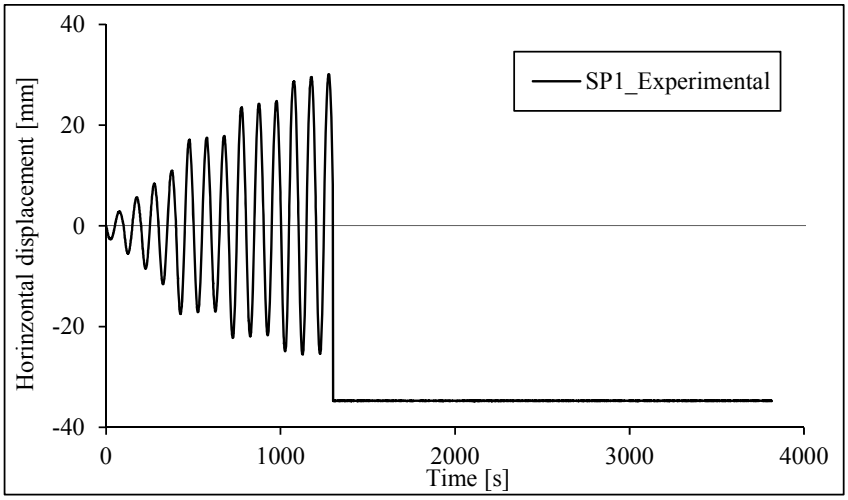

Figure 6.11 – Horizontal displacement due to ovalization of SP1 specimen.

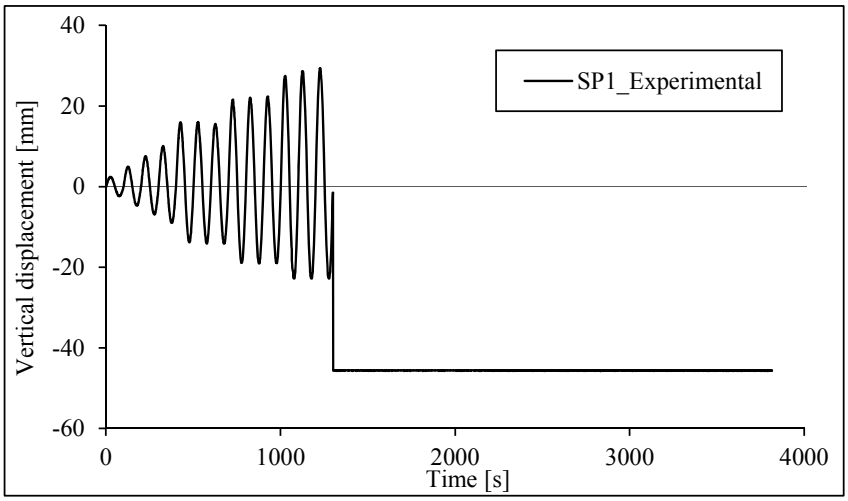

Figure 6.12 –Vertical displacement due to ovalization of SP1 specimen.

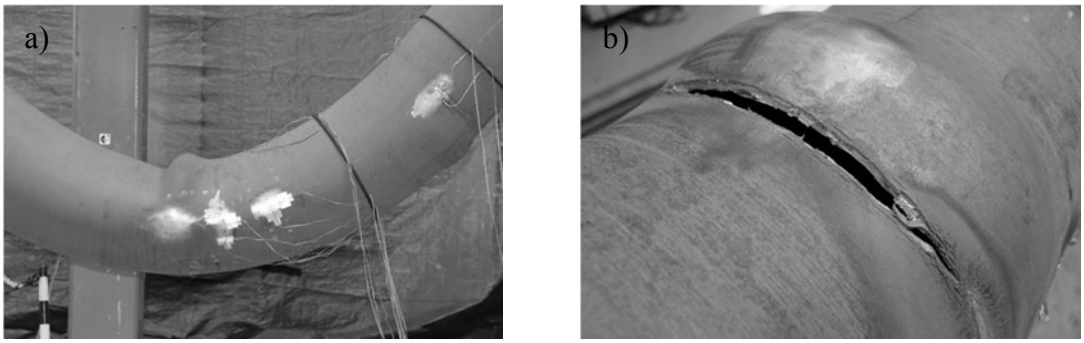

Figure 6.13 – Failure aspect of SP1 specimen: a) buckle detail; b) detail of the crack at the end of the test.

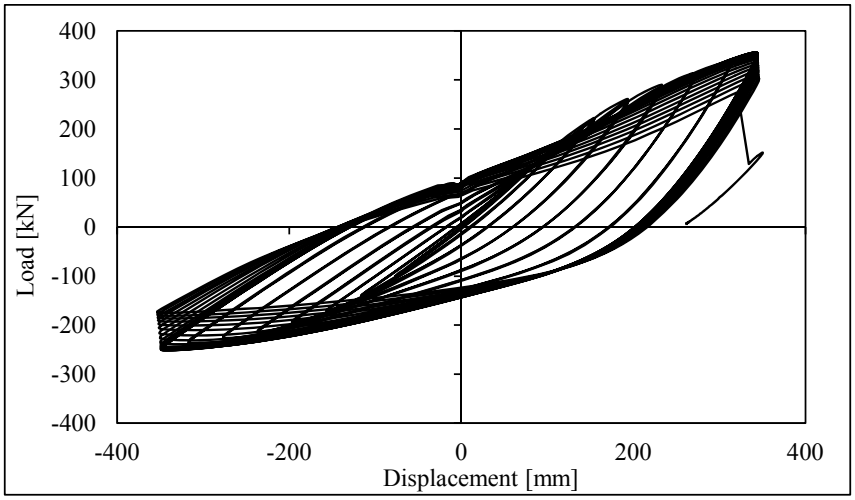

Figure 6.14 – Experimental cyclic load-displacement curves obtained for the SP2 elbow.

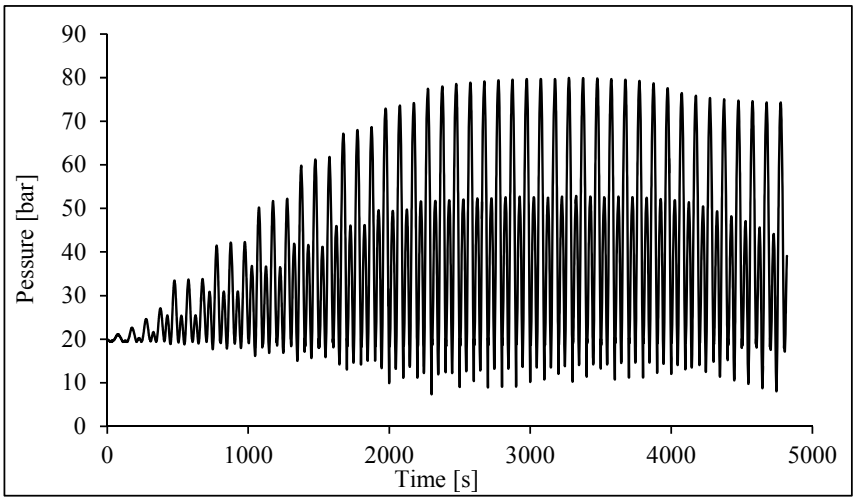

Figure 6.15 – Evolution of inner pressure during the cyclic loading of SP2 specimen.

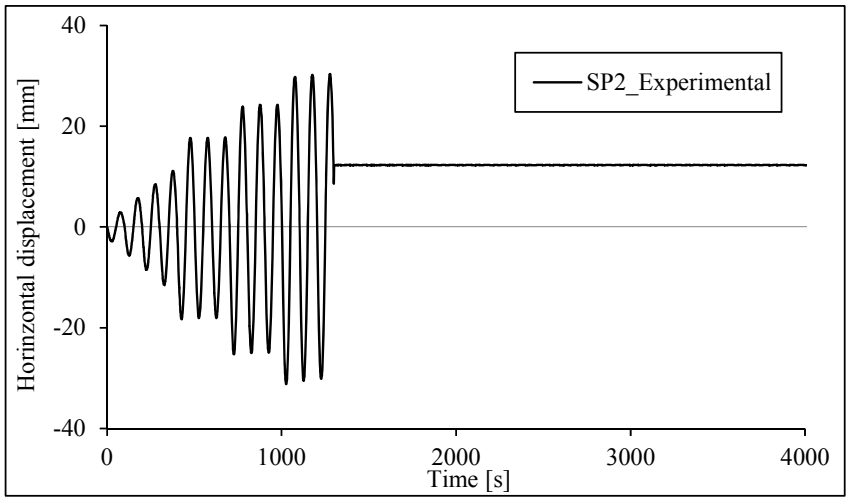

Figure 6.16 – Horizontal displacement due to ovalization of SP2 specimen.

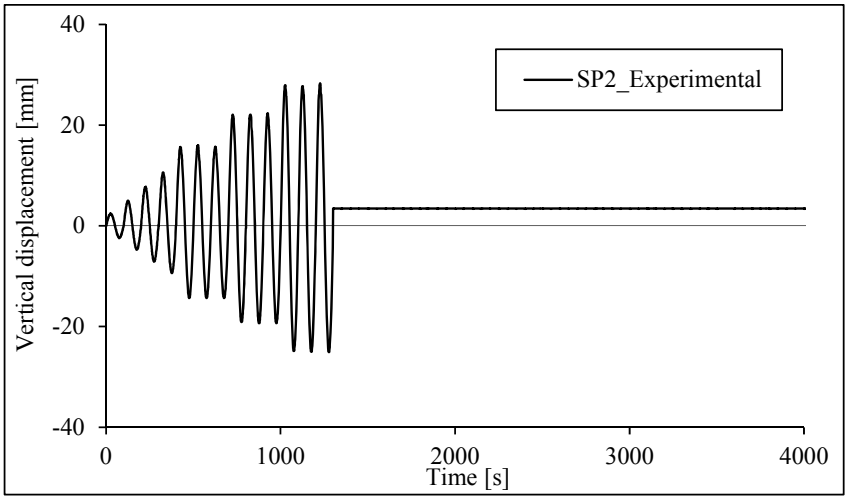

Figure 6.17 –Vertical displacement due to ovalization of SP2 specimen.

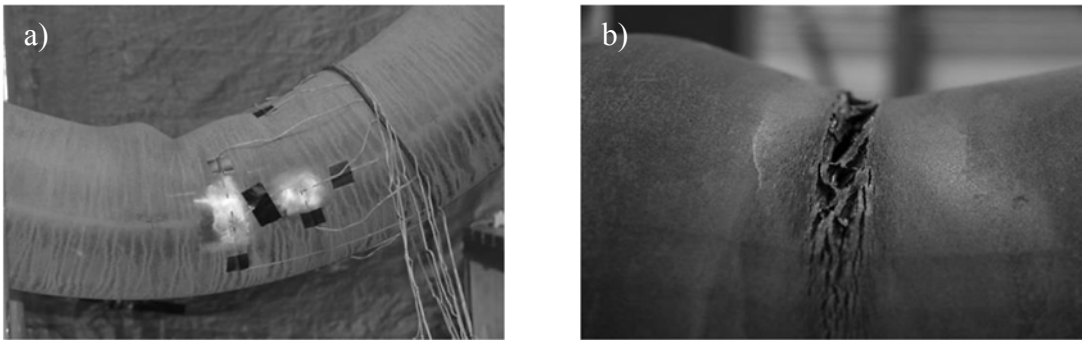

Figure 6.18 – Failure aspect of SP2 specimen: a) buckle detail; b) detail of the crack at the end of the test.

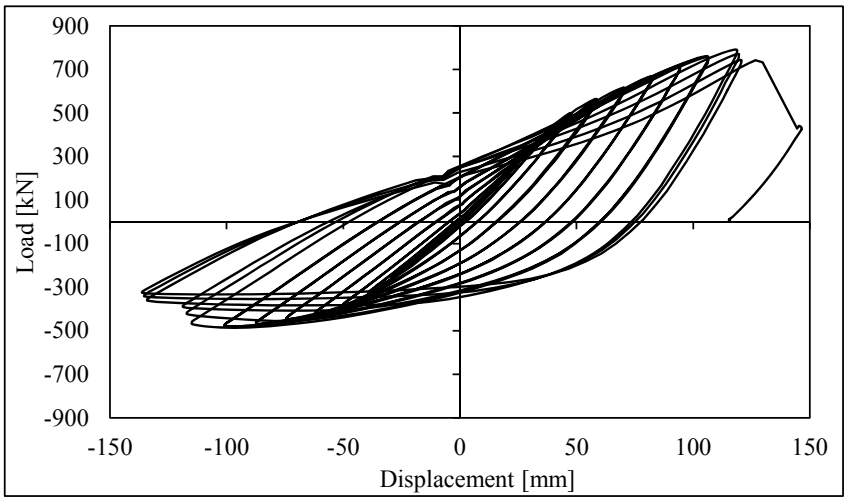

Figure 6.19 – Experimental cyclic load-displacement curves obtained for the SP3 elbow.

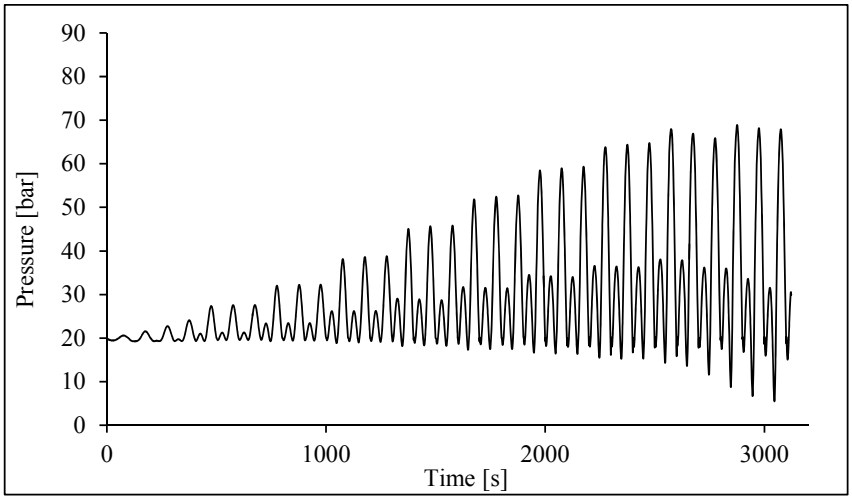

Figure 6.20 – Evolution of inner pressure during the cyclic loading of SP3 specimen.

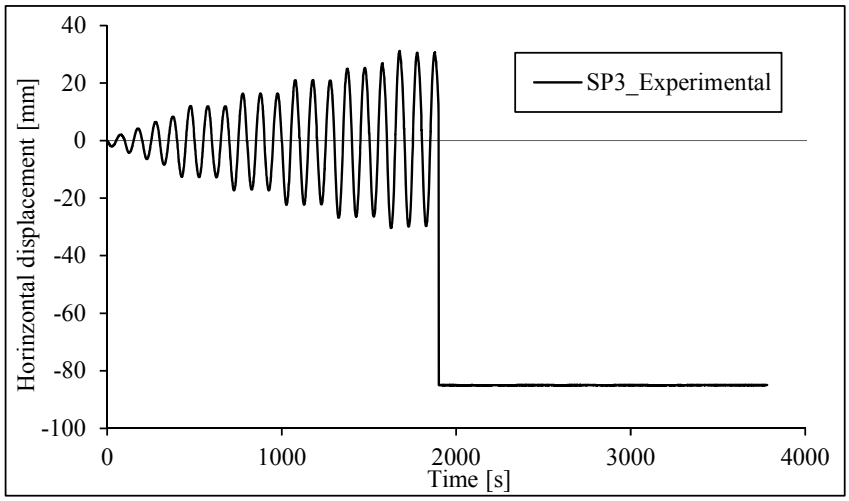

Figure 6.21 – Horizontal displacement due to ovalization of SP3 specimen.

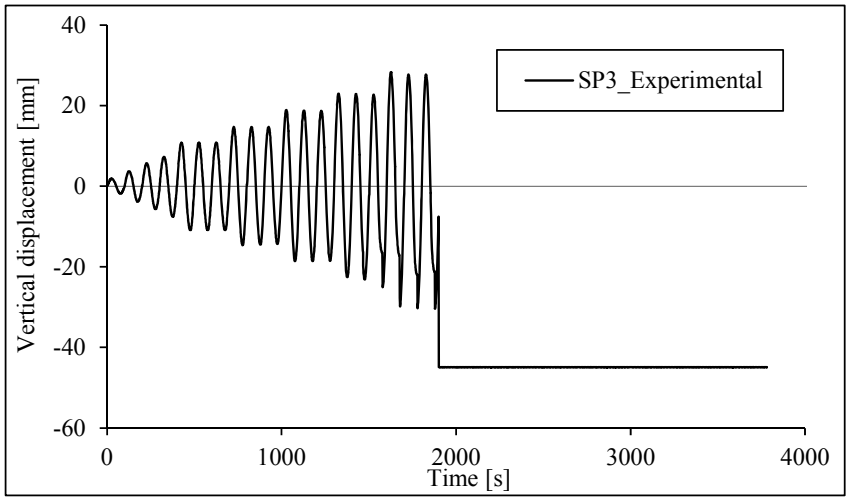

Figure 6.22 – Vertical displacement due to ovalization of SP3 specimen.

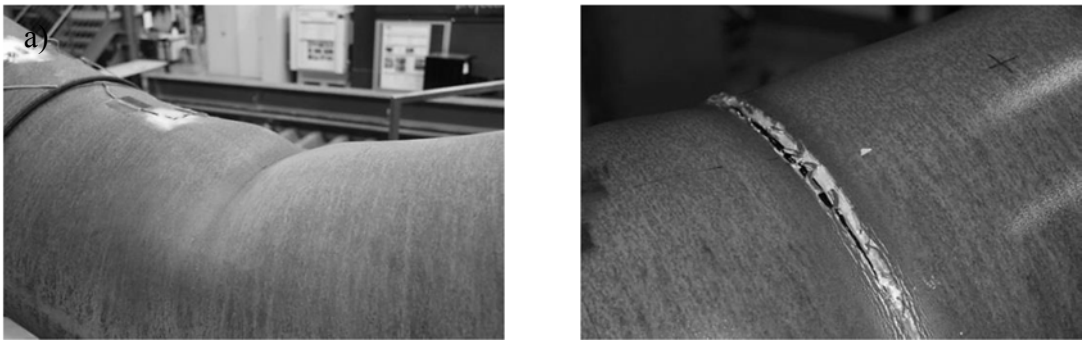

Figure 6.23 – Failure aspect of SP3 specimen: a) buckle detail; b) detail of the crack at the end of the test.

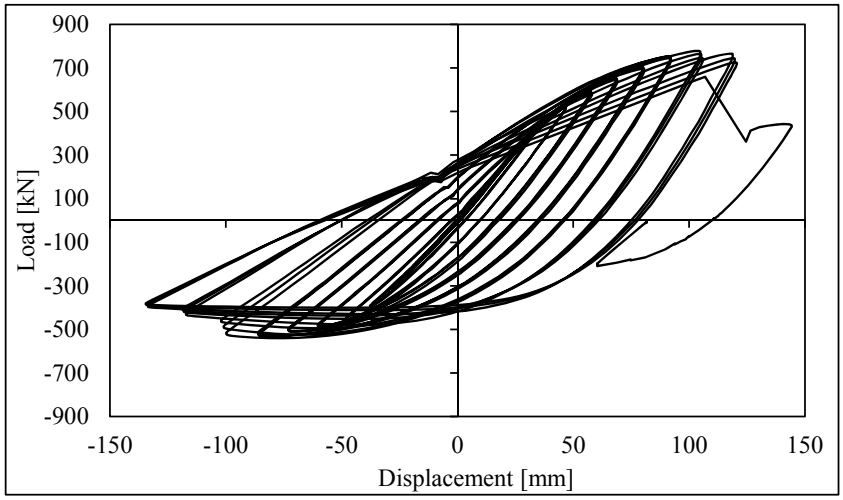

Figure 6.24 – Experimental cyclic load-displacement curves obtained for the SP4 elbow.

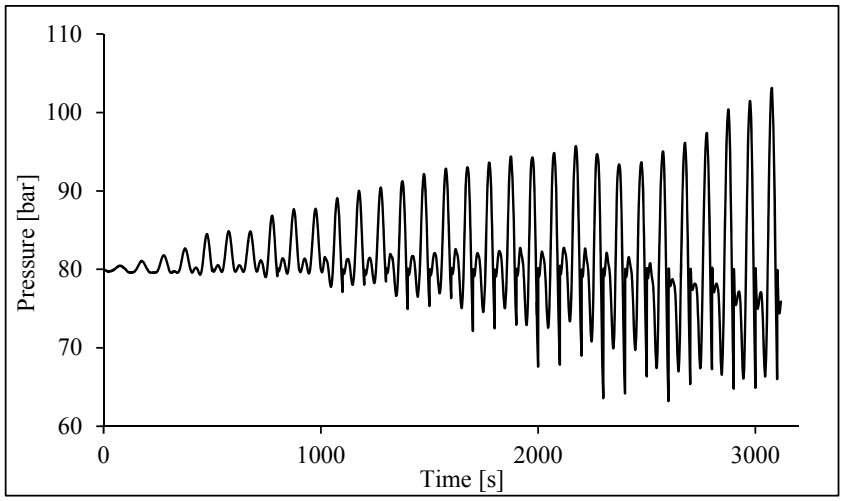

Figure 6.25 – Evolution of inner pressure during the cyclic loading of SP4 specimen.

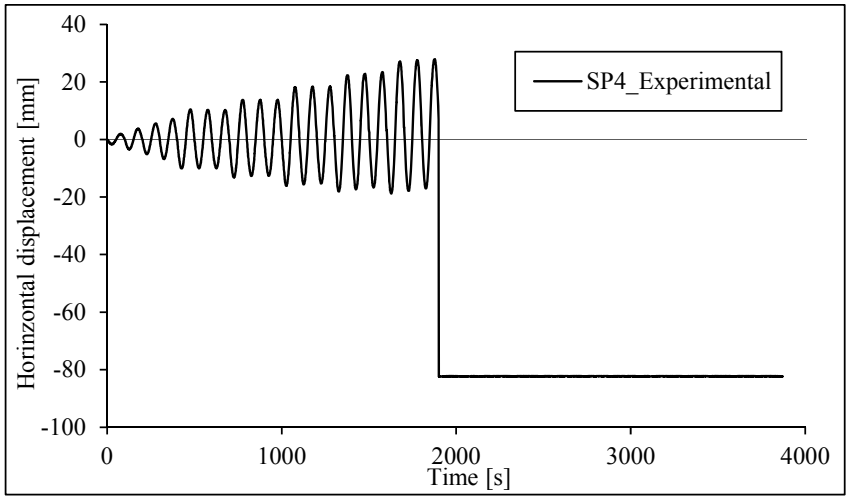

Figure 6.26 – Horizontal displacement due to ovalization of SP4 specimen.

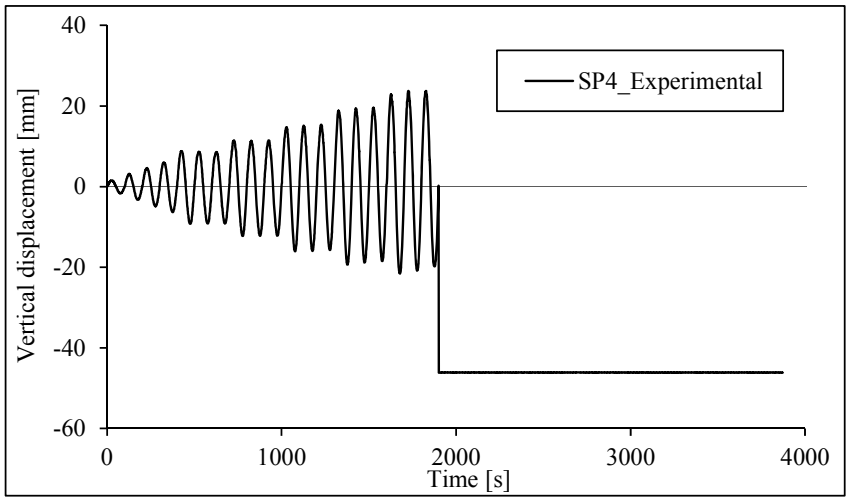

Figure 6.27 – Vertical displacement due to ovalization of SP4 specimen.

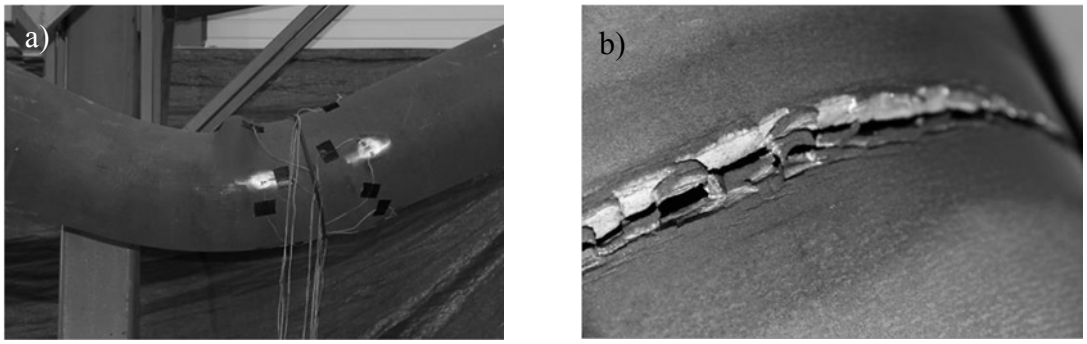

Figure 6.28 – Failure aspect of SP4 specimen: a) buckle detail; b) detail of the crack at the end of the test.

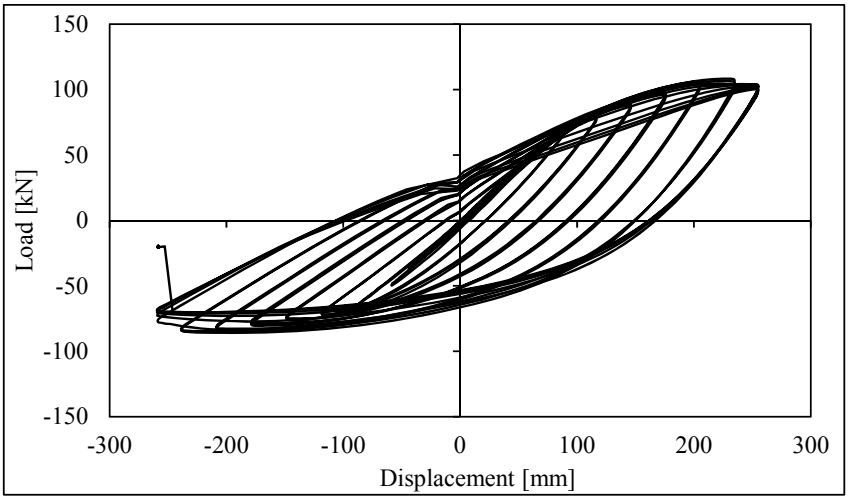

Figure 6.29 – Experimental cyclic load-displacement curves obtained for the SP5 elbow.

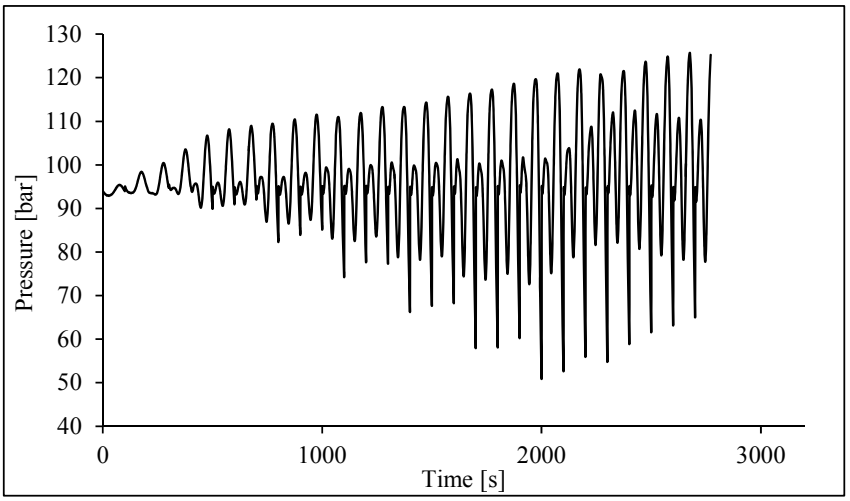

Figure 6.30 – Evolution of inner pressure during the cyclic loading of SP5 specimen.

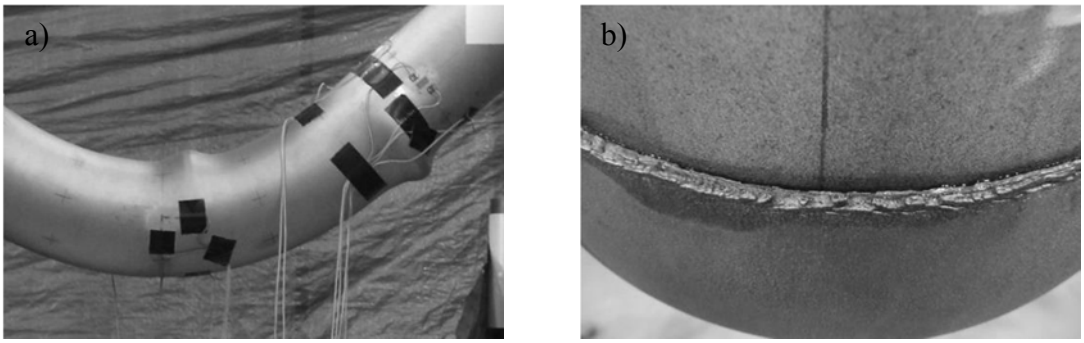

Figure 6.31 – Failure aspect of SP5 specimen: a) buckle detail; b) detail of the crack at the end of the test.

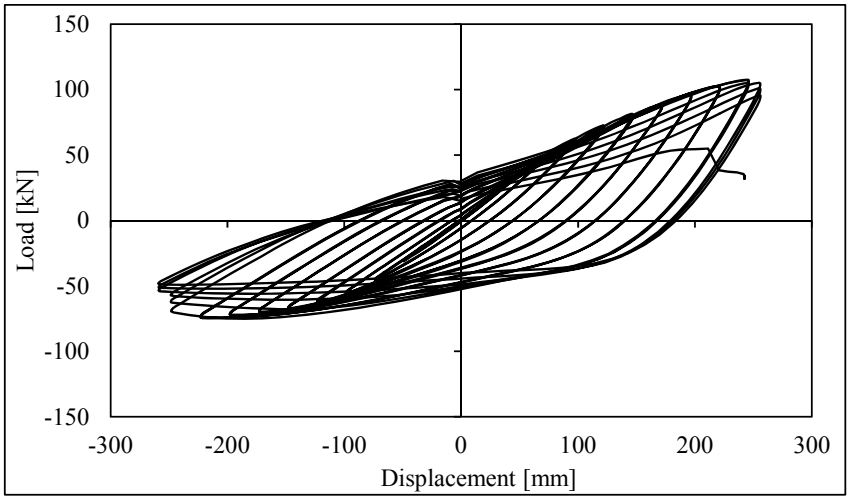

Figure 6.32 – Experimental cyclic load-displacement curves obtained for the SP6 elbow.

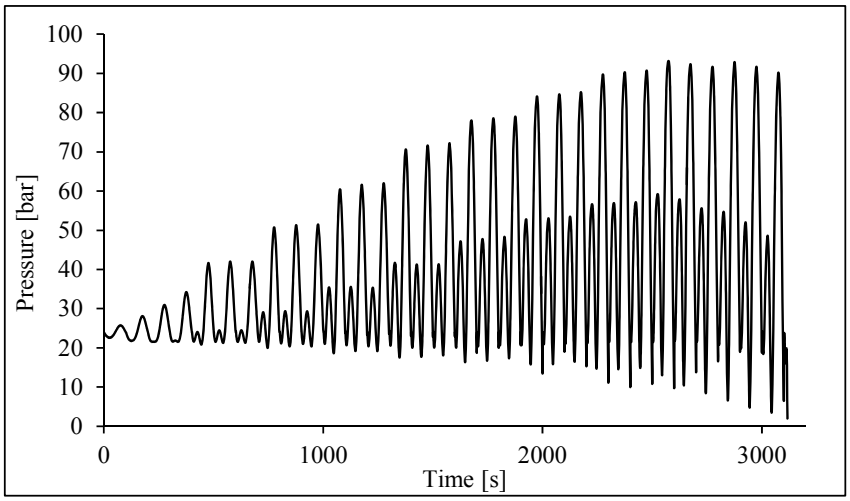

Figure 6.33 – Evolution of inner pressure during the cyclic loading of SP6 specimen.

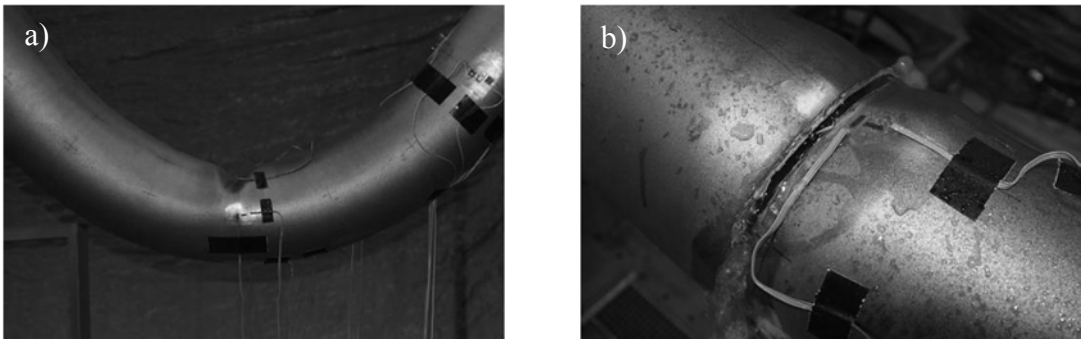

Figure 6.34 – Failure aspect of SP6 specimen: a) buckle detail; b) detail of the crack at the end of the test.

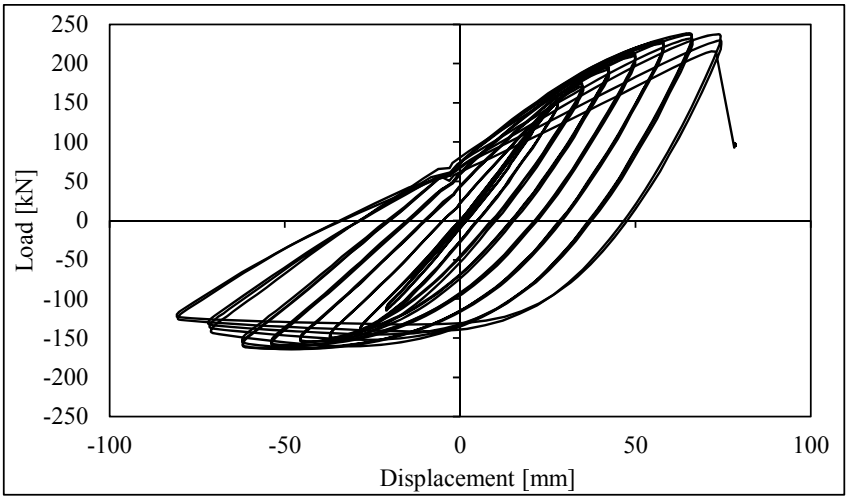

Figure 6.35 – Experimental cyclic load-displacement curves obtained for the SP7 elbow.

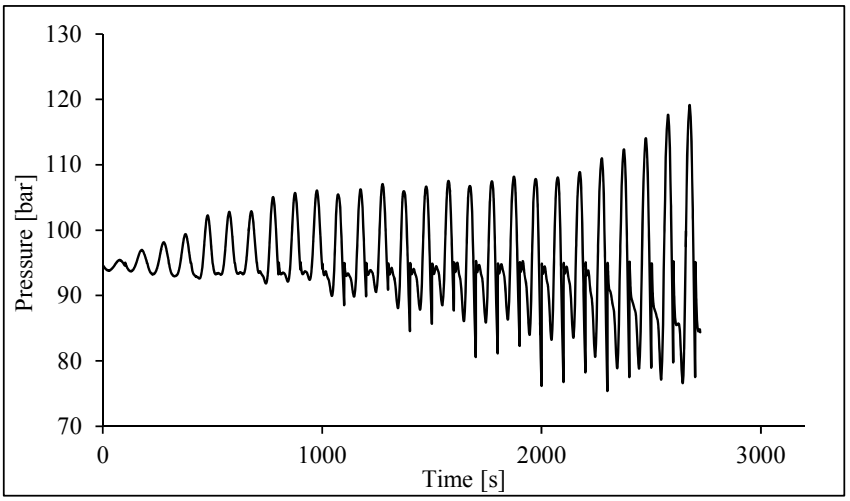

Figure 6.36 – Evolution of inner pressure during the cyclic loading of SP7 specimen.

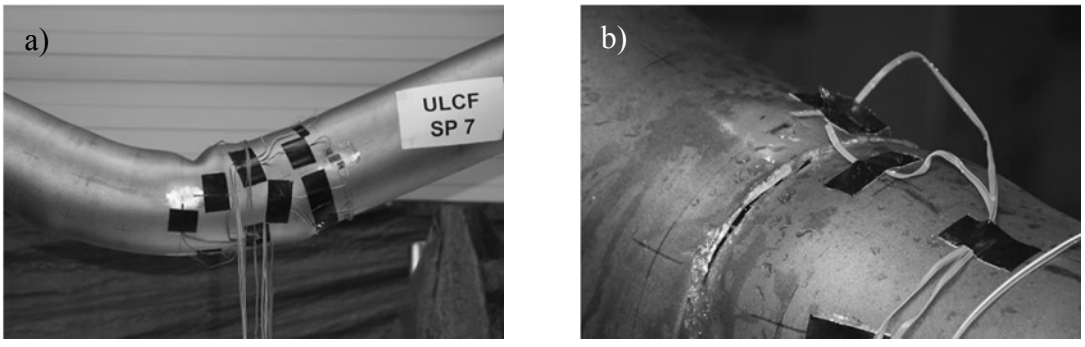

Figure 6.37 – Failure aspect of SP7 specimen: a) buckle detail; b) detail of the crack at the end of the test.

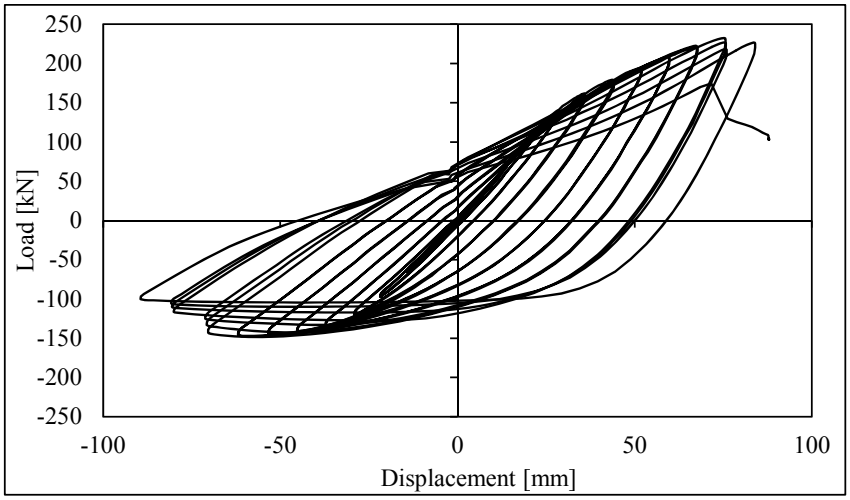

Figure 6.38 – Experimental cyclic load-displacement curves obtained for the SP8 elbow.

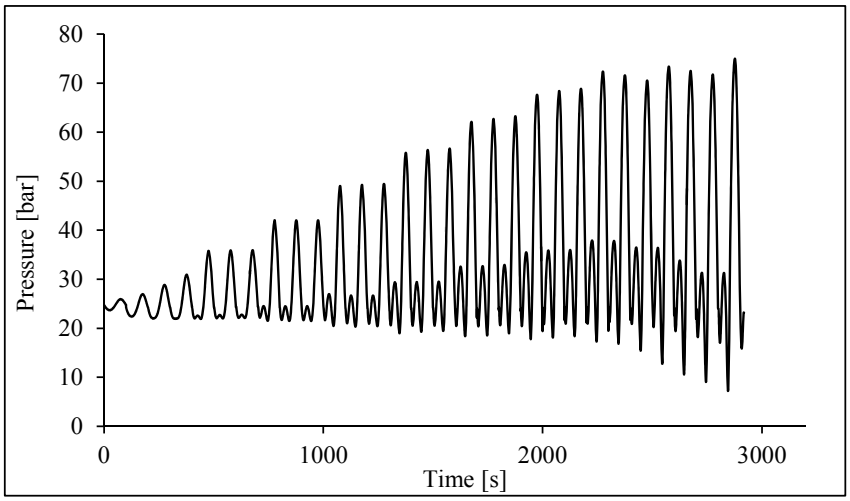

Figure 6.39 – Evolution of inner pressure during the cyclic loading of SP8 specimen.

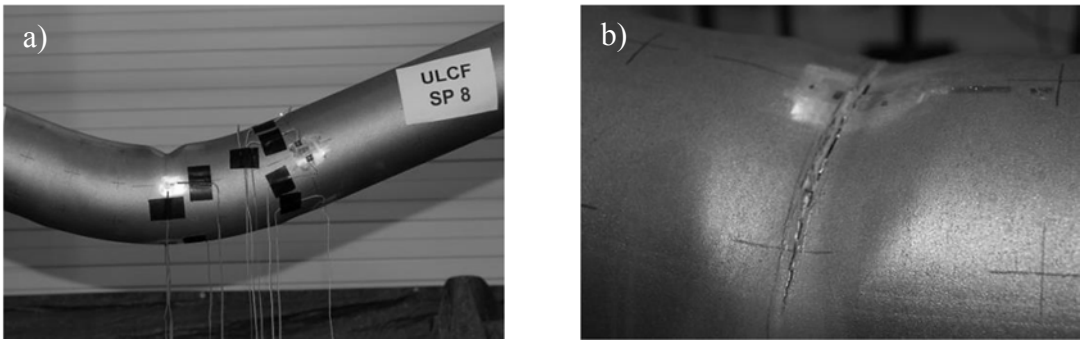

Figure 6.40 – Failure aspect of SP8 specimen: a) buckle detail; b) detail of the crack at the end of the test.

The analysis of the results revealed that in all tests the failure was preceded by plastic buckles that induced strain localization responsible for the damage concentration and

consequent crack initiation. The analysis of the experimental results presented in the Table 6.7 reveals that the number of cycles to develop a visible buckle ranged between the minimum value of 19 (SP5) and a maximum of 26 (SP6) with a range of 7 cycles. It is interesting to note that the higher internal pressure led always to a lower number of cycles to initiate a visible buckle. The same conclusion stands for the macroscopic crack initiation and final failure. After the visible buckle formation, the number of cycles to initiate the macroscopic crack ranged between 2 (SP8) and 18 (SP2). SP2 specimen showed an uncharacteristic duration when compared to the other specimens. However it can be justified by the maintenance of the last displacement level without further increments in the displacements (see Table 6.6). Excluding this case, the other specimens showed a crack initiation after buckle formation between 2 and 6 cycles. Also, after the crack initiation the number of cycles to propagate the crack and produce the final failure ranged between 3 and 6. It is also interesting to note that the buckle can be developed outward or inward directions. Also, in some cases, besides the buckle formation at the central inner radius part of the elbow some buckles were formed at the transition elbow-straight pipe segments.

6.3 FULL-SCALE TESTS OF STRAIGHT PIPES UNDER CYCLIC LOADING

In this section, cyclic ULCF bending tests performed on straight pipes were performed on two full-scale specimens of X60 steel as well as of X65 steel grades. These materials were already characterized by small-scale tests covered by the previous chapters. These tests were performed by the responsibility of OCAS N.V. This section describes the experimental program of cyclic pure bending tests that will be used latter to validate the proposed ULCF modelling approaches. The test loading consisted in pure bending, combined with a small internal pressure.

6.3.1 Description of the experimental setup

Figure 6.41 illustrates the experimental setup used for the full-scale testing of straight pipes including the main components of the setup. The setup is equipped with hydraulic cylinders with a load capacity of 500 kN acting on a moment arm of 2 m, which provides a bending

capacity of 1000 kN.m. The bending moment is provided by the hydraulic cylinders (2). To avoid bending loads on the load cell, the cylinders lay on supports (3). The bending moment is transmitted to the test sample (7) by the tubeholders (6). In order to allow free motion on the test floor, the tubeholders are supported by wheels (4). The test sample (7) is bent against a curved former (1) which is attached to the modular test floor of the Soete Laboratory of Ghent University. The cylinder displacements are measured using the wire sensors (5) [7]. The tubeholders, former and cylinder supports are specifically designed for these tests. To adapt the tubeholder to the different pipe sizes (8 5/8" and 16" diameters) adaptor sleeves are used. Additionally, two different configurations to adapt both pipe sizes are adopted. In detail, for the case of configuration 1, the tubeholders are oriented to each other resulting in a free specimen length of 1980 mm. The radius of curvature of the former is 7.50 m (which is representative for pipeline reeling) [7]. The complete setup in this configuration is illustrated in the Figure 6.42. In the configuration 2 (see Figure 6.43), the tubeholders are oriented outwards resulting in a free specimen length of 3480 mm. The radius of curvature of the former is 19.9 m.

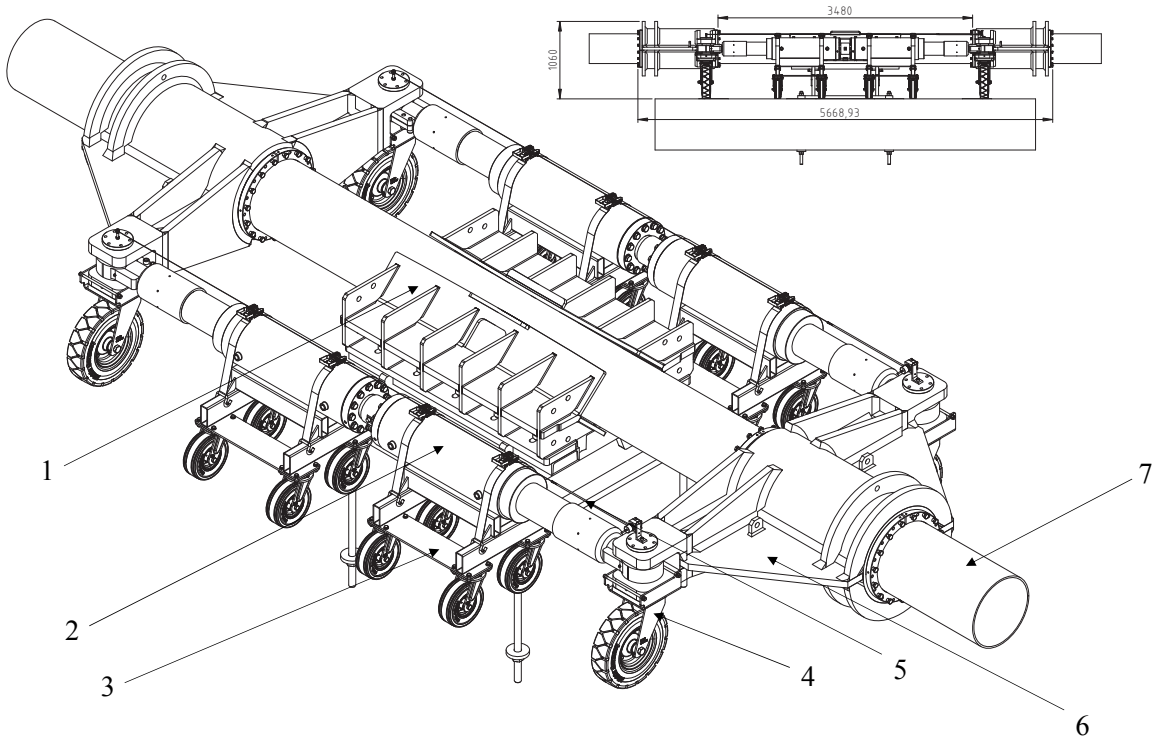

Figure 6.41 –Pure cyclic bending setup for straight pipes [7].

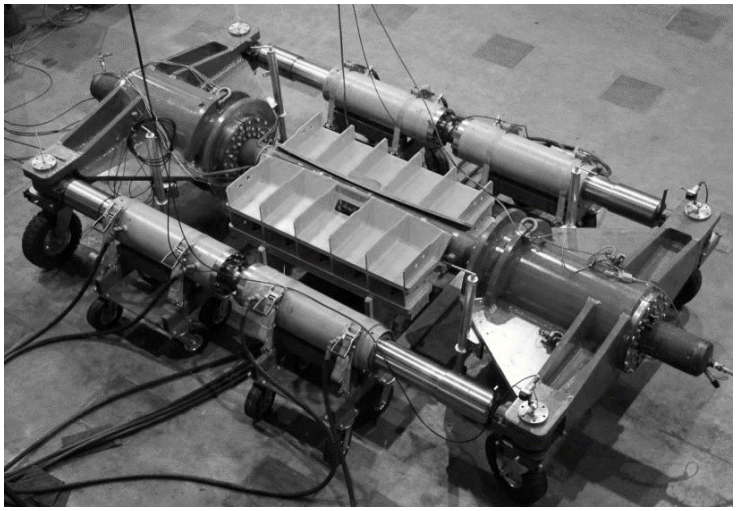

Figure 6.42 – Pure cyclic bending setup: configuration 1 [7].

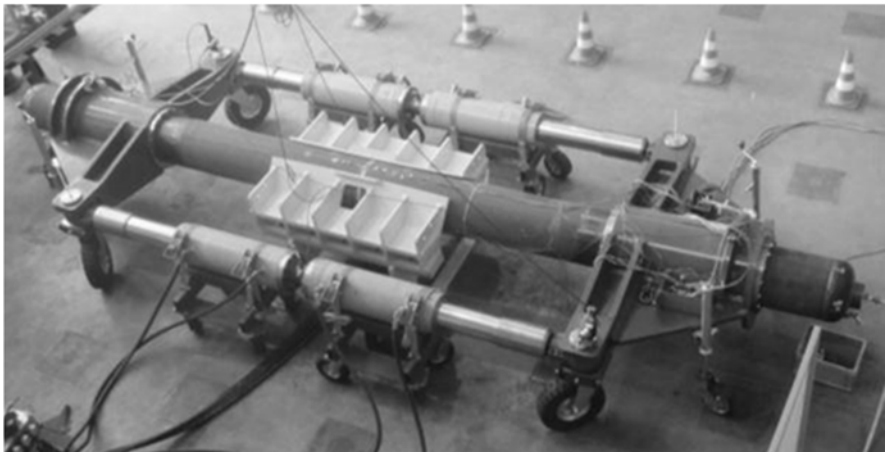

Figure 6.43 – Pure cyclic bending setup: configuration 2 [7].

6.3.2 Description of tests procedure for cyclic bending of straight pipes

A total of four full-scale cyclic tests on straight pipes were carried out, two on each steel grade (X60 and X65). For each pipe/material two distinct pipe section orientations were tested as described in the Table 6.8. During sample preparation, strain gauges were attached to pipe external surface. The location of the strain gauges and the respective identification are explained in the Table 6.9 and Figure 6.44.

Table 6.8 – Overall dimensions of the straight pipes.

Specimen	Orientation	Pipe average measured OD at 0° - 180° plane	Pipe average measured OD at 90° - 270° plane	Thickness [mm]
Test A (X65)	90° - 270° plane max strain / 0° - 180° plane is neutral fibre	220.55	220.01	5.59
Test B (X65)	0° - 180° plane max strain / 90° - 270° plane is neutral fibre	220.84	219.83	5.59
Test C (X60)	90° - 270° plane max strain / 0° - 180° plane is neutral fibre	407.37	407.79	9.5
Test D (X60)	90° - 270° plane max strain / 0° - 180° plane is neutral fibre	407.58	407.23	9.5

Table 6.9 – Numbering of strain gauges used in bending cyclic tests in straight pipes [7].

Strain gauge numbering					
Circumferential position	0°	90°	180°	270°	Gauge direction
Left	1	7	13	19	hoop
Left	2	8	14	20	axial
Center	3	9	15	21	hoop
Center	4	10	16	22	axial
Right	5	11	17	23	hoop
Right	6	12	18	24	axial

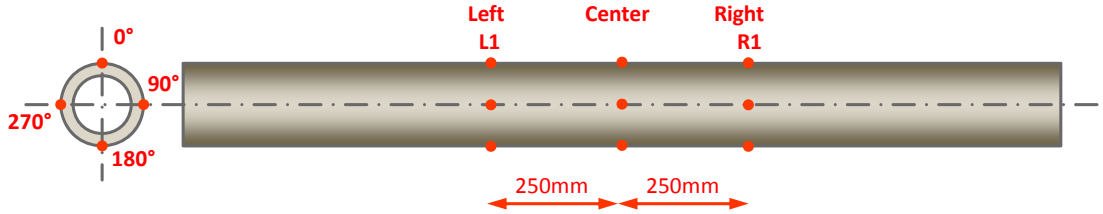

Figure 6.44 – Location of strain gauges used in the ULCF bending tests of straight pipes [7].

Similarly to what was adopted for the ULCF tests of elbows described in the Section 6.2.2, the procedure for the cyclic loading definition of the straight pipes was also based on ECCS recommendations [6]. The “short testing procedure”, as described in the referred document was applied. In the ECCS testing procedure, the displacement amplitude is gradually increased over a prescribed number of cycles [7]. Consequently, the displacement amplitude is obtained from the displacement limit, e_y. The e_y was computed by means of finite element analysis due to the limited amount of test specimens available. The number of cycles for each displacement amplitude of each straight pipe cyclic tests are presented in Table 6.10. Figure 6.45 and Figure 6.46 illustrate the numerical curves that were used to evaluate the yield displacement, e_y, for the pipes and that was used as a basis for the definition of the loading histories for each piping test.

Table 6.10 – Loading histories applied in each straight pipe cyclic bend testing [7].

Cycles	e_y (factor)	X60 (e_y=40)	X65 (e_y=85)
1	1/4	10mm	21mm
1	1/2	20mm	43mm
1	3/4	30mm	64mm
1	1	40mm	85mm
3	1.5	60mm	128mm
3	2	80mm	170mm
3	2.5	100mm	213mm
Max. displacement (due to curved former)		180mm	245mm

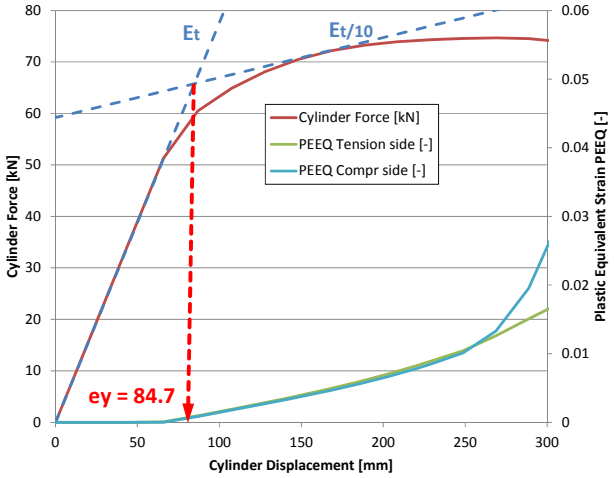

Figure 6.45 – Determination of e_y for the X65 straight pipe (specimens A and B) [7].

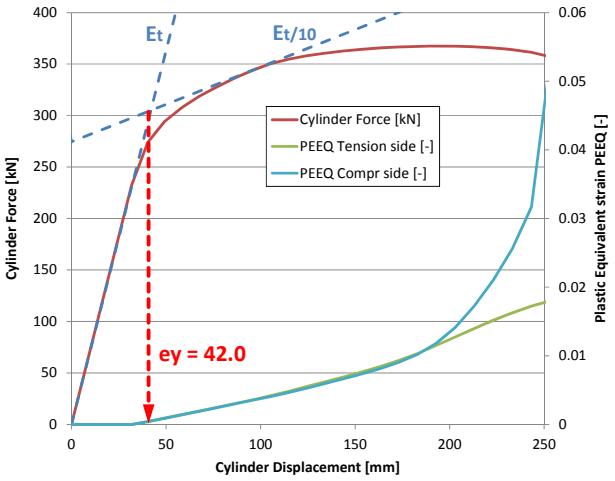

Figure 6.46 – Determination of e_y for the X60 straight pipe (specimens C and D) [7].

6.3.3 Experimental results

The experimental results of cyclic bending tests of the straight pipes are summarized in the Table 6.7, which specifies the number of cycles until buckling and the number of cycles until the macroscopic crack initiation that coincides with the specimen failure.

Table 6.11 – Experimental results of bending cyclic tests of straight pipes [7].

Specimen	Cycles to buckling [-]	Cycles to fracture[-]
Test A	14	17
Test B	8	11
Test C	122	129
Test D	33	39

Test sample A was mounted with the 0° section reference at the 12h position in the setup. Thus, the 90° position with the smallest diameter is subjected to the highest bending strains [7]. The experimental data that includes the average cylinder displacement, bending moment, hysteresis cycles, strain values and inner pressure are shown in Figure 6.47 to Figure 6.51. It should to be noted that the cyclic bending tests on straight pipes were carried out under displacement control. The plotted “average cylinder displacement” is the average of the extension of the pushing cylinder and the retraction of the pulling cylinder [3]. Concerning the buckle location it appeared in the pipe, next to tubeholder, during the cycle 14. After this buckling, the resulting bending moment reduced appreciably. The final fracture appeared during cycle 17. The experimental data of strain gauge 22 is illustrated in Figure 6.50. The strain amplitude during cycles 11 to 13 is approximately 1%. It is clear that following the local buckling of the pipe in cycle 14, the strain amplitude at the pipe center starts reducing.

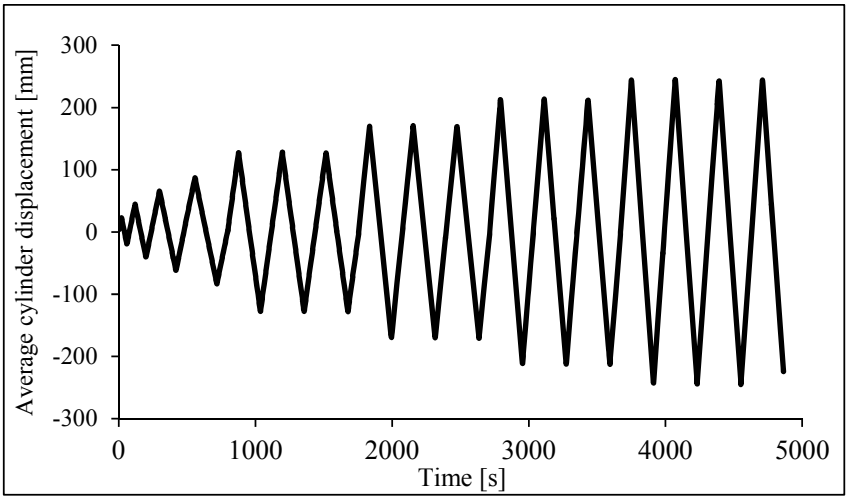

Figure 6.47 – Average displacement *versus* time corresponding to the Test A performed on X65 piping [7].

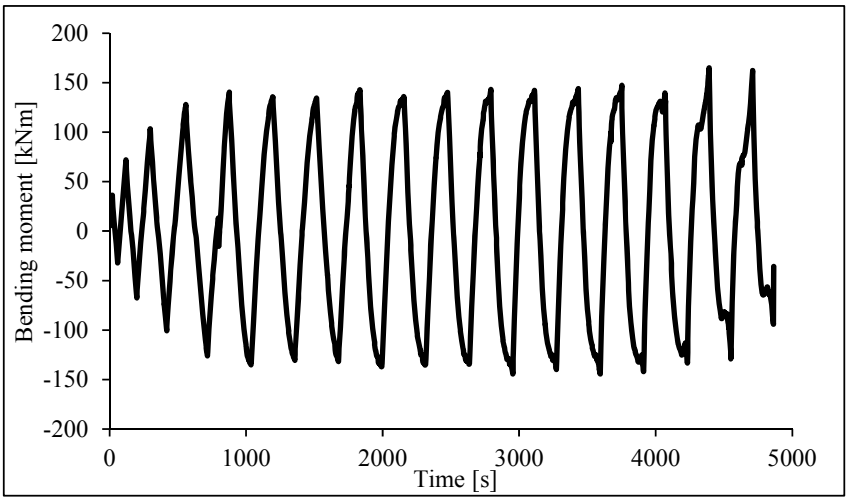

Figure 6.48 – Bending moment *versus* time corresponding to the Test A performed on X65 piping [7].

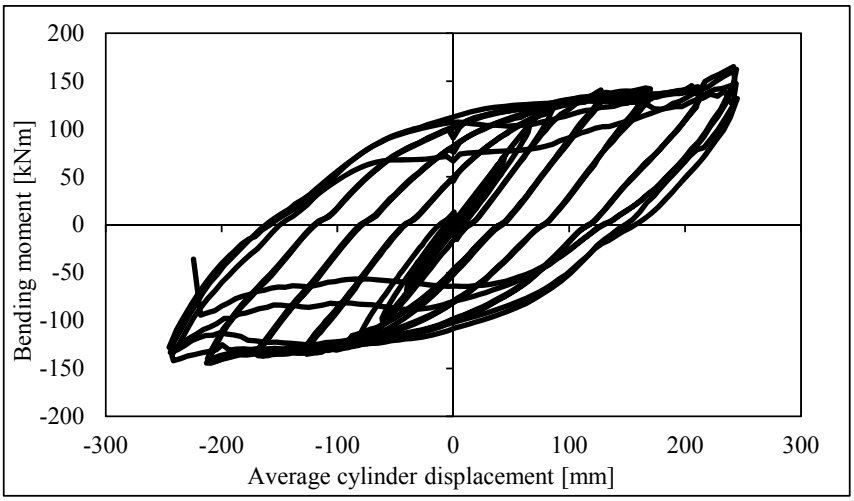

Figure 6.49 – Bending moment *versus* average cylinder displacement corresponding to Test A performed on X65 piping [7].

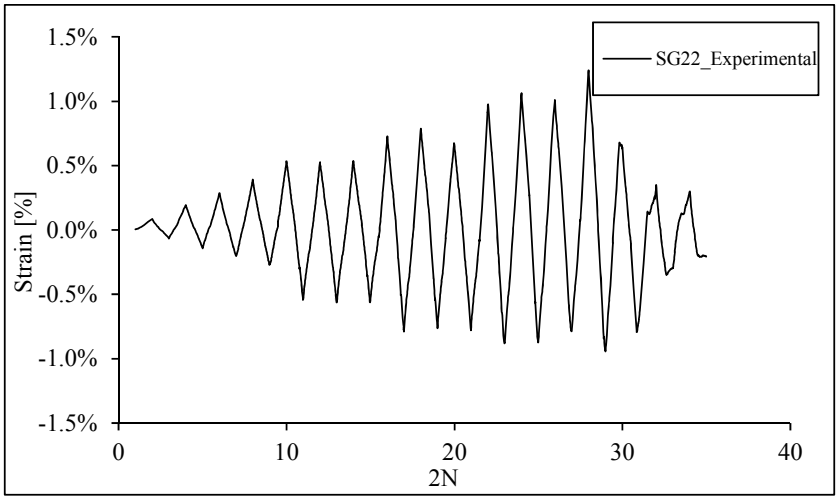

Figure 6.50 – Axial strain at pipe centre (gauge 22) corresponding to Test A performed on X65 piping [7].

The evolution of inner pressure of Test A is represented in Figure 6.51. Initially, an inner pressure of 2.2 Bar was set. Nevertheless the cyclic bending test was paused after the 4th cycle during which the pressure was removed from the specimen. Then, a pressure of 2.7 Bar was applied assuming that this increase did not influence the test. Due to pipe deformation, the inner pressure increased from cycle 14, which corresponds to the moment of buckle formation. The analysis of the figure shows that, at the moment of fracture of the pipe, the internal pressure was 3.3 Bar. Figure 6.52 shows the fracture location of Test A. The crack propagated from a buckle next to the tubeholder and it was located at the 90° position around the pipe circumference [7]. Figure 6.52b) illustrates a side view of the buckled specimen. The dashed line corresponds to the neutral axis of the pipe (0° position).

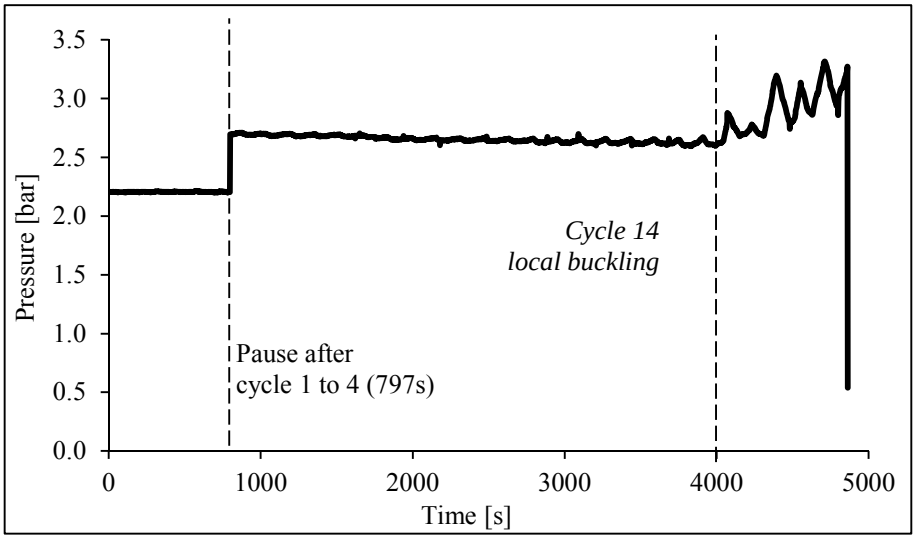

Figure 6.51 – Inner pressure history corresponding to Test A performed on X65 piping [7].

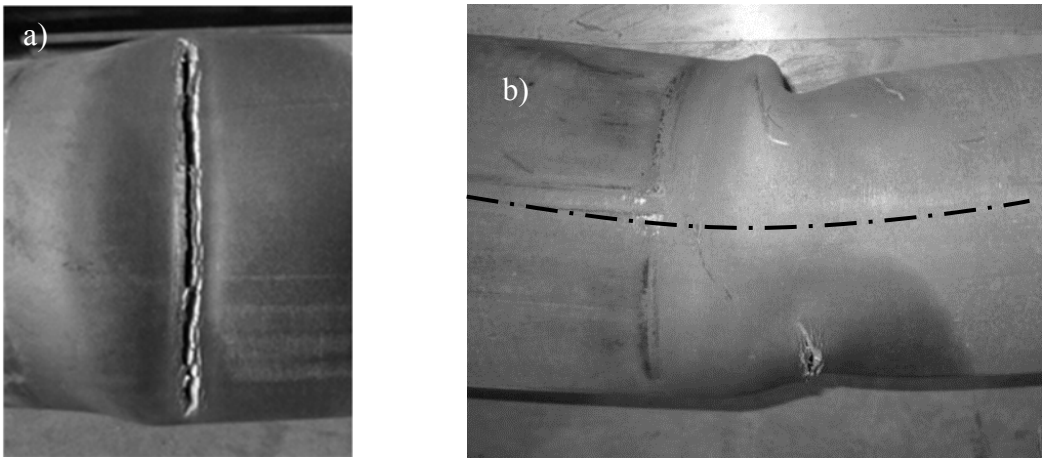

Figure 6.52 – Fracture location from Test A: a) detail view of a macroscopic crack; b) side view of the buckled pipe [7].

Following the description of Test A, the experimental data for Test B is also defined in this section. Test B was mounted with the 90° reference at the 12h position in the setup. To induce the crack initiation at the pipe center, the specimen was slightly ground at 0° and 180°, as schematically represented in the Figure 6.53. The experimental data including the average cylinder displacement, bending moment, hysteresis cycles, strain values and inner pressure are shown in Figure 6.54 to Figure 6.58. The buckle appeared at the center of the pipe, during the cycle 8. Consequently from this point, the inner pressure was removed. After that, the test was continued until the specimen final fracture at the 11th cycle. The fracture location of Test B is represented in Figure 6.59. In detail, view of macroscope crack and a section view of ULCF fracture in buckled section is observed.

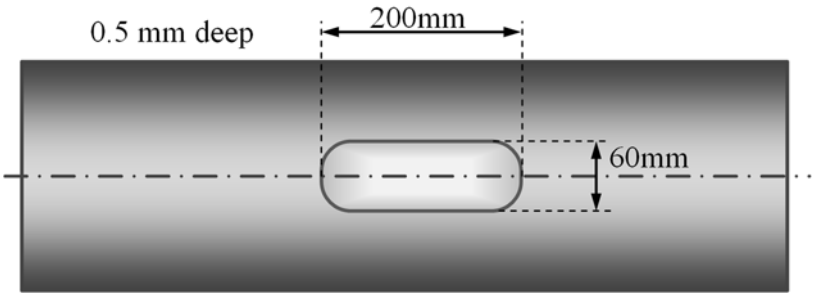

Figure 6.53 – Wall thickness reduction at the pipe center corresponding to the Test B specimen [7].

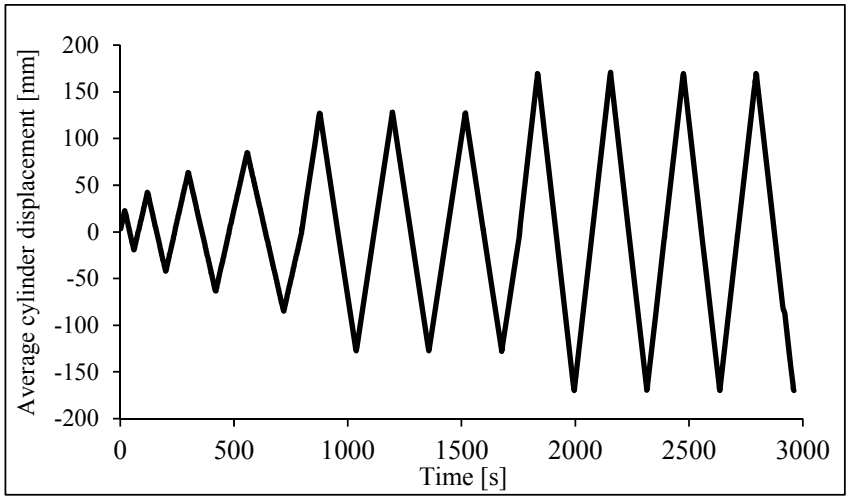

Figure 6.54 – Average displacement *versus* time corresponding to the Test B performed on X65 piping [7].

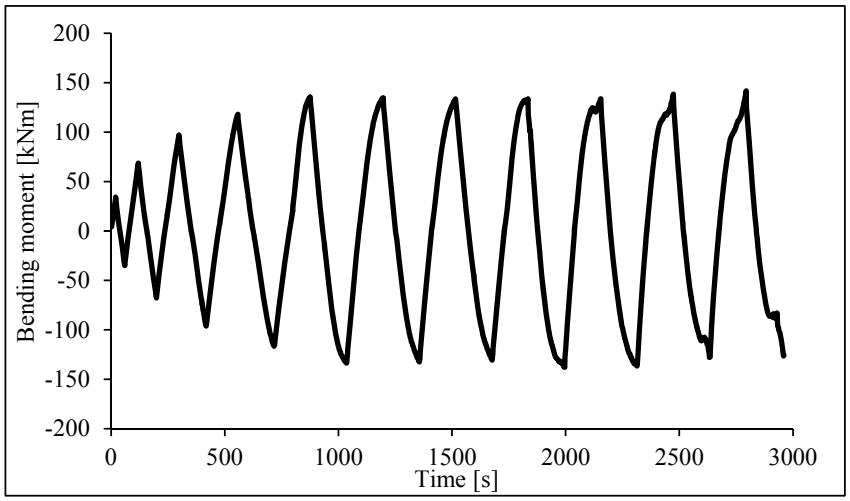

Figure 6.55 – Bending moment *versus* time corresponding to the Test B performed on X65 piping [7].

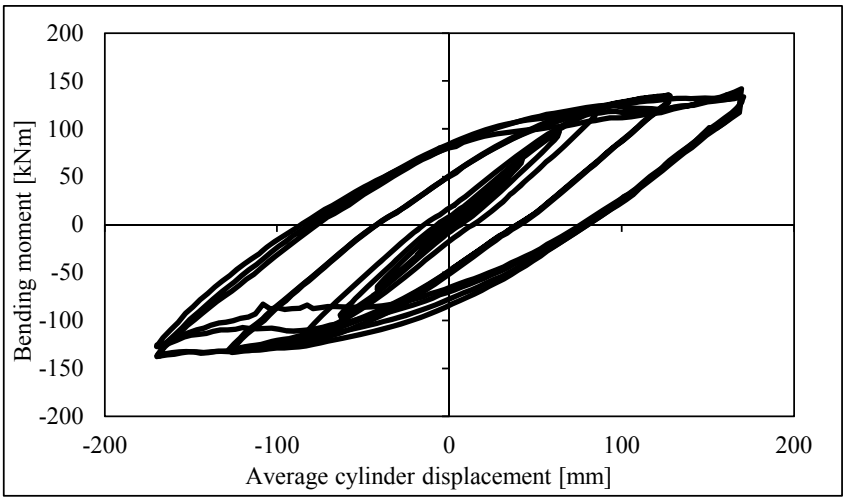

Figure 6.56 – Bending moment *versus* average cylinder displacement corresponding to Test B performed on X65 piping [7].

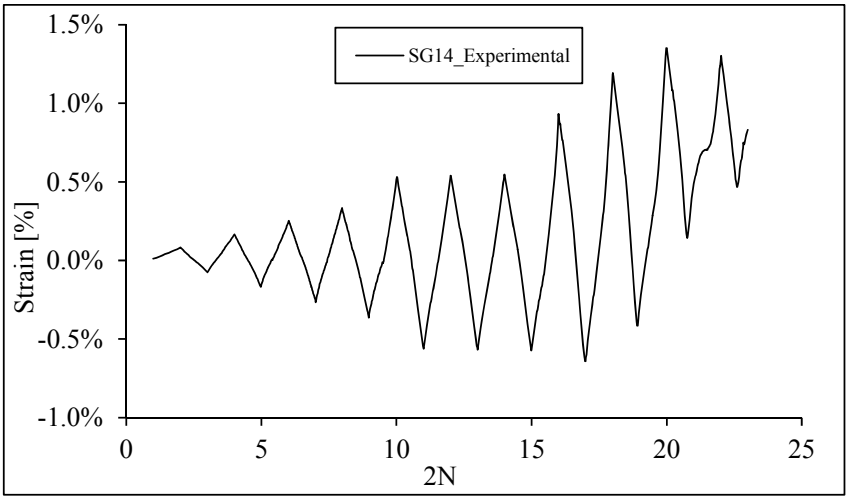

Figure 6.57 – Axial strain at pipe centre (gauge 14) corresponding to Test B performed on X65 piping [7].

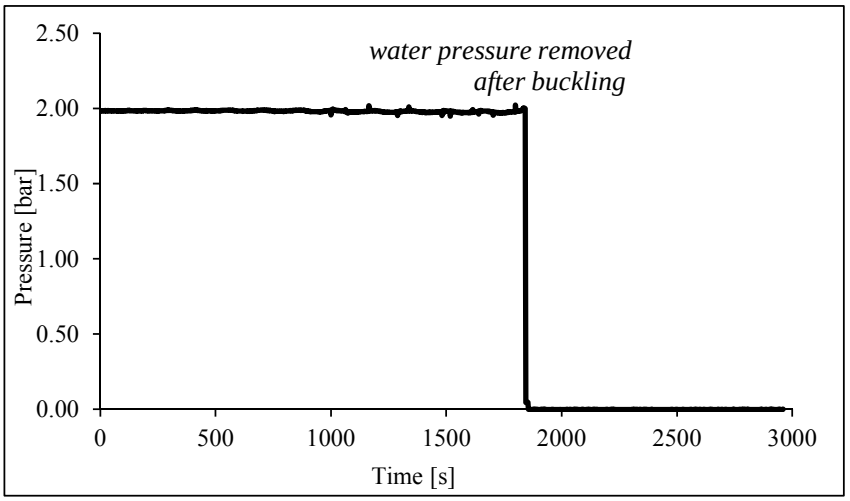

Figure 6.58 – Inner pressure history corresponding to Test B performed on X65 piping [7].

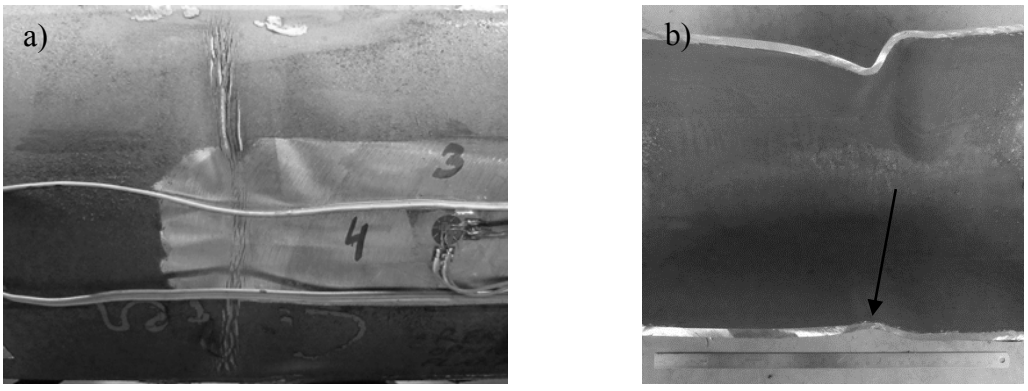

Figure 6.59 – Fracture location from Test B: a) detail view of a macroscopic crack; b) section view of the buckled section [7].

Due to the dimensions of the pipes of X60 steel grades the experimental set-up was rearranged according to the Configuration 2, as illustrated in Figure 6.43. The specimen relative to the Test C was mounted with the 0° reference at the 12h position in the setup. The experimental data, resulted from this test can be observed in Figure 6.60 to Figure 6.64, which includes the cylinder displacement, bending moment, the strain values obtained from strain gauges and the hysteresis loops. In this tests the buckle was visible after 122 cycles and located at a distance of 40 cm from the tubeholder. The final fracture occurred after 129 cycles. In order to avoid the figure to be overloaded with information, the data between the 25 to 120 cycles was discarded from the plots. To avoid the axial and rotational movement of the pipe in the setup, some small blocks were welded to the specimen which reacted against the tubeholder [7]. However, the blocks failed during the test and the pipe shifted approximately 30 cm in axial direction over the complete test.

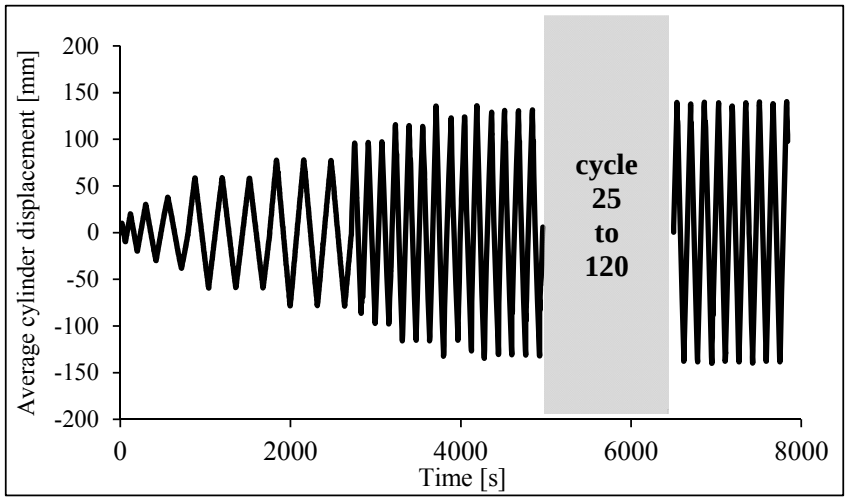

Figure 6.60 – Average displacement *versus* time corresponding to the Test C performed on X60 piping [7].

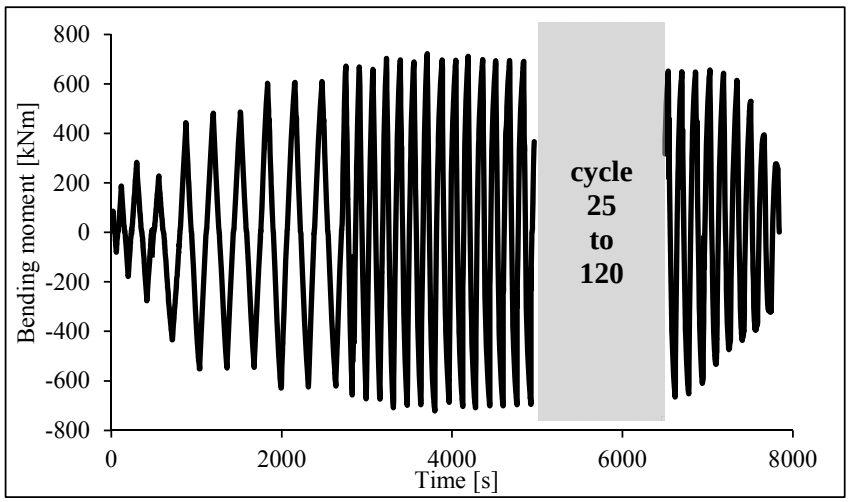

Figure 6.61 – Bending moment *versus* time corresponding to the Test C performed on X60 piping [7].

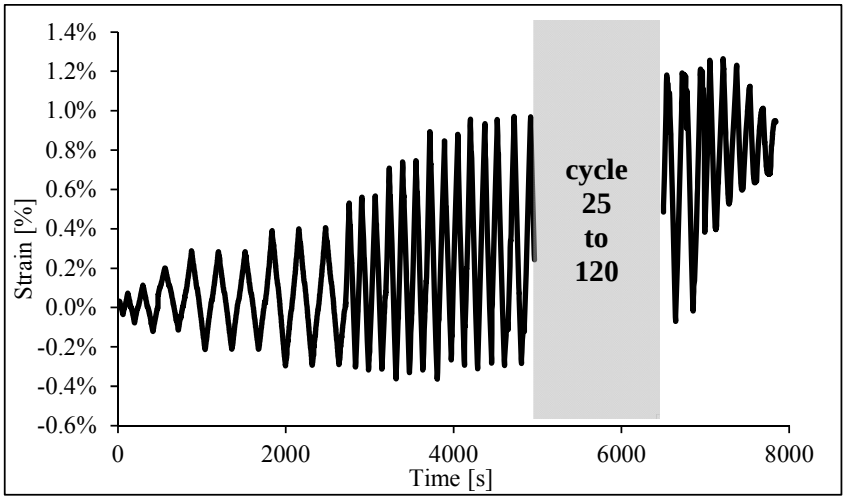

Figure 6.62 – Axial strain at pipe centre (gauge 22) corresponding to Test C performed on X60 piping [7].

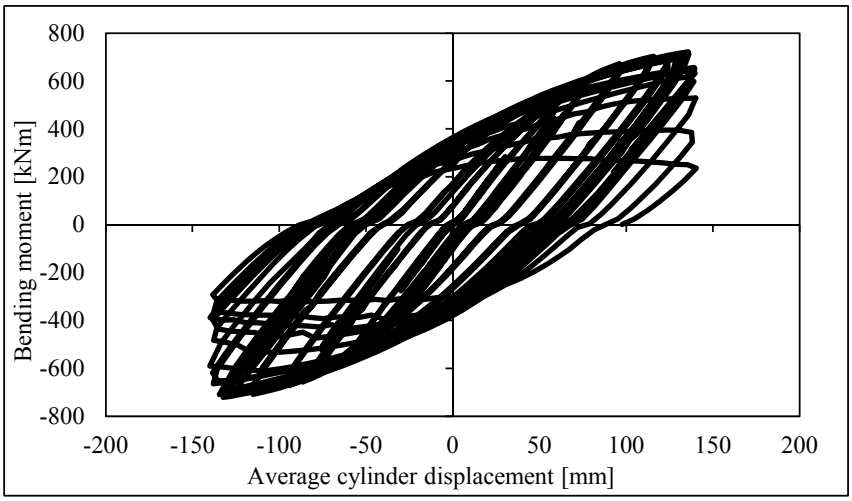

Figure 6.63 – Bending moment *versus* average cylinder displacement corresponding to Test C performed on X60 piping [7].

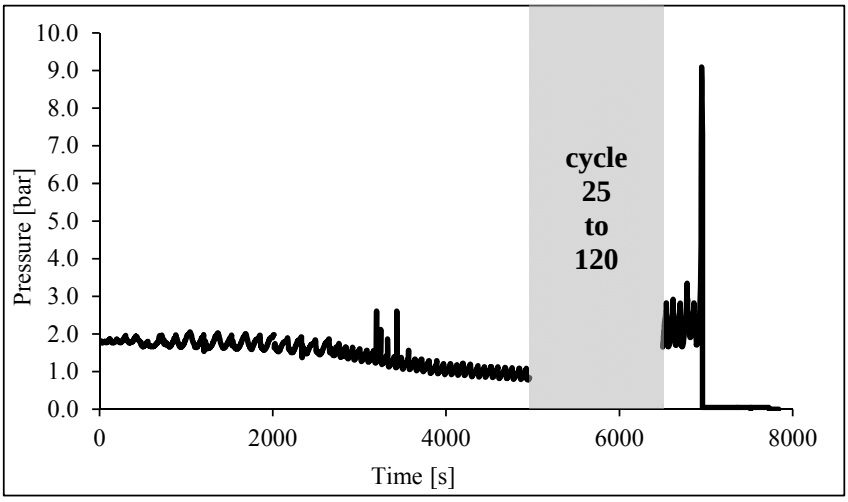

Figure 6.64 – Inner pressure history corresponding to Test C performed on X60 piping [7].

Figure 6.65 illustrates the buckle after cycle 122 and the axial displacement of 30 cm due to the failure of the welded fittings. The instability appeared next to the material that was initially inside the tubeholder. Due to this effect, the Test C will not be considered in the numerical simulations to be presented in the Chapter VII. The fracture location of Test C is represented in Figure 6.61. In detail, a view of a macroscopic crack and a top view of the ULCF fracture in the buckled section is observed, including the representation of the neutral axis.

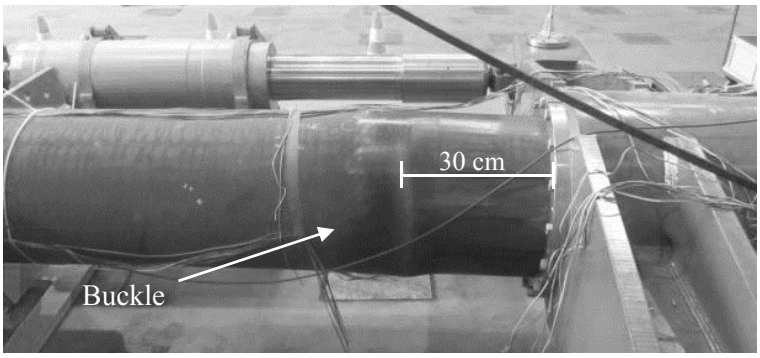

Figure 6.65 – Illustration of the axial movement of the pipe of Test C [7].

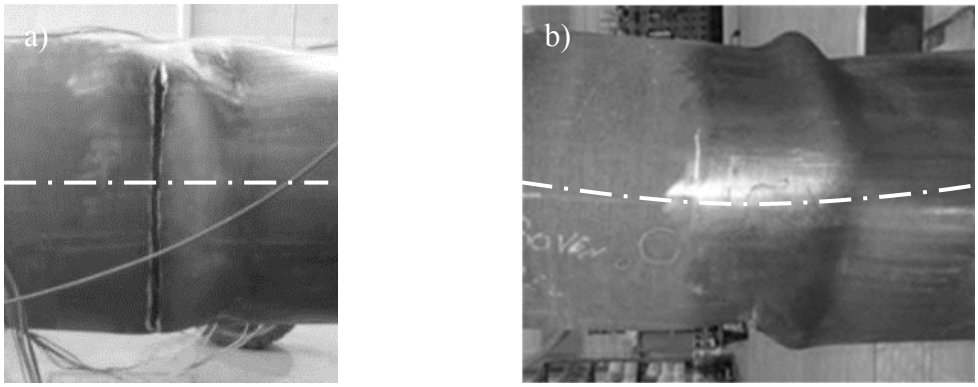

Figure 6.66 – Fracture location from Test C: a) detail view of the macroscopic crack; b) top view of the buckled section [7].

The specimen of Test D was mounted with the 0° reference at the top position (12h00) in the setup. Also, to induce the crack initiation at the pipe center, the specimen was slightly ground at 0° and 180°, with 0.8 mm thickness reduction over an 250mm x 100mm area, as represented in Figure 6.67. The experimental data including the average cylinder displacement, bending moment, hysteresis cycles, strain values and inner pressure are shown in Figure 6.68 to Figure 6.72. The buckle appeared at the center of the pipe during the cycle 33, consequently from this point the inner pressure was removed. After that, the

test was continued until the specimen final fracture at the 39 cycle. It is clear from the strain measurements shown in Figure 6.70 that the local strains at the location of the buckle start to decrease before the macroscopic buckle appearance: from cycle 22, the local strain start decreasing [7]. The fracture location of the specimen of Test D is represented in the Figure 6.73. As can be observed, the thickness reduction at the pipe center was essential to induce the macroscope crack initiation.

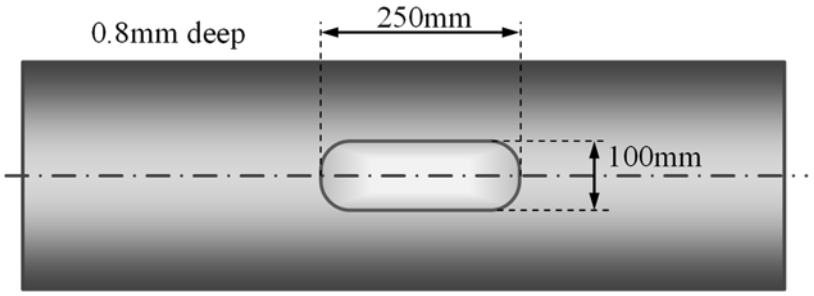

Figure 6.67 – Wall thickness reduction at the pipe center of Test D [7].

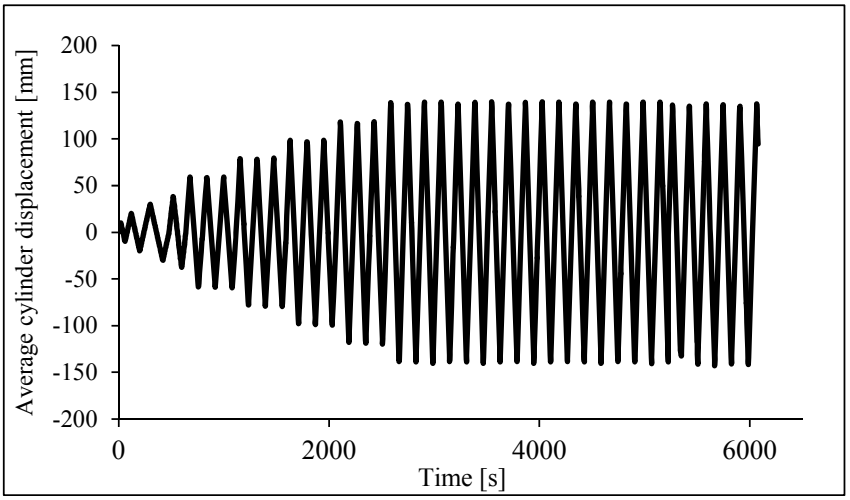

Figure 6.68 – Average displacement *versus* time corresponding to the Test D performed on X60 piping [7].

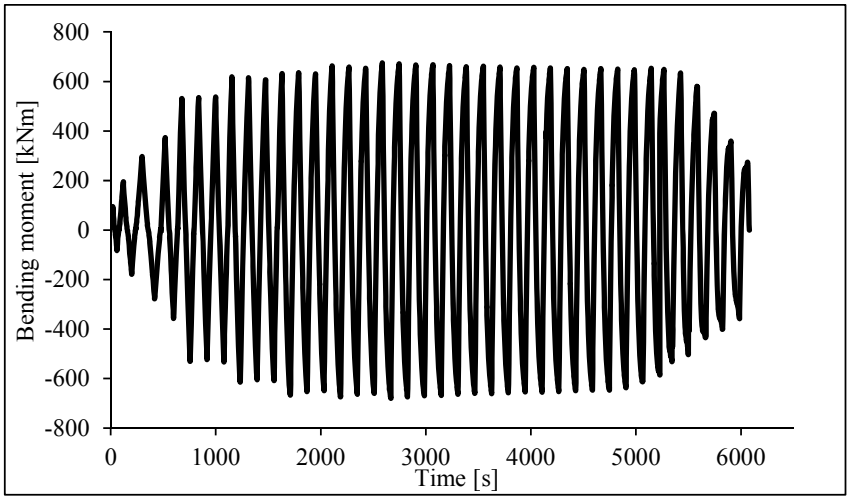

Figure 6.69 – Bending moment *versus* time corresponding to the Test D performed on X60 piping [7].

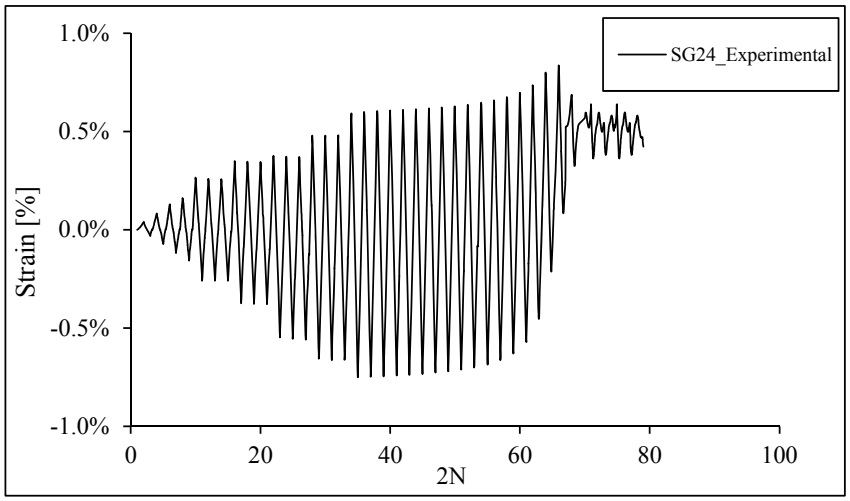

Figure 6.70 – Axial strain at pipe centre (gauge 24) corresponding to Test D performed on X60 piping [7].

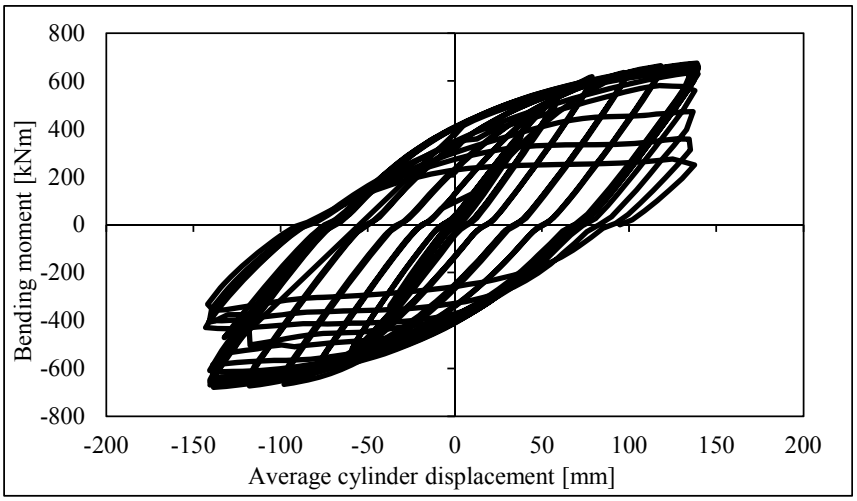

Figure 6.71 – Bending moment *versus* average cylinder displacement corresponding to Test D performed on X60 piping [7].

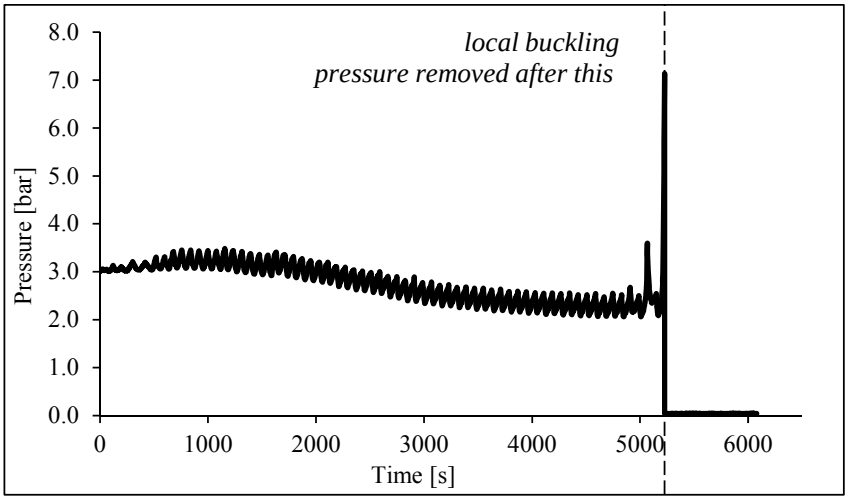

Figure 6.72 – Inner pressure history corresponding to Test D performed on X60 piping [7].

Figure 6.73 – Detail view of fracture location of Test D [7].

In summary, concerning the 4 ULCF tests of the straight pipes, 3 accomplished with the expected purpose. The Test C was not successful due to the non-controlled relative displacements between the pipe and the tube-holder. The tests performed with the X65 pipes resulted in very short lives, within the ULCF domain. The valid test on the X60 pipe resulted in a fatigue life that was about two times the lives obtained for the X65 pipes. In all cases the fatigue cracks were preceded by the plastic instabilities. Fatigue cracks appeared very few cycles after the buckle appearance.

6.4 CONCLUSIONS

In this chapter the experimental program carried out on full-scale elbows and straight pipes of X60 and X65 steel grades was described. These tests were performed by RWTH and OCAS, partners of the European project *Ultra low cycle fatigue of steel under cyclic high-strain loading conditions*, coordinated by FEUP. The experimental results obtained with these tests were presented in a brief form in this chapter and will be used to validate the finite element models and fatigue simulations that will be developed in the Chapter VII. This experimental program aiming at characterizing the ULCF of elbows and straight pipes used in the pipelines.

With respect to the cyclic tests of full-scale elbows, two distinct configurations regarding the elbows' angles (45º and 90º) were tested for X60 and X65 steel grades. Additionally, the straight pipes that resulted in the elbows showed different dimensions which required an adequate experimental setup to be adjusted for each piping section. Measurements were carried out over all specimens and different displacement amplitudes and different inner pressures were applied, which allowed the investigation of the influence of these parameters in the ULCF behavior of the referred components. It should be referred that the displacement amplitudes applied on both cyclic tests of elbows and straight pipes were based on the ECCS recommendations. Preliminary finite element simulations were conducted to achieve the proportional displacement limit, e_y. The elbows ovalization at the central section was measured and the strain gauges were attached to the straight pipes at the critical location, which allowed the measurement of the strain evolution during the cyclic tests. Since the inner pressure showed significant fluctuations during the tests, it was also measured until the specimen final failure. In general, the buckle formation occurred at the central section of the elbows, which is affected by the displacement amplitude and inner pressure. The inner pressure is directly related with the shape of buckle. On effect, when the specimens are subjected to a higher internal pressure, it was verified that the instability tends to assume a "bubble" shape towards the exterior of the pipe. In contrast, for the lower values of internal pressure the instability assumes a dent shape. Concerning the straight pipes the instability occurred at two different locations, in detail at the central section (Test B and Test D) and the next to the tubeholder (Test A and Test C). The buckle formation at

the central section was induced by a process of thickness reduction at this location. The tubeholder was initially fixed to the tube by using a small weld, in order to avoid a rotational and longitudinal movement of the tube inside the tube holder. However, the tubeholder shifted a little towards the outside of the tube due to a failure in the weld for the Test D. The instabilities formation causes a considerable increase in the accumulated plastic strain promoting a very fast damage evolution and quick failure. As expected, the macroscopic crack appearance and the propagation until final failure occurred within a few cycles after the buckle formation.

6.5 REFERENCES

[1] Fernandes A.A. et al, (2015), "Ultra low cycle fatigue of steel under cyclic high strain loading conditions," Final Report, European Commission RFSR CT 2011 00029.

[2] Pereira J.C.R., Ruano J., Schaffrath S., de Jesus A.M.P., Fernandes A.A., Feldmann M., (2015), "Ultra-low-cycle fatigue behavior of full-scale elbows", ASME 2015 PVP July 19-23, 2015, Boston, Massachusetts USA.

[3] Pereira J.C.R., Wittenberghe J.V., de Jesus A.M.P., Thibaux P., Fernandes A.A., (2016) "Ultra-low-cycle fatigue behavior of full-scale straight pipes under alternating bending", ASME 2016 PVP July 17-21, 2016, Vancouver, BC, Canada.

[4] Pereira J.C.R., Wittenberghe J.V., de Jesus A.M.P., Thibaux P., Fernandes A.A., (2016), "Study of full-scale straight pipes under ultra-low-cycle fatigue bending loading", International journal of pressure vessels and piping" (submitted for publication).

[5] Schaffrath, S., Eichler, B., Feldmann, M., (2014). “Full Scale tests of elbows under cycle loading (ULCF).” ULCF internal report, RWTH Aachen - Institute of steel construccion.

[6] ECCS-European Convention for Constructional Steelwork, (1986). “Recommended Testing Procedure for Assessing the Behaviour of Strutctural Steel Elements under Cyclic Loads.” ECCS, Belgium.

[7] Wittenberghe J.V., (2014). “Full scale tests of straight pipes under cyclic.” ULCF internal report, OCAS NV.

Chapter VII

Finite element simulation and damage assessment of full-scale cyclic tests of elbows and straight pipes

7.1 INTRODUCTION

In this chapter, the cyclic tests of the full-scale elbows and straight pipes (presented in Chapter VI) will be modelled using the finite element method, aiming at evaluating the stress/strain histories at the critical locations and the application of the damage models identified at Chapter IV to assess the damage behaviour of the tested full-scale pipe components. The finite element models will be developed in the ABAQUS® software [1]. The numerical models of the full-scale elbows and straight pipes were built taking into account the actual geometries of each component based on measurements performed prior the tests (diameters, thicknesses, ovalities). The boundary conditions of the numerical models were supported by the experimental measurements during the tests, in particular the displacement amplitudes and the inner pressure histories registered during the cyclic loading, will be inputted in the numerical models. The numerical results are compared with experimental load and bending moment histories which were registered as reactions. A comparison between the experimental and numerical deformed shape of specimens, specifically at the plastic instabilities location will be also presented. Based on the elastoplastic strain histories evolution obtained by means of the finite element simulations, the performance of the damage models used for fatigue life prediction will be evaluated. The Coffin-Manson [2][3] relation and Xue [4] model are proposed to estimate the fatigue life of the pipe components. Additionally, the recommendations of *ASME Boiler & Pressure Vessel Code, Section VIII, Div. 2* [5] were also applied to make alternative damage predictions and to allow a comparison with the experimental results and with the predictions performed with models identified and validated in this thesis using small-scale testing data.

7.2 SIMULATION OF FULL-SCALE TESTS OF ELBOWS UNDER CYCLIC LOADING

In this section, a numerical approach for the simulation of the elbows under cyclic loading was proposed based on an uncoupled plastic-damage approach. This approach was supported by an elastoplastic analysis performed using the plasticity models with

kinematic hardening. The plasticity and damage model parameters were identified using small-scale test data from smooth specimens subjected to tension-compression ULCF loading conditions. In particular, it is emphasized that material subjected to the same thermal cycle as the one used in elbows manufacturing was tested for the generation of relevant cyclic plasticity data. The numerical results resulted from the simulation of the 8 elbows tested at RWTH are presented. A detailed presentation of the finite element model of the full-scale tests, the comparisons between numerical and experimental results and the fatigue damage assessment are given below.

7.2.1 Finite element model

As referred above, the numerical simulations of cyclic bending tests of the full-scale elbows were performed on commercial code ABAQUS® [1], using 8-noded isoparametric solid elements with reduced integration (C3D8R). In order to minimize the computational cost of the numerical simulations, symmetry conditions were taken into account in the numerical model. The symmetry conditions are detailed in the Figure 7.1, consisting on modelling only half of the elbow. As previously mentioned, each specimen was modelled taking into account the real dimensions, which are summarized in Table 7.1. The diameter and thickness of the pipe, D_R and t_R, were computed from the average values of perimeter and thickness measured for all sections of the pipe. The vertical and horizontal diameters, $D_{1\text{-}5}$ and $D_{3\text{-}7}$ were used to model the central section of the elbow (see Figure 7.2). Concerning the pipe thickness at the central section, the values obtained at the points 1, 3 and 5 were used to define a variable thickness (see Figure 6.4). Due to the supposed symmetry between the points 3 and 7, the thickness value, t_3, was assumed as the average of these values. Figure 7.2 illustrates the central section of the elbows, including the typical finite element mesh.

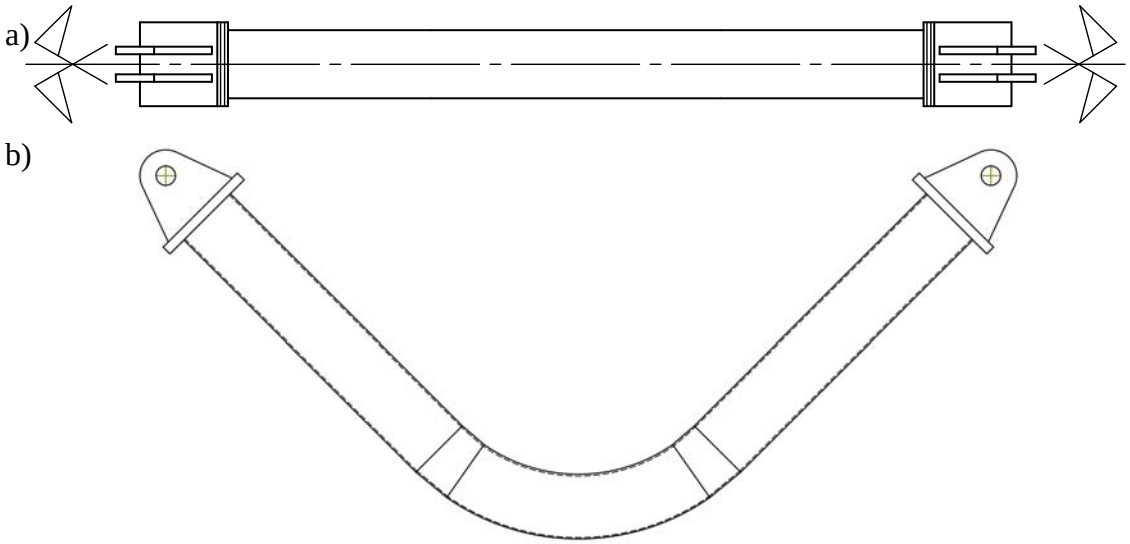

Figure 7.1 – a) Symmetry condition assumed on numerical modelling of elbows (longitudinal symmetry plane); b) front view assumed on numerical modelling.

Table 7.1 – Dimensions used in the numerical models of elbows (mm) (see Figure 6.1 and Figure 7.2).

Parameters	**SP1**	**SP2**	**SP3**	**SP4**	**SP5**	**SP6**	**SP7**	**SP8**
L	2032	2032	2032	2032	1100	1100	1100	1100
R	1219	1219	1219	1219	657	657	657	657
D	408.45	408.43	408.47	408.39	220.73	220.77	220.22	219.66
t	9.49	9.44	9.57	9.52	5.65	5.64	5.57	5.65
D_{1-5}	401.80	401.60	400.70	402.20	213.40	212.90	212.70	212.80
D_{3-7}	408.80	408.50	409.80	408.20	222.40	223.10	223.10	222.90
t_1	11.15	11.25	11.13	11.26	6.68	6.67	6.88	6.79
t_3	9.43	9.52	9.45	9.49	5.60	5.61	5.62	5.66
t_5	8.32	8.37	8.32	8.37	5.07	5.09	4.99	5.12

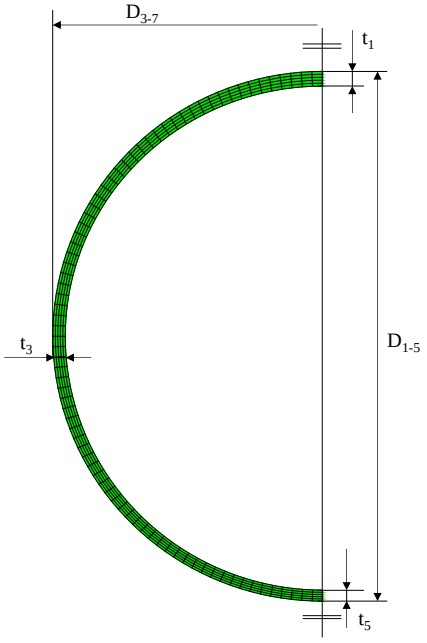

Figure 7.2 – Central section of the numerical model of the elbows.

In order to reduce the mesh size effect, a considerable refinement was adopted, mainly at the central section of the elbows (critical zone). Thus, a progressive reduction of the element size was used with the proximity to the central section of the elbow. The typical finite element mesh of an elbow is represented in Figure 7.3. A refined finite element mesh was set for the center of the elbows, where the instability is expected to occur, with minimum size of 3 mm in the longitudinal direction and 8 mm in the circumferential direction and 5 solid elements in the thickness direction. A coarse finite element mesh was implemented on the gripping system (see Figure 7.4), since these components are only used to apply the displacement amplitudes of each specimen. The different components of the gripping system show independent finite element meshes. The connection of the multiple surfaces was obtained by means of bonded contact pairs to guarantee the continuity. The material of the pipe was simulated using the Von Mises plasticity model with the non-linear kinematic hardening, using the Chaboche constants achieved from LCF and ULCF experimental tests carried out on smooth and notched small-scale specimens of the material subjected to the thermal treatment, as described in the Chapter IV (see Table 4.7 and Table 4.9) The pin-joint was modelled using the MPC constraint and link option available in the ABAQUS®. The experimental displacement histories derived from the wire sensors were imposed in the left and right pin joints. Comparisons between the numerical and experimental displacements are represented in Figure 7.5 for SP3 specimen, showing a perfect agreement between the two records.

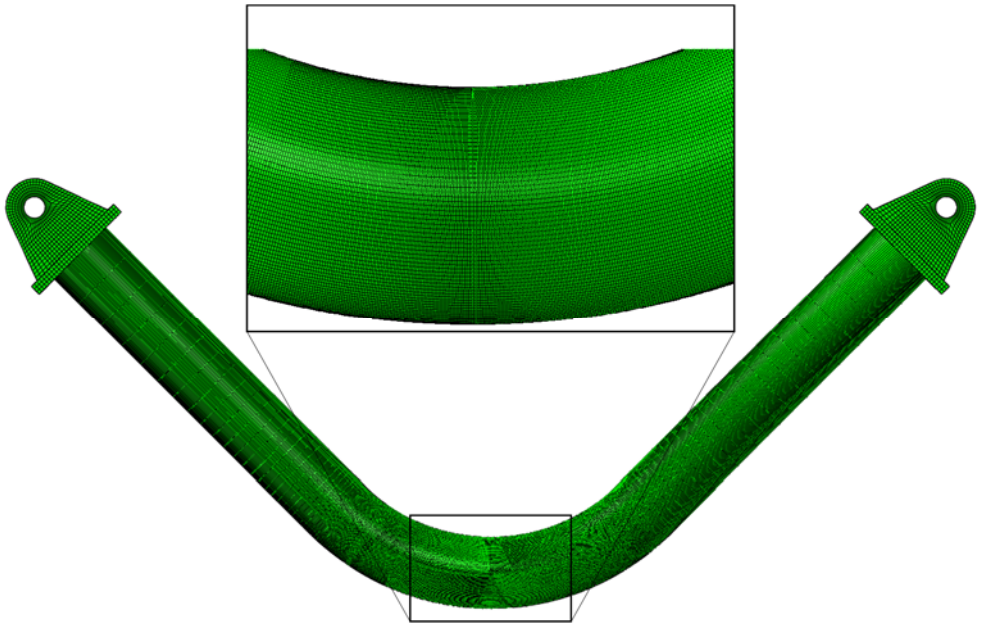

Figure 7.3 – Typical finite element mesh with detail view at the specimen central section (SP1).

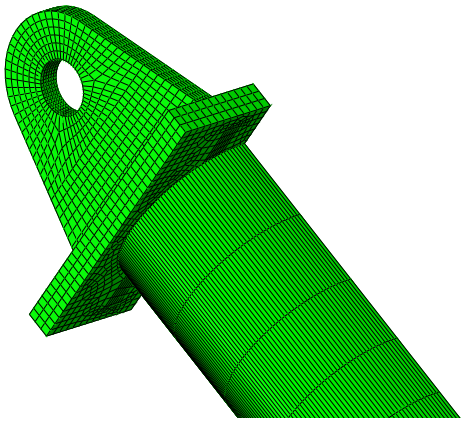

Figure 7.4 – Finite element mesh of gripping system.

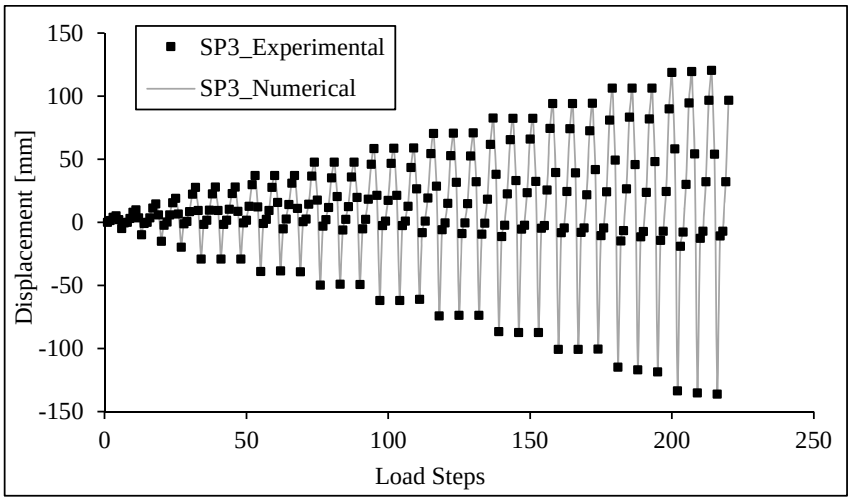

Figure 7.5 – Comparison between experimental and numerical displacement histories inputted as boundary conditions.

7.2.2 Numerical results

The numerical results of the elastoplastic simulations of the full-scale elbows tests are presented in this section. In order to validate the finite element models, numerical data are compared with experimental results, in particular the load-displacement curves are presented as also the evolution of horizontal and vertical diameters for the specimens SP1 to SP4. In addition, the experimental deformed shapes of the local plastic buckles are compared with the numerical simulation. Except for the remaining models, the simulation of SP1 specimen did not account for the fluctuation of the inner pressure, which hindered the formation of local plastic instability. In fact, in this model a constant internal pressure was applied. This evidence demonstrates the great influence of the variation of the internal pressure during the formation of plastic buckles. As mentioned along this work, the formation of the plastic instabilities causes a significant increase in the plastic

deformation, leading to the rupture of the components in a small number of cycles, after its formation. For the above reasons, and in order to reproduce the plastic buckle in the SP1 specimen, a concentrated load was applied at the central section of the elbow, along to the vertical direction. Thus, a load of 1000 N was applied at the interior node from the first cycle in the plastic regime. Comparisons between the numerical and experimental data of horizontal and vertical ovalization can be found in Figure 7.6 and Figure 7.9, for the specimens SP1 to SP4 specimens. As mentioned above, due to instabilities of the measuring equipment during the cyclic tests, these correlations will not be demonstrated until the final of numerical simulation due to the lack of experimental data. The evolution of the horizontal diameter during the cyclic loading reports a progressive ovalization, mainly for the high displacement amplitudes. This evidence supports the material continuous plastic yielding. Regarding to the evolution of vertical diameter a constant behavior until the buckle formation is observed.

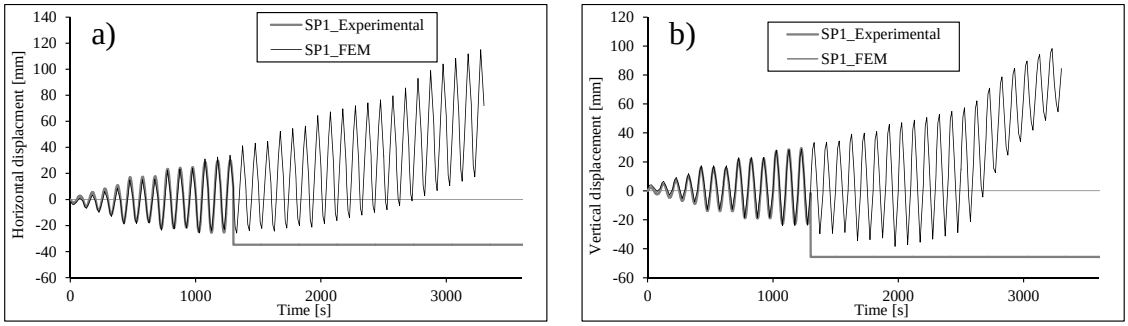

Figure 7.6 – Comparisons of experimental and numerical data of specimen SP1: a) horizontal diameter; b) vertical diameter.

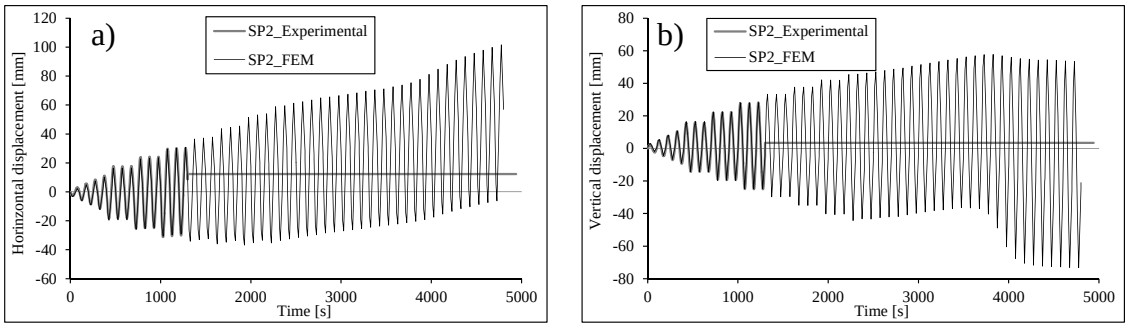

Figure 7.7 – Comparisons of experimental and numerical data of specimen SP2: a) horizontal diameter; b) vertical diameter.

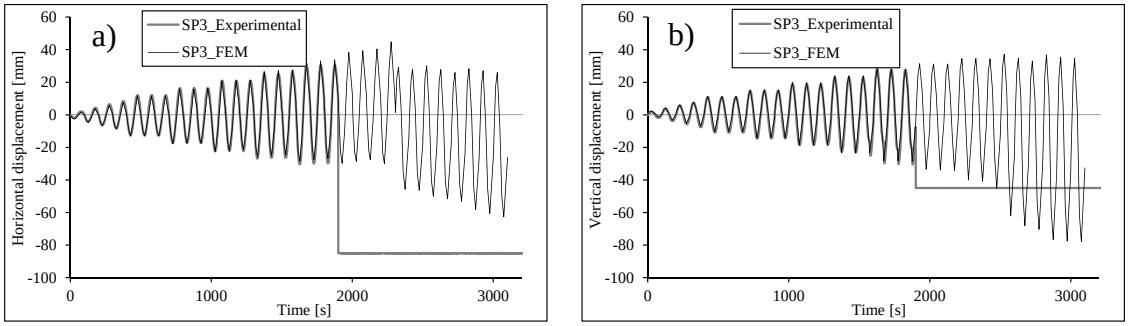

Figure 7.8 – Comparisons of experimental and numerical data of specimen SP3: a) horizontal diameter; b) vertical diameter.

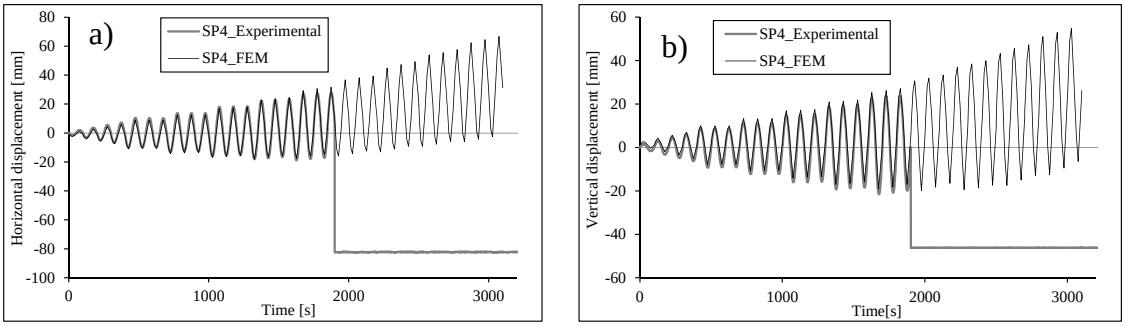

Figure 7.9 – Comparisons of experimental and numerical data of specimen SP4: a) horizontal diameter; b) vertical diameter.

Figure 7.10 to Figure 7.17 illustrate results of the simulations performed on elbows including the comparisons between the simulated load history and the experimental load history. Since the load is an output of the experimental and numerical simulations, the comparison of both histories gives a good indication of the quality of the simulations. In order ensure the damage evolution until the failure conditions, the numerical simulations of specimens, SP3, SP4, SP5, SP6 and SP7 were extended for a few more cycles than tested in the laboratory. This extrapolation was performed taking into account the displacement and inner pressure values registered for the last cycle applied in the experimental cyclic tests. Afterwards the accumulated equivalent plastic strain (PEEQ) and deformation are presented illustrating the numerical deformed shape at the final of simulation.

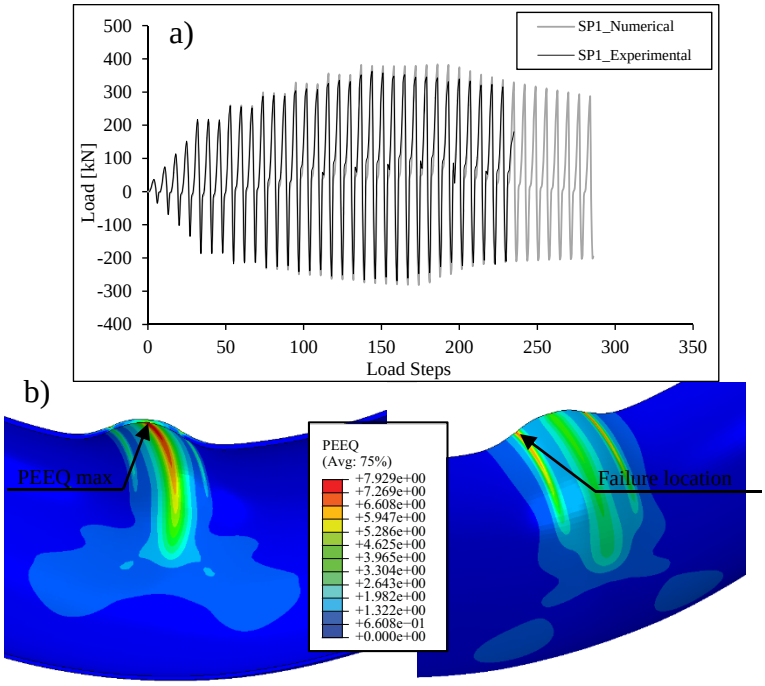

Figure 7.10 – Results of cyclic test of SP1 elbow: a) load-time history; b) elbow at the moment of failure.

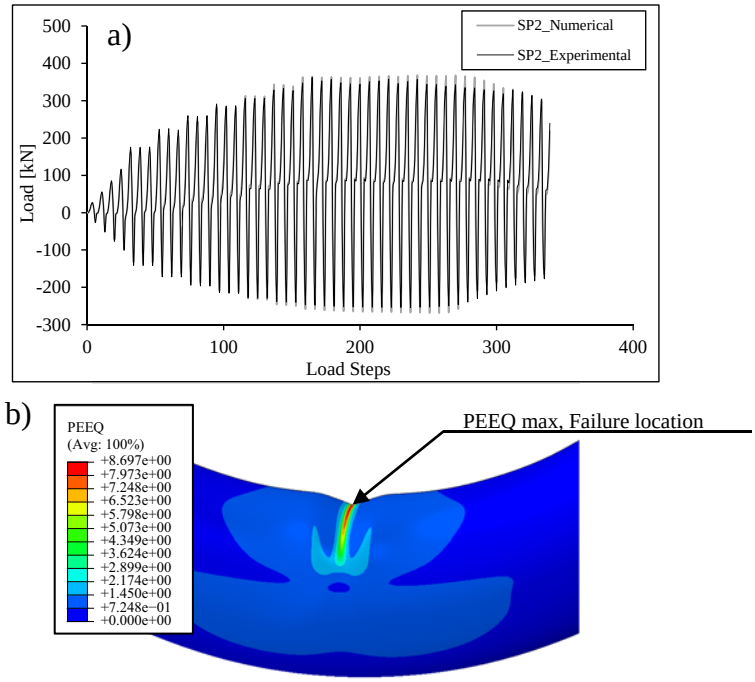

Figure 7.11 – Results of cyclic test of SP2 elbow: a) load-time history; b) elbow at the moment of failure.

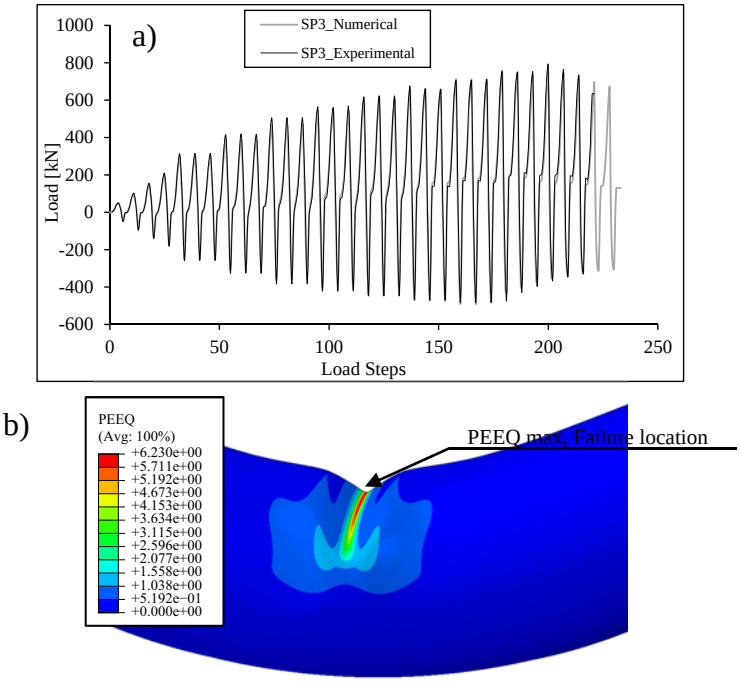

Figure 7.12 – Results of cyclic test of SP3 elbow: a) load-time history; b) elbow at the moment of failure.

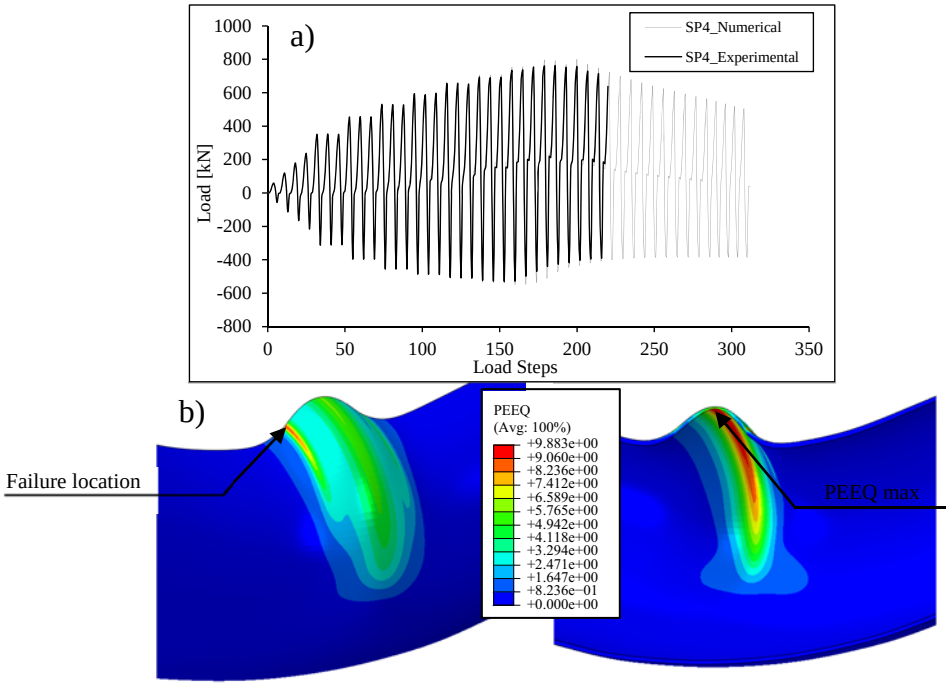

Figure 7.13 – Results of cyclic test of SP4 elbow: a) load-time history; b) elbow at the moment of failure.

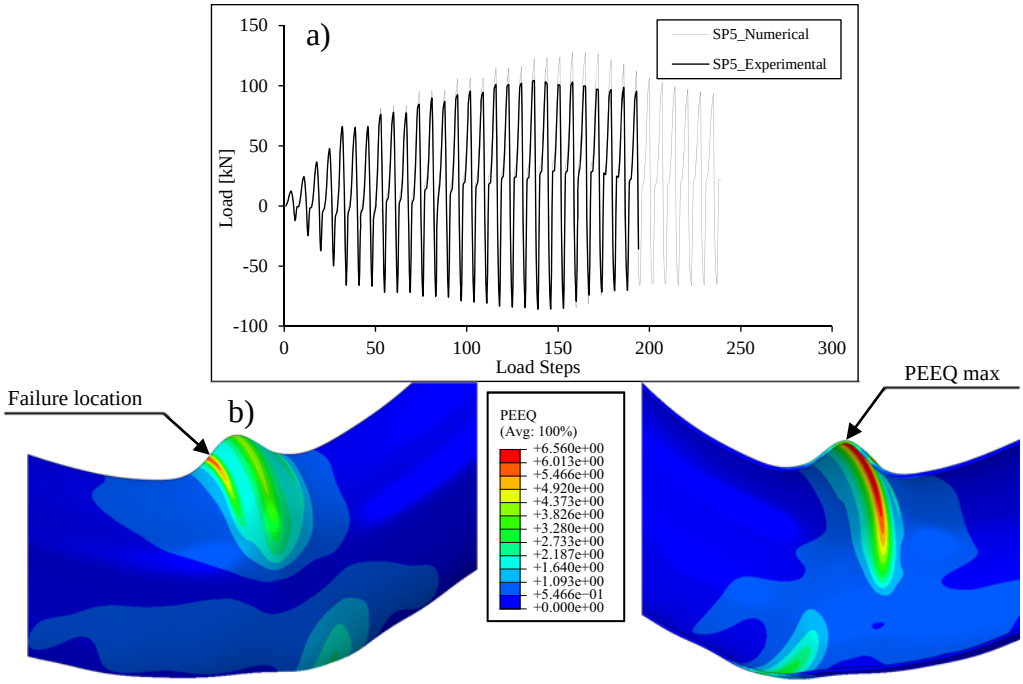

Figure 7.14 – Results of cyclic test of SP5 elbow: a) load-time history; b) elbow at the moment of failure.

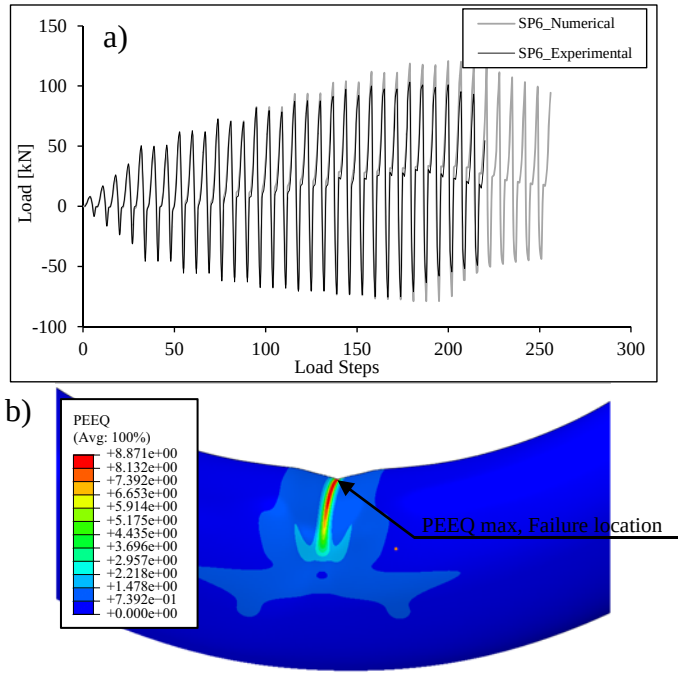

Figure 7.15 – Results of cyclic test of SP6 elbow: a) load-time history; b) elbow at the moment of failure.

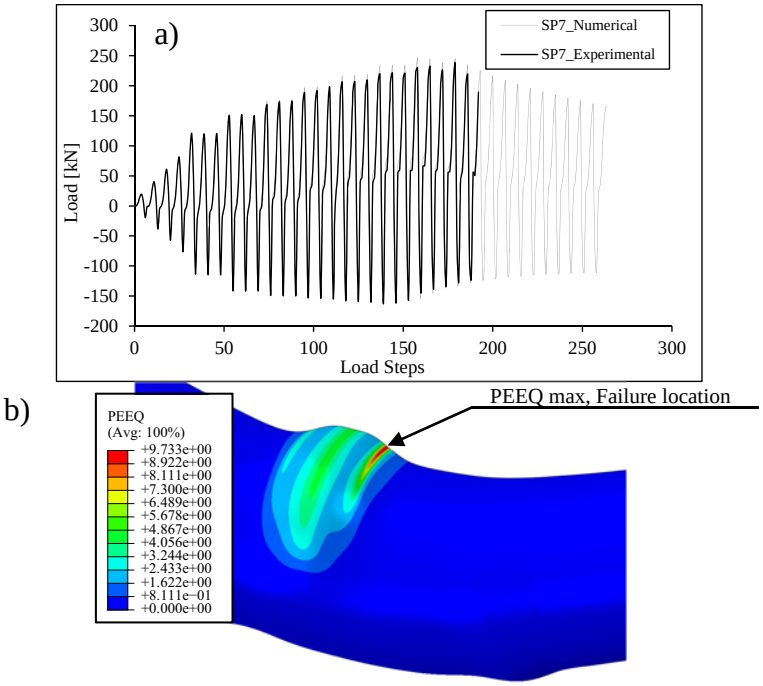

Figure 7.16 – Results of cyclic test of SP7 elbow: a) load-time history; b) elbow at the moment of failure.

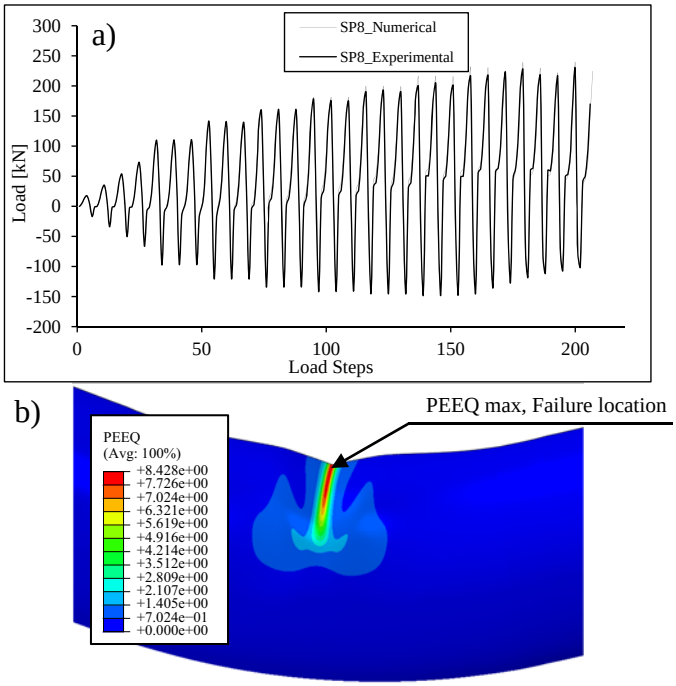

Figure 7.17 – Results of cyclic test of SP8 elbow: a) load-time history; b) elbow at the moment of failure.

In general, very good agreements were observed between both numerical and experimental load histories. The major differences were found at compression stages, in latter stages of the load histories, where local plastic instabilities started to develop in the

elbows. Nevertheless, in many cases the models were able to capture this strength reduction which is an indication that local plastic buckles were accurately captured by the numerical models. In all tests, failures occurred only after a local buckle was generated that contributed to the strain localization and damage evolution. Therefore the success of the fatigue life predictions depends on the capacity of the model to simulate the buckle formation. The numerical models were able to model the shape the buckle (inward/ outward) as a function of the applied inner pressure. It was observed that for the lower values of the internal pressure, the formed buckle was directed inside the pipe; for the higher pressure, the buckled formed outward of the pipe. This feature was clearly captured by the finite element analysis. It was also observed that the failure location may not coincide with the maximum accumulated equivalent plastic strain location, as demonstrated by the analysis of numerical results of SP1, SP4 and SP5 specimens. The experimental evidence of the specimens with the buckle formed toward the interior of the pipe indicates that the failure occurs at the root of the buckle in the exterior of the pipe. The correspondence between the failure and maximum accumulated equivalent plastic strain location was only obtained for the specimen SP7.

7.2.3 Damage models evaluation

It was verified previously that the finite element models with a Von Mises plasticity yield criterion and kinematic hardening reproduces satisfactory the elastoplastic cyclic behavior of the tested elbows on the experimental program described in the Chapter VI. In this section a fatigue life assessment will be performed by means of Coffin-Mason [2][3] and Xue models [4]. In addition, the ASME code Division VIII, Section II recommendations are also applied to compute the fatigue lives for the tested elbows. The damage analysis was conducted using a cycle-by-cycle analysis. A multiaxial strain approach was used to compute the total and plastic strain ranges. This approach was defined in the Chapter IV, Eq. (4.6). As mentioned previously, in this research the fatigue life predictions are concerned with the macroscopic crack initiation. The damage evolution associated with each specimen and comparisons between the numerical and experimental fatigue life durations will be presented.

Based on the Coffin-Manson and Xue model formulations, the numbers of cycles to failure corresponding to the computed equivalent plastic strain amplitudes, corresponding to each loading cycle, were computed. In order to account for the damage for each cycle loading, the Miner's rule was applied as follows:

$$D = \frac{n}{N} \tag{7.1}$$

where D represents the damage variable, n is applied the number of cycles ($n=1$ in this analysis, cycle-by-cycle damage analysis) and N is the number of cycles to macroscopic crack initiation computed from the Coffin-Manson and Xue models, for the same conditions of the n applied cycles. In order to compute the number of cycles to failure the global parameters of the Coffin-Manson relation were used (see Table 4.17 and Table 4.20).

Concerning the identification of the elbows critical location, the accumulated equivalent plastic strain, stress triaxiality and the Lode angle parameter maps around the plastic buckle were analyzed. It is important to note that the criteria of maximum accumulated equivalent plastic strain and maximum equivalent plastic range is equivalent. This information is important for the application of the Xue damage model. Figure 7.18 and Figure 7.19 illustrate this information for SP2 and SP7 specimens. It was observed that the shape of the buckle is related to the inner pressure applied during the cyclic tests. Thus, one case with the buckle directed toward the interior of the pipe (SP2) and the other with the buckle formed toward the exterior of the pipe (SP7) were selected. The combined analysis of these parameters results the crack initiation location which is supported by the experimental evidences.

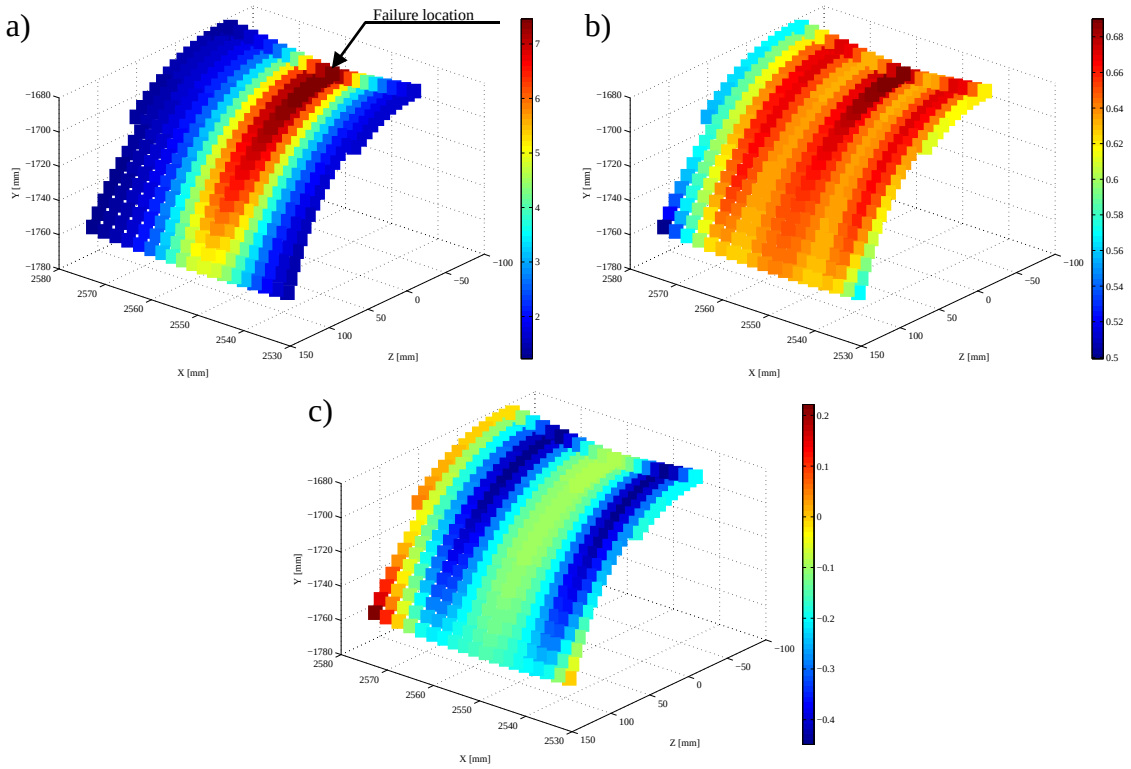

Figure 7.18 – Maps of the variables involved on the evaluation of the critical location of SP2 elbow: a) accumulated equivalent plastic strain; b) stress triaxiality; c) Lode angle parameter.

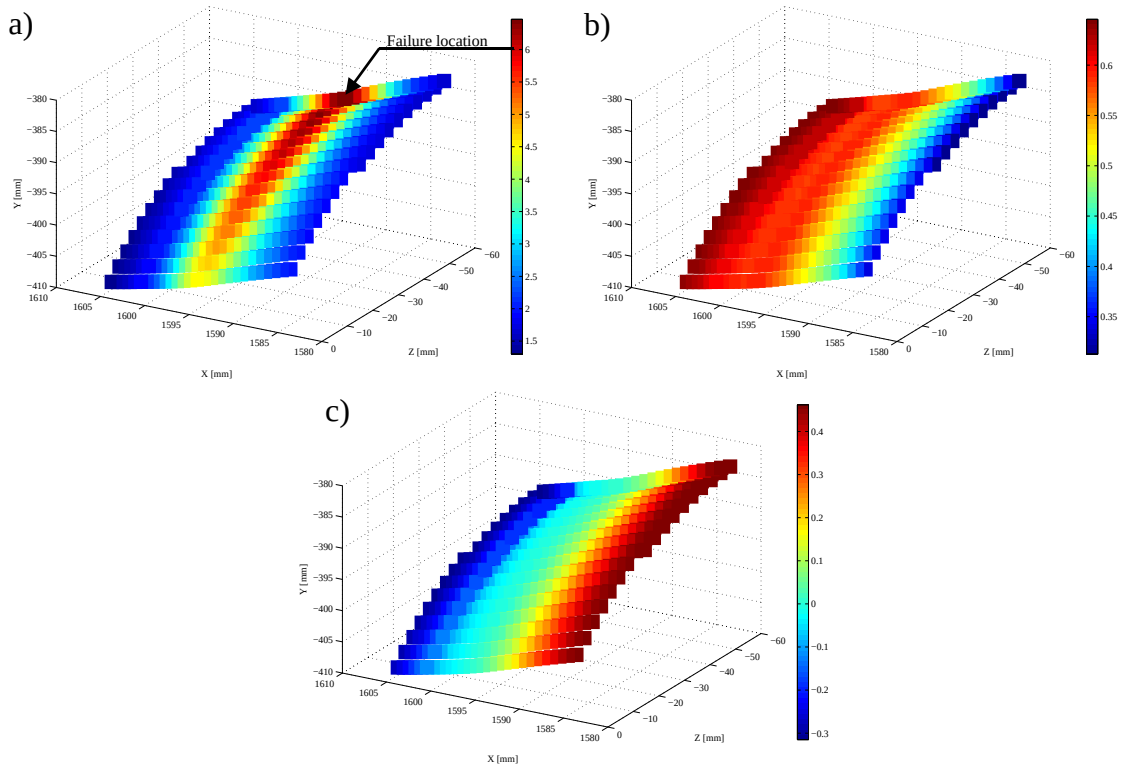

Figure 7.19 – Maps of the variables involved on the evaluation of the critical location of SP7 elbow: a) accumulated equivalent plastic strain; b) stress triaxiality; c) Lode angle parameter.

Moreover, the evolution of the triaxiality and the Lode angle parameter were acquired at the peaks of tensile stages and plotted against the number of cycles in the Figure 7.20. The analysis of this figure reports a practically constant behavior regarding the triaxiality, around η=0.6. In contrast, the Lode angle parameter shows a variation under the negative domain, which can be associated to the geometric effect of large-scale specimens. The appearance of the plastic instability leads to a gradual approximation to plastic plane strain conditions, since the Lode angle parameter tends to $\bar{\theta}$=0.

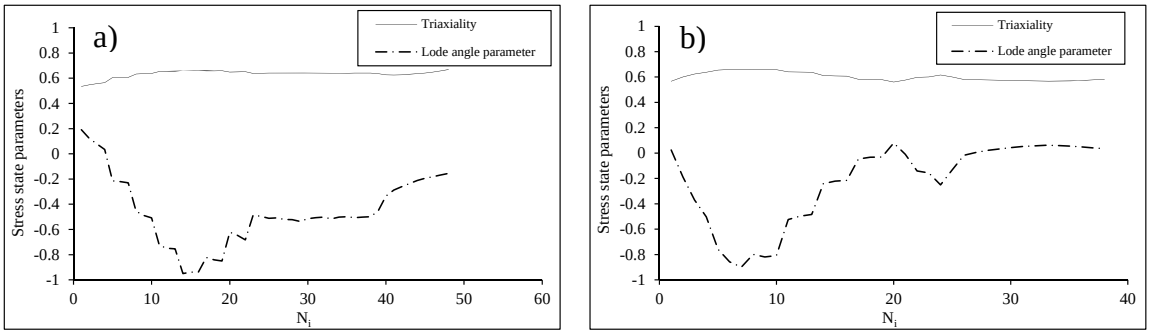

Figure 7.20 – Evolution of the stress state parameters during the cyclic loading at tensile peaks (assumed critical node): a) SP2 elbow; b) SP7 elbow.

As demonstrated in the Chapter IV the fatigue life assessment by means of Xue model, requires the monotonic fracture strain that corresponds to a normalizing factor to be applied to the equivalent plastic strain range. An approach based on the direct application of the 3D ductile surface proposed by Bai and Wierzbicki model [7] can be considered a good practice to compute this fracture strain, knowing the triaxiality and Lode angle parameters evolution at the critical location. However, the 3D fracture surface was only calibrated for the X60 piping steel since respective small-scale tests covered the necessary range of stress triaxialities and Lode angle parameter values. Thus, the effect of stress state conditions on the identification of monotonic fracture strain can be accounted assuming the influence introduced from these two parameters on cyclic behavior of X60 piping steel.

Since the ductile fracture surfaces were not fully evaluated for the X60TT and X65TT steels, a simplified methodology was proposed for these materials to account the influence of the Lode angle parameter in the number of cycles to crack initiation. It consisted in adopting a correction for the number of cycles taking into account a similar dependency of the number of cycles with the Lode angle parameter as observed for the

X60 steel grade. This approximation is illustrated in the diagram of the Figure 7.21. For a given pair of stress parameters $(\eta, \bar{\theta})$, the fracture strain is computed using an exponential function obtained from small-scale data (see Table 7.2) as represented in Figure 7.22. Using the computed fracture strain for the X60TT and X65TT steels, the Xue relation for these materials is used to compute the number of cycles to crack initiation. This number of cycles could be considered a trial value, N_i^{Trial}, if the Lode angle parameter does not coincide with the value for which the exponential function of both steel were derived ($\bar{\theta}$=0.58 for X60TT and $\bar{\theta}$=0.60 for X65TT). The correction procedure for the number of the cycles is executed taking into account data from the X60 steel. Two fracture strains are computed for X60 steel, one taking into account the known $(\eta, \bar{\theta})$ stress parameters; the other is computed for $(\eta, \bar{\theta} = const)$. With that fracture strains, the number of cycles to crack initiation are computed using the Xue relation for the X60 steel. Comparing the resulting lives we realize the effect of the Lode angle correction for the X60 steel which is adopted for the both X60TT and X65TT steels and the trial number of cycles is finally corrected. For this approach, a symmetric surface around η=0 [7] was considered since the Lode angle parameter shows negative values at the tensile peaks during the cyclic loading. Based on these assumptions the accumulated damage was computed for the critical node based on Xue model. Figure 7.23 to Figure 7.30 represent the evolution of the damage resulted from Coffin-Manson and Xue models.

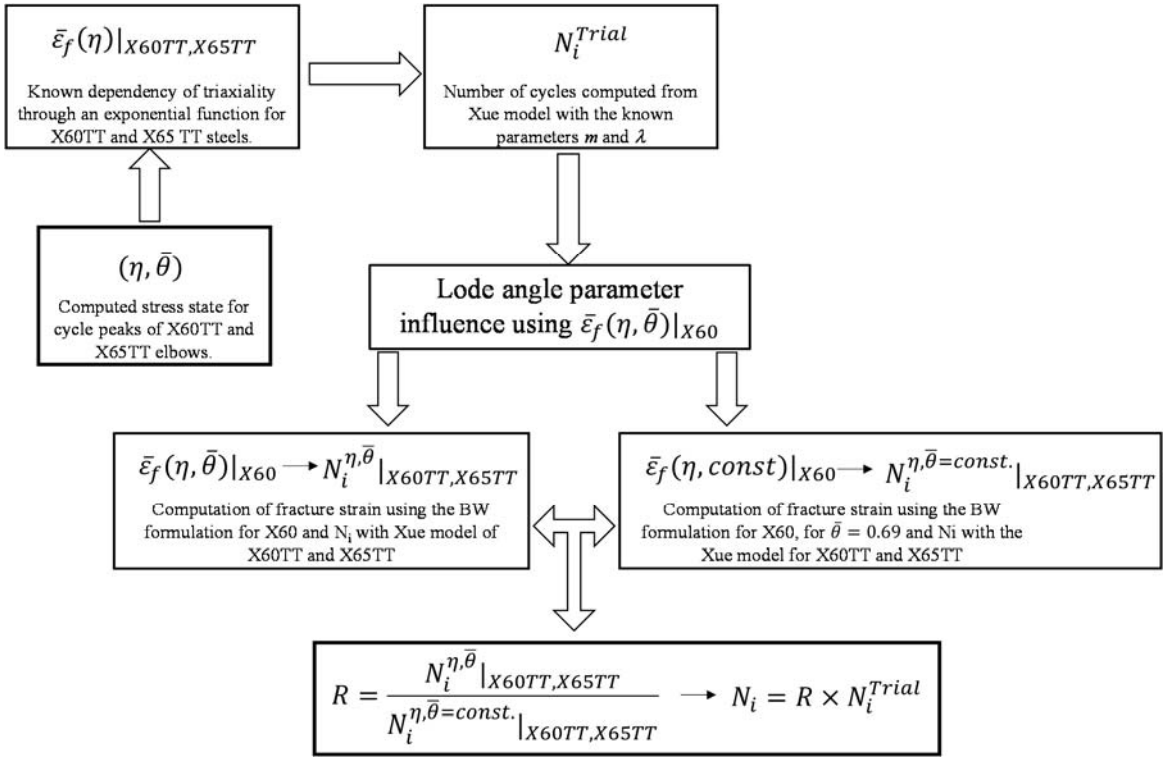

Figure 7.21 – Procedure for the computation of the number of cycles to crack initiation corrected for the triaxiality and Lode angle parameter influence.

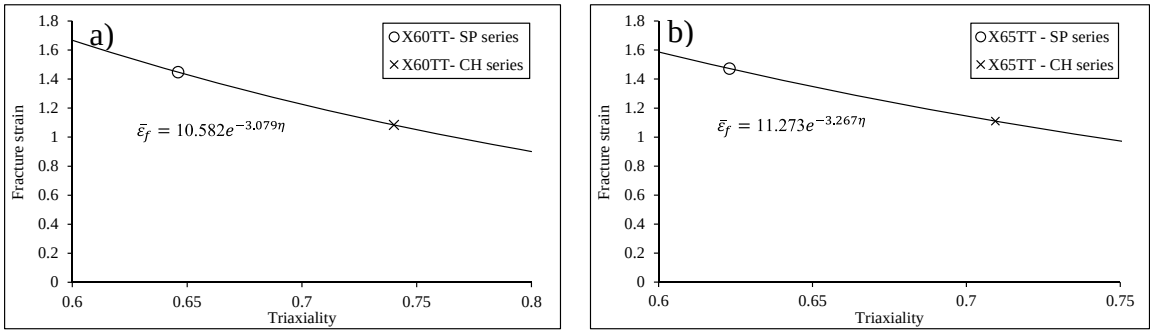

Figure 7.22 – Exponential relation between fracture strain and triaxiality for: a) X60 piping steel with thermal treatment; b) X65 piping steel with thermal treatment.

Table 7.2 – Monotonic fracture strains and stress triaxialities obtained using monotonic tensile small-scale tests of X60 and X65 steel grades with thermal treatment.

Specimens series	$\bar{\varepsilon}_f$	η_{av}	$\bar{\theta}_{av}$
X60TT_SP	1.45	0.65	0.58
X60TT_CH	1.08	0.74	0.57
X65TT_SP	1.47	0.62	0.60
X65TT_CH	1.11	0.71	0.59

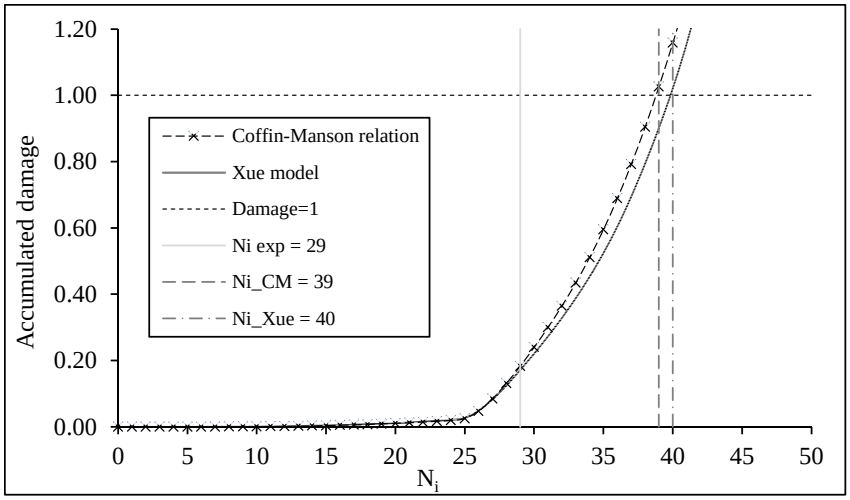

Figure 7.23 – Damage evolution of SP1 specimen.

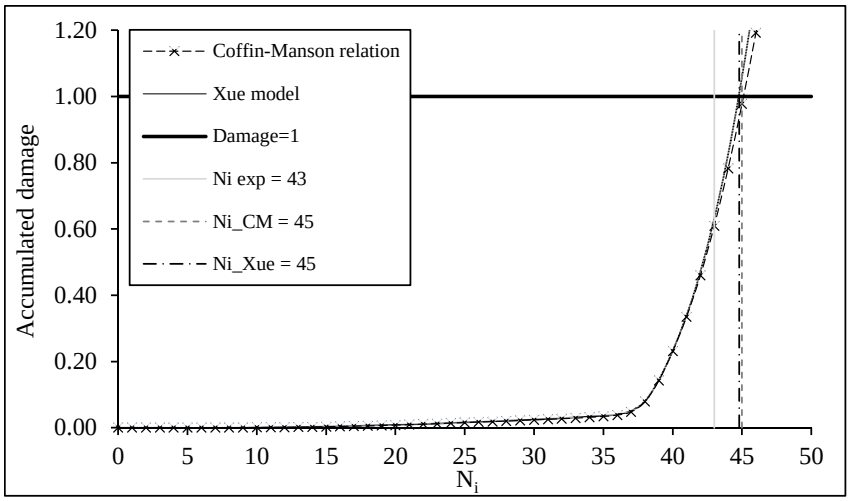

Figure 7.24 – Damage evolution of SP2 specimen.

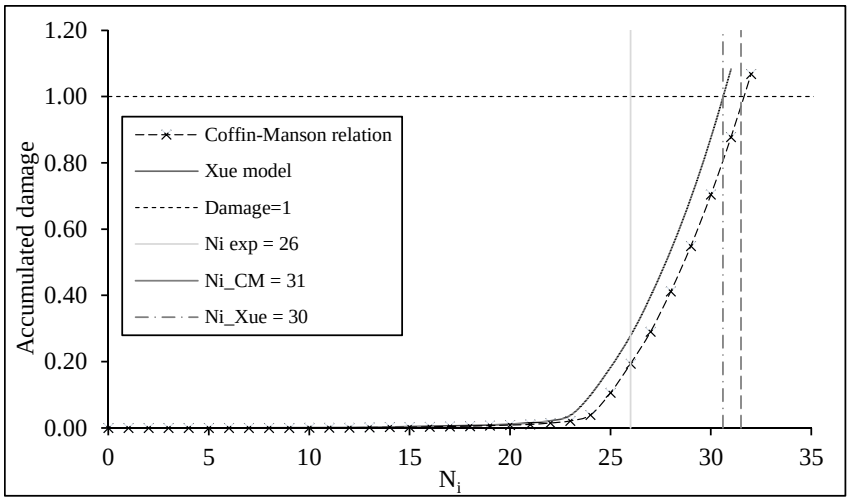

Figure 7.25 – Damage evolution of SP3 specimen.

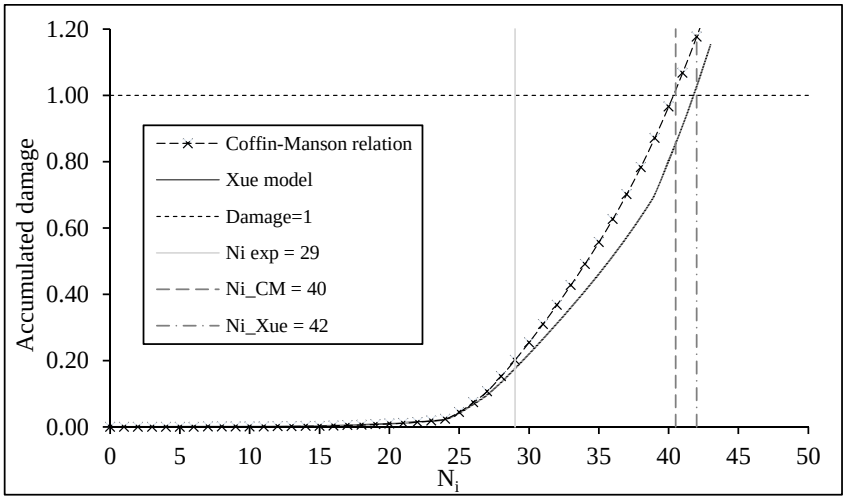

Figure 7.26 – Damage evolution of SP4 specimen.

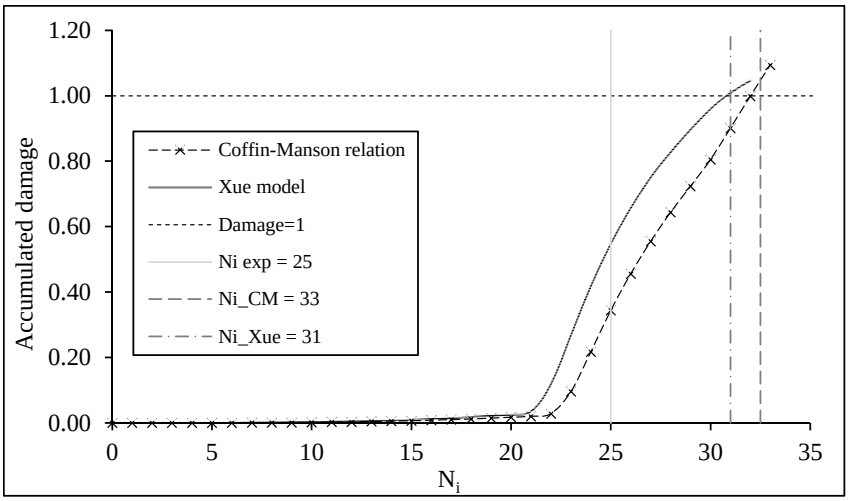

Figure 7.27 – Damage evolution of SP5 specimen.

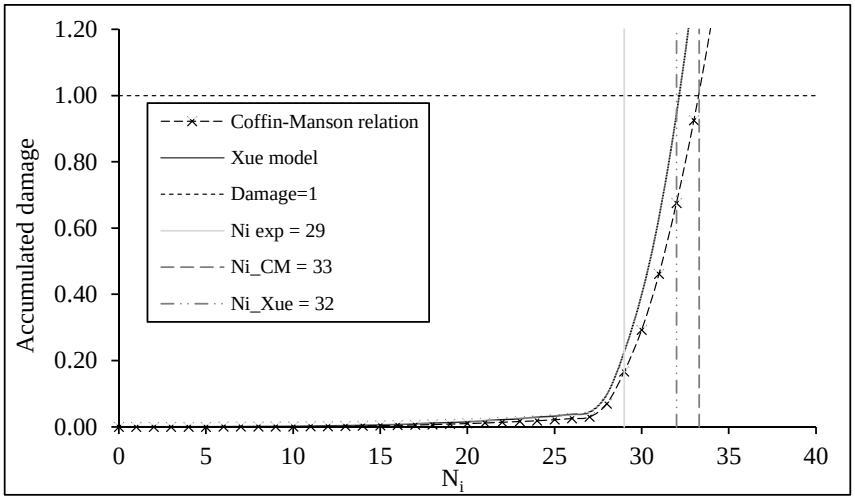

Figure 7.28 – Damage evolution of SP6 specimen.

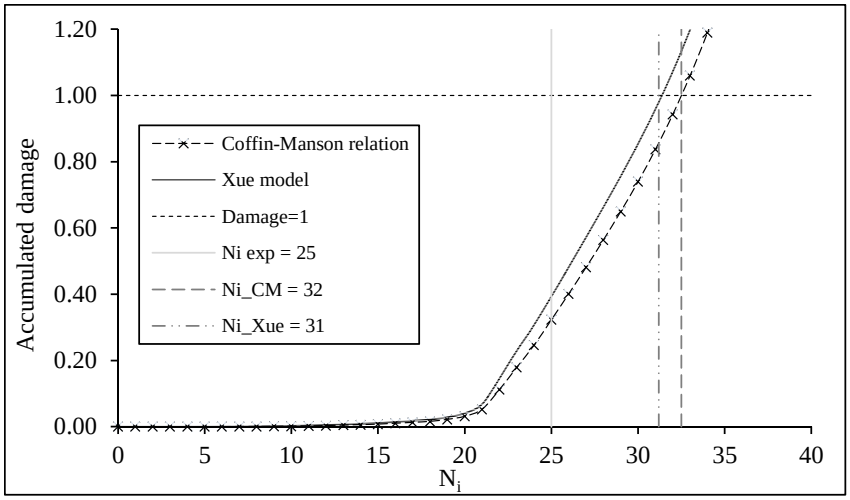

Figure 7.29 – Damage evolution of SP7 specimen.

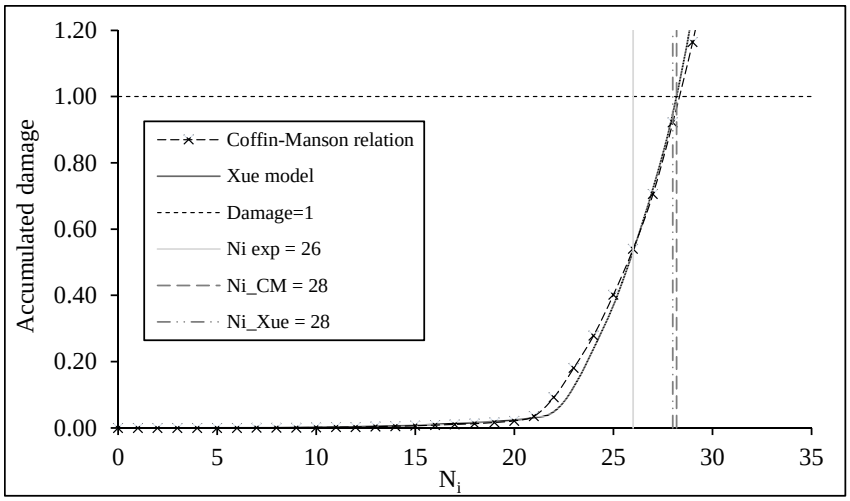

Figure 7.30 – Damage evolution of SP8 specimen.

Alternatively to the Coffin-Manson relation and Xue model, the S-N curves provided in the ASME B&PVC, Section VIII, Division 2 [5] were used in the analysis, but with the same strain-life histories computed with the numerical models and material elastoplastic properties considered in this study. For this approach, the total strain components were directly addressed from the finite element model. As performed for the Coffin-Manson relation and Xue model a cycle-by-cycle damage analysis was considered. The equivalent total strain, $\Delta\varepsilon^{T}_{eq}$ is defined by the Eq. (7.2) and the stress amplitude S_a is given by Eq. (7.3).

$$\Delta\varepsilon^{T}_{eq} = \frac{\sqrt{2}}{3}\sqrt{\begin{aligned}&(\Delta T_{11}-\Delta T_{22})^2+(\Delta T_{22}-\Delta T_{33})^2+(\Delta T_{33}-\Delta T_{11})^2+\\&+\frac{3}{2}(\Delta T_{12}^2+\Delta T_{23}^2+\Delta T_{31}^2)\end{aligned}} \tag{7.2}$$

$$S_a = \frac{E \cdot \Delta\varepsilon_{eq}^{T}}{2} \tag{7.3}$$

where E represents the elastic modulus of the material. The number of cycles predicted by the ASME recommendations are given by:

$$N = 10^{X} \tag{7.4}$$

where X is defined as:

$$X = \frac{C_1 + C_3 Y + C_5 Y^2 + C_7 Y^3 + C_9 Y^4 + C_{11} Y^5}{1 + C_2 Y + C_4 Y^2 + C_6 Y^3 + C_8 Y^4 + C_{10} Y^5} \tag{7.5}$$

$$Y = \left(\frac{S_a}{C_{us}}\right) \cdot \left(\frac{E_{FC}}{E_T}\right) \tag{7.6}$$

The parameter C_{us} represents the units correction factor from ksi to MPa (C_{us}=6.894757) and was assumed (E_{FC}/E_T)=1. The coefficients C_1 to C_{10} were obtained from the Table 7.3, which are in accordance to the ultimate tensile strength obtained for the X60 and X65 steel grades, subjected to the thermal process and presented in Table 3.21 and Table 3.38, respectively.

Table 7.3 – Coefficients of ASME recommendations [5].

$\sigma_{uts} \leq$ 552 MPa		
C_i	**48≤ S_a <214 [MPa]**	**214≤ S_a <3999 [MPa]**
1	2.25451	7.999502
2	-4.64E-01	5.83E-02
3	-8.31E-01	1.50E-01
4	8.63E-02	1.27E-04
5	2.02E-01	-5.26E-05
6	-6.94E-03	0.00
7	-2.08E-02	0.00
8	2.01E-04	0.00
9	7.14E-04	0.00
10	0.00	0.00
11	0.00	0.00

Since the original S-N curves available in the ASME code incorporate safety factors, alternative curves were used in an attempt to remove the safety factors and to use average strain-life data, to allow a direct comparison with the predictions performed in this study. The development of design fatigue curves of ASME code were based on the experimental fatigue tests carried out by Langer [8] on small-scale smooth round polished bars, covering a wide range of fatigue cycles 10^0-10^6, where the last one was assumed the fatigue limit [9]. The ASME design S-N curves incorporates safety factors of 20 on the number of cycles or 2 on the stresses (pseudo-elastic); the more conservative one was used to reproduce the design curves [9]-[10]. Taking into account these assumptions, three fatigue curves are considered for each experimental tests and represented in Figure 7.31 to Figure 7.38. In these S-N curves, the points represent the stress conditions for each cycle applied in the experimental testing of the elbows, the resulting lives will be used to compute the damage of each cycle ($D=1/N_i$). It is clearly observed that eliminating the safety factors from the ASME base curve, for the same stress level, the number of cycles increase, mainly for the S-N curve with a factor of 20 on the number of cycles. Therefore, this latter S-N curve was selected as the most representative one for the ASME S-N curve without safety factors.

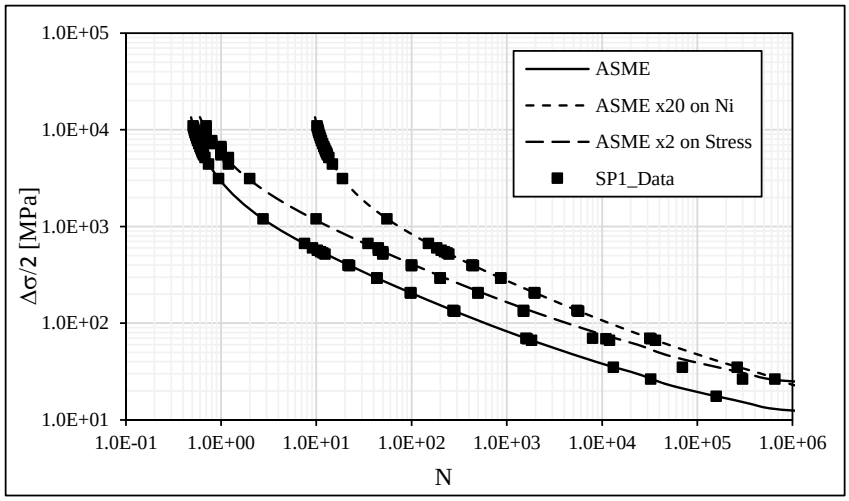

Figure 7.31 – Stress data obtained for SP1 specimen plotted on the ASME S-N curves for damage analysis.

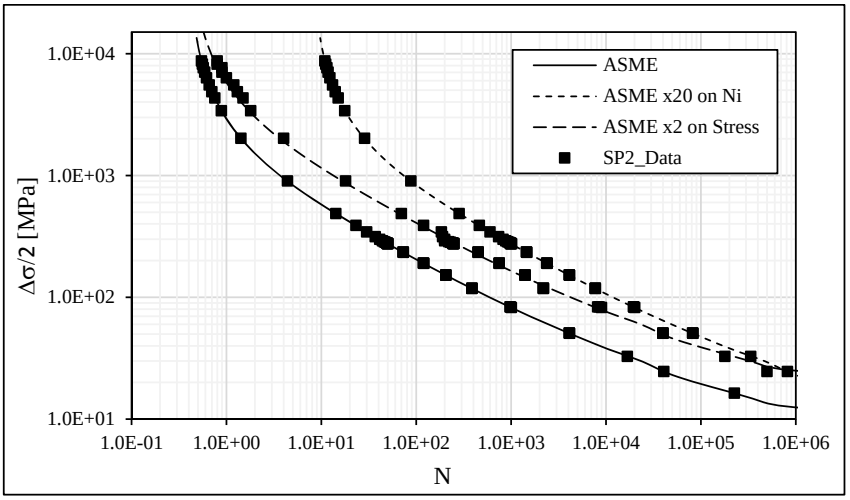

Figure 7.32 – Stress data obtained for SP2 specimen plotted on the ASME S-N curves for damage analysis.

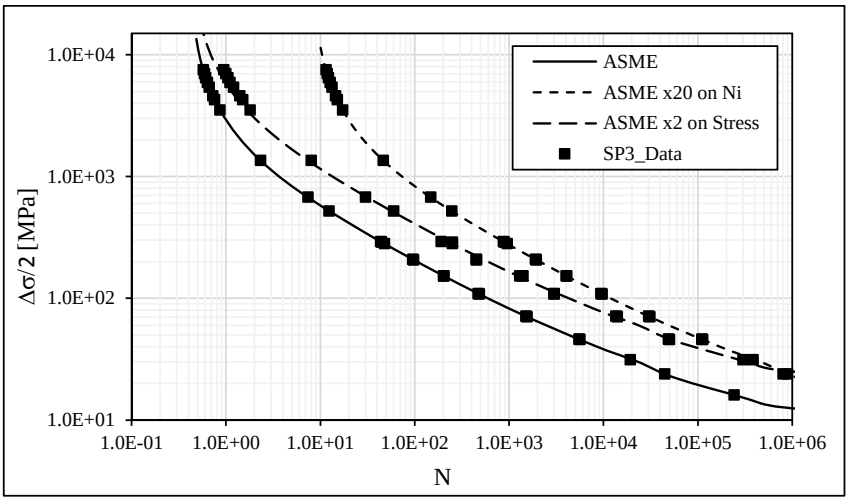

Figure 7.33 – Stress data obtained for SP3 specimen plotted on the ASME S-N curves for damage analysis.

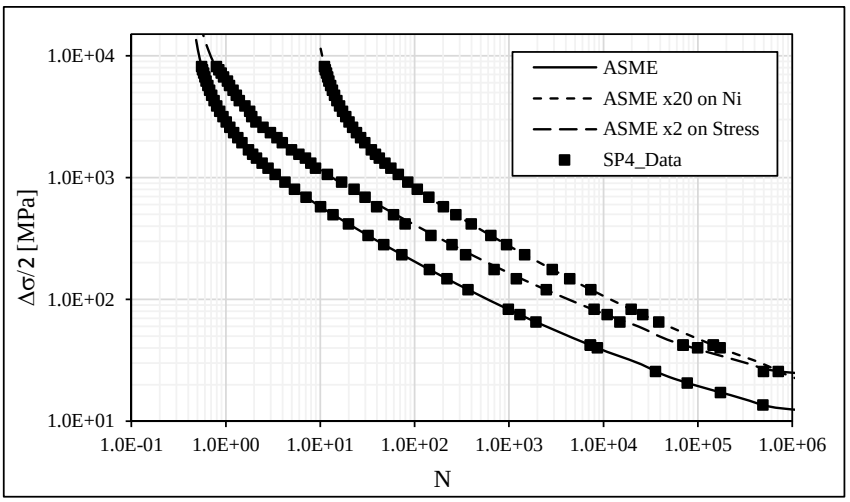

Figure 7.34 – Stress data obtained for SP4 specimen plotted on the ASME S-N curves for damage analysis.

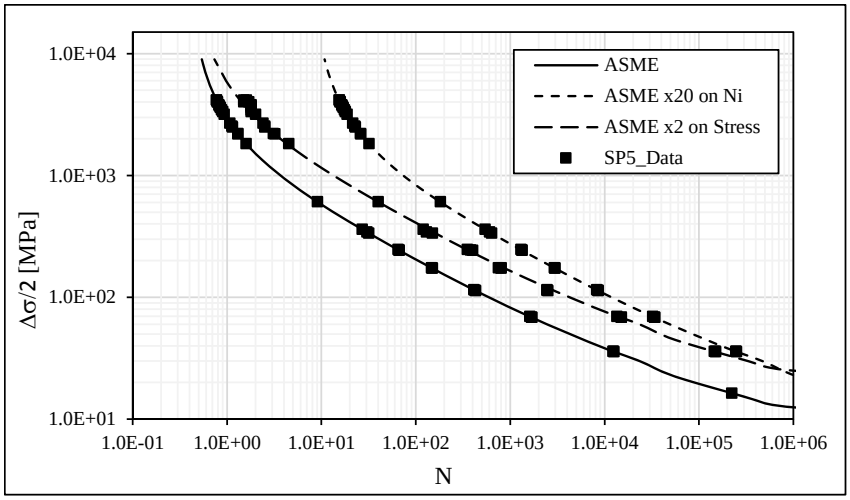

Figure 7.35 – Stress data obtained for SP5 specimen plotted on the ASME S-N curves for damage analysis.

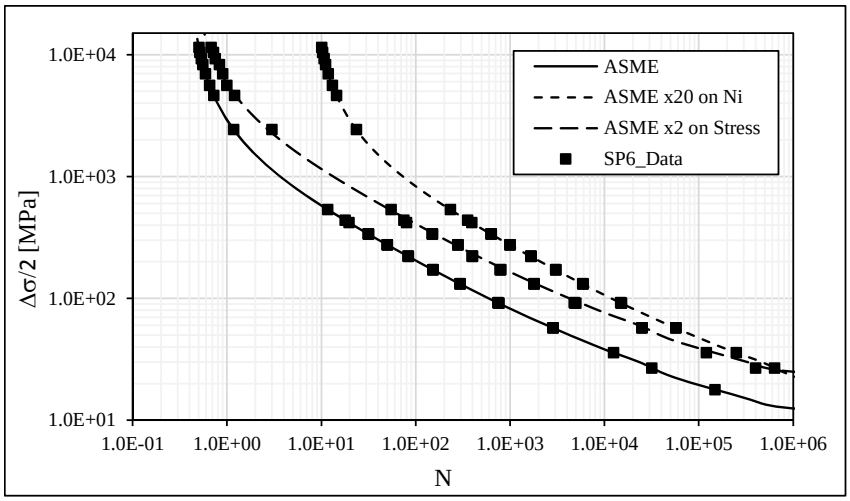

Figure 7.36 – Stress data obtained for SP6 specimen plotted on the ASME S-N curves for damage analysis.

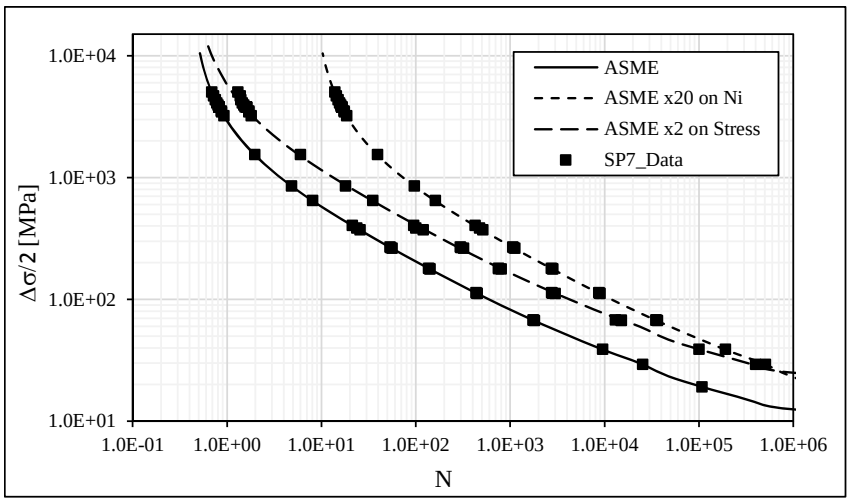

Figure 7.37 – Stress data obtained for SP7 specimen plotted on the ASME S-N curves for damage analysis.

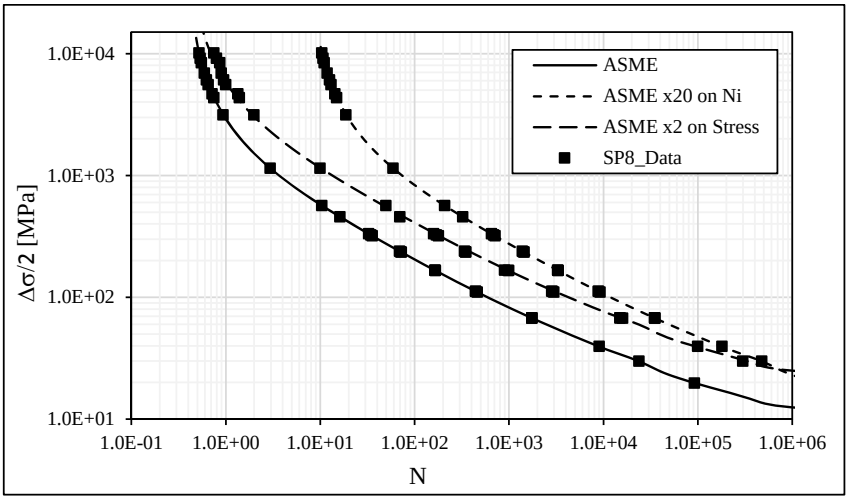

Figure 7.38 – Stress data obtained for SP8 specimen plotted on the ASME S-N curves for damage analysis.

The numerical fatigue life predictions obtained from Coffin-Manson relation, Xue model and ASME code, which includes the original formulation with the safety margin and the correction of 20 times on the number of cycles, are compared with the experimental number of cycles in the Figure 7.39. Additionally, to the usual accuracy bands used in this work (see Chapter IV), improved accuracy bands, 1.5x and 0.66x of life were also introduced, aiming to reinforce the quality of numerical predictions. As expectable the original ASME S-N curves originates the most conservative results, underestimating consistently the number of cycles. In contrast, an overestimation concerning the numerical fatigue life prediction of elbows is verified when the factor of 20 is applied on the number of cycles to failure estimated with ASME fatigue design curves. With respect to the estimations obtained from the fatigue damage models considered in this study, a slight overestimation is observed however the satisfactory quality of numerical predictions is not affected. A typical approach based on the application of Coffin-Manson relation, which only depends of the material parameters and the equivalent plastic strain range produced very satisfactory results. The assessment of Xue model was also performed taking into account a monotonic fracture strain derived approximately according to the procedure schematized in the Figure 7.21. On effect, the evolution of Lode angle parameter during the cyclic loading tends to the plastic plane strain conditions and according to the ductile damage model, for the monotonic failure proposed by Bai [7], this condition results on lower fracture strains (Figure 4.117) affecting the fatigue strength of the material. The influence of the stress state parameters on the fatigue life predictions of the full-scale elbows was accounted indirectly through the 3D fracture ductile surface of X60 piping steel. This methodology results on satisfactory fatigue life

predictions however, no significant differences are observed between the numerical results obtained with the Coffin-Manson relation and Xue model. On effect, the assessment of the monotonic fracture strain, using a simple exponential function is not the most accurate method, leading to an overestimation of this parameter resulting on non-conservative fatigue life predictions.

The numbers of fatigue life cycles, predicted by ASME code for each specimen, are summarized in the Table 7.4. This table also includes the number of cycles obtained with the Coffin-Manson relation and Xue model as well as the experimental data. The relative errors between the experimental and predicted fatigue cycles were also included in this table. A maximum deviation of 60% is observed for the fatigue estimations resulted from the ASME code application with a factor of 20 applied to the number of cycles, confirming the largest deviations with this approach. The fatigue damage models resulted in a maximum deviation of 38%, nevertheless all data points are inside an improved accuracy band.

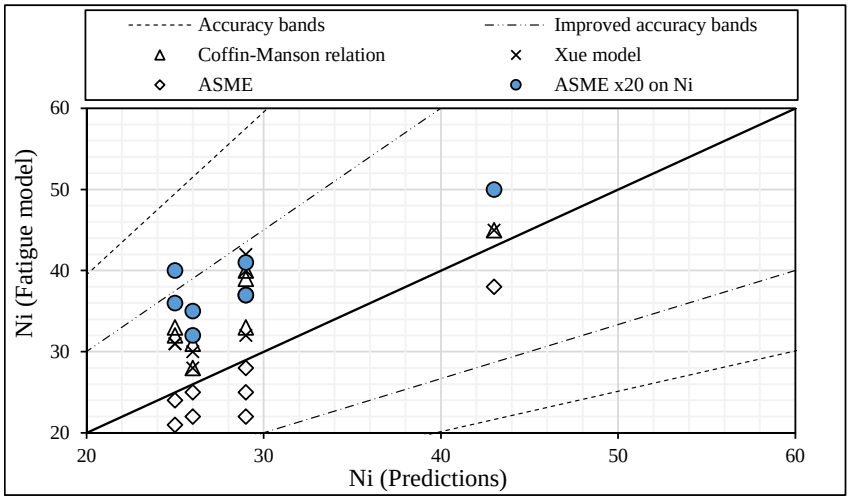

Figure 7.39 – Comparisons between experimental number of cycles and fatigue life predictions for elbows.

Table 7.4 – Fatigue life predictions for elbows.

Specimens	Experimental	Coffin-Manson	Xue	ASME	ASME x20 on Ni
SP1	29	39 (+34%)	40 (+38%)	25 (-14%)	37 (+28%)
SP2	43	45 (+5%)	45 (+5%)	38 (-12%)	50 (+16%)
SP3	26	31 (+19%)	30 (+15%)	25 (-4%)	35 (+35%)
SP4	29	40 (+38%)	42 (+45%)	22 (-24%)	41 (+41%)
SP5	25	33 (+32%)	31 (+24%)	24 (-4%)	40 (+60%)
SP6	29	33 (+14%)	32 (+10%)	28 (-3%)	37 (+28%)
SP7	25	32 (+28%)	31 (+24%)	21 (-16%)	36 (+44%)
SP8	26	28 (+8%)	28 (+8%)	22 (-15%)	32 (+23%)

7.3 SIMULATION OF FULL-SCALE TESTS OF STRAIGHT PIPES UNDER CYCLIC LOADING

In this section, the full-scale cyclic tests performed by OCAS on straight pipes are revisited. Numerical models based on solid finite elements are presented for the pipes and the tubeholders using ABAQUS® [1] software. Tubeholders were simulated in fine detail. A detailed presentation of the finite element models of the full-scale tests, comparisons between numerical and experimental results and the fatigue damage assessments are given below. As referred in the Chapter VI, which describes the experimental results of the cyclic bending tests carried out on straight pipes, during experimental tests, the tubeholder was initially fixed to the pipe by using a small weld, aiming to avoid a rotational and longitudinal movement of the tube inside the tubeholder. In the Test C, the weld failed and the tubeholder shifted axially with respect to the pipe [11]. For that reason, the numerical simulation and consequent fatigue damage assessment was not performed for this experimental test.

7.3.1 Finite element model

Besides the modelling of the straight pipes, this numerical approach also considered the modelling of the tubeholder and the central bending plates in the numerical model. To adjust the tubeholder to the different pipe sizes (8 5/8" and 16" diameter) two configurations for bending tests were used as mentioned in the Chapter VI. The tubeholder was the same in both configurations however the central bending plates show different dimensions when associated to the configurations for the X60 or X65 pipes. The connection between the tubeholder and the pipe is performed through two endcaps, located at the ends of tubeholder as illustrated in Figure 7.40. These considerations were helpful to build the geometry of the numerical models which are detailed. Figure 7.41 shows the tubeholder geometry and the pin joint; the central bending plates are represented in Figure 7.42 and a cut view of tubeholder illustrating the endcaps for the two configurations is presented in Figure 7.43.

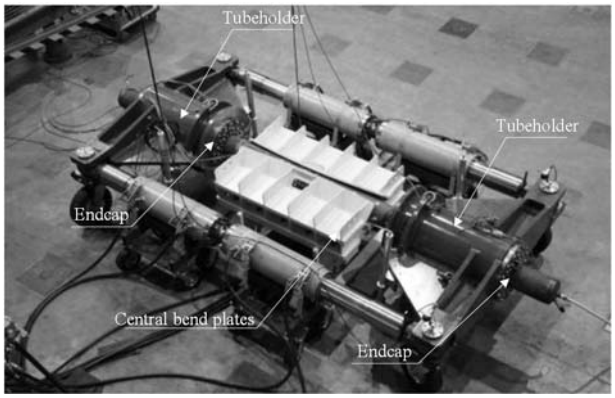

Figure 7.40 – Pure bending setup used to tests the straight pipes.

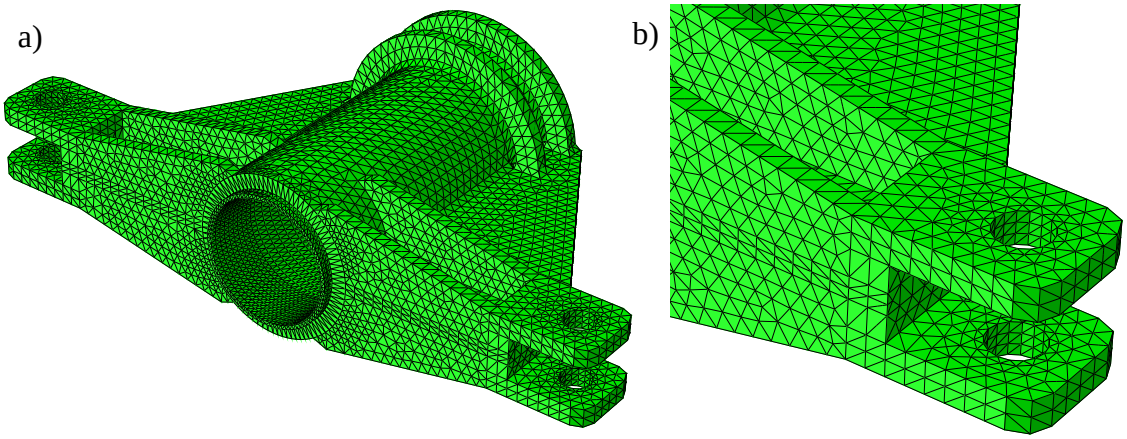

Figure 7.41 – Finite element mesh of the tubeholder (a) and detail view of the pin joint (b).

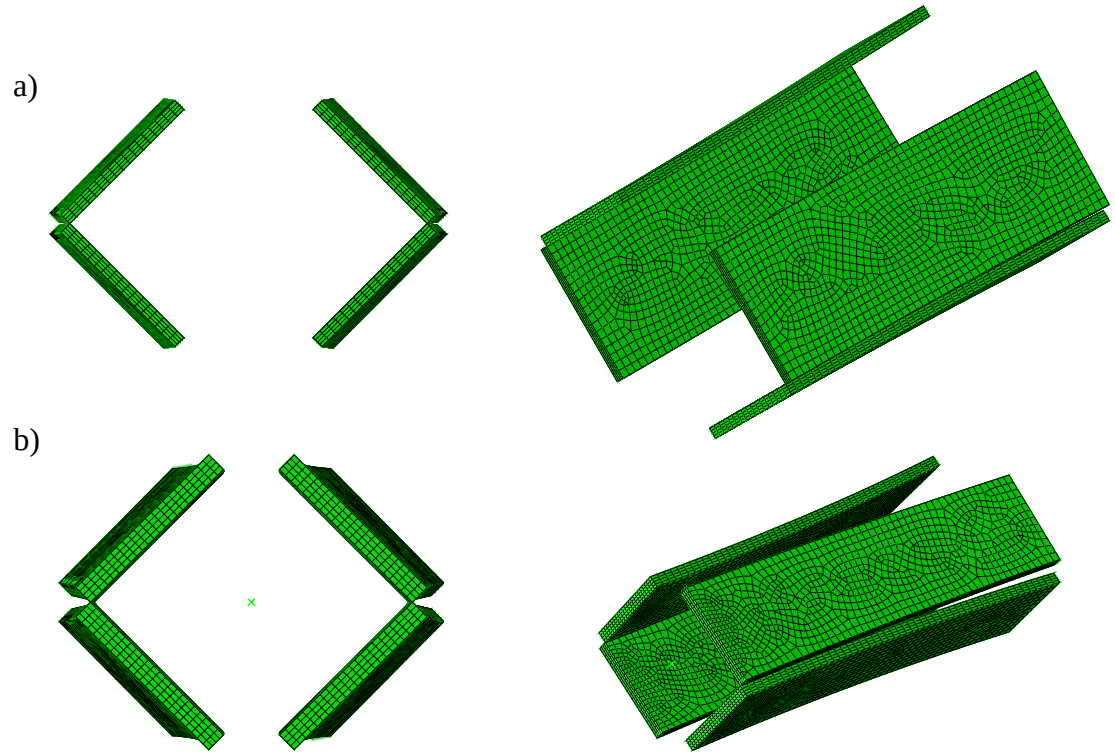

Figure 7.42 – Central bending plates used in test configuration for the X60 pipes (a) and X65 pipes (b).

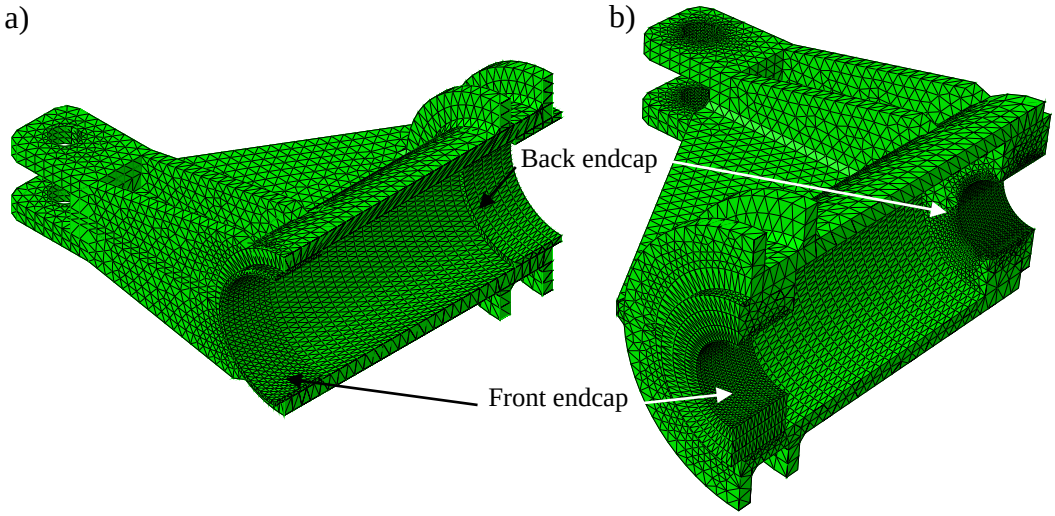

Figure 7.43 – Location of endcaps at the tubeholder: a) X60 pipe test configuration (Tests C & D); b) X65 pipe test configuration (Tests A & B).

The numerical models of the pipes used for the simulation are represented in the Figure 7.44 and Figure 7.45, respectively. A refined finite element mesh was set for the center of the straight pipes, with minimum size of 3 mm in the longitudinal direction and 10 mm in the circumferential direction and 4 solid elements in the thickness direction. The pipes were built taking into account the ovalization and the wall thickness reduction at the piper center in accordance with Table 6.9. In order to improve the accuracy of the stress/strain field and contact convergence a refined mesh was imposed at the critical locations (pipe

center and endcaps/pipe contact zone). The element type associated with each component described above is summarized in the Table 7.5. Concerning the materials definition, different properties were assigned to each component. The tubeholder was modelled as a linear elastic material and the central bending plates were simulated as rigid bodies. The plasticity model based on the second invariant of the stress tensor with nonlinear kinematic hardening (Chaboche model) was used for pipe definition (see Table 4.6 and Table 4.8). The kinematic hardening parameters were obtained through an inverse procedure, based on the LCF and ULCF experimental results carried out on smooth and notched specimens, as expressed in the Chapter IV.

Table 7.5 – Element types used in the numerical models.

Numerical model	Element type
Pipe	C3D8R (Hexahedral elements with reduced integration)
Tubeholder	C3D4 (Tetrahedral)
Central bending plates	R3D4 (Quadrilateral)

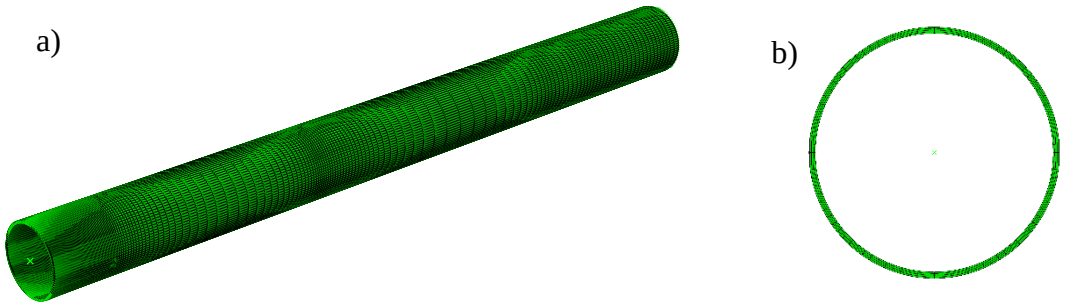

Figure 7.44 – Finite element mesh of the pipe used in the Test B: a) full view of pipe; b) view of the finite element mesh at the central section.

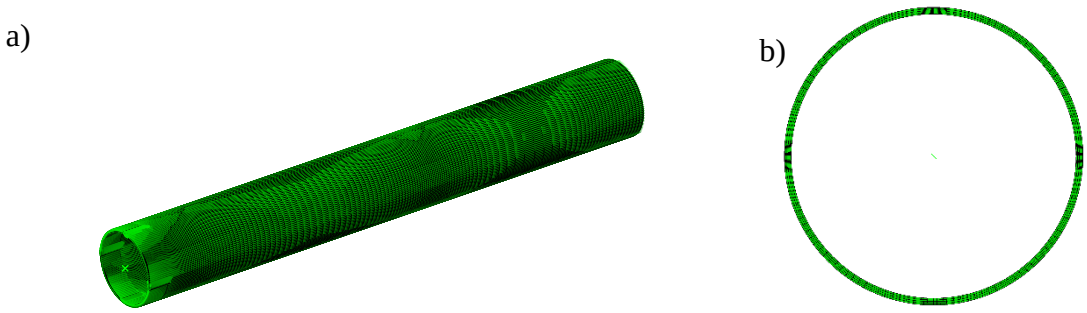

Figure 7.45 – Finite element mesh of the pipe used in the Test D: a) full view of pipe; b) view of the finite element mesh at the central section.

The simulation of cyclic bending tests were performed considering the following contact pairs: i) between the central supporting/guiding plates and the external surface of the pipe

and ii) between the tubeholder and external surface of the pipe. A surface-to-surface contact definition was selected with normal and tangential behaviors governed by the penalty algorithm formulation. For the three simulations covered in this study a very small friction coefficient of 0.01 was implemented. Concerning the boundary conditions, experimental displacements measured using wire sensors placed between cylinder/tubeholder pin joints connections were applied in the numerical models. The pin joint was modelled using the MPC constraint and link option available in the ABAQUS®. Comparisons between the experimental values and the applied displacements in the numerical model for the Test A are illustrated in Figure 7.46, showing a perfect agreement between the two curves. In order to reduce the computational costs, a plane of symmetry, normal to the longitudinal pipe direction, was considered and the displacements of the nodes at the symmetry plane were restrained along the normal direction. A full representation of one numerical model is shown in Figure 7.47.

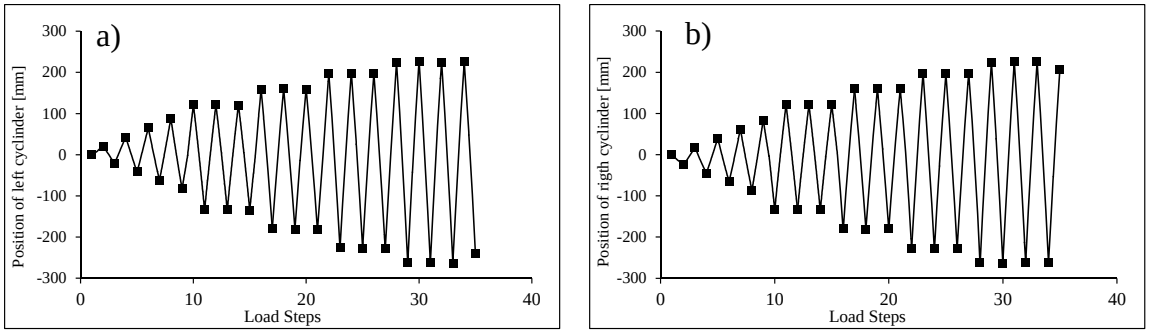

Figure 7.46 – Comparison between the experimental and numerical displacement inputted as boundary condition in the numerical model of Test A: a) left pin; b) right pin.

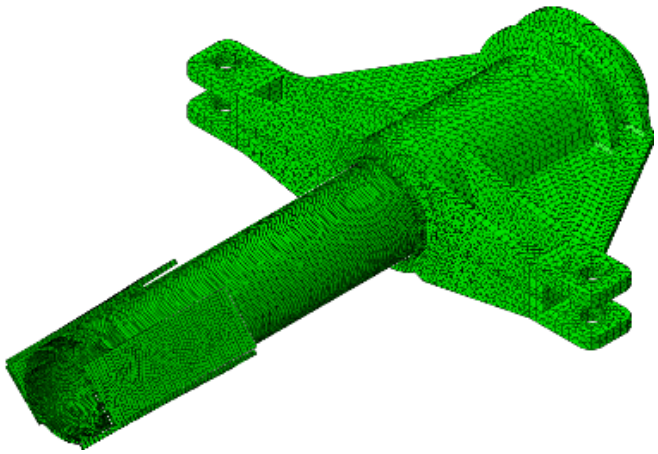

Figure 7.47 – Full representation of the numerical model used on the simulation of cyclic bending tests on straight pipes (Test D setup).

7.3.2 Numerical results

In this section the numerical results obtained from the simulation of cyclic tests on straight pipes are reported. Comparisons between experimental and numerical bending moment results are illustrated in Figure 7.48 to Figure 7.50. In general, a very good compromise is observed between the numerical and experimental data and the numerical models are able to reproduce the strength reductions (bending moment reduction) which coincide with the starting of the buckling instability. This effect contributes to the strain localization and damage evolution leading to the failure of the pipe. With respect to the location of the local instability, the numerical model of the Test A was able to reproduce it at the connection of pipe and tubeholder as experimentally verified (see Figure 7.51). Preliminary simulations of the Test B and Test D exhibited an instability also generated at the connection of the pipe and tubeholder, as verified in the Test A. In contrast, for the Tests B and D, a small thickness reduction was machined at the centre of the pipes to localize the instability at the centre of the pipes. That thickness reduction was also included in the numerical models. Also, a small external load at the centre of pipe, perpendicular to the pipe longitudinal direction, was applied to facilitate the buckle localization. The analysis of the numerical results is supported by the experimental evidence concerning the location and the shape of the instabilities. The local instability obtained for Test B and Test D from finite element model for the conditions of the simulated last load step visible are illustrated in Figure 7.52 and Figure 7.53, respectively. The analysis of these figures supports the experimental evidences since reports appropriately the location and the shape of the instabilities. The simulations of Test A and Test B was extended for a few more cycles aiming to ensure the failure conditions of the pipe, according to less conservative damage models. Additionally, the experimental data obtained from strain gauges is compared with the numerical information in Figure 7.54 to Figure 7.56. A good correlation is observed between experimental and numerical data from the start of cyclic test until the buckle formation.

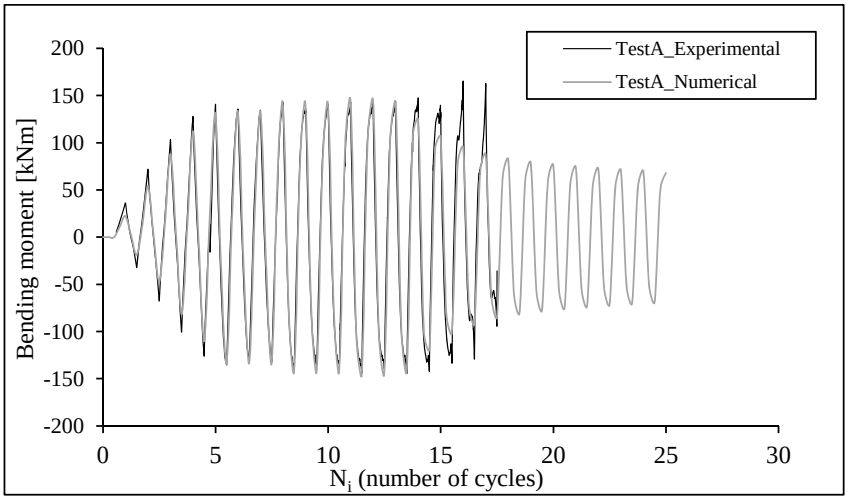

Figure 7.48 – Experimental *versus* numerical bending moment history for Test A.

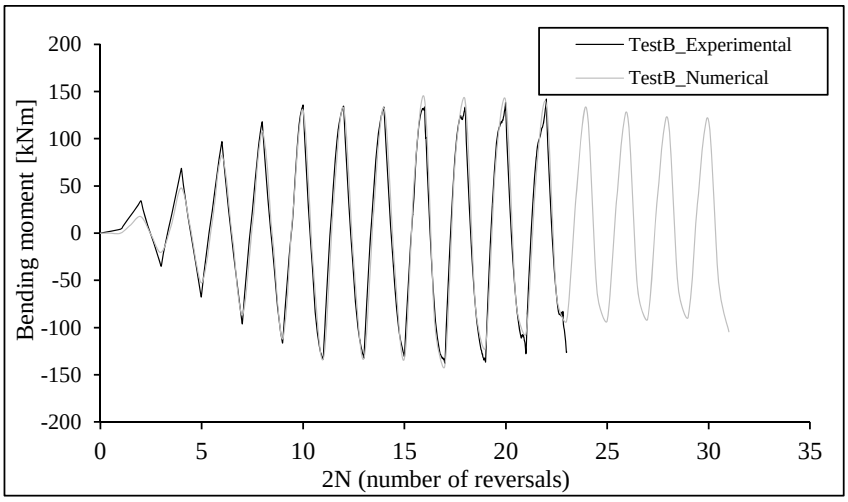

Figure 7.49 – Experimental *versus* numerical bending moment history for Test B.

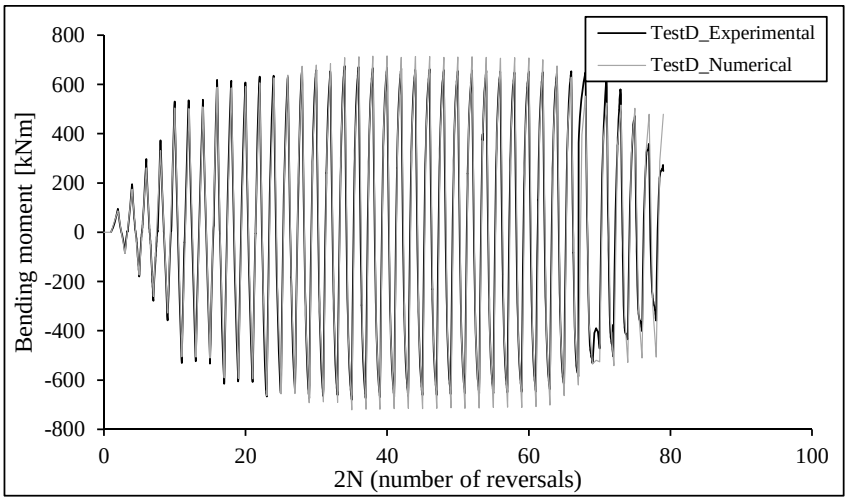

Figure 7.50 – Experimental *versus* numerical bending moment history for Test D.

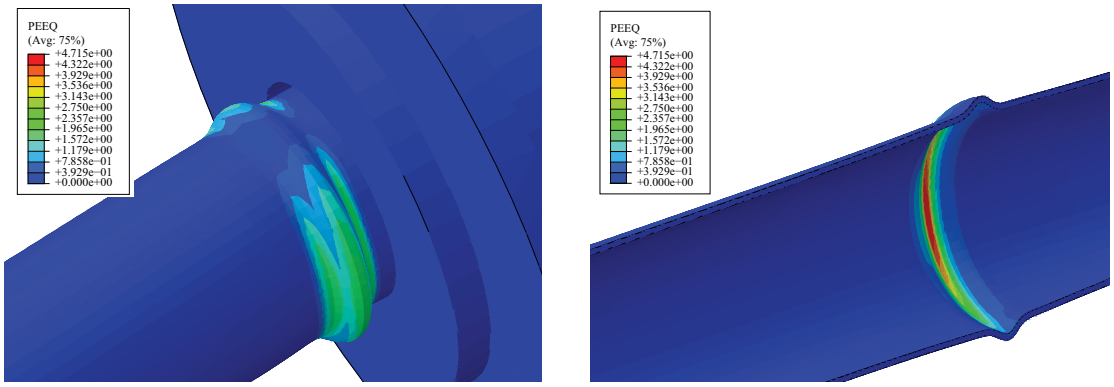

Figure 7.51 – Local instability obtained for numerical simulation of Test A.

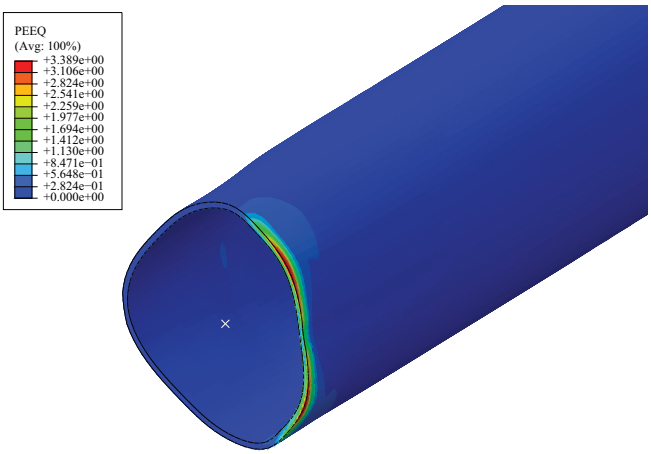

Figure 7.52 – Local instability obtained for numerical simulation of Test B.

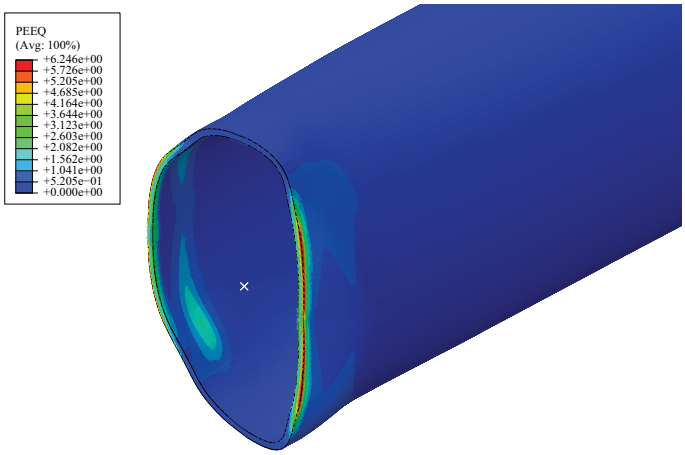

Figure 7.53 – Local instability obtained for numerical simulation of Test D.

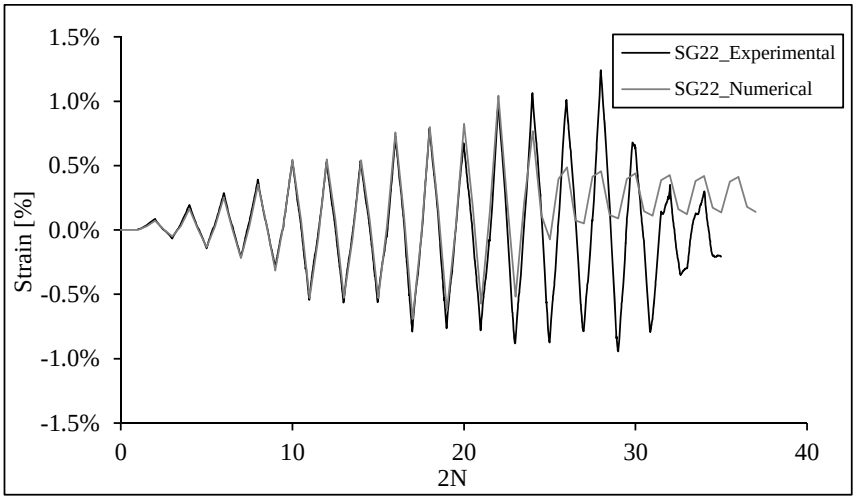

Figure 7.54 – Comparison between numerical and experimental axial strain measured from strain gauge 22 of Test A.

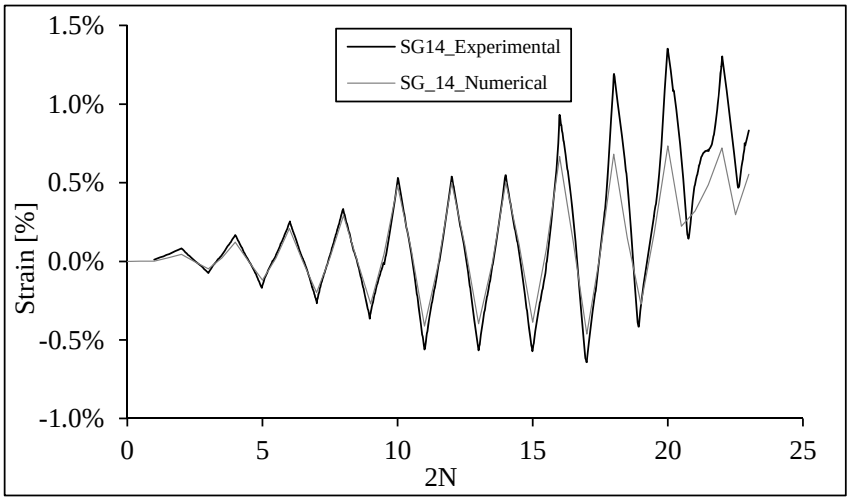

Figure 7.55 – Comparison between numerical and experimental axial strain measured from strain gauge 14 of Test C.

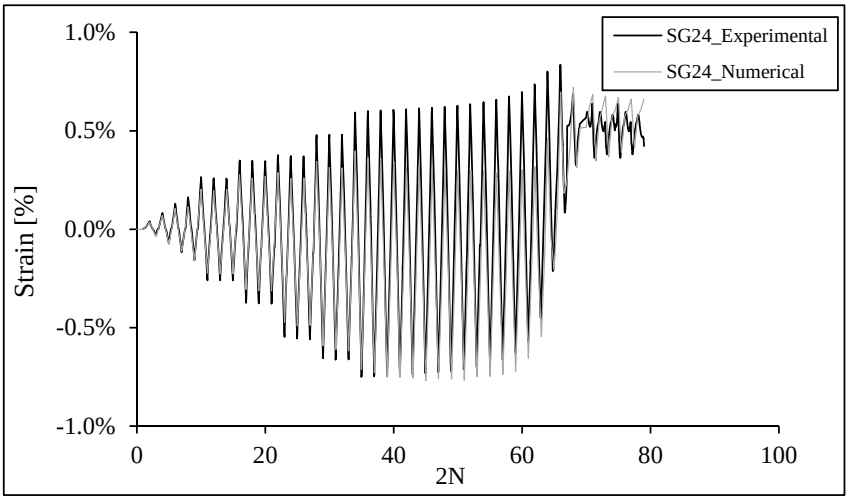

Figure 7.56 – Comparison between numerical and experimental axial strain measured from strain gauge 24 of Test D.

7.3.3 Damage models evaluation

Fatigue life estimations resorting to the Coffin-Manson relation [2][3] and Xue model [4], taking into account the numerical data derived from elastoplastic cyclic simulations will be presented. Moreover, the ASME code, Section VIII, Div. 2 [5] recommendations were also applied to compute the fatigue life of the straight pipes. In order to calculate the accumulated damage during the bending cyclic tests, a similar methodology to the one already applied for elbows was used. The global parameters of the Coffin-Manson relation derived from small-scale test data were used. The Xue model previously identified using the small-scale data, was also applied in the fatigue assessments. The identification of the critical location was based on the observation of the maps of accumulated equivalent plastic strain range, the triaxiality and the Lode angle parameter as illustrated for Test A and Test B in the Figure 7.57 and Figure 7.58, respectively. In order to identify the monotonic fracture strain for the application of Xue model, the methodology discussed for the fatigue life assessment of the elbows was used (see Figure 7.21). A reduced small-scale testing program was performed for the X65 steel (see Table 7.6) not allowing the evaluation of the full fracture surface for this material, since it was not possible to cover different Lode angle parameters. Figure 7.59 shows the fracture strains that were obtained for the X65 steel, for an average Lode angle parameter, $\bar{\theta}$=0.69, covering distinct triaxialities. Since the Lode angle parameter is constant, the classical Johnson-Cook ductile failure relation was used to fit the results. The Lode angle parameter $\bar{\theta}$=0.69, resulted as the average value of the numerical data of smooth (SP) and notched (OH and SN) specimens series, made of X65 piping steel, according to Table 7.6.

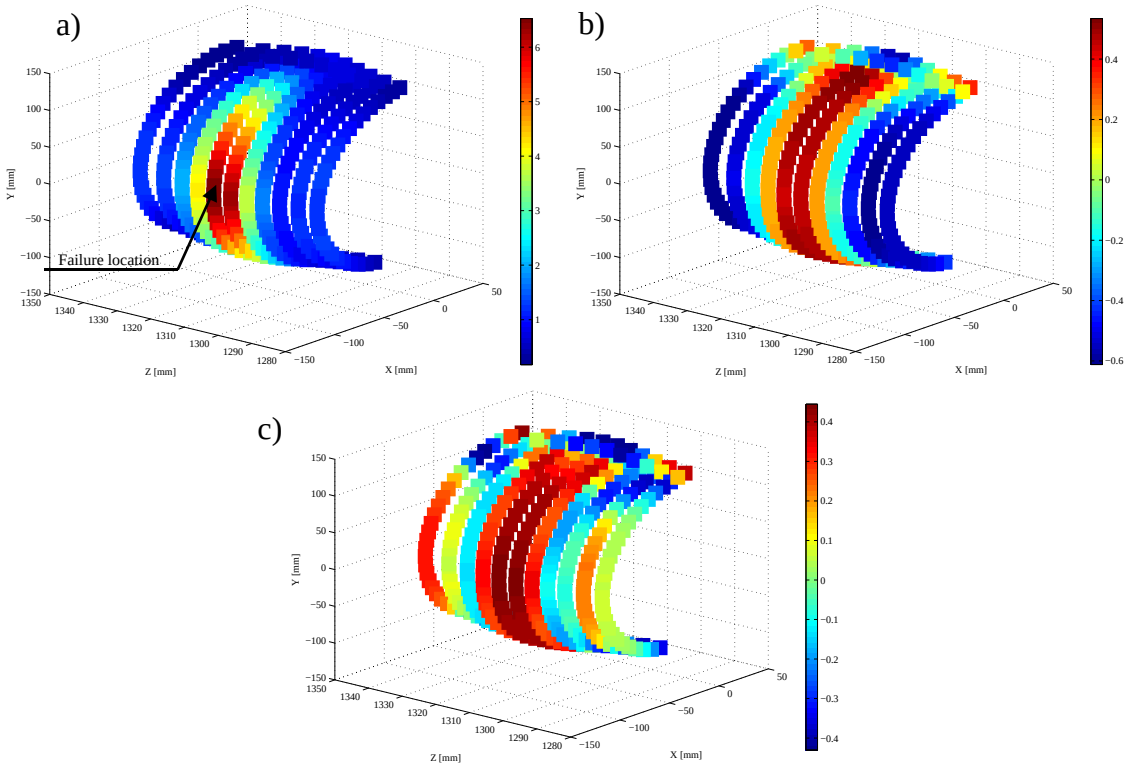

Figure 7.57 – Maps of the variables involved on the evaluation of the critical location of the Test A: a) accumulated equivalent plastic strain; b) stress triaxiality; c) Lode angle parameter.

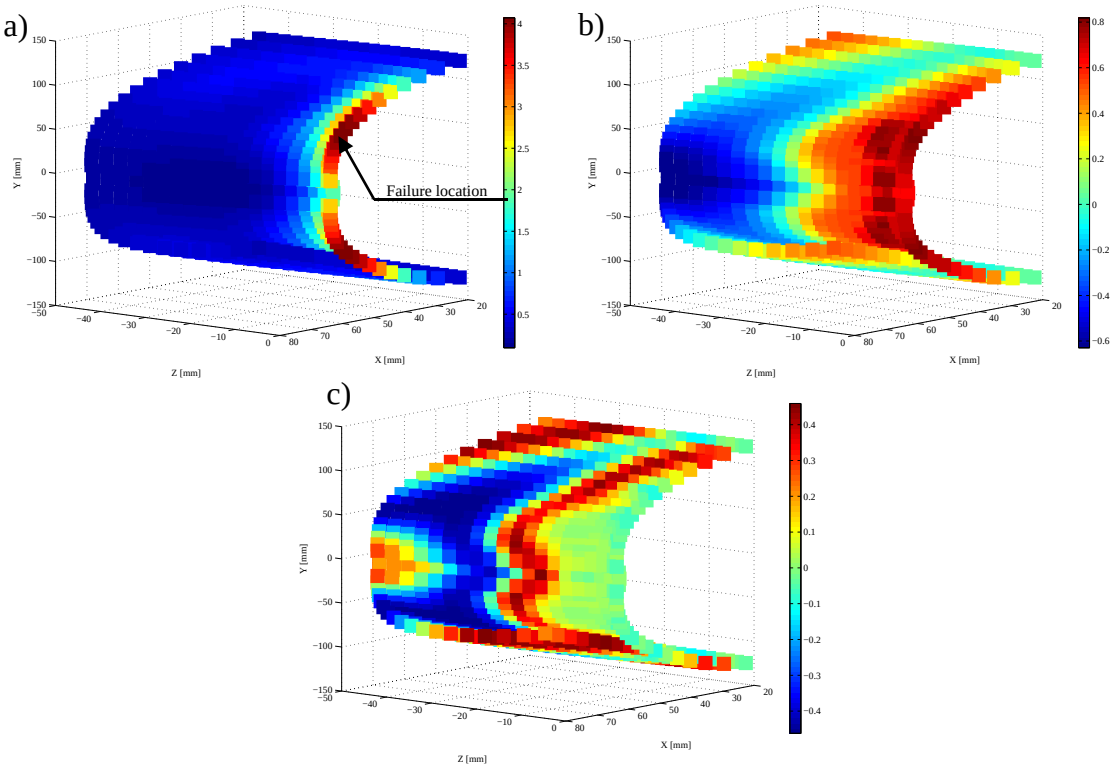

Figure 7.58 – Maps of the variables involved on the determination of fracture strain of Test B: a) accumulated equivalent plastic strain; b) triaxiality; c) Lode angle parameter.

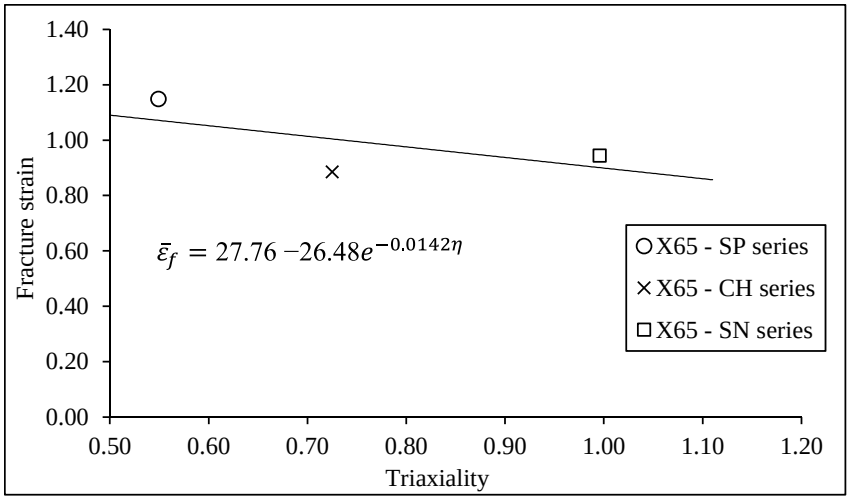

Figure 7.59 – Ductility curve of the X65 piping steel, for $\bar{\theta}$=0.69.

Table 7.6 – Monotonic fracture strain, stress triaxiality and Lode angle parameter obtained for monotonic tensile small-scale tests of the X65 steel grade.

Specimens series	$\bar{\varepsilon}_f$	η_{av}	$\bar{\theta}_{av}$
X65_SP	1.15	0.55	0.69
X65_CH	0.88	0.72	0.72
X65_OH	0.87	0.76	0.54
X65_SN	0.94	1.00	0.66

The evolution of both triaxiality and Lode angle parameters, for Test A and Test B, can be observed in the graphs of the Figure 7.60, at the critical node. A constant behavior of triaxiality and Lode angle parameter around η=0.4 and $\bar{\theta}$=0.8 is observed for Test A. In the case of Test B, the triaxiality practically assumes a constant behavior around η=0.4 showing an increase for η=0.6 at the last cycles. The Lode angle parameter also assumes a constant behavior for the tensile peaks around $\bar{\theta}$=1 decreasing for values close to $\bar{\theta}$=0 at the last cycles. It is interesting to retain that the formation of plastic instability leads to a change on the behavior of these parameters in the case of Test B. This data will be assessed to compute the monotonic fracture strain for each cycle.

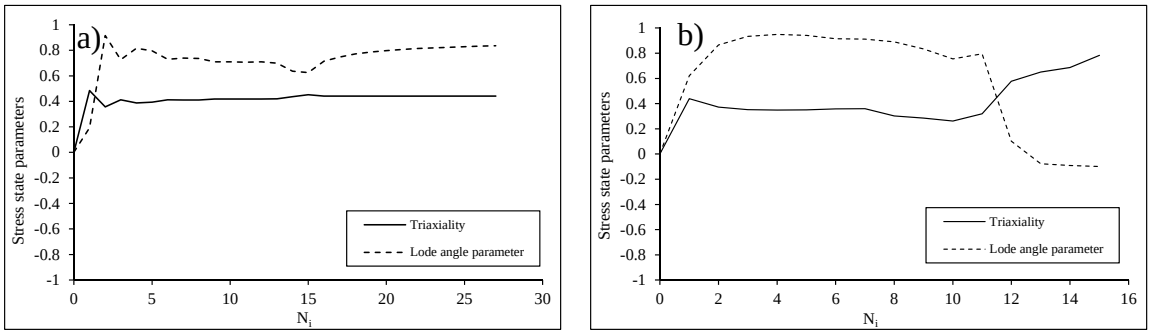

Figure 7.60 – Evolution of the stress state parameters during the cyclic loading at tensile peaks for critical node: a) Test A; b) Test B.

As described in the Chapter IV, the 3D fracture surface proposed by Bai and Wierzbicki was identified for X60 piping steel using the numerical data from monotonic tensile tests. This information allows computing directly the monotonic fracture strain as a function of the triaxiality and Lode angle parameter, for each tensile loading path. The evolution of both parameters for the Test D can be observed in the graph of the Figure 7.62, which assumes an identical behavior to the Test B.

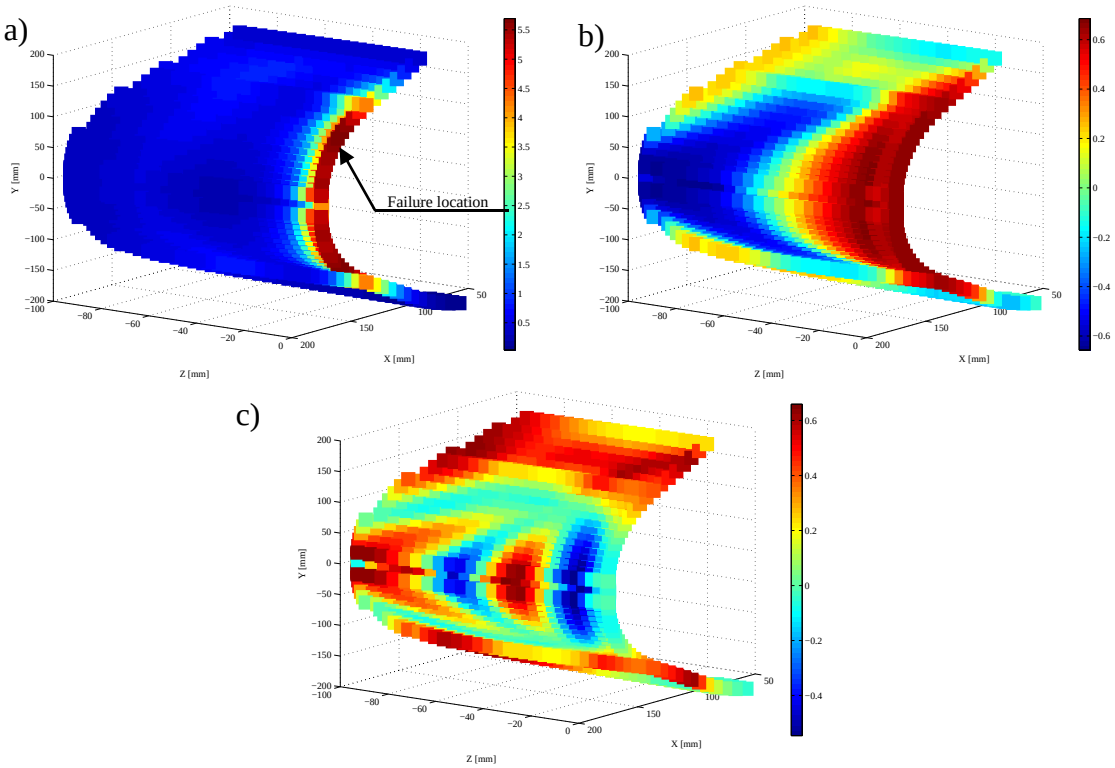

Figure 7.61 – Maps of the variables involved on the determination of fracture strain of Test D: a) accumulated equivalent plastic strain; b) triaxiality; c) Lode angle parameter.

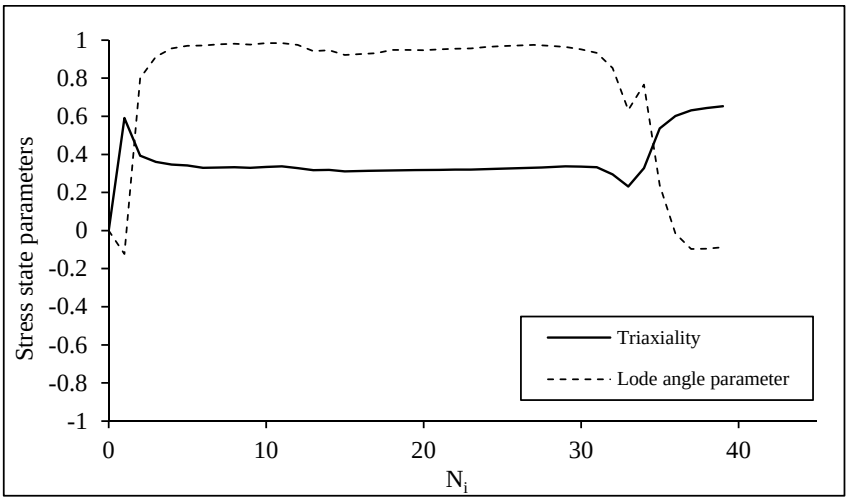

Figure 7.62 – Evolution of the stress state parameters during the cyclic loading at tensile peaks for Test D.

Figure 7.63 and Figure 7.65 show the computation of the accumulated damage using the Coffin-Manson relation and the Xue model for Test A, B and D. As occurred for the fatigue life assessment of full-scale elbows, the ASME code recommendations [5] were also considered to estimate the fatigue life of straight pipes. Consequently, a similar procedure was conducted to obtain the S-N curves for these experimental tests. The coefficients C_1 to C_{10}, were also obtained from the Table 7.3, taking into account the mechanical properties requirements specified for X60 and X65 piping steels, presented in the Table 3.20 and Table 3.37. A total of three S-N curves are tested for each experimental test. In detail, the base S-N curve, a S-N curve without a safety factor based on the stresses correction and another S-N curve without a safety factor formulated on the number of cycles correction, as can be observed in the Figure 7.66 to Figure 7.68. As expectable, the elimination of the safety factors, results on non-conservatives S-N curves, the less conservative one resulting from the elimination of a safety factor of 20 applied in the number of cycles.

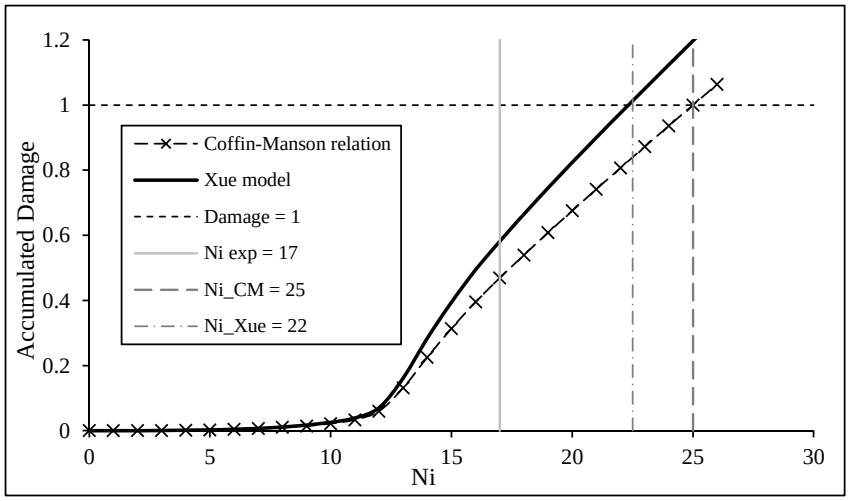

Figure 7.63 – Simulated damage evolution for Test A.

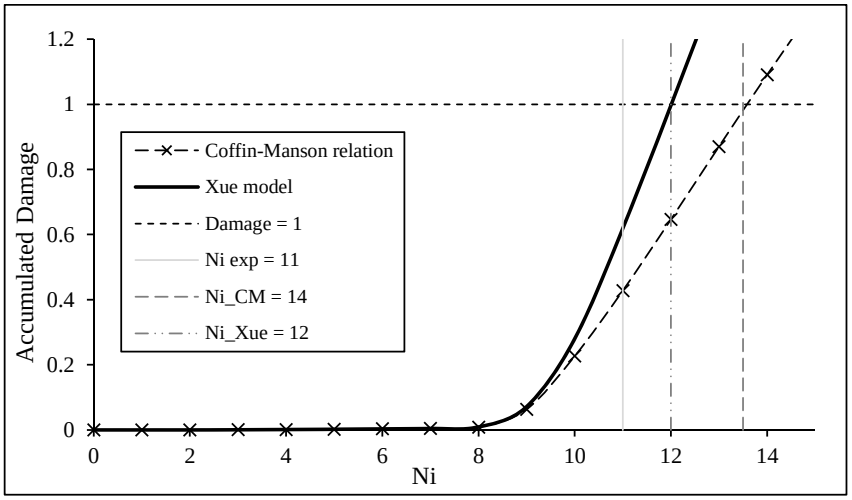

Figure 7.64 – Simulated damage evolution for Test B.

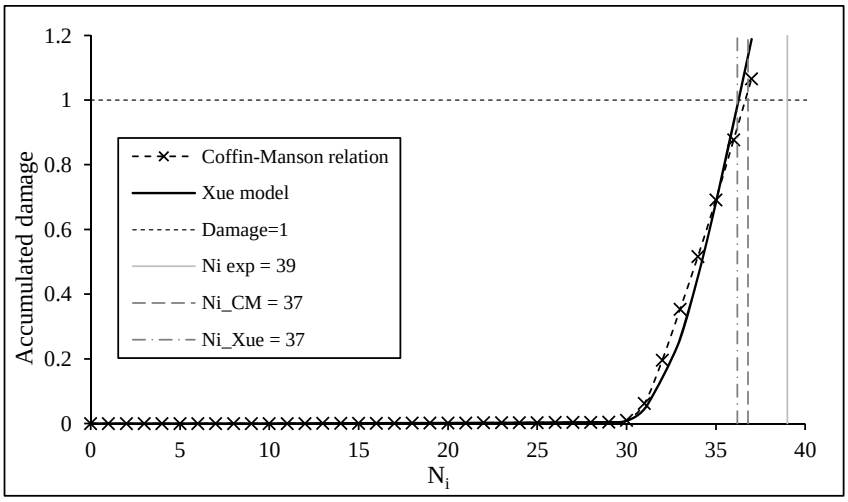

Figure 7.65 – Simulated damage evolution for Test D.

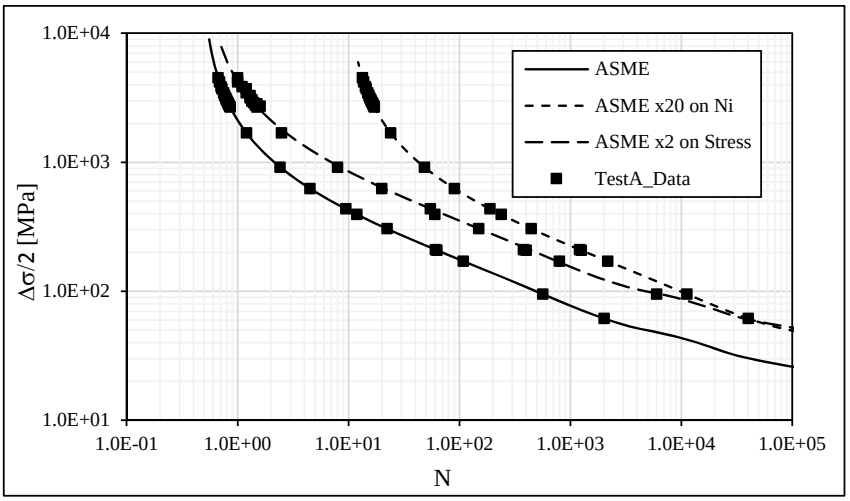

Figure 7.66 – Stress data obtained for Test A plotted on the ASME S-N curves for damage analysis.

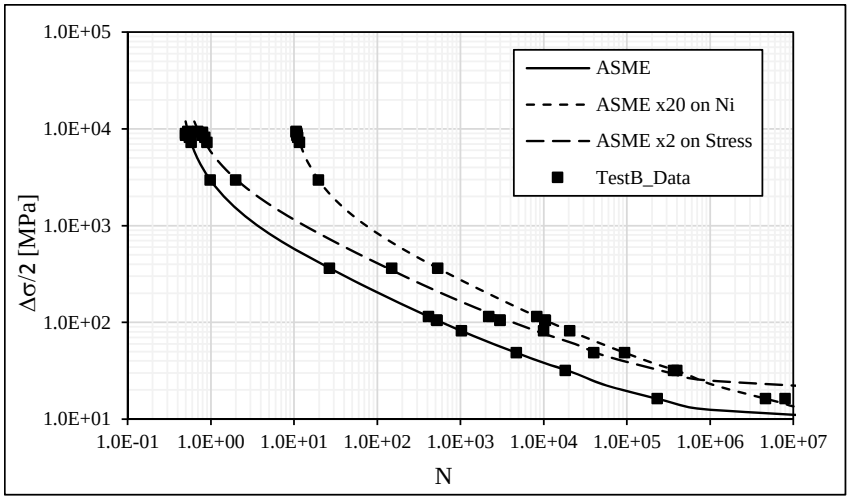

Figure 7.67 – Stress data obtained for Test B plotted on the ASME S-N curves for damage analysis.

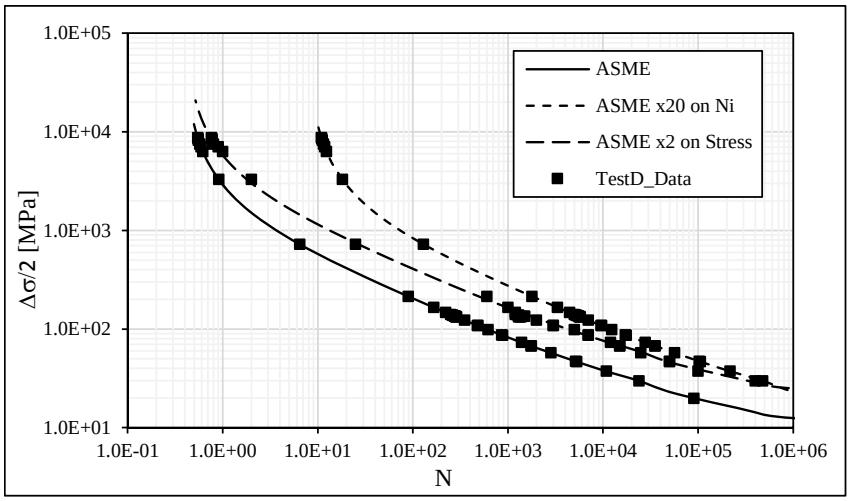

Figure 7.68 – Stress data obtained for Test D plotted on the ASME S-N curves for damage analysis.

Figure 7.69 reports the comparisons between the experimental and numerical fatigue life predictions obtained with the Coffin-Manson relation, Xue model and ASME code including the base S-N curve and the S-N curve with the safety factor on the number of cycles. The same accuracy bands proposed for elbows were also considered for this analysis. In general, very good fatigue life estimations were attained with the fatigue damage models investigated in this work. Concerning the predictions obtained with the Coffin-Manson relation and Xue models, the resulted fatigue lives were higher than the experimental results for Test A and Test B, which resulted in a non-conservative prediction. However, for the Test A and Test B a better performance of Xue model is evidenced, which comprises the effect of both strain and stress parameters evolution during the cyclic loading. On effect, these results support the condition of considered the influence of stress/state parameters on the fatigue life estimations under large plastic strain amplitudes. In contrast the Coffin-Manson relation and Xue model underestimates

in 1 cycle the fatigue life of Test D. It was observed prediction errors in the 5%/47% (see Table 7.7) range for the Coffin-Manson relation and 5%/29% (see Table 7.7) for the Xue model. The main differences are observed for the fatigue life predictions for the Test A, namely 8 cycles for Coffin-Manson relation and 5 cycles for the Xue model, which results on significantly unconservative predictions. It should be noted that for this case, the plastic instability was detected at the pipe-tubeholder junction and it revealed a very complex pattern not fully reproduced by the finite element model. An accurate prediction of the plastic instabilities is of primordial importance to capture the correct strain concentrations. In addition, the recommendations proposed by the ASME code were also applied derive the number of cycles of the straight pipes. Using the original design curve (with safety factors), fatigue lives were underestimated with errors in the range -24%/-15% (see Table 7.7), representing adequate conservative predictions. Again the worst predictions were obtained for the Test A. Finally, using the ASME code S-N curve without safety factors (removed safety factor of 20 on fatigue lives) all predictions were in the range of +8%/+65% (see Table 7.7) all being non-conservative, with the maximum error on Test A, among all the predictions presented (+65%).

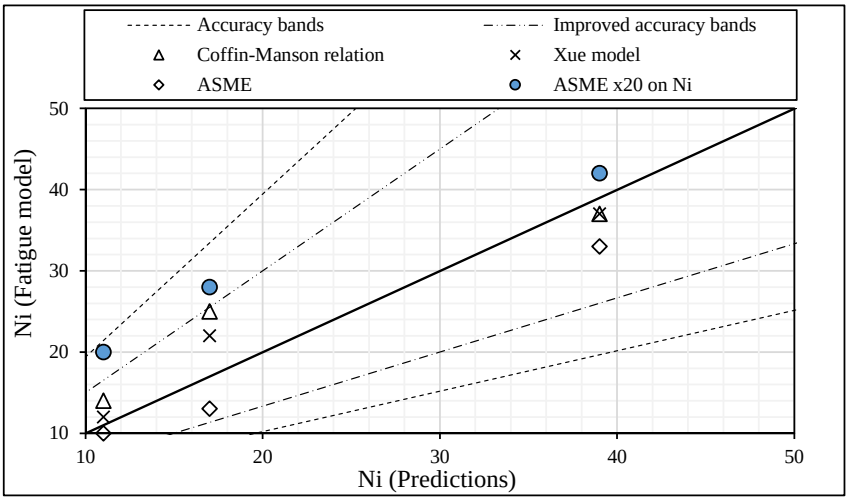

Figure 7.69 – Comparisons of experimental data and predictions for full-scale tests on straight pipes.

Table 7.7 – Fatigue life predictions of fatigue tests on straight pipes.

Specimens	Experimental	Coffin-Manson	Xue	ASME	ASME x20 on Ni
Test A	17	25 (+47%)	22 (+29%)	13 (-24%)	28 (+65%)
Test B	11	14 (+27%)	12 (+9%)	10 (-9%)	20 (+82%)
Test D	39	37 (-5%)	37 (-5%)	33 (-15%)	42 (+8%)

7.4 CONCLUSIONS

In this chapter, numerical simulations of the ULCF cyclic tests carried out on full-scale elbows and straight pipes were presented. Comparisons between the experimental results and numerical data including the load/reaction values, pipe ovalization, bending moment and numerical deformed shape were performed allowing validating the finite element models.

Concerning the finite element simulation of full-scale elbows, the elastoplastic properties of the materials subjected to the thermal process were used. In general, very good correlations were accomplished between both numerical and experimental load histories. Moreover, the finite element models were able to reproduce the plastic strain localization and consequent formed buckle. It was observed that the shape of the buckles (inward/outward) arises as a function of the applied internal pressure. For the higher tested pressure, the buckled formed toward the exterior of the pipe and for the lower values of the tested inner pressure, the formed buckle was directed to the inner part of the pipe. The fluctuation of internal pressure was not applied in the simulation of SP1 specimen, being considered a constant value during the cyclic loading. As observed from the remaining experimental tests, the buckle formation and plastic localization are dependent of the pressure fluctuation. Thus, a small concentrate load was applied to SP1 specimen to assist the buckle formation in accordance with experimental evidences.

With respect to the straight pipes a good agreements were also confirmed between the numerical and experimental data. Two distinct locations for the buckle formation were observed for the straight pipes, namely at the central section of the pipe (Test B and Test D) and the other at the connection of the pipe and tubeholder (Test A). The instability of the pipes of Test B and Test D were assisted by means of a small concentrated load establishing a compromise between the buckle formation and the global response in terms of bending moment data. For the three cases, the fatigue failure occurred after the development of plastic instabilities in the straight pipe.

After the validation of the plasticity models, the stress and strain (total and plastic components) histories were computed for the critical locations. The identification of the critical locations resulted from the compromise between the observations of the fields of equivalent accumulated plastic strain, triaxiality and Lode angle parameter and the failure location observed in the experimental tests. On effect, the identification of the critical location should result from the combination of the higher values of accumulated equivalent plastic strain and triaxiality and in contrast, the lower values of Lode angle parameter.

The history of the strain components were acquired and correlated by means of the multiaxial strain approach definition given by ASME resulting the equivalent plastic strain ranges. Concerning the fatigue life predictions, the Coffin-Manson relation produced satisfactory results for the fatigue lives of elbows and straight pipes with a maximum of eleven and eight, respectively, cycles difference between the numerical and experimental results. Additionally, the performance of Xue model was also investigated in this work. The main difference of this model resides on the normalization of the equivalent plastic strain range by the monotonic fracture strains, which in turns is dependent of the stress triaxiality and Lode angle parameter. In general, it was observed that Lode angle parameter tends to the plastic plane strain conditions for the elbows and straight pipes. This effect promotes the fatigue strength reduction. Therefore the fracture strain dependency should be incorporated in the formulation of the fatigue damage models for generalized yielding conditions with high plastic intensity. In detail, the impact of the stress state parameters were incorporated in the fatigue life predictions of the full-scale elbows and straight pipes. As regard the straight pipes, Test A and Test B were simulated considering the 3D monotonic fracture surface of X60 piping steel evaluated in the Chapter IV since the full 3D fracture surface for the X65 steel was not available. The full methodology proposed in the Chapter IV was applied for the Test D. Both procedures results on satisfactory fatigue life predictions of elbows and straight pipes with a maximum of thirteen and eleven cycle differences, respectively, between the numerical and experimental results.

Moreover, the ASME VIII-Div.2 procedures were applied to simulate the fatigue life of the straight pipes, considering two distinct approaches. In the first one, the original ASME S-N curve was used resulting the best fatigue live predictions, all of them in the

conservative side and close to the experimental results. Another computation was performed using the ASME code but without safety factors, resulting non-conservative predictions with the major deviations of all calculations.

7.5 REFERENCES

[1] ABAQUS, (2012), User's manual version 6.12, Hibbitt, Karlsson, and Sorensen, Inc., Providence, R.I.

[2] Coffin L.F., (1954). "A study of the effects of cyclic thermal stresses on a ductile metal." Transactions of the American Society of Mechanical Engineers, 76: 931 – 950.

[3] Manson, S.S., (1954). "Behavior of materials under conditions of thermal stress." Technical Report NACA-TR-1170, National Advisory Committee for Aeronautics.

[4] Xue, L., (2008). "A unified expression for low cycle fatigue and extremely low cycle fatigue and its implication for monotonic loading." International Journal of Fatigue, 30: 1691–1698.

[5] ASME Boiler & Pressure Vessel Code, Section VIII, (2013). "Rules for Construction of Pressure Vessels, Division 2 – Alternative Rules." The American Society of Mechanical Engineers (ASME), New York, USA.

[6] Miner M.A., (1945). "Cumulative damage in fatigue." Journal of Applied Mechanics Transactions ASME, 67:159 – 164.

[7] Bai Y., (2003). "Effect of Loading History on Necking and Fracture". Ph.D. thesis. Cambridge, MA: Department of Ocean Engineering, Massachusetts Institute of Technology.

[8] Langer B.F., (1962). “Design of pressure vessels for Low-cycle fatigue.” Journal of Basic Engineering, 84:389 – 399.

[9] Sokolov Y., (2013). “A critical review of ASME weld detail fatigue analysis methods.” published in Research Gate.

[10] Keisler J., Chopra O. K., (1955). “Statistical analysis of fatigue strain-life data for carbon and low-alloy steels” ASME/PVP conference, July 23-27, Honolulu, HI.

[11] Wittenberghe J.V., (2014). “Full scale tests of straight pipes under cyclic”, ULCF internal report, OCAS NV.

[12] Bai Y., (2003). “Effect of Loading History on Necking and Fracture”. Ph.D. thesis. Cambridge, MA: Department of Ocean Engineering, Massachusetts Institute of Technology.

Chapter VIII

Final conclusion and future works

8.1 SUMMARY OF MAIN CONCLUSIONS

In the present thesis the damage mechanism associated with high plastic strain conditions under monotonic and cyclic loading was investigated for three steel grades, namely X52, X60 and X65 steel grades. An extensive experimental program under extreme loading conditions, including ultra-low-cycle fatigue and monotonic tests considering distinct multiaxial stress states was conducted. Distinct monotonic fracture strains, pressure and deviatoric stress parameters were covered by means of distinct specimens design/testing configurations. In addition, the effect of thermal cycle applied in the elbows conformation was studied in the ULCF behaviour of the X60 and X65 piping steels. Also, the experimental data of a significant full-scale testing program was addressed, aiming at assessing the damage mechanisms of pipelines under extreme loading conditions combining the internal pressure with bending cyclic loading. Besides the experimental work, numerical simulations represented an essential part of this work. The numerical plasticity models of different materials were calibrated and validated by comparison with the experimental results. The stress/strain history was achieved at the critical locations which allowed identifying the damage models parameters. Finite element simulations were also conducted on full-scale tested elbows and straight pipes in order to reproduce numerical instabilities similar to the experimentally observed.

In the Chapter III the entire experimental program performed on small-scale specimens was described and the main conclusions are summarized as follows:

i. X65 piping steel presents a higher yield stress as also a higher ultimate tensile strength. X52 and X60 exhibit a similar ultimate tensile strength and X52 steel grade assumes the lowest yield stress value. X60 piping steel reveals higher ductility at fracture;
ii. Concerning the cyclic behaviour of the X60 piping steel, it exhibits an higher fatigue strength under both LCF and ULCF;
iii. The cyclic curves of the piping steels were obtained joining together the LCF and ULCF data. The cyclic curve suffered a stress softening when ULCF data is considered;

iv. The effect of thermal treatment on X60 and X65 was also investigated in the Chapter III and a reduction of mechanical strength was observed. In addition, the X60 and X65 piping steels with thermal process exhibits a pronounced yield plateau, typical of carbon steels, which was caused by the tempering treatment applied after the forming of the elbows;

v. The thermal effect does not promote significant modifications as regards the fatigue life and elastoplastic behaviour of X60 steel grade. However, for X65 steel grade an increase in the fatigue strength and a reduction in the cyclic yield stress was observed;

vi. Exiting standards for LCF are not applicable for ULCF loading since significant instabilities may occur during the cyclic loading. In order to minimize these instabilities an anti-buckling system was developed and adopted to perform the ULCF of smooth plane specimens. However, those anti-buckling devices are not fully effective. Therefore LVDT sensors were used to measure accurately the lateral displacements of the actuator in order to provide accurate boundary conditions for the numerical simulations of the tests;

vii. The use of the notched specimens may be considered an alternative to investigate the ULCF behaviour of materials since the notch presence promotes the strain concentration, which reduces the instability of the specimens. Nevertheless to address the non-linear stress/strain fields is required to perform numerical simulations;

viii. The monotonic fracture surfaces exhibits the classical characteristics of a monotonic ductile fractures, namely the fibrous appearance, the porosity and have larger necking regions and an overall rougher appearance. The fracture surfaces of ULCF tests show a similar aspect of the cyclic and ductile failures.

The numerical simulations of the experimental tests described in the Chapter III were presented in the Chapter IV. A new proposal for the imposition of the boundary conditions on smooth specimens as a function of the lateral instabilities was described. The numerical data extracted from numerical models was accounted in the assessment of the Coffin-Manson relation and Xue model. Thus, the main conclusions of this chapter will be presented:

i. The plasticity models with isotropic and kinematic hardening were calibrated for each pipe steel using a trial and error procedure, resulting a good compromise with monotonic and cyclic experimental results, respectively;

ii. The conventional stress-strain curves from monotonic tests of smooth specimens were determined until the damage onset for the three steels grades. The X60 piping steel exhibits a higher ductility and X52 and X65 shows a similar elongation until the failure;

iii. The thermal treatment leads to a significant modifications in the monotonic ductile behaviour of the X60 and X65 steel grades, reducing the ductility of the first one and increase the ductility of the last one;

iv. The small-scale geometries of X60 piping steel were concentrated on the identification of lower and upper boundary limits of the damage locus. Moreover, the results of notched plane specimens which provided intermediate values of Lode angle parameters were included in the 3D fracture surface a satisfactory agreement being found;

v. The boundary conditions applied on the smooth specimens were corrected considering the actuator lateral displacements in the cyclic simulations. This step results on the increasing of the equivalent plastic strain of smooth specimens. Based on these results and considering the numerical data of notched specimens the parameters of Coffin-Manson relation and Xue model were computed and fatigue life estimations for small-scale data were performed. In general, the model proposed by Xue that includes the effect of the fracture strain reports the best fatigue life predictions;

vi. A new preposition for the computation of fracture strain, which is dependent of pressure and deviatoric stress parameters, was proposed in the Chapter IV. On effect, updated fracture strains were computed from the 3D ductile surface of X60 piping steel and new life predictions were estimated. This indirect procedure will allow overcoming some limitations associated to the fracture strain computation, requiring reduced number of experimental tests associated to the ULCF life estimation and the Xue model can be applied in full-scale cases where the determination of the fracture strain shows some difficulties. This procedure may be indicated as new strain-based approach that can be used for design guidelines that includes the effect of both triaxiality and Lode angle parameter in the monotonic ductile as well as the ULCF failure. This

represents a step forward to the widely accepted Coffin-Manson classical relation.

vii. The fatigue strength reduces with the increasing of triaxiality and the decreasing of Lode angle parameter;

viii. The process for the fatigue life assessment under different stress/strain conditions presented in this work can be considered as a new methodology;

ix. A new approach based on the application of local boundary conditions directly obtained from DIC was proposed in this work. This procedure allowed to conclude that the effect of local boundary conditions is negligible regards the computation of equivalent plastic strain for the critical nodes;

x. The ULCF behaviour of X52 piping steel was also investigated by means of bending cyclic tests carried out on smooth plane, notched and flat-grooved specimens. Xue model allow to estimate the fatigue life of both notched and flat-grooved specimens considering the fracture strain derived from monotonic tensile tests and considering positive stress triaxiality levels and a lode angle parameter within the range $0 \leq \bar{\theta} \leq 1$.

Considering a strain based approach, the performance of the Theory of Critical Distances on LCF and ULCF life predictions was also assessed. The TCD was applied in the form of the Point method (PM), the Line method (LM) and the Area method (AM), leading to the computation of the effective elastic and plastic strain amplitudes. These data was correlated to the number of cycles of small-scale tests, including the smooth and notched geometries, in order to assess the parameters of the Morrow's relation. The main conclusions of this analysis are as follows:

i. The critical distances were found for each material and should be considered a material property;

ii. The computation of the critical distance was based on the maximization of the determination coefficient between the experimental results and the numerical results predicted by the Morrow relation. This critical distance was applied using the three methodologies and the best performance in terms of fatigue life estimation was obtained from AM;

iii. The X60 steel grade can be considered as the least sensitive to the TCD since assumes the lower values for the critical distance. On effect, satisfactory

fatigue life predictions were achieved for this material with the critical node approach;

iv. Also, bending cyclic tests of notched and flat-grooved specimens were included in this study. Different monotonic fracture strains, triaxialities and Lode angle parameters are covered by this set of specimens. The application of the TCD with the Morrow's multiaxial strain-life approach was not enough to address the diversity of fatigue data. Nevertheless the use of the TCD together with a good damage estimator can lead to improved predictions. It is expected that using the Xue model approach to account properly for both stress triaxiality and Lode angle parameters effect, predictions would result very satisfactory and improved with respect to the critical node approach.

In the Chapter VI the experimental program of full-scale tests performed on elbows and straight pipes was presented. The cyclic tests on elbows were performed by Department of Ferrous Metallurgy (RWTH Aachen University) and OCAS N.V. (Zwijnaarde, Belgium) carried out the bending cyclic test on straight pipes. The main remarks of this chapter are presented below:

i. ULCF failures on pipe components were always preceded by plastic instabilities;

ii. As regards the elbows tests, in general the buckle formation occurred at the central section of the elbows and the inner pressure is directly related with the shape of instability;

iii. For the lower values of nominal inner pressure a dent type shape was observed, and in contrast for the higher pressure values, the instability tends to assume a "bubble" shape towards the exterior of the pipe;

iv. Concerning the straight pipes the buckle occurred at two different locations, namely, next to the tubeholder (Test A and Test C) and at central section of the pipes (Test B and Test D). For the last tests, the plastic instabilities were intentionally introduced in the components by a thickness reduction;

v. The plastic instabilities assumes an important role for the plastic strain localization leading to the damage mechanism evolution and final failure of components;

Numerical simulations of full-scale tests were presented in the Chapter VII. The validation of the finite element models were performed establishing comparisons between load values, pipe ovalization, bending moment and numerical deformed shape mainly at the instability location. In addition, a fatigue assessment of these experimental tests was conducted using the classical Coffin-Manson relation, the Xue model and the ASME VIII-Div.2 procedures. The main conclusions of these procedures are as follows:

i. The finite element models of full-scale elbows were able to reproduce the plastic strain localization and consequent formed buckle. It was observed that the shape of the buckles (inward/outward) arises as function of the applied internal pressure and this result was confirmed by the numerical simulations;

ii. Two distinct locations for the buckle formation were observed for the straight pipes. For the Test A the instability occurred at the pipe center. The instability of the pipes of Test B and Test D was induced from a concentrated load;

iii. The identification of the critical location resulted from a compromise between the observations of the equivalent accumulated plastic strain, the triaxiality and Lode angle parameter fields and the failure location observed in the experimental tests;

iv. The Coffin-Manson relation produced satisfactory results for the fatigue lives performed for the full-scale tests;

v. The influence of the triaxiality and Lode angle parameter was accounted on the fatigue life estimations by means of Xue model. The triaxiality practically assumes a constant behaviour and in general, the Lode angle parameter tended to values around $\bar{\theta}$=0 for the final cycles after the buckle formation.

vi. The influence of both parameters was accounted indirectly in the fatigue life predictions of full-scale elbows and Test A and Test B considering the 3D ductile surface of X60 piping steel due to the lack of data for the X65 and X60TT and X65TT steels as regards the full ductile failure surface. The methodology proposed in the Chapter IV was directly applied for the Test D, since it consisted of X60 steel grade. The predictions using the Xue model were not always the best ones but the absence of an accurate ductile failure surface may justify such discrepancies. For the Test D the predictions using the Xue model were very accurate.

vii. ASME VIII-Div.2 procedures were applied to simulate the fatigue life of the straight pipes, considering two distinct approaches. The base S-N curve

formulation resulted on the best fatigue life predictions, in the safe side and very close to the experimental results. However, is S-N curves are cleared from safety margins, non-conservative predictions were obtained using the ASME procedures, being the wort predictions of the ones presented in the work.

8.2 PROPOSALS FOR FUTURE RESEARCH

Although comprehensive studies have been performed in the present thesis on the characterization of X52, X60 and X65 steels, under monotonic and ULCF loadings, the following topics are suggested for future studies.

i. Perform monotonic tensile tests on cylindrical specimens and flat-grooved specimens with different notch severities for X52 and X65 piping steels, in order to calibrate the 3D fracture locus of these materials. In addition, the same experimental program should be applied for the material subjected to a thermal treatment. The 3D monotonic ductile surface will be used on the validation of the methodology for the fatigue life assessment proposed in the Chapter IV;

ii. Testing additional shear specimens for different loading conditions combining tension and shear as well as compression and shear using distinct angle of loading. This task will consist on the identification of a 3D fracture locus for the X60 piping steel that should be compared to the one assessed in this work;

iii. Investigate the performance of others fatigue damage models presented in the literature on the fatigue life assessment;

iv. Concerning the numerical simulations, it is suggested to calibrate plasticity models with combined hardening aiming to describe the material softening during the cyclic loading. Afterwards, this plasticity models should be used on full-scale simulations investigating it influence on the buckles formation;

v. In accordance with the numerical data available from the full-scale tests it can be proposed the application of the TCD in order to compute an effective equivalent total range leading to new estimations based on this technique. The

TCD theory should also be extended to the Xue damage formulation in order to use the concepts of characteristic length to the strains at fracture.

vi. A parametric study on full-scale elbows and straight pipes could be conducted. In detail, different dimensions and loading conditions should be assumed in order to study the effect of these parameter on the fatigue behavior of this components.

vii. The ULCF studies should be extended also to welded joints and anisotropic piping materials since both aspects are important for large diameter line pipes.

viii. The investigation of the ULCF behaviour of the steels under combined torsion/tension-compression loading is also suggested, exploring the possibilities for non-proportional loading effects.